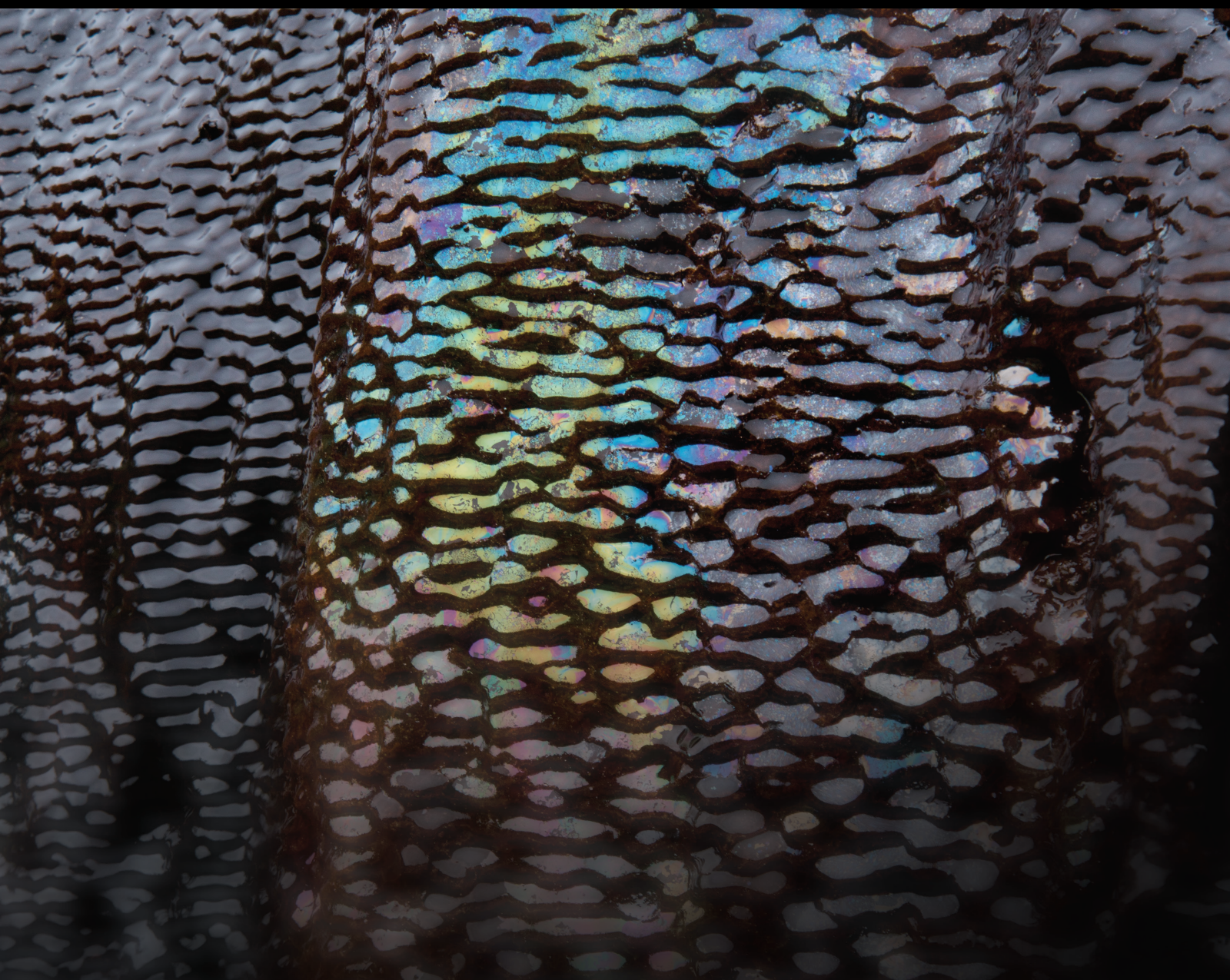


Hydro-Mechanical Behaviors of Rock Fractures and Fracture Networks

Lead Guest Editor: Richeng Liu

Guest Editors: Qian Yin and Bo Li





Hydro-Mechanical Behaviors of Rock Fractures and Fracture Networks

Geofluids

Hydro-Mechanical Behaviors of Rock Fractures and Fracture Networks

Lead Guest Editor: Richeng Liu

Guest Editors: Qian Yin and Bo Li







Copyright © 2020 Hindawi Limited. All rights reserved.

This is a special issue published in "Geofluids." All articles are open access articles distributed under the Creative Commons Attribution License, which permits unrestricted use, distribution, and reproduction in any medium, provided the original work is properly cited.





























Chief Editor

































Umberta Tinivella, Italy

Associate Editors

Paolo Fulignati , Italy
Huazhou Li , Canada
Stefano Lo Russo , Italy
Julie K. Pearce , Australia

Academic Editors

Basim Abu-Jdayil , United Arab Emirates
Hasan Alsaedi , USA
Carmine Apollaro , Italy
Baojun Bai, USA
Marino Domenico Barberio , Italy
Andrea Brogi , Italy
Shengnan Nancy Chen , Canada
Tao Chen , Germany
Jianwei Cheng , China
Paola Cianfarra , Italy
Daniele Cinti , Italy
Timothy S. Collett , USA
Nicoló Colombani , Italy
Mercè Corbella , Spain
David Cruset, Spain
Jun Dong , China
Henrik Drake , Sweden
Farhad Ehya , Iran
Lionel Esteban , Australia
Zhiqiang Fan , China
Francesco Frondini, Italy
Ilaria Fuoco, Italy
Paola Gattinoni , Italy
Amin Gholami , Iran
Michela Giustiniani, Italy
Naser Golsanami, China
Fausto Grassa , Italy
Jianyong Han , China
Chris Harris , South Africa
Liang He , China
Sampath Hewage , Sri Lanka
Jian Hou, China
Guozhong Hu , China
Lanxiao Hu , China
Francesco Italiano , Italy
Azizollah Khormali , Iran
Hailing Kong, China

Karsten Kroeger, New Zealand
Cornelius Langenbruch, USA
Peter Leary , USA
Guangquan Li , China
Qingchao Li , China
Qibin Lin , China
Marcello Liotta , Italy
Shuyang Liu , China
Yong Liu, China
Yueliang Liu , China
Constantinos Loupasakis , Greece
Shouqing Lu, China
Tian-Shou Ma, China
Judit Mádl-Szonyi, Hungary
Paolo Madonia , Italy
Fabien Magri , Germany
Micòl Mastroicco , Italy
Agnes Mazot , New Zealand
Yuan Mei , Australia
Evgeniy M. Myshakin , USA
Muhammad Tayyab Naseer, Pakistan
Michele Paternoster , Italy
Mandadige S. A. Perera, Australia
Marco Petitta , Italy
Chao-Zhong Qin, China
Qingdong Qu, Australia
Reza Rezaee , Australia
Eliahu Rosenthal , Israel
Gernot Rother, USA
Edgar Santoyo , Mexico
Mohammad Sarmadivaleh, Australia
Venkatramanan Senapathi , India
Amin Shokrollahi, Australia
Rosa Sinisi , Italy
Zhao-Jie Song , China
Ondra Sracek , Czech Republic
Andri Stefansson , Iceland
Bailu Teng , China
Tivadar M. Tóth , Hungary
Orlando Vaselli , Italy
Benfeng Wang , China
Hetang Wang , China
Wensong Wang , China
Zhiyuan Wang , China
Ruud Weijermars , Saudi Arabia




Bisheng Wu , China
Da-yang Xuan , China
Yi Xue , China
HE YONGLIANG, China
Fan Yang , China
Zhenyuan Yin , China
Sohrab Zendeboudi, Canada
Zhixiong Zeng , Hong Kong
Yuanyuan Zha , China
Keni Zhang, China
Mingjie Zhang , China
Rongqing Zhang, China
Xianwei Zhang , China
Ye Zhang , USA
Zetian Zhang , China
Ling-Li Zhou , Ireland
Yingfang Zhou , United Kingdom
Daoyi Zhu , China
Quanle Zou, China
Martina Zucchi, Italy

Contents


The Influential Factors and Characteristics of Tight Sandstone Gas Reservoir: A Case Study in Ordos Basin in China

Dazhong Ren , Fu Yang, Rongxi Li, Yuhong Li, and Dengke Liu 
Research Article (11 pages), Article ID 6690043, Volume 2020 (2020)



Modeling and Simulation of Deformation Mechanism of Soft Rock Roadway considering the Mine Water

Yanlong Chen , Qiang Li, Hai Pu, Peng Wu , Liang Chen, Deyu Qian, Xuyang Shi , Kai Zhang, and Xianbiao Mao
Research Article (22 pages), Article ID 8812470, Volume 2020 (2020)


Investigation on Nonlinear Flow Behavior through Rock Rough Fractures Based on Experiments and Proposed 3-Dimensional Numerical Simulation

Xianshan Liu , Man Li, Nandou Zeng, and Tao Li
Research Article (34 pages), Article ID 8818749, Volume 2020 (2020)

Effect of Sea-Level Change on Deep-Sea Sedimentary Records in the Northeastern South China Sea over the past 42 kyr

Bin Wang , Huaiyan Lei , Fanfan Huang, Yuan Kong, Fulong Pan, Weidong Cheng, Yong Chen, and Limei Guo
Research Article (17 pages), Article ID 8814545, Volume 2020 (2020)


Numerical Simulation of Cracking Behavior of Precracked Rock under Mechanical-Hydraulic Loading

Zhong Zhang, Chun-Chi Ma , Tianbin Li, Tao Song, and Huilin Xing
Research Article (14 pages), Article ID 8852572, Volume 2020 (2020)

Equivalent Permeability Distribution for Fractured Porous Rocks: Correlating Fracture Aperture and Length

Tao Chen 
Research Article (12 pages), Article ID 8834666, Volume 2020 (2020)

Stability Monitoring and Analysis of High and Steep Slope of a Hydropower Station

Guangcheng Shi, Gongkai Gu, Hua Zhou, Zhigang Tao , Hongyue Pan, and Ting Tang
Review Article (16 pages), Article ID 8840269, Volume 2020 (2020)


Failure Behavior of Hot-Dry-Rock (HDR) in Enhanced Geothermal Systems: Macro to Micro Scale Effects

Hongwei Zhang , Zhijun Wan , and Derek Elsworth 
Research Article (13 pages), Article ID 8878179, Volume 2020 (2020)

Experimental Investigation on the Stress-Dependent Permeability of Intact and Fractured Shale




Yongxiang Zheng , Jianjun Liu , Yichen Liu, Di Shi, and Bohu Zhang
Research Article (16 pages), Article ID 8897911, Volume 2020 (2020)

Scale Dependence of Waviness and Unevenness of Natural Rock Joints through Fractal Analysis

Yingchun Li , Shengyue Sun, and Hongwei Yang

Research Article (18 pages), Article ID 8818815, Volume 2020 (2020)

A New Decision Method of Filling Ratio Based on Energy Matching of Surrounding Rock and Backfill

Yanlong Zhou , Keping Zhou , and Yun Lin 



Research Article (7 pages), Article ID 8856537, Volume 2020 (2020)

Numerical Simulation on Heat Transfer Characteristics of Water Flowing through the Fracture of High-Temperature Rock

Xiaohu Zhang, Zhaolun Wang, Yanhua Sun, Chun Zhu, Feng Xiong, and Qiongqiong Tang 





Research Article (14 pages), Article ID 8864028, Volume 2020 (2020)

Model Experimental Study on the Seepage and Failure Features of Tunnel under Wetting-Drying Alternation with Increasing Water Pressure

Haijian Su , Yujie Feng, Qingzhen Guo, Hongwen Jing , and Wenxin Zhu

Research Article (11 pages), Article ID 8845528, Volume 2020 (2020)

Visualization of Gas Diffusion-Sorption in Coal: A Study Based on Synchrotron Radiation Nano-CT

Yingfeng Sun , Yixin Zhao , Hongwei Zhang , and Cun Zhang 


Research Article (11 pages), Article ID 8835848, Volume 2020 (2020)

Numerical Simulation on Non-Darcy Flow in a Single Rock Fracture Domain Inverted by Digital Images

Jianli Shao , Qi Zhang , Wenbin Sun , Zaiyong Wang, and Xianxiang Zhu 

Research Article (13 pages), Article ID 8814327, Volume 2020 (2020)

Permeability Experiment of Fractured Rock with Rough Surfaces under Different Stress Conditions

Zilong Zhou, Jing Zhang, Xin Cai , Shanyong Wang, Xueming Du, and Haizhi Zang

Research Article (15 pages), Article ID 9030484, Volume 2020 (2020)

Research Article

The Influential Factors and Characteristics of Tight Sandstone Gas Reservoir: A Case Study in Ordos Basin in China

Dazhong Ren ^{1,2,3,4}, Fu Yang,² Rongxi Li,³ Yuhong Li,¹ and Dengke Liu ^{2,5}

¹*Xi'an Geological Survey Center, China Geological Survey, Xi'an 710054, China*

²*Key Laboratory of Coal Resources Exploration and Comprehensive Utilization Ministry of Land and Resources, Xi'an, Shaanxi 710021, China*

³*School of Earth Science and Resources, Chang'an University, Xi'an 710054, China*

⁴*Shaanxi Key Laboratory of Advanced Stimulation Technology for Oil&Gas Reservoirs, College of Petroleum Engineering, Xi'an Shiyou University, Xi'an 710021, China*

⁵*School of Human Settlements and Civil Engineering, Xi'an Jiaotong University, Xi'an 710054, China*

Correspondence should be addressed to Dazhong Ren; petro_gas@163.com

Received 2 December 2020; Accepted 10 December 2020; Published 29 December 2020

Academic Editor: Qian Yin

Copyright © 2020 Dazhong Ren et al. This is an open access article distributed under the Creative Commons Attribution License, which permits unrestricted use, distribution, and reproduction in any medium, provided the original work is properly cited.

To analyze the impact of the factors on physical properties and the mechanism of tightness as well as favorable accumulation space of tight sandstone reservoir, comprehensive analysis is conducted using various kinds of experiments. The results show that the predominant rock type is medium-coarse grained lithic quartzarenite, and the main accumulating space is the dissolved secondary pores. Reservoir pore-throat structures can be divided into four categories. Based on morphologies and parameters which derived from capillary pressure curves, the physical properties rank in the following descending sequence: Type I > Type II > Type III > Type IV. The reservoir quality is influenced by both sedimentation and diagenesis synthetically. The underwater distributary channel is the dominant space for favorable reservoir. Compaction and cementation play dominant roles in the reduction of permeability. The loss of primary pores caused by both those diagenesis are 20.52% and 16.91%, respectively. Secondary pores formed by dissolution improve the reservoir quality by increase the porosity (2.68%). This suggests that weak diagenesis greatly contributes to the improvement of reservoir quality.

1. Introduction

Tight sandstone is a heterogeneous porous media with tiny pore body and narrow pore throat [1–6]. The physical properties, sedimentary characteristics, and pore structures of tight sandstone influence their storage, migration, and transport properties. Therefore, understanding the basic information and microscopic features of the tight sandstone is the basis of figuring out the percolation mechanisms, development capabilities, and hydrocarbon occurrence states of the reservoirs [7–10]. Although lots of literature focus on those properties, the study on tight sandstone still is not enough when compared to conventional reservoirs [11–14]. Therefore, it is of great significance to study the influential factors and characteristics of the tight sandstone reservoirs.

The physical properties of tight sandstone are very complicated due to the heterogeneously distributed grains and pore network, and the mechanism of tightness is dependent on those properties [15, 16]. Numerous studies on those properties and abundant methods have been applied, and the results show that large pores dominate the pore storage while tiny pores control the percolation ability [17–19]. When it comes to favorable accumulation space of tight sandstone reservoir, currently, various techniques including observations and quantitative determination are adopted [20, 21]. Apart from direct observation and indirect testing methods, some calculation algorithms, such as fractal theory, are applied to describe the microscopic features of tight sandstone [3, 22]. Hence, the study on the pore structures, sedimentary features, and morphological characteristics of tight sandstone plays a key role in governing the favorable

accumulation spaces. Thus, we picked a typical area in the Ordos basin to achieve our goals.

This paper aims to study the microscopic characteristics of tight sandstone of Shan-2 Member. We analyzed the influential factors of physical properties, the mechanism of tightness, and favorable accumulation space of tight sandstone reservoir by various kinds of tests, such as casting thin slices (CTS), scanning electron microscope (SEM), cathodoluminescence (CL), X-ray diffraction (XRD), high-pressure mercury intrusion (HPMI), physical property testing, core testing, and well logging.

2. Methodology

2.1. Geological Setting. Yanchang Oil and Gas Field, mainly located in Yanan City, Shaanxi Province (China), i.e., in the southeastern part of Shaanbei Slope of Ordos Basin (Figures 1(a) and 1(b)), covers $1.7 \times 10^4 \text{ km}^2$ and has small basement undulations. The depositional caprock has a gentle slope with no obvious anticlines, where nose-like structure develops [23–25]. With the successful gas testing in many wells in Nanniwan, Ganyegu, Qili, and Wangjiachuan in recent years, natural gas exploration shows good prospects in the Yanchang Oilfield which has took a position as the large-scale gas field. Sedimentary facies of the Shan-2 Member, the main gas production layer in the research area, is mainly braided river delta front underwater distributary channel sand body (Figure 1(c)) [26, 27]. It has poor physical properties and is a typical low porosity and low permeability tight sandstone reservoir, where the gas accumulation zone is mainly controlled by sedimentation and diagenesis [27].

2.2. Observation Methods. The CTS and SEM methods were applied for direct observation. Before CTS observation, the samples were milled to produce flat surfaces, and the rock slices were stuck in the middle. Prior to the SEM, all samples were mechanically ground, polished, and coated with carbon. ZEISS MERLIN 6174 apparatus were used for observation.

2.3. XRD. A BRUKER D8 ADVANCE X-ray diffractometer was employed for XRD measurements. The samples were crushed to the size of 80 mesh and tested at 40 kV voltage and 30 mA.

2.4. HPMI. The capillary pressure curves were determined using the mercury intrusion method on a Micromeritics Autopore IV 9400 apparatus. Prior to the tests, the samples were dried in an oven, evacuated at vacuum, and tested at the pressure of 1–200 MPa, the interfacial tension of mercury/air of 0.485 N/m, and the wetting angle of Hg of 140° . The calculation methods were derived from the Washburn equation and the results from Purcell [28, 29].

3. Result and Discussion

3.1. Petrographic Characteristics. According to core observation and the quantitative statistics of 107 sandstone slices, Shan-2 Member is mainly lithic quartzarenite and quartzarenite with medium-coarse grains (Figure 2). The average volume fraction of terrigenous clastic is 86.2%, including 75.32%

quartz, 1.94% feldspar, and 18.81% debris. The debris contains 17.62% metamorphic, 4.37% volcanic debris, and 1.28% mica.

Detrital particles have good sorting performance and low roundness and mainly contain subrounded and subangular. The particles are mainly in long contact. Cementation is mainly porous and increased porous cementation, showing that sandstone has high compositional maturity and low textural maturity in the Shan-2 Member.

The interstitial material in the Shan-2 Member has average volumetric coefficient of 14.07% and mainly consists of siliceous, kaolinite, illite, and I/S mixed layer and carbonate with the average volume coefficient of 5.81%, 2.9%, 1.72%, and 2.6%, respectively.

3.2. Physical Properties of the Reservoir. The analysis results of 159 samples from 47 wells in the research area show that the samples have the porosity between 5.0%–12.0% and 7.22% on average and permeability mainly between $0.1 \sim 250 \times 10^{-3} \mu\text{m}^2$ and $15.69 \times 10^{-3} \mu\text{m}^2$ on average. The porosity is obviously positive related to the permeability (Figure 3), suggesting that the permeability is mainly controlled by void spaces, while the physical properties and gas content are controlled by the development of pores [30–32].

3.3. Pore Development Characteristics of the Reservoir. The observations of 107 sandstone CTS under a microscope and the results from SEM and CL show that the sandstone in the Shan-2 Member provides the surface porosity of 5.57% and has about 38.82% residual primary intergranular pores, about 28.17% intergranular solution pores, about 24.25% intragranular solution pores, 8.26% intercrystalline pores, about 0.5% microfractures, etc. (Figure 4).

3.3.1. Primary Intergranular Pores. Three types of primary intergranular pores develop in this area: (1) primary intergranular pores remained after the particles are covered by chlorite lining, (2) primary intergranular pores remained after the quartz secondary overgrowth or microcrystalline calcite cement formation in the early diagenetic stage, and (3) primary pores remained after the pseudomatrix is filled in the pores formed by the deformation of plastic particles such as biotite, phyllite, and siltstone fragments. These pores have too small diameters to be identified under ordinary microscopes. Primary intergranular pores of the sandstone in the target zone are mainly fracture interstitial pores filled by quartz secondary overgrowth (Figure 4(a)).

3.3.2. Secondary Pores. Secondary pore is the dominant type developing in the upper Paleozoic sandstone reservoir in the research area. The pores are transformed by late diagenesis, such as pores formed due to dissolution, metasomatism, and cementation. Dissolved components are detrital particles, matrix, cements, and authigenic metasomatic minerals, including intergranular dissolution pores and intragranular dissolution pores (Figure 4(b)):

- (1) Intergranular dissolution pores: there are developed by the dissolution of interstitial particles. They have obvious corrosion traces at the edge of grains and

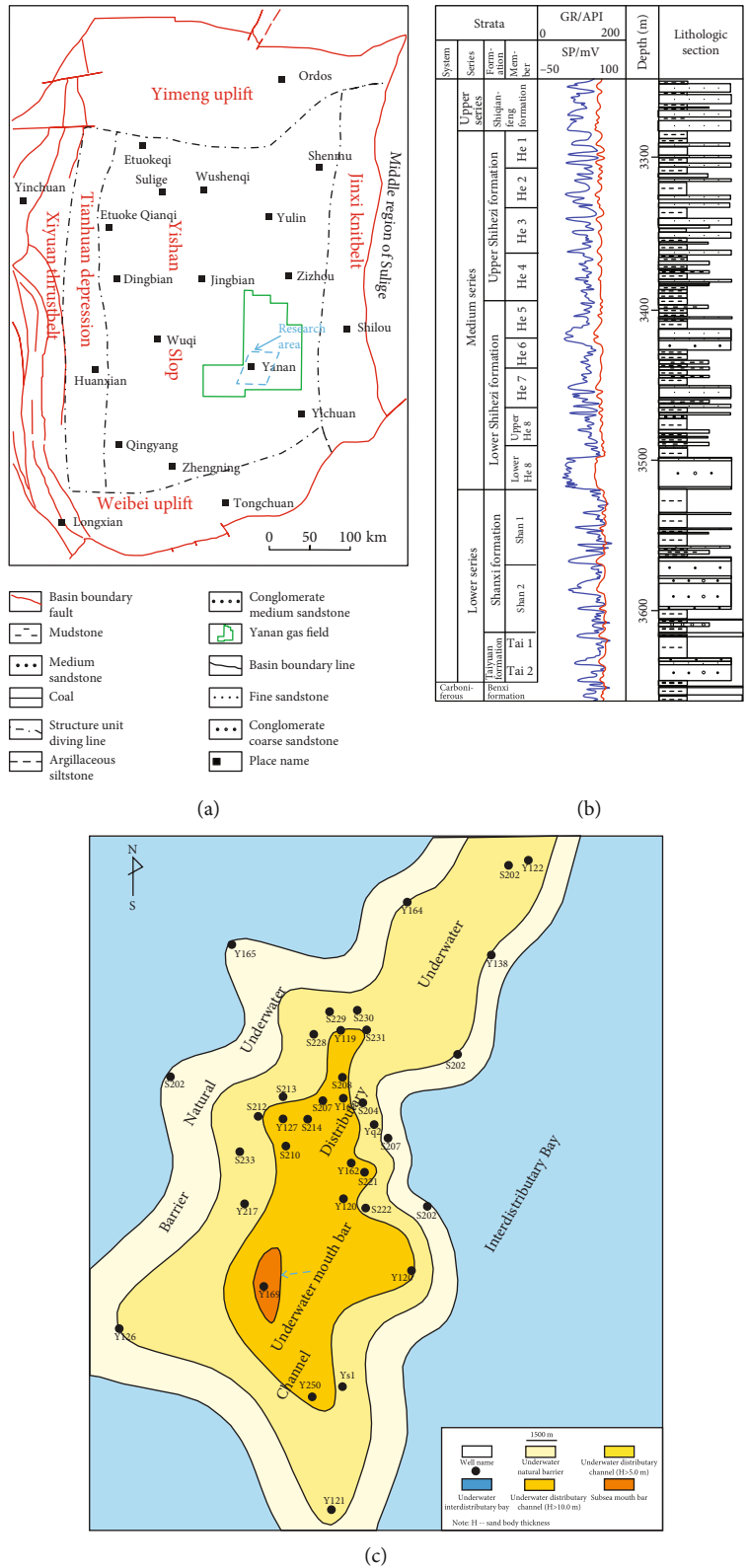


FIGURE 1: (a) Location of the research area. (b) Well logs of the Shanxi Formation. (c) Sedimentary characteristics of the research area (modified from [26, 27]).

mainly distribute in sandstone. The edges are rough and like a bay, long strip, and hemisphere. Solution pores are usually irregular, with the size

between $5\ \mu\text{m}$ and $50\ \mu\text{m}$, associated with feldspar, rock debris, etc., and connected by fine dissolved joints

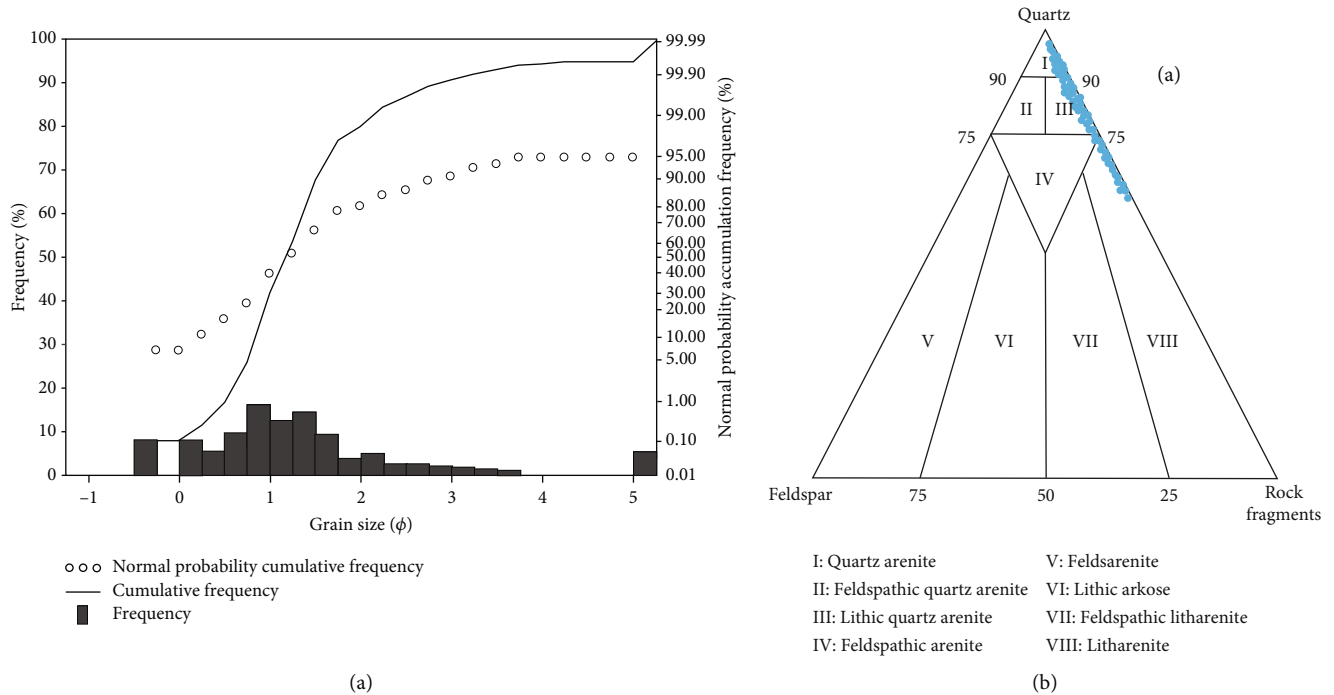


FIGURE 2: Grain size distribution and rock classification of Shan-2 Member in the Shanxi Formation.

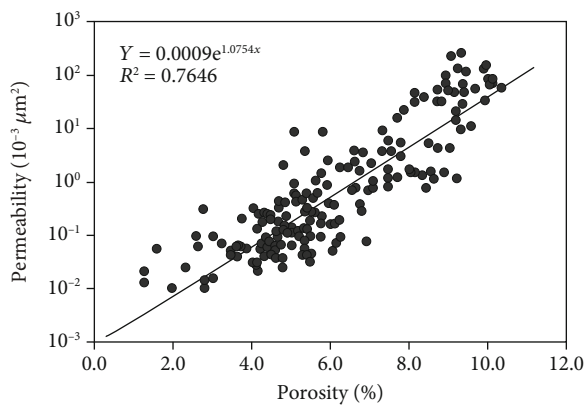


FIGURE 3: Relationship between porosity and permeability of Shan-2 Member of the Shanxi Formation in the research area.

- (2) Intragranular dissolution pores: feldspar is generally subjected to dissolution under the acidic diagenetic condition. Honeycomb-like intragranular solution pores develop following the dissolution of feldspar granules and matrix in volcanic rock fragments. Phyllite, biotite, and other pseudomatrix are dissolved to form intragranular micropores

3.3.3. Intercrystalline Micropores. The interstitial material pores, which can be identified through CTS, and the kaolinite intercrystalline micropores, which have good crystallinity and pore size of higher than $3.0 \mu\text{m}$, are the main types (Figure 4(c)). Such pores, which mainly distribute in the intergranular pores and secondary dissolution pores of feld-

spars and debris, are commonly seen in sandstone in each layer in the research area. The pores have nonuniform sizes, which are dominated by crystal sizes and packing degree, and distribute nonuniformly. Kaolinite crystals formed by rock fragment alteration are so poorly crystallized that kaolinite crystal accounts for less than 10% of kaolinite and has the pore diameter of less than $2.0 \mu\text{m}$.

3.3.4. Microfractures. The observations of CTS and SEM show that the microfracture pores in the research area are not developed very well and thereby classified into intergranular joints and rock fractures. Rock fractures are so narrow as to penetrate plastic debris and matrix (Figure 4(d)). Although rock fractures distribute much less common than intergranular joints, they provide the pathways for large-scale fluid migration, creating the potential conditions for generation of dissolved secondary pores [11, 32–34].

3.4. Pore Structure Characteristics. According to the analysis of thin slices and mercury intrusion experiment, the pores in the Shan-2 Member include 38.16% fine pores ($1.0 \mu\text{m} < r < 10 \mu\text{m}$), 25.75% small pores ($10 \mu\text{m} < r < 50$), 22.81% medium pores ($50 \mu\text{m} < r < 100$), and 8.61% micro pores ($r < 1.0 \mu\text{m}$). Throat types are mainly microthroat ($0.1 \mu\text{m} < r < 1.0 \mu\text{m}$), accounting for 65.22% of the total throat, followed by sorption throat ($r < 0.1 \mu\text{m}$), accounting for 25.47% of the statistics; fine throat ($1.0 \mu\text{m} < r < 2.0 \mu\text{m}$) only takes up 7.78% of the total throat; other throats of which radius is higher than $2.0 \mu\text{m}$ are throat or fractures formed by strong dissolution, and this throat takes only a small percentage of the total throat amount ($< 5.0\%$). Plateau of the mercury intrusion curve is not obvious, and a steep slope is

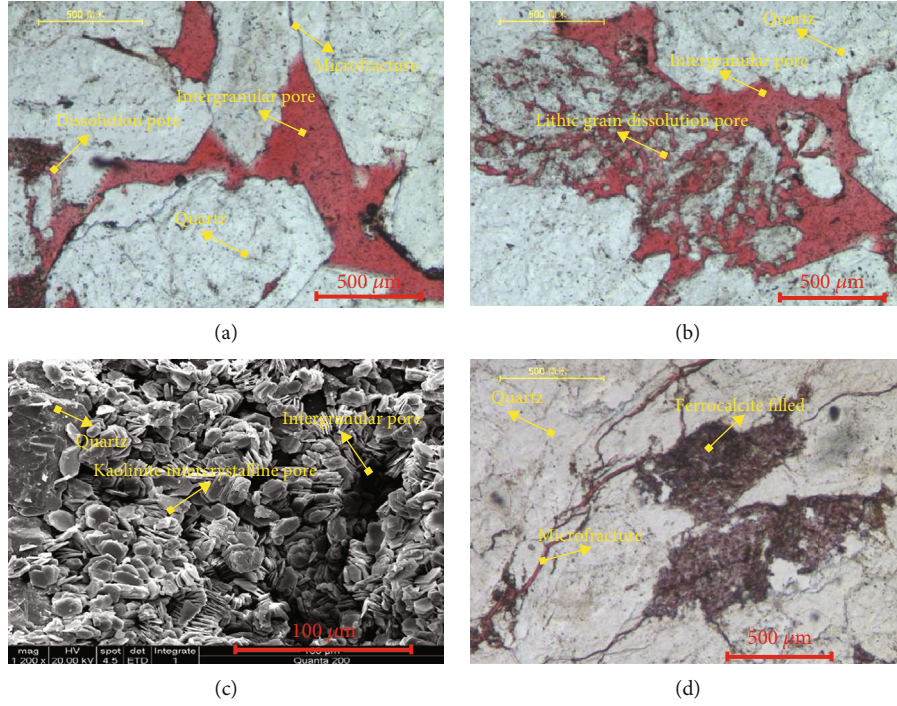


FIGURE 4: Micropore structure of the samples in the research area. (a) Well Y169, 2763.47 m, CTS. (b) Well Y120, 2677.41 m, CTS. (c) Well Y123, 2587.62 m, SEM. (d) Well Y162, 2727.26 m, CTS.

TABLE 1: Mercury-injection data of the Shan-2 Member of the Shanxi Formation in the research area.

Type	Φ , %	K , $10^{-3} \mu\text{m}^2$	P_d , MPa	P_{50} , MPa	r_{50} , μm	S_{Hgmax} , %	P_C	SN
I	>6.0	>1.0	<0.5	<1.5	>0.5	>80.0	IP, DP-IP	7
II	5.0~9.0	0.1~2.0	0.5~1.5	2.0~10	0.1~0.5	70~90	DP-IP, IP-DP	24
III	4.0~7.5	0.1~0.5	1.0~10.0	15~30	0.05~0.1	50~80	DP, MP-DP	30
IV	<6.0	/	/	/	/	<50.0	MF, DP-MF	9

Φ : porosity; K : permeability; P_d : displacement pressure; P_{50} : medium pressure; r_{50} : medium radius; S_{Hgmax} : maximum mercury saturation; P_C : pore combination; SN: sample number; IP: intergranular pore; DP: dissolution pore; MP: micropore; MF: microcrack.

shown, indicating poor pore throat sorting and strong pore structure microscopic heterogeneity. According to capillary pressure curves of the reservoir, pore throats can be divided into the following four types: type I (medium-small pore and fine-microthroat); type II (small-fine pore and microthroat); type III (fine pore and micro sorption throat); and type IV (fine-micropore and fine-microthroat) (Table 1, Figure 5).

3.5. Analysis of Influencing Factors of Reservoir Characteristics. The pores in the Shan-2 Member have a complicated structure and strong microscopic heterogeneity. This gas reservoir has low porosity and ultra-low permeability, and its characteristics are mainly controlled by sedimentation and diagenesis.

3.5.1. Sedimentation. Sedimentation plays an important role in reservoir development and properties [35]. Sedimentary microfacies, such as subaqueous distributary channel, chan-

nel mouth bar, subaqueous levee, and subaqueous interdistributary bay develop in the Shan-2 Member, which is formed by delta front subfacies sedimentation. As the favorable zone in the research area, the subaqueous distributary channel has strong hydrodynamic force and good sorting performance, contains relatively small amount of clay and matrix, and shows high compositional maturity and relatively high porosity and permeability, so it becomes a good accumulation space. For other sedimentary facies, however, its porosity and permeability decrease drastically under compaction and cementation due to weak hydrodynamic force and the high content of interstitial substances, such as fine particles and matrix (Figures 6 and 7).

It is found that the size of terrigenous debris that makes up the sandstone determines the intergranular pore size. Generally, larger pores often exist in coarse sandstone, while smaller pore often exists in smaller sandstone. Therefore, the sandstone with bigger grain size has the higher porosity and permeability (Figure 7). Thus, it is concluded that high-

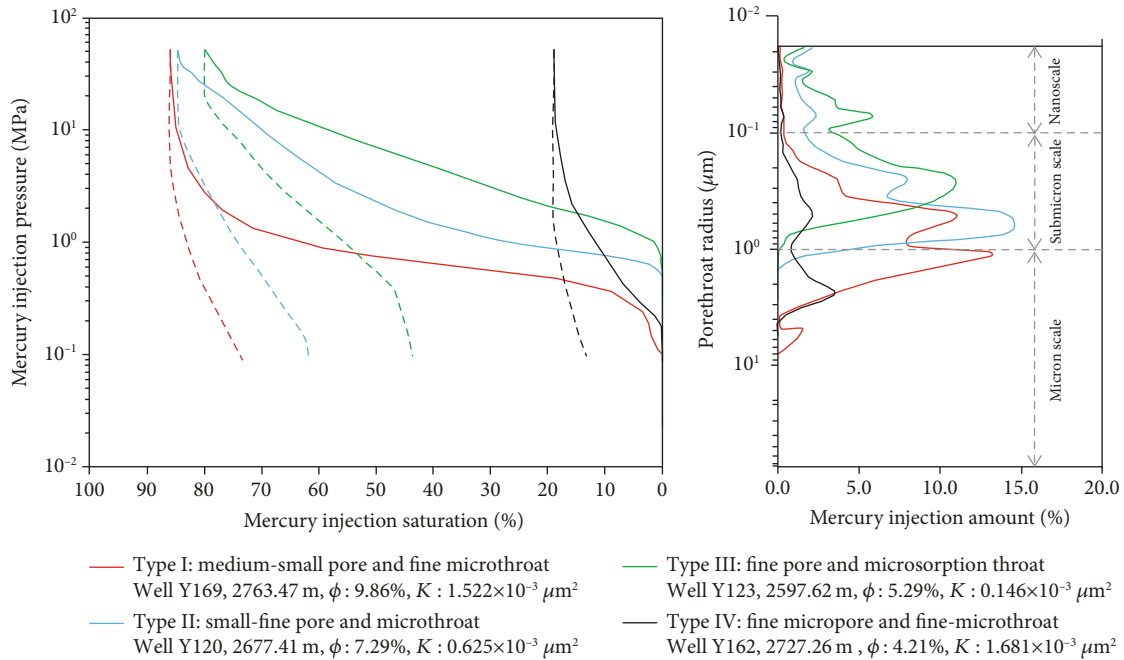


FIGURE 5: Characteristics of mercury intrusion curves and pore structure of samples in the research area.

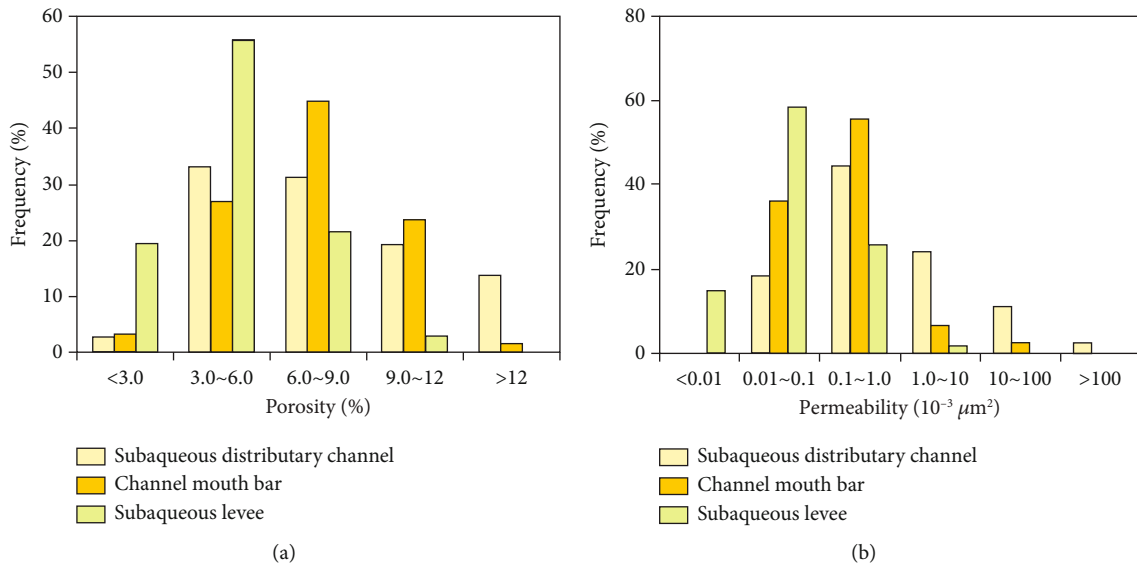


FIGURE 6: Distribution of porosity and permeability of different sedimentary microfacies.

quality reservoirs often develop in sandstone with good roundness and sorting performance and big grain size. This is because primary pores develop in the rocks with coarse grains (coarse and fine sandstone), good sorting performance, and low matrix content. The acidic fluid easily permeates into the rock and the dissolution pervades the reservoir, resulting in good physical properties [34, 36, 37]. Comprehensive research shows that the grains with good physical properties are generally fine or above in the reservoirs.

3.5.2. Diagenesis

(1) *Effects of Compaction and Pressure Solution on Reservoir Porosity.* The deeply buried quartz in the Shan-2 Member undergoes brittle fracture due to formation stress (Figure 8(a)). Flexible detrital particles (such as mica and argillaceous debris) are bent and orientated or semiorientated due to compaction and pseudomatrixization. It is commonly seen that grains show long contact due to quartz secondary overgrowth. Concave-convex or suture contact is also observed.

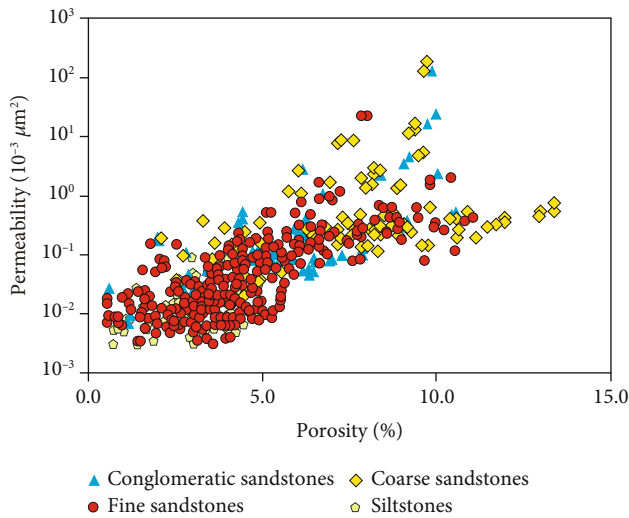


FIGURE 7: Relationship between porosity and permeability of different sandstone types.

These phenomena indicate that the sandstone in this area has undergone strong compaction and pressure solution. The compaction rate could quantitatively indicate the compaction degree (Table 2) [38, 39]. Primary porosity is set between 33.5 and 39.7%, 35.8% on average, and the calculated compaction rate of sandstone in the Shan-2 Member is 36.5~76.2%, 53.45% on average. The loss of primary porosity is 20.52% due to compaction.

(2) *Effects of Cementation on Reservoir.* Clay mineral cementation, siliceous cementation, and carbonate cementation are commonly seen in the research area. Illite and I/M mixed layers widely develop in the sandstone with the high rock fragment content and distribute in the intergranular pores in the forms of fine scaly, colloid, or locular aggregates. Under SEM, the I/M mixed layer unit is like bent flake, and the aggregate is honeycomb-shaped and has a spike-like protrusion. Illite is irregular, fibrous, acicular, and hair-like (Figure 8(b)). The I/M mixed layer in the research area is the intermediate product of the transformation of montmorillonite to illite and is dominated by the illite-rich layer in its late evolution stage. Clay minerals of the I/M mixed layer barely results in the loss of primary intergranular pores, but greatly influences the permeability due to the fact that the bridged coil-like and silk-like crystals clog the throats [41, 42]. Chlorite, which is rarely seen in Shan-2 sandstone, shows thin film or pore-filling form (Figure 8(c)).

Kaolinite, which widely develops in the reservoir, can be divided into two types according to particle morphology, crystallinity, etc. [43, 44]: one forms in the early stage of diagenesis, has imperfect crystal shape, distributes on the worm-like or scattered flaky particle surfaces, develops by the dissolution of feldspar in acidic water, and mainly fills the pores; intergranular pores do not develop, and irregular dissolved edges develop locally (Figure 8(d)). The other one forms in

the late stage of diagenesis and has relatively good crystal shape, and its single crystal is pseudohexagonal. It is precipitated directly from pore solution or evolved from the earlier kaolinite with small crystal. The aggregation is loosely packed in book-like form in intergranular pores or feldspar secondary pores. Intergranular pores are well develop (Figure 8(d)). On one hand, the intergranular authigenic kaolinite forms a large amount of intercrystalline micropores. On the other hand, it also increases the pressure resistance of sandstone [45].

Authigenic siliceous cements, which are common in the research area, are mainly in the form of quartz overgrowth. The observation under the CTS and the cathodoluminescent slice shows most of quartz crystals that exhibit secondary overgrowth, which belongs to grades II to III. The quartz secondary overgrowth edges are separated from the detrital quartz by a very thin clay film. Its authigenic crystal surfaces develop well. The enlarged quartz is mutually fitted or tightly mosaic in concave-convex contact and mostly grows in the pore-filling form in the pore walls or in solution pores of feldspar (Figures 8(a), 8(d), and 8(e)). Although the secondary quartz overgrowth partially inhibits the compaction, the pores are blocked due to authigenic rock overgrowth along the pore space with diagenesis (Figures 8(a), 8(d), and 8(e)). Thus, the porosity and permeability of the reservoir decrease [46].

Carbonate cements are very common in sandstone in the Shan-2 Member and mainly occur as intergranular cements, metasomatic materials, or fillings in the secondary pores. They always show a fine-medium crystalline structure or sometimes muddy structure and mainly contain calcite, iron calcite (the main components), iron dolomite, and siderite. (Iron) calcite cements in the research area can be divided into two phases, early phase and late phase. The late phase is abundant. Early calcite cements are mainly microcrystalline calcite itself or the mixture with clay minerals filled in the particles (Figure 8(f)); late calcite cements are mainly iron calcite with coarse grains in the anhedral shape. It distributes irregularly among the debris particles mainly in long or concave-convex contact. Partial precipitation of calcite formed in late phase takes place after dissolution (Figures 8(f) and 8(g)). Transformation from early precipitation to dissolution and to late precipitation reflects that the pore water properties change from alkaline to acidic and then back to alkaline [46].

Carbonate minerals are major cements that reduce the sandstone properties and play a dual effect on the reservoirs. One effect is that carbonates formed in the early stage of diagenesis strengthen the sandstone's pressure resistance and protect some of the residual intergranular pores [47]. The other effect is that authigenic carbonates mainly form in the form of precipitate in the intergranular pore walls and intra-granular solution pores and thereby reduce the porosity and the accumulation properties of the reservoir (Figure 9). It is calculated by cementation rate formula (Table 2) [38, 39, 48]. The analysis of precipitate content of various cements shows that the cementation rate of sandstone in the Shan-2 Member is 9.0~63.5%, 44.42% on average, and the porosity loss is 16.91%.

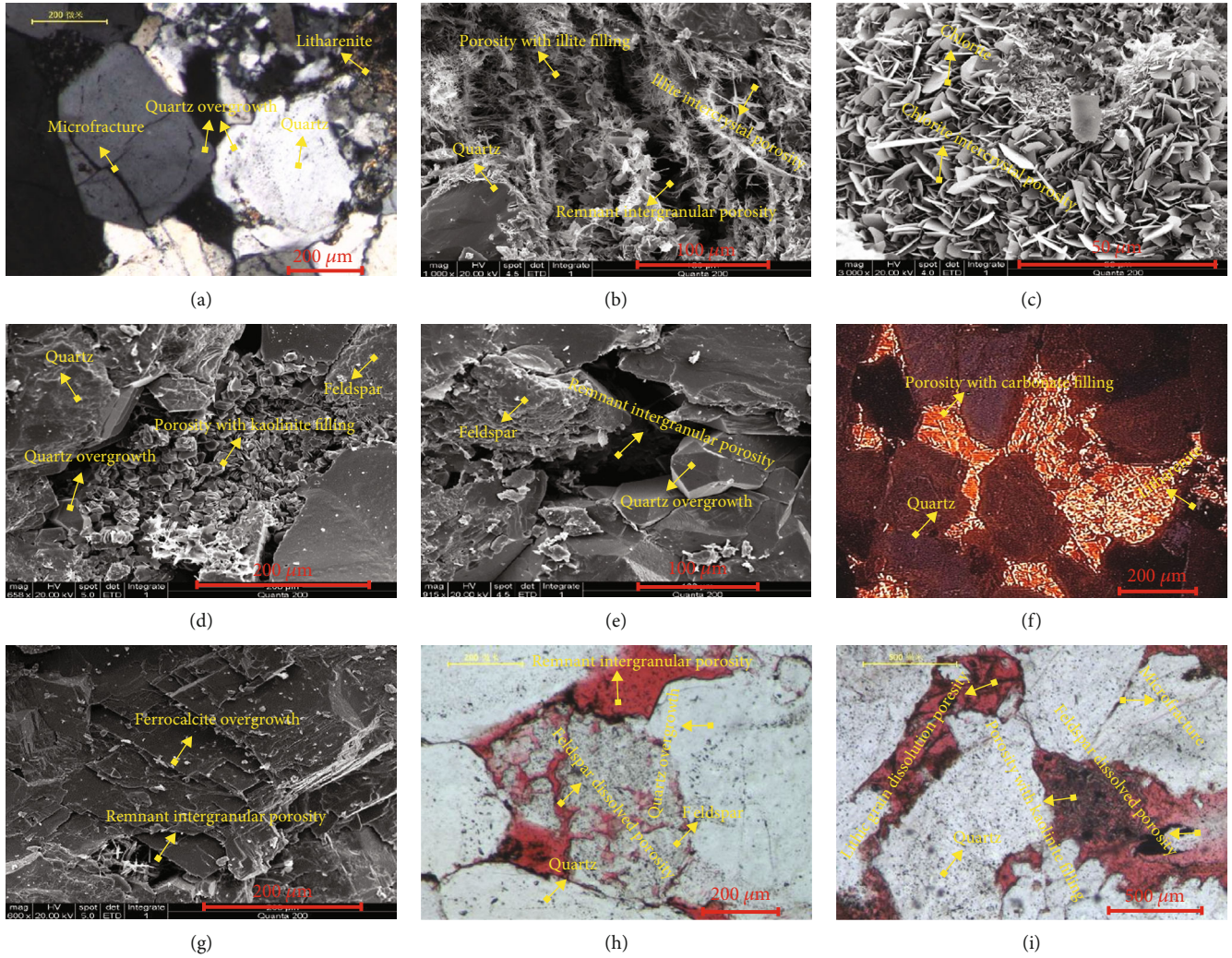


FIGURE 8: Microscope features of diagenesis of samples in the research area. (a) Well Y169, 2629.70 m, CTS. (b) Well Y168, 2513.97 m, SEM. (c) Well Y120, 2560.29 m, SEM. (d) Well Y126, 2718.98 m, SEM. (e) Well Y120, 2708.69 m, SEM. (f) Well Y165, 2501.65 m, CL. (g) Well Y126, 2718.98 m, SEM. (h) Well Y165, 2614.57 m, CTS. (i) Well Y218, 2612.53 m, CTS.

TABLE 2: Quantitative calculation method of porosity evolution in sandstone reservoir (modified from [39, 40]).

Parameters of porosity evolution	Formula
Primary porosity, %	$\Phi_1 = 20.91 + 22.90/S_d$
Residual porosity after compaction, %	$\Phi_2 = \Phi_1 \text{EXP}^{-nh}$
Porosity reduction due to cementation, %	$\Phi_3 = C$
Porosity increase due to dissolution, %	$\Phi_4 = P_1 \times P_2/P_3$

Note: this research is not involved in microscopic fractures and pores of interstitial material due to the difficulty in their statistical approach.

(3) *Effects of Dissolution and Metasomatism on Physical Properties of Reservoir.* The most common metasomatism occurring in sandstone in the Shan-2 Member includes calcite replacing detrital particles, calcite replacing cements, calcite replacing argillaceous matrix, calcite argillaceous heterogeneity, and hydromica replacing quartz secondary overgrowth

and intergranular microcrystalline quartz, etc. In addition, the transformation of montmorillonite to illite and chlorite, kaolinitization to feldspar, and transformation between kaolinite and illite is common in this area. From the pore distribution in this area, most of the solution pores formed by metasomatism are destroyed by cementation.

Dissolution in the research area is very strong. The examination of SEM shows that a limited amount of secondary pores form by the dissolution of clay minerals, carbonate minerals, and quartz grains mainly in the surface and inside of rock fragments (Figure 8(h)), followed by the dissolution of feldspar (Figure 8(i)). Grains could dissolve in two cases: one is that the unstable particles such as feldspar and rock fragments are dissolved to form the dissolved intergranular pores directly; the other is that the feldspar and rock fragments are replaced by carbonate minerals and then dissolved in the metasomatic materials leading to the dissolved intra-granular pores and dissolved intergranular pores formed by

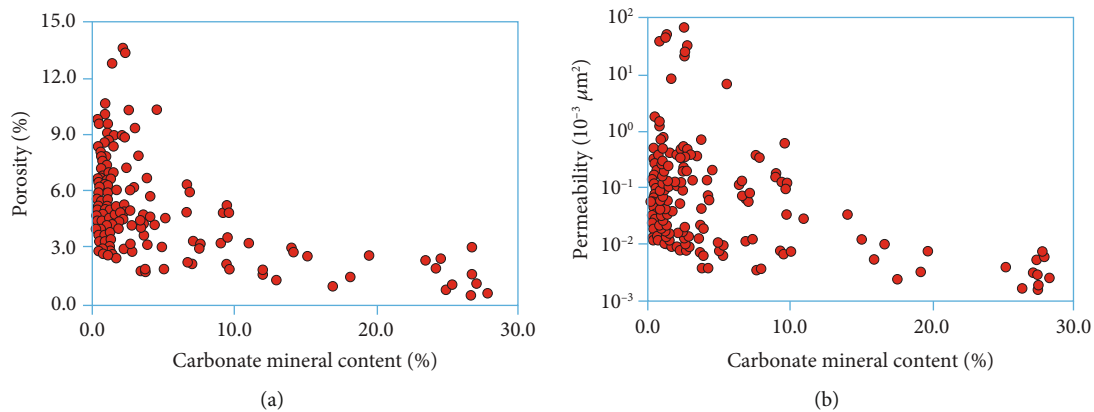


FIGURE 9: Relationship between content of carbonate minerals and petrophysical properties of samples in the research area.

dissolution of the grains [49]. Dissolution plays a constructive role in improvement of the accumulation properties of the sandstone reservoir. Although some of the solution pores are filled by iron carbonate cements in the late stage, some secondary pores remained. The amount of new pores formed by dissolution is calculated from the cementation rate formula (Table 2). The calculation result is about 2.68%.

4. Conclusion

- (1) Lithology of the Shan-2 Member is mainly medium-coarse lithic quartzarenite and quartzarenite with high compositional maturity and low structural maturity. Solution pores are the main accumulation spaces, followed by primary pores. Intragranular solution pores are mainly feldspar and rock fragment solution pores. The pore types are dominated by microfine pores
- (2) Shan-2 Member has four types of pores: medium-small pore with fine-microthroat, small-fine pore with microthroat, fine pore with microthroat, and fine-micropore with fine-microthroat. The main pore type is small-medium pores, and the main throat type is microthroat. The reservoir has poor physical properties, an average porosity of 7.22% and average value of $15.69 \times 10^{-3} \mu\text{m}^2$, and thereby belongs to a low porosity and low permeability gas reservoir
- (3) Sedimentation is the fundamental factor affecting the reservoir characteristics. Rock types, rock grain sizes, sorting performance, and matrix components are very different at different sedimentary facies. The rocks with good physical properties are fine and above sandstone, and the most favorable sedimentary facies is the underwater distributary channel in the research area
- (4) Diagenesis is also an important factor affecting the accumulation properties of the Shan-2 Member. Compaction and cementation are the main factors of reducing the physical properties. The average loss

of porosity due to compaction in the Shan-2 Member is 20.52%, and the loss of porosity is 16.91% due to cementation. Corrosion results in a certain increase of porosity, 2.68% on average

Data Availability

The thin section and SEM images are provided by Shaanxi Key Laboratory of Advanced Stimulation Technology for Oil & Gas Reservoirs, Xi'an Shiyou University. The physical properties and PCMI data used for this study are from the State Engineering Laboratory for Exploration and Development of Low permeability Oil and Gas Fields in China.

Conflicts of Interest

The authors declare that there are no conflicts of interest regarding the publication of this paper.

Acknowledgments

This research was supported by the Open Fund of Key Laboratory of Coal Resources Exploration and Comprehensive Utilization, Ministry of Land and Resources (grant numbers KF2019-1 and KF2020-2), China Postdoctoral Science Foundation (grant number 2018M643554), National Natural Science Foundation of China (grant numbers 41702146 and 51934005), Young science and Technology Talents Foundation of Shaanxi Province (grant number 2019KJXX-054), and Open Fund of Shaanxi Key Laboratory of Advanced Stimulation Technology for Oil & Gas Reservoirs, grant number 20JS120.

References




- [1] J. Lai, G. Wang, Z. Wang et al., "A review on pore structure characterization in tight sandstones," *Earth-Science Reviews*, vol. 177, pp. 436–457, 2018.
- [2] B. Ghanbarian, C. Torres-Verdín, L. W. Lake, and M. Marder, "Gas permeability in unconventional tight sandstones: scaling up from pore to core," *Journal of Petroleum Science and Engineering*, vol. 173, pp. 1163–1172, 2019.

- [3] D. Liu, Z. Gu, R. Liang et al., "Impacts of pore-throat system on fractal characterization of tight sandstones," *Geofluids*, vol. 2020, Article ID 4941501, 17 pages, 2020.
- [4] H. Huang, T. Babadagli, X. Chen, H. Li, and Y. Zhang, "Performance comparison of novel chemical agents for mitigating water-blocking problem in tight gas sandstones," *SPE Reservoir Evaluation & Engineering*, vol. 23, pp. 1150–1158, 2020.
- [5] S. Chen, D. Yin, N. Jiang, F. Wang, and Z. Zhao, "Mechanical properties of oil shale-coal composite samples," *International Journal of Rock Mechanics and Mining Sciences*, vol. 123, p. 104120, 2019.
- [6] G. Sheng, Y. Su, and W. Wang, "A new fractal approach for describing induced-fracture porosity/permeability/compressibility in stimulated unconventional reservoirs," *Journal of Petroleum Science and Engineering*, vol. 179, pp. 855–866, 2019.
- [7] J. Lai, X. Fan, B. Liu et al., "Qualitative and quantitative prediction of diagenetic facies via well logs," *Marine and Petroleum Geology*, vol. 120, 2020.
- [8] D. Ren, D. Zhou, D. Liu, F. Dong, S. Ma, and H. Huang, "Formation mechanism of the upper Triassic Yanchang formation tight sandstone reservoir in Ordos Basin—take Chang 6 reservoir in Jiyuan oil field as an example," *Journal of Petroleum Science and Engineering*, vol. 178, pp. 497–505, 2019.
- [9] D. Liu, W. Sun, D. Ren, and C. Li, "Quartz cement origins and impact on storage performance in Permian Upper Shihezi Formation tight sandstone reservoirs in the northern Ordos Basin, China," *Journal of Petroleum Science and Engineering*, vol. 178, pp. 485–496, 2019.
- [10] S. Hu, Y. Tan, H. Zhou et al., "Anisotropic modeling of layered rocks incorporating planes of weakness and volumetric stress," *Energy Science & Engineering*, vol. 8, no. 3, pp. 789–803, 2020.
- [11] D. Liu, W. Sun, D. Li, J. Shi, and D. Ren, "Pore structures characteristics and porosity evolution of tight sandstone reservoir: taking the Chang 63 tight sandstones reservoir of Huaqing area in Ordos Basin as an instance," *FEB-Fresenius Environmental Bulletin*, vol. 27, pp. 1043–1052, 2018.
- [12] D. Liu, W. Sun, and D. Ren, "Experimental investigation of pore structure and movable fluid traits in tight sandstone," *PRO*, vol. 7, no. 3, p. 149, 2019.
- [13] N. Zhang, W. Liu, Y. Zhang, P. Shan, and X. Shi, "Microscopic pore structure of surrounding rock for underground strategic petroleum reserve (SPR) caverns in bedded rock salt," *Energies*, vol. 13, no. 7, p. 1565, 2020.
- [14] G. Sheng, H. Zhao, Y. Su et al., "An analytical model to couple gas storage and transport capacity in organic matter with non-circular pores," *Fuel*, vol. 268, p. 117288, 2020.
- [15] J. Qiao, J. Zeng, S. Jiang, and Y. Wang, "Impacts of sedimentology and diagenesis on pore structure and reservoir quality in tight oil sandstone reservoirs: implications for macroscopic and microscopic heterogeneities," *Marine and Petroleum Geology*, vol. 111, pp. 279–300, 2020.
- [16] W. Dou, L. Liu, K. Wu, Z. Xu, X. Liu, and X. Feng, "Diagenetic heterogeneity, pore throats characteristic and their effects on reservoir quality of the upper Triassic tight sandstones of Yanchang Formation in Ordos Basin, China," *Marine and Petroleum Geology*, vol. 98, pp. 243–257, 2018.
- [17] D. Xiao, S. Jiang, D. Thul, S. Lu, L. Zhang, and B. Li, "Impacts of clay on pore structure, storage and percolation of tight sandstones from the Songliao Basin, China: implications for genetic classification of tight sandstone reservoirs," *Fuel*, vol. 211, pp. 390–404, 2018.
- [18] X. Wang, J. Hou, S. Song et al., "Combining pressure-controlled porosimetry and rate-controlled porosimetry to investigate the fractal characteristics of full-range pores in tight oil reservoirs," *Journal of Petroleum Science and Engineering*, vol. 171, pp. 353–361, 2018.
- [19] C. Wang, B. Shen, J. Chen et al., "Compression characteristics of filling gangue and simulation of mining with gangue backfilling: an experimental investigation," *Geomechanics and Engineering*, vol. 20, no. 6, pp. 485–495, 2020.
- [20] A. Reinicke, E. Rybacki, S. Stanchits, E. Huenges, and G. Dresen, "Hydraulic fracturing stimulation techniques and formation damage mechanisms—implications from laboratory testing of tight sandstone–proppant systems," *Geochemistry*, vol. 70, pp. 107–117, 2010.
- [21] Y. Zhang, S. Cao, N. Zhang, and C. Zhao, "The application of short-wall block backfill mining to preserve surface water resources in Northwest China," *Journal of Cleaner Production*, vol. 261, 2020.
- [22] P. Shan and X. Lai, "An associated evaluation methodology of initial stress level of coal-rock masses in steeply inclined coal seams, Urumchi coal field, China," *Engineering Computations*, vol. 37, no. 6, pp. 2177–2192, 2020.
- [23] Y. Yang, W. Li, and L. Ma, "Tectonic and stratigraphic controls of hydrocarbon systems in the Ordos basin: a multicycle cratonic basin in Central China," *AAPG Bulletin*, vol. 89, no. 2, pp. 255–269, 2005.
- [24] S. Dai, D. Ren, C.-L. Chou, S. Li, and Y. Jiang, "Mineralogy and geochemistry of the no. 6 coal (Pennsylvanian) in the Junger Coalfield, Ordos Basin, China," *International Journal of Coal Geology*, vol. 66, no. 4, pp. 253–270, 2006.
- [25] W.-Z. Zhang, H. Yang, J.-F. Li, and J. Ma, "Leading effect of high-class source rock of Chang 7 in Ordos Basin on enrichment of low permeability oil-gas accumulation-Hydrocarbon generation and expulsion mechanism," *Shiyou Kantan Yu Kaifa (Petroleum Exploration and Development)*, vol. 33, no. 3, pp. 289–293, 2006.
- [26] J. Dai, J. Li, X. Luo et al., "Stable carbon isotope compositions and source rock geochemistry of the giant gas accumulations in the Ordos Basin, China," *Organic Geochemistry*, vol. 36, no. 12, pp. 1617–1635, 2005.
- [27] L. Zhang, G. Bai, X. Luo et al., "Diagenetic history of tight sandstones and gas entrapment in the Yulin gas field in the central area of the Ordos Basin, China," *Marine and Petroleum Geology*, vol. 26, no. 6, pp. 974–989, 2009.
- [28] E. W. Washburn, "The dynamics of capillary flow," *Physical Review*, vol. 17, no. 3, pp. 273–283, 1921.
- [29] W. R. Purcell, "Capillary pressures—their measurement using mercury and the calculation of permeability therefrom," *Journal of Petroleum Technology*, vol. 1, no. 2, pp. 39–48, 2013.
- [30] D. J. K. Ross and R. M. Bustin, "The importance of shale composition and pore structure upon gas storage potential of shale gas reservoirs," *Marine and Petroleum Geology*, vol. 26, no. 6, pp. 916–927, 2009.
- [31] Y. Wang, Y. Zhu, S. Chen, and W. Li, "Characteristics of the nanoscale pore structure in Northwestern Hunan shale gas reservoirs using field emission scanning electron microscopy, high-pressure mercury intrusion, and gas adsorption," *Energy & Fuels*, vol. 28, no. 2, pp. 945–955, 2014.
- [32] N. Jiang, C. Wang, H. Pan, D. Yin, and J. Ma, "Modeling study on the influence of the strip filling mining sequence on

- mining-induced failure,” *Energy Science & Engineering*, vol. 8, no. 6, pp. 2239–2255, 2020.
- [33] J. Su, G. Chai, L. Wang et al., “Pore-scale direct numerical simulation of particle transport in porous media,” *Chemical Engineering Science*, vol. 199, pp. 613–627, 2019.
- [34] G. Feng, Y. Kang, X. Wang, Y. Hu, and X. Li, “Investigation on the failure characteristics and fracture classification of shale under Brazilian test conditions,” *Rock Mechanics and Rock Engineering*, vol. 53, pp. 1–16, 2020.
- [35] C. Legout, I. G. Droppo, J. Coutaz, C. Bel, and M. Jodeau, “Assessment of erosion and settling properties of fine sediments stored in cobble bed rivers: the arc and Isère alpine rivers before and after reservoir flushing,” *Earth Surface Processes and Landforms*, vol. 43, no. 6, pp. 1295–1309, 2018.
- [36] S. Zhi, D. Elsworth, J. Wang, Q. Gan, and S. Liu, “Hydraulic fracturing for improved nutrient delivery in microbially-enhanced coalbed-methane (MECBM) production,” *Journal of Natural Gas Science and Engineering*, vol. 60, pp. 294–311, 2018.
- [37] G. Feng, X. Wang, M. Wang, and Y. Kang, “Experimental investigation of thermal cycling effect on fracture characteristics of granite in a geothermal-energy reservoir,” *Engineering Fracture Mechanics*, vol. 235, 2020.
- [38] J. L. Luo, X. S. Liu, X. Y. Fu, R. Kang, and Y. Jia, “Impact of petrologic components and their diagenetic evolution on tight sandstone reservoir quality and gas yield: a case study from the 8 gas-bearing reservoir of upper Paleozoic in northern Ordos Basin,” *Earth Science*, vol. 39, no. 5, pp. 537–545, 2014.
- [39] T. R. Taylor, M. R. Giles, L. A. Hathorn et al., “Sandstone diagenesis and reservoir quality prediction: models, myths, and reality,” *AAPG Bulletin*, vol. 94, no. 8, pp. 1093–1132, 2010.
- [40] C. Zhang, W. Sun, and H. Gao, “Reservoir diagenetic facies and porosity evolution pathways of Chang 8 formation in Huachi Ordos Basin,” *Earth Science*, vol. 39, no. 4, pp. 411–420, 2014.
- [41] K. Xi, Y. Cao, J. Jahren et al., “Diagenesis and reservoir quality of the lower cretaceous Quantou Formation tight sandstones in the southern Songliao Basin, China,” *Sedimentary Geology*, vol. 330, pp. 90–107, 2015.
- [42] Y. Wang, L. Liu, S. Li et al., “The forming mechanism and process of tight oil sand reservoirs: a case study of chang 8 oil layers of the upper triassic yanchang formation in the western jiyuan area of the ordos basin, china,” *Journal of Petroleum Science and Engineering*, vol. 158, pp. 29–46, 2017.
- [43] S. Huang, Y. Wu, X. Meng, L. Liu, and W. Ji, “Recent advances on microscopic pore characteristics of low permeability sandstone reservoirs,” *Advances in Geo-Energy Research*, vol. 2, no. 2, pp. 122–134, 2018.
- [44] L. Wang, J. Su, Z. Gu, and L. Tang, “Numerical study on flow field and pollutant dispersion in an ideal street canyon within a real tree model at different wind velocities,” *Computers & Mathematics with Applications*, vol. 81, no. 6, pp. 679–692, 2021.
- [45] J. Yan, S. Zhang, J. Wang, Q. Hu, M. Wang, and J. Chao, “Applying fractal theory to characterize the pore structure of lacustrine shale from the Zhanhua depression in Bohai Bay Basin, Eastern China,” *Energy & Fuels*, vol. 32, no. 7, pp. 7539–7556, 2018.
- [46] J. Wang, Y. Cao, K. Liu, A. Costanzo, and M. Feely, “Diagenesis and evolution of the lower Eocene red-bed sandstone reservoirs in the Dongying Depression, China,” *Marine and Petroleum Geology*, vol. 94, pp. 230–245, 2018.
- [47] L. Wu, Y. Lu, S. Jiang, Y. Lu, X. Liu, and H. Hu, “Pore structure characterization of different lithofacies in marine shale: a case study of the upper Ordovician Wufeng-Lower Silurian Longmaxi formation in the Sichuan Basin, SW China,” *Journal of Natural Gas Science and Engineering*, vol. 57, pp. 203–215, 2018.
- [48] O. Walderhaug, “Kinetic modeling of quartz cementation and porosity loss in deeply buried sandstone reservoirs,” *AAPG bulletin*, vol. 80, no. 5, pp. 731–745, 1996.
- [49] H. Zhang, J. Peng, X. Lin, B. Li, and Q. Xia, “Diagenesis and its controlling factors of lower Donghetang formation tight sandstone reservoir in Bachu area, Tarim Basin, China,” *Geosciences Journal*, vol. 22, no. 2, pp. 327–336, 2018.

Research Article

Modeling and Simulation of Deformation Mechanism of Soft Rock Roadway considering the Mine Water

Yanlong Chen ¹, Qiang Li,² Hai Pu,^{1,3} Peng Wu ¹, Liang Chen,¹ Deyu Qian,⁴
Xuyang Shi ⁴, Kai Zhang,¹ and Xianbiao Mao²

¹State Key Laboratory for Geomechanics and Deep Underground Engineering, China University of Mining and Technology, Xuzhou 221116, China

²School of Mechanics and Civil Engineering, China University of Mining and Technology, Xuzhou 221116, China

³College of Mining Engineering and Geology, Xinjiang Institute of Engineering, Urumqi 830091, China

⁴School of Mines, China University of Mining and Technology, Xuzhou 221116, China

Correspondence should be addressed to Yanlong Chen; chenyanlong@cumt.edu.cn and Peng Wu; pengw@cumt.edu.cn

Received 25 May 2020; Revised 23 June 2020; Accepted 9 November 2020; Published 21 November 2020

Academic Editor: Fabien Magri

Copyright © 2020 Yanlong Chen et al. This is an open access article distributed under the Creative Commons Attribution License, which permits unrestricted use, distribution, and reproduction in any medium, provided the original work is properly cited.

The existence of coal mine water has an important influence on the instability of soft rock roadway in mining engineering. Considering the effect of mine water, a case study on the fracture mechanism and control technology of soft rock roadway was performed in this paper. The results showed that with the increase of moisture content, the uniaxial compressive strength of mudstone nonlinearly decreased, while the tensile strength, Young's modulus, cohesion, and friction angle tended to a linear decrease approximately. Meanwhile, with the increase of the weakening coefficient, the axial force of the anchorage body increased gradually, while the maximum shear stress decreased gradually. With the increase of moisture content, the failure zone was further propagated into the deep surrounding rock, resulting in a larger stress relaxation around the roadway, especially in the roof and floor. Finally, the supporting technology of the roadway was proposed, and then its support principle, design process, and parameters were also analyzed in detail. The field monitoring data showed that the support technology can control the surrounding rock deformation effectively and maintain the long-term stability of the roadway.

1. Introduction

Coal resources play an important role in the energy structure, accounting for more than 70% of the total resources in China. With the increasing intensity of coal mining and the exhaustion of shallow coal resources, the coal mining depth gradually increases at a speed of 10 m to 25 m per year [1]. Under the influence of high temperature, hyperosmosis, high in situ stress, and dynamic pressure disturbance, internal fractures of the rock masses develop and expand, eventually leading to the deformation of the roadway [2, 3]. Therefore, the failure mechanism of deep roadway is more complex than that of shallow roadway, especially in the soft rock. Engineering data have indicated that deep soft rock roadway accounts

for about 28%-30% of the total roadways, nevertheless, the repair rates are as high as 70% [4, 5]. Besides, the maintenance cost for the overall safety of the roadway is extremely expensive. Therefore, research on soft surrounding rock roadway is one of the pressing issues at home and abroad.

Grasping the instability mechanism of soft rock roadway is essential for the establishment of a support scheme in underground engineering. Theoretical analysis, numerical simulation, and engineering practice on the instability mechanism of soft rock roadway have been studied in the previous studies. Xue et al. [6] analyzed the theory of stacked arch bearing arch strength and applied this theory into the design of roadway support. Wang et al. [7] claimed that the unreasonable support scheme cannot effectively bear the

deformation and loosening pressure, resulting in the large deformation of deep roadway. Li et al. [8] applied PFC^{2D} to simulate the rock breakage modes under the confining pressure in deep mining. Zhang et al. [9] used FLAC^{3D} to study the instability of gypsum mining goaf under the influence of typical faults. Zhu et al. [10] explored the temporal and spatial evolution of stress at the floor of the coal seam by FLAC^{3D}. Considering that the high horizontal in situ stress is the major cause of roadway instability, Mark et al. [11] and Shen [12] simulated the failure mechanism of soft rock roadway by UDEC. Tang and Tang [13] simulated the floor heave processes of a swelling rock tunnel under the high humidity through simulation with RFPA. González-Nicieza et al. [14] investigated the influence of the depth and cross-section of the tunnel on the radial displacement by the convergence-confinement method (CCM). In addition, the low compressive and shear strength and the development of joints and cracks have important influences on the large deformation of the soft rock roadway [15, 16]. These studies have shown that the failure mechanism of soft rock roadway is not only related to the geological condition, in situ stress state, and rock mass parameters but also closely related to roadway size and section shape. In other words, the failure mechanism of soft rock roadway is complex, and some special supporting methods are required under different characteristics of the soft roadway [17, 18].

Recently, studies on the large deformation of soft rock roadway have been carried out, and some achievements have been obtained [19–21]. Based on the previous research and application, basic control techniques of soft rock roadway are summarized from the following four aspects: (1) the active support method is mainly used to improve the shear stiffness and tensile strength of the shallow surrounding rock and resist the harmful deformation of the roadway, such as bolt and cable [2, 22–24]. (2) The flexible passive support structure can resist the residual deformation of surrounding rock effectively, such as traditional U-steel, concrete-filled steel tubular, building arch, and steel tube confined concrete supports [25–28]. (3) Grouting reinforcement can improve the bearing capacity of the shallow surrounding rock [16, 29–31]. (4) A certain thickness of the compressive layer is reserved between the roadway surface and the passive support structure to effectively release the deformation energy of surrounding rock [4, 32–34]. Due to the complexity of geological conditions of soft rock roadway, the large and long-duration deformation in soft rock tunnel engineering is difficult to be controlled by a single support method. In the engineering practice, the combination support scheme has been proved to be an effective solution for such a support problem.

Due to the unique geological conditions, control technologies of soft rock roadway may not be applicable in different underground engineering. In this paper, the failure mechanism and control technology were studied to effectively control the large deformation of water-dripping soft rock roadway. Firstly, evolution laws of mudstone parameters with the moisture content were discussed comprehensively by the laboratory test. Secondly, the influence of mine water on the stress state of the anchorage body was researched by introducing a weakening coefficient. Thirdly,

with the change of moisture content, the deformation and plastic zone development process of surrounding rock were analyzed by the numerical simulation with FLAC^{3D}. Finally, the new waterproof supporting method was proposed to support the roadway.

2. Engineering Properties of the Soft Roadway

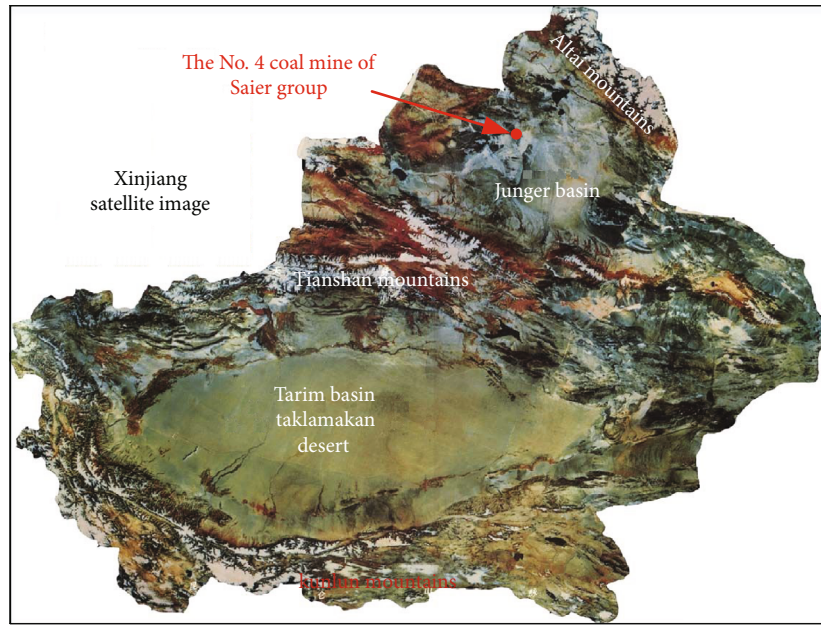
2.1. Engineering Setting. As shown in Figure 1(a), No. 4 coal mine of Saier Group is located in the northwest of the Xinjiang Autonomous Region, China. The B1002 haulage roadway of No.4 coal mine is excavated in the 10# coal seam, with a total length of 1200 m and an average burial depth of 320.66 m. In addition, both the belt and rail transportation functions are used in the haulage roadway, so there is a large section for the haulage roadway. The detailed arrangement of the haulage roadway is shown in Figure 1(b).

The cross-section of the haulage roadway is rectangular and excavated in the 10# coal seam with the width and height of 5000 mm and 3600 mm. The surrounding rock of the haulage roadway is mainly composed of mudstone and pack sand. The mudstone is mainly distributed on the surface of the roadway surrounding rock, with the soft property and poor cementing effect. The average distance from the roadway to the pack sand in roof and pack sand in floor is 5.0 m and 3.2 m, and pore water is rich in pore water. Figure 2 shows the lithological column of the roadway. In addition, bolt-mesh-cable combined support is mainly adopted in the primary support method of the haulage roadway. Two kinds of bolt and cable are used: (1) 2000 mm with the pretightening force of 30 kN; and (2) 5400 mm with the pretightening force of 60 kN. The cross-section and support patterns are shown in Figure 3.

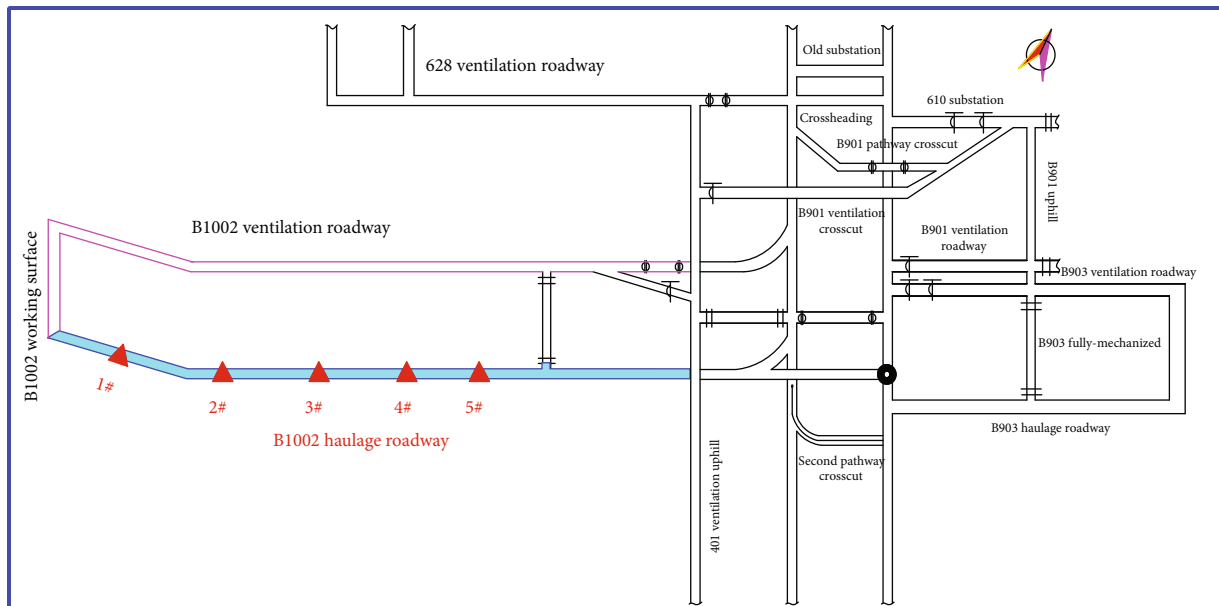
2.2. Mineral Composition Analysis. The average mineral composition of mudstone was obtained by an X-ray diffraction spectrum, as shown in Figure 4. It can be seen that rock specimens include abundant minerals such as quartz, kaolinite, smectite, illite, and less feldspar, calcite. The clay mineral composition is up to 74.5%, indicating that mudstone specimens belong to the swelling soft rock. When it encounters mine water, great expansive force will be generated by the mudstone, resulting in accelerated damage to the roadway stability.

2.3. Deformation Characteristics of Soft Rock Roadway. After roadway excavation, based on the investigation and monitoring data of the haulage roadway in two months, the deformation and support structure failure characteristic of the roadway are summarized as follows:

- (1) Large deformation and high deformation speed. The large deformation of surrounding rock appeared after two months of the roadway excavation. The average roof subsidence, floor heaves, and side walls convergence were 450 mm, 420 mm, and 930 mm, respectively. In some areas, the accumulative deformation was as large as 1.2–1.4 times compared with the above results, and the maximum side walls convergence reached 1400 mm and the section shrinkage rate reached 65%. In addition, due to the influence of



(a)



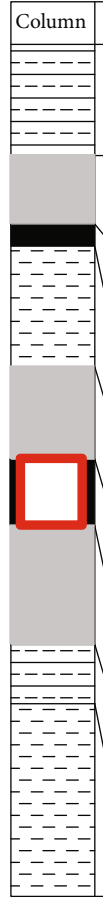
(b)

FIGURE 1: The detailed arrangement of the haulage roadway. (a) Location of the No.4 coal mine of Saier Group. (b) B1002 haulage roadway layout in No.4 coal mine.

packstone pore water on the mudstone, the strength of the rock mass decreased gradually with time, and the deformation of the surrounding rock lasted for a long period, resulting in extremely poor stability. The monitoring data indicated that the general deformation speed of surrounding rock was 5 mm/d-8 mm/d, while some were up to 12 mm/d

(2) Support structure failure. Due to unreasonable support methods, the phenomena of roof collapse, mesh tearing failure, and corrosion failure of bolt, as well as weakening of surrounding rock, were easily occurred

under the effect of the high in situ stress and pack sand pore water. With the influence of mine water, corrosion failure of support structure was more serious (Figure 5(a)), and the bolt (cable) support strength decreased significantly. Next, the extrusion and stagger displacement appeared in the roof, resulting in the roof subsidence (Figure 5(b)). The two sides moved towards the free surface, and then metal mesh and trapezoidal beam were subject to the tensile and shear failure (Figure 5(c)). Finally, the roof collapse accident happened along the weak



Column	No	Lithology	Thickness (m)	Lithological characters
	1	Siltstone	6.0	Gray green, horizontal bedding, thin sandstone interbed.
	2	Mudstone	3.7	Grey, gently slope bedding, containing plants fossils, broken.
	3	9# coal mine	1.2	Anthracite coal, banded structure, fractured
	4	Packsand	6.5	Gray, main containing quartz and felpar, good integrity.
	5	Mudstone	5.0	Gray, gently slope bedding, containing plants fossils, broken.
	6	10# coal mine	3.6	Anthracite coal, banded structure, fractured
	7	Mudstone	6.4	Gray, gently slope bedding, containing plants fossils, broken.
	8	Sandy mudstone	3.2	Black gray, gently slope bedding, containing plants fossils, moderate weathering.
	9	Packsand	10.4	Gray, main containing quartz and felpar, good integrity.

FIGURE 2: Strata histogram and lithological characters.

interface with the serious caved side walls (Figure 5(d)). The surrounding rock presented large deformation characteristic

- (3) The roadway deformation presented the time-dependent characteristic. After being excavated, the surrounding rock of the roadway always kept a high deformation ratio over time. Deformation duration lasted for about 4 months

2.4. The Influence of Moisture Content on Rock Mass. Based on the field investigation, the mine water was the main cause of the large deformation of surrounding rock [35]. Therefore, it was necessary to research the influence of mine water on the mudstone parameters by laboratory tests to obtain the instability mechanism of haulage roadway. In this test, moisture contents were adjusted to a predetermined value by a spraying method. The tensile (σ_t) and compressive strengths (σ_c) evolution law with the moisture content (ρ) were shown in Figure 6. It is seen that the compressive strength decreases nonlinearly with the increase of moisture content. As shown in Table 1, ρ increases from 1.43% to 3.33%-5.56%, and σ_c decreases by 13.45%-68.42%, respectively. In addition, the relationship between tensile strength and moisture content is linear approximately. For instance, ρ increases from 1.43% to 3.33% or from 3.33% to 5.56%, and ρ decreases by 57.14%

and 83.33%, respectively. Figure 7 shows the influences of moisture content on the Young's modulus (E), cohesion (c), and friction angle (φ) of mudstone. It should be noted that the Young's modulus can be determined by taking the slope of 40%-60% of the stress-strain curve. It is seen that parameters (E , c , and φ) decrease linearly with the increase of moisture content. For example, ρ increases from 2.42% to 4.54%, the Young's modulus decreases by 59.62%, cohesion decreases by 37.5%, and friction angle decreases by 12%. Therefore, the mine water has an important effect on the mudstone parameter attenuation, and the influence of mine water should be considered in the instability mechanism and support method optimization of surrounding rock. The relationships between moisture content and mechanical parameters of mudstone are shown in the following equation.

$$\begin{cases} \sigma_c = -0.5199\rho^2 + 0.7101\rho + 18.1225 (R^2 = 0.9113), \\ \sigma_t = -0.3289\rho + 1.7750 (R^2 = 0.9798), \\ E = -0.2948\rho + 1.8191 (R^2 = 0.9401), \\ c = -0.5247\rho + 3.9443 (R^2 = 0.9282), \\ \varphi = -1.2863\rho + 27.8713 (R^2 = 0.9856). \end{cases}$$

(1)

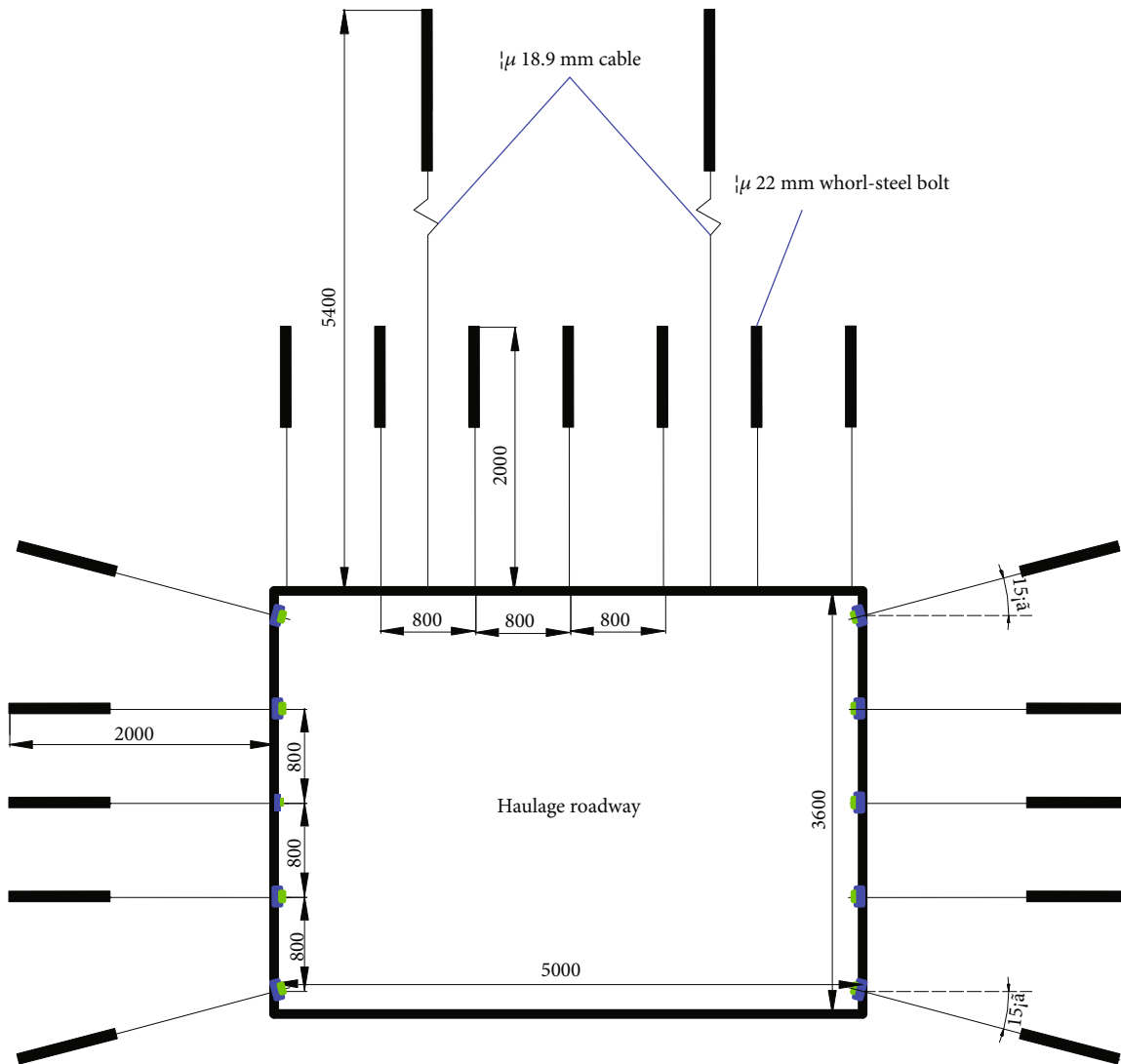


FIGURE 3: Primary support of the haulage roadway.

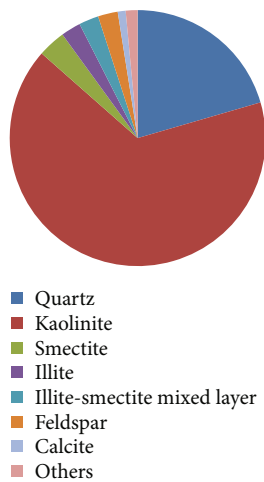


FIGURE 4: The mineral composition of mudstone located on the surrounding rock surface of the roadway.

3. The Support Mechanical Characteristics of a Bolt under Water-Dripping Condition

Based on the results of laboratory tests in Section 2.4, the existence of mine water reduces the rock masses mechanical properties effectively and weakens the bearing capacity of surrounding rock. Since bolt support can effectively change the stress state of surrounding rock and enhance the strength and stability of the anchorage rock mass, it has been widely used in different kinds of soft rock engineering in China [2, 31]. However, mine water not only corrodes the bolt body but also weakens the anchorage strength at the grout-bolt or grout-rock mass interface. As a result, the bolt support effect is greatly reduced, and the instability risk of surrounding rock is enhanced. Therefore, it was necessary to research the stress evolution process of the rock bolt under different water-dripping conditions.

3.1. Mechanical Model Establishment. The mechanical calculation model of the grout bolt drilled into rock mass is shown

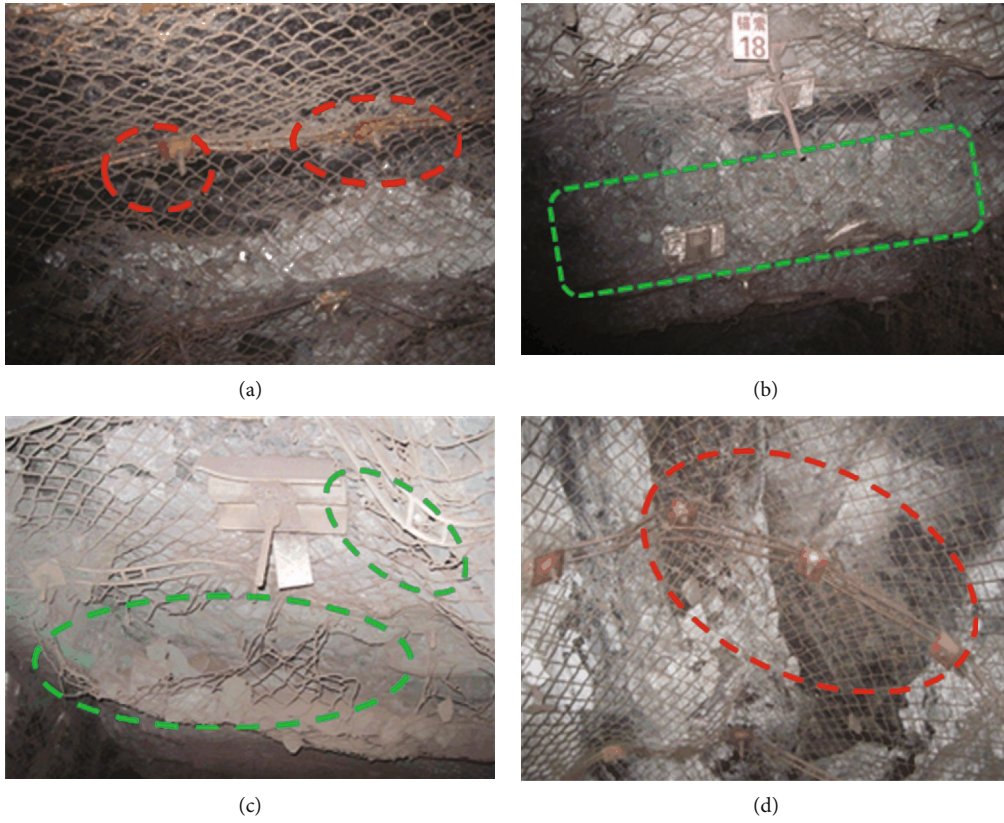


FIGURE 5: The deformation and support structure failure characteristic of surrounding rock. (a) Water-dripping corrosion of supporting structure; (b) roof subsidence; (c) mesh tearing and trapezoidal beam failure; (d) roof collapse.

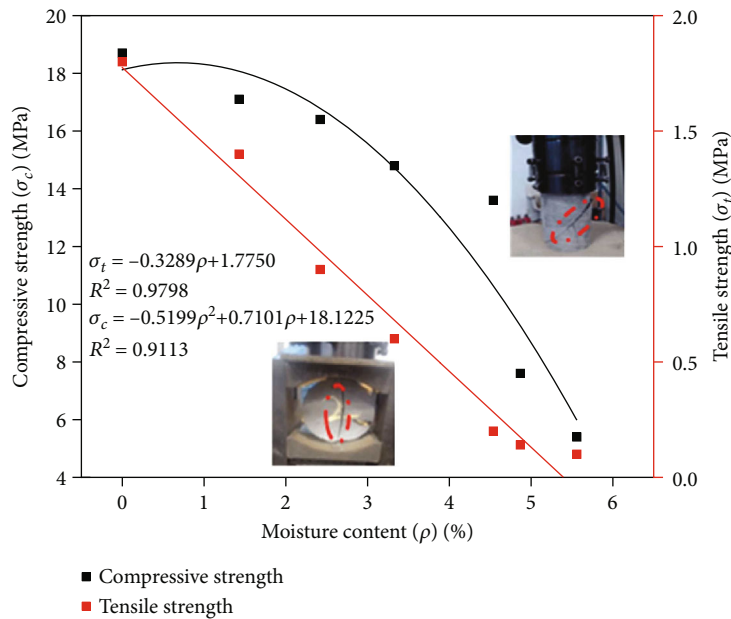


FIGURE 6: Influence of moisture content on the compressive and tensile strength of mudstone.

in Figure 8. The outer radius of the bolt and grout is represented as r_a and r_i , respectively. The total bolt length and anchorage length are L and L_z , respectively. F is the initial pretightening force applied to the rock bolt, and $\tau(z)$ is the

shear stress along the anchorage failure interface. It should be noted that the possible failure interface may be located at (1) the grout-bolt interface, (2) grout-rock mass interface, and (3) internal grout, as shown in Figure 8. Due to the

TABLE 1: Mudstone parameters under different moisture contents.

Moisture content (%)	Compressive strength (MPa)	Tensile strength (MPa)	Bulk modulus (GPa)	Shear modulus (GPa)	Young's modulus (GPa)	Cohesion (MPa)	Friction angle (°)
0.00	18.7	1.8	1.20	0.72	1.80	4.3	28
1.43	17.1	1.4	1.07	0.64	1.60	3.1	26
2.42	16.4	0.9	0.69	0.42	1.04	2.4	25
3.33	14.8	0.6	0.42	0.25	0.63	1.9	23
4.54	13.6	0.2	0.28	0.17	0.42	1.5	22
5.56	5.4	0.1	0.22	0.13	0.33	1.4	21

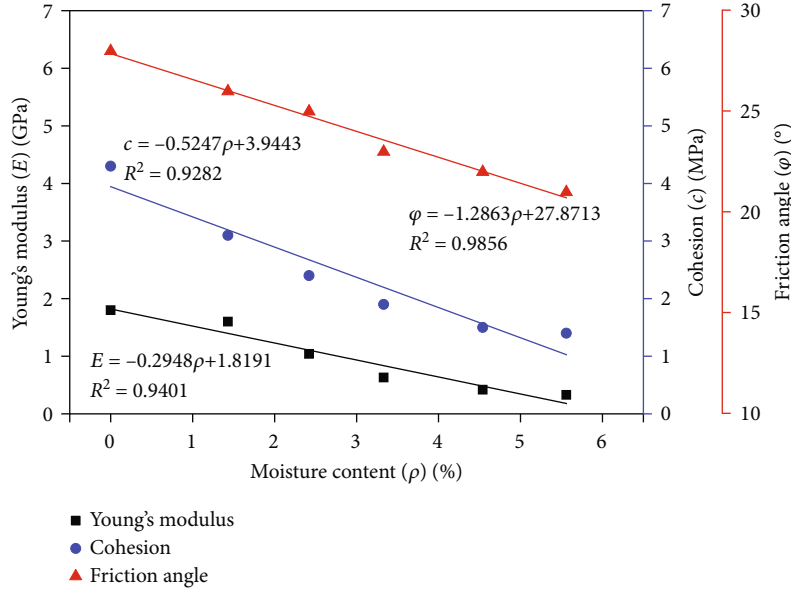


FIGURE 7: Influence of moisture content on the parameters (E , c , and φ) of mudstone.

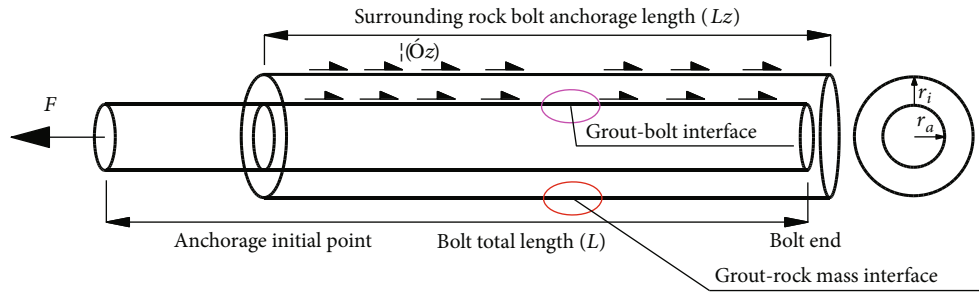


FIGURE 8: Mechanical calculation model of the mortar bolt drilled into rock mass.

relatively high strength of grout, grout-bolt interface and grout-rock mass interface are considered as the possible decoupling places. Therefore, the decoupling radius is written as follows:

$$r_j = \begin{cases} r_a & \text{Failure location at the grout-bolt interface,} \\ r_i & \text{Failure location at the grout-rock mass interface.} \end{cases} \quad (2)$$

According to the elastic theory, the relationship between the shear stress and shear displacement can be expressed as the following equation [2].

$$\tau(z) = k_j u(z), \quad (3)$$

where k_j represents interface shear stiffness without considering the effect of mine water; the subscripts “ j ” represents “ a ” for the grout-bolt interface and “ i ” for the grout-rock

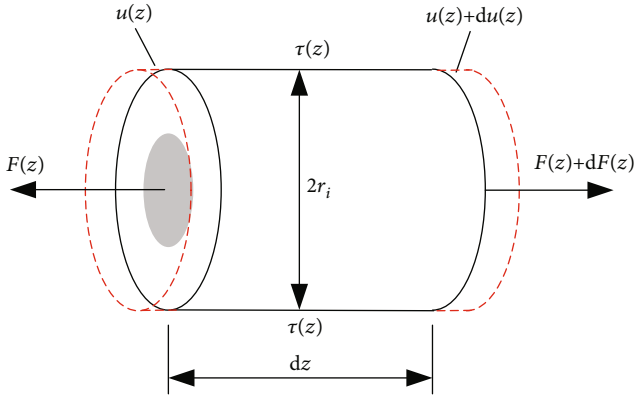


FIGURE 9: Microunit stress analysis of the anchoring body.

TABLE 2: The geometric and mechanical parameters of grout-bolt and bolt.

Bolt parameters			Grout parameters		Other parameters			
L	L_z	r_a	E_b	r_i	E_g	k_a	k_j	F
(m)	(m)	(mm)	(GPa)	(mm)	(GPa)	(GPa)	(GPa)	(kN)
2.0	1.2	10	200	13	120	75	35	60

mass interface, respectively. $u(z)$ is the relative displacement between the anchorage body and surrounding rock.

When the rock encounters the mine water, mechanical properties of rock are weakened at the interface. Hence, the weakening coefficient (λ) is introduced to define the weakening degree of rock mass, as shown in the following equation.

$$\lambda = \frac{k_j - k_m}{k_j}, \quad (4)$$

where λ is called weakening coefficient and satisfies $0 \leq \lambda < 1$. If $\lambda = 0$, then the rock mass is not affected by the water dripping. If $\lambda \rightarrow 1$, then rock mass is seriously affected by water and the bolt loses its anchoring action. k_m is the weakened interface shear stiffness by water. Then, the shear stress at the interface is obtained by substituting Equation (4) into Equation (3).

$$\tau(z) = (1 - \lambda)k_j u(z). \quad (5)$$

Deformation coordination conditions should be satisfied by the anchorage body and surrounding rock. Figure 9 shows the microunit stress analysis model of the anchoring body. Hence, according to the Hook's law, the relationship between the relative displacements of the anchoring body $u(z)$ and the pretightening force of the bolt $F(z)$ is expressed by the following equation [31].

$$\frac{F(z)}{\pi r_j^2} = \frac{du(z)}{dz} E_j, \quad (6)$$

where E_j is the equivalent elastic modulus of the anchoring body; $E_j = E_b$ is valid for the failure location at the grout-

bolt interface or $E_j = [E_g(r_i^2 - r_a^2) + E_b r_a^2]/r_i^2$ for the failure location at the grout-rock mass interface. E_g and E_b is the elastic modulus of the grout and bolt, respectively.

Based on the stress equilibrium condition of the microelement body, the relationship between shear stress of the anchorage body and pretightening force along direction is expressed by the following equation.

$$\frac{dF(z)}{dz} = 2\pi r_j \tau(z). \quad (7)$$

By integrating the Equations (5) and (7) into Equation (6), Equation (8) is obtained as follows:

$$\frac{d^2 u(z)}{dz^2} - \frac{2(1 - \lambda)k_j}{r_j E_j} u(z) = 0. \quad (8)$$

According to the solution of Equation (8), the boundary conditions $F(L) = 0$ and $F(L - L_z) = F$, the axial force and shear stress of the anchorage body along the z direction under the effect of the water dripping are obtained as follows:

$$\begin{cases} F(z) = \frac{F}{1 - e^{2L_z \sqrt{2(1-\lambda)k_j/r_j E_j}}} \left[e^{\sqrt{\frac{2(1-\lambda)k_j}{r_j E_j}}(-L+L_z+z)} - e^{\sqrt{\frac{2(1-\lambda)k_j}{r_j E_j}}(L+L_z-z)} \right], \\ \tau(z) = \frac{1}{\pi} \sqrt{\frac{(1-\lambda)k_j}{2r_j^3 E_j}} F(z). \end{cases} \quad (9)$$

3.2. Parameters Analysis. To research the influence of the weakening coefficient on the axial force and shear stress of anchorage body under different failure interfaces, different weakening coefficients (0, 0.2, 0.4, 0.6, and 0.8) were selected. The geometric and mechanical parameters of grout-bolt and bolt are shown in Table 2.

Figure 10 presents the influence of different weakening coefficients on the axial force and shear stress of the anchorage body. It indicates that the weakening coefficient has an extremely important effect on the axial force and shear stress distribution of the anchorage body whether the failure location at the grout-bolt interface or the grout-rock mass interface. With the increase of the weakening coefficient, the axial force of the anchorage body increases gradually from the anchorage initial point to the end of the bolt under the same pretightening force, while the maximum shear stress decreases gradually. In addition, when the weakening coefficient is small, the shear stress is mainly concentrated near the anchorage initial point. With the increase of the weakening coefficient, the distribution of shear stress transforms from the anchorage initial point to the whole length of the bolt gradually. The above analysis shows that the mine water not only affects the anchoring action of the bolt to the surrounding rock but also causes the redistribution of bolt axial stress.

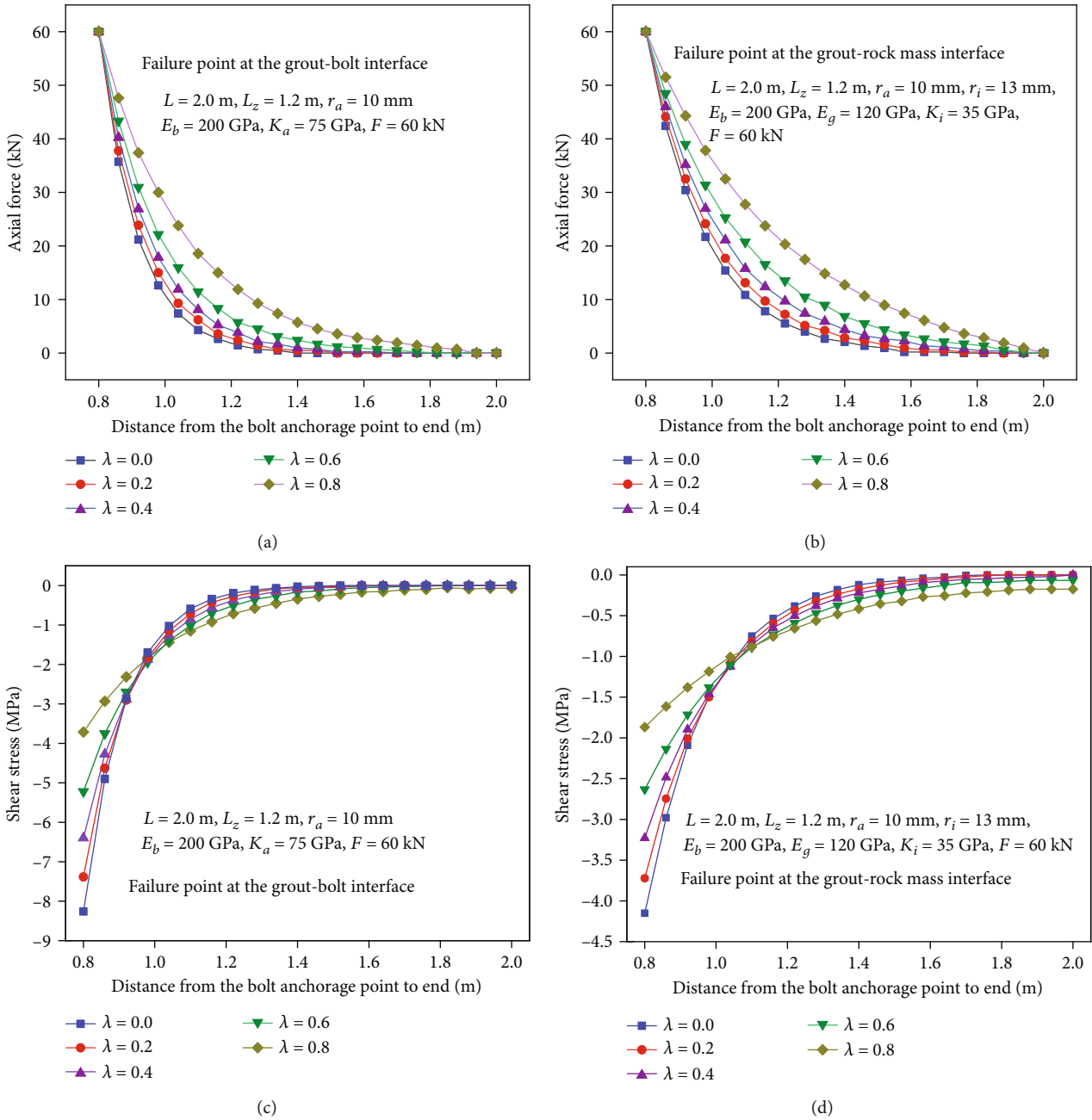


FIGURE 10: Axial force and shear stress evolution law of the anchorage body under different weakening coefficients. (a) Axial force (failure point at the grout-bolt interface); (b) axial force (failure point at the grout-rock mass interface); (c) shear stress (failure point at the grout-bolt interface); (d) shear stress (failure point at the grout-rock mass interface).

4. Establishment of a Numerical Simulation Model

4.1. *Establishment of a Numerical Simulation Model.* The Fast Lagrangian Analysis of Continua in 3-Dimension (FLAC^{3D}) software can effectively simulate the progressive failure and large deformation problem of the underground engineering compared with the ABAQUS or ANSYS software. Hence, FLAC^{3D} has been widely applied to tunnel excavation and support design, slope, or foundation reinforcement engineering and mining engineering. From the previous analysis in

this study, the B1002 haulage roadway of No.4 coal mine in Saier Group encountered a typical large deformation problem of soft rock roadway. Therefore, the FLAC^{3D} software was selected to research the failure mechanism of this roadway under different moisture contents. To remove the influence of the boundary effect on calculation results, the length, width, and height of the simulation model were set as 100 m, 25 m, and 50 m, respectively, as shown in Figure 11. The model size of the haulage roadway was 5.0 m (width) \times 3.6 m (height); both the left-right boundary and the bottom boundary were subject to displacement

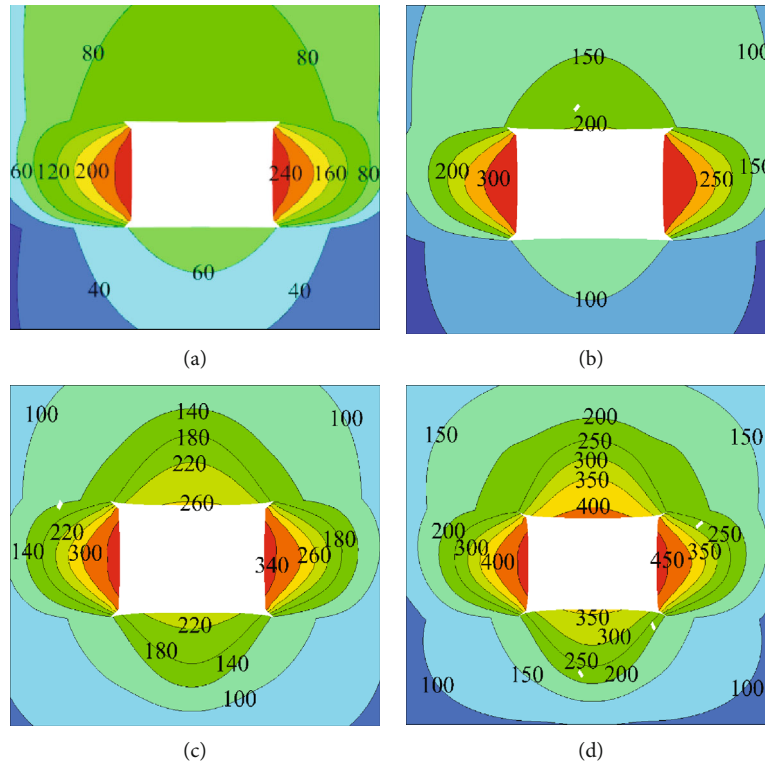


FIGURE 13: Total displacement maps of roadway without support under different moisture contents. (a) 2.42%; (b) 3.33%; (c) 4.54%; (d) 5.56%.

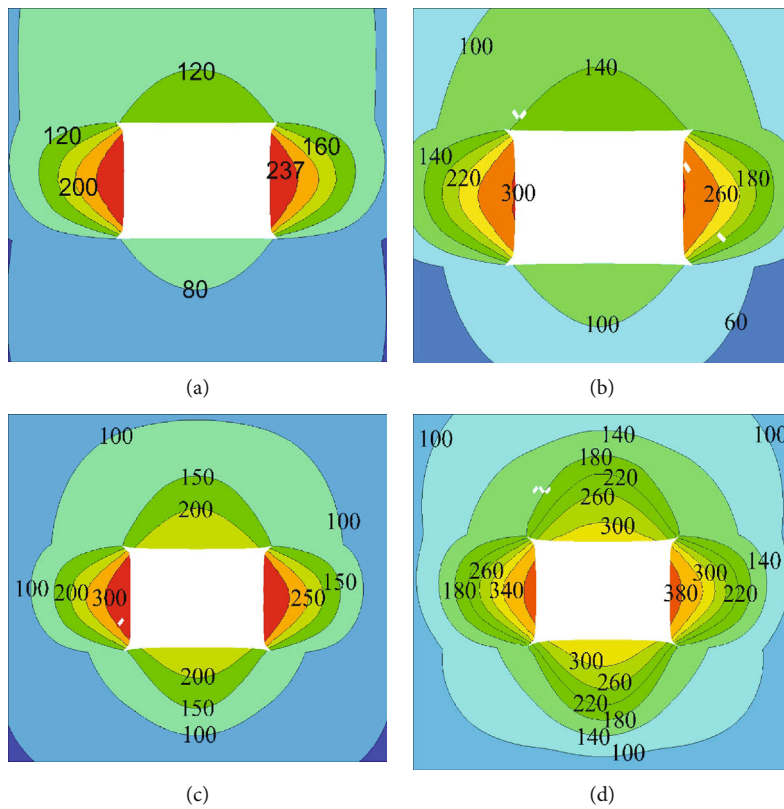


FIGURE 14: Total displacement maps of roadway with primary support under different moisture contents. (a) 2.42%; (b) 3.33%; (c) 4.54%; (d) 5.56%.

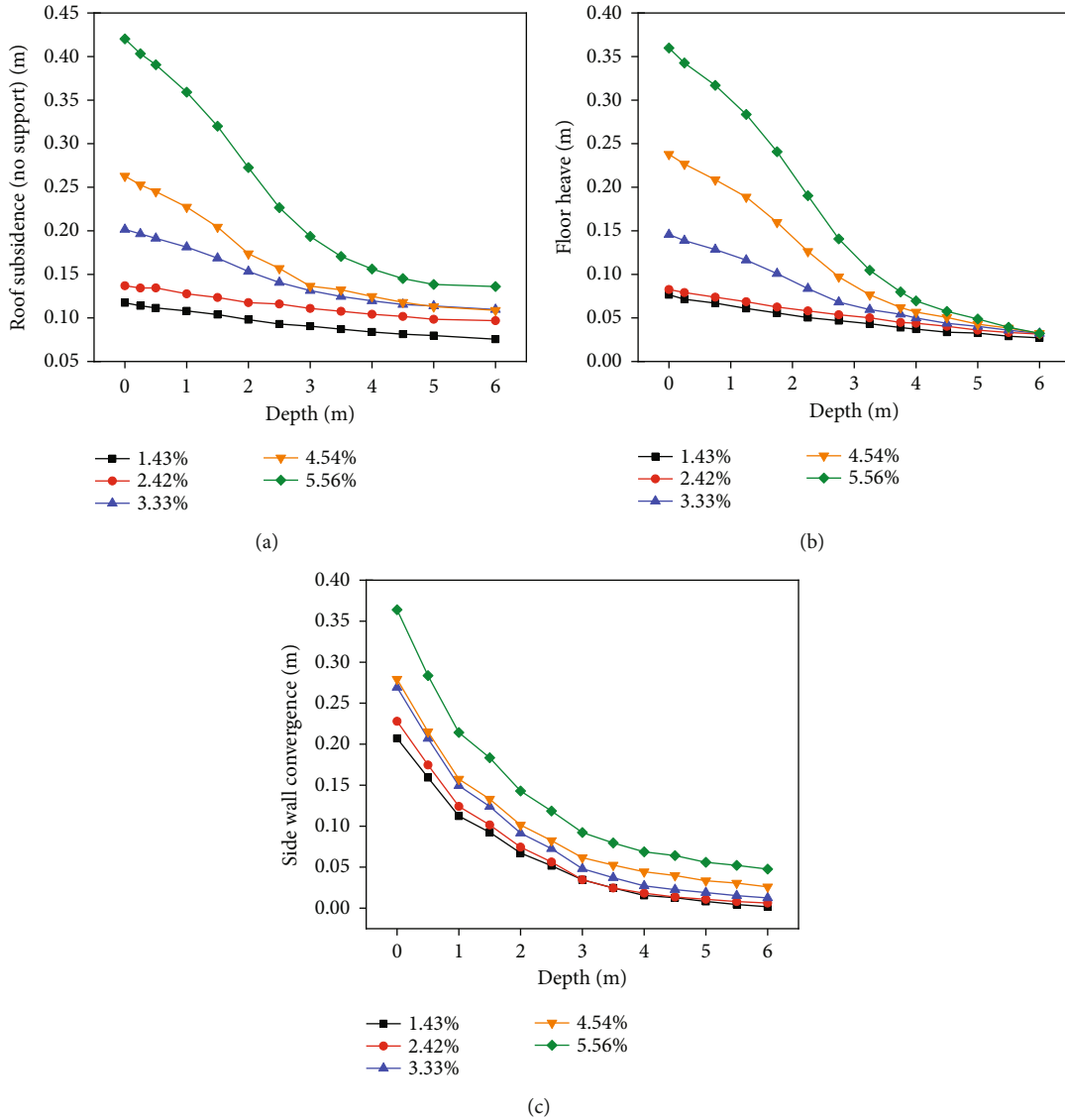


FIGURE 15: Displacement of roadway without support along the depth direction under different moisture contents. (a) Roof subsidence; (b) floor heave; (c) side wall convergence.

constraint, while the top boundary was subject to stress constraint with 10.5 MPa, which was measured by the field in situ stress test. To improve the calculation accuracy, the grid around the haulage roadway was encrypted. In this simulation, the in situ stress balance was first carried out, and then the total displacement and plastic zone of surrounding rock were extracted to research the failure process of haulage roadway considering the effect of different moisture contents after roadway excavation.

The mechanical parameters of the rock mass at different levels were easily obtained by laboratory tests. Table 2 presents the initial mechanical parameters of coal and rock mass taken from the geological report of the B1002 haulage roadway. To research the influence of mine water on the instability mechanism of the haulage roadway with the primary support and without any support, mudstone parameters were derived from Table 1 under different moisture contents. In addition, the Mohr-Coulomb criterion was used

to simulate the failure of coal and rock masses. According to the engineering practice, the bolt-mesh-cable combined support was mainly adopted in the primary support of the haulage roadway. Geometric and mechanical parameters of bolt and cable are shown in Tables 3 and 4.

4.2. Failure Criterion. Since the tensile strength of the rock mass was much lower than its compressive strength, the Mohr-Coulomb failure criterion was selected to realize the tension failure of the rock mass in this numerical simulation. The failure criterion might be represented in the plane $(\sigma_1 - \sigma_3)$ as illustrated in Figure 12, and the failure envelope $f(\sigma_1, \sigma_3) = 0$ is defined from point A to B by the Mohr-Coulomb failure function with

$$f^s = \sigma_1 - \sigma_3 N_\varphi + 2c\sqrt{N_\varphi}, \quad (10)$$

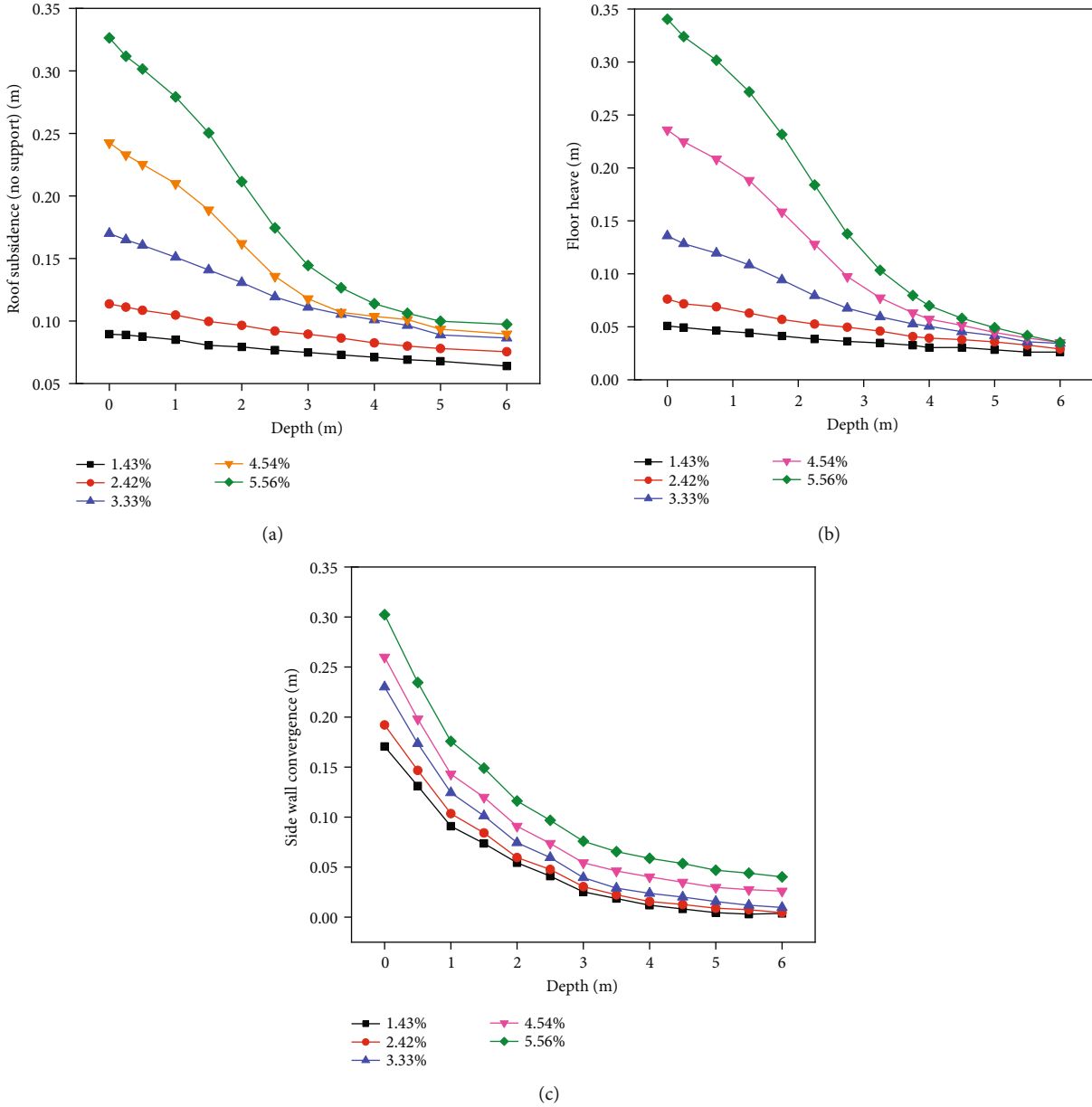


FIGURE 16: Displacement of roadway with primary support along the depth direction under different moisture contents. (a) Roof subsidence; (b) floor heave; (c) side wall convergence.

where c is the cohesion; φ is the internal friction angle, $N_\varphi = (1 + \sin \varphi)/(1 - \sin \varphi)$. In addition, the tensile failure function from point B can be expressed as follows:

$$f^t = \sigma_t - \sigma_3, \tag{11}$$

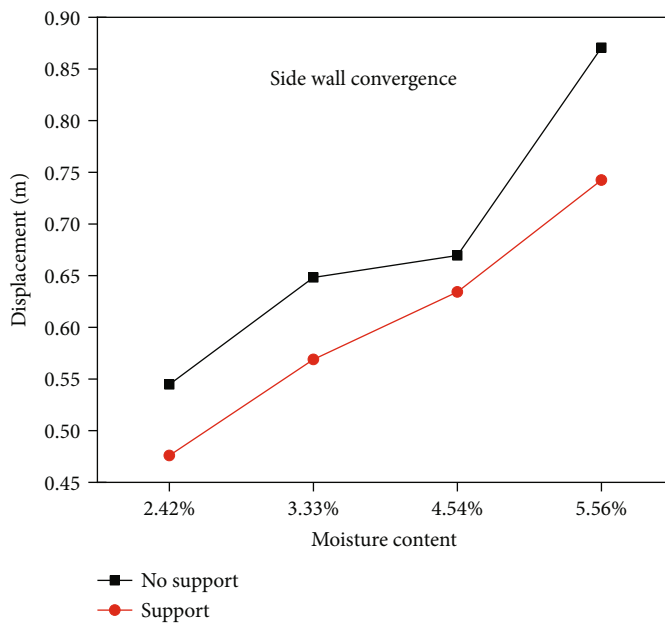
where σ_t is the tensile strength.

4.3. Failure Mechanism of Water-Dripping Mudstone Roadway

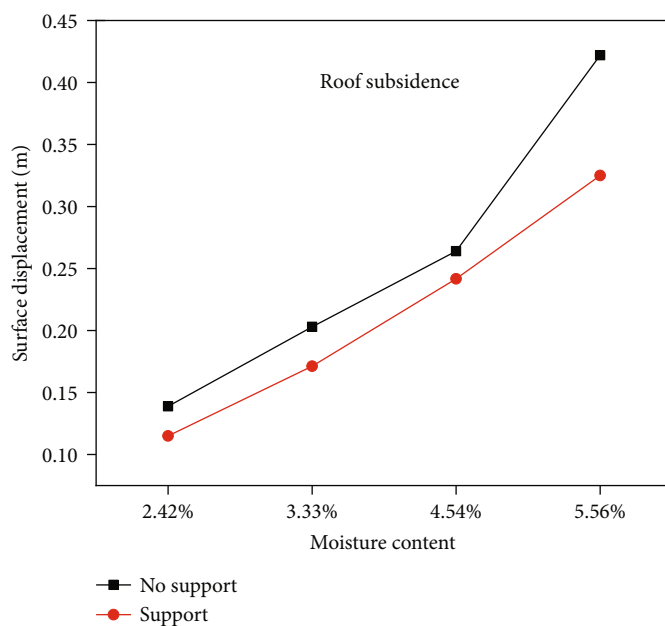
4.3.1. Displacement Analyses. Figures 13 and 14 show the total displacement maps of surrounding rock with the primary support and without support under different moisture contents after the haulage roadway excavation. It is seen that

the serious nonuniform deformation of roadway surrounding rock is caused by excavation and independent with the primary support or without support. The convergence deformation of side walls is obviously larger than that of the roof subsidence, while the floor heave is the smallest. For instance, when the moisture content is 4.54%, the side wall convergence, roof subsidence, and floor heave of the roadway with the primary support are 669 mm, 264 mm, and 237 mm without support, and 633 mm, 242 mm, and 235 mm, respectively.

In addition, with the increase of the moisture content, the deformation of surrounding rock of the roadway with the primary support and without support increases gradually, as shown in Figures 15–17. For instance, as the moisture content increases from 2.42% to 4.54%, the side wall convergence, roof subsidence, and floor heave increase by 22.53%,

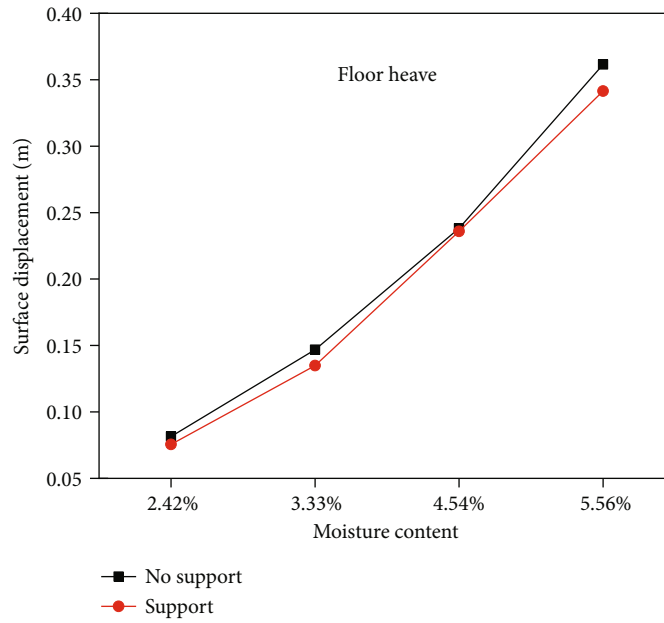


(a)



(b)

FIGURE 17: Continued.



(c)

FIGURE 17: Surface displacement evolution law with the different moisture contents. (a) Side walls convergence; (b) roof subsidence; (c) floor heave.

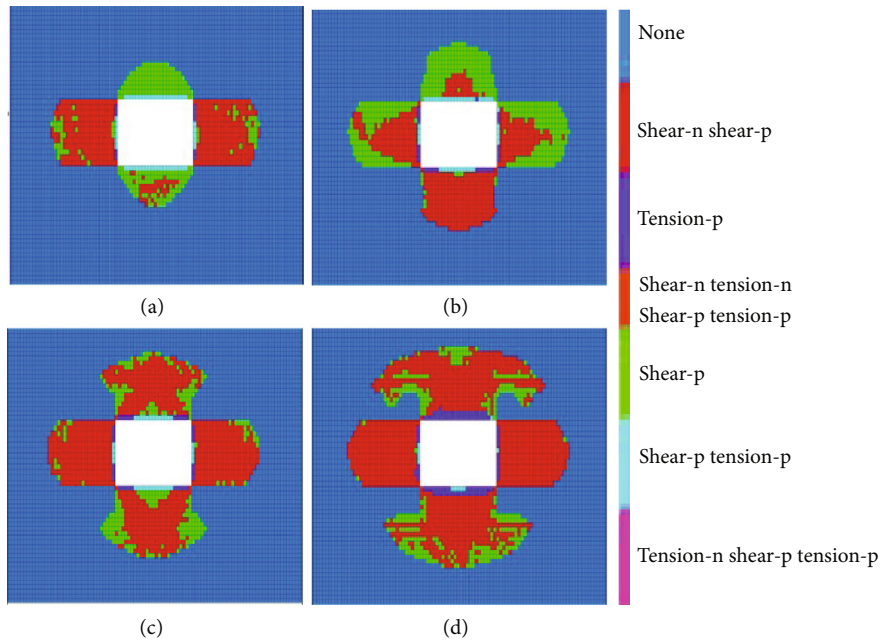


FIGURE 18: Plastic zone distribution of roadway without support under different moisture contents. (a) 2.42%; (b) 3.33%; (c) 4.54%; (d) 5.56%.

91.30%, and 185.54% for the roadway without the support and increase by 33.26%, 112.28%, and 209.21% with the primary support, respectively. However, when the moisture content reaches 4.54%, the deformation rate of side walls and roof begins to increase sharply for the roadway without the support, while the floor remains unchanged basically. In other words, the mine water has a great influence on the

stability of surrounding rock, especially on the side walls and roof deformation.

Meanwhile, compared with the roadway without support, the maximum side wall convergence, roof subsidence, and floor heave of the roadway with the primary support only decrease by 13%-14.94%, 8.33%-22.57%, and 0.84%-8.4%, respectively, at the moisture content range of 2.42%-5.56%.

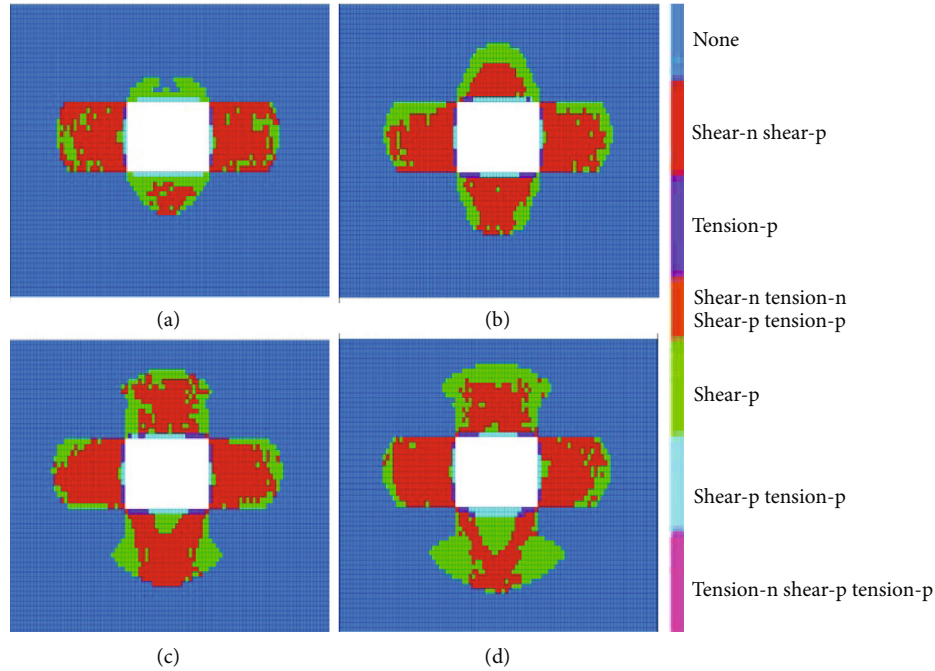


FIGURE 19: Plastic zone distribution of roadway with primary support under different moisture contents. (a) 2.42%; (b) 3.33%; (c) 4.54%; (d) 5.56%.

TABLE 5: Plastic zone distribution of roadway without support and with primary support.

Moisture content (%)	Roof (m)		Floor (m)		Side walls (m)	
	No support	Primary support	No support	Primary support	No support	Primary support
2.42	2.4	1.5	2.7	2.7	4.4	4.2
3.33	3.9	3.6	4.2	3.9	4.6	4.4
4.54	4.5	4.2	4.8	4.8	4.6	4.4
5.56	4.8	4.5	5.4	5.4	4.8	4.4

It indicates that harmful deformation of surrounding rock is hardly controlled by the primary support, especially the side wall convergence under the high moisture content condition, as shown in Figure 14.

4.3.2. Crack and Plastic Region Analysis. Previous research has shown that engineering accidents in mine coal, such as roof caving and wall caving, are closely related to the propagation of the plastic zone. Therefore, the extension process of the plastic zone caused by excavation is urgent to be investigated. Figures 18 and 19 show plastic zone distribution maps of roadway without support and with primary support under different moisture contents. It is seen that tension-shear combined failure mainly occurred in the surface of the roadway, and shear failure occurred in deep surrounding rock, whether the roadway with the primary support or without the support. The plastic zone around the surrounding rock is in a shape of a cross.

In addition, with the increase of moisture contents, the plastic zone range for the roof and floor significantly increases, while that of side walls changes slightly. For instance, as the moisture content increases from 2.42% to 5.56%, the ranges of the side walls only increase by 0.4 m

for the roadway without support and 0.2 m with primary support, but the roof and floor increase by 2.4 m and 2.7 m without support or 3.0 m and 2.7 m without support, respectively, as shown in Table 5. In other words, the moisture content has the greatest influence on the plastic zone range of roof and floor, but has little influence on side walls.

As shown in Table 5, compared with the roadway without support, when the moisture content is 5.56%, the ranges of plastic zone of the roadway with the primary support at 4.5 m roof and 4.4 m side walls only decrease by 0.3 m and 0.4 m, respectively, while 5.4 m floor is unchanged. It indicates that the primary support cannot effectively control the development of the plastic zone, and there is still a large amount of shear failure around the roadway, especially on the floor.

4.3.3. Failure Mechanism Analysis. From the above analysis, the failure mechanism of the haulage roadway under the primary support can be summarized as follows:

High in situ stress, low-strength coal, and rock mass. The average burial depth of the haulage roadway is 320.66 m with relatively higher in situ stress (10.5 MPa) combined with the influence of the tectonic stress. The natural compressive

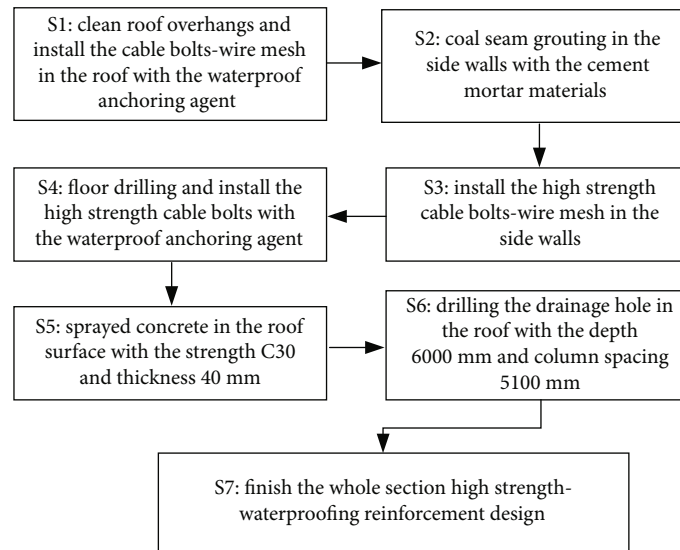


FIGURE 20: WSHSWRT support design.

strength of the coal and mudstone in the roof and floor is, respectively, 16.4 MPa and 3.24 MPa, belonging to the typical “three soft” coal seam roadway. The stress redistribution can occur after roadway excavation, and then, overburden stress exceeds the compressive strength of the rock masses, so that the shallow surrounding rock enters into the postfailure state first. The plastic zone is propagated from the shallow to the interior over time, resulting in the large broken rock mass zone finally.

Mudstone is weakened seriously, accelerating the deformation of surrounding rock. Pack sand layers near the roof and floor are rich in fissure water, which easily weakens the mudstone parameters. Then, the anchorage force and support strength of the bolt sharply drop with the attenuation of rock mass parameters. As a result, the harmful deformation of surrounding rock is accelerated to move towards the free face and reduce the instability process of haulage roadway.

Low-strength and incomplete support structure. Initial pretightening forces of the bolt and cable used in the primary support are only 30 kN and 60 kN. However, they cannot provide enough compressive stress to prevent the tensile failure of shallow surrounding rock. The “bolt-mesh-cable” combined support is only used in the roof and side walls; then, a whole-section support structure around the haulage roadway cannot be formed to effectively resist the floor heave.

5. The Support Approach of “Whole Section High Strength-Waterproofing Reinforcement Technology (WSHSWRT)”

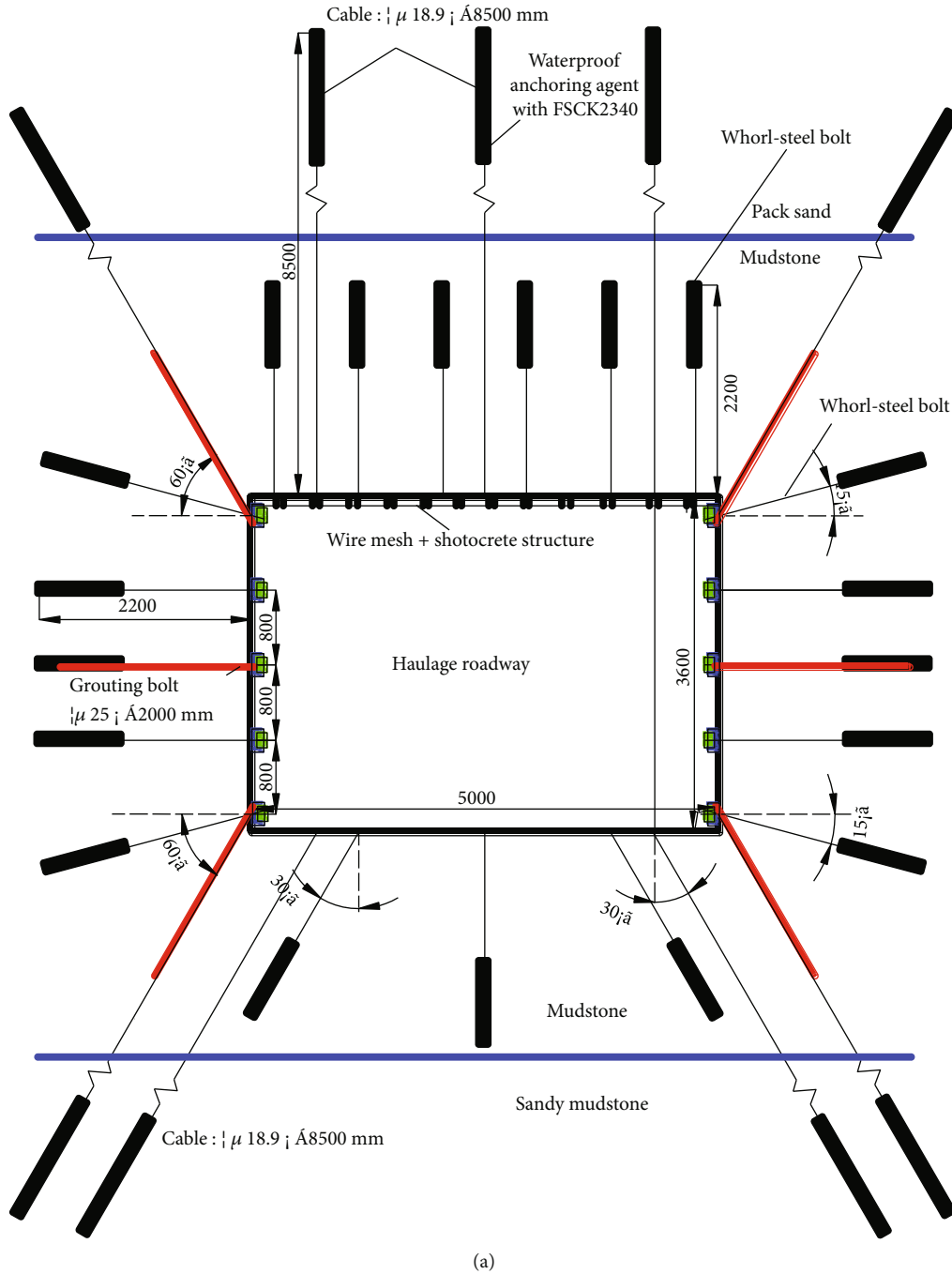
5.1. Control Principal. The support approach of WSHSWRT is mainly composed of the whole section high pretension bolt-cable, waterproof anchoring agent, shotcrete, and drainage hole in the roof as well as side wall grouting layer. Previous research has indicated that the confining pressure has an

extremely important effect on the residual strength of rock mass [4]. The residual strength gradually increases with the increase of the confining pressure. Therefore, the whole section-high pretension bolt-cable support should be used to improve mechanical parameters and reduce the tensile failure of shallow surrounding rock including the floor heave. Furthermore, the cables of the roof and side walls should be anchored to packstone layers, so as to fully play the suspension action for the shallow surrounding rock. The strength of the coal is much lower than that of rock masses, which is the main reason for the large deformation of the two sides. The grouting technology improves the bond strength and the residual bearing capacity of cracked surrounding rock effectively and has been widely used in tunnel excavation engineering [23]. Therefore, the large deformation and plastic region of side convergence can be effectively controlled by the coal seam grouting. A series of drainage holes in the roof is arranged to reduce the influence of mine water on the mechanical properties of shallow surrounding rock. In addition, a hermetic high-strength integrated support structure is formed in the roof through the high strength shotcrete layer, so that the high resistance is provided to control the roof subsidence, and the surrounding rock is sealed to reduce the weathering of shallow mudstone. As we know, the weakening effect of mine water on the surrounding rock and anchoring agent is one of the main reasons for the bolt support failure. Therefore, the waterproof anchoring agent should be used to reduce the influence of mine water. Figure 20 shows the design process of the WSHSWRT support.

5.2. Support Parameters and Scheme. In the above analysis, WSHSWRT is proposed to solve the large deformation of the “three soft” mining roadway. The support technology is divided into the following aspects: the whole section bolt-cable high strength support structure (high strength bolt-cable-wire mesh), the coal seam grouting reinforcement, and supplementary support including shotcrete and drilling drainage holes in the roof. The excavation section of the

TABLE 6: Bolt and cable properties of the combined support.

Parameters	Density (kg·m ⁻³)	Cross-sectional area (cm ²)	Elastic moduli (GPa)	Tensile capability (kN)	Bond stiffness (N/m ²)	Bond cohesion (N/m)	Preload (kN)
Bolt	7500	3.80	200	120	2×10^9	4×10^5	80
Cable	7500	2.81	200	300	2×10^9	4×10^5	120



(a) FIGURE 21: Continued.

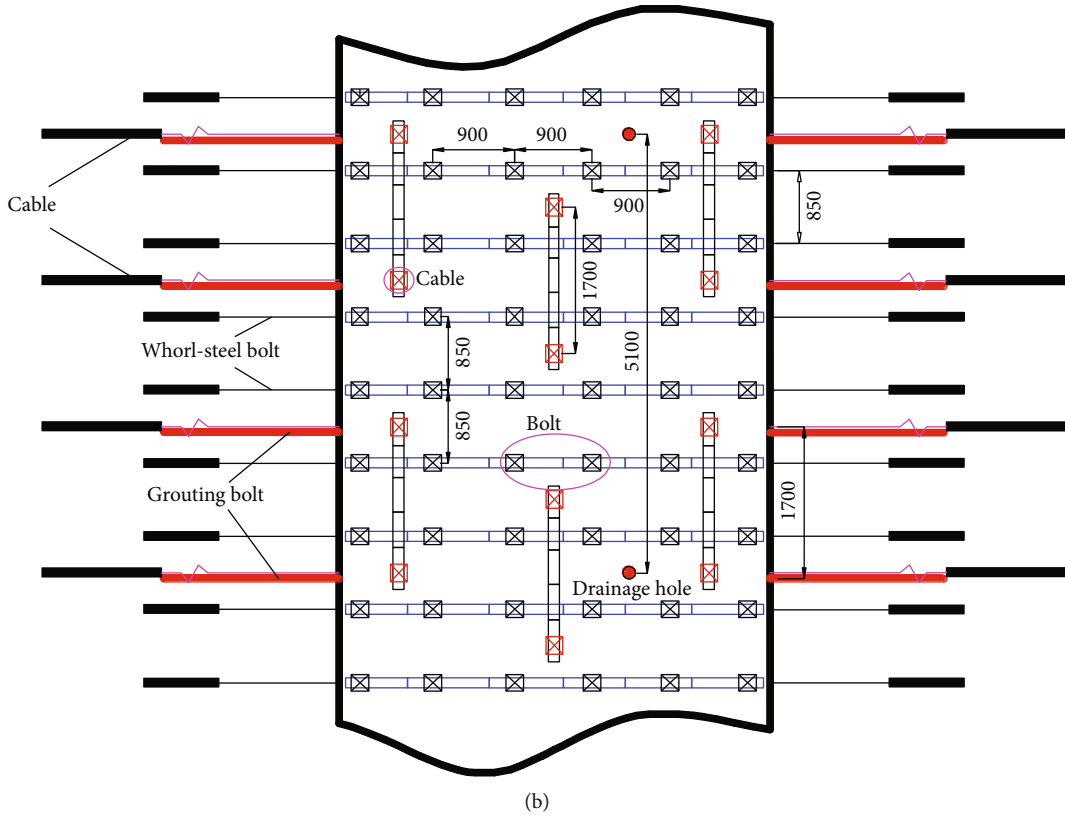


FIGURE 21: WSHSWRT of the haulage roadway. (a) Support section; (b) roof and side support.

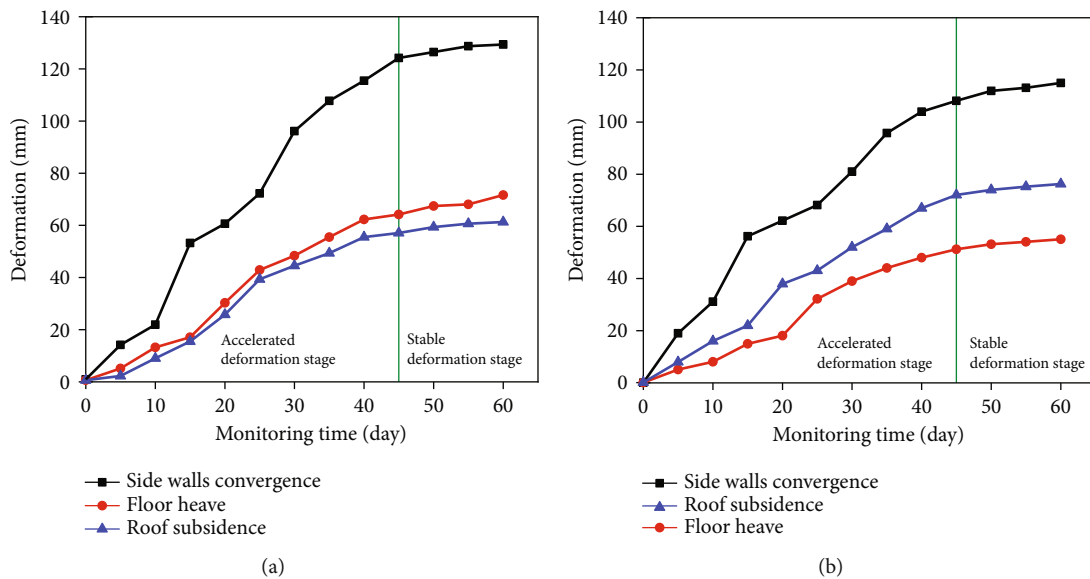


FIGURE 22: Surface convergence of haulage roadway at different monitoring points. (a) 2# monitoring point; (b) 4# monitoring point.

haulage roadway was rectangular with a width of 5.0 m and a height of 3.6 m. The specific support parameter design is shown as follows.

Whole section bolt-cable high strength support. Sixteen $\Phi 22 \text{ mm} \times 2200 \text{ mm}$ high-strength bolts were installed in the roof and two sides with the row spacing and column

spacing of $900 \text{ mm} \times 850 \text{ mm}$ and $800 \text{ mm} \times 850 \text{ mm}$. Three $\Phi 22 \text{ mm} \times 2200 \text{ mm}$ high-strength bolts were installed on the floor with the row spacing and column spacing of $1350 \text{ mm} \times 850 \text{ mm}$. The bolts installed in the top and bottom of the two sides were inclined at 15° . Nine $\Phi 18.9 \text{ mm} \times 8500 \text{ mm}$ high-strength cables were installed in the roof, two sides,

TABLE 7: Surface convergence of surrounding rock.

Time (d)	Roof subsidence (mm)	Floor heave (mm)	Side walls convergence (mm)
0	0	0	0
5	8	5	19
10	16	8	31
15	22	15	56
20	38	18	62
25	43	32	68
30	52	39	81
35	59	44	96
40	67	48	104
45	72	51	108
50	74	53	112
55	75	54	113
60	76	55	115

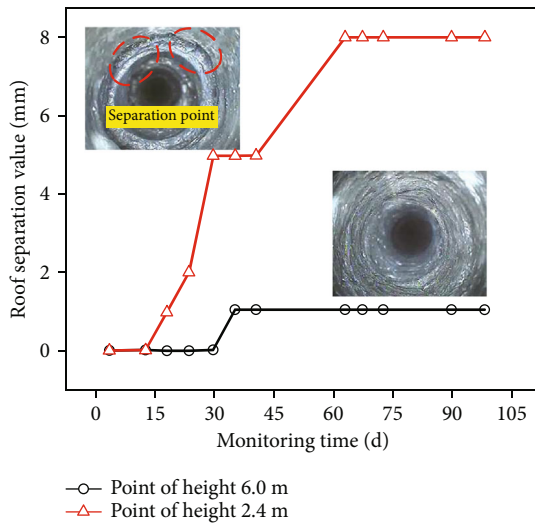


FIGURE 23: Separation monitoring of the roof with different heights.

and floor with the row spacing and column spacing of 1800 mm \times 1700 mm, 3200 mm \times 1700 mm, and 3600 mm \times 1700 mm, respectively. The longitudinal connection along the roadway was adopted between two roof cables by the rebar beam, while vertical connection for the two sides cables. Cables installed in the top and bottom of the two sides were inclined at 60°. Bolts were designed to be installed with a steel strip 4700 mm long for the roof and 3400 mm long for the two sides as well as the wire mesh with a grid size of 50 mm \times 50 mm. The limit anchorage force of bolts and cables was no less than 120 kN and 300 kN, respectively.

The waterproof anchoring agent with FSCK2340 \times 4 for cables and FSCK2340 \times 2 for bolts was applied to the roof to reduce the influence of mine water. The properties of bolts and cables are shown in Table 6.

Coal seam grouting reinforcement. Six Φ 25 mm \times 2000 mm hollow grouting anchors were symmetrically installed on the two sides with the row spacing and column spacing

of 1600 mm \times 1700 mm. The grouting bolts of the top and bottom were inclined at 60°. The grouting pressure was maintained at 0.6 MPa. As cement grout has the characteristics of environmental protection, economy, and good durability compared with chemical grout, cement grout is selected as the grouting material. The grouting material was mainly composed of cement, sand, water reducer, and water in a ratio of 1 : 1 : 0.01 : 0.32.

The strength and average thickness of the shotcrete in the roof was C30 and 40 mm, respectively. The drainage hole was drilled in the roof with a depth of 6000 mm and column spacing of 5100 mm. The concrete combined support scheme is shown in Figure 21.

5.3. WSHSWRT Engineering Application. WSHSWRT was applied to the B1002 haulage roadway of No.4 coal mine. Five sections of the roadway were selected to monitor the surface convergence, fracture, and separation state of the roof to obtain the supporting effect of the proposed support scheme. The layout of the five monitoring points is shown in Figure 21(b).

5.3.1. Deformation Monitoring. The roof subsidence, floor heave, and side wall convergence at the 2# and 4# monitoring points are shown in Figure 22. Monitoring results indicated that the deformation can be divided into two stages. (1) Accelerated deformation stage: the surface deformation increased obviously with the monitoring time within 47 days after roadway excavation, owing to the release of surrounding rock deformation energy under the effect of supporting structures. However, the deformation ratio decreased gradually. (2) Stable deformation stage: the surface deformation tended to be stable after the excavation for 47 days. As shown in Table 7, the final roof subsidence, floor heave, and side wall convergence are only in the range of 71 mm-76 mm with the average deformation rate of 0.4 mm/d, 55 mm-61 mm with the average deformation rate of 0.6 mm/d, and 115 mm-129 mm with the average deformation rate of 0.5 mm/d, respectively. From the above analysis, the deformation is within the allowable range, and the new supporting scheme can effectively control the large deformation of the haulage roadway.

5.3.2. Separation Monitoring. To evaluate the internal support effect of roof surrounding rock, the separation state of the roof at the 3# monitoring points with different heights of 2.4 m and 6.0 m was monitored by the separation instrument and JL-IDOI(A) electronic drilling peep instrument, as shown in Figure 23.

From Figure 23, it is seen that the maximum separation values of two monitoring points under WSHSWRT are only 1 mm with a height of 6.0 m and 8.0 mm with a height of 2.4 m after a 2-month roadway excavation, respectively. The above information indicated that the integrity of the roadway roof is good, and there will be no large-scale collapse and roof caving accidents. In other words, WSHSWRT can control the roof bed aspiration effectively and provide important maintenance for the long-term stability of the roof.

6. Conclusions

- (1) The surface deformation for the water-dripping roadway is noticeable and characterized by the large deformation and time-dependent properties during the roadway excavation, owing to the low strength support structure and the influence of mine water. The support structure failure, such as roof collapse, wire mesh tearing failure, and bolt corrosion failure, is not only related to unreasonable supporting structure and strength but also closely related to the weakening effect of mine water on the shallow mudstone
- (2) With the increase of moisture contents, the compressive strength nonlinearly decreases, while tensile strength, Young's modulus, cohesion, and friction angle have an approximately linear decrease. Therefore, the influence of mine water should be considered in the instability mechanism and support scheme design
- (3) With the increase of the weakening coefficient, the axial force of the anchorage body increases gradually from the anchorage initial point to the end of the bolt, while the maximum shear stress decreases gradually; when the weakening coefficient is small, the shear stress is mainly concentrated near the anchorage initial point, while the distribution of shear stress gradually transforms from the anchorage initial point to the whole length of the bolt with the increase of the weakening coefficient. The above analysis shows that the mine water not only affects the anchoring action of the bolt but also causes the redistribution of bolt axial force
- (4) WSHSWRT is proposed to adjust the stress state and improve the support strength of surrounding rock. Field monitoring results show that the proposed support technology can effectively control the harmful deformation of the surrounding rock and maintain the long-term stability of the roadway. The case provides an important reference for studies on the failure mechanism and control technology in water-dripping soft rock roadway

Data Availability

The data used to support the findings of this study are included within the article.

Conflicts of Interest

The authors declare that they have no conflicts of interest.

Acknowledgments

This work was financially supported by the National Natural Science Foundation of China (51974295, U1803118, 51974296, and 51704277) and the Fundamental Research Funds for the Central Universities (2015XKZD06).


References

- [1] M. C. He, "Rock mechanics and hazard control in deep mining engineering in China," in *Proceedings ISRM International Symposium 2006 4th Asian Rock Mechanics Symposium*, pp. 29–46, Singapore, SG, November 2006.
- [2] C. Q. Ma, P. Wang, L. S. Jiang, and C. S. Wang, "Deformation and control countermeasure of surrounding rocks for water-dripping roadway below a contiguous seam goaf," *Processes*, vol. 6, no. 7, p. 77, 2018.
- [3] P. Kang, L. Hong, Y. Fazhi, Z. Quanle, S. Xiao, and L. Zhaopeng, "Effects of temperature on mechanical properties of granite under different fracture modes," *Engineering Fracture Mechanics*, vol. 226, p. 106838, 2020.
- [4] S. Q. Yang, M. Chen, H. W. Jing, K. F. Chen, and B. Meng, "A case study on large deformation failure mechanism of deep soft rock roadway in Xin'an coal mine, China," *Engineering Geology*, vol. 217, pp. 89–101, 2017.
- [5] D. Ma, J. J. Wang, X. Cai et al., "Effects of height/diameter ratio on failure and damage properties of granite under coupled bending and splitting deformation," *Engineering Fracture Mechanics*, vol. 220, p. 106640, 2019.
- [6] Y. Xue, F. Gao, X. G. Liu, and X. Liang, "Permeability and pressure distribution characteristics of the roadway surrounding rock in the damaged zone of an excavation," *International Journal of Mining Science and Technology*, vol. 27, no. 2, pp. 211–219, 2017.
- [7] Q. Wang, R. Pan, B. Jiang et al., "Study on failure mechanism of roadway with soft rock in deep coal mine and confined concrete support system," *Engineering Failure Analysis*, vol. 81, pp. 155–177, 2017.
- [8] X. F. Li, S. B. Wang, R. Malekian, S. Q. Hao, and Z. X. Li, "Numerical simulation of rock breakage modes under confining pressures in deep mining: an experimental investigation," *IEEE Access*, vol. 4, pp. 5710–5720, 2016.
- [9] C. R. Zhang, X. C. Yang, G. F. Ren, B. Ke, and Z. L. Song, "Instability of gypsum mining goaf under the influence of typical faults," *IEEE Access*, vol. 7, pp. 88635–88642, 2019.
- [10] L. Zhu, Q. L. Yao, Z. Xia, W. N. Wang, and X. H. Li, "Study on the movement characteristics of the overlying stratum and surrounding rock control in ultraclose coal seams: a case study," *Energy Science & Engineering*, vol. 8, no. 4, pp. 1231–1246, 2020.
- [11] C. Mark, W. Gale, D. Oyler, and J. Chen, "Case history of the response of a longwall entry subjected to concentrated horizontal stress," *International Journal of Rock Mechanics and Mining Sciences*, vol. 44, no. 2, pp. 210–221, 2007.
- [12] B. T. Shen, "Coal mine roadway stability in soft rock: a case study," *Rock Mechanics and Rock Engineering*, vol. 47, no. 6, pp. 2225–2238, 2014.
- [13] S. B. Tang and C. A. Tang, "Numerical studies on tunnel floor heave in swelling ground under humid conditions," *International Journal of Rock Mechanics and Mining Sciences*, vol. 55, no. 10, pp. 139–150, 2012.
- [14] C. González-Nicieza, A. E. Álvarez-Vigil, A. Menéndez-Díaz, and C. González-Palacio, "Influence of the depth and shape of a tunnel in the application of the convergence-confinement method," *Tunnelling and Underground Space Technology*, vol. 23, no. 1, pp. 25–37, 2008.
- [15] R. Pan, Q. Wang, B. Jiang et al., "Failure of bolt support and experimental study on the parameters of bolt-grouting for

- supporting the roadways in deep coal seam,” *Engineering Failure Analysis*, vol. 80, pp. 218–233, 2017.
- [16] D. Ma, H. Y. Duan, X. B. Li, Z. H. Li, Z. L. Zhou, and T. B. Li, “Effects of seepage-induced erosion on nonlinear hydraulic properties of broken red sandstones,” *Tunnelling and Underground Space Technology*, vol. 91, p. 102993, 2019.
- [17] S. M. Chen, A. Wu, Y. Wang, X. Chen, R. Yan, and H. Ma, “Study on repair control technology of soft surrounding rock roadway and its application,” *Engineering Failure Analysis*, vol. 92, pp. 443–455, 2018.
- [18] K. Peng, Y. Q. Wang, Q. L. Zou, Z. P. Liu, and J. H. Mou, “Effect of crack angles on energy characteristics of sandstones under a complex stress path,” *Engineering Fracture Mechanics*, vol. 218, p. 106577, 2019.
- [19] W. J. Yu, B. Pan, F. Zhang, S. F. Yao, and F. F. Liu, “Deformation characteristics and determination of optimum supporting time of alteration rock mass in deep mine,” *KSCE Journal of Civil Engineering*, vol. 23, no. 11, pp. 4921–4932, 2019.
- [20] L. Sun, H. Wu, B. Yang, and Q. Li, “Support failure of a high-stress soft-rock roadway in deep coal mine and the equalized yielding support technology: a case study,” *International Journal of Coal Science & Technology*, vol. 2, no. 4, pp. 279–286, 2015.
- [21] P. Lin, H. Y. Liu, and W. Y. Zhou, “Experimental study on failure behaviour of deep tunnels under high in-situ stresses,” *Tunnelling and Underground Space Technology*, vol. 46, pp. 28–45, 2015.
- [22] L. Jiang, P. Wang, P. Zheng, H. Luan, and C. Zhang, “Influence of different advancing directions on mining effect caused by a fault,” *Advances in Civil Engineering*, vol. 2019, Article ID 7306850, 10 pages, 2019.
- [23] W. Fangtian, Z. Cun, W. Shuaifeng, Z. Xiaogang, and G. Shenghua, “Whole section anchor-grouting reinforcement technology and its application in underground roadways with loose and fractured surrounding rock,” *Tunnelling and Underground Space Technology*, vol. 51, pp. 133–143, 2016.
- [24] H. Yu, L. G. Kong, Z. Y. Niu, S. T. Zhu, and D. Y. Jing, “Numerical simulation of bolt-mesh-anchor support technology at soft rock roadway,” *Advanced Materials Research*, vol. 868, pp. 251–254, 2013.
- [25] X. Chang, Y. Y. Wei, and Y. C. Yun, “Analysis of steel-reinforced concrete-filled-steel tubular (SRCFST) columns under cyclic loading,” *Construction and Building Materials*, vol. 28, no. 1, pp. 88–95, 2012.
- [26] Y. Wu, Y. Hao, J. Tao, Y. Teng, and X. Dong, “Non-destructive testing on anchorage quality of hollow grouted rock bolt for application in tunneling, lessons learned from their uses in coal mines,” *Tunnelling and Underground Space Technology*, vol. 93, article 103094, 2019.
- [27] H. B. Ge and T. Usami, “Strength analysis of concrete-filled thin-walled steel box columns,” *Journal of Constructional Steel Research*, vol. 30, no. 3, pp. 259–281, 1994.
- [28] Y. Y. Jiao, L. Song, X. Z. Wang, and A. Coffi Adoko, “Improvement of the U-shaped steel sets for supporting the roadways in loose thick coal seam,” *International Journal of Rock Mechanics and Mining Sciences*, vol. 60, pp. 19–25, 2013.
- [29] D. Ma, J. J. Wang, and Z. H. Li, “Effect of particle erosion on mining-induced water inrush hazard of karst collapse pillar,” *Environmental Science and Pollution Research*, vol. 26, no. 19, pp. 19719–19728, 2019.
- [30] Y. Sun, G. Li, J. Zhang, and D. Qian, “Experimental and numerical investigation on a novel support system for controlling roadway deformation in underground coal mines,” *Energy Science & Engineering*, vol. 8, no. 2, pp. 490–500, 2020.
- [31] Z. Yin, W. Chen, H. Hao et al., “Dynamic compressive test of gas-containing coal using a modified Split Hopkinson pressure bar system,” *Rock Mechanics and Rock Engineering*, vol. 53, no. 2, pp. 815–829, 2020.
- [32] P. Wang, L. S. Jiang, P. Q. Zheng, G. P. Qin, and C. Zhang, “Inducing mode analysis of rock burst in fault-affected zone with a hard-thick stratum occurrence,” *Environmental Earth Sciences*, vol. 78, no. 15, 2019.
- [33] F. Zhang, L. Liu, J. Cao, X. Yan, and F. Zhang, “Mechanism and application of concrete-filled steel tubular support in deep and high stress roadway,” *Construction and Building Materials*, vol. 186, pp. 233–246, 2018.
- [34] C. Li, J. H. Xu, C. S. Fu, R. Wu, and Q. Q. Ma, “Mechanism and practice of rock control in deep large span cut holes,” *Mining Science and Technology (China)*, vol. 21, no. 6, pp. 891–896, 2011.
- [35] H. L. Liu, W. C. Zhu, Y. J. Yu, T. Xu, R. F. Li, and X. G. Liu, “Effect of water imbibition on uniaxial compression strength of sandstone,” *International Journal of Rock Mechanics and Mining Sciences*, vol. 127, article 104200, 2020.

Research Article

Investigation on Nonlinear Flow Behavior through Rock Rough Fractures Based on Experiments and Proposed 3-Dimensional Numerical Simulation

Xianshan Liu ^{1,2}, Man Li,^{1,2} Nandou Zeng,^{1,2} and Tao Li^{1,2}

¹Key Laboratory of New Technology for Construction of Cities in Mountain Area (Chongqing University), Ministry of Education, Chongqing 400045, China

²School of Civil Engineering, Chongqing University, Chongqing 400045, China

Correspondence should be addressed to Xianshan Liu; lzmoumou@163.com

Received 23 June 2020; Revised 1 August 2020; Accepted 10 August 2020; Published 12 November 2020

Academic Editor: Richeng Liu

Copyright © 2020 Xianshan Liu et al. This is an open access article distributed under the Creative Commons Attribution License, which permits unrestricted use, distribution, and reproduction in any medium, provided the original work is properly cited.

Rock fractures as the main flow channels, their morphological features, and spatial characteristics deeply influence the seepage behavior. Reservoir sandstones as a case study, four splitting groups of fractures with different roughness were scanned to get the geometric features, and then the seepage experiments were taken to analyze the relationship of the pressure gradient ∇P and flow rate Q , and the critical Reynolds number (Re_c) and wall friction factor (f) were determined to explain the translation of linear seepage to nonlinear seepage condition. Based on the scanning cloud data of different rough fractures, the fractures were reconstructed and introduced into the COMSOL Multiphysics software; a 3-dimensional seepage model for rough fractures was calibrated and simulated the seepage process and corresponding pressure distribution, and explained the asymmetry of flow velocity. And also, the seepage characteristics were researched considering aperture variation of different sample fractures; the results indicated that increasing aperture for same fracture decreased the relative roughness, the fitting coefficients by Forchheimer formula based on the data $\nabla P \sim Q$ decreased, and the figures about the coefficients and corresponding aperture described nonlinear condition of the above rough fractures. In addition, the expression of wall friction factor was derived, and relationship of f , Re_c and relative roughness indicated that f increased with increasing fracture roughness considering the same aperture, resulting in nonlinear flow more easily, otherwise is not, showing that f could be used to describe the seepage condition and corresponding turning point. Finally, it can be seen from the numerical results that the nonlinearity of fluid flow is mainly caused by the formation of eddies at fracture intersections and the critical pressure gradient decreases with increasing angle. And also, analysis about the coefficient B in the Forchheimer law corresponding to fracture intersections considering the intersecting angle and surface roughness is proposed to reveal the flow nonlinearity. The above investigations give the theoretical support to understand and reveal the seepage mechanism of the rock rough fractures.

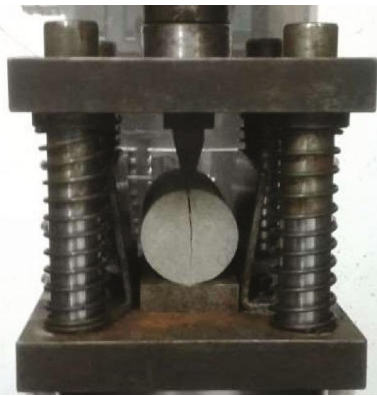
1. Introduction

Rock fractures are common in the field of the rock engineering. And the fractures as the controlled seepage channels play an important role on the groundwater assessment, oil and gas development, and mass transportation; how to solve the flow behavior through the complex fractures is key to above engineering [1].

And many researches indicate that natural fractures with complex morphology form tortuous seepage channels to influence the seepage behavior. Some researchers such as Babadagli et al. [2] and Singh et al. [3] have researched the cubic law to describe the low-velocity flow in the fractures considering the fracture morphology. Considering the flow velocity increasing, Yuan et al. [4] and Zimmerman et al. [5] have conducted flow tests and explained the flow



(a) Sandstones samples



(b) Brazilian test



(c) Fracture surface after the Brazilian testing

FIGURE 1: Arrangement of rock rough fractures.

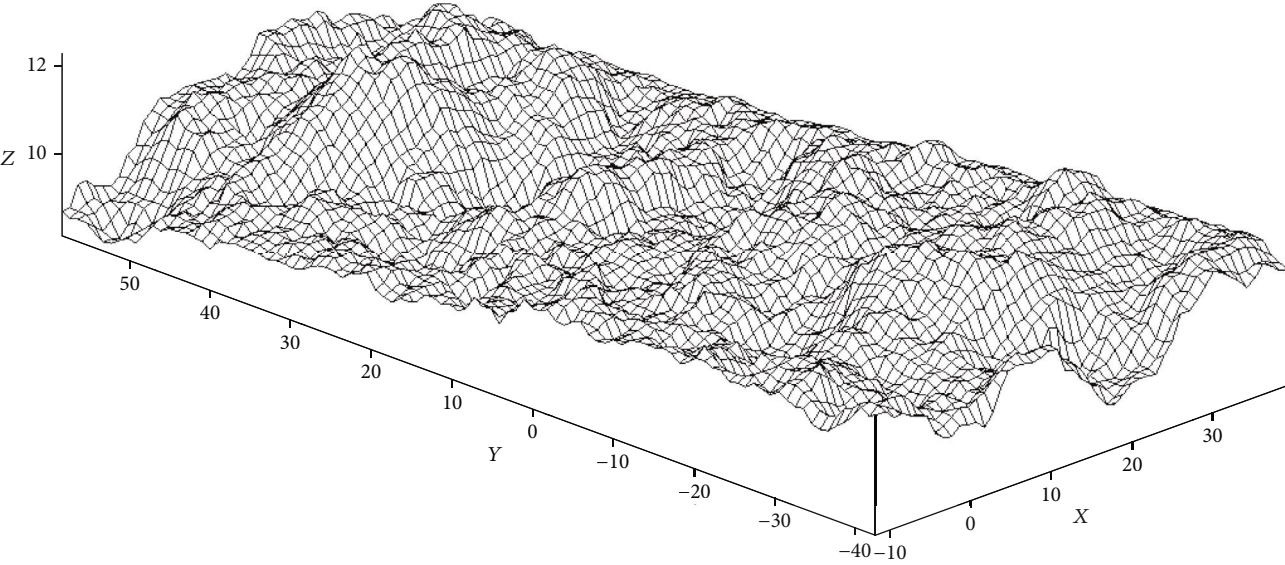
nonlinearity, indicating that greater flow velocity in the rough fractures and wall friction coefficient enlarge the inertial forces to show nonlinear flow behavior; therefore, the cubic law considering the viscous forces cannot be applicable for the flow through the rough fractures, especially under higher flowing conditions.

In recent years, many researchers have conducted nonlinear flow tests, theories, and numerical simulations; Ranjith and Darlington [6], Qian et al. [7], Zhang and Nemcik [8], Zoorabadi et al. [9] Chen and Zhou [10], and Xiong et al. [11] have conducted flow tests considering different fracture roughness of a large amount of rocks to analyze the influence of the fracture roughness on the flow nonlinearity under loading and unloading conditions, revealing the seepage mechanism of the nonlinear flow behavior through the rough fractures. The testing achievements mentioned above give supports to set up a rational model to describe the flow nonlinearity. Therefore, some researchers have proposed a few theoretical models such as seepage cavity model by Weimin et al. [12], improved cubic model by Hongguang et al. [13], T model similar to the Forchheimer model by Javadi et al. [14], and a model based on corrected Reynolds equation by Lee et al. [15] to illuminate the seepage characteristics. However, the theoretical models with many simplifications cannot completely describe the nonlinear flow behavior through the rough fractures. Therefore, numerical simulations based on the experiments and theories have been developed for complex flow behavior through the rough fractures.

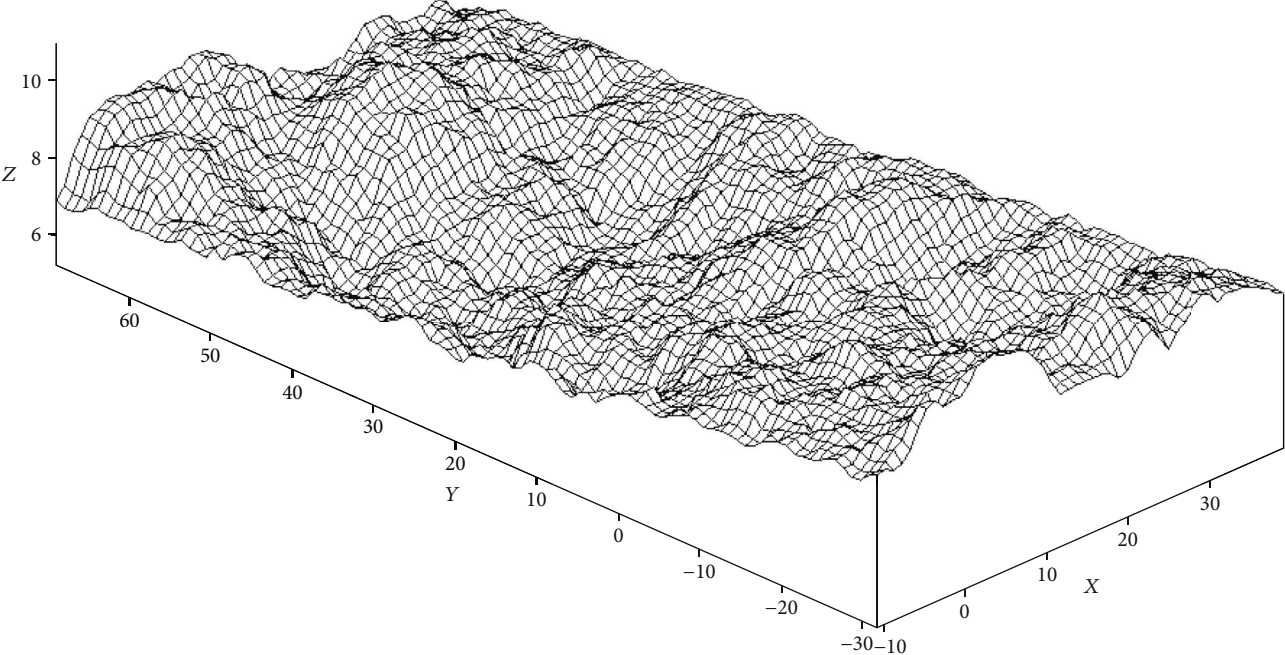
Wang et al. [16] and Zou et al. [17] have proposed some numerical models based on Boltzmann and Fluent software to analyze the flow nonlinearity in the rough fractures.

Furthermore, the above tests, theoretical analysis, and numerical simulations have given many useful achievements for deep investigation of the flow behavior through the complex fractures. However, rougher fracture surfaces may influence on the friction loss, inertial forces, and seepage behavior, while the fluid flowing through rough fractures. Nazridoust et al. [18], Yang et al. [19], Zhang et al. [20], Zhou et al. [21], and Xiaopeng et al. [22] have conducted experiments and theories to propose the seepage model considering wall friction effect and reveal the evolution mechanism of the fluid flow in rough fractures considering the wall friction effect, which deeply explains that the seepage mechanism of the flow through rough fractures especially represents the transformation of the seepage behavior from the linearity to the nonlinearity while the fracture roughness and flow velocity change suddenly. However, above investigations are focused on flow behavior through the 2-dimensional fractures; advanced research on the flow characteristics in 3-dimensional fractures should be deeply conducted.

In addition, when fluid is injected into a fracture intersection, the flow pressure and flow rate distribution are affected by many factors such as fluid properties [23], fracture intersection angle [24, 25], fracture surface roughness [23], and pressure gradient [26]. The fluid flow behavior derived for a single fracture [27–29] is not applicable to the case of fracture



(a) Specimen S1: $\Delta = 0.58$ mm



(b) Specimen S2: $\Delta = 0.86$ mm

FIGURE 2: Continued.

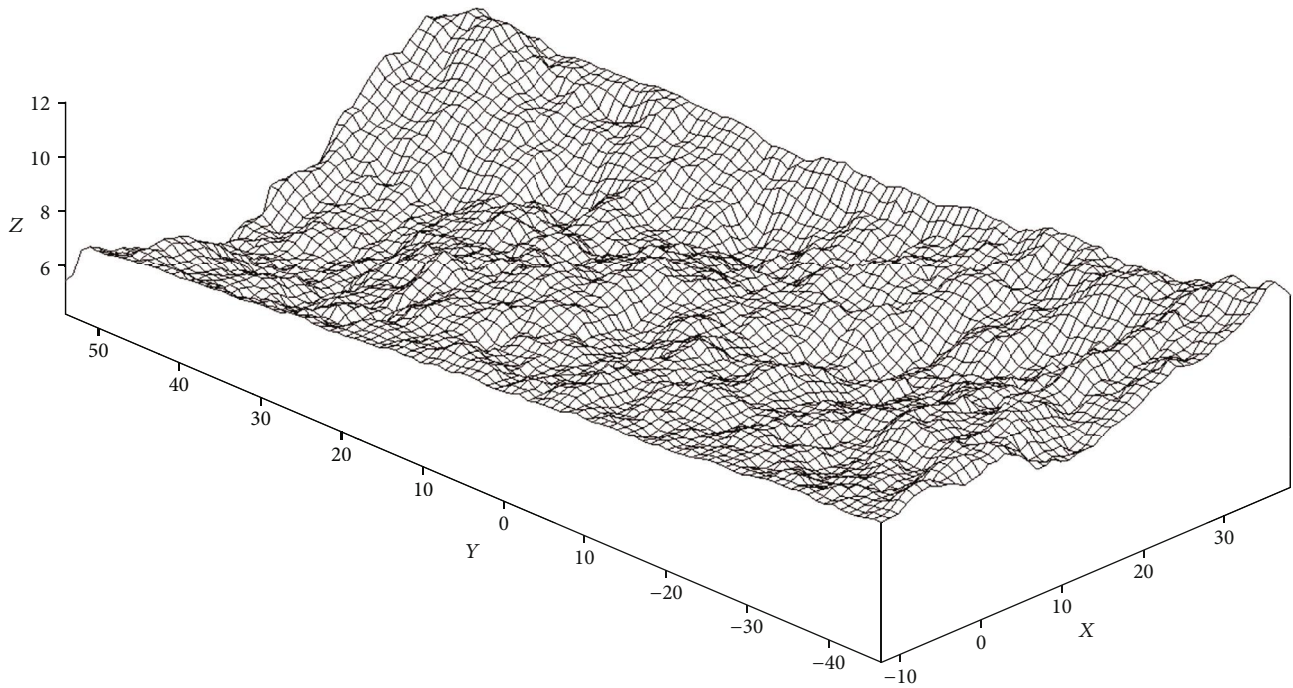
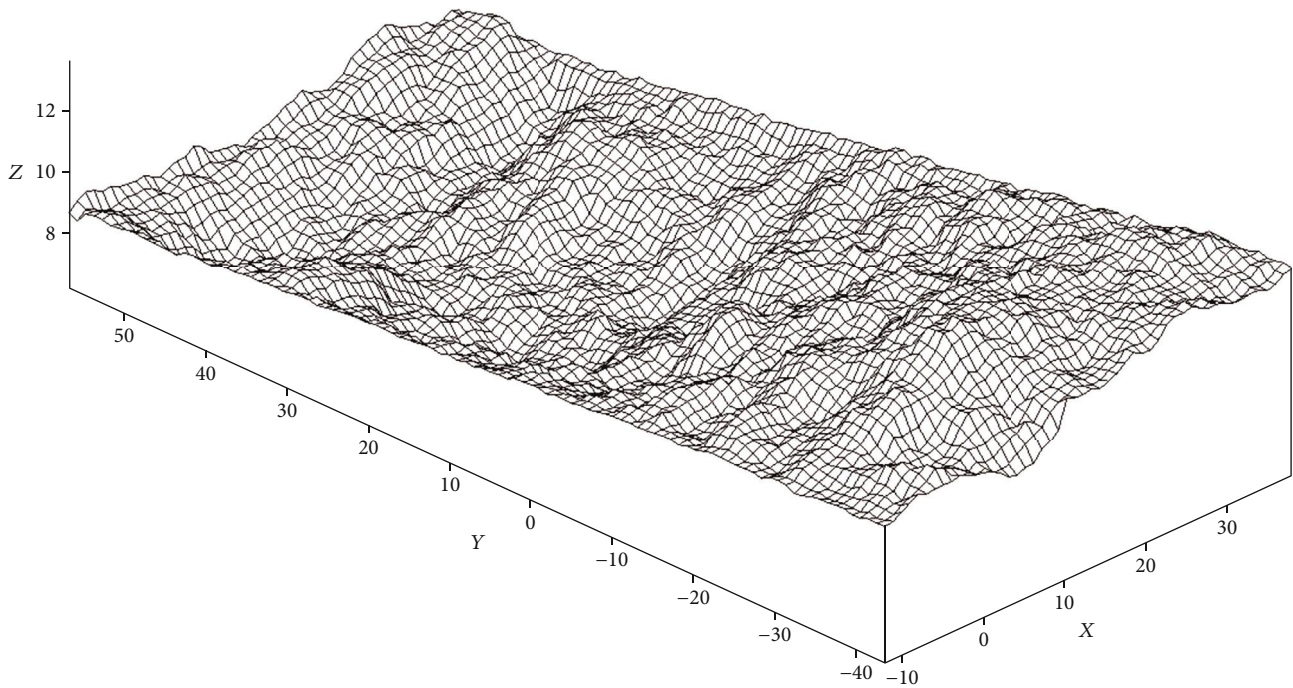
(c) Specimen S3: $\Delta = 1.01$ mm(d) Specimen S4: $\Delta = 1.59$ mm

FIGURE 2: 3-dimensional morphology reconstruction of rough fracture of specimens S1-S4.

intersections, especially when the nonlinear flow regime is considered. Numerical simulations have been performed by Liu et al. [30] and Xiong et al. [31] to estimate the effects of fracture intersections on the nonlinear flow behaviors in crossing fractures. It is found that a nonlinear flow regime occurs in which the inertial effects caused by the fracture intersections should not be neglected. Although many studies described have been conducted experimentally and numeri-

cally, the influence mechanisms of fracture intersection angle and roughness on fluid flow behavior are rarely discussed. In addition, the corresponding nonlinear flow model is also rarely reported.

Although many studies described were conducted experimentally, theoretically, and numerically, the flow through 3-dimensional rough fractures considering the space distribution has not been deeply investigated. Taking a reservoir

TABLE 1: Geometric parameters of the rough fractures.

Specimen no.	Length L (mm)	Diameter D (mm)	Average aperture b_m (mm)	Absolute roughness Δ (mm)	Relative roughness (Δ/b_m)
S1	100.04	50.08	0.87	0.58	0.67
S2	99.94	50.04	1.26	0.86	0.68
S3	100.08	50.01	0.64	1.01	1.58
S4	100.02	49.98	0.99	1.59	1.61



FIGURE 3: Triaxial multifield coupling test system.

sandstone as a case study, fractures with different roughness are formed and scanned the point cloud data to obtain the key parameters describing the rough fracture. And then, flow tests have been conducted on these fracture models and the corresponding numerical simulations have been carried out by solving the Navier-Stokes equations based on software COMSOL Multiphysics to characterize the nonlinear relationship and flow distribution behavior. And also, groups of 3-dimensional fracture intersections have been studied with particular focus on the nonlinear flow behavior. And semi-empirical expressions for the nonlinear term in the Forchheimer law have been proposed for different cases of rough fractures and fracture intersections, revealing the flow non-linearity of 3-D rough fractures. The achievements can help to verify all kinds of seepage theories, especially promoting the general application in corresponding engineering.

2. Flow Tests of Rock Rough Fractures

2.1. Preparation of Rock Rough Fractures. The testing sandstones taken from western Xindianzi anticline in Chongqing City are selected for the experimental study considering different seepage designs. It is observed from Figure 1(a) that the sandstone is gray and white, and the size of all tested sandstone specimens is cylindrical with 50 mm in diameter and 100 mm in length approximately according to the method by the International Society for Rock Mechanics (ISRM). And then, the Brazilian test plotted in (Figure 1(b)) is taken to obtain the artificial rough fractures. As for this testing process, the prepared samples are placed in the special clamp and then loaded with different loading rates to form fractures with obvious roughness plotted in Figure 1(c). And greater loading rate

causes stress concentration to form fractures with smaller waviness and roughness; otherwise, the fractures with rougher surface are formed normally.

2.2. Acquisition and Analysis of 3-D Morphology of the Rough Fractures. Four different groups of splitting sandstone fractures mentioned above with different roughness named S1, S2, S3, and S4 are selected for laser scanning system to get the geometric morphology. And the laser scanning system is composed by the 3-dimensional noncontact optical scanner named OKIO-B and corresponding scanning software, so it can be taken to scan the fracture surface contactlessly to obtain high precision and large amount of data and exhibit the real-time photographs to get the point cloud data of the 3-dimensional fracture surface. Furthermore, the point cloud data based on the scanning system are optimized by noise reduction and patching and then imported to the software Surfer to reconstruct the 3-dimensional fracture surface [24] plotted in Figures 2(a)–2(d) (unit: mm).

In addition, the above point cloud data is changed into Cartesian coordinates, suppose Z_T, Z_B as the coordinates of the upper surface and the lower surface in Z direction considering the upper surface and lower surface of the fractures in the same coordinates system, as in the following equations.

$$Z_T = \begin{pmatrix} Z_{T11} & \cdots & Z_{T1n} \\ \vdots & \ddots & \vdots \\ Z_{Tm1} & \cdots & Z_{Tmn} \end{pmatrix}, \quad (1)$$

$$Z_B = \begin{pmatrix} Z_{B11} & \cdots & Z_{B1n} \\ \vdots & \ddots & \vdots \\ Z_{Bm1} & \cdots & Z_{Bmn} \end{pmatrix}, \quad (2)$$

where, Z_{Tij}, Z_{Bij} are the coordinates in Z direction at nodes (i, j) in a common coordinate system for upper and lower fracture surfaces, respectively. So, the fracture aperture (F_r) can be written by the following equations.

$$F_r = Z_T - Z_B, \quad (3)$$

$$F_r = \begin{pmatrix} b_{11} & \cdots & b_{1n} \\ \vdots & \ddots & \vdots \\ b_{m1} & \cdots & b_{mn} \end{pmatrix}, \quad (4)$$

where b_{ij} is the fracture aperture at nodes (i, j) , which is the subtraction of Z_{Tij}, Z_{Bij} shown in the following equation.

$$b_{ij} = Z_{Tij} - Z_{Bij} \geq 0. \quad (5)$$

So the average aperture b_m of the 3-dimensional fracture surface can be written by

$$b_m = \frac{1}{m \times n} \sum_{i=1}^m \sum_{j=1}^n b_{ij}. \quad (6)$$

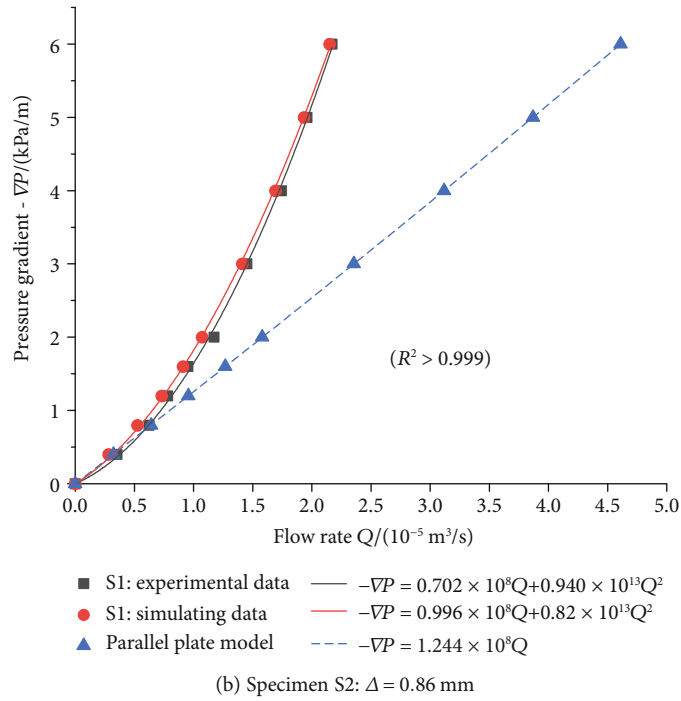
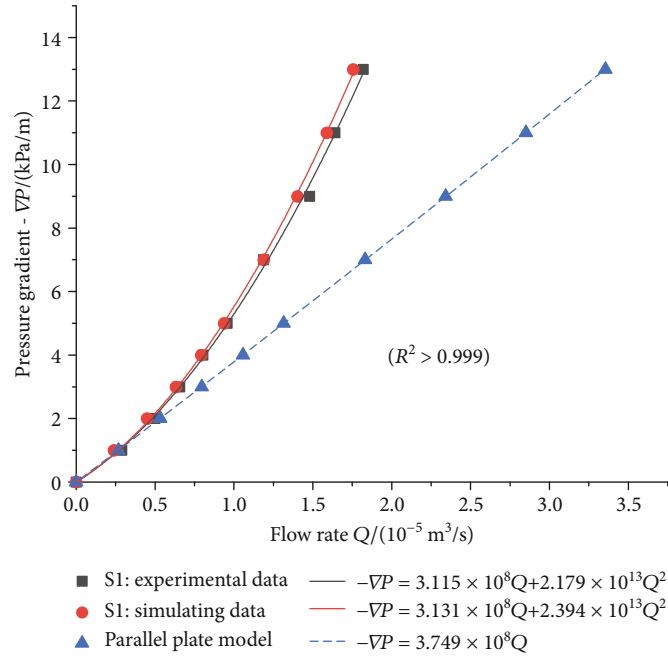


FIGURE 4: Continued.

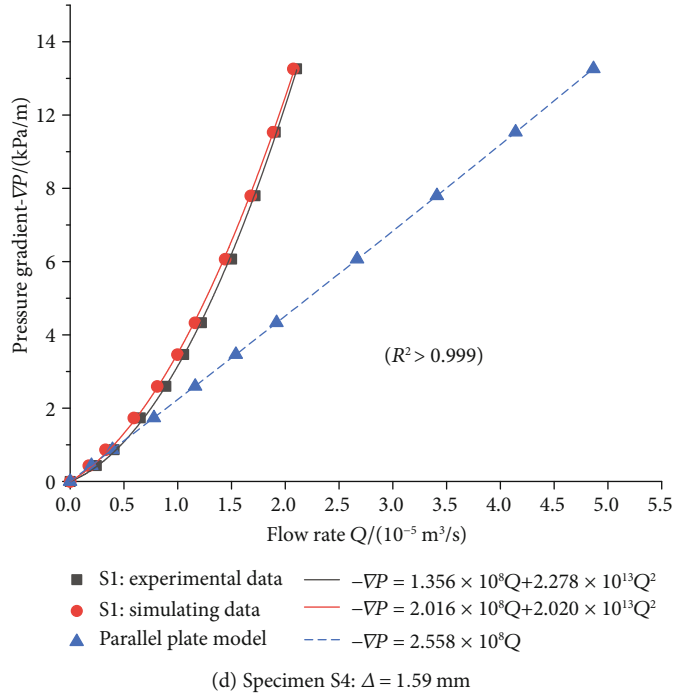
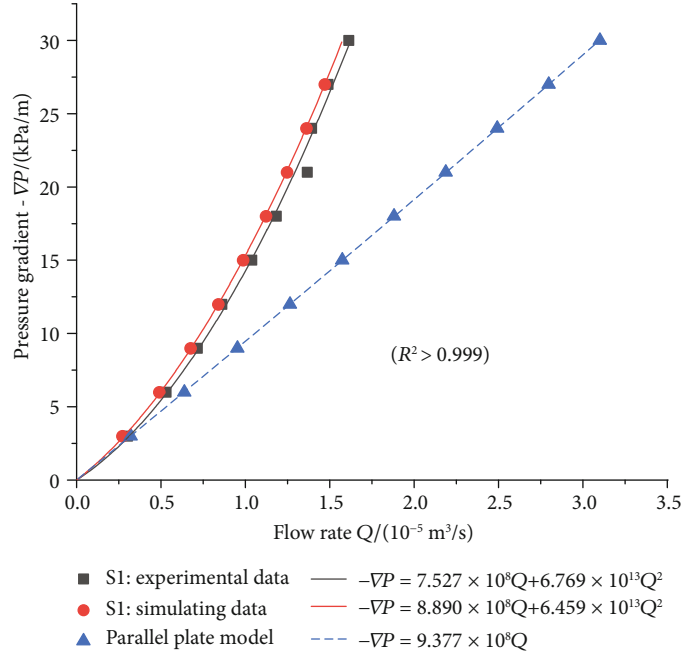


FIGURE 4: Curves of $\nabla P - Q$ for specimens S1-S4.

And then, based on the point cloud data calculated by Equations (1) and (2), the average surface Z coordinates (\bar{Z}_T) and absolute roughness (Δ_T) may be, respectively, obtained by Equations (7) and (8) for upper fracture surfaces. Similarly, the absolute roughness of the lower fracture surface (Δ_B) can be obtained.

$$\bar{Z}_T = \frac{1}{(m+1)(n+1)} \sum_{i=0}^m \sum_{j=0}^n Z_{Tij}, \quad (7)$$

$$\Delta_T = \frac{1}{(m+1)(n+1)} \sum_{i=0}^m \sum_{j=0}^n |Z_{Tij} - \bar{Z}_T|. \quad (8)$$

Thus, the average absolute roughness of fracture surface (Δ) for upper and lower fracture surfaces can be calculated by Equation (9). The average aperture, absolute average roughness, and relative roughness for the samples

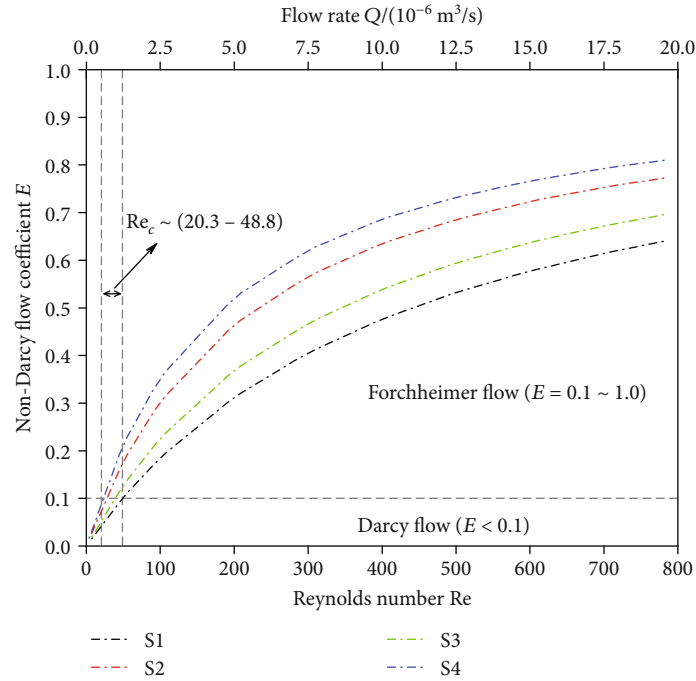


FIGURE 5: Variation of non-Darcy coefficient of fracture surface for samples S1-S4.

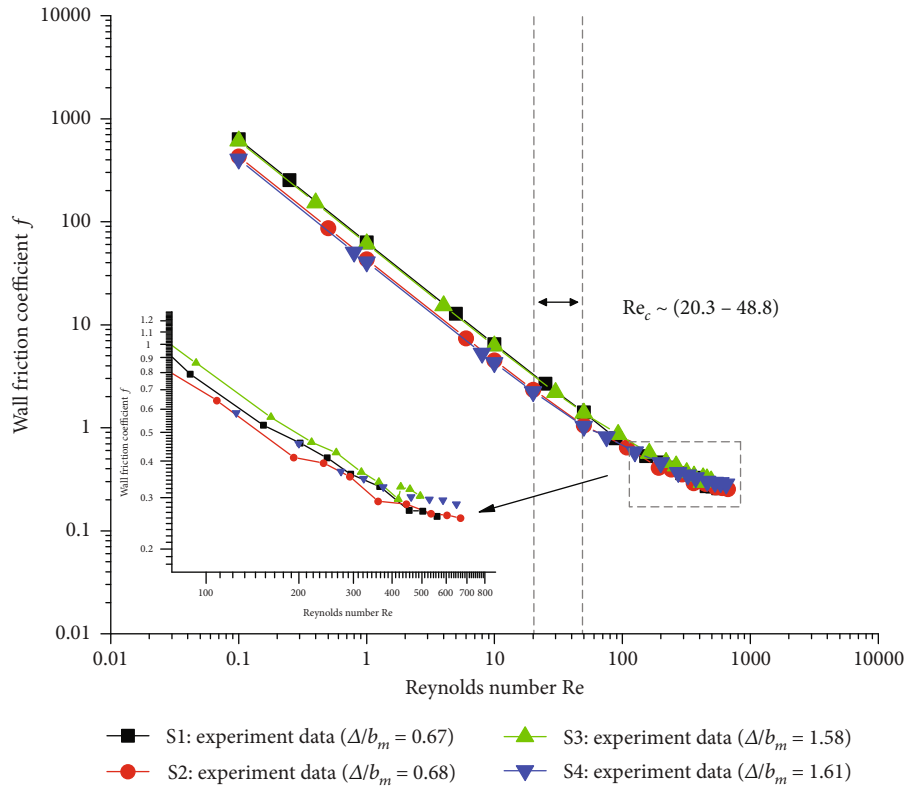


FIGURE 6: Wall friction coefficient of rough fractures for specimens S1-S4.

S1, S2, S3, and S4 are shown in Table 1.

$$\Delta = \frac{\Delta_T + \Delta_B}{2}. \quad (9)$$

2.3. *The Procedure of the Flow Test about the Rock Rough Fractures.* All tests will be carried out on a rock servocontrolled triaxial equipment named Rock 600-50HT PLUS manufactured by TOP INDUSTRIE in France plotted in

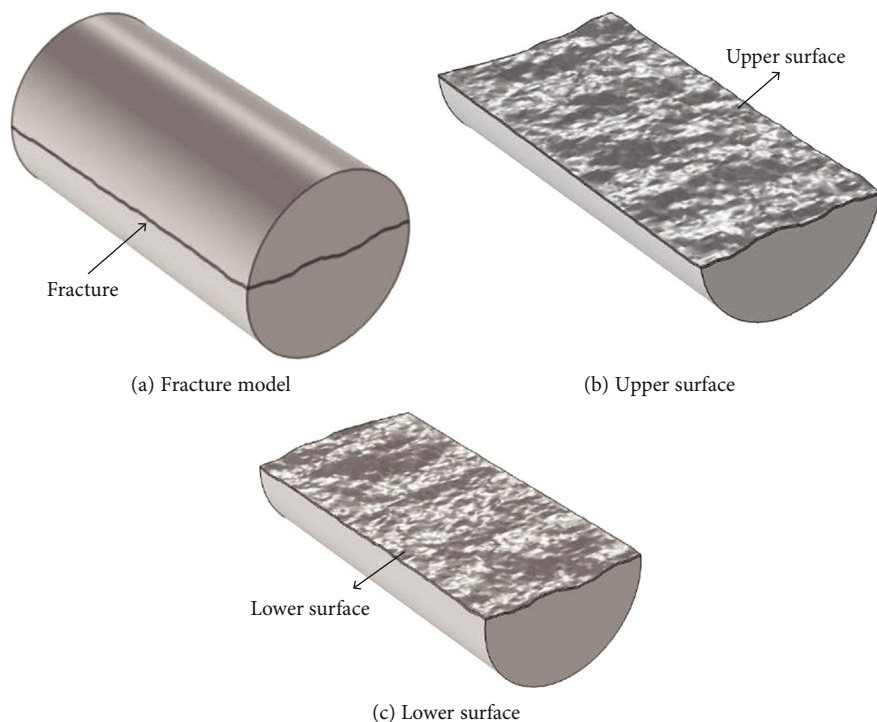


FIGURE 7: Physical model of rough fractured for specimen S1.

Figure 3. The triaxial cell is capable of performing triaxial compression tests at confining pressures (P_2) up to 60 MPa, with increasing deviatoric stress (P_1) up to 500 MPa, with increasing transducer that has a resolution of 0.01 MPa. The system can deal with the constant head, constant flow rate, and transient pulse permeability tests under low or high confining and water pressures, and a high-precision electronic balance is selected to measure the real-time flow rate [27]. The servocontrolled fluid pump can produce pore pressure up to 60 MPa (P_3/P_4). Furthermore, the upstream and downstream fluid pressures can be regulated with pore pressure pumps P_3 and P_4 ; as a result, the seepage tests can be performed on constant fluid pressure or constant volume condition according to the experimental target.

As for the flow procedure, the sandstone specimens are firstly saturated, then vacuumized for 4 hours by the vacuum pump, wet pumped for 4 hours with distilled water, and finally soaked for 16 hours to ensure the specimens are full of water. And then, the specimens are enclosed in a 3 mm thick Viton rubber jacket and then placed in the sample assembly. Porous spacers are inserted on to the ends of the samples to ensure even distribution of pore pressure over the ends of the samples. Considering the influence of the temperature on deformation and seepage response, all the tests are all performed at room temperature ($25 \pm 2^\circ\text{C}$). The seepage tests under different load combinations can be performed as follows. The samples are firstly applied with the confining pressure of the desired value, and in this stage, the axial stress is proportionally increased to the value of the confining pressure, bringing the samples to an initial isotropic stress or zero deviatoric stress to ensure that there is no

gap between the specimen and the rubber jacket to prevent the fluid leakage. Furthermore, the saturated specimens are conducted at a constant pore pressure indicating the balance of the upstream pressure (P_3) and downstream pressure (P_4) to ensure the fluid in a single phase in the process of the seepage testing. Afterwards, water is introduced into the fractures through the inlet and collected at the outlet. A series of flow pressures at the inlet were tested and their corresponding flow rates were recorded. Therefore, the relationships between flow rate and pressure gradient or hydraulic gradient for the rough fractures can be obtained.

3. Analysis of Seepage Characteristic of 3-Dimensional Rough Fractures

3.1. Variation of the Pressure Gradient and Flow Rate of the Fractures. The testing data about the pressure gradient ∇P and the flow rate Q at the outlet for the specimens S1-S4 has been obtained and fitted into $\nabla P \sim Q$ curves plotted in Figure 4.

It can be observed from the comparisons plotted in Figures 4(a)–4(d) of $\nabla P \sim Q$ about the specimens S1-S4 (black curves) and the $\nabla P \sim Q$ about the parallel plate model (blue curves) that the flow behavior through the rough fractures has changed obviously. These results suggest that pressure gradient ∇P increases linearly initially and then nonlinearly inclined to the flow rate axis as the flow rate Q increases. It can be concluded that rough fractures with smaller pressure gradient, the fluid flow mainly shows viscous forces, then inertial forces when increasing the pressure gradient, especially the roughness of the fractures surface causing obvious friction effect increases the pressure loss to transform the

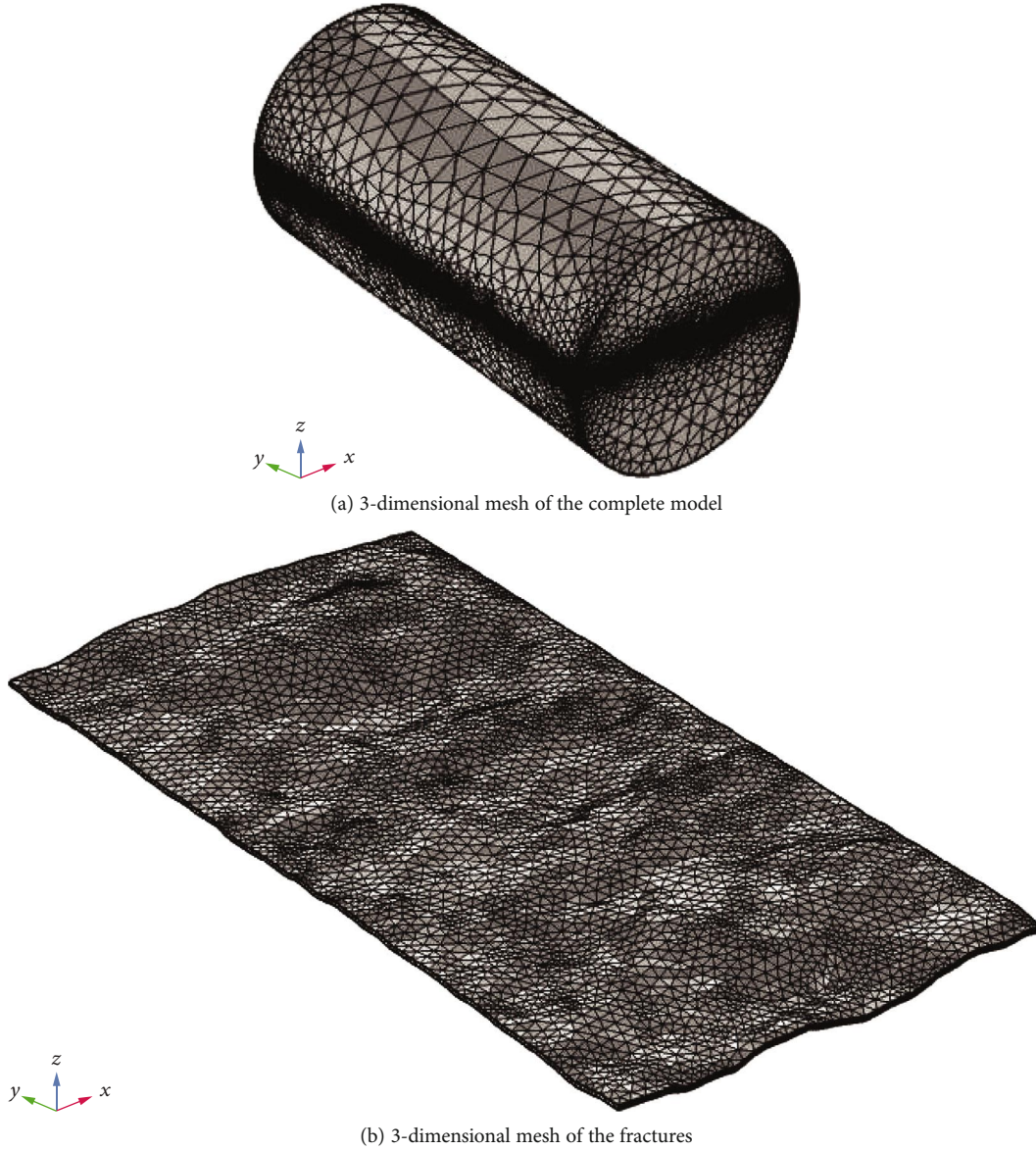


FIGURE 8: 3-dimensional numerical model of sample S1 with rough surface.

TABLE 2: Comparison of flow rate between the experiments and numerical simulation of specimen S1.

Pressure gradient ∇P (kPa/m)	Flow rate at outlet $Q(\times 10^5 \text{ m}^3/\text{s})$		
	Experimental value	Simulated value	Relative error
1	0.289	0.239	17.3%
2	0.499	0.449	10.0%
3	0.656	0.633	3.5%
4	0.803	0.794	1.1%
5	0.956	0.938	1.9%
7	1.188	1.189	0.1%
9	1.480	1.402	5.3%
11	1.642	1.589	3.2%
13	1.821	1.756	3.6%

linear flow to the nonlinear flow. In addition, it can be seen from the mentioned variation that in view of different average apertures and absolute roughness, the pressure gradient corresponding to the $\nabla P \sim Q$ deviating from the linear curves is also different, meaning that the critical pressure gradient is different for different rough fractures, indicating that the surface morphology is the key factor to influence on the seepage characteristics.

3.2. Nonlinear Characteristics of the Flow in Rough Fractures.

In can be seen from the curves $\nabla P \sim Q$ plotted in Figures 4(a)–4(d) that increasing inertial forces has controlled the seepage behavior while increasing the pressure gradient, so the relationship of the curves $\nabla P \sim Q$ is nonlinear and the cubic law only considering the viscous forces cannot be suitable to describe the flow nonlinear through the rough fractures. Therefore, the equation named Navier-Stokes (N-S)

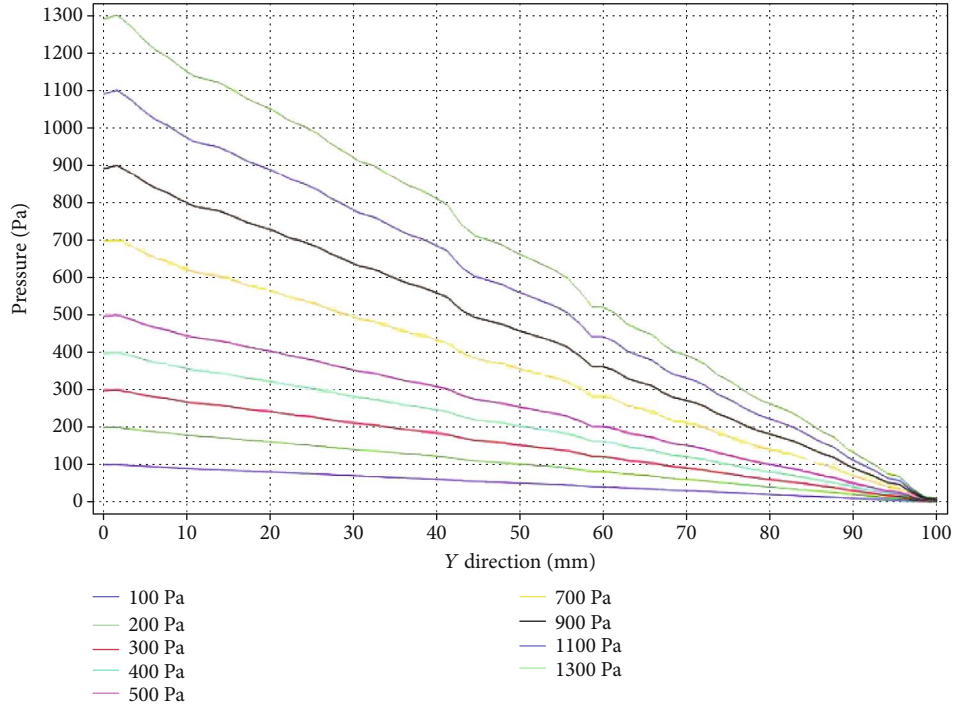


FIGURE 9: Distribution of seepage pressure on the fracture surface of specimen S1.

describing the complex flow is introduced to analyze the fracture flow. However, the solution about the complete N-S equation is very difficult; some researchers have proposed some rational models to quantitatively present the flow non-linear caused by the flow inertial forces, and the very common model named the Forchheimer model [10, 11] is as follows:

$$-\frac{dP}{dL} = AQ + BQ^2, \quad (10)$$

where AQ is the linear item by viscous forces, BQ^2 is the non-linear item by inertial forces, dP/dL is the pressure gradient (Pa/m), Q is the flow rate through the fractures, A, B represent the linear coefficients ($\text{kg}/(\text{m}^5 \cdot \text{s})$) and nonlinear coefficients (kg/m^8), $A = 12\mu/wb^3$, $B = \beta\rho/w^2b^2$, ρ is the fluid density (kg/m^3), w is the fracture width (m), μ is the dynamic viscosity, and b is the equivalent hydraulic aperture (m).

In addition, the Forchheimer model has been proposed to fit corresponding data of ∇P and Q for specimens S1-S4 based on flow tests; the fitting expressions with correlation coefficient 0.99 show a good agreement with the experimental results in Section 3.1, indicating that the Forchheimer model is used to represent the flow linearity considering viscous forces with smaller pressure gradient and flow nonlinearity considering inertial forces with greater pressure gradient, revealing the complete transformation of the linear flow to nonlinear flow in the rough fractures.

3.3. The Transformation of the Flow Behavior through the Rough Fractures. It can be seen that the curves $\nabla P \sim Q$ that the seepage behavior can be transformed from the linearity to the nonlinearity, so the transformation of the seepage

behavior should be deeply investigated to apply in the related geotechnical engineering. Reynolds number Re written by Equation (11) is an important parameter to describe the ratio of the inertial forces and the viscous forces, and the parameter reveals that Re will increase with greater flow velocity causing greater inertial forces to reflect the variation of the fluid density, viscous parameters, flow velocity, and flow paths, representing the transformation points of the seepage behavior while flowing in the rough fractures.

$$Re = \frac{\rho u D_h}{\mu} = \frac{2\rho Q}{\mu w}, \quad (11)$$

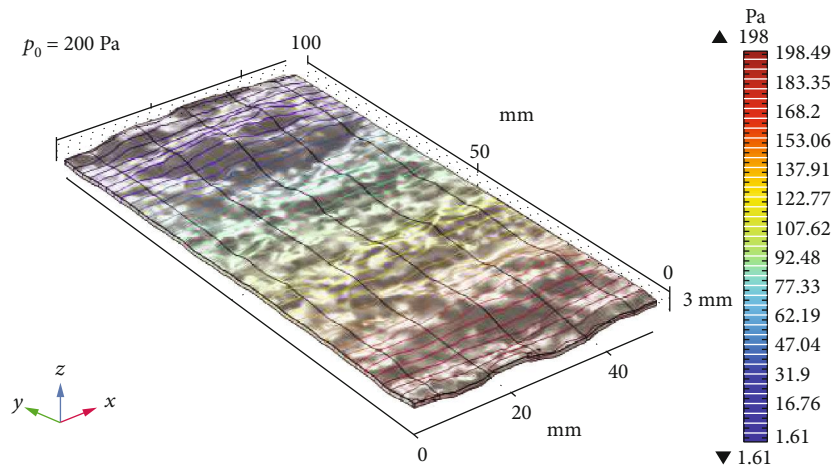
where D_h is the hydraulic diameter (m), $D_h = 2b$.

For determining the influence of the nonlinear item based on Forchheimer formula, non-Darcy coefficient E written by Equation (12) proposed by Zeng and Grigg [26] is introduced to explain the mechanism of nonlinear flow in the rough fractures.

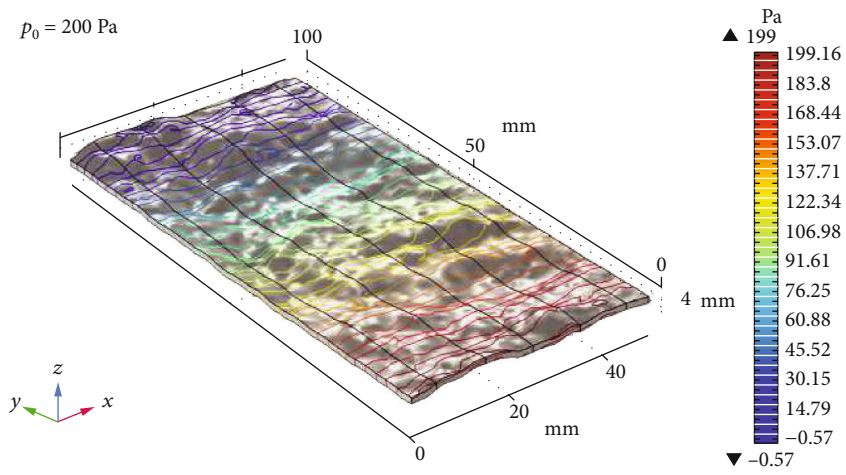
$$E = \frac{BQ^2}{AQ + BQ^2}, \quad (12)$$

where E represents the intensity influenced by the flow nonlinearity. And in the geotechnical field, the inertial forces cannot be ignored while the parameter E reaches 10% [5], indicating the nonlinear flow behavior has been triggered. Thus, the critical Reynolds number Re_c based on the Equations (11) and (12) can be derived as follows [31]:

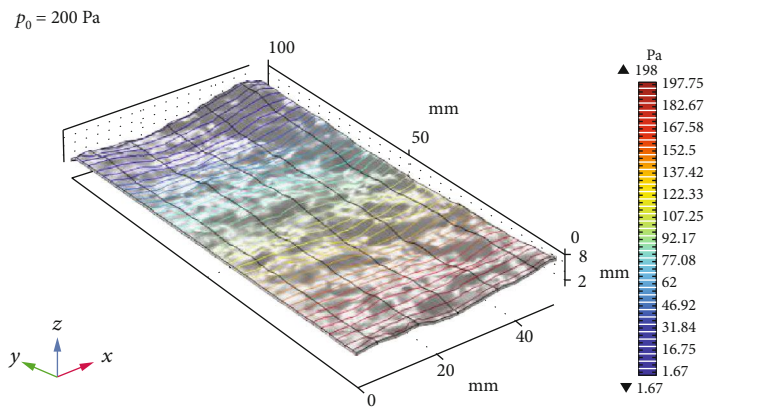
$$Re_c = \frac{2A\rho E}{B\mu w(1-E)}. \quad (13)$$



(a) Specimen S1

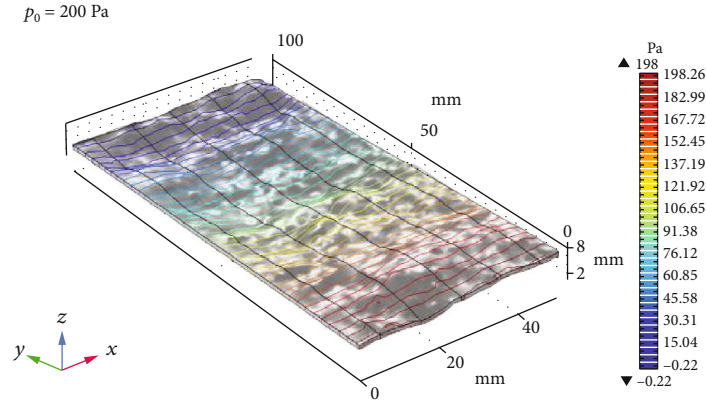


(b) Specimen S2



(c) Specimen S3

FIGURE 10: Continued.



(d) Specimen S4

FIGURE 10: Comparison of surface pressure of specimens S1-S4.

Therefore, non-Darcy coefficients considering different testing conditions can be calculated based on fitting coefficients A, B , and the curves $E \sim Q$ and $E \sim Re$ are plotted in Figure 5. It can be seen from the figure that E increases with increasing Reynolds number or flow rate, and greater inertial forces cause greater loss of the nonlinear pressure gradient, indicating that nonlinear flow in rough fractures is more intense with smooth amplification, which shows a good agreement with the conclusions in Zhou et al. [21]. Furthermore, the critical Re_c of the specimens S1-S4 are also calculated as 48.8, 25.5, 37.9, and 20.3; it can be seen that E increases with rougher fractures surface considering some Reynolds number, indicating that greater loss of the pressure gradient will cause smaller critical Reynolds number Re_c ; the reason is mainly that the rougher fractures caused larger tortuosity of the seepage paths and stronger inertial forces to trigger the nonlinear flow more easily. Therefore, different roughness and aperture will generate different seepage paths, resulting in different transformation points for the linear flow to nonlinear flow in the rough fractures.

It can be also concluded that nonlinear flow through the rough fractures is closely related to the wall morphology, and increasing pressure gradient causes greater inertial forces to strengthen the friction effect due to the contact of the fluid and rough wall. Then, the wall friction coefficient f can be written by Equations (15) and (16) based on Darcy-Weisbach equation shown by Equation (14), and mentioned by Forchheimer formula, the formulas can be applied to represent the influence of the fracture roughness on the flow behavior and reveal the mechanism of nonlinear flow through rough fractures.

$$-\nabla P = f \frac{1}{D_h} \frac{\rho u^2}{2} = f \frac{\rho Q^2}{4b^3 w^2}, \quad (14)$$

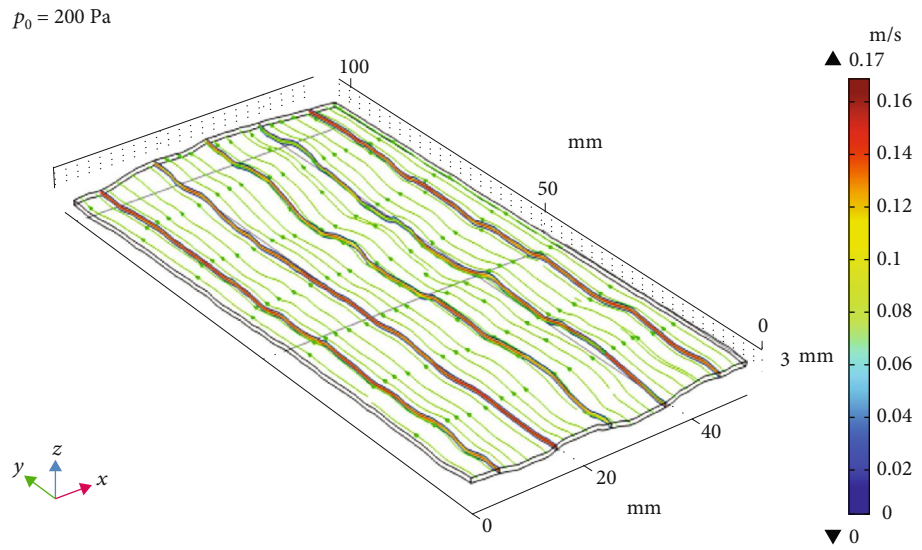
$$f = -\frac{4\nabla P b^3 w^2}{\rho Q^2}, \quad (15)$$

$$f = \frac{4b^3 w^2}{\rho Q^2} (AQ + BQ^2). \quad (16)$$

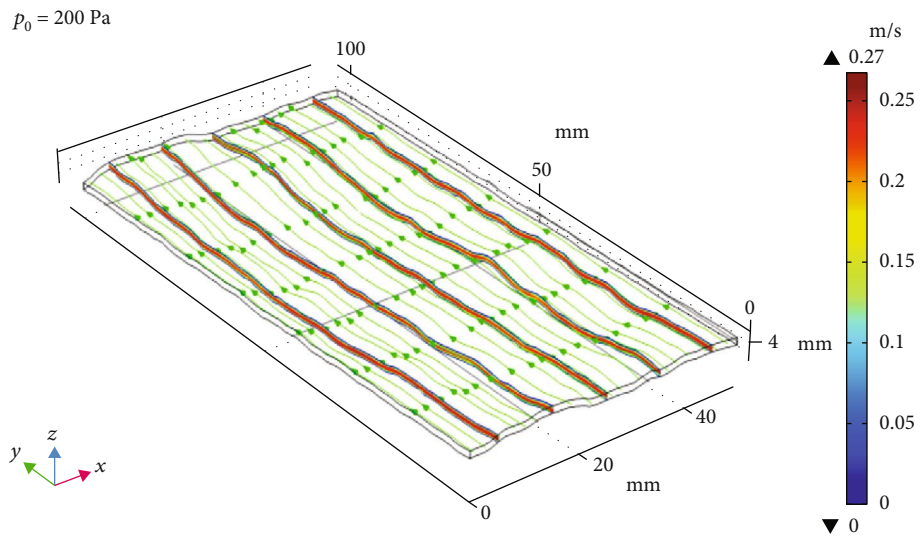
And then, the experimental data of $\nabla P \sim Q$ are used for calculating the wall friction coefficients f based on Equations (15) and (16) to build curves of $f \sim Re$ plotted in Figure 6. It can be seen from the figure that smaller flow velocity will cause negative relationship of wall friction coefficient f and Reynolds number Re in the initial stage. However, the nonlinear relationship of f and Re is obvious when increasing the flow rate. And the critical wall friction coefficient f can be obtained as 1.44, 1.65, 1.78, and 1.96, indicating that the seepage state is from the linear to nonlinear; f exceeds the above values, and variation of f is induced by the variation of the seepage state; however, the seepage state is caused by velocity variation resulting from the pressure gradient, so f is only an assessment index. And the results also show that rougher fracture surface will result in larger wall friction coefficient. Also, it can be observed from the local enlarged figure plotted in Figure 6 that different fracture roughness cause obvious variation of the curves $f \sim Re$, deeply illuminating that different surface morphologies cause tortuous seepage paths [23] resulting in stronger wall friction effect to change the seepage behavior.

4. The Numerical Simulation of Flow Behavior through 3-Dimensional Rough Fractures

For better describing the flow variation in rough fractures, 3-dimensional numerical model is proposed to simulate the seepage behavior and reveal the variation of some seepage parameters such as pressure, flow velocity, and flow rate. According to the experimental and theoretical data of the rough fractures mentioned above, the software named COMSOL Multiphysics is proposed to reconstruct the 3-dimensional fracture surface of the specimens S1, S2, S3, and S4 to form numerical models considering different rough fractures. And then, the comparison has been conducted to prove the feasibility of the proposed numerical model and

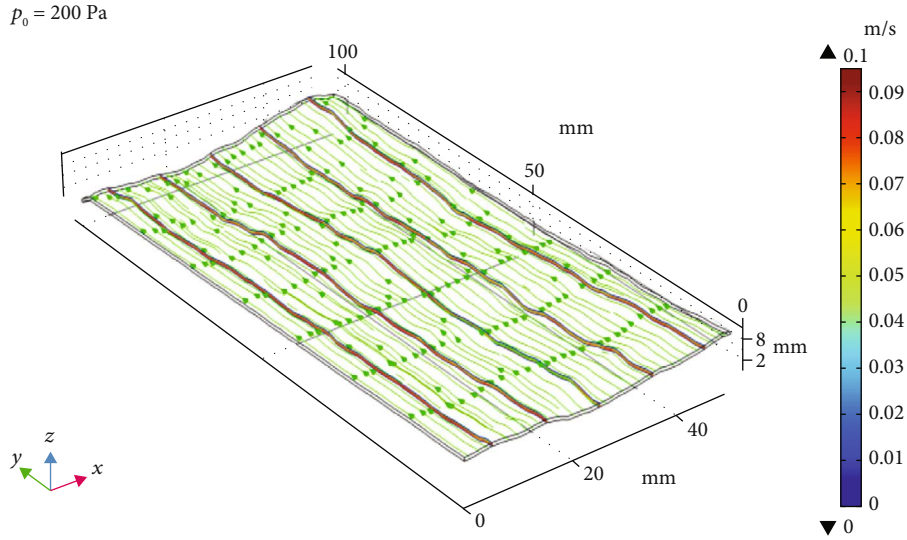


(a) Specimen S1

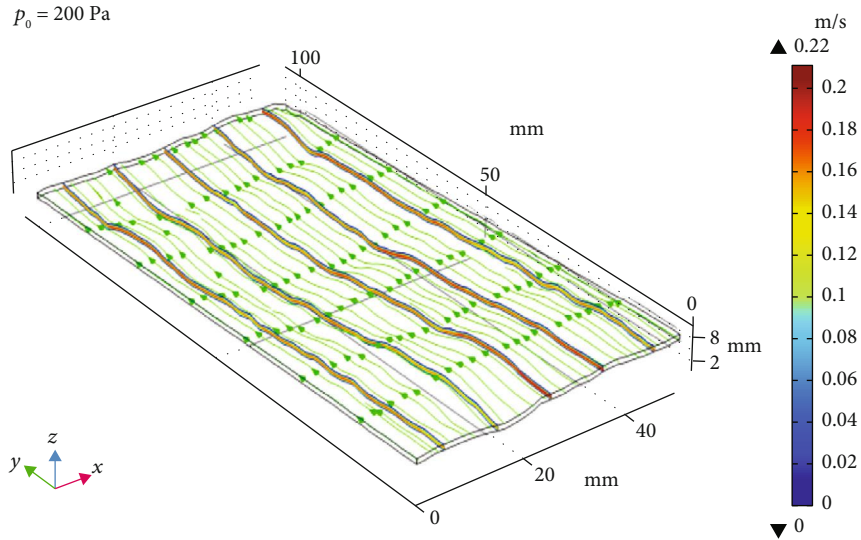


(b) Specimen S2

FIGURE 11: Continued.



(c) Specimen S3



(d) Specimen S4

FIGURE 11: Velocity distribution on fracture surface of specimens S1-S4.

then analyzes the seepage characteristics in detail considering different conditions.

4.1. The Model Setup and Corresponding Calibration of the Seepage Model through the 3-D Rough Fractures

4.1.1. The Model Setup for the Fracture Seepage. The software named COMSOL Multiphysics is a popular numerical software solving the multiphysics coupling problems in many fields of solid mechanics, fluid mechanics, and thermal mechanics. For the model setup of the flow in rough fractures, the scanning data about the 3-D fracture surface is introduced into the software to form the 3-D rough models shown in Figure 7(a), and the complete specimens, corresponding upper surface and lower surface, are plotted in Figures 7(b) and 7(c). And also, the mesh of the fracture models is shown in Figures 8(a) and 8(b).

As for 3-D seepage calculation, suppose the incompressible fluid, constant viscosity and fluid density, and the laminar flow, the continuity equation and Navier-Stokes equation are included in Equations (17) and (18). And then, initial boundary is set with no-flow and no-slip on the upper, lower, left, and right boundaries, and the pressure is loaded at the inlet and outlet to complete the seepage numerical model.

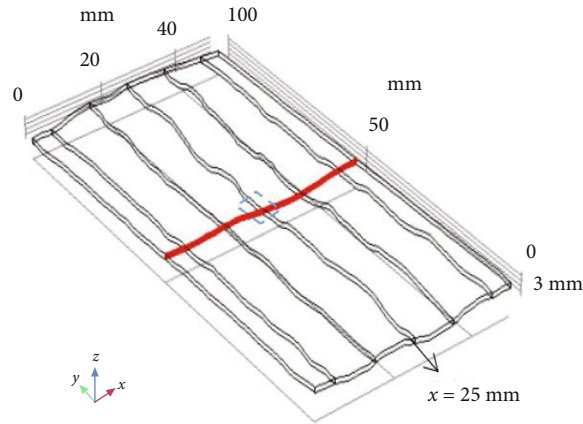
The continuity equation is written as follows:

$$\nabla u = 0. \tag{17}$$

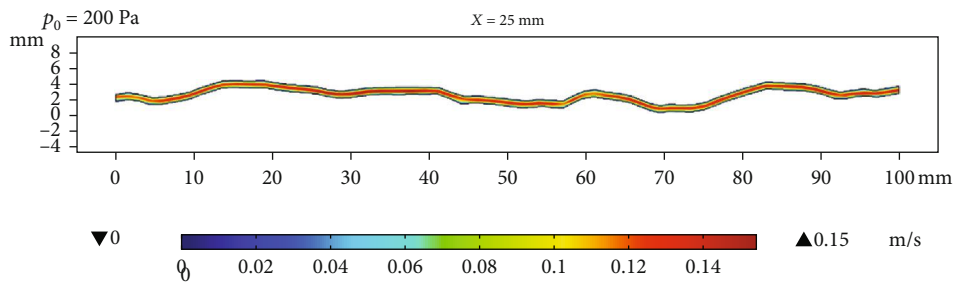
The Navier-Stokes equation is shown as follows:

$$\rho(u \cdot \nabla)u = \mu \nabla^2 u - \nabla P, \tag{18}$$

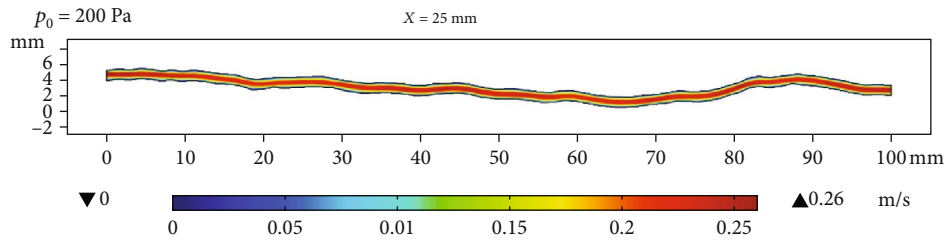
where ρ is the fluid density, valued 998.2 kg/m^3 , μ is the dynamic viscosity coefficient, valued $0.001 \text{ Pa} \cdot \text{s}$, P is the fluid



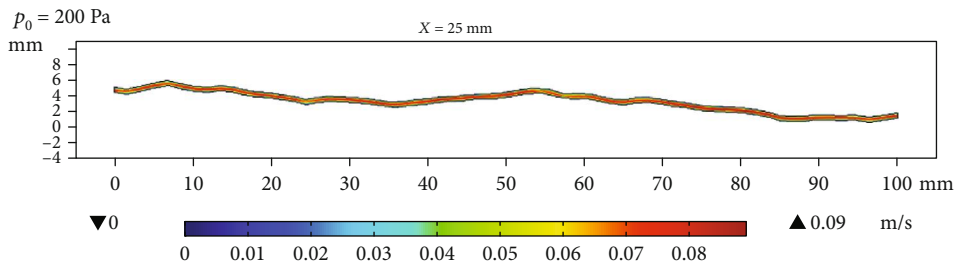
(a) The diagram of the researched line



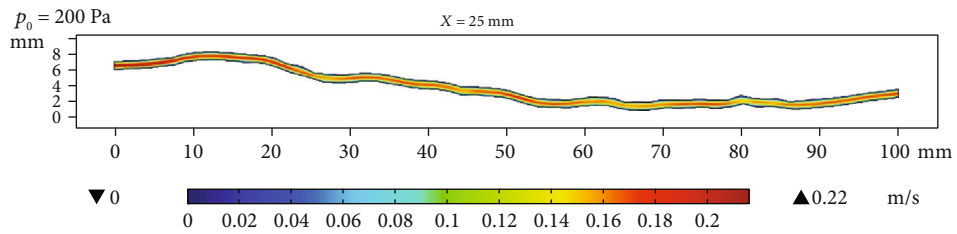
(b) Specimen S1



(c) Specimen S2



(d) Specimen S3



(e) Specimen S4

FIGURE 12: Velocity distribution along the lines ($X = 25$ mm) of specimens S1-S4.

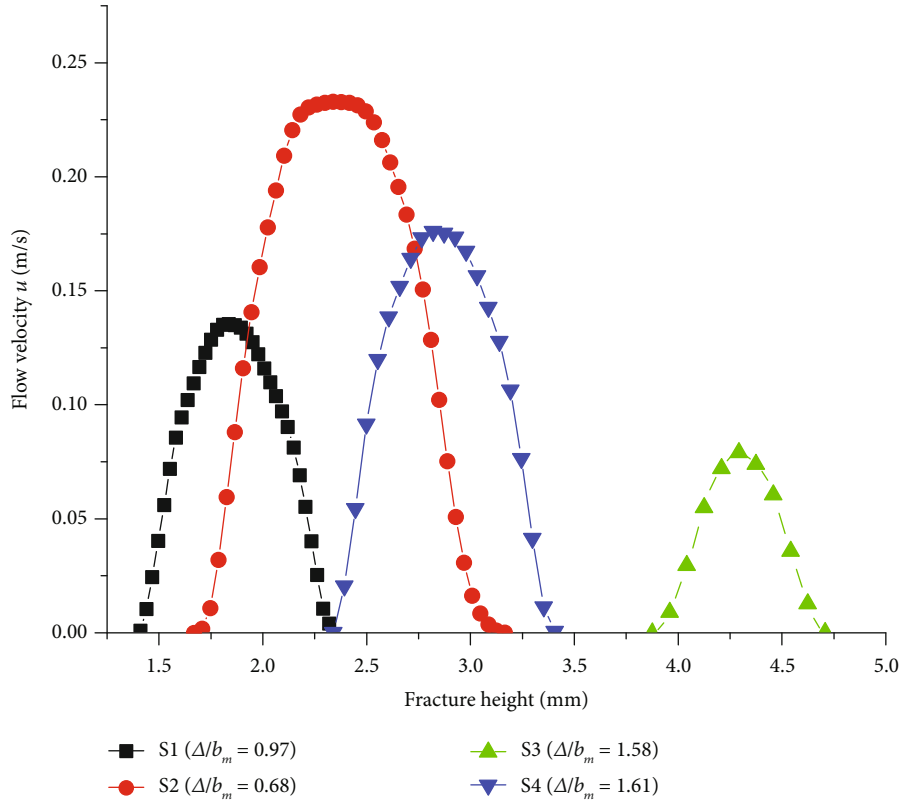


FIGURE 13: Velocity distribution along the fracture height (Z direction) of specimens S1-S4 ($X = 25$ mm interested $Y = 50$ mm).

pressure (Pa), u is the flow velocity (m/s), $\rho(u \cdot \nabla)u$ represents the item describing the fluid inertial forces, and $\mu \nabla^2 u$ represents the item describing the fluid viscous forces.

4.1.2. Calibration of the Numerical Model for Seepage in Rough Fractures. In order to calibrate the proposed seepage model, the specimen S1 as a case study, the flow rate Q calculated by the formula $Q = \int u dA$ under same conditions for the experiments has been obtained in Table 2. It can be seen from the comparisons that the simulated flow rate is close to the testing value (less than 5% discrepancy). And then, the simulated curves in red of ∇P and Q plotted in Figure 4 show a good agreement with the fitting curves by Forchheimer formula and smaller discrepancy with increased pressure gradient. Therefore, the proposed seepage model can be applicable to analyze the nonlinear flow through the rough fractures.

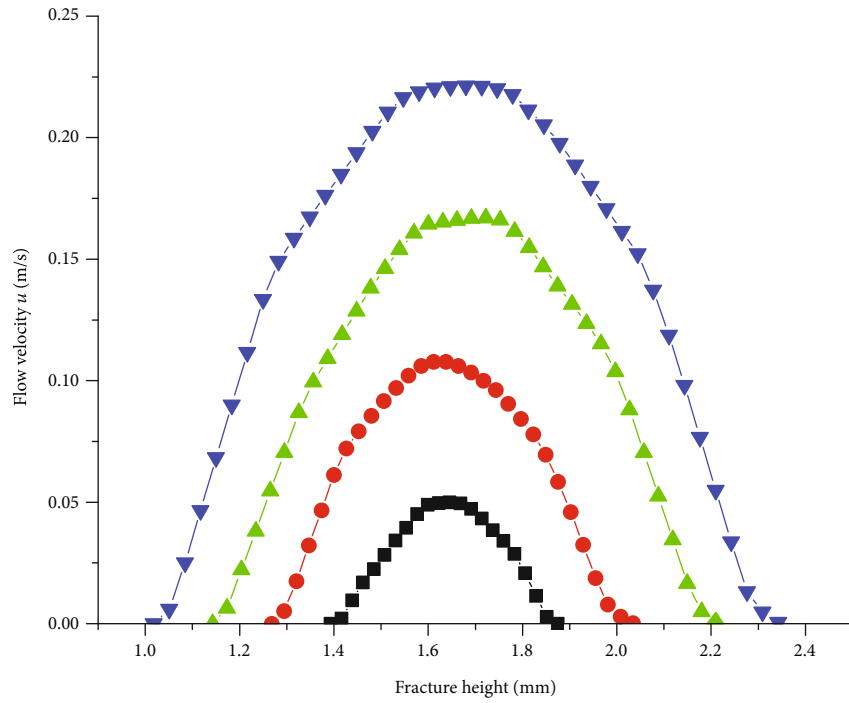
4.2. Analysis of the Seepage Behavior through 3-D Rough Fractures

4.2.1. The Description of the Flow Behavior. The flow behavior of the specimens S1-S4 is deeply investigated based on the calibrated seepage model. And the pressure distribution under different pressure gradients is plotted in Figure 9, and the pressure decreases from the inlet to the outlet and the pressure lines are uneven along the flow direction, indicating that rough fracture wall blocks the fluid flow forward and the curves are bended obviously to spread to the left and right while increasing the pressure gradient. Meanwhile, the pressure $p_0 = 200$ Pa is supposed to get the pressure dis-

tribution on the fracture surface plotted in Figures 10(a)–10(d), and different pressures are obvious for same points under same conditions, illuminating the fracture roughness plays an important role on the seepage characteristics.

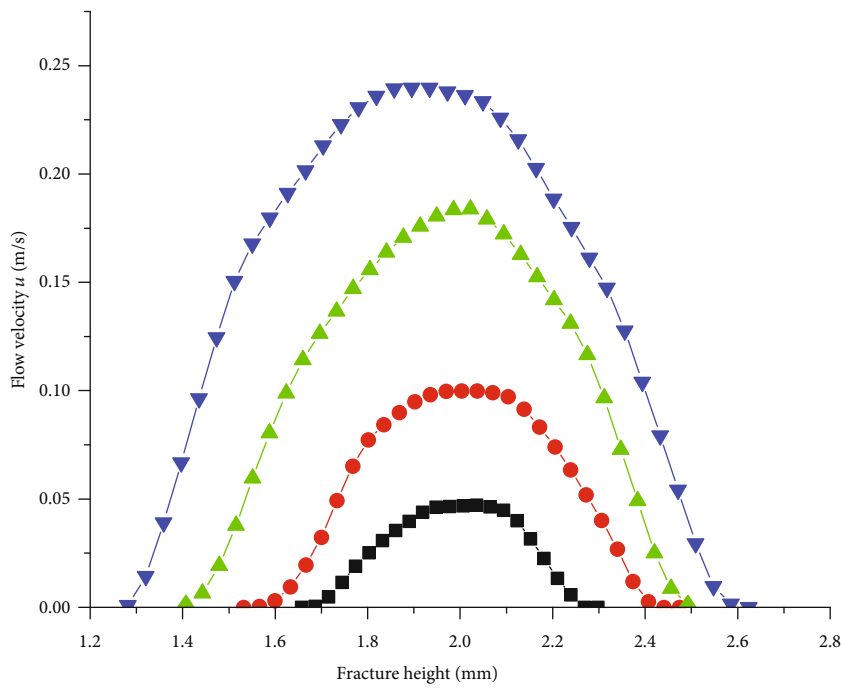
For deeply investigating the flow characteristics, cloud figures plotted in Figures 11(a)–11(d) and the velocity distribution on section $X = 25$ mm of the specimens S1-S4 plotted in Figures 12(a)–12(e) are treated to describe the flow velocity on the different sections. It can be observed from the figures mentioned above that the smallest flow velocity is close to zero near the upper wall and lower wall, otherwise the greatest in the middle of the fracture, which is in accordance with the velocity variation described by the Darcy-Weisbach equation. In order to display the flow variation along the fracture height, the intersected line on the section $Y = 50$ mm and $X = 25$ mm of four specimens is selected to show the curves variation plotted in Figure 13 based on the software Tecplot, which illuminates the curve shape which obeys the parabola shape. And in addition, the curves of the flow velocity for four specimens in the middle of the fractures with maximum values [21] show unsmooth characteristics, even though in the same intersected lines, the main reason is that different roughness cause different wall friction effects resulting in the different velocity distributions, which emphasizes the ignorance of the fracture roughness and corresponding spatial distribution influencing on the flow through the rough fractures.

4.2.2. Analysis of the Seepage Behavior considering the Aperture Variation. The seepage behavior considering the



Specimen S1
 ■ $b = 0.50$ mm ▲ $b = 1.00$ mm
 ● $b = 0.75$ mm ▼ $b = 1.25$ mm

(a) Specimen S1



■ $b = 0.50$ mm ▲ $b = 1.00$ mm
 ● $b = 0.75$ mm ▼ $b = 1.25$ mm

(b) Specimen S2

FIGURE 14: Continued.

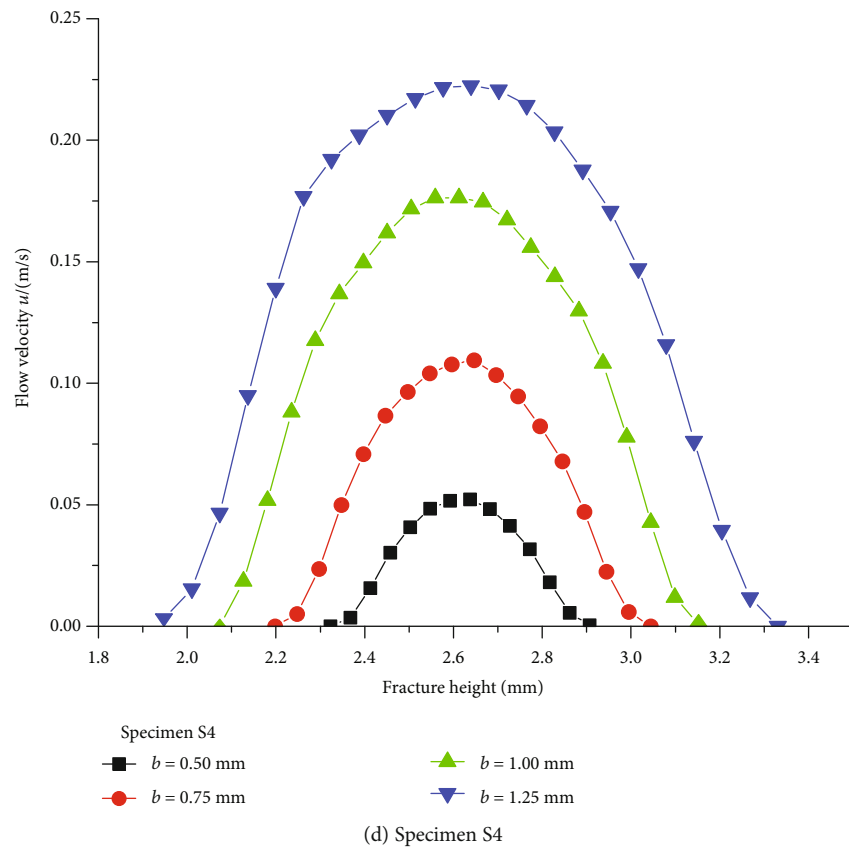
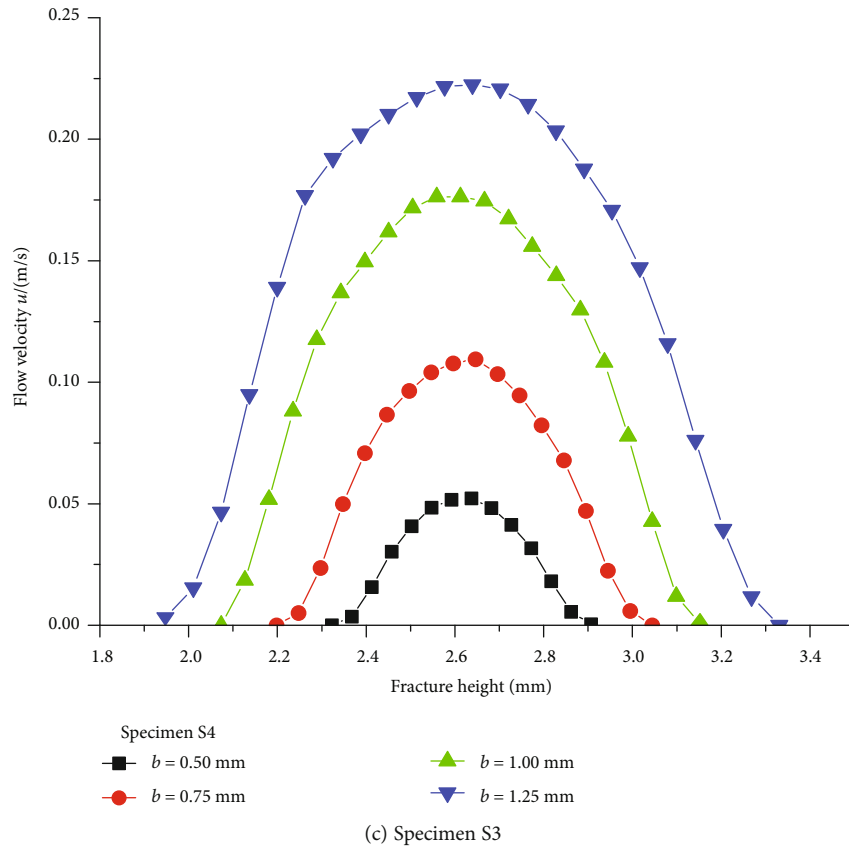
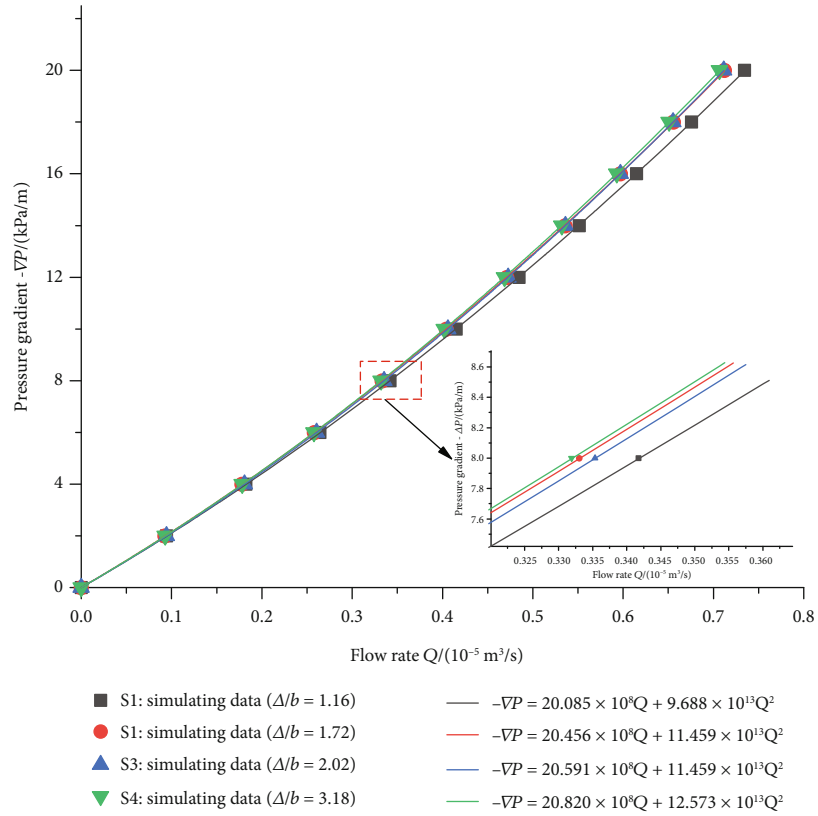
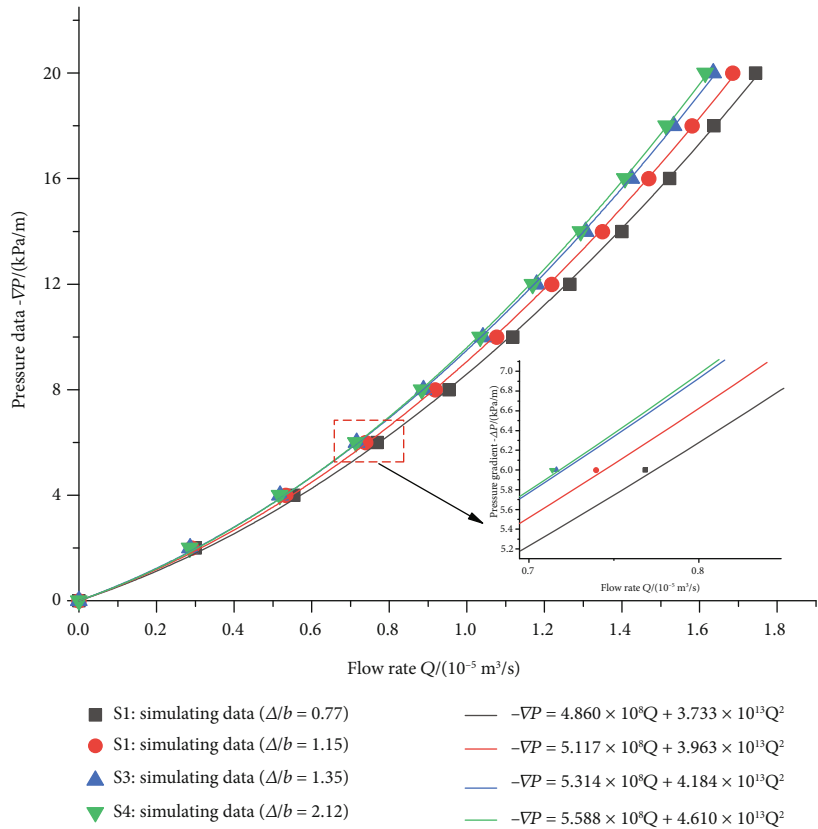


FIGURE 14: Comparison of flow velocity of fractures in samples S1-S4 considering varied aperture.

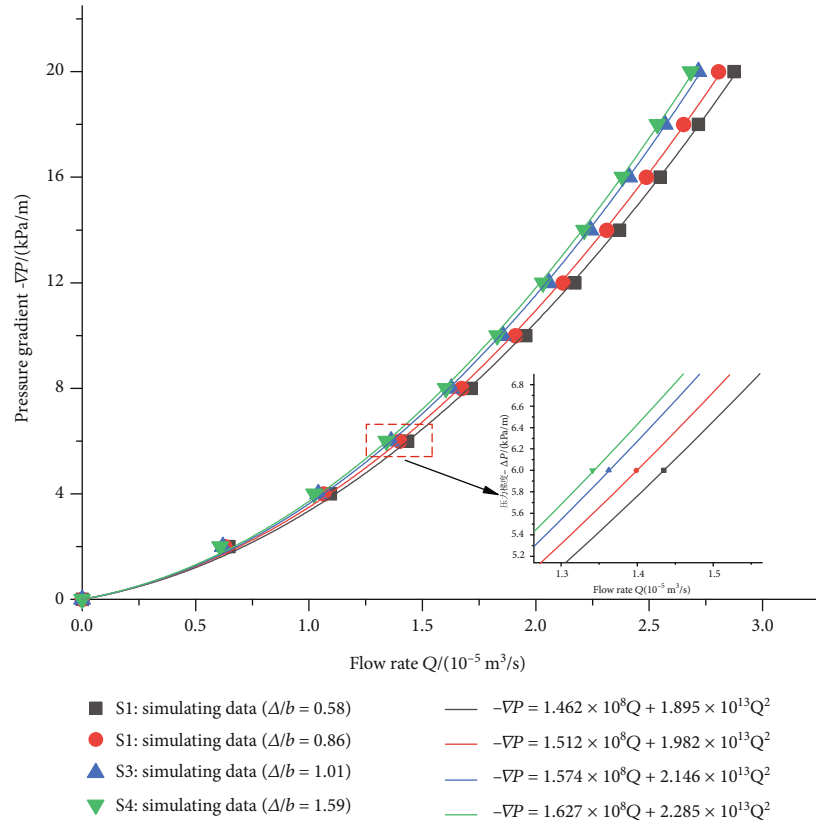


(a) Fracture aperture $b = 0.50 \text{ mm}$

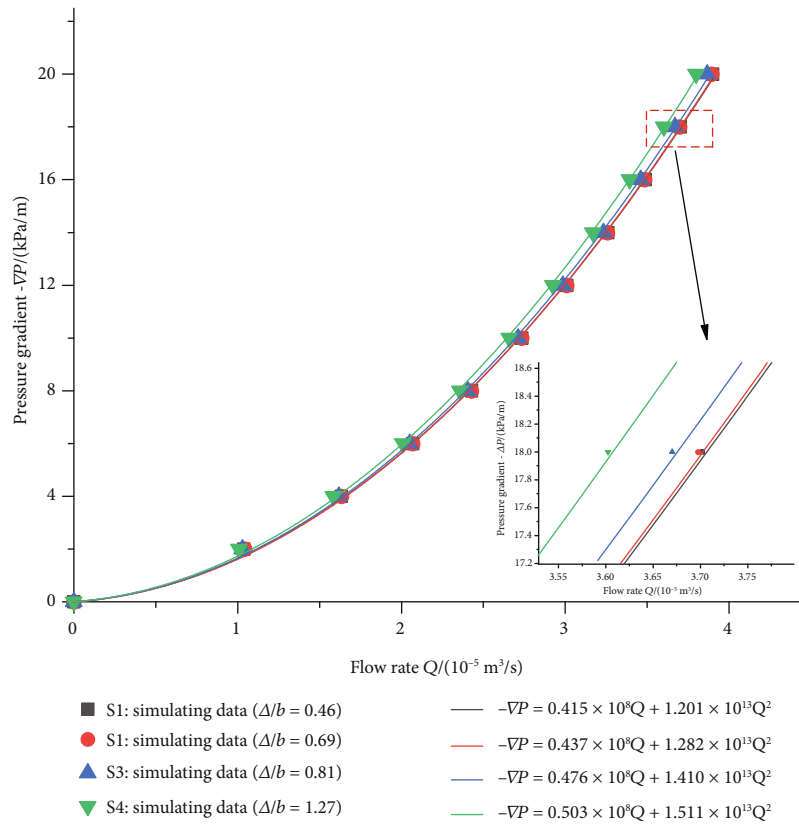


(b) Fracture aperture $b = 0.75 \text{ mm}$

FIGURE 15: Continued.



(c) Fracture aperture $b = 1.00$ mm



(d) Fracture aperture $b = 1.25$ mm

FIGURE 15: Curves of ∇P and Q considering the variation of the hydroaperture for samples.

TABLE 3: Fitting coefficients A and B in the Forchheimer equation and corresponding critical Reynolds numbers.

Fracture aperture b (mm)	Specimen S1			Specimen S2			Specimen S3			Specimen S4		
	A (10^8)	B (10^{13})	f	A (10^8)	B (10^{13})	f	A (10^8)	B (10^{13})	f	A (10^8)	B (10^{13})	f
0.50	20.085	9.688	5.06	20.456	10.668	5.57	20.591	11.459	5.98	20.82	12.573	6.56
0.75	4.86	3.733	1.95	5.117	3.953	2.06	5.314	4.184	2.18	5.588	4.61	2.41
1.00	1.462	1.895	0.99	1.512	1.982	1.03	1.574	2.146	1.12	1.627	2.285	1.19
1.25	0.415	1.201	0.63	0.437	1.282	0.67	0.476	1.410	0.74	0.503	1.511	0.79

aperture variation has been deeply researched in this section. Considering the aperture with 0.50 mm, 0.75 mm, 1.00 mm, and 1.25 mm and same intersected lines on section $X = 25$ mm and $Y = 50$ mm, the curves of the flow velocity along the fracture height representing the aperture direction (Z direction) are compared shown in Figures 14(a)–14(d). Observed from the velocity distribution, it can be concluded that for the same rough fracture, increasing fracture aperture will enlarge the seepage channel to decrease the relative roughness, so the wall friction coefficient decreases resulting in greater flow velocity. And also, the flow velocity shows asymmetric because of the fracture roughness changing the seepage paths, which is in accordance with the seepage characteristics through the rough fractures, deeply indicating the importance of the fracture roughness on correct description of the seepage characteristics.

5. Seepage Mechanism of the Rough Fractures considering Multifactor Combinations

In order to generally describe the flow behavior through the rough fractures, the seepage mechanism based on the proposed numerical model will be deeply investigated considering the combination of the fracture roughness and aperture variation, revealing the seepage mechanism of the rough fractures under the combination of multifactors.

5.1. Nonlinear Behavior of the Flow through 3-D Rough Fractures. According to the analysis mentioned above, once the fracture aperture for the same fracture changes causing the variation of the relative roughness, the curves $\nabla P \sim Q$ will change greatly. Considering different combinations of the roughness and aperture, the curves $\nabla P \sim Q$ of four specimens S1-S4 are plotted in Figures 15(a)–15(d). It can be observed from the curve variation that the curves show linear in the initial stage but nonlinear while increasing the pressure gradient, which is in accordance with the experimental curves. However, once the fracture aperture increases causing smaller relative roughness, corresponding flow rate and velocity will increase.

Therefore, the seepage behavior based on combination of the roughness and aperture can be described by the Forchheimer model, and the fitting curves show good agreement with the simulated values. The calculated coefficients A , B are listed in Table 3. The results indicate that considering the same aperture for the four specimens, increasing roughness will narrow the seepage channel to weaken the flow rate; the fitting coefficients are greater; otherwise, increasing aperture of same specimen causing smaller relative roughness causes

smaller fitting coefficients and greater flow rate and velocity. And in addition, the relationship between the fitting coefficients A , B is modeled by the power function plotted in Figures 16(a)–16(d), which shows a good agreement with the variation in the reference written by Chen et al. [10]. It can be concluded that the fitting coefficient based on the Forchheimer model considering the geometric parameters of the rough fractures can describe the nonlinear flow behavior through the rough fractures.

5.2. Triggering Mechanism of the Nonlinear Flow Behavior through 3-D Rough Fractures. It can be concluded from the seepage analysis mentioned in Section 3 that Re_c will decrease with roughness increasing considering same pressure and aperture, showing that nonlinear flow will occur with smaller Reynolds number; otherwise, Re_c will be greater with aperture increasing considering same pressure and roughness, showing that nonlinear flow is difficult to occur because of smaller relative roughness. Therefore, the aperture variation causes the relative roughness (Δ/b) representing the fracture roughness changing greatly resulting in tortuous seepage paths and different interactions of the fracture wall and fluid.

Furthermore, according to the analysis about the wall friction coefficient f , another formula describing the wall friction coefficient can be obtained by Equations (19) and (20) based on the Darcy-Weisbach equation and Forchheimer formula, and it can be seen that the wall friction coefficient f is closely related to the Reynolds number, fracture aperture, and roughness.

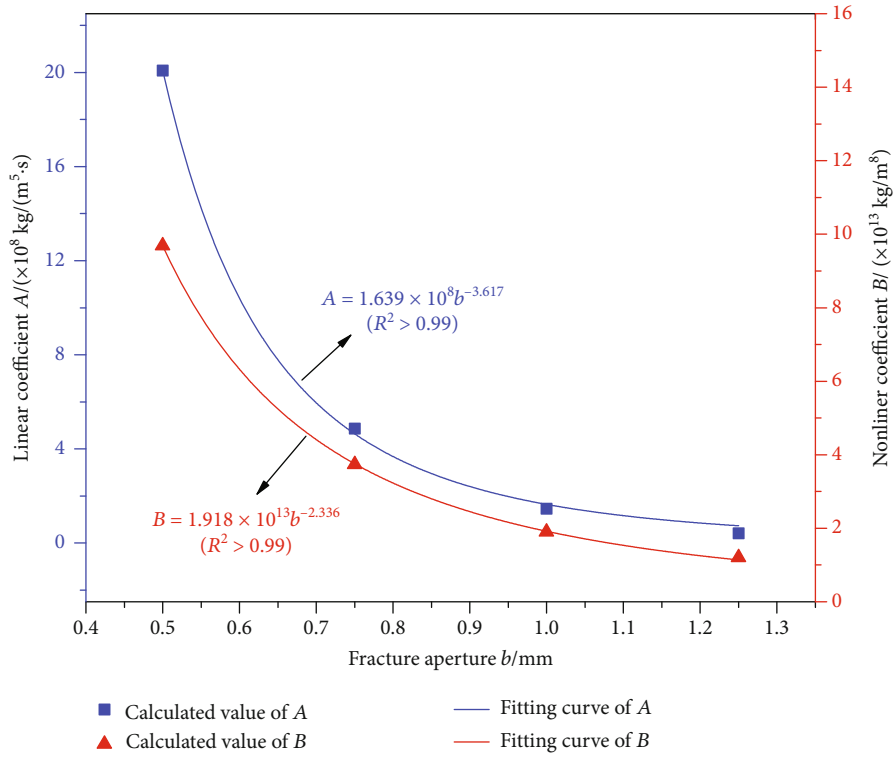
$$f = \frac{96}{Re} + 4b\beta, \quad (19a)$$

$$4b\beta = a_1 \left(\frac{\Delta}{b} \right)^{c_1}, \quad (19b)$$

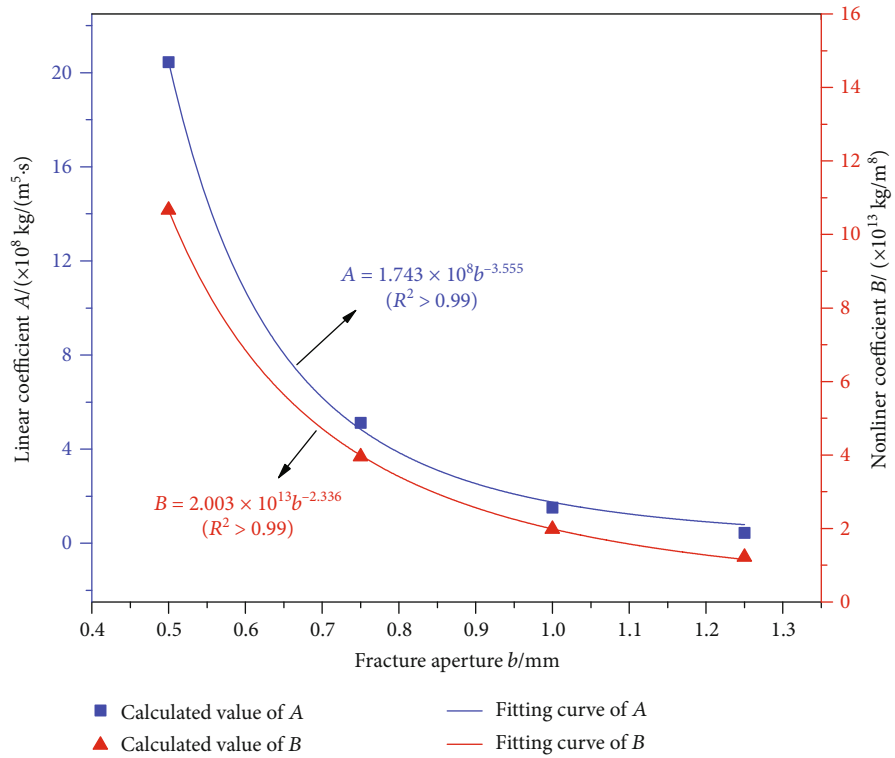
where a_1 and c_1 are the fitting coefficients for calculating the wall friction coefficient. The best-fit curve of f and the variables Re and Δ/b is plotted in Figure 17, which indicates a strong relationship. The best regression values of the coefficients in Equation (20) are $a_1 = 0.067$ and $c_1 = -1.128$ with coefficient of determination $R^2 = 0.944$.

$$f = \frac{96}{Re} + 0.067 \left(\frac{\Delta}{b} \right)^{-1.128}. \quad (20)$$

In addition, the wall friction coefficients considering aperture variation of specimens S1-S4 are calculated to build the curves of f and Re plotted in Figures 18(a)–18(d). It can

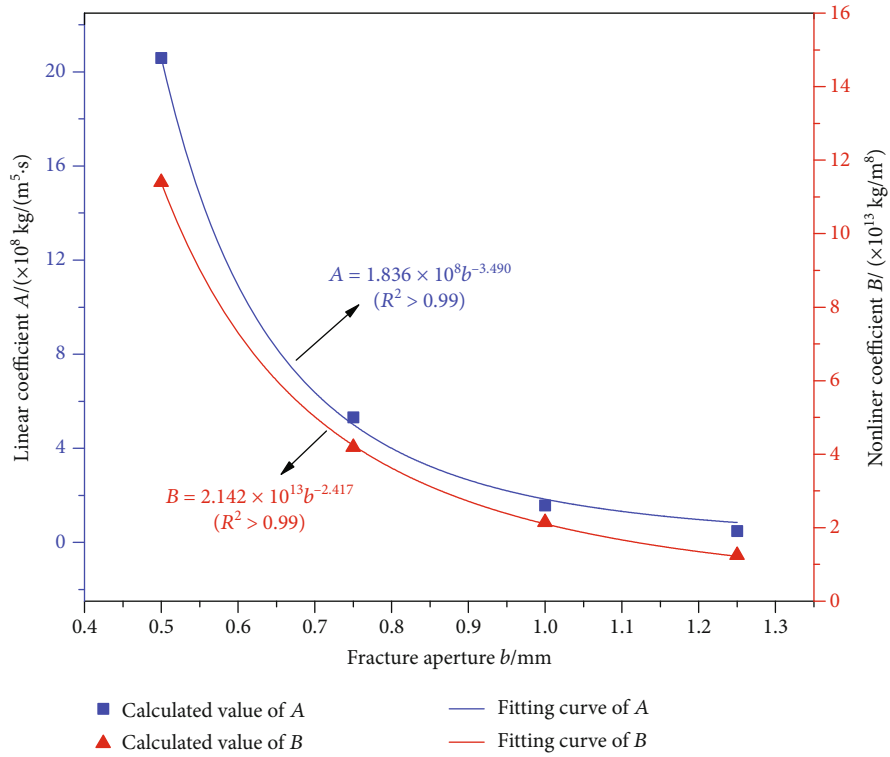


(a) Specimen S1

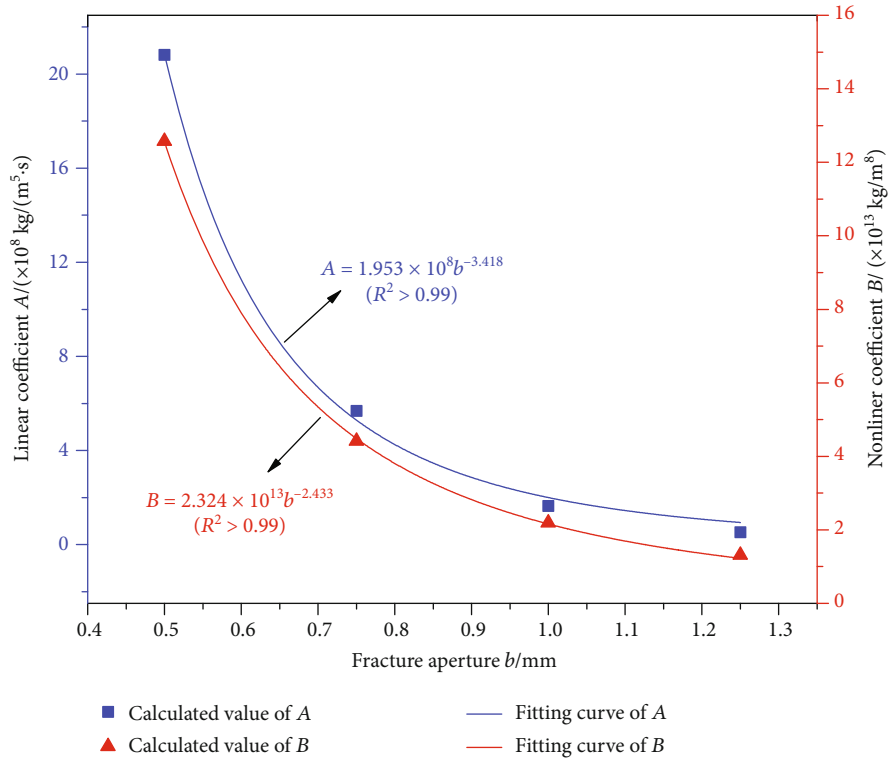


(b) Specimen S2

FIGURE 16: Continued.



(c) Specimen S3



(d) Specimen S4

FIGURE 16: Fitting curves of the coefficients A and B based on Forchheimer equation and fracture aperture for samples.

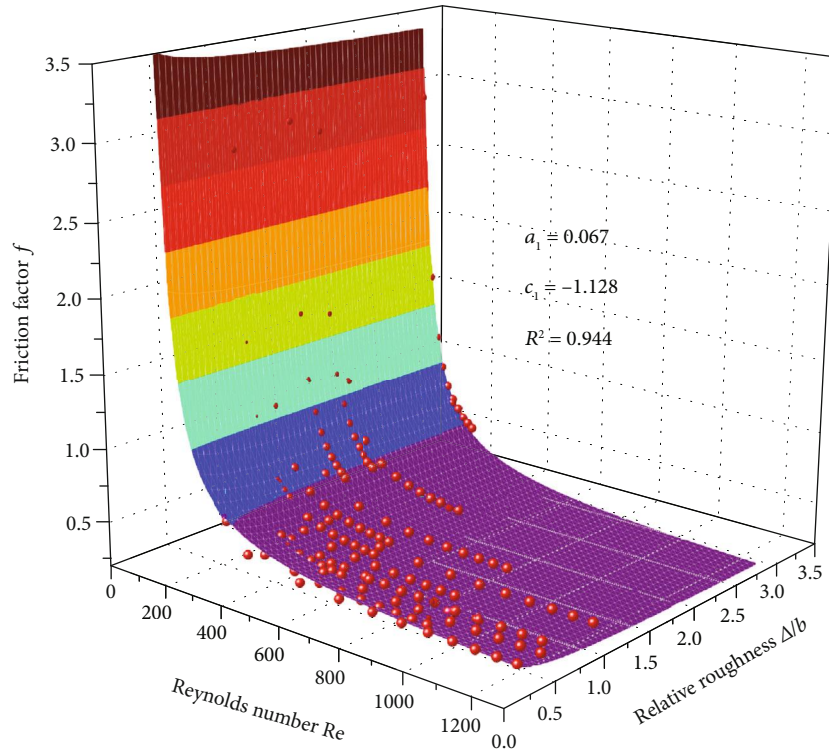


FIGURE 17: Relationship of $f \sim Re$ and relative roughness.

be seen that for some specimen, the curves of f and Re are linear with smaller Reynolds number and then show nonlinear characteristics and deviate the curve considering the parallel plate model. And the conclusion can be done that greater relative roughness causes obvious flow nonlinearity, and f is controlled by the Reynolds number with smaller flow velocity; otherwise, f is controlled by multifactors with greater flow velocity.

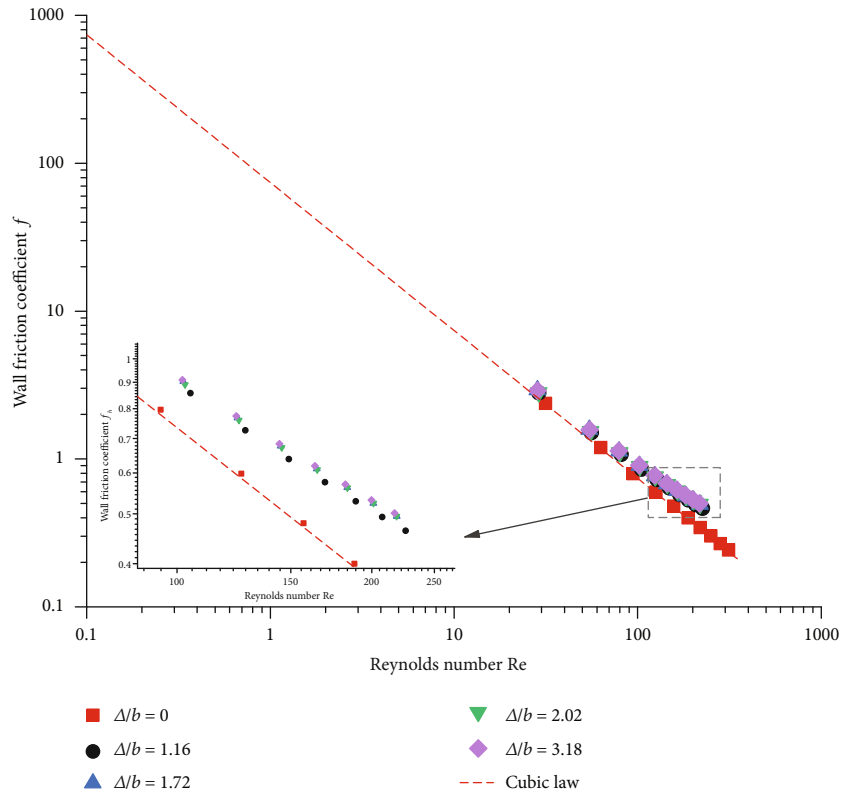
In addition, comparison of critical wall friction coefficients is listed in Table 3. It can be seen that f equals to 5.06, 5.57, 5.98, and 6.56 with aperture 0.50 mm, f equals to 1.95, 2.06, 2.18, and 2.41 with aperture 0.75 mm, f equals to 0.99, 1.03, 1.12, and 1.19 with aperture 1.0 mm, and f equals to 0.63, 0.67, 0.74, and 0.79 with aperture 1.25 mm. And the figure about f , Re , and relative roughness plotted in Figure 17 is setup to show that greater roughness caused the frictional resistance work and pressure loss increasing to get greater wall friction coefficient and smaller Reynolds number, and greater aperture caused smaller wall friction coefficient and greater Reynolds number. As for the former condition, the nonlinear flow occurs more easily; otherwise, the nonlinear flow for the latter condition may not occur probably. Therefore, the wall friction coefficients related to the fracture morphology, Reynolds number, and so on can explain the seepage characteristics of rough fractures and also describe the transformation points representing the occurrence of the nonlinear flow.

5.3. Nonlinear Flow Behavior of 3-D Intersected Fractures. For deeply investigating the seepage behavior through the rough fractures, the central part of the specimens S1 and S4

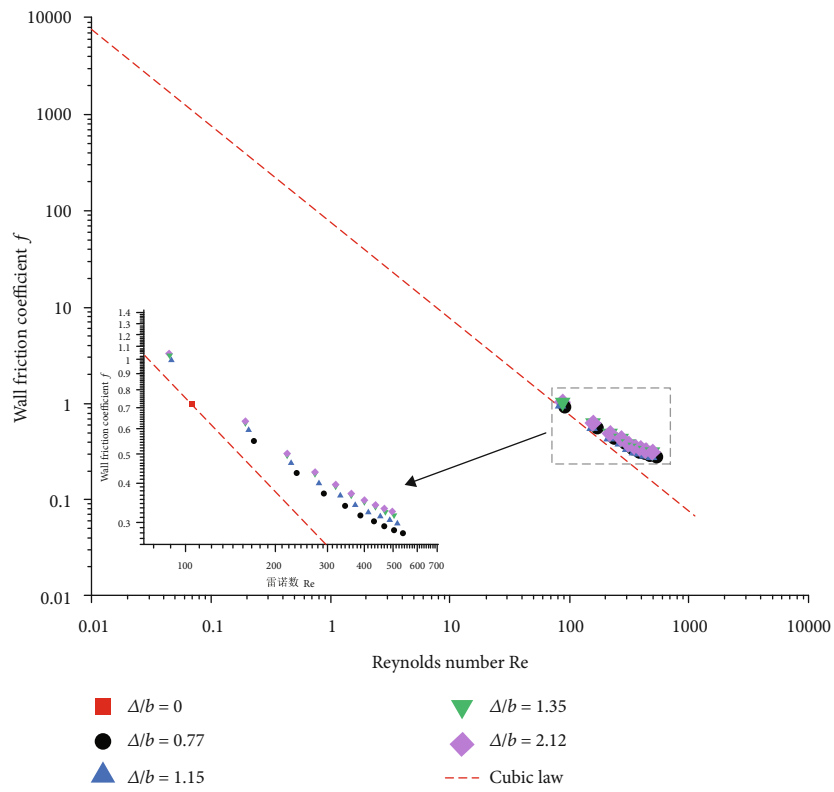
($15 \leq X \leq 35$, $30 \leq Y \leq 70$) is selected to reveal the seepage behavior considering fractures intersection. This cooperation not only can save the computational cost but also the roughness of S1 and S4 is almost in good with the original specimens. Thus, the data based on the scanning system is introduced to the software COMSOL and forms the intersected fractures plotted in Figure 19; then, corresponding flow behavior is analyzed in detail in the following sections.

5.3.1. Seepage Flow considering Different Interested Angles of the Rough Fractures. The experimental results of curves $\nabla P - Q$ for the specimens S1 and S4 are shown in Figures 20(a)–20(b). These results suggest that pressure gradient increases linearly initially and then nonlinearly as flow rate increases. The data in the linear stage is used to calculate hydraulic apertures. The aperture of the corresponding numerical model uses the same value of hydraulic aperture obtained by experimental data. Simulations are also plotted in Figures 21 and 22.

The quadratic polynomial regression in the form of Equation (10) is used to fit the $\nabla P - Q$ curves in the cases of crossing fracture intersection (CFI). The high coefficients of determination of R^2 (>0.99) demonstrate that the Forchheimer law adequately describes the nonlinear flow behavior at fracture intersections. When flow rate is small (Figures 20(a)–20(b)), the inertial force is much less than the viscous force and pressure gradient increases linearly with increasing Q . In this condition, the nonlinear term BQ^2 could be ignored and the cubic law is introduced to describe the relationship between flow rate and pressure gradient. The nonlinearity and the deviations from the cubic law are



(a) $b = 0.50$ mm



(b) $b = 0.75$ mm

FIGURE 18: Continued.

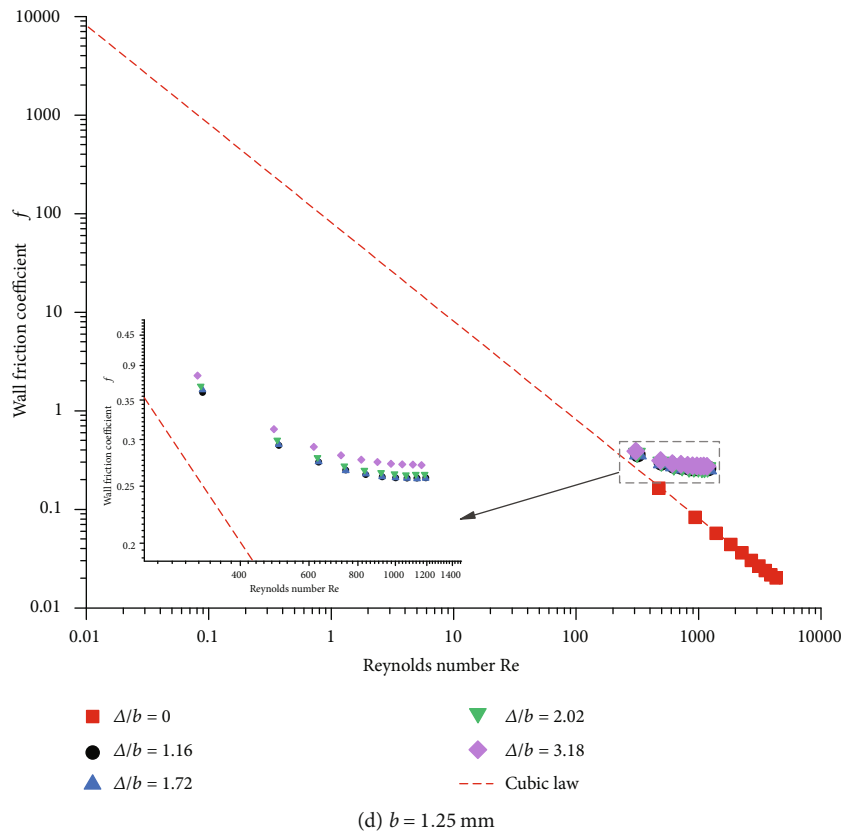
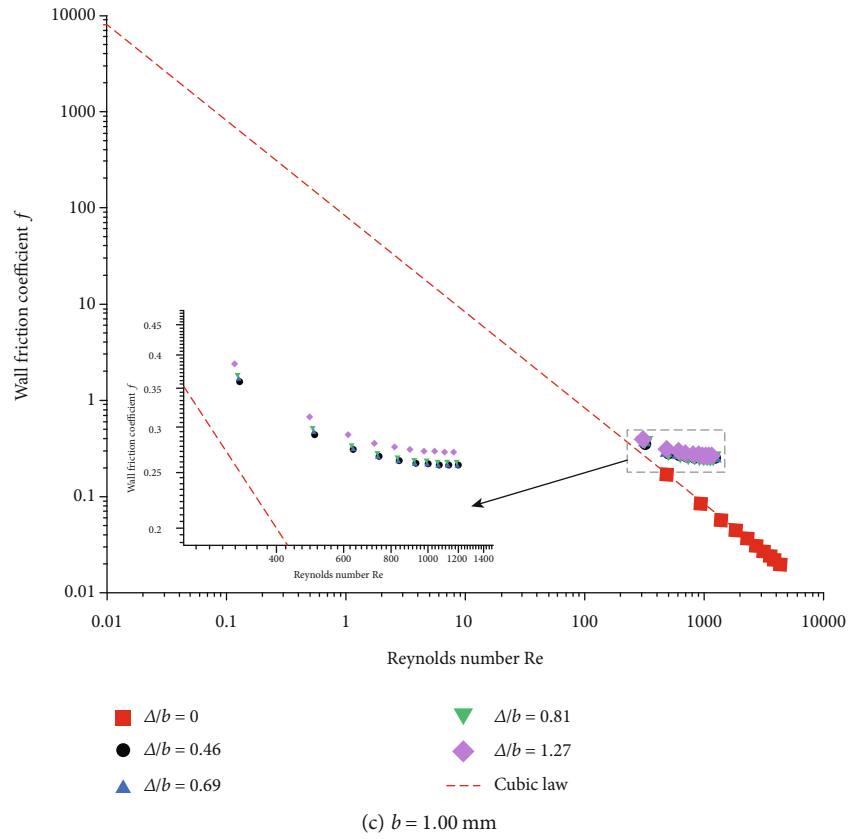


FIGURE 18: Curves of wall friction factor and Reynolds.

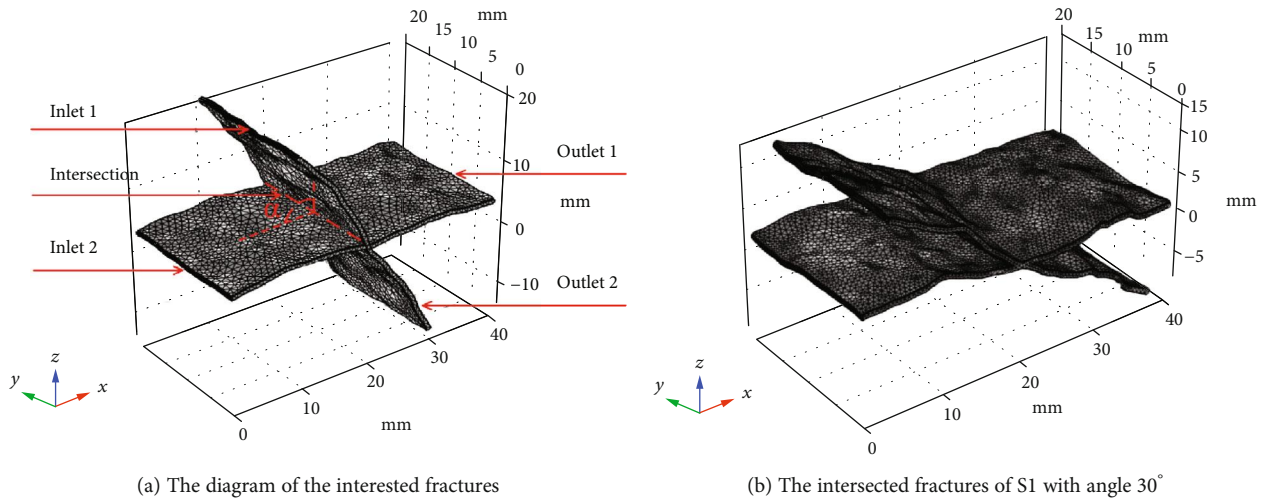


FIGURE 19: The intersection of rough fractures.

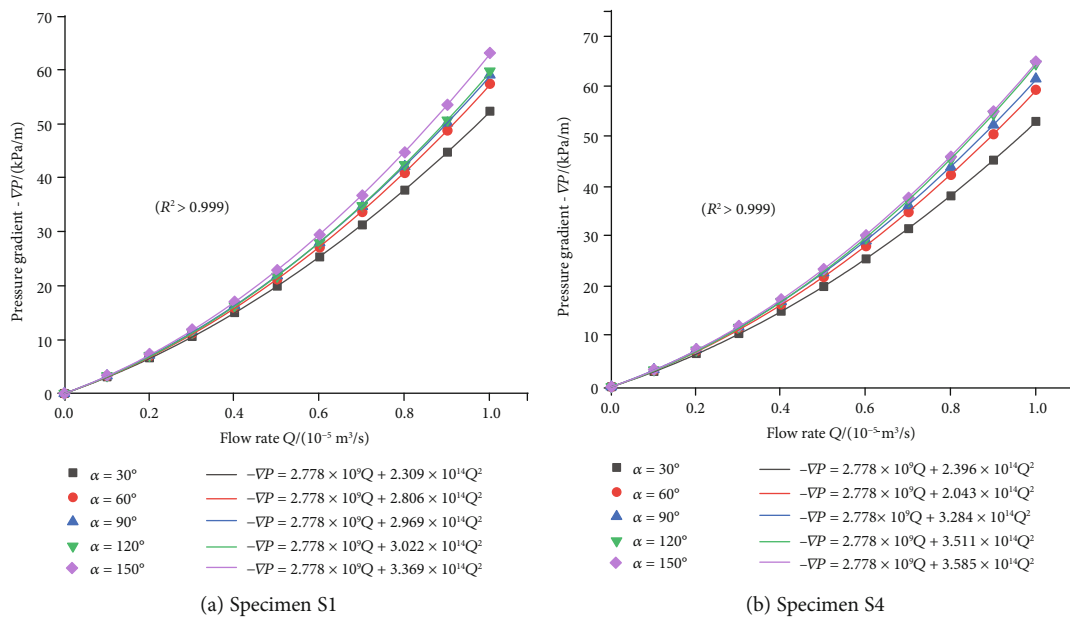


FIGURE 20: Curves of pressure gradient and flowrate.

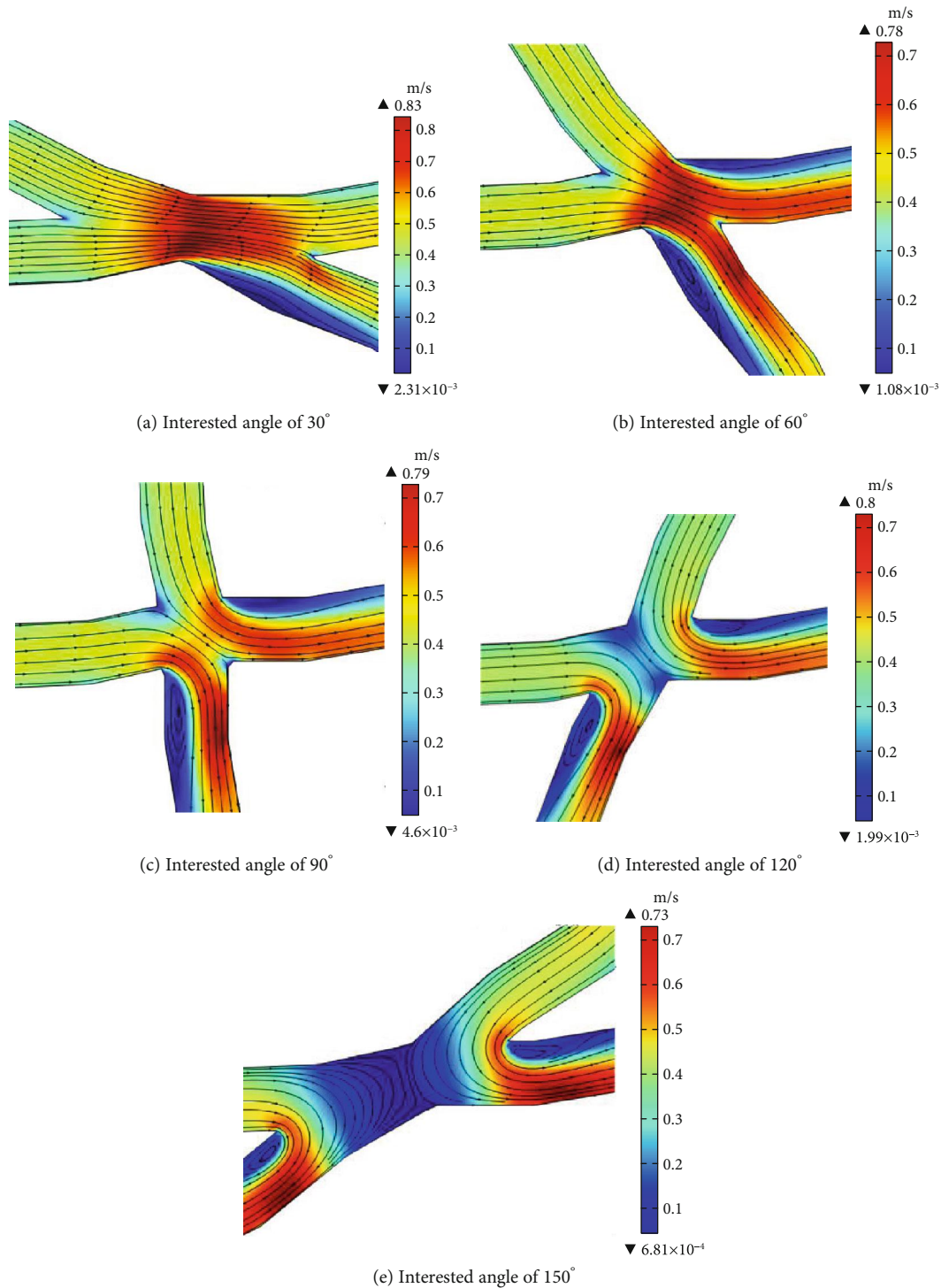


FIGURE 21: Velocity distribution of specimen S1.

enhanced as flow rate increases. According to the definition of critical Reynolds number in Equation (13), the Re_c is ranging from 85.94 to 133.42 listed in Table 4.

Figures 21 and 22 deeply researched on the flow characteristics at fracture intersections and their influences on the nonlinear flow behavior for two types of rough intersected fractures. For crossing angle α of 30° , the flow streamlines follow closely the curvatures of the fracture walls. For crossing

angles α of 60° changing to 150° , two eddies emerge in lower parts of the fracture which cause the reduction in the effective area available for flow when Reynolds number Re is 100. This result is consistent with that of Liu et al. [30].

To systematically investigate the nonlinear flow behavior in single fracture intersections, many extended numerical models beyond the flow experimental cases were established. Models have been established with crossing angle α of 30° ,

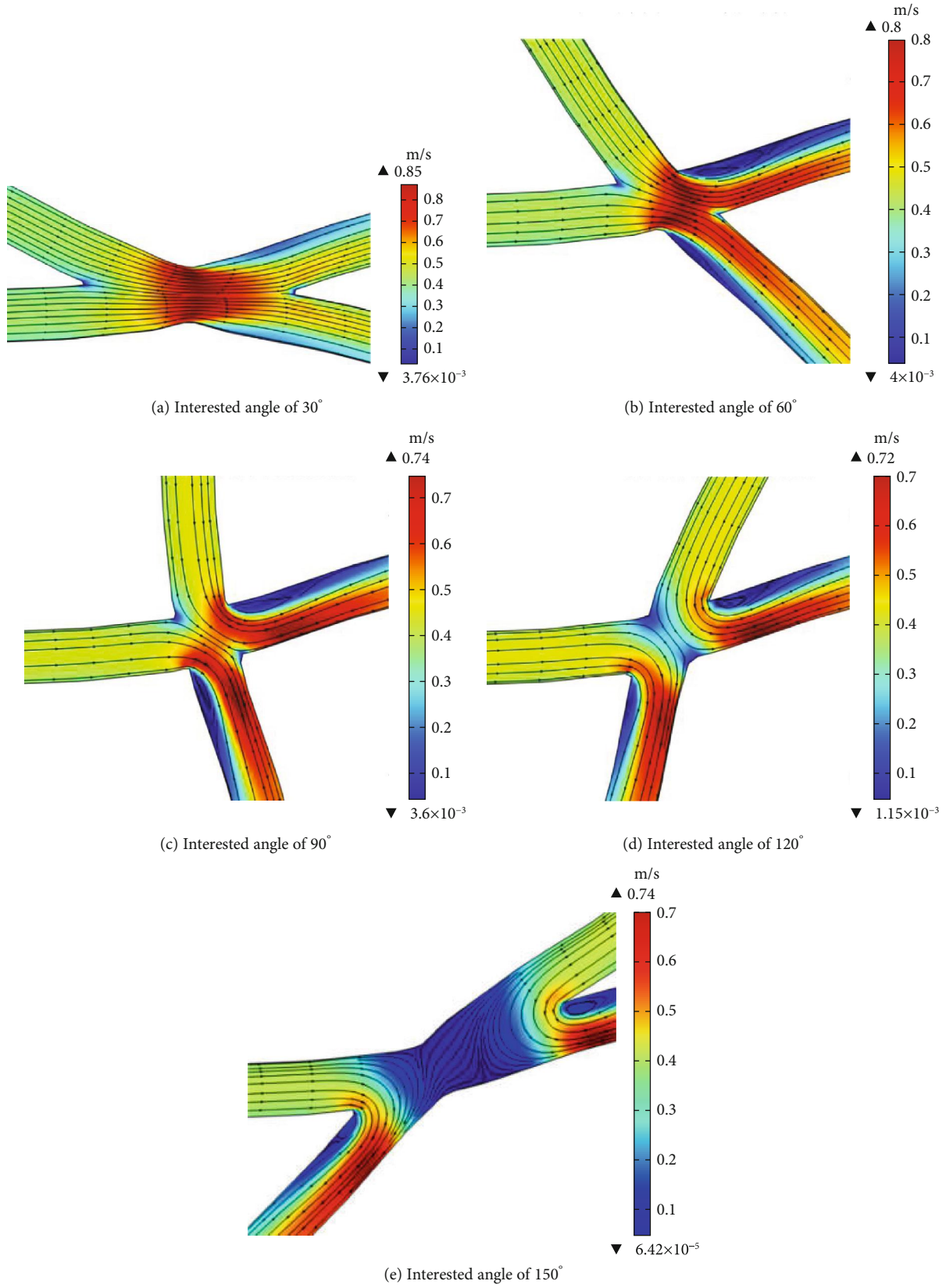
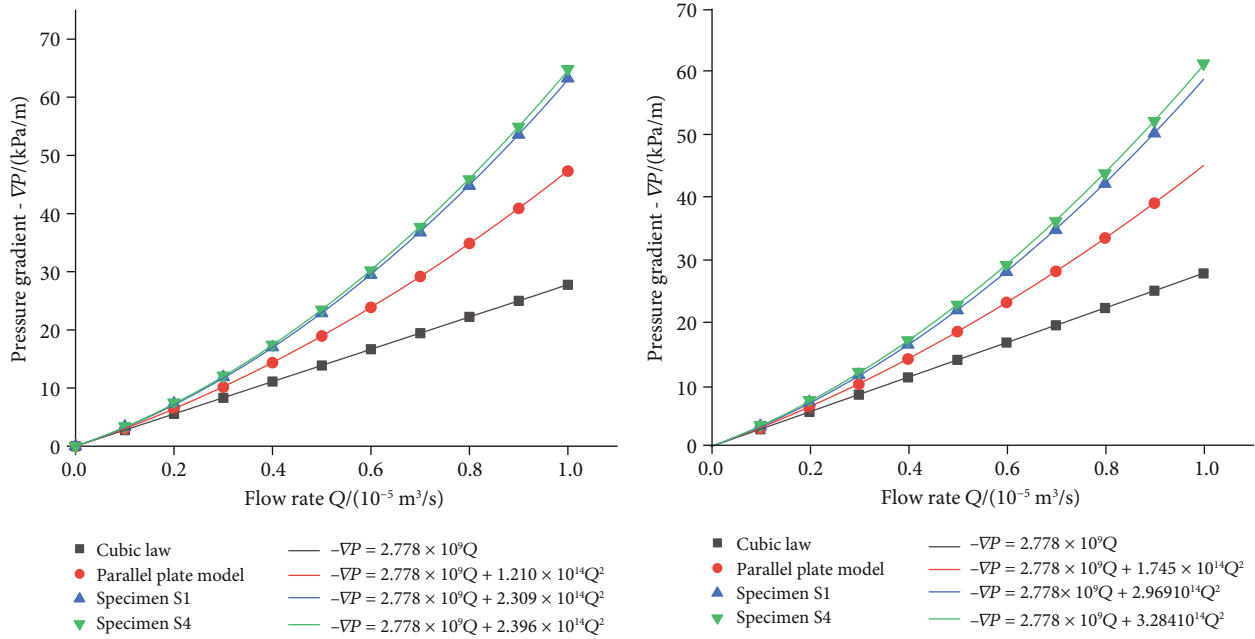


FIGURE 22: Velocity distribution of specimen S4.

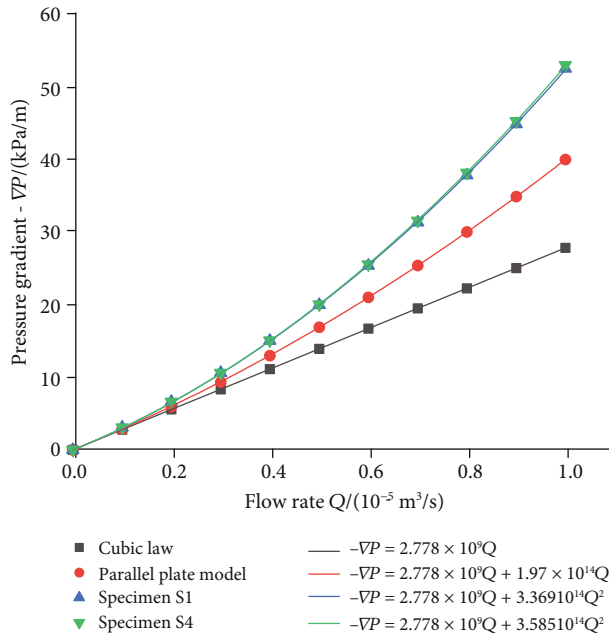
TABLE 4: The seepage parameters considering different intersected angles of rough fractures.

CFI $\alpha/^\circ$	Specimen S1			Specimen S4		
	B ($\text{kg}/\text{m}^8/10^{14}$)	Re_c	β	B ($\text{kg}/\text{m}^8/10^{14}$)	Re_c	β
30	2.309	133.42	0.020	2.396	128.61	0.021
60	2.806	109.81	0.024	3.043	101.23	0.026
90	2.969	103.78	0.026	3.284	93.83	0.028
120	3.022	101.93	0.026	3.511	87.76	0.030
150	3.369	91.44	0.029	3.585	85.94	0.031



(a) Interested angle of 30°

(b) Interested angle of 90°



(c) Interested angle of 150°

FIGURE 23: Curves of $\nabla P \sim Q$ for rough fractures with different interested angles.

60°, 90°, 120°, and 150°. The numerical simulations by solving the Navier-Stokes equations were also performed by COMSOL Multiphysics. In order to better understand the influence of fracture intersections on the nonlinear flow behavior, the Forchheimer coefficient B listed in Table 4 (mentioned in Section 3.2: $B = \beta\rho/w^2b^2$) is calculated and the values for different cases. The relationships between B and intersected angle are also listed in Table 4. Hence, it is also proved that the intersected angle has significant influences on nonlinear flow behavior of fracture intersections.

Therefore, the formation of eddies is related to the fracture intersected angle, which demonstrates that the intersected angle plays a significant role in the nonlinear behavior of flow through the intersected fractures.

5.3.2. The Fracture Roughness Influencing on the Seepage Characteristics. In addition, in order to describe the flow characteristics through fractures with different roughness considering some intersected angles, the simulations are plotted in Figure 23. The results indicate that the curves of $\nabla P - Q$ increased linearly initially and then nonlinearly as flow rate increased, which show a good agreement with the variation in Figure 20. Observed from the curves considering same intersection angle plotted in Figure 24 described by histogram, the variation of the nonlinear fluid coefficients B increased with the greater roughness. Therefore, the fracture surface roughness and intersection angle are both important factors influencing on the flow behavior of rough fractures.

6. Conclusions

In this work, flow tests have been carried out on single rough fractures to study the nonlinear behavior of fluid flow through rough fractures. Corresponding extended numerical simulations have been conducted to supplement the analyses and also analysis about influence of the fracture intersections on seepage behavior transformation of the fluid flow. The main conclusions are drawn as follows:

- (1) The flow tests through the rough fractures of specimens S1-S4 show that increasing pressure gradient can enlarge the flow velocity and weaken the viscous forces, and then increasing inertial forces cause the transformation of the seepage behavior from the linearity to nonlinearity. And also, the non-Darcy coefficient is introduced to explain the transformation points of the flow behavior, and the wall friction coefficient is derived based on equation Darcy-Weisbach and Forchheimer formula to reveal the transformation mechanism of fluid flow through the rough fractures
- (2) The 3-D fractures are reconstructed based on the scanning point cloud data, and the seepage numerical model using the Navier-Stokes equation based on the software COMSOL Multiphysics is proposed considering different roughness about four specimens S1-S4. The comparison of the $\nabla P \sim Q$ calibrates the feasibility of the above model

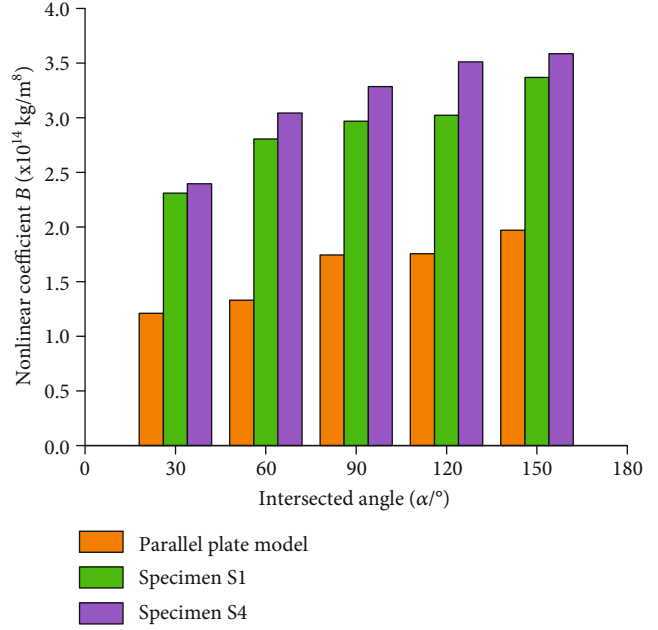


FIGURE 24: The comparison of nonlinear coefficients for rough fractures with different interested angles.

- (3) It can be seen from the distribution of the pressure gradient and velocity of mentioned fractures based on the proposed model that pressure decreases along the flow direction; however, greater pressure causes uneven pressure distribution and obvious nonlinear flow behavior. And also, the velocity shape is close to the parabola shape along the fracture height direction (aperture direction); however, the velocity shape shows asymmetry because of nonlinear flow behavior through rough fractures
- (4) The curves of the $\nabla P \sim Q$ considering combination of the aperture variation indicate that greater absolute roughness weakens the flow rate to enlarge the Forchheimer coefficients; however, greater aperture causes larger velocity and flow rate to get smaller Forchheimer coefficients, which reveals the relationship of the coefficients $A, B, \text{aperture}$ and the flow nonlinearity
- (5) The triggering mechanism of the transformation of the flow behavior from the linearity to the nonlinearity is deeply researched, and another expressions of the wall friction coefficient have been derived to calculate f . It can be concluded that greater roughness causes larger f and smaller Re considering same apertures resulting in nonlinear flow; otherwise, increasing aperture representing smaller relative causes smaller f and larger Re considering same roughness resulting in nonlinear flow more difficultly. The results indicate that the wall friction coefficients related to the fracture morphology, Reynolds number, and so on can explain the seepage characteristics of rough fractures and also describe the

transformation points representing the occurring of the nonlinear flow

- (6) The flow nonlinearity is strongly affected by the fracture intersected angle. The nonlinearity of fluid flow is mainly caused by the formation of eddies at fracture intersections, which are clearly observable in numerical models. And it can be observed from the numerical results that the critical Reynolds number decreases with increasing angle. Furthermore, the relationships based on simulations that relate the nonlinear coefficient B in Forchheimer law to intersected angle and surface roughness have been proposed to reveal the flow nonlinearity through the rough fractures

Data Availability

The data in this manuscript are obtained by the experiments in Chongqing University, and the data based on software are extended from the experimental data.

Conflicts of Interest

The authors declare that there are no conflicts of interest regarding the publication of this paper.

Acknowledgments

The research is financially supported by the National Natural Science Foundation of China (No. 51779021) and the Fundamental Research Funds for the Central Universities (No. 2020CDCGJ021).

References

- [1] B. Berkowitz, "Characterizing flow and transport in fractured geological media: a review," *Advances in Water Resources*, vol. 25, no. 8-12, pp. 861-884, 2002.
- [2] T. Babadagli, X. Ren, and K. Develi, "Effects of fractal surface roughness and lithology on single and multiphase flow in a single fracture: an experimental investigation," *International Journal of Multiphase Flow*, vol. 68, pp. 40-58, 2015.
- [3] K. K. Singh, D. N. Singh, and P. G. Ranjith, "Laboratory simulation of flow through single fractured granite," *Rock Mechanics and Rock Engineering*, vol. 48, no. 3, pp. 987-1000, 2015.
- [4] W. Yuan, G. Zhigang, and N. Xiaodong, "Experimental study of non-Darcy water flow through a single smooth fracture," *Chinese Journal of Rock Mechanics and Engineering*, vol. 29, no. 7, pp. 1404-1407, 2010.
- [5] R. W. Zimmerman, A. AL-Yaarubi, C. C. Pain, and C. A. Grattoni, "Nonlinear regimes of fluid flow in rock fractures," *International Journal of Rock Mechanics and Mining Sciences*, vol. 41, no. 3, pp. 163-169, 2004.
- [6] P. G. Ranjith and W. Darlington, "Nonlinear single-phase flow in real rock joints," *Water Resources Research*, vol. 43, no. 9, pp. 146-156, 2007.
- [7] J. Qian, Z. Chen, H. Zhan, and H. Guan, "Experimental study of the effect of roughness and Reynolds number on fluid flow in rough-walled single fractures: a check of local cubic law," *Hydrological Processes*, vol. 25, no. 4, pp. 614-622, 2011.
- [8] Z. Zhang and J. Nemcik, "Fluid flow regimes and nonlinear flow characteristics in deformable rock fractures," *Journal of Hydrology*, vol. 477, no. 16, pp. 139-151, 2013.
- [9] M. Zoorabadi, S. Saydam, W. Timms, and B. Hebblewhite, "Non-linear flow behavior of rough fractures having standard JRC profiles," *International Journal of Rock Mechanics and Mining Sciences*, vol. 76, pp. 192-199, 2015.
- [10] Y. F. Chen, J. Q. Zhou, S. H. Hu, R. Hu, and C. B. Zhou, "Evaluation of Forchheimer equation coefficients for non-Darcy flow in deformable rough-walled fractures," *Journal of Hydrology*, vol. 529, pp. 993-1006, 2015.
- [11] Q. Xiong, D. Yang, and W. Chen, "Multi-scale modelling of gas flow in nanoscale pore space with fractures," *Journal of Rock Mechanics and Geotechnical Engineering*, vol. 12, no. 1, pp. 32-40, 2020.
- [12] X. Weimin, X. Caichu, W. Wei et al., "Study of void model for fluid flow through rough fractures-taking Reynolds equation as governing equation," *Rock and Soil Mechanics*, vol. 33, no. 12, pp. 3680-3688, 2012.
- [13] Z. Hongguang, Y. Cheng, X. Heping et al., "A new geometrical model for non-linear flow in rough-walled fractures based on the cubic law," *Journal of China Coal Society*, vol. 41, no. 4, pp. 822-828, 2016.
- [14] M. Javadi, M. Sharifzadeh, and K. Shahriar, "A new geometrical model for non-linear fluid flow through rough fractures," *Journal of Hydrology*, vol. 389, no. 1-2, pp. 18-30, 2010.
- [15] H. B. Lee, I. W. Yeo, and K. K. Lee, "The modified Reynolds equation for non-wetting fluid flow through a rough-walled rock fracture," *Advances in Water Resources*, vol. 53, no. 1, pp. 242-249, 2013.
- [16] M. Wang, Y. F. Chen, G. W. Ma, J. Q. Zhou, and C. B. Zhou, "Influence of surface roughness on nonlinear flow behaviors in 3D self-affine rough fractures: lattice Boltzmann simulations," *Advances in Water Resources*, vol. 96, pp. 373-388, 2016.
- [17] L. Zou, L. Jing, and V. Cvetkovic, "Roughness decomposition and nonlinear fluid flow in a single rock fracture," *International Journal of Rock Mechanics and Mining Sciences*, vol. 75, pp. 102-118, 2015.
- [18] K. Nazridoust, G. Ahmadi, and D. H. Smith, "A new friction factor correlation for laminar, single-phase flows through rock fractures," *Journal of Hydrology*, vol. 329, no. 1-2, pp. 315-328, 2006.
- [19] J. Yang, Z. Qingang, Y. Yang et al., "An experimental investigation on the mechanism of fluid flow through single rough fracture of rock," *Scientia Sinica Technologica*, vol. 43, no. 10, pp. 1144-1154, 2013.
- [20] Z. Zhang, J. Nemcik, Q. Qiao, and X. Geng, "A model for water flow through rock fractures based on friction factor," *Rock Mechanics and Rock Engineering*, vol. 48, no. 2, pp. 559-571, 2015.
- [21] J.-Q. Zhou, S.-H. Hu, Y.-F. Chen, M. Wang, and C.-B. Zhou, "The friction factor in the Forchheimer equation for rock fractures," *Rock Mechanics and Rock Engineering*, vol. 49, no. 8, pp. 3055-3068, 2016.
- [22] S. Xiaopeng, Z. Lei, L. Honglian et al., "Experimental and numerical modelling of nonlinear flow behavior in single fractured granite," *Geofluids*, vol. 50, 19 pages, 2019.
- [23] M. Wenqiang, L. Lianchong, Y. Tianhong et al., "Numerical investigation on a grouting mechanism with slurry-rock coupling and shear displacement in a single rough fracture,"

- Bulletin of Engineering Geology and the Environment*, vol. 78, no. 8, pp. 6159–6177, 2019.
- [24] W. A. M. Wanniarachchi, P. G. Ranjith, M. S. A. Perera, T. D. Rathnaweera, C. Zhang, and D. C. Zhang, “An integrated approach to simulate fracture permeability and flow characteristics using regenerated rock fracture from 3-D scanning: a numerical study,” *Journal of Natural Gas Science and Engineering*, vol. 53, pp. 249–262, 2018.
- [25] J. Bi, X. P. Zhou, and Q. H. Qian, “The 3D numerical simulation for the propagation process of multiple pre-existing flaws in rock-like materials subjected to biaxial compressive loads,” *Rock Mechanics and Rock Engineering*, vol. 49, no. 5, pp. 1611–1627, 2016.
- [26] Z. Zeng and R. Grigg, “A criterion for non-Darcy flow in porous media,” *Transport in Porous Media*, vol. 63, no. 1, pp. 57–69, 2006.
- [27] X. Liu, M. Xu, and K. Wang, “Mechanism of permeability evolution for reservoir sandstone with different physical properties,” *Geofluids*, vol. 2018, 16 pages, 2018.
- [28] J. Yu, X. Chen, Y. Y. Cai, and H. Li, “Triaxial test research on mechanical properties and permeability of sandstone with a single joint filled with gypsum,” *KSCE Journal of Civil Engineering*, vol. 20, no. 6, pp. 2243–2252, 2016.
- [29] D. S. Yang, W. Wang, W. Z. Chen et al., “Investigation on stress sensitivity of permeability in a natural fractured shale,” *Environmental Earth Sciences*, vol. 78, no. 55, pp. 1–10, 2019.
- [30] R. Liu, B. Li, and Y. Jiang, “Critical hydraulic gradient for nonlinear flow through rock fracture networks: the roles of aperture, surface roughness, and number of intersections,” *Advances in Water Resources*, vol. 88, pp. 53–65, 2016.
- [31] F. Xiong, W. Wei, C. Xu, and Q. Jiang, “Experimental and numerical investigation on nonlinear flow behaviour through three dimensional fracture intersections and fracture networks,” *Computers and Geotechnics*, vol. 121, article 103446, 2020.

Research Article

Effect of Sea-Level Change on Deep-Sea Sedimentary Records in the Northeastern South China Sea over the past 42 kyr

Bin Wang ¹, Huaiyan Lei ^{1,2}, Fanfan Huang,¹ Yuan Kong,¹ Fulong Pan,¹ Weidong Cheng,¹ Yong Chen,³ and Limei Guo^{1,2}

¹College of Ocean & Earth Sciences, Xiamen University, Xiamen 361102, China

²State Key Laboratory of Marine Environmental Science, Xiamen University, Xiamen 361102, China

³Island Research Center, Ministry of Natural Resources, Pingtan, 350400, China

Correspondence should be addressed to Huaiyan Lei; lhy@xmu.edu.cn

Received 7 June 2020; Revised 19 August 2020; Accepted 18 September 2020; Published 23 October 2020

Academic Editor: Qian Yin

Copyright © 2020 Bin Wang et al. This is an open access article distributed under the Creative Commons Attribution License, which permits unrestricted use, distribution, and reproduction in any medium, provided the original work is properly cited.

We integrated multiple geochemical analysis of a 13.75 m-long core 973-4 recovered from the northeastern South China Sea (SCS) to detect the response of deep-sea sediment archives to sea-level change spanning the last 42 kyr. The age-depth model based on AMS ¹⁴C dating, together with the sediment grain size, shows an occurrence of turbidity current at around 14 kyr, which was associated with submarine landslides caused by gas hydrate dissociation. A dominantly terrigenous sediment input was supplied from southwestern Taiwan rivers. By synthesizing environment-sensitive indexes, four distinct stages of paleoenvironmental evolutions were recognized throughout the studied interval. Well-oxygenated condition occurred during the stage I (42.4–31.8 kyr) with low sea-level stand below -80 m, accompanied by flat terrigenous input. The largest amounts of terrigenous sediment input occurred during the late phase of stage II (31.8–20.4 kyr) with the lowest sea-level stand below -120 m because of a short distance from paleo-Taiwan river estuaries to the core location. An occurrence of Ca-enriched turbidity current disturbed the original sediments during the stage III (20.4–13.9 kyr). The stepwise elevated sea-level stand resulted in an enclosed (semi-enclosed) system and contributed to a relatively low-oxygen environment in deep ocean during the stage IV (13.9 kyr—present). Temporal variations of TOC and CaCO₃ display contrary pattern synchronously, indicating a decoupled relationship between organic carbon burial and carbonate productivity. Our results highlight that these sedimentary records as reflected in the paleoenvironmental changes in the northeastern SCS were mainly driven by sea-level fluctuations and later, since the mid-Holocene, the strengthening East Asian summer monsoon (EASM) overwhelmed the stable sea level in dominating the environmental changes.

1. Introduction

As the largest marginal sea of the western Pacific, the South China Sea (SCS) receives large amounts of sediment annually, with possible terrigenous supplies from the Pearl, Red, and Yangtze Rivers, as well as the island of Taiwan and Luzon [1–4]. It is considered that more than 700 Mt/year of fluvial sediments are transported to the SCS from surrounding rivers [3], amounting to 3.7% of estimated global fluvial sediment discharge to the world ocean [5]. Among various fluvial drainage systems, the mountainous rivers from southwestern (SW) Taiwan discharge the largest number of

suspended sediments directly to the SCS, with a total load of 176 Mt/year, South China contributes about 102 Mt/year, and the supply from Luzon Island is more than 13 Mt/year (Figure 1) [3]. Recently, the area in the east of the Pearl River (EPR) has been considered as another potential source for sediment supply to the northern SCS [6]. These fluvial sediments are further transported by various coastal, surface, and deep currents after entering the SCS, such as the East Asian monsoon (EAM), which is the major control on the surface circulation. Meanwhile, the deep-water current from the Western Pacific through the Luzon Strait and the intrusion of shallower Kuroshio Current are considered to be the

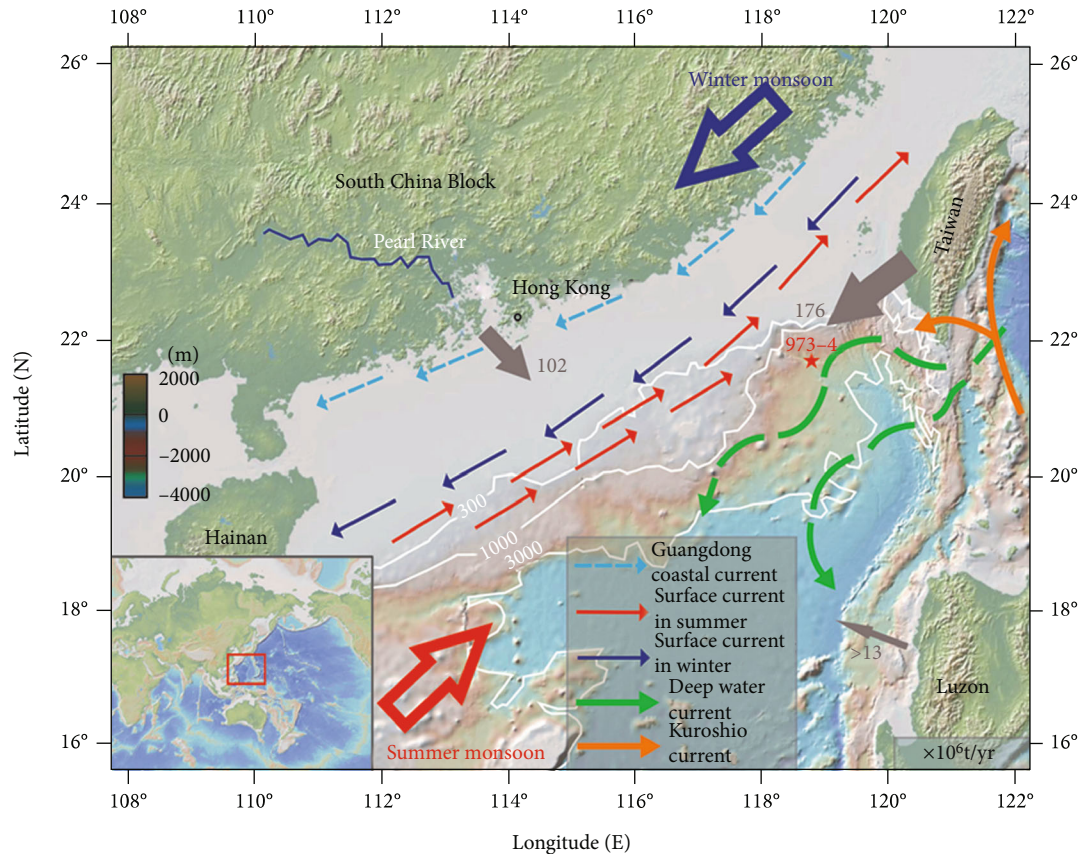


FIGURE 1: Overview map of the northern part of the SCS, including core location 973-4, monsoon and current systems, fluvial drainage systems, and their annual suspended sediment discharge to the South China Sea. Core 973-4 is labeled by red star. Monsoon and current systems are labeled by colored arrows. Monsoon winds after Webster [11], Guangdong coastal currents after Fang et al. [8], Kuroshio Current after Caruso et al. [7], deep water currents after Zhao et al. [12]. Fluvial drainage systems and their annual discharge to SCS are represented by grey arrows with numbers (in million metric tons, Mt/yr), and the size represents the flux (summarized by [3]). The base map was generated from GeoMapApp.

main pathways that can transport sediments derived from Taiwan to the northern SCS. Moreover, the Guangdong Current impacted by EAM flows northeastward in summer and southwestward in winter, which is important for sediment transport from the Pearl River to the northern SCS (Figure 1) [3, 7–12]. Consequently, the SCS is commonly regarded as the largest receptacle of fluvial sediments among semi-enclosed marginal seas around the world [5], and this area provides a natural laboratory for deciphering paleoenvironmental changes from high-resolution sedimentary records.

In comparison with continental basin affected by significant modification of diagenetic processes [13–15], marine sediments in ocean basin have more clearer fingerprints for the deposition history; hence, they are robust archives for reconstructing the past variations of both climate and environment. Over the last decade, many studies attempted to elucidate the paleoenvironmental changes by using multiple paleoproxies, such as elemental geochemistry [16, 17], foraminiferal characteristics ([18, 19]), magnetism [20], clay minerals [3, 9, 21], and granularity [22, 23]. The key conclusion from these results is that sea-level fluctuations placed a

significant impact on climate change and dominated the environmental development. For example, during the Last Glacial Maximum (LGM) when the global sea level dropped below -120 m, the coastline retreated, and larger areas of continental shelf were exposed; fluvial sediments could be discharged into outer shelf and deep ocean more easily [24].

The continental margin off SW Taiwan is located in the northeastern SCS, which is a greatly suitable area for studying the sedimentary responses to the sea-level change because this area has received large amounts of fluvial sediments. A recent research demonstrated that Taiwan-sourced sediments could be delivered into the SCS for a long distance [25]. In such a case, frequent turbidity currents induced by sea-level changes have been observed [26], and lowstand is more likely to trigger seafloor instability [27, 28]. As a result, the exogenous materials carried by paroxysmal currents are able to disrupt the original sequence during the process of sedimentation. Because of active methane seepage, published reports have paid more attention to the dissociation of deep methane-hydrated reservoirs [29–31], few studies concentrated on the paleoenvironmental changes in the northeastern SCS over the studied time scales, and the sedimentary

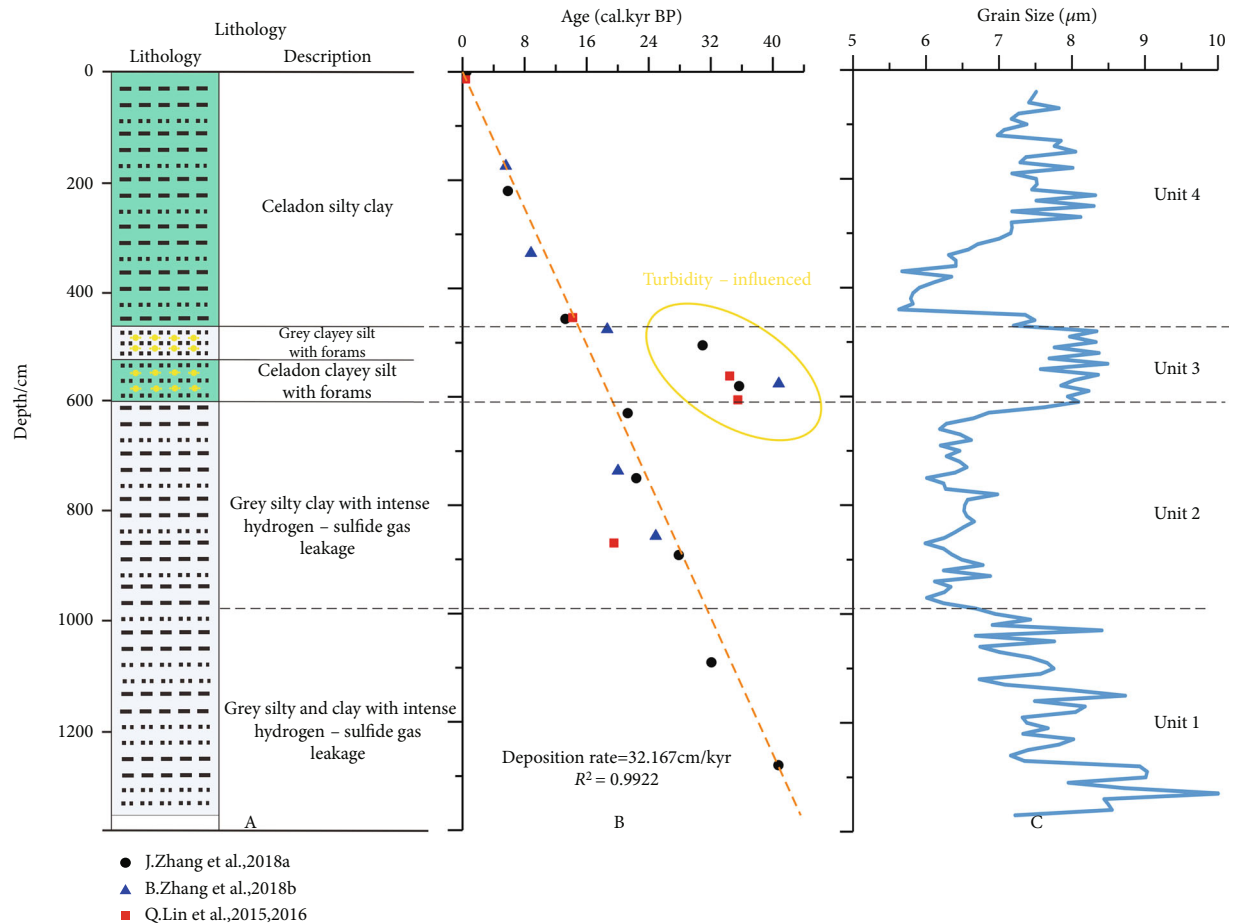


FIGURE 2: Downcore variations in lithology (a), calibrated age-depth model (b) and mean grain size (c). Lithological characteristics were summarized from [51]. The calibrated AMS ^{14}C dating was collected from [3, 19, 31, 52]. The yellow circle represents the abnormal intervals resulted from turbidity current, and the calibrated age presents great linear feature and high deposition rate (32.167 cm/kyr) except for several turbidite-influenced data. Grain size data were taken from [31], and units 1-4 are defined correspondingly.

records related to sea-level variations remained ambiguous. In this work, detailed sedimentary records from core 973-4 are used to better constrain the paleoenvironmental changes related to the sea-level variations since the last glaciation.

2. Materials and Methods

2.1. Materials and Age-Depth Model. Due to special location and tectonic characteristics, the SCS was greatly affected by surrounding units such as Eurasian, Pacific, and Indo-Australian plates, which resulted in complicated submarine topography. The study area is located in the SW Taiwan Basin of the northeastern South China Sea, where submarine faults, bottom channels, and mud diapirs were developed [32]. Many studies have analyzed the hydraulic properties of rock fractures [33–40] and suggested that these fracture systems in strata are favorable pathway for fluid migration [41–45], but the fracture systems develop heterogeneously in natural environments, and the fracture prediction is quite difficult and needs more experimental investigations [46–49]. Additionally, large-scale seep carbonates associated with gas hydrate and CH_4 -enriched fluid migration, named as “Jiulong methane reef”, were discovered nearby the study

area in 2004 [50]. The studied core 973-4 (Figure 1) ($118^\circ 49.0818' \text{E}$, $21^\circ 54.3247' \text{N}$; 1666 m water depth; 13.75 m long) was retrieved from the lower continental slope in the northeastern SCS conducted by the “Haiyang-6” vessel in 2011. After core retrieval, the collected sediments were divided into segments and then freeze-dried for the further analysis. Simultaneously, the core was described immediately. The lithology of core 973-4 is characterized by dark-green silty clay and grey silty clay, and the abnormal intervals between 450 and 605 cm consist of a silty layer, accompanied by enhanced abundances of foraminifera as described by Qu [51] in details (Figure 2(a)).

On the basis of the geochronological framework (Figure 2(b)), core 973-4 had a high linear deposition rate with an average of 32.167 cm/kyr, and the oldest sediments were from the phase of the Marine Isotope Stage (MIS) 3 recorded at the age of 42.4 kyr. An obvious discontinuity in the age-depth model was observed at the intervals between 450 and 605 cm aged from around 14 to 20 kyr, in accordance with the core observation, and the younger strata was disturbed by older sediments. The inconsecutive sequence was identified as the potential occurrence of turbidity currents, which have been simply mentioned before [29, 31].

2.2. Analytical Methods. Samples were taken at 30 cm intervals, and 40 samples were obtained from top to bottom of core 973-4. The samples were freeze-dried and then crashed into powders with an agate pestle and mortar. To remove the organic matter and carbonate, 10% H₂O₂ at 60°C for 1 h and 0.5 N HCl at 60°C for 2 h were treated to react with sediments, respectively. Afterwards, sediments were washed three times with deionized water and then were freeze-dried for further treatment. For each sample, about 30 mg freeze-dried sediments were placed into the digestion vessel and microwaved (Top Wave) along with an acid mixture of 3 ml HF and 6 ml HNO₃. After cooling, the remaining solutions were transferred into the Teflon Crucible on a hotplate for heating overnight until the samples were evaporated to dryness. Subsequently, the residues were dissolved in 2 ml HNO₃ (2%) and diluted to 20 ml with Milli-Q water. The obtained solutions were collected for the determination of major metal concentrations (Al, Ba, Ca, Fe, K, Mg, Mn, Na, P, Ti) by using an Inductively Coupled Plasma-Optical Emission Spectrometer (ICP-OES) at the Institute of Soil Science, Chinese Academy of Sciences (Nanjing). The precisions for chemical analysis of major elements were better than 3%, and the results were reliable. For the analysis of trace element concentrations (Sr, Li, Be, V, Cr, Co, Ni, Cu, Zn, Rb), the digested solution was determined at the Institute of Earth Environment, Chinese Academy of Sciences (Xi'an) by using an Inductively Coupled Plasma Mass Spectrometry (ICP-MS). Within the elemental detection ranges, precision and accuracy were both better than 5% for trace elements.

Several sedimentary segments were collected for the analysis of total nitrogen (TN) and nitrogen isotope ($\delta^{15}\text{N}$). For the TN measurement, dry samples were dealt with 1 N HCl to react with carbonate and then rinsed with deionized water thoroughly, followed by drying at 40°C for 24 h. Subsequently, about 3 mg processed subsamples were analyzed for TN using a PE 2400 SERIES-II Elemental Analyzer. About 20 mg each subsample was taken for the measurements of nitrogen isotopes ($\delta^{15}\text{N}$) by a Thermo Scientific Delta V Advantage mass spectrometer. All the measurements were conducted at the State Key Laboratory of Marine Environment Science, Xiamen University. The analytical precision was better than 0.2% for TN and 0.3‰ for $\delta^{15}\text{N}$.

In addition, published data from core 973-4 were also synthesized in this study to detail the dominated controls of sea level on sedimentary records.

3. Results

According to the downcore variations in grain size, the overall core of 973-4 has four distinctive horizons (Figure 2(c)). Unit 4 (40-450 cm) exhibits the grain size ranging from 5.67 to 8.32 μm with a mean grain size of 7.07 μm and mainly consists of celadon silty clay. There is a rapid increase in grain size in unit 3 (450-610 cm) to an average of 7.95 μm due to the influence of turbidity current, and the sediments are foraminifera-enriched silt with plant fragments. Unit 2 (610-980 cm) shows the lowest grain size value with a mean of 6.45 μm and consists of grey silty clay. A gradual increase in grain size is presented in the lower unit 1 (980-1370 cm),

ranging between 6.24 and 10.06 μm with an average of 7.77 μm , and this interval constitutes grey silt and grey clay (Table 1).

The measured major and trace elements for core 973-4 in this study are mainly composed of Al (5.57-9.59%), Fe (3.03%-4.61%), Ca (2.00%-10.25%), Mg (1.07%-2.07%), Na (1.38%-1.92%), K (1.69%-3.21%), Ti (0.32%-0.55%), Mn (273.89-827.10 ppm), P (432.86-879.41 ppm), V (92.65-157.29 ppm), Cr (52.72-94.58 ppm), Rb (55.28-156.27 ppm), and Sr (125.05-411.20 ppm). As similar with variability of grain size, the elemental profiles have also been divided into the same four intervals from top to bottom (Figure 3). Vertical variations of Al, K, Fe, Mg, Ti, V, and Cr show a similar temporal pattern, which exhibits more depleted in unit 3 while a dramatic increase in concentrations is observed in unit 2. Al concentrations decreased with depth from 7.22% at the top to 6.19% at the depth of 600 cm, following by an increase to 9.59% at the depth of 830 cm, and then the Al values vary little until the bottom. Ti concentrations show stable trend in unit 1 and unit 4, but fluctuations are observed in unit 2 and unit 3 ranging between 0.32% and 0.55%. Similarly, V and Cr show steady variations in unit 1 and unit 4, while nonsteady trends are displayed in unit 2 and unit 3, increasing from 92.65 $\mu\text{g/g}$ to 157.29 $\mu\text{g/g}$ for V and 52.57 $\mu\text{g/g}$ to 94.58 $\mu\text{g/g}$ for Cr with depth, respectively. Mn concentrations generally increase with depth from 0.04% to 0.08% except for the intervals of unit 3 featuring a minimum of 0.03%. The profiles of Ca and Sr display a similar temporal pattern, which is characterized by extraordinarily high values in unit 3 with a peak of 10.25% for Ca and 411.20 $\mu\text{g/g}$ for Sr, while the concentrations in other depths are low and vary slightly, with an average of 2.57% for Ca and 152.77 $\mu\text{g/g}$ for Sr, respectively. The more detailed variations of elemental contents in core 973-4 are presented in Table 1 and Figure 3.

Accordingly, it is noticeable that these vertical profiles exhibit special variations in unit 3 relative to other intervals, which may be related to the modification by the turbidity current. In order to better constrain this anomaly, the major element concentrations from core 973-4 sediments, together with those from the Pearl River [54], the Southwestern Taiwan Rivers [55], and the Luzon River [56] were all used for comparison after normalizing them to the upper continental crust (UCC) (Figure 4) [57].

Our results show that most of the normalized elements including Al, Ca, Fe, Mg, Mn, Na, P, and Ti in core 973-4 are depleted with the exception of K. In addition, the values in unit 3 affected by the turbidity current are significantly different from those deposited in normal strata (unit 1, unit 2 and unit 4), especially for the Ca content. The normalized concentrations of Ca in core 973-4 within unit 3 are greatly high, such an abnormal variation significantly deviates from normal deposition sequence and other river sediments. In addition, there are no obvious similarities in UCC-normalized concentrations between those from core 973-4 and other river samples (Figure 4).

Biogenic proxies in sediments including TN, $\delta^{15}\text{N}$, TOC, and CaCO₃ are mainly driven by marine productivity and oceanic processes [58]. In this work, the TN and $\delta^{15}\text{N}$ values within selected depths ($n = 20$) were mainly used to

TABLE 1: Average (avg) and standard deviation (std) of geochemical parameters in different intervals of the core 973-4. Major elements are given in weight percent (%) while trace elements are in $\mu\text{g/g}$.

Parameters	Unit 4 (70-450 cm)		Unit 3 (450-610 cm)		Unit 2 (610-980 cm)		Unit 1 (980-1280 cm)		
	Avg	Std	Avg	Std	Avg	Std	Avg	Std	
Major elements (%)	Al	7.13	0.38	6.10	0.26	7.59	0.62	7.37	0.21
	Ca	2.49	0.43	7.64	1.38	2.64	0.16	2.59	0.08
	Fe	3.82	0.14	3.13	0.07	4.06	0.20	4.06	0.09
	K	2.26	0.05	1.90	0.13	2.54	0.21	2.43	0.04
	Mg	1.23	0.09	1.21	0.06	1.64	0.14	1.52	0.06
	Mn	0.04	0.00	0.03	0.00	0.06	0.01	0.07	0.00
	Na	1.78	0.11	1.53	0.07	1.57	0.10	1.54	0.06
	P	0.06	0.00	0.05	0.00	0.06	0.01	0.07	0.01
Trace elements ($\mu\text{g/g}$)	Ti	0.46	0.01	0.36	0.02	0.46	0.03	0.45	0.01
	V	123.57	6.24	102.46	6.15	130.03	8.30	129.59	4.91
	Cr	71.04	4.58	56.95	2.70	79.02	4.68	79.58	2.51
	Rb	79.32	16.14	89.03	4.87	99.42	22.08	87.68	4.62
	Sr	162.70	25.70	320.33	50.14	154.37	13.87	141.25	7.23
Grain size(μm)	7.07	0.75	7.95	0.38	6.45	0.31	7.77	0.76	
$\delta^{13}\text{C}_{\text{TOC}}(\text{‰})$	-25.08	0.88	-24.11	0.76	-25.18	0.49	-25.36	1.04	
TOC(%)	0.65	0.25	0.74	0.13	0.88	0.16	0.64	0.19	
$\text{CaCO}_3(\text{‰})$	6.82	3.00	21.32	4.64	4.47	1.33	7.50	1.72	
$\delta^{15}\text{N}(\text{‰})$	4.29	0.79	4.38	1.21	4.75	0.96	4.77	0.91	
TN(%)	0.09	0.13	0.07	0.08	0.08	0.10	0.06	0.07	

Data sources: grain size data and CaCO_3 content [31], $\delta^{13}\text{C}_{\text{TOC}}$ and TOC data [53], and other data (this study).

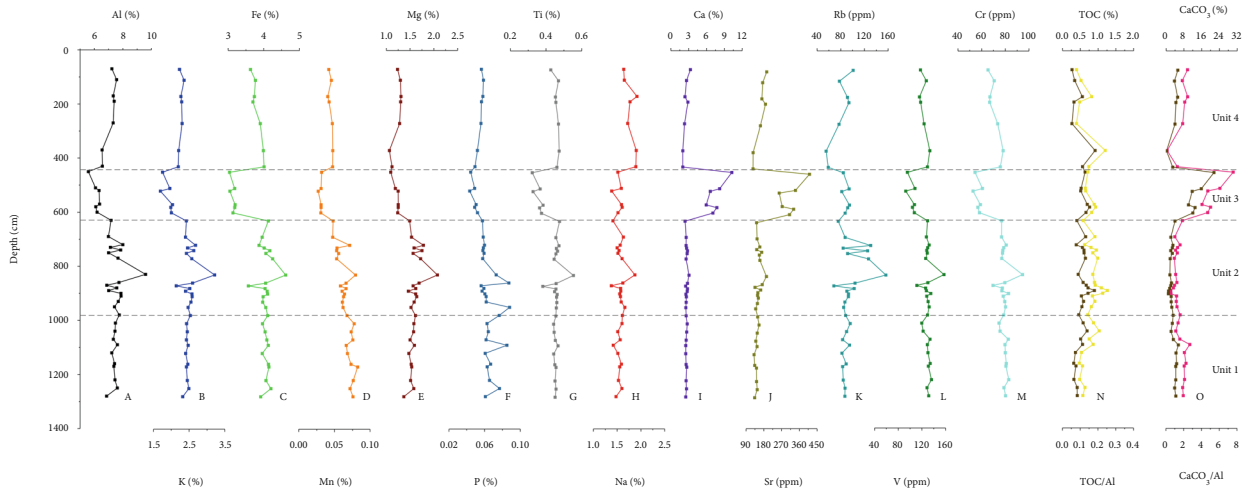


FIGURE 3: Variations in major and trace elemental concentrations, together with TOC (yellow line), CaCO_3 (red line) content, and their normalized to Al values (black line) at core 973-4 in the northeastern SCS over the past 42 kyr.

determine the source of organic matter, the TN values vary in a narrow range from 0.06% to 0.10% (average 0.08%), and TN contents in unit 1 are apparently lower than upper layers. The $\delta^{15}\text{N}$ values exhibited in four units are between 3.97‰ and 5.24‰ (average 4.59‰), and a gradually increasing trend of the mean $\delta^{15}\text{N}$ value is observed with respect to depth.

The content of TOC and CaCO_3 has been reported before [31, 53]. Over the past 42 kyr, the content of TOC varies in the range between 0.39% and 1.26%, which shows relatively higher values in unit 2 and unit 3 but lower values in unit 1 and unit 4. Temporal variations of CaCO_3 present extremely high values in unit 3 and reach a maximum of 30.19%, while lower values are displayed in unit 2, and relatively higher

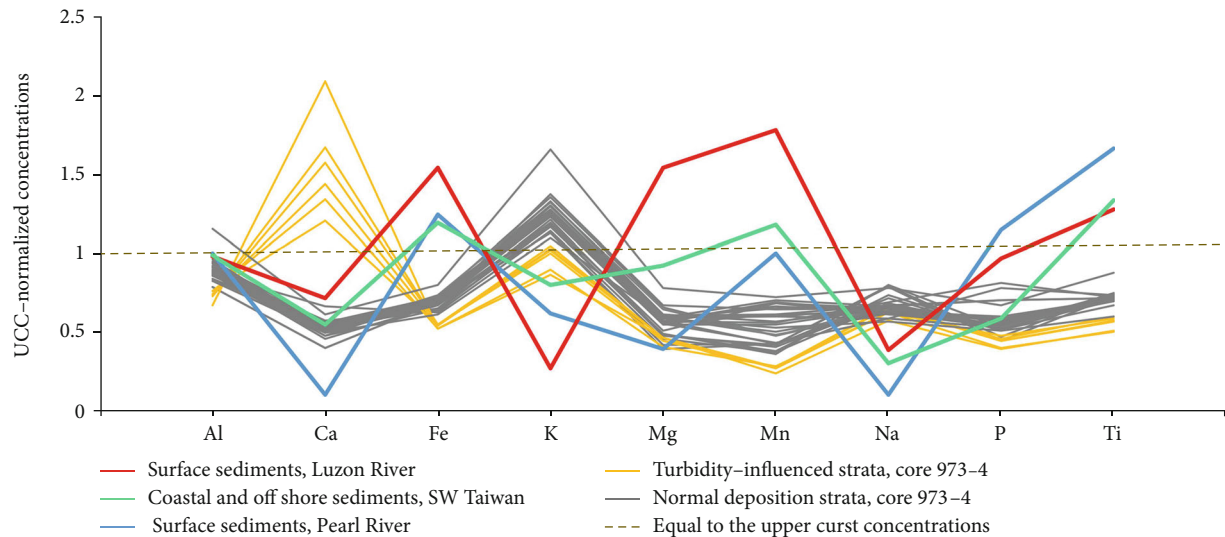


FIGURE 4: UCC-normalized major element concentrations at core 973-4 since the past 42 kyr, showing comparisons with those from the Pearl River [54], Luzon River [56], and offshore of SW Taiwan [55].

values are showed in unit 1 and unit 4. The Al normalized ratio of biogenic records (TOC/Al and CaCO_3/Al) displays a consistency in vertical changes with their content data (Figures 3(n) and 3(o)).

4. Discussion

4.1. The Occurrence of Turbidity Current. Based on sedimentological and geochemical evidences, the unit 3 at core 973-4 was characterized by the largest mean grain size and the highest CaCO_3 content; additionally, the sedimentary strata were disturbed by ex situ sediments, resulting in a sedimentary discontinuity along the normal deposition sequence. Previous studies have confirmed this phenomenon and mentioned the occurrence of turbidity current event briefly [19, 31], but no synthetical description was focused on the overall processes. In this study, we attempt to explain the inducing factors, development process, and the impact of the turbidite event on sedimentation, which could provide further detailed information for investigating environmental evolution in the northeastern SCS.

Core 973-4 is located in the northeastern SCS, where methane hydrate has been considered to accumulate into deep-sea sediments [59]. Generally, gas hydrate is stable under low-temperature and high-pressure environment. When hydrated reservoir forms, an enhanced strength of gas hydrate-bearing sediments has been indicated from laboratory simulation [60], yet the hydrate-free sediment is unconsolidated and differs from the tight reservoirs, such as coal and oil shale [61, 62, 63]. Zhang et al. [31] reported the methane hydrate dissociation history by using stable carbon and oxygen isotope composition of carbonate in bulk sediment, the results revealed that during past 14 kyr, methane hydrate decomposition events were significant and let to the largest methane flux from deep sediments to the overlying layer, and the experimental study indicated that tectonic zones may serve as a favorable pathway for fluid migration [64, 65].

At around 14 kyr, a significant increase in water temperature was concluded [66], which was likely to promote the gas hydrate decomposition, and the high values of oxygen isotopes of benthic foraminifera during this interval [31] were closely related to the warm seawater temperature. Besides, the relatively low sea-level condition (-90 m) during this period might be another crucial factor to accelerate the dissociation process. As a consequence, intense release of gas from deep reservoirs can directly destabilize the seafloor, resulting in the loss of reservoir strength and the occurrence geological hazards, such as earthquake, submarine landslides, and turbidity current [67, 68]. Moreover, both steep slope and developed submarine channel can contribute to the hyperpycnal flow and sediment transportation to the deep ocean.

The intervals of turbidite at core 973-4 range from 450 cm to 605 cm, where mean grain size and stratigraphic chronology vary significantly due to instantaneously enhanced hydrodynamic condition. Furthermore, the concentration of all major elements deposited in turbidite-influenced strata, with the exception of calcium, is less than that of normal deposition strata (Figure 4), and the extreme enrichment in Ca content is attributed to the external input of biogenic content and coincides with an increasing abundance and diversity of foraminiferal assemblages [19]. In return, those materials could result in the enhanced dilution effect to other elements. Chen [69] reported that the nearby core 973-3 (1026 water depth) (Figure 5) occurred turbidity current within the intervals between 220 cm and 770 cm. Interestingly, the strata from these two adjacent sites was overturned at nearly the same time according to the age-depth model. Yet, the shallow-water core 973-3 received more turbidites than that at core 973-4, resulting in much thicker turbidite-influenced layer. Therefore, we can infer that the location of the submarine landslides was situated in the area closed to the river mouth.

At around 14 kyr, both low sea-level condition and rising temperature of seawater were responsible for dissociating the

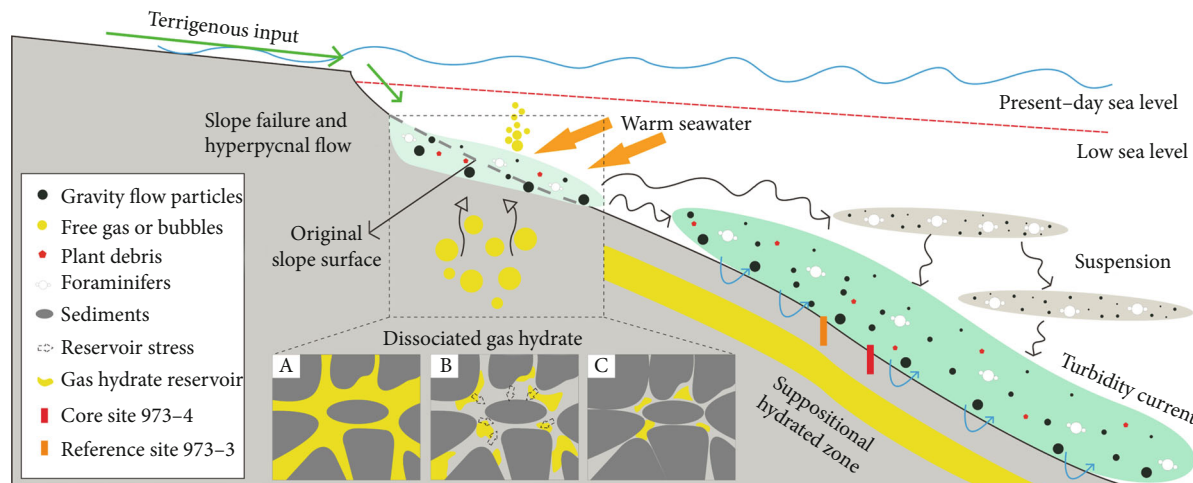


FIGURE 5: A conceptual picture showing the possible processes, including the occurrence of turbidite, sediment delivery, and sedimentation due to the slope failure induced by gas hydrate dissociation. The three drawings in the bottom display the evolution of the hydrated reservoir from a microscopic aspect during gas hydrate dissociation owing to unstable environmental condition. (a). When formed within sediment, gas hydrate filled into pores and cemented particles with high saturation, resulting in an increase in bulk sediment strength (b). When the perturbations to the thermodynamic equilibrium of the gas hydrate system occurred due to the change of sea level and seawater temperature, hydrate began to dissociate from the stability zone (hydrated zone). This process released water and free gas, which diffused upward to the subsurface layer or even to the seafloor shaped as gas plumes, accordingly, the strength in sediments decreased, and sediment particles showed a tendency to be compressed (the dotted arrows) (c). As the hydrate dissociates and gas releases, the sediment particles were redistributed, and the reservoirs became instability. Consequently, those factors were sufficient to trigger an occurrence of submarine landslide and then induced the turbidity current. The turbidity current transported large block of sediments into the deep ocean along the steep slope; finally, the fine materials in suspension deposited on the top of coarse particles. The exogenous components mixed with in situ marine sediments and redeposited on the seafloor, which caused the destruction of the original deposition sequence with certain depth.

hydrated reservoirs, which subsequently led to the release of gas and slope failure, and the contemporaneous turbidity current began to form. During the early stage of the turbidity current formation, plenty of materials were transported from the parent location to deep sea along the steep slope. After delivering for a long distance, turbidity current evolved to a relatively low-density flow. In the form of sediment plume, fine components in suspension were finally deposited on the top of coarse-particle layer due to weakened hydrodynamic condition, which was reflected in the profile of sediment granularity that a sharp drop in mean grain size overlay the turbidite-influenced strata (Figure 2). Below the turbidite-influenced layer, age-depth discontinuity caused by episodically active turbidity currents within some intervals was also speculated during the low sea-level period, but the scale was so small that it had little effect on the environmental reconstruction throughout the studied timescale.

Turbidity current could disturb the original sedimentation rate, and the concomitant materials would mix with local layer; as a consequence, the newly assembled sediments redeposited on the top of normal deposition strata, which led to a discontinuity in the chronological framework. The overall process including the occurrence of submarine landslide, formation of turbidity current, sediment delivery, and deposition process is conceptually illustrated in Figure 5. Large-scale submarine landslides associated with dissociation of gas hydrate have been reported world-

wide, such as the West African margin [70]. Gas hydrate dissociation controlled by climate change has been recognized as a geohazard, which is related to the fate of human activity, and it has been drawn increasing international concern for a long time.

4.2. *The Sources of Organic Matter and Sediment Provenance.* The high deposition rate was identified from the age-depth model, and some plant fragments and rotten wood were also observed during core recovery [31], which indicated that core 973-4 was influenced by the input of terrigenous matters. More specifically, the TOC/TN ratio and organic carbon isotope values ($\delta^{13}C_{TOC}$) are widely used to distinguish the source of organic matter [71]. Generally, MOM (marine organic matter) has more positive $\delta^{13}C_{TOC}$ values and lower TOC/TN ratios than TOM (terrestrial organic matter) [72–74]. By contrast, the TOC/TN ratios in core 973-4 (average 9.39) (Figure 6) are distinctly higher than those from adjacent region of the Dongsha area (average 4.86) [75], presenting a significant contribution from the terrestrial origin. Moreover, the $\delta^{15}N_{TN}$ values in core 973-4 fluctuate in the range from 3.97‰ to 5.24‰, which are in accordance with nitrogen isotope compositions from surface sediments in SCS (3.4‰–6.6‰) [76]. $\delta^{15}N_{TN}$ values in sediment are mainly controlled by the availability of nitrogen and the original nitrogen isotope compositions [77]. Due to the instability during cyclic process, nitrogen isotope ratios ($\delta^{15}N$) are prone to generate disagreement. In comparison, $\delta^{13}C_{TOC}$ is

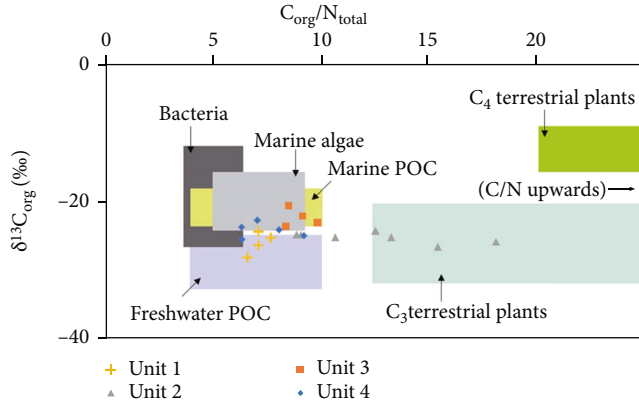


FIGURE 6: $\delta^{13}\text{C}_{\text{org}}$ values vs. $\text{C}_{\text{org}}/\text{N}_{\text{total}}$ ratios of sediments from core 973-4. Data fields after Lamb et al. [71].

a more dependable proxy for indicating the organic-matter sources. Previous research reported that the $\delta^{13}\text{C}_{\text{TOC}}$ of MOM typically varies between -19‰ and -22‰ [78]. The studied core confirmed a mainly terrestrial-sourced carbon source as indicated by depleted $\delta^{13}\text{C}_{\text{TOC}}$ values ranged from -22.69‰ to -26.94‰ with an average of -25.04‰ . Additionally, a simple balance model of carbon isotope was used to calculate the relative proportion of the organic matter contribution between TOM and MOM to core 973-4 [79]:

$$\begin{aligned} \delta^{13}\text{C}_{\text{sed}} &= W_T \times \delta^{13}\text{C}_{\text{terr}} + W_M \times \delta^{13}\text{C}_{\text{mari}}, \\ 100\% &= W_T + W_M, \end{aligned} \quad (1)$$

where $\delta^{13}\text{C}_{\text{terr}}$ and $\delta^{13}\text{C}_{\text{mari}}$ are $\delta^{13}\text{C}$ end-member for terrestrial (-27‰) and marine (-19.5‰) organic origin, respectively; $\delta^{13}\text{C}_{\text{sed}}$ is the carbon isotope ratios from core 973-4 samples; W_T and W_M represent the TOC contribution ratios from terrestrial and marine source, respectively.

As a consequence, about 73.9% of the calculated TOM in sediment from core 973-4 was contributed to the total organic materials, suggesting a dominantly terrestrial sedimentary environment spanning the long-term time scale. Besides, some marine-derived organic matter was also contributed to the core 973-4 during the certain depositional cycles (Figure 6).

It is widely accepted that REE compositions are considered as a reliable indicator for provenance because of their conservative behavior during the sediment transportation and formation [57, 80]. Wu [81] measured the REE compositions from the same core to decipher the influence of cold seeps on the geochemical characteristics, but not to discuss the sediment provenance. Thus, we normalize the REE concentrations at core 973-4 to the upper continental crust (UCC-normalized) [57]. Accordingly, the UCC-normalized REE compositions of three potential provenances including sediments from the Pearl River, SW Taiwan, and Luzon Island, which present a distinct difference to discriminate the sediment sources in the northern SCS, are displayed for comparison. As a result, it is evident that most of the sediment samples in core 973-4 have similar REE patterns to

the SW Taiwan River sediments characterized by relatively flat variation with a slightly positive anomaly in middle REEs (Sm, Eu, Gd, Tb, Dy) and a negative anomaly in other REEs (La, Ce, Pr, Nd, Ho, Er, Tm, Yb, Lu) (Supplementary Figure S1), coinciding with the clay mineral results [3]. The generally high REE values in the Pearl River relative to the SW Taiwan Rivers and Luzon Island may be related to the strong chemical weathering and stable morphology in the Pearl River basin [82]. In addition, two discrimination plots of δEu vs. δCe and $(\text{La}/\text{Sm})_{\text{UCC}}$ vs. $(\text{Gd}/\text{Lu})_{\text{UCC}}$ are effectively used to reflect sediment sources [80], and the δEu and δCe are defined as $\text{Eu}_N/(\text{Sm}_N \times \text{Gd}_N)^{1/2}$ and $\text{Ce}_N/(\text{La}_N \times \text{Pr}_N)^{1/2}$, respectively, where N indicates chondrite normalization (data from [57]). Notably, the REE pattern from core 973-4 samples over the last 42 kyr is also similar with the SW Taiwan Rivers with higher values of δCe and $(\text{La}/\text{Sm})_{\text{UCC}}$ (Supplementary Figure S2).

To summarize, the accumulated sediments in core 973-4 were predominantly originated from Taiwanese rivers over the past 42 kyr, and no REE pattern is similar to the Pearl River or Luzon Island sediments, indicating little sediment contribution from these two sources to the investigated area. Due to the formation of the Taiwan orogen and strengthening deep-water current, the fluvial-derived sediments are considered to be the significant sedimentary inputs to the northern SCS since 3 Ma [10]. Various oceanic currents, such as surface Asian monsoon, intrusion of the subsurface Kuroshio Current, and deep-water current via Luzon Strait (Figure 1), are believed to further promote the transport process of Taiwan-sourced sediments into northern SCS thousands of kilometers away from the source region [52].

4.3. Reconstruction of Paleoenvironments. According to our data above, sea-level fluctuations have a dominated impact on the sedimentary archives responding to the environmental change, such as the occurrence of turbidite. Here, reliable paleorecords, such as grain size, major, and trace elements, together with biogenic proxies (Figure 7), are used to detect the detailed evolution process about how the sea-level variations have an influence on the paleoenvironmental change at core 973-4 in the northeastern SCS since the last glaciation, including the terrigenous input, redox condition, organic matter burial, and ocean productivity.

The fact that Al and Ti are mainly from terrigenous input and behave conservatively during the transport process, which serve as valid signs for estimating the amount of terrigenous input during the geological past. Generally, elevated terrigenous input indicated by higher Al and Ti content occurred during the glacial episodes with low sea-level stand because of the short distance from paleoestuary to the deep ocean. However, in warming stage with relative high sea level, most terrestrial sediment carried by various currents deposited in the inner shelf close to the river mouth. The similar pattern was also confirmed at core 973-4 throughout the past 42 kyr in this study (Figures 7(h) and 7(i)).

Ratios of Rb/Sr and K/Na are applied to reflect the chemical weathering. The increasing chemical weathering intensity rapidly leaches Sr compared to Rb [89]. Similarly, the K/Na ratio is also indicative of sediment recycling, which

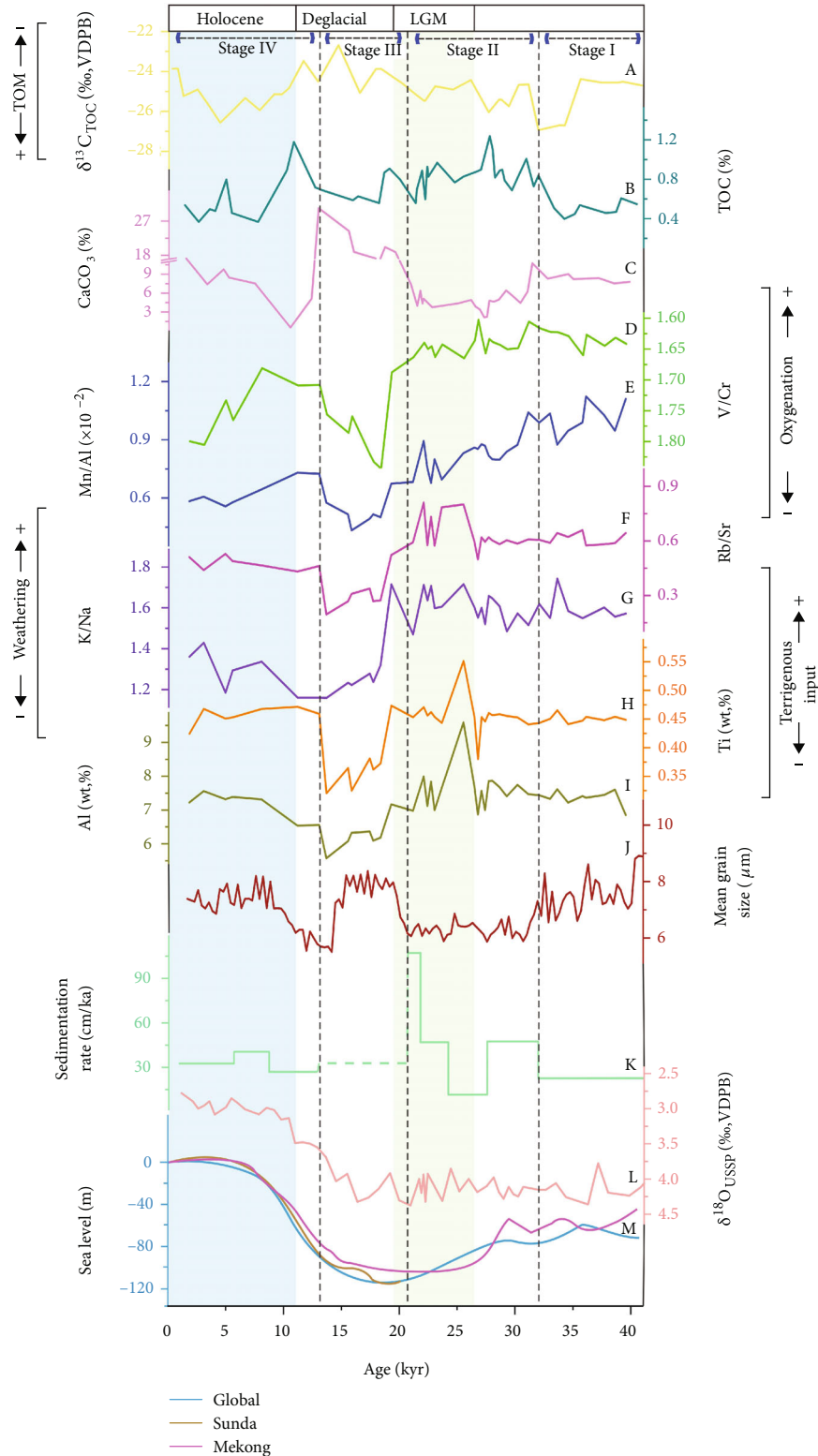


FIGURE 7: Temporal variations of paleorecords at core 973-4 sediments over the past 42 kyr. (a). Carbon isotope of total organic carbon [53]. (b) The TOC content [53]. (c) The CaCO₃ content [31]. (d)–(i) Elements and elemental ratios (this study). (j) mean grain size [31]. (k) sedimentation rate (summarized by [19, 29, 31, 83]), and the dotted line during stage III represents the average sedimentation rate. (l) Oxygen isotope of *Uvigerina* spp. [31]. (m) Sea-level curves for global change, represented by the blue line [84], Mekong River Estuary, represented by the pink line [85], and Sunda Shelf represented by the orange line [86]. Last Glacial Maximum (LGM) and Holocene are marked in green and blue shades, respectively [87, 88]. The dashed lines are the boundary between each evolutionary stage. LGM: Last Glacial Maximum. “+” and “-” in two sides represent increase and decrease, respectively.

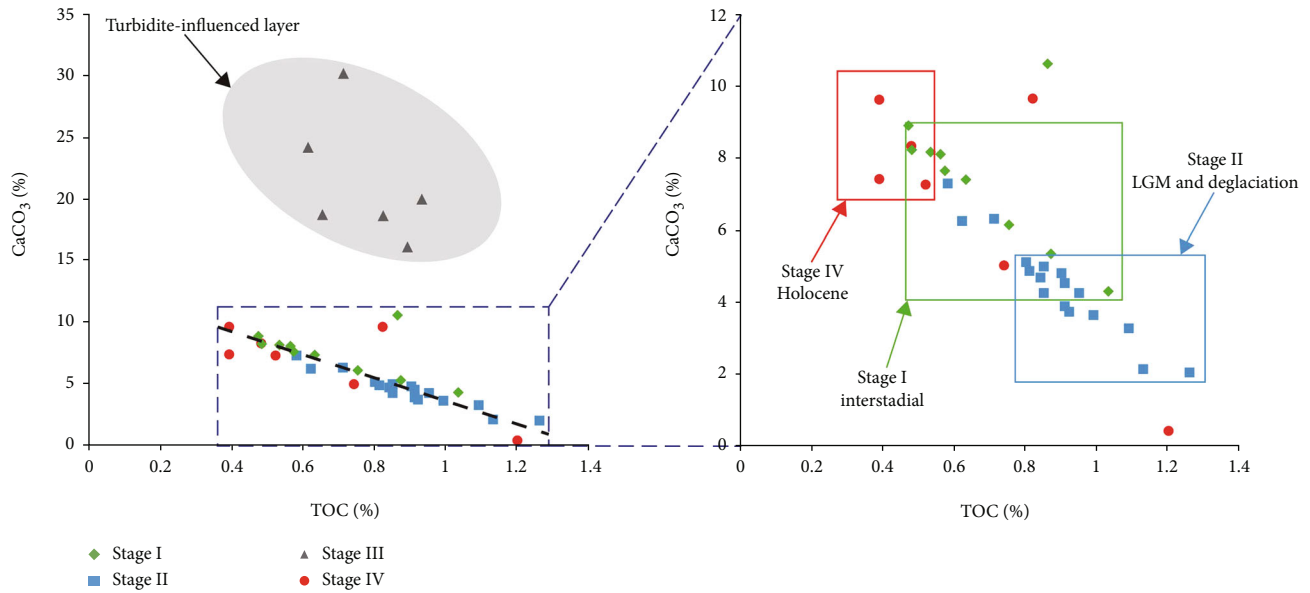


FIGURE 8: Correlation plots for TOC vs. CaCO_3 of samples from core 973-4. Colored patterns represent the data in different stages over the past 42 kyr.

increases with weathering due to more liable nature of plagioclase relative to K-feldspar [89]. Therefore, higher ratios of Rb/Sr and K/Na are indicative of intense chemical weathering. As discussed above, relatively higher Rb/Sr and K/Na ratios in core 973-4 are displayed during the glaciation, especially LGM; but lower ratios are observed in the early Holocene, afterward, the ratios gradually increase since middle Holocene (Figures 7(f) and 7(g)). The variability in Rb/Sr and K/Na ratios confirms that the sediments at core 973-4 had experienced a distinct change in chemical weathering over the past 42 kyr, and we attribute the controlling factors on weathering to the climatic alternation and sea-level variations. The rates of chemical weathering and physical erosion are often coupled, and higher chemical weathering rates are always together with rapid erosion [90]. Enhanced erosion is marked by global cooling due to the increased atmospheric CO_2 [91]. Moreover, Kump [92] presented a clear correlation between chemical erosion rates and river runoff, and as a result, higher chemical weathering intensity in low sea-level period was potentially associated with the strong hydraulic condition. To adequately explain the link between weathering rates and climatic conditions is really a hard work; additionally, the interference from Taiwan makes it more tough to define the substantially erosion rates, monsoon strength, and intensity of chemical weathering in the investigated region [93].

CaCO_3 is an indicative proxy for ocean productivity [94], whereas its content is generally low in deep ocean owing to the dissolution process [95]. Core 973-4 lies above the current carbonate compensation depth (CCD) of about 3400 m [96], so weak dissolution of CaCO_3 in study area is likely. To eliminate the detrital dilution effect, the marine biogenic proxies (TOC and CaCO_3) are normalized to Al concentration. For core 973-4, consistency in vertical variations between Al normalized ratios (TOC/Al and CaCO_3 /Al) and

their biogenic contents is illustrated spanning the last 42 kyr, which suggests that the dilution effect can be neglected (Figures 3(n) and 3(o)). Recently, Cartapanis et al. [97] reported the global organic carbon burial in marine sediments over the last 150 kyr, and the result showed that higher accumulation rate of organic carbon was observed during the glacial period relative to the interglaciation. Core 973-4 showed the similar variability over the past 42 kyr (Figure 7(b)), with higher values during the LGM and deglacial period and lower values during the interstadial and Holocene. Interestingly, the content of organic carbon deviated from the productivity records, e.g., CaCO_3 . The temporal variations of TOC and CaCO_3 displayed polar trend over the studied time scales, indicating a decoupled relationship between organic carbon burial with ocean productivity.

As illustrated in Figure 8, there is a quite excellent negative correlation between TOC and CaCO_3 content on orbital time scales with some exceptions for abnormal values within the turbidite-influenced layer. During the cooling period with low sea level, higher TOC content was ascribed to the increasing terrigenous input, accompanied by low content of CaCO_3 , which was related to the low temperature cooled by intensified winter monsoon. In contrast, the synchronous concurrence of higher CaCO_3 content and lower TOC content was exhibited during the warm episode with sea-level highstand. This phenomenon may be environment-specific and has been proved in much of the marginal seas [58, 97, 98].

Trace metal records in sediment are good indicators for redox condition in oceanic systems, and these metal concentrations are often depleted under well-oxygenated conditions and accumulated in sediment under low-oxygen conditions [99]. In oxic conditions, V (V) and Cr (IV) are soluble phase in aquatic systems, while in the euxinic conditions, reduced V (III) is enriched in the sediments [99]. Jones [100] proposed that the V/Cr ratio is sensitive to the redox change; generally,

higher V/Cr ratios suggest a more reduced condition in the sediment-water interface. Moreover, Mn is also a redox-sensitive and labile element. Under oxygen-enriched conditions, oxidized Mn (III) and Mn (IV) as the insoluble phase are accumulated in the sediment; however, under oxygen-limited conditions, it will be reduced to the Mn (II) existed in the aquatic systems [101]. Hence, the higher Mn/Al ratios suggest an oxygenated condition, and lower Mn/Al ratios suggest a low-oxygen environment. During the glacial stage with low sea-level stand, oxygenated conditions in the water-sediment interface documented by higher Mn/Al and lower V/Cr ratios were displayed, such an environment was not favoring for organic carbon preservation. After entering the Holocene with sea-level highstand, a gradual shift to reducing environment occurred in the seafloor as indicated by lower Mn/Al and higher V/Cr ratios. Bottom water redox condition was controlled by the deep-water ventilation induced by the sea-level change [58]. Low sea-level stand was more likely to promote the vertical and advective water circulation, resulting in higher bottom water O₂ concentrations, but in sea-level highstand, weakening of vertical water mixing led to low-oxygen conditions and generated a relatively enclosed system in deep ocean.

Based on these records, we recognized four conceptual stages of evolution of the paleoenvironmental change at core 973-4 in the northeastern SCS throughout the last 42 kyr, and each proxy is clearly correlated to the sea-level variations (Figure 7).

4.3.1. Stage I: Weak Warm Period in Last Glaciation with Slightly Low Sea-Level Stand (42.4-31.8 kyr). During 42.4-31.8 kyr, which was an interstadial and belonged to a special period characterized by a weak warm episode during the last glaciation, sea level was low below -80 m. The core 973-4 was typical of stable Al and Ti content, accompanied by decreasing $\delta^{13}\text{C}_{\text{TOC}}$ values (Figure 7(a)), indicating an accelerated contribution of organic matter from terrestrial origin. Meanwhile, the oxygenated condition in bottom water was exhibited by high Mn/Al ratios and low V/Cr ratios compared to other stages (Figures 7(d) and 7(e)), which was not favoring for TOC preservation, resulting in low TOC content (Figure 7(b)). Due to sensibility to the redox conditions in the process of diagenesis, the burial efficiency of organic carbon is still questioned [58]. The biogenic CaCO₃ recorded in sediments showed moderate to high values, which demonstrated a relatively high paleo-productivity during this stage (Figure 9(a)). High CaCO₃ content indicated that the weak warm climate during the interstadial increased the seawater temperature and further promoted the calcareous biological activity. The decoupled relationship between organic carbon and ocean paleoproductivity has been confirmed above.

4.3.2. Stage II: Cold Period with Significantly Sea-Level Drop (31.8-20.4 kyr). The episode of 31.8-20.4 kyr belonged to the glacial period. When sea level dropped below -120 m during the Last Glacial Maximum (LGM) in the late phase of this stage, the abrupt environmental change was showed from the sedimentary records. The clearly higher Al and Ti content, especially during the LGM, indicated a greatly high terrige-

nous sediment input to the core 973-4 off the Taiwan Shelf, which was also demonstrated by the markedly high sedimentation rate (Figure 7(k)). Extremely low sea-level stand shortened the distance between the core site location and paleo-Taiwan river mouth during the last glacial period, resulting in an increasing flux of fluvial sediments to the lower continental slope (Figure 9(b)). The fluctuated $\delta^{13}\text{C}_{\text{TOC}}$ values and low C/N ratios supported an additional contribution from marine organic matter (Figure 6). A shift to weak oxygenated condition relative to the stage I in a water-sediment interface documented by redox-sensitive elemental ratios was still not favorable for organic matter preservation. However, the enhanced terrigenous inputs brought large amount of terrigenous debris matter (TDM) to the core location; consequently, the TOC content during this stage was high (Figure 7(b)). The oxygenated condition was a possibility that the low sea-level stand induced a strong deep-water ventilation and then led to higher O₂ concentration in the bottom water. Additionally, the higher CaCO₃ content was apparently interrupted, and its low values were synchronous with the high TOC values. Owing to the rapid sea-level drop and the polar front entrance from the North Pacific to the SCS, the southwest SCS passage was closed, which caused a significant decrease of the seawater temperature [24, 102]. As a result, low temperature produced low productivity in the ocean.

4.3.3. Stage III: Alternation of Cold to Warm Period with Sea-Level Rise (20.4-13.9 kyr). During the 20.4-13.9 kyr, this stage belonged to the late glacial period and the overall deglaciation with stepwise sea-level rise. Nevertheless, a significant turbidity current occurred during the late period of this stage and then disturbed the in situ sedimentary layer. As a result, sedimentary records exhibited abrupt changes, and the original information within sediments was covered up by the extraneous materials. Therefore, it is impossible to reconstruct the paleoenvironment during this interval. However, we can infer some potential information from the variations of several geochemical parameters. It is noteworthy that Al displayed an obviously decreased trend after the occurrence of turbidity current (13.9 kyr) compared to that in the late phase of stage II (20.4 kyr), implying a potential decline in terrigenous sediment input to the lower continental slope in the northeastern SCS, which may be associated with the rapid sea-level rise (Figure 7(m)). Continuous sea-level rise resulted in most terrigenous sediments to be deposited in the proximal area on the inner continental shelf rather than the outer continental slope [16]. The elevated $\delta^{13}\text{C}_{\text{TOC}}$ values indicated an increasing marine-sourced sediment input during this period; moreover, the content of CaCO₃ reached a peak due to the increasing abundance of foraminifer. As reported by previous research [103], calcareous foraminiferal fauna could contribute to about 55% of total CaCO₃ in the marine environment with the water depth shallower than CCD. Accordingly, further evidence was concluded to demonstrated that turbidity current brought Ca-enriched oceanic materials to accumulate in the studied area. Therefore, the sea-level fluctuations had a dominant influence on terrigenous sediment input and sources of organic matter in core 973-4.

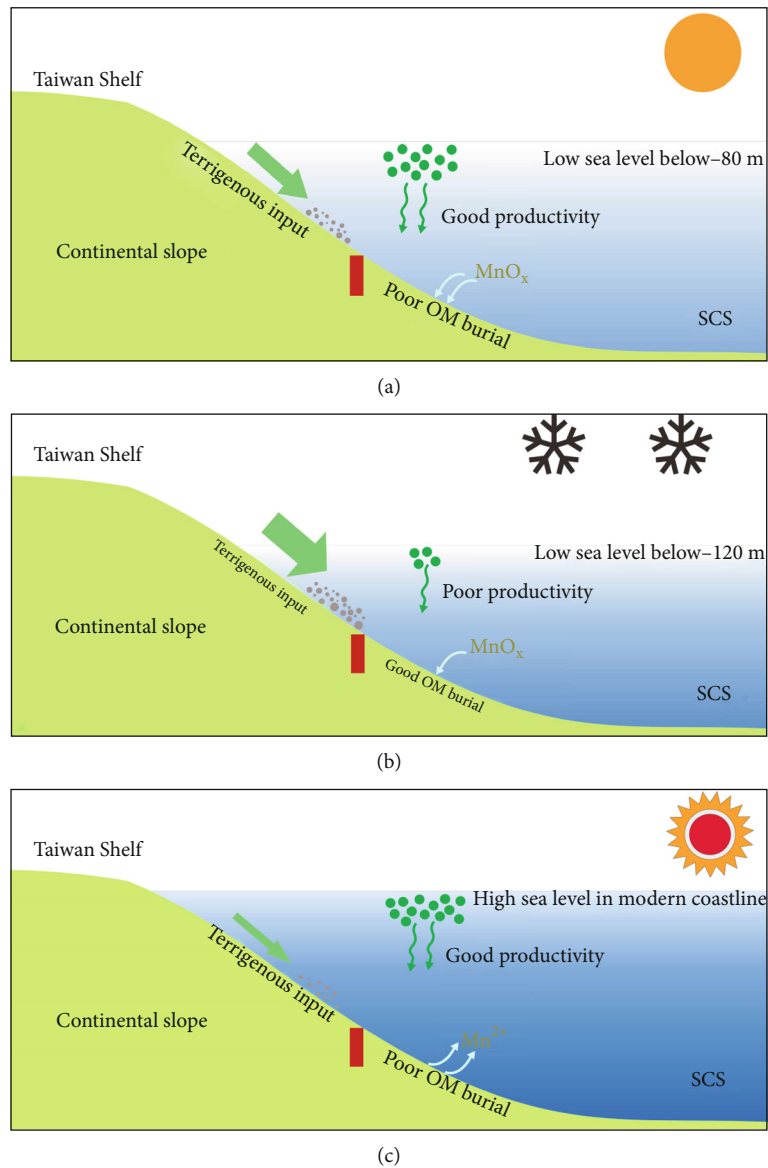


FIGURE 9: Schematic cartoons showing the terrigenous input, organic carbon burial, redox condition in the water-sediment interface, and ocean productivity at core 973-4 located in the northeastern SCS at the (a) interstadial phase during the last glaciation with low sea level (stage I), (b) period of glaciation with the lowest sea level (stage II), and (c) Holocene in sea-level highstand with warm and humid climate (stage IV), with the exception of the stage III influenced by the turbidity current. The size of shallow green arrows indicates the flux of terrigenous input. Core 973-4 is labeled as a red pillar. The ocean productivity in the surface water is expressed by bottle green circles, and higher productivity as indicated by more circles represents the enhanced biogenic CaCO₃ input to deep sea and the seafloor. Dashed area with color from blue to white represents dissolved O₂ content from low to high in the ocean documented by the phase of manganese.

4.3.4. Stage IV: Cold to Warm and Humid Holocene with Further Sea-Level Rise until the Modern Coastline (13.9 kyr—Present). The climate began to be warm and humid since 13.9 kyr, except for several transient cold events, such as the Younger Dryas events (YD) in the early phase of this stage. The sea level gradually rose and reached to the present-day highstand at around 8 kyr [104]. As discussed above, the terrigenous sediment input responding to the sea-level change has been well documented by the variability of Al and Ti. Since the middle Holocene, coastline gradually reached to the modern level, and large amount of sediments

discharged from Taiwan-sourced rivers were restricted to the estuarine areas and inner shelf. Lower flux of terrestrial input resulted in low TOC content, although a gradual change to oxygen-depletion environment supported by higher V/Cr and lower Mn/Al ratios, such a condition was a favorable condition for TOC preservation. The reducing condition was attributed to the relatively enclosed system in the bottom water resulted from the high sea-level stand (Figure 9(c)). Enhanced TOM was contributed to the core location in the early Holocene, but elevated MOM was supplied since the middle Holocene as suggested by the gradually

increasing $\delta^{13}\text{C}_{\text{TOC}}$ values (Figures 6 and 7(a)). During the early Holocene at around 10 kyr, a significant drop of CaCO_3 content (Figure 7(c)) might indicate a carbonate minimum event (CM), featuring a pattern with a rapid decrease following by a slow increase in the CaCO_3 content, while the TOC content varied inversely. The decoupled relationship between TOC and CaCO_3 reminded us that organic matter preservation is not a simple function of ocean productivity [58].

Since the middle Holocene, stable sea-level stand exerted little effect on sediment flux into the sea, but the Al and Ti content increased slightly. Meanwhile, the chemical weathering also increased as indicated by K/Na and Rb/Sr ratios (Figures 7(f) and 7(g)). Therefore, we proposed that the effect of rapidly strengthening East Asian summer monsoon (ESAM) overwhelmed that of the stable sea level and dominated the environmental changes in the northeastern SCS during the Holocene with sea-level highstand.

5. Conclusion

In summary, a detailed sedimentary analysis for core 973-4 collected from northeastern SCS spanning the past 42 kyr suggested that sea-level changes dominated the deposition history. Due to warm seawater temperature and relatively low sea level, the dissociation of gas hydrated reservoir caused a significant turbidity current at around 14 kyr. The organic matter was primarily from terrestrial supply as indicated by negative $\delta^{13}\text{C}_{\text{TOC}}$ values and higher TOC/TN ratios, and Taiwanese rivers were considered to be the dominant sediment provenance. We recognized four distinct stages responding to sea-level change on the basis of geochemical variations recorded in sediments: stage I (42.4-31.8 kyr) was characterized by low sea-level stand with weak warm climate, lowstand promoted the water ventilation and then induced the oxygenated condition in bottom water, which was not favoring for the organic matter burial, accompanied by consistent terrigenous input; during the period of stage II (31.8-20.4 kyr), the prominently high terrigenous input to the study area was presented by high Al and Ti content due to a short distance from the paleo-Taiwan river mouth to core location when the sea level stood below -120 m, the large TDM input resulted in the increasing TOC content though the redox condition in water-sediment interface was still oxygenated, while the CaCO_3 content decreased during this stage, and the contrary pattern showed that ocean productivity was decoupled from organic carbon burial; the turbidity current occurred during the late period of stage III (20.4-13.9 kyr), which brought large amount of Ca-enriched oceanic materials and subsequently disturbed the original sedimentary sequence, and we inferred that the terrigenous input gradually declined due to stepwise rise in sea-level stand as showed by potential decrease of Al content; during the episode of stage IV (13.9 kyr-present), high sea-level stand promoted a reducing environment in the bottom water because of weak ventilation with well-oxygenated surface water. Warm climate induced the enhanced productivity while the TOC content was low. Since the middle Holocene, the variations of terrigenous input, redox condition, and

chemical weathering were mainly controlled by East Asian summer monsoon when sea level reached to the modern coastline.

Data Availability

The data used to support the findings of this study are included within the manuscript and the supplementary materials.

Conflicts of Interest

The authors declare that there are no conflicts of interest regarding the publication of this paper.

Authors' Contributions

Bin Wang and Huaiyan Lei contributed equally to this work.

Acknowledgments

We thank the crew of HaiYang-6 vessel for collecting core samples. The authors are grateful to Dr. Jie Zhang and anonymous reviewers for their constructive comments that substantially improved the manuscript. This work was financially supported by National Natural Science Foundation of China (Grant Nos. 41773078 and 41276046) and Fundamental Research Funds for Xiamen University (Grant No. 20720180114).

Supplementary Materials

Supplementary material contains Figure S1 and Figure S2, which show the sediment provenance derived from REE compositions. (*Supplementary Materials*)

References

- [1] P. D. Clift, J. I. Lee, M. K. Clark, and J. Blusztajn, "Erosional response of South China to arc rifting and monsoonal strengthening: a record from the South China Sea," *Marine Geology*, vol. 184, no. 3-4, pp. 207-226, 2002.
- [2] Z. F. Liu, A. Trentesaux, S. C. Clemens et al., "Clay mineral assemblages in the northern South China Sea: implications for east Asian monsoon evolution over the past 2 million years," *Marine Geology*, vol. 201, no. 1-3, pp. 133-146, 2003.
- [3] Z. F. Liu, Y. L. Zhao, C. Colin et al., "Source-to-sink transport processes of fluvial sediments in the South China Sea," *Earth-Science Reviews*, vol. 153, pp. 238-273, 2016.
- [4] S. M. Wan, A. C. Li, P. D. Clift, and J.-B. W. Stuut, "Development of the east Asian monsoon: mineralogical and sedimentological records in the northern South China Sea since 20 Ma," *Palaeogeography Palaeoclimatology Palaeoecology*, vol. 254, no. 3-4, pp. 561-582, 2007.
- [5] J. D. Milliman and K. L. Farnsworth, *River Discharge to the Coastal Ocean: A Global Synthesis*, Cambridge University Press, Cambridge, 2011.
- [6] J. Liu, L. Cao, W. Yan, and X. Shi, "New archive of another significant potential sediment source in the South China Sea," *Marine Geology*, vol. 410, pp. 16-21, 2019.

- [7] M. J. Caruso, G. G. Gawarkiewicz, and R. C. Beardsley, "Interannual variability of the Kuroshio intrusion in the South China Sea," *Journal of Oceanography*, vol. 62, no. 4, pp. 559–575, 2006.
- [8] G. H. Fang, G. Wang, Y. Fang, and W. Fang, "A review on the South China Sea western boundary current," *Acta Oceanologica Sinica*, vol. 31, no. 5, pp. 1–10, 2012.
- [9] Z. F. Liu, C. Colin, X. J. Li et al., "Clay mineral distribution in surface sediments of the northeastern South China Sea and surrounding fluvial drainage basins: source and transport," *Marine Geology*, vol. 277, no. 1–4, pp. 48–60, 2010.
- [10] S. M. Wan, A. C. Li, P. D. Clift, S. G. Wu, K. H. Xu, and T. G. Li, "Increased contribution of terrigenous supply from Taiwan to the northern South China Sea since 3Ma," *Marine Geology*, vol. 278, no. 1–4, pp. 115–121, 2010.
- [11] P. J. Webster, "The role of hydrological processes in ocean-atmosphere interactions," *Reviews of Geophysics*, vol. 32, no. 4, pp. 427–476, 1994.
- [12] W. Zhao, C. Zhou, J. W. Tian et al., "Deep water circulation in the Luzon Strait," *Journal of Geophysical Research, Oceans*, vol. 119, no. 2, pp. 790–804, 2014.
- [13] H. Huang, T. Babadagli, and X. Chen, "Performance comparison of novel chemical agents for mitigating water-blocking problem in tight gas sandstones," *SPE Reservoir Evaluation & Engineering*, vol. 23, pp. 1–9, 2020.
- [14] W. Ji, Y. Song, Z. Rui, M. Meng, and H. Huang, "Pore characterization of isolated organic matter from high matured gas shale reservoir," *International Journal of Coal Geology*, vol. 174, pp. 31–40, 2017.
- [15] D. Z. Ren, D. S. Zhou, D. K. Liu, F. Dong, S. Ma, and H. Huang, "Formation mechanism of the upper Triassic Yanchang formation tight sandstone reservoir in Ordos Basin—take Chang 6 reservoir in Jiyuan oil field as an example," *Journal of Petroleum Science and Engineering*, vol. 178, pp. 497–505, 2019.
- [16] T. Jiwrungrueangkul, Z. Liu, and Y. Zhao, "Terrigenous sediment input responding to sea level change and east Asian monsoon evolution since the last deglaciation in the southern South China Sea," *Global and Planetary Change*, vol. 174, pp. 127–137, 2019.
- [17] D. B. Zhao, S. M. Wan, P. D. Clift et al., "Provenance, sea-level and monsoon climate controls on silicate weathering of Yellow River sediment in the northern Okinawa trough during late last glaciation," *Palaeogeography Palaeoclimatology Palaeoecology*, vol. 490, pp. 227–239, 2018.
- [18] H. R. Grenfell, B. W. Hayward, R. Nomura, and A. T. Sabaa, "A foraminiferal proxy record of 20th century sea-level rise in the Manukau Harbour, New Zealand," *Marine and Freshwater Research*, vol. 63, no. 4, pp. 370–384, 2012.
- [19] B. D. Zhang, M. D. Pan, D. D. Wu, and N. Y. Wu, "Distribution and isotopic composition of foraminifera at cold-seep site 973-4 in the Dongsha area, northeastern South China Sea," *Journal of Asian Earth Sciences*, vol. 168, pp. 145–154, 2018.
- [20] M. T. Whalen and J. E. Day, "Cross-Basin variations in magnetic susceptibility influenced by changing sea level, paleogeography, and paleoclimate: Upper Devonian, Western Canada Sedimentary Basin," *Journal of Sedimentary Research*, vol. 80, no. 12, pp. 1109–1127, 2010.
- [21] J. G. Liu, R. Xiang, S. J. Kao, S. Y. Fu, and L. P. Zhou, "Sedimentary responses to sea-level rise and Kuroshio current intrusion since the Last Glacial Maximum: grain size and clay mineral evidence from the northern South China Sea slope," *Palaeogeography Palaeoclimatology Palaeoecology*, vol. 450, pp. 111–121, 2016.
- [22] M. K. Li, T. P. Ouyang, C. J. Tian et al., "Sedimentary responses to the east Asian monsoon and sea level variations recorded in the northern South China Sea over the past 36 Kyr," *Journal of Asian Earth Sciences*, vol. 171, pp. 213–224, 2019.
- [23] L. Yi, H. J. Yu, J. D. Ortiz et al., "A reconstruction of late Pleistocene relative sea level in the south Bohai Sea, China, based on sediment grain-size analysis," *Sedimentary Geology*, vol. 281, pp. 88–100, 2012.
- [24] W. Pinxian and S. Xiangjun, "Last glacial maximum in China: comparison between land and sea," *Catena*, vol. 23, no. 3–4, pp. 341–353, 1994.
- [25] X. Tian, F. J. Xu, S. Z. Wu, J. Zhang, C. Guo, and J. Dong, "Clay mineral characteristics and provenance of continental shelf sediments in eastern Hainan Island since middle Holocene," *Earth Science-Journal of China University of Geosciences*, vol. 40, pp. 1497–1504, 2015, (in Chinese with English abstract).
- [26] S.-W. Yu, L. L. Tsai, P. J. Talling et al., "Sea level and climatic controls on turbidite occurrence for the past 26, kyr on the flank of the Gaoping Canyon off SW Taiwan," *Marine Geology*, vol. 392, pp. 140–150, 2017.
- [27] N. Li, D. Feng, L. Y. Chen, H. B. Wang, and D. F. Chen, "Compositions of foraminifera-rich turbidite sediments from the Shenhu area on the northern slope of the South China Sea: implication for the presence of deep water bottom currents," *Journal of Asian Earth Sciences*, vol. 138, pp. 148–160, 2017.
- [28] X. T. Liu, R. Rendle-Bühning, and R. Henrich, "Climate and sea-level controls on turbidity current activity on the Tanzanian upper slope during the last deglaciation and the Holocene," *Quaternary Science Reviews*, vol. 133, pp. 15–27, 2016.
- [29] Q. Lin, J. S. Wang, T. J. Algeo, F. Sun, and R. X. Lin, "Enhanced framboidal pyrite formation related to anaerobic oxidation of methane in the sulfate-methane transition zone of the northern South China Sea," *Marine Geology*, vol. 379, pp. 100–108, 2016.
- [30] J. R. Liu, G. Izon, J. S. Wang et al., "Vivianite formation in methane-rich deep-sea sediments from the South China Sea," *Biogeosciences*, vol. 15, no. 20, pp. 6329–6348, 2018.
- [31] J. Zhang, H. Y. Lei, Y. Chen et al., "Carbon and oxygen isotope composition of carbonate in bulk sediment in the Southwest Taiwan Basin, South China Sea: methane hydrate decomposition history and its link to mud volcano eruption," *Marine and Petroleum Geology*, vol. 98, pp. 687–696, 2018.
- [32] C. S. Liu, I. L. Huang, and L. S. Teng, "Structural features off southwestern Taiwan," *Marine Geology*, vol. 137, no. 3–4, pp. 305–319, 1997.
- [33] S. C. Hu, Y. L. Tan, H. Zhou et al., "Anisotropic modeling of layered rocks incorporating planes of weakness and volumetric stress," *Energy Science & Engineering*, vol. 8, no. 3, pp. 789–803, 2020.
- [34] F. Q. Ren, C. Zhu, and M. C. He, "Moment tensor analysis of acoustic emissions for cracking mechanisms during schist strain burst," *Rock Mechanics and Rock Engineering*, vol. 53, no. 1, pp. 153–170, 2020.
- [35] J. Wang, Y. Zhang, Z. Qin, S. G. Song, and P. Lin, "Analysis method of water inrush for tunnels with damaged water-

- resisting rock mass based on finite element method-smooth particle hydrodynamics coupling,” *Computers and Geotechnics*, vol. 126, p. 103725, 2020.
- [36] B. Chen, C. Zhang, Y. Y. Li, Z. K. Li, and H. J. Zhou, “Physical simulation study of crack propagation and instability information discrimination of rock-like materials with faults,” *Arabian Journal of Geosciences*, vol. 13, no. 18, pp. 1–24, 2020.
- [37] J. Xu, A. Haque, W. Gong et al., “Experimental study on the bearing mechanisms of rock-socketed piles in soft rock based on micro X-ray CT analysis,” *Rock Mechanics and Rock Engineering*, vol. 53, no. 8, pp. 3395–3416, 2020.
- [38] Q. Yin, H. W. Jing, H. J. Su, and H. H. Zhao, “Experimental study on mechanical properties and anchorage performances of rock mass in the fault fracture zone,” *International Journal of Geomechanics*, vol. 18, no. 7, article 04018067, 2018.
- [39] Q. Yin, R. C. Liu, H. W. Jing, H. J. Su, L. Y. Yu, and L. X. He, “Experimental study of nonlinear flow behaviors through fractured rock samples after high-temperature exposure,” *Rock Mechanics and Rock Engineering*, vol. 52, no. 9, pp. 2963–2983, 2019.
- [40] C. Zhu, M. C. He, M. Karakus, X. B. Cui, and Z. G. Tao, “Investigating toppling failure mechanism of anti-dip layered slope due to excavation by physical modelling,” *Rock Mechanics and Rock Engineering*, vol. 53, 2020.
- [41] N. Jiang, C. X. Wang, H. Y. Pan, D. Yin, and J. Ma, “Modeling study on the influence of the strip filling mining sequence on mining-induced failure,” *Energy Science & Engineering*, vol. 8, no. 6, pp. 2239–2255, 2020.
- [42] G. L. Sheng, Y. L. Su, and W. D. Wang, “A new fractal approach for describing induced-fracture porosity/permeability/compressibility in stimulated unconventional reservoirs,” *Journal of Petroleum Science and Engineering*, vol. 179, pp. 855–866, 2019.
- [43] G. L. Sheng, H. Zhao, Y. L. Su et al., “An analytical model to couple gas storage and transport capacity in organic matter with noncircular pores,” *Fuel*, vol. 268, p. 117288, 2020.
- [44] N. Zhang, W. Liu, Y. Zhang, P. F. Shan, and X. L. Shi, “Microscopic pore structure of surrounding rock for underground strategic petroleum reserve (SPR) caverns in bedded rock salt,” *Energies*, vol. 13, no. 7, p. 1565, 2020.
- [45] Y. Zhang, S. G. Cao, N. Zhang, and C. Z. Zhao, “The application of short-wall block backfill mining to preserve surface water resources in Northwest China,” *Journal of Cleaner Production*, vol. 261, p. 121232, 2020.
- [46] J. T. Chen, J. H. Zhao, S. C. Zhang, Y. Zhang, F. Yang, and M. Li, “An experimental and analytical research on the evolution of mining cracks in deep floor rock mass,” *Pure and Applied Geophysics*, vol. 177, 2020.
- [47] G. Feng, X. C. Wang, M. Wang, and Y. Kang, “Experimental investigation of thermal cycling effect on fracture characteristics of granite in a geothermal-energy reservoir,” *Engineering Fracture Mechanics*, vol. 235, article 107180, 2020.
- [48] C. X. Wang, B. T. Shen, J. T. Chen et al., “Compression characteristics of filling gangue and simulation of mining with gangue backfilling: an experimental investigation,” *Geomechanics and Engineering*, vol. 20, no. 6, pp. 485–495, 2020.
- [49] X. Wang, C. Liu, S. Chen, L. Chen, K. Li, and N. Liu, “Impact of coal sector’s de-capacity policy on coal price,” *Applied Energy*, vol. 265, p. 114802, 2020.
- [50] X. Q. Han, E. Suess, Y. Y. Huang et al., “Jiulong methane reef: microbial mediation of seep carbonates in the South China Sea,” *Marine Geology*, vol. 249, no. 3–4, pp. 243–256, 2008.
- [51] Y. Qu, *Response of cold seep benthic foraminifera and methane eruption in northern slope of the South China Sea [M.S. thesis]*, China University of Geosciences, Beijing, 2013.
- [52] J. G. Liu, P. D. Clift, W. Yan et al., “Modern transport and deposition of settling particles in the northern South China Sea: sediment trap evidence adjacent to Xisha trough,” *Deep Sea Research Part I: Oceanographic Research Papers*, vol. 93, pp. 145–155, 2014.
- [53] W. J. Ou, *Sedimentary organic geochemistry research of source rocks of the potential gas hydrate-bearing areas in the northern South China Sea [Ph.D. thesis]*, Xiamen University (Xiamen), 2013.
- [54] Z. F. Liu, C. Colin, W. Huang et al., “Climatic and tectonic controls on weathering in South China and Indochina Peninsula: clay mineralogical and geochemical investigations from the Pearl, Red, and Mekong drainage basins,” *Geochemistry, Geophysics, Geosystems*, vol. 8, no. 5, article Q05005, 2007.
- [55] K. Selvaraj and C.-T. A. Chen, “Moderate chemical weathering of subtropical Taiwan: constraints from solid-phase geochemistry of sediments and sedimentary rocks,” *Journal of Geology*, vol. 114, no. 1, pp. 101–116, 2006.
- [56] Z. F. Liu, Y. L. Zhao, C. Colin, F. P. Siringan, and Q. Wu, “Chemical weathering in Luzon, Philippines from clay mineralogy and major-element geochemistry of river sediments,” *Applied Geochemistry*, vol. 24, no. 11, pp. 2195–2205, 2009.
- [57] S. R. Taylor and S. M. McLennan, *The Continental Crust: Its Composition and Evolution*, Blackwell, Oxford, 1985.
- [58] D. W. Li, Y. P. Chang, Q. Li, L. W. Zheng, X. D. Ding, and S. J. Kao, “Effect of sea-level on organic carbon preservation in the Okinawa trough over the last 91 kyr,” *Marine Geology*, vol. 399, pp. 148–157, 2018.
- [59] H. Ye, T. Yang, G. R. Zhu, S. Y. Jiang, and L. S. Wu, “Pore water geochemistry in shallow sediments from the northeastern continental slope of the South China Sea,” *Marine and Petroleum Geology*, vol. 75, pp. 68–82, 2016.
- [60] D. C. Mosher, R. C. Shipp, L. Moscardelli et al., *Submarine Mass Movements and their Consequences*, Springer, Netherlands, 2011.
- [61] G. Feng, Y. Kang, X. C. Wang, Y. Hu, and X. Li, “Investigation on the failure characteristics and fracture classification of shale under brazilian test conditions,” *Rock Mechanics and Rock Engineering*, vol. 53, no. 7, pp. 3325–3340, 2020.
- [62] P. F. Shan and X. P. Lai, “An associated evaluation methodology of initial stress level of coal-rock masses in steeply inclined coal seams, Urumchi coal field, China,” *Engineering Computations*, vol. 37, no. 6, pp. 2177–2192, 2020.
- [63] D. K. Liu, Z. L. Gu, R. X. Liang et al., “Impacts of pore-throat system on fractal characterization of tight sandstones,” *Geofluids*, vol. 2020, no. 9, Article ID 4941501, pp. 1–17, 2020.
- [64] Q. Yin, G. W. Ma, H. W. Jing et al., “Hydraulic properties of 3D rough-walled fractures during shearing: an experimental study,” *Journal of Hydrology*, vol. 555, pp. 169–184, 2017.
- [65] Q. Yin, H. W. Jing, G. W. Ma, H. J. Su, and R. C. Liu, “Investigating the roles of included angle and loading condition on the critical hydraulic gradient of real rock fracture networks,”

- Rock Mechanics and Rock Engineering*, vol. 51, no. 10, pp. 3167–3177, 2018.
- [66] M. Kienast, S. Steinke, K. Statterger, and S. E. Calvert, “Synchronous tropical South China Sea SST change and Greenland warming during deglaciation,” *Science*, vol. 291, no. 5511, pp. 2132–2134, 2001.
- [67] T. H. Kwon, G. C. Cho, and J. C. Santamarina, “Gas hydrate dissociation in sediments: pressure-temperature evolution,” *Geochemistry, Geophysics, Geosystems*, vol. 9, no. 3, article Q03019, 2008.
- [68] N. Sultan, “Comment on “Excess pore pressure resulting from methane hydrate dissociation in marine sediments: a theoretical approach” by Wenyue Xu and Leonid N. Germanovich,” *Journal of Geophysical Research*, vol. 112, no. B2, 2007.
- [69] F. Chen, C. Zhuang, G. X. Zhang et al., “Abnormal sedimentary events and gas hydrate dissociation in Dongsha area of the South China Sea during last glacial period,” *Earth Science*, vol. 39, no. 11, pp. 1617–1626, 2014, (in Chinese with English abstract).
- [70] R. J. Davies, K. E. Thatcher, S. A. Mathias, and J. X. Yang, “Deepwater canyons: an escape route for methane sealed by methane hydrate,” *Earth and Planetary Science Letters*, vol. 323–324, pp. 72–78, 2012.
- [71] A. L. Lamb, G. P. Wilson, and M. J. Leng, “A review of coastal palaeoclimate and relative sea-level reconstructions using $\delta^{13}\text{C}$ and C/N ratios in organic material,” *Earth-Science Reviews*, vol. 75, no. 1–4, pp. 29–57, 2006.
- [72] P. A. Meyers, “Organic geochemical proxies of paleoceanographic, paleolimnologic, and paleoclimatic processes,” *Organic Geochemistry*, vol. 27, no. 5–6, pp. 213–250, 1997.
- [73] K. Selvaraj, K. Y. Wei, K. K. Liu, and S. J. Kao, “Late Holocene monsoon climate of northeastern Taiwan inferred from elemental (C, N) and isotopic ($\delta^{13}\text{C}$, $\delta^{15}\text{N}$) data in lake sediments,” *Quaternary Science Reviews*, vol. 37, pp. 48–60, 2012.
- [74] J. Zhang, Y. Wu, T. C. Jennerjahn, V. Ittekkot, and Q. He, “Distribution of organic matter in the Changjiang (Yangtze River) estuary and their stable carbon and nitrogen isotopic ratios: implications for source discrimination and sedimentary dynamics,” *Marine Chemistry*, vol. 106, no. 1–2, pp. 111–126, 2007.
- [75] C. Cao, H. Y. Lei, and B. C. Guan, “Carbon and nitrogen concentration and stable isotopic composition of sediments from Dongsha area to Indicator of methane-rich environment,” *Journal of Xiamen University (Natural Science)*, vol. 49, pp. 838–844, 2010, (in Chinese with English abstract).
- [76] M. Kienast, “Unchanged nitrogen isotopic composition of organic matter in the South China Sea during the last climatic cycle: global implications,” *Paleoceanography*, vol. 15, no. 2, pp. 244–253, 2000.
- [77] R. S. Robinson, M. Kienast, A. L. S. Albuquerque, M. Altabet, and S. Contreras, “A review of nitrogen isotopic alteration in marine sediments,” *Paleoceanography*, vol. 27, pp. 89–108, 2012.
- [78] M. R. Fontugne and J. M. Jouanneau, “Modulation of the particulate organic carbon flux to the ocean by a macrotidal estuary: evidence from measurements of carbon isotopes in organic matter from the Gironde system,” *Estuarine, Coastal and Shelf Science*, vol. 24, no. 3, pp. 377–387, 1987.
- [79] J. P. Wu, S. E. Calvert, and C. S. Wong, “Carbon and nitrogen isotope ratios in sedimenting particulate organic matter at an upwelling site off Vancouver Island,” *Estuarine, Coastal and Shelf Science*, vol. 48, no. 2, pp. 193–203, 1999.
- [80] S. Yang, H. Jung, M. Choi, and C. Li, “The rare earth element compositions of the Changjiang (Yangtze) and Huanghe (yellow) river sediments,” *Earth and Planetary Science Letters*, vol. 201, no. 2, pp. 407–419, 2002.
- [81] D. D. Wu, F. Yang, X. Huang et al., “Rare earth elemental geochemistry of the sediment in cold-seep area in Dongsha area of South China Sea,” *Marine Geology & Quaternary Geology*, vol. 37, pp. 59–69, 2017, (in Chinese with English abstract).
- [82] Z. Liu, C. Colin, W. Huang, Z. Chen, A. Trentesaux, and J. Chen, “Clay minerals in surface sediments of the Pearl River drainage basin and their contribution to the South China Sea,” *Chinese Science Bulletin*, vol. 52, no. 8, pp. 1101–1111, 2007.
- [83] Q. Lin, J. S. Wang, S. Y. Fu et al., “Elemental sulfur in northern South China Sea sediments and its significance,” *Science China Earth Sciences*, vol. 58, no. 12, pp. 2271–2278, 2015.
- [84] C. Waelbroeck, L. Labeyrie, E. Michel et al., “Sea-level and deep water temperature changes derived from benthic foraminifera isotopic records,” *Quaternary Science Reviews*, vol. 21, no. 1–3, pp. 295–305, 2002.
- [85] T. J. J. Hanebuth, H. K. Voris, Y. Yokoyama, Y. Saito, and J. I. Okuno, “Formation and fate of sedimentary depocentres on Southeast Asia’s Sunda shelf over the past sea-level cycle and biogeographic implications,” *Earth-Science Reviews*, vol. 104, no. 1–3, pp. 92–110, 2011.
- [86] S. H. Zhao, Z. F. Liu, Q. Chen et al., “Spatiotemporal variations of deep-sea sediment components and their fluxes since the last glaciation in the northern South China Sea,” *Science China Earth Sciences*, vol. 60, no. 7, pp. 1368–1381, 2017.
- [87] P. U. Clark, A. S. Dyke, J. D. Shakun et al., “The last glacial maximum,” *Science*, vol. 325, no. 5941, pp. 710–714, 2009.
- [88] P. U. Clark, J. D. Shakun, P. A. Baker et al., “Global climate evolution during the last deglaciation,” *Proceedings of the National Academy of Sciences*, vol. 109, no. 19, pp. E1134–E1142, 2012.
- [89] H. W. Nesbitt and G. M. Young, “Early Proterozoic climates and plate motions inferred from major element chemistry of lutites,” *Nature*, vol. 299, no. 5885, pp. 715–717, 1982.
- [90] C. S. Riebe, J. W. Kirchner, and R. C. Finkel, “Erosional and climatic effects on long-term chemical weathering rates in granitic landscapes spanning diverse climate regimes,” *Earth and Planetary Science Letters*, vol. 224, no. 3–4, pp. 547–562, 2004.
- [91] M. E. Raymo and W. F. Ruddiman, “Tectonic forcing of late Cenozoic climate,” *Nature*, vol. 359, no. 6391, pp. 117–122, 1992.
- [92] L. R. Kump, S. L. Brantley, and M. A. Arthur, “Chemical weathering, atmospheric CO_2 , and climate,” *Annual Review of Earth and Planetary Sciences*, vol. 28, no. 1, pp. 611–667, 2000.
- [93] P. D. Clift, S. M. Wan, and J. Blusztajn, “Reconstructing chemical weathering, physical erosion and monsoon intensity since 25Ma in the northern South China Sea: a review of competing proxies,” *Earth-Science Reviews*, vol. 130, pp. 86–102, 2014.
- [94] J. W. Farrell and W. L. Prell, “Climatic change and CaCO_3 -preservation: an 800,000 year bathymetric reconstruction from the central equatorial Pacific Ocean,” *Paleoceanography*, vol. 4, no. 4, pp. 447–466, 1989.

- [95] C. Prakash Babu, H.-J. Brumsack, B. Schnetger, and M. E. Böttcher, "Barium as a productivity proxy in continental margin sediments: a study from the eastern Arabian Sea," *Marine Geology*, vol. 184, no. 3-4, pp. 189–206, 2002.
- [96] R. H. Chen, J. Xu, Y. Meng et al., "Microorganisms and carbon lysocline depth and CCD in surface sediment of the northeastern South China Sea," *Acta Oceanologica Sinica*, vol. 25, pp. 48–56, 2003.
- [97] O. Cartapanis, D. Bianchi, S. L. Jaccard, and E. D. Galbraith, "Global pulses of organic carbon burial in deep-sea sediments during glacial maxima," *Nature Communications*, vol. 7, no. 1, 2016.
- [98] K. E. Kohfeld and Z. Chase, "Controls on deglacial changes in biogenic fluxes in the North Pacific Ocean," *Quaternary Science Reviews*, vol. 30, no. 23-24, pp. 3350–3363, 2011.
- [99] N. Tribouillard, T. J. Algeo, T. Lyons, and A. Riboulleau, "Trace metals as paleoredox and paleoproductivity proxies: an update," *Chemical Geology*, vol. 232, no. 1-2, pp. 12–32, 2006.
- [100] B. Jones and D. A. C. Manning, "Comparison of geochemical indices used for the interpretation of palaeoredox conditions in ancient mudstones," *Chemical Geology*, vol. 111, no. 1-4, pp. 111–129, 1994.
- [101] S. E. Calvert and T. F. Pedersen, "Sedimentary geochemistry of manganese; implications for the environment of formation of manganiferous black shales," *Economic Geology*, vol. 91, no. 1, pp. 36–47, 1996.
- [102] M. Zhao, C. Y. Huang, C. C. Wang, and G. Wei, "A millennial-scale U37K' sea-surface temperature record from the South China Sea (8°N) over the last 150 kyr: monsoon and sea-level influence," *Palaeogeography Palaeoclimatology Palaeoecology*, vol. 236, no. 1-2, pp. 39–55, 2006.
- [103] W. S. Broecker and E. Clark, "CaCO₃ size distribution: a paleocarbonate ion proxy?," *Paleoceanography*, vol. 14, no. 5, pp. 596–604, 1999.
- [104] S. Steinke, H.-Y. Chiu, P.-S. Yu et al., "On the influence of sea level and monsoon climate on the southern South China Sea freshwater budget over the last 22,000 years," *Quaternary Science Reviews*, vol. 25, no. 13-14, pp. 1475–1488, 2006.
- [105] J. C. Marini, C. Chauvel, and R. C. Maury, "Hf isotope compositions of northern Luzon arc lavas suggest involvement of pelagic sediments in their source," *Contributions to Mineralogy and Petrology*, vol. 149, no. 2, pp. 216–232, 2005.
- [106] Z. F. Xu and G. L. Han, "Rare earth elements (REE) of dissolved and suspended loads in the Xijiang River, South China," *Applied Geochemistry*, vol. 24, no. 9, pp. 1803–1816, 2009.

Research Article

Numerical Simulation of Cracking Behavior of Precracked Rock under Mechanical-Hydraulic Loading

Zhong Zhang,¹ Chun-Chi Ma ,¹ Tianbin Li,¹ Tao Song,¹ and Huilin Xing²

¹State Key Laboratory of Geohazard Prevention and Geoenvironment Protection, Chengdu University of Technology, Chengdu 610059, China

²Frontiers Science Center for Deep Ocean Multispheres and Earth System, Key Lab of Submarine Geosciences and Prospecting Techniques, MOE and College of Marine Geosciences, Ocean University of China, Qingdao 266100, Australia

Correspondence should be addressed to Chun-Chi Ma; machunchi17@cdut.edu.cn

Received 16 June 2020; Revised 19 July 2020; Accepted 21 September 2020; Published 17 October 2020

Academic Editor: Richeng Liu

Copyright © 2020 Zhong Zhang et al. This is an open access article distributed under the Creative Commons Attribution License, which permits unrestricted use, distribution, and reproduction in any medium, provided the original work is properly cited.

The cracking behavior of precracked rocks under mechanical-hydraulic loading is of great significance in underground openings or petroleum engineering. In this study, an advanced in-house finite element code PANDAS proved to be effective in simulating coupled fracturing processes under complex geological conditions was used to simulate the cracking propagation of the precracked rocks under mechanical loading and mechanical-hydraulic loading with different strength parameters. The simulation results demonstrated that (1) the cracks initiate by the induced stresses, and multiple types of tensile cracks originate from the preexisting flaws; (2) crack propagation patterns under mechanical-hydraulic loading were studied with different strength parameters, and the multiple patterns of pure tensile, main tensile, tensile-shear, main shear, and pure shear were observed; and (3) the timing of hydraulic loading has a significant impact on the fracturing process: when hydraulic loading was carried out in the phase of main crack propagation, the tensile fracture was promoted and the shear fracture was inhibited; when hydraulic loading was carried out in the phase of shear crack propagation, the shear fracture and tensile fracture were stimulated. The numerical simulation results are in good agreement with the experimental results by previous studies. The research on the cracking behavior of precracked rocks under mechanical and hydraulic loading will expand the application prospect in the fields of coal seam gas reservoir and tunnel water inrush.

1. Introduction

In the process of underground engineering construction such as traffic tunnel excavation, water conservancy project, and coal and oil exploitation, the geological environment of high ground stress and strong seepage pressure is becoming more and more complex. Under the joint action of in situ stress and seepage water pressure, the primary cracks in engineering rock mass are easy to expand and evolve, which leads to the change of macroscopic mechanical behavior and fracture mode of rock mass [1, 2]. Preexisting cracks or fractures determine the initiation of new cracking and dominate the formation of macroscopic failure planes [3]. When a load is applied, new cracks originate from preexisting cracks and propagate by the influence of major principal stress, sometimes coalescing with other cracks. The cracking of rock

masses affected by the coupling effect of mechanical-hydraulic loading is increasingly investigated in engineering.

In past decades, a large number of experimental studies were conducted to characterize the cracking behaviors and the law of fracture in rock samples containing preexisting flaws, where the term flaws refer to those preexisting artificial cracks [4–6]. The fracturing processes and crack coalescence patterns under compression were characterized and estimated on different rock materials [4]. Some studies suggested that tensile cracks are initially originating from flaws under compressive loading, and the tensile cracks are subsequently followed by shear cracks [5]. Another study investigated the failure mode and cracking process of marble specimens with different precracks by the uniaxial compression test. Lee and Jeon [6] carried out uniaxial compression tests on three different materials and obtained the initiation, propagation,

and coalescence laws of presingle crack and predouble crack. Yin et al. [7] conducted experimental investigations into hydraulic properties of 3D rough-walled fractures during shearing. At the same time, the high temperature and included angle of preexisting cracks had been experimentally studied to observe macroscopic cracks emanating from the flaws [8, 9].

Moreover, several numerical studies were conducted to explain better the fracturing processes in precracked models, including the finite element methods (FEM) [10–12], boundary element methods (BEM), and displacement discontinuity methods (DDM) [13]. To model the crack behaviors reasonably, appropriate cracking criteria need to be incorporated [14]. A numerical simulation code (RFPA) can be used to analyze the crack propagation in a rock while simulating both global failure of rock and local cracking at flaws [15]. Also, cracking behavior in rock and rock-like materials has been modeled by using particle flow code (PFC) [16].

Numerical models are not only useful for analyzing and interpreting the crack types observed in physical experiments but also useful tools for observing the dynamic images of the stress field and seepage field evolution in the process of fracture propagation [17, 18]. However, many studies have only focused on the analysis of preset single crack growth, which cannot completely simulate the whole process of crack initiation, development, and interpenetration under different strength parameters and hydraulic coupling environment [19, 20]. Therefore, some more complex conditions of the actual work need to be further considered to simulate the cracking behavior and propagation mechanism of precracked rock, such as different strength parameters and hydraulic coupling.

To address this knowledge gap, this study was based on the porous mechanical-hydraulic coupled FEM and the continuum damage theory, and an in-house finite element code PANDAS was used to simulate the cracking behavior of precracked rock [21–23]. Moreover, the cracking behaviors that originate and propagate from the flaws with different strength parameters in rock samples were also investigated in this study. On this basis, how the crack behaviors propagate under the mechanical-hydraulic loading and the influence of hydraulic action time sequence was examined. The numerical simulation strategy considering the influence of different rock strength parameters and hydraulic time series on crack growth is innovative. This research is expected to enhance the awareness of the instability process of crack damage evolution under complex stress environments, as well as the mechanism of crack formation and propagation.

2. Methodologies

Many scholars have used the numerical simulation method (RFPA, PFC, and FLAC3D) to study the fracture mechanism of the fissured rock mass, which helps to understand the stress state and provides a powerful criterion for the initiation and propagation of cracks [10–20].

In this study, an in-house code PANDAS (Parallel Adaptive Nonlinear Deformation Analysis Software) was used to simulate the crack propagation patterns of a precracked

model under mechanical-hydraulic loading [21]. PANDAS is an advanced computing program in which the in-house finite element code has implemented the advanced unstructured mesh generation of extremely heterogeneous fractured porous media by using a nonlinear coupled finite element solver [22, 23]. It is a finite element code developed and verified for simulating coupled fracturing processes in a complex geological condition, which were set in 3D subjected to the affecting hydraulic and thermal factors for simulating coupled crustal dynamics [24, 25]. The related equations used in this study are briefly listed below [5, 11, 26–29].

The stress balance equation is defined as

$$\frac{\partial \sigma_{ij}}{\partial X_{ij}} + X_j = 0 \quad (i, j = 1, 2, 3), \quad (1)$$

where σ_{ij} is the component of the Cauchy stress tensor and X_j is the body force in the j th direction.

Jaumann rate is introduced for the stress:

$$\sigma'_{ij} = C_{ijkl} D_{kl}, \quad (2)$$

where σ'_{ij} is the Jaumann rate of the Cauchy stress tensor and C_{ijkl} is the elastoplastic material matrix. The geometrical equation is defined as

$$D_{ij} = \frac{1}{2} (V_{i,j} + V_{j,i}) = \frac{1}{2} (L_{ij} + L_{ji}), \quad (3)$$

where $V_{i,j}$ is the partial derivative of the i th velocity at the j th direction and L is the velocity gradient tensor. D and W are the symmetric and antisymmetric parts of L , respectively.

The fluid and stress coupling equation is defined as

$$\sigma'_{ij} = \sigma_{ij} - \alpha p \delta_{ij}, \quad (4)$$

where p is the pore pressure, α is the coefficient of pore pressure, and δ_{ij} is the Kronecker constant.

The seepage equation is expressed as follows:

$$k \nabla^2 p = \frac{1}{Q} \frac{\partial P}{\partial t} - \alpha \frac{\partial \varepsilon_v}{\partial t}, \quad (5)$$

where k is the permeability, Q is the Biot constant, and ε_v is the volume strain.

The permeability follows the exponential law of effective stress:

$$k(\sigma, p) = \xi k_i \exp \left(-\beta \left(\frac{\sigma_{ii}}{3} - \alpha p \right) \right), \quad (6)$$

where k_i is the initial permeability and β and ζ are the material constants. Once the element is failed, relevant stresses are released, and the element is granted with the properties of air material (i.e., Young's modulus is reduced to a minimal value, and the permeability is corresponding to a fractured state).

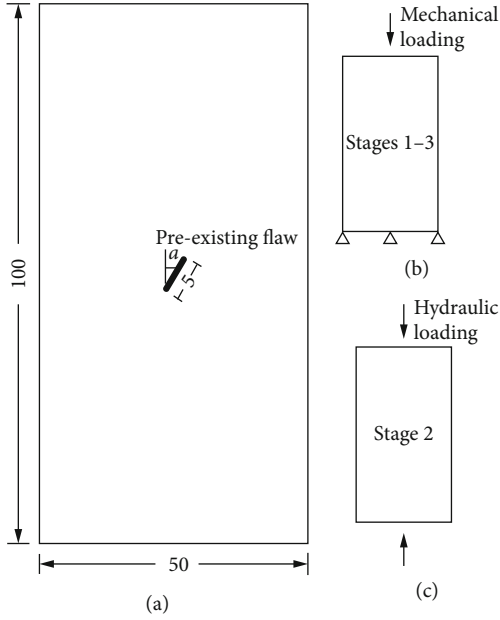


FIGURE 1: Designed rock sample and loading conditions.

Maximum principal stress criterion and Mohr-Coulomb theory are used as the cracking criteria of the poroelastic-brittle rock sample based on the effective stress concept. Tensile cracks occur when the maximum tensile stress exceeds the tensile strength:

$$\sigma_1 \geq \sigma_t. \quad (7)$$

Shear cracks are determined by the Mohr-Coulomb criterion:

$$\sigma_1 - \sigma_3 \frac{1 + \sin \phi}{1 - \sin \phi} \leq \sigma_c, \quad (8)$$

where σ_3 is minimum principal stress, σ_1 is maximum principal stress, ϕ is the friction angle, and σ_c is the shear strength.

3. Numerical Simulation

3.1. Model. To study the fracture behavior of precracked rock under mechanical hydraulic load, the calculation model is set up in this paper as shown in Figure 1. The precracked rock sample is designed at 50 mm (width) and 100 mm (height) in two dimensions (Figure 1(a)). Three loading stages are designed to include the development of crack initiation (stage 1), crack propagation (stage 2), and fracturing (stage 3). Mechanical loading is performed at stages 1–3 with applied axial displacement on the top boundary and fixed displacement at the bottom boundary (Figure 1(b)). Hydraulic loading is performed at stage 2 at both the top and bottom boundaries (Figure 1(c)). Besides, five cases of preexisting flaws with diverse angles α (in the range 15°–75° and 15° in the interval) are designed at the center of the rock samples. The crack initiation and crack propagation patterns under

uniaxial compression and mechanical-hydraulic loading are discussed in Sections 3.2 and 3.3, respectively.

3.2. Crack Behaviors of Preexisting Flaw under Uniaxial Compression

3.2.1. Stress Field around the Flaw and Crack Initiation. Five cases of rock samples were performed at stage 1 with a displacement up to 0.2 mm, wherein cracks were originating, and crack-induced stresses were formed. Figure 2 shows the stress field around a 60-degree flaw. The maximum and minimum principal stresses and maximum shear stress were recorded. The contour mapping of the minimum principal stress exhibits the compressive and tensile stress areas (Figure 2(a)). There are two concentrated areas of tensile stress (which resemble an auriform area) on each tip of the flaw that was recorded in the indicators of “MIN1” and “MIN2.” The contour mapping of the maximum principal stress also exhibits an auriform concentrated area on each tip of the flaw (Figure 2(b)), and the indicator “MAX” was used to record the value. The contour mapping of the maximum shear stress exhibits the orthogonal areas of the stress concentration around the flaw (Figure 2(c)), and the indicator “MAXSH” was used to record the value.

Figures 3 and 4 show the evolution of the stresses (MIN1, MIN2, MAX, and MAXSH) with the variation of flaw angles (15°, 30°, 45°, 60°, and 75°). Stress MIN1 decreases after increasing to the maximum value in the 45-degree flaw. Stress MIN2 increases continuously; stresses MAX (absolute value) and MAXSH smoothly decrease continuously.

Diverse tensile cracks originate from the flaws under compressive loading (Figure 5). Type I and II wing cracks are both emerging in the flaws at 15°, 30°, and 45° because of the stress concentrations of MIN1 and MIN2, respectively; moreover, type I crack is followed by type II crack in time history by the reason that stress MIN2 is generally smaller than stress MIN1. Type III crack emerges along the same direction of the flaw at 60°. Type IV crack occurs in the flaw at 75°, wherein cracks are simultaneously emerging from the directions of MIN1 and MIN2 by the reason that stresses of MIN1 and MIN2 are much closer.

3.2.2. Crack Propagation Patterns Affected by Strength Parameters. During stages 2 and 3 of the mechanical loading, crack propagations are highly related to the specific strength parameters in the rock samples. As shown in Table 1, the tensile strength gradually increases in the five schemes of strength parameter (i.e., SP1, SP2, SP3, SP4, and SP5), which is equivalent to the decrease of the ratio between shear strength to tensile strength. SP1 and SP5 are the minimum and maximum tensile strengths, respectively. From SP2 to SP4, the tensile strengths gradually increase.

Crack propagation patterns (e.g., in the flaw at 60°) affected by the five schemes of strength parameters are shown in Figure 6. A single main fracture forms in the schemes SP1 and SP2. The main (first) fracture and the second fracture approximately perpendicular to each other are forming in the schemes SP3, SP4, and SP5. The crack propagation patterns of the five schemes are pure tensile, main tensile,

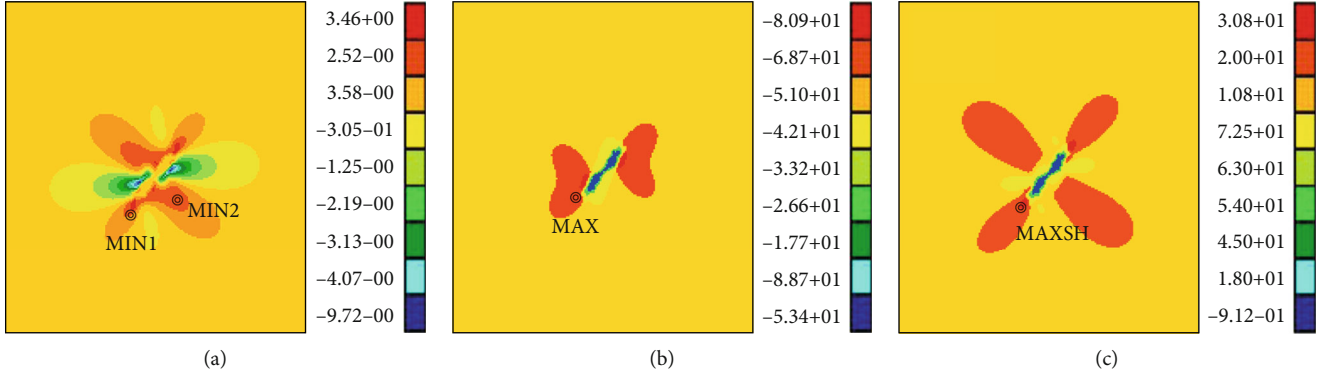


FIGURE 2: Stress field around the existing flaw: (a) minimum principal stress; (b) maximum principal stress; (c) maximum shear stress.

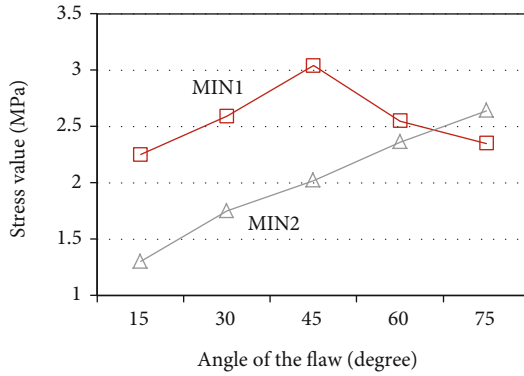


FIGURE 3: Evolution of the minimum principal stress.

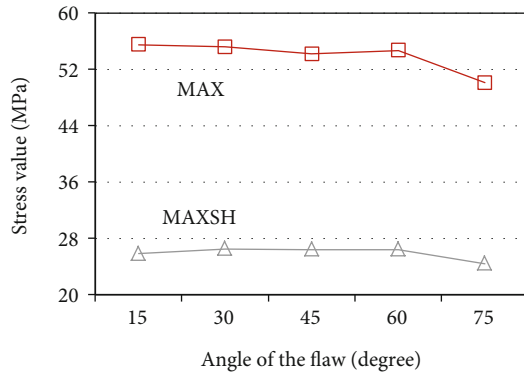


FIGURE 4: Evolution of the maximum principal stress.

tensile-shear, main shear, and pure shear, respectively. From SP1 to SP5, the proportion of shear cracks gradually increases in the main fracture, which induces the decrease of the angle (concerning the horizontal direction) of the main fracture plane. The appearance of the second fracture is affected by the increase of the shear crack proportion in the main fracture plane—as the shear cracks increase in the main fracture from SP3 to SP5, the second fracture appears earlier and develops more significantly. Figure 7 shows the shear stress evolution of the initial crack in the second fracture. From SP2 to SP4, the shear stress develops more quickly, and the earliest stress drop (shear crack) appears in SP4. The three moments of the shear stress evolution (A, B, and C) are exhibited by the contour mapping of the maximum shear

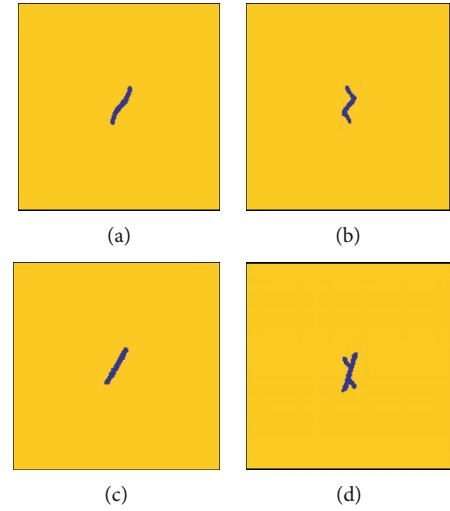


FIGURE 5: Initiation of the tensile cracks: (a) type I; (b) type II; (c) type III; (d) type IV.

TABLE 1: Schemes of the strength parameters.

Nos.	E1 (GPa)	E2 (GPa)	Poisson's ratio	Yield strength (MPa)	Tensile strength (MPa)
SP1	20	5	0.2	60	1.0
SP2	20	5	0.2	60	4.5
SP3	20	5	0.2	60	5.0
SP4	20	5	0.2	60	5.5
SP5	20	5	0.2	60	10.0

E1 and E2 denote Young's modulus of the rock and flaw, respectively.

stress, wherein the shear stress (red area) develops and concentrates in the orthogonal directions leading to the formation of the fractures.

The relationships between the angles of the main fracture planes and the schemes of strength parameters are shown in Figure 8. From SP2 to SP4, the angles of the main fracture planes decrease. From 15° to 75° of the flaws, angles of the main fracture planes increase.

3.3. Crack Behaviors under Mechanical-Hydraulic Loading. To explore the hydraulic effect acting in propagated cracks,

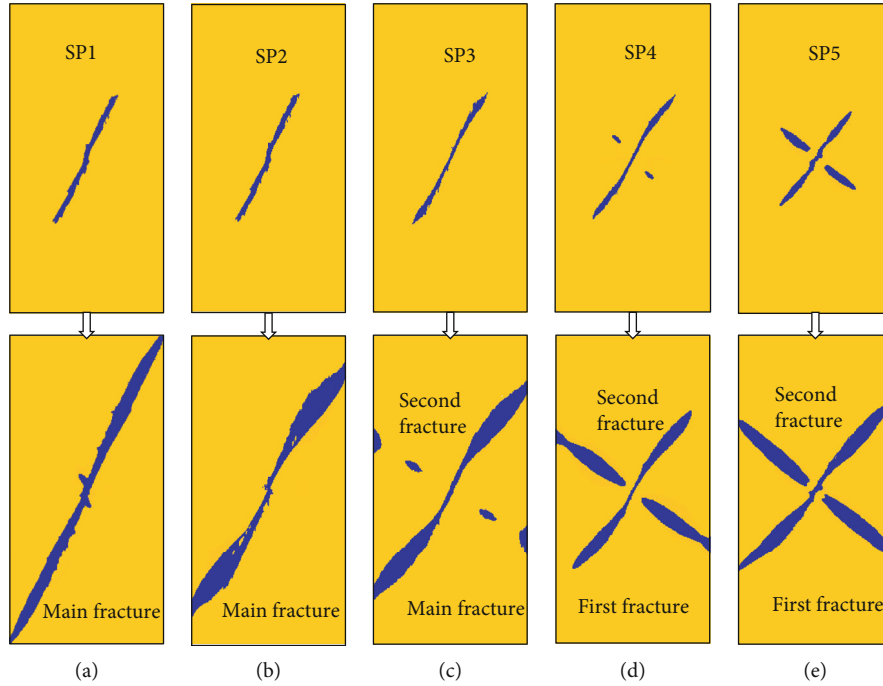


FIGURE 6: Crack propagation patterns affected by the different schemes of the strength parameters: (a) pure tensile; (b) main tensile; (c) tensile-shear; (d) main shear; (e) pure shear.

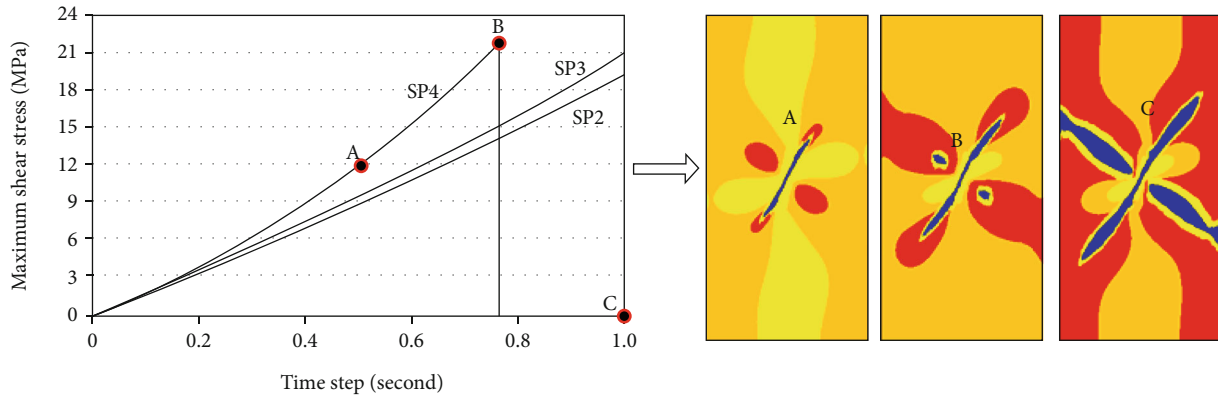


FIGURE 7: Shear-stress evolution of the initial cracks in the second fracture.

hydraulic pressures were imposed at both ends of the rock sample after stage 2 of the mechanical loading was performed. Two schemes of hydraulic loading (SH1 and SH2) were designed in the simulation (Figure 9). Under SH1, hydraulic pressures were applied after the main fracture had been developing for a specific period wherein only tensile cracks occurred (including the schemes SP2, SP3, and SP4). Under SH2, hydraulic pressures were applied at a period when the shear cracks were occurring after tensile cracking (including the schemes SP3 and SP4). Table 2 shows the process of mechanical-hydraulic loading in the rock samples (e.g., in the flaw at 60°). The three schemes of strength parameters SP2, SP3, and SP4, are included to study the conditions of nonhydraulic loading (NonHy), hydraulic loading scheme 1 (SH1), and hydraulic loading scheme 2 (SH2). Hydraulic loading was applied after the axial displacement of the rock sample reached stage 2 (crack propagation), and

the sample was subsequently continually loading to stage 3 (fracturing). SH2 is not considered in SP2 because of the absence of shear cracks.

3.3.1. Mechanical-Hydraulic Action under SH1 Scheme. The contour mapping of the minimum principal stress (tensile) before and after hydraulic loading and the seepage field is shown in Figure 10. The related seepage parameters are introduced in Table 3. The initial permeability (isotropic) is the base value independent from the stress field. Coefficient 1 defines the adjustment of the permeability affected by the stress field (anisotropic), and coefficient 2 defines the increase of the permeability when cracking occurs. Figure 11(a) shows the evolution of the hydraulic pressures in SP2 by the three monitoring points MA, MB, and MC. The hydraulic pressures increase to the constant value of 3.5 MPa by following the sequence MA>MB>MC. Figure 11(b) shows the evolution of

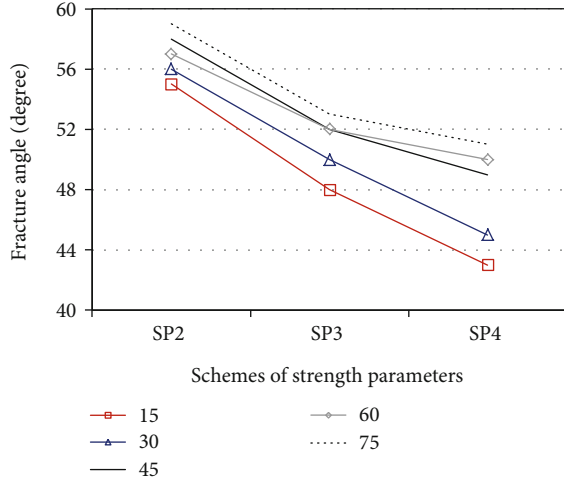


FIGURE 8: Evolution of fracture angles.

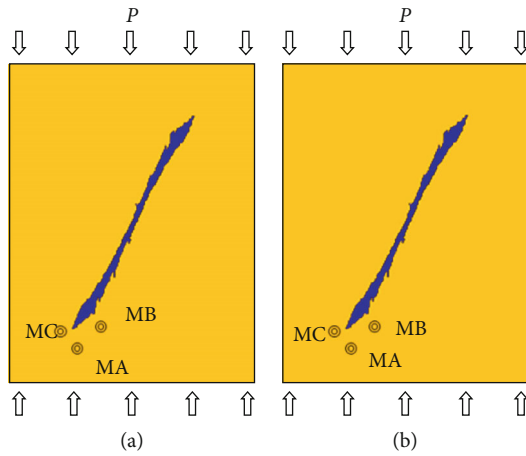


FIGURE 9: Two schemes of hydraulic loading: (a) SH1; (b) SH2.

the incremental tensile stresses ($\Delta\sigma_3$), and 0.713 MPa, 0.695 MPa, and 0.688 MPa are reached at the points MA, MC, and MB, respectively (following the sequence MA>MC>MB). The total tensile stresses (σ_3) 4.01 MPa, 2.98 MPa, and 2.70 MPa are reached at the points MA, MB, and MC, respectively (following the sequence MA>MB>MC).

Figure 12(a) shows the evolutions of the incremental tensile stresses with different flaw angles in SP2. The value of $\Delta\sigma_3$ increases with flaw angles from 15° to 75°, and the stress values follow the sequence MA>MC>MB. Figure 12(b) shows the evolutions of the total tensile stresses. The value of σ_3 increases with flaw angles, and stress values follow the sequence MA>MB>MC.

Continued mechanical loading (the loading stage 3) is applied after hydraulic loading. Evolutions of the maximum shear stresses (refer to the initial cracks in the second fracture) are exhibited in Figure 13 under the conditions of non-hydraulic and hydraulic actions. Under the hydraulic action, the maximum shear stresses develop slowly, and the stress drops (shear cracks) occur lately. The comparison between SP4 and SP3 shows that the maximum shear stress develops more quickly, and the stress drop occurs earlier. According

to the crack propagation patterns in Figure 14, the angles of the main fracture increase because of the hydraulic action.

3.3.2. Mechanical-Hydraulic Action under SH2 Scheme. Figure 15(a) shows the evolution of the hydraulic pressures in SP3 monitored by the three points MA, MB, and MC. Under SH2, the hydraulic pressures increase to the constant value 3.5 MPa by following the sequence MA>MB>MC. Figure 15(b) shows the evolution of the incremental tensile stresses ($\Delta\sigma_3$), and 0.736 MPa, 0.713 MPa, and 0.698 MPa are reached at the points MC, MA, and MB, respectively (following the sequence MC>MA>MB). The total tensile stresses (σ_3) 4.17 MPa, 2.93 MPa, and 2.91 MPa are reached at the points MA, MB, and MC, respectively (following the sequence MA>MB>MC).

Figure 16(a) shows the evolution of incremental tensile stresses with different flaw angles in SP3. The value of $\Delta\sigma_3$ increases with the flaw angles from 15° to 75°, and the stress values follow the sequence MC>MA>MB. Figure 16(b) shows the evolutions of the total tensile stresses. The value of σ_3 increases with the flaw angles, and the stress values follow the sequence MA>MB>MC.

Continued mechanical loading was applied after hydraulic loading. The evolutions of the maximum shear stresses (refer to the initial cracks in the second fracture) are shown in Figure 17 under the conditions of nonhydraulic and hydraulic actions. Under the hydraulic action SH2, the maximum shear stresses develop quickly, and the stress drops occur earlier. According to the crack propagation patterns in Figure 14, the cracking area expanded under the hydraulic action.

4. Discussion

In this study, we investigated: the stress field around the flaw and the mode of crack initiation under different strength parameters, as well as the role of hydraulic loading in crack growth. This section will further discuss the influence of a crack growth model and hydraulic loading time sequence on the fracturing process.

4.1. On the Propagation Mode of Crack Growth. The results of this study indicate that the initiation of crack types is controlled by the stress and the angle of precrack. Firstly, the stress field around the flaw (Figure 2) reflects the position that the minimum principal stress (Figure 2(a)) and the maximum principal stress (Figure 2(b)) exert on the tip of the defect and the maximum shear stress (Figure 2(c)) exerts on the orthogonal region of the stress concentration around the defect. Secondly, Figures 3 and 4 show the evolution of the stresses with the variation of flaw angles. Types I and II wing cracks sequentially occur in the flaws at 15°, 30°, and 45°. Type III crack (along the same direction of the flaw) generally occurs in the flaw at 60°. Type IV crossed crack occurs in the flaw at 75°.

Furthermore, we identified that with the increase of rock sample strength, the shear force tends to increase, the secondary crack develops and concentrates in the vertical direction of the precrack, and the main fracture angle decreases.

TABLE 2: Process of the mechanical-hydraulic loading.

Loading stages	SP2			SP3			SP4		
	NonHy	SH1	SH2	NonHy	SH1	SH2	NonHy	SH1	SH2
Stage 2 (mm)	–	0.63	–	–	0.63	0.65	–	0.63	0.64
Stage 3 (mm)	0.75	0.75	–	0.77	0.77	0.77	0.79	0.79	0.79

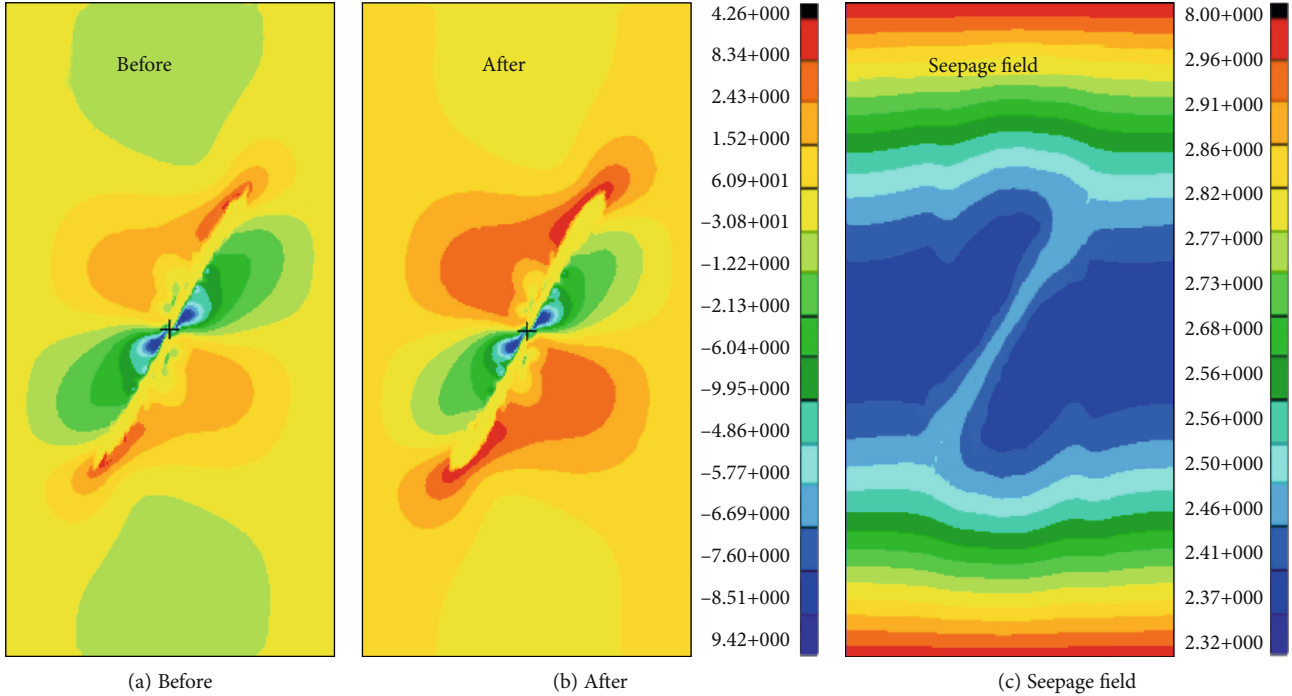


FIGURE 10: Distributions of the principal stress and hydraulic pressure.

TABLE 3: Related seepage parameters.

E1 (GPa)	E2 (GPa)	Poisson's ratio	Initial permeability (10^{-16} m^2)	Porosity (%)	Permeability coefficient 1	Permeability coefficient 2
20	5	0.2	1.0	0.13	0.1	1000

The proportion of shear fractures in the main fractures tends to increase, and the occurrence.

time of the second fracture is earlier and more obvious (Figure 6). Shear cracks were first found in SP4, through shear stress statistics (Figure 7).

Our numerical results are in agreement with previous experimental studies [30–32]. Lajtai [30] conducted uniaxial compression loading tests and found the following crack initiation sequence: (a) tensile fractures, (b) normal shear fractures, (c) additional normal shear fractures leading to the formation of shear zones, and (d) inclined shear fractures (Figure 18). Experimental result shows that there are various initial defects, such as cracks and crack-like in materials. And the microcracks always appear in the defects or local stress concentration areas. Fracture behavior of rock samples should be based on stress and energy [32]. The cracking behavior in specimens containing single flaws under uniaxial compression was evaluated systematically by Wong and Einstein [31]. Three of the crack types are tensile, and three of the crack types are shear. The remaining one is of mixed

tensile-shear nature, with shearing occurring adjacent to the flaw tips and simultaneous tensile opening occurring farther away. The experimental study showed that seven crack types with different trajectories and initiation mechanism (tensile/shear) could originate from the preexisting flaws under uniaxial compression (Figure 19).

From our study, we derived some knowledge on the crack propagation mode. With the increase of the strength parameters, the crack growth mode develops from tension to shear. And the crack growth modes from SP1 to SP5 are pure tension, main tension, tension shear, main shear, and pure shear, respectively.

4.2. Influence of Hydraulic Loading Time Sequence on the Fracturing Process. In this study, the crack propagation patterns were affected significantly by the hydraulic loading time sequence. Under SH1, hydraulic pressures were applied after the main fracture had been developing for a specific period wherein only tensile cracks occurred (including the schemes SP2, SP3, and SP4). The simulation shows that the tensile

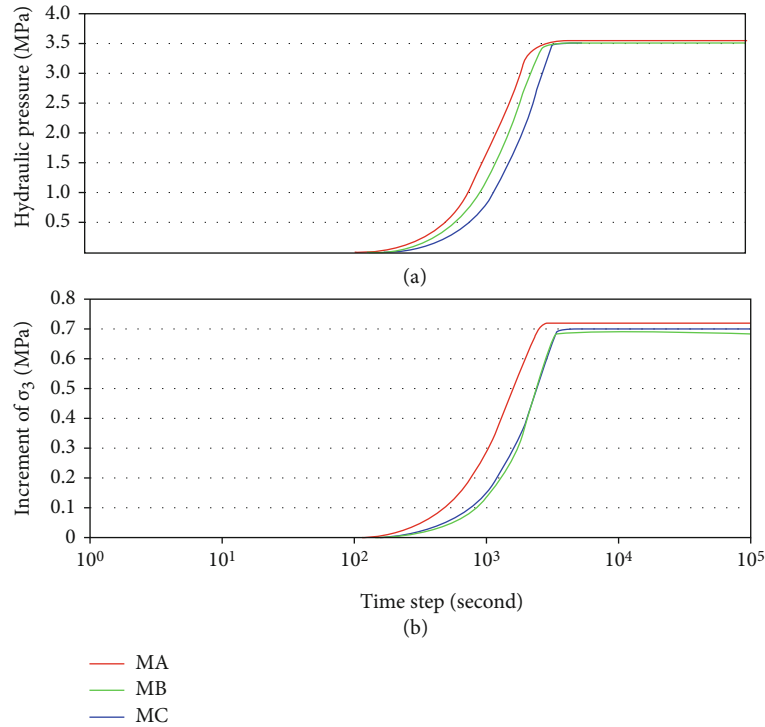


FIGURE 11: Evolutions of the hydraulic pressures and incremental tensile stresses.

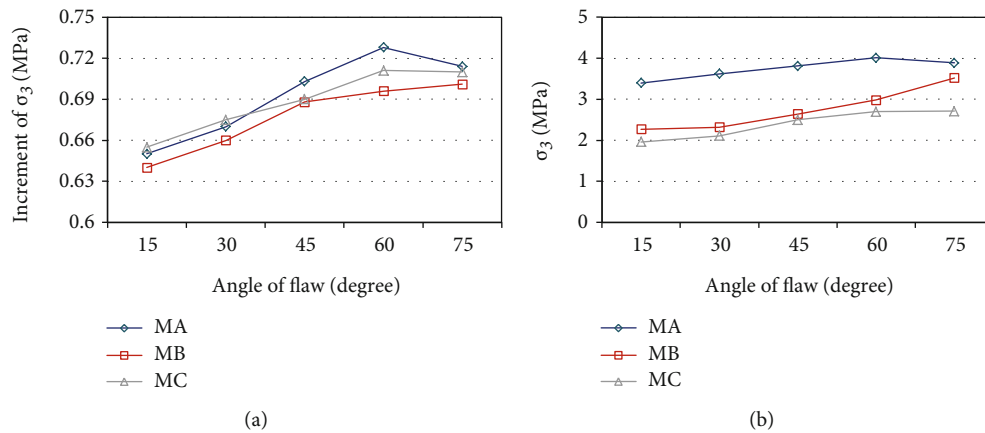


FIGURE 12: Evolutions of $\Delta\sigma_3$ and σ_3 by monitoring points: (a) incremental tensile stress; (b) total tensile stress.

stress and the angle of the main fracture crack also increase when SP2 is applied with hydraulic loading (Figures 11 and 12). For SP3 and SP4, the stress drop (shear crack) under mechanical-hydraulic loading occurs later than that under mechanical loading (Figures 13(a) and 13(b)). It shows that the growth of tensile crack on the main fracture surface is enhanced and the shear crack is restrained by mechanical-hydraulic loading. The occurrence time of stress drop (shear crack) of SP4 is earlier than that of SP3, indicating that the increase of rock strength is beneficial to the development of shear crack (Figure 13).

Under SH2, hydraulic pressures were applied at a period when the shear cracks were occurring after tensile cracking (including the schemes SP3 and SP4). The simulation shows that the tensile stress increases with hydraulic loading

(Figures 15 and 16). With the increase of the strength ratio of the rock sample, the crack propagation develops from tensile to shear. The occurrence time of stress drop (shear crack) under mechanical-hydraulic loading is earlier than that under mechanical loading (Figures 17(a) and 17(b)). The reason is that the maximum shear stress develops quickly and the shear crack occurs earlier; the shear crack growth is enhanced by mechanical-hydraulic loading. Compared with SP3 and SP4, it is also concluded that the increase of rock strength is beneficial to the development of shear crack (Figure 17).

Previous physical experiments by our team have also shown that mechanical-hydraulic loading can stimulate crack growth and fracture [33, 34]. Through the acoustic emission test under the mechanical-hydraulic loading, Chen

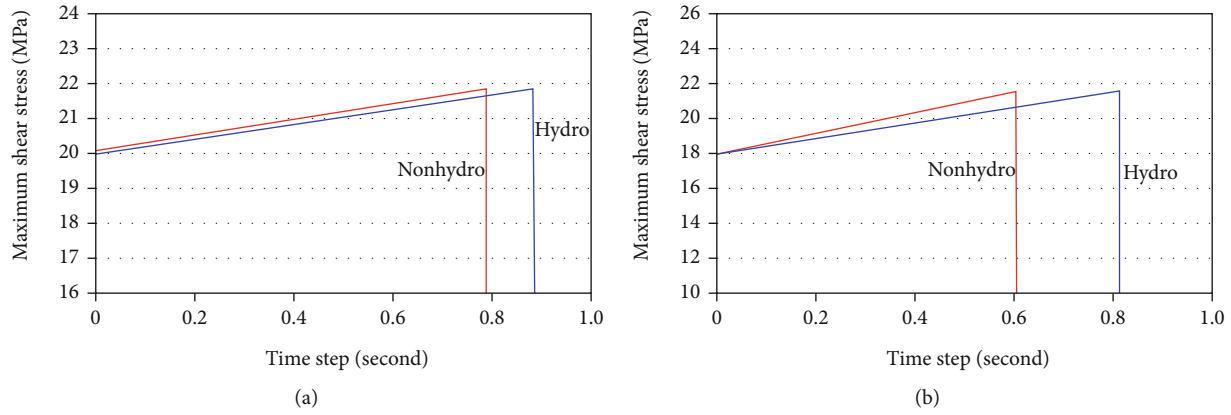


FIGURE 13: Evolutions of the maximum shear stress under continued mechanical loading: (a) scheme 3 of the strength parameters; (b) scheme 4 of the strength parameters.

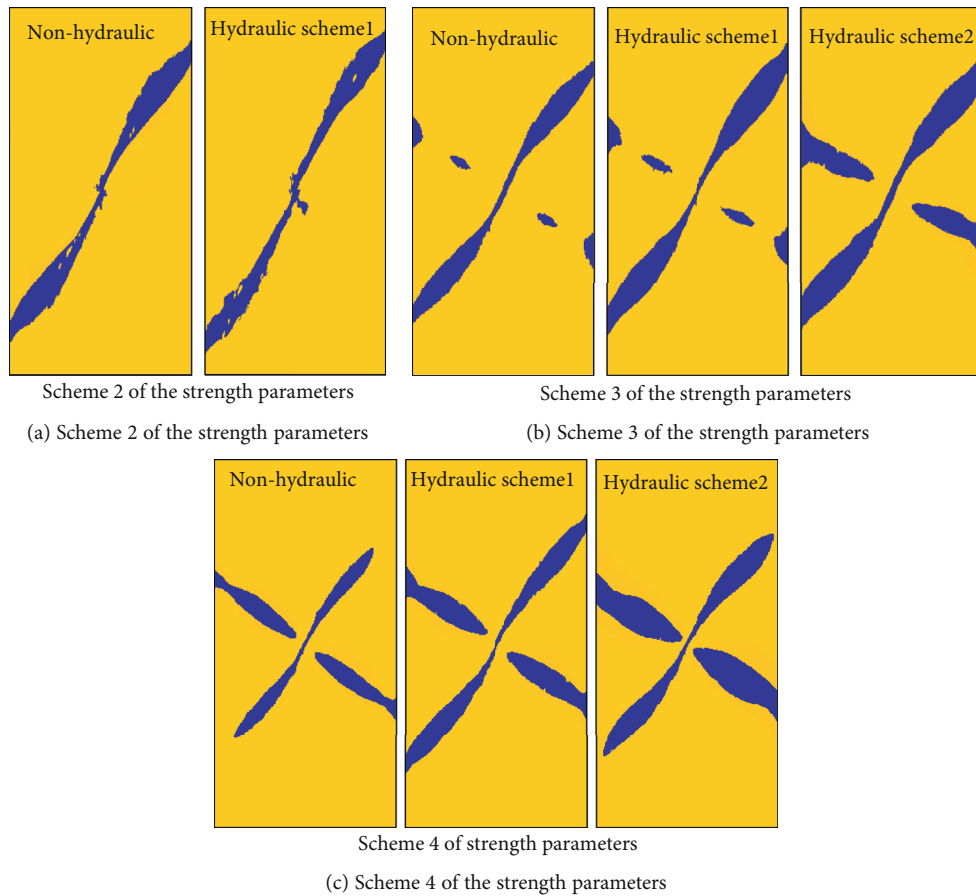


FIGURE 14: Crack propagation patterns under nonhydraulic and hydraulic actions.

[33, 34] found that with the increase of water pressure, the number of internal cracks in the rock increases at the time of final instability (Figure 20). These results may be explained by the fact that the splitting effect of water pressure is produced in the process of crack propagation, which leads to the initiation and propagation of new cracks. The propagation and penetration of primary crack and secondary crack may further accelerate the fracture of rock.

In conclusion, the main strength of this investigation is that the formation and propagation modes of the crack in precracked rock mass are simulated under different strength parameters and different mechanical-hydraulic loading time sequence. However, the following shortcomings exist in this study: (1) only a single precrack is simulated herein, and (2) the influence of high geotherm is not considered. Based on the complexity of internal crack defects and multifield

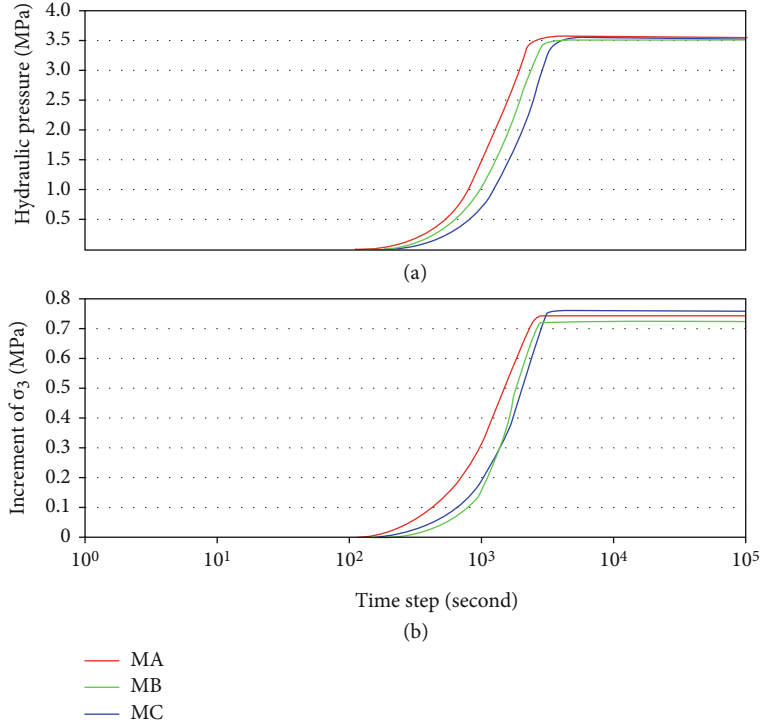


FIGURE 15: Evolutions of the hydraulic pressures and incremental tensile stresses.

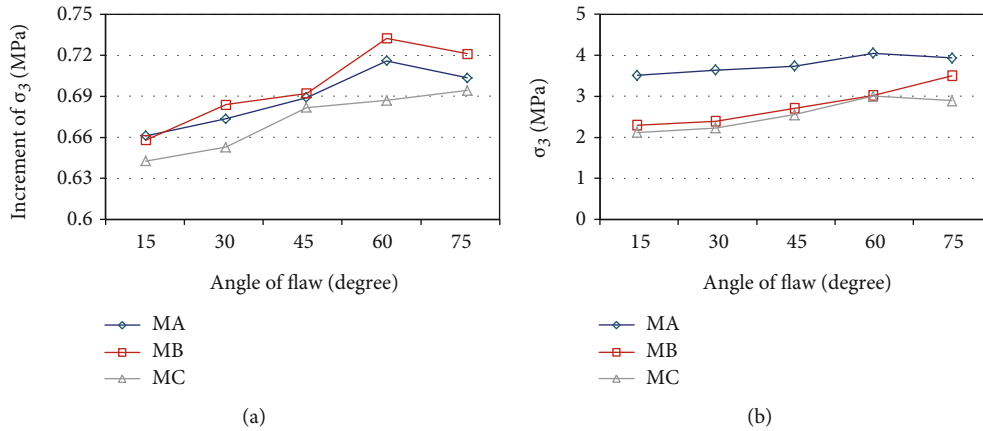


FIGURE 16: Evolutions of $\Delta\sigma_3$ and σ_3 by monitoring points: (a) incremental tensile stress; (b) total tensile stress.

coupling environments in the rock mass, the combination of multiple precracking and high geotherm can be considered to further explain cracking index and fracture mechanism.

5. Conclusions

In this paper, an in-house finite element code PANDAS was used to simulate the cracking behavior of precracked rocks under mechanical-hydraulic loading. The influence of different strength parameters and mechanical-hydraulic loading factors on the law of crack propagation is mainly considered. The major conclusions of this study are as follows:

- (1) The crack types are controlled by the crack-induced stresses and angle of the flaw. Types I

and II wing cracks sequentially occur in the flaws at 15°, 30°, and 45°. Type III crack (along the same direction of the flaw) generally occurs in the flaw at 60°. Type IV crossed crack occurs in the flaw at 75°

- (2) Crack propagation patterns were strongly affected by the different schemes of strength parameters. As the tensile strength gradually increased, the crack propagation patterns corresponding to the five schemes included pure tensile, main tensile, tensile-shear, main shear, and pure tensile, respectively. The larger the strength ratio of the rock mass is, the earlier the second fracture (roughly perpendicular to the main fracture) appears and develops more obviously

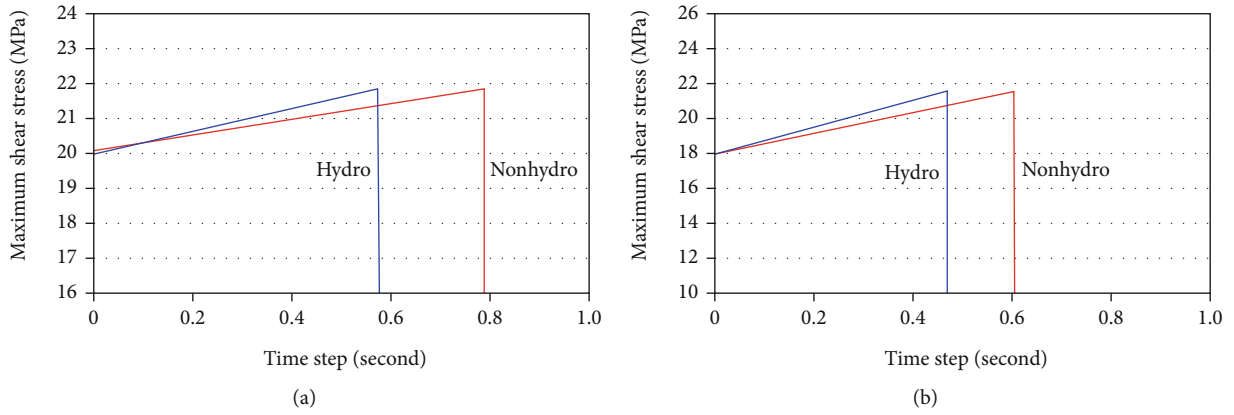


FIGURE 17: Evolutions of the maximum shear stress under continued mechanical loading: (a) scheme 3 of the strength parameters; (b) scheme 4 of the strength parameters.

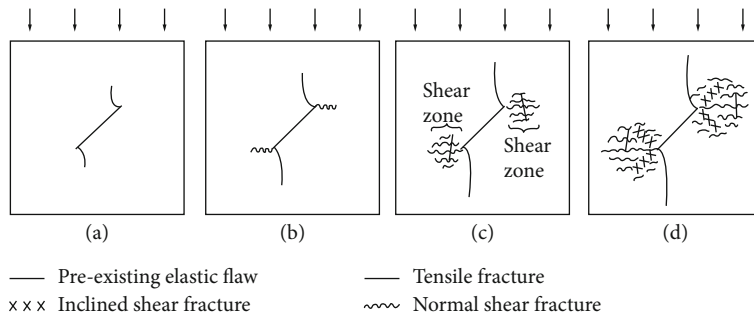


FIGURE 18: The evolution of fracture from a single open flaw observed by Lajtai [30].

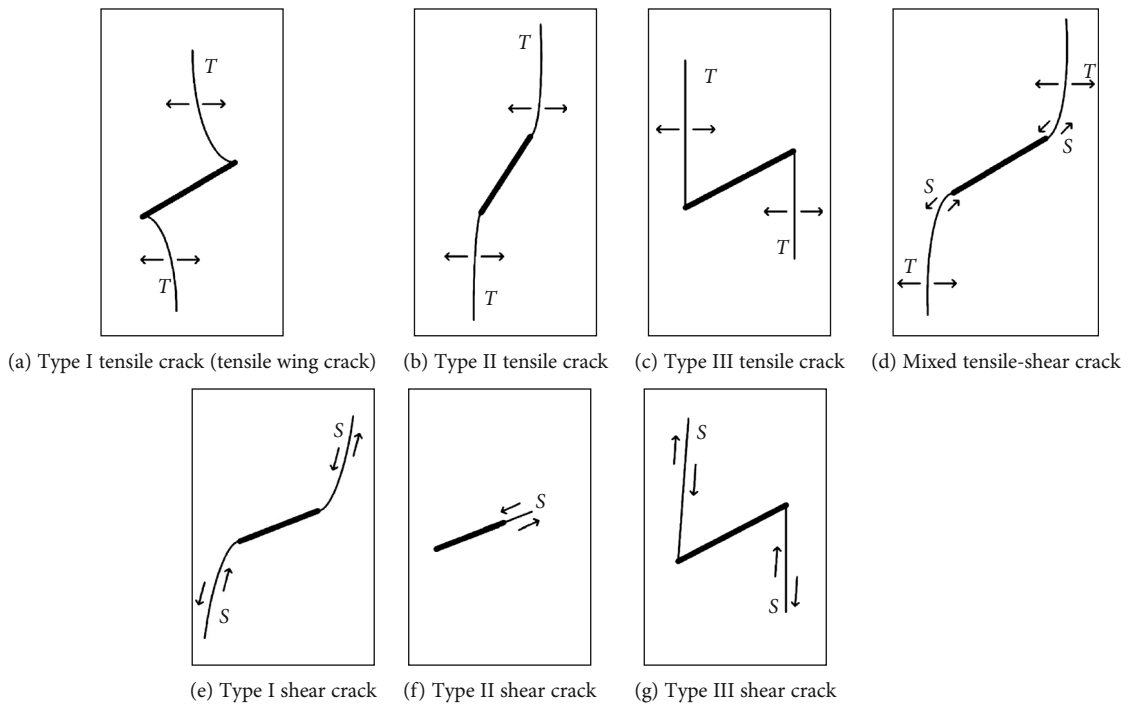


FIGURE 19: The tensile crack types initiated from the preexisting flaws by Wong and Einstein [31]. *T*: tensile cracking opening; *S*: shearing displacement.

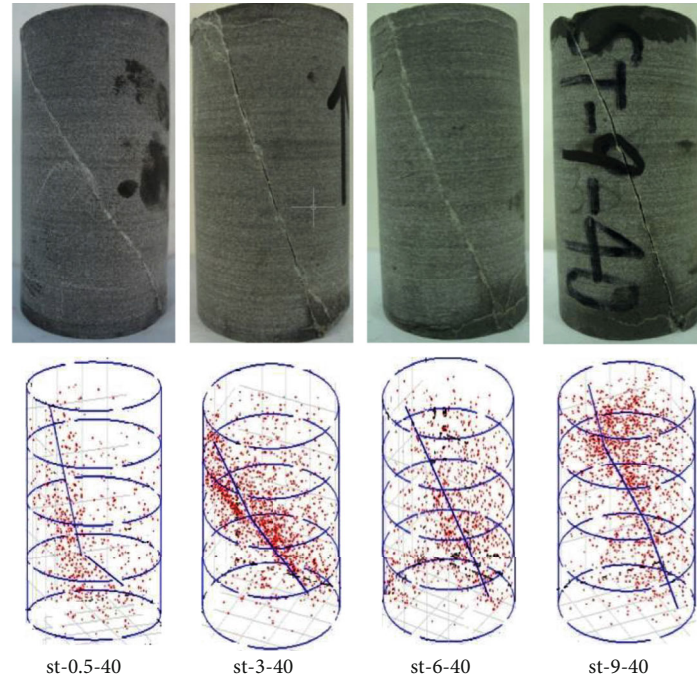


FIGURE 20: Positioning results of acoustic emission test and broken rock sample under different hydraulic loading by Wang and Shrive [32].

- (3) The applied timing of hydraulic action has a significant impact on the crack propagation patterns. When hydraulic loading is carried out in the main crack propagation stage, the shear fracture appears later and the maximum shear stress (the initial fracture of the second fracture) develops slowly. It shows that the tensile crack is promoted during the rock fracture and the shear crack is restrained by hydraulic loading
- (4) When hydraulic loading is carried out in the phase of shear crack propagation, the maximum shear stress develops faster and the shear fracture appears earlier. The results show that both shear fracture and tensile fracture are strengthened under the condition of shear fracture. The splitting effect of water pressure is produced in the process of crack propagation, which leads to the initiation and propagation of new cracks and further accelerates the fracture of rock

This study not only helps to understand the mechanism of crack formation and propagation under complex stress environments but also further expands the research of new engineering scenarios, such as coalbed methane logging and tunnel water inrush [15, 35]. Based on this study, further experimental and theoretical research can be carried out by comprehensively considering multiple groups of precrack and high geotherm factors.

Abbreviations

MIN: Minimum principal stress
 MAX: Maximum principal stress
 MAXSH: Maximum shear stress

SP (1-5): Five schemes of strength parameter
 SH (1, 2): Two schemes of hydraulic loading.

Data Availability

All data, models, and code generated or used in the research process have appeared in the manuscript. According to the calculation formula and method in the paper, interested readers can reproduce these results and data and can make improvements to obtain different results.

Conflicts of Interest

The authors declared that they have no conflicts of interest in this work.

Acknowledgments

We would like to thank Dr. Quanshu Li and Dr. Zhiting Han of the University of Queensland for the helpful discussions. The related calculation was carried out by running the PANDAS software on the Savanna Supercomputer at UQ. The work is financially supported by the National Natural Science Foundation of China (Grant Numbers 52074251, 9205820028, and U19A20111) and the open fund (Grant Numbers SKLGP2015K004 and SKLGP2017Z001) from the State Key Laboratory of Geohazard Prevention and Geoenvironment Protection, China

References

- [1] G. L. Feng, X. T. Feng, B. R. Chen, Y. X. Xiao, and Y. Yu, "A microseismic method for dynamic warning of rockburst

- development processes in tunnels,” *Rock Mechanics and Rock Engineering*, vol. 48, no. 5, pp. 2061–2076, 2015.
- [2] G. L. Feng, X. T. Feng, B. R. Chen, Y. X. Xiao, and Z. N. Zhao, “Effects of structural planes on the microseismicity associated with rockburst development processes in deep tunnels of the Jinping-II Hydropower Station, China,” *Tunnelling and Underground Space Technology*, vol. 84, pp. 273–280, 2019.
 - [3] L. F. Vesga, L. E. Vallejo, and S. Lobo-Guerrero, “DEM analysis of the crack propagation in brittle clays under uniaxial compression tests,” *International Journal for Numerical and Analytical Methods in Geomechanics*, vol. 32, no. 11, pp. 1405–1415, 2008.
 - [4] Y. J. Xie, Y. L. Duo, and H. Yuan, “Potential fracture paths for cracked rocks under compressive-shear loading,” *International Journal of Rock Mechanics and Mining Sciences*, vol. 128, article 104216, 2020.
 - [5] A. Manouchehrian and M. F. Marji, “Numerical analysis of confinement effect on crack propagation mechanism from a flaw in a pre-cracked rock under compression,” *Acta Mechanica Sinica*, vol. 28, no. 5, pp. 1389–1397, 2012.
 - [6] H. Lee and S. Jeon, “An experimental and numerical study of fracture coalescence in pre-cracked specimens under uniaxial compression,” *International Journal of Solids and Structures*, vol. 48, no. 6, pp. 979–999, 2011.
 - [7] Q. Yin, G. Ma, H. Jing et al., “Hydraulic properties of 3D rough-walled fractures during shearing: an experimental study,” *Journal of Hydrology*, vol. 555, pp. 169–184, 2017.
 - [8] Q. Yin, H. Jing, G. Ma, H. Su, and R. Liu, “Investigating the roles of included angle and loading condition on the critical hydraulic gradient of real rock fracture networks,” *Rock Mechanics and Rock Engineering*, vol. 51, no. 10, pp. 3167–3177, 2018.
 - [9] Q. Yin, R. Liu, H. Jing, H. Su, L. Yu, and L. He, “Experimental study of nonlinear flow behaviors through fractured rock samples after high-temperature exposure,” *Rock Mechanics and Rock Engineering*, vol. 52, no. 9, pp. 2963–2983, 2019.
 - [10] A. Golshani, M. Oda, Y. Okui, T. Takemura, and E. Munkhtogoo, “Numerical simulation of the excavation damaged zone around an opening in brittle rock,” *International Journal of Rock Mechanics and Mining Sciences*, vol. 44, no. 6, pp. 835–845, 2007.
 - [11] Y. Sumer and M. Aktas, “Finite element modeling of existing cracks on pre-loaded reinforced concrete beams,” *Arabian Journal for Science and Engineering*, vol. 39, no. 4, pp. 2611–2619, 2014.
 - [12] H. Haeri, K. Shahriar, M. F. Marji, and P. Moarefvand, “Experimental and numerical study of crack propagation and coalescence in pre-cracked rock-like disks,” *International Journal of Rock Mechanics and Mining Sciences*, vol. 67, pp. 20–28, 2014.
 - [13] Y. Wang, X. Zhou, and X. Xu, “Numerical simulation of propagation and coalescence of flaws in rock materials under compressive loads using the extended non-ordinary state-based peridynamics,” *Engineering Fracture Mechanics*, vol. 163, pp. 248–273, 2016.
 - [14] S. Q. Yang, W. L. Tian, Y. H. Huang, P. G. Ranjith, and Y. Ju, “An experimental and numerical study on cracking behavior of brittle sandstone containing two non-coplanar fissures under uniaxial compression,” *Rock Mechanics and Rock Engineering*, vol. 49, no. 4, pp. 1497–1515, 2016.
 - [15] X. P. Zhou and Y. T. Wang, “Numerical simulation of crack propagation and coalescence in pre-cracked rock-like Brazilian disks using the non-ordinary state-based peridynamics,” *International Journal of Rock Mechanics and Mining Sciences*, vol. 89, pp. 235–249, 2016.
 - [16] C. Ma, Y. Jiang, H. Xing, and T. Li, “Numerical modelling of fracturing effect stimulated by pulsating hydraulic fracturing in coal seam gas reservoir,” *Journal of Natural Gas Science and Engineering*, vol. 46, pp. 651–663, 2017.
 - [17] C. Zhao, J. Niu, Q. Zhang, S. Yu, and C. Morita, “Numerical simulations on cracking behavior of rock-like specimens with single flaws under conditions of uniaxial and biaxial compressions,” *Journal of Materials in Civil Engineering*, vol. 31, no. 12, article 04019305, 2019.
 - [18] G. Liu, J. Peng, Z. Zhang, Z. Wang, and Y. Yang, “Numerical investigation of fluid-driven crack propagation and coalescence in granite specimen with two pre-existing flaws,” *Journal of Natural Gas Science and Engineering*, vol. 75, article 103132, 2020.
 - [19] D. Roubinet, S. Demirel, E. B. Voytek, X. Wang, and J. Irving, “Hybrid analytical and numerical approach for modeling fluid flow in simplified three-dimensional fracture networks,” *Geofluids*, vol. 2020, Article ID 3583817, 14 pages, 2020.
 - [20] W. Lu, Y. Wang, and X. Zhang, “Numerical simulation on the basic rules of multihole linear codirectional hydraulic fracturing,” *Geofluids*, vol. 2020, Article ID 6497368, 14 pages, 2020.
 - [21] H. L. Xing and A. Makinouchi, “Three dimensional finite element modeling of thermomechanical frictional contact between finite deformation bodies using R-minimum strategy,” *Computer Methods in Applied Mechanics and Engineering*, vol. 191, no. 37–38, pp. 4193–4214, 2002.
 - [22] H. L. Xing, P. Mora, and A. Makinouchi, “A unified friction description and its application to the simulation of frictional instability using the finite element method,” *Philosophical Magazine*, vol. 86, no. 21–22, pp. 3453–3475, 2006.
 - [23] H. L. Xing, J. Zhang, and C. Yin, “A finite element analysis of tidal deformation of the entire earth with a discontinuous outer layer,” *Geophysical Journal International*, vol. 170, no. 3, pp. 961–970, 2007.
 - [24] H. Xing, “Finite element simulation of transient geothermal flow in extremely heterogeneous fractured porous media,” *Journal of Geochemical Exploration*, vol. 144, pp. 168–178, 2014.
 - [25] Q. Li and H. Xing, “Numerical analysis of the material parameter effects on the initiation of hydraulic fracture in a near well-bore region,” *Journal of Natural Gas Science and Engineering*, vol. 27, pp. 1597–1608, 2015.
 - [26] A. R. Ingraffea and F. E. Heuze, “Finite element models for rock fracture mechanics,” *International Journal for Numerical and Analytical Methods in Geomechanics*, vol. 4, no. 1, pp. 25–43, 1980.
 - [27] H. C. M. Chan, V. Li, and H. H. Einstein, “A hybridized displacement discontinuity and indirect boundary element method to model fracture propagation,” *International Journal of Fracture*, vol. 45, no. 4, pp. 263–282, 1990.
 - [28] C. A. Tang and S. Q. Kou, “Crack propagation and coalescence in brittle materials under compression,” *Engineering Fracture Mechanics*, vol. 61, no. 3–4, pp. 311–324, 1998.
 - [29] A. Bobet and H. H. Einstein, “Numerical modeling of fracture coalescence in a model rock material,” *International Journal of Fracture*, vol. 92, no. 3, pp. 221–252, 1998.
 - [30] E. Z. Lajtai, “Brittle fracture in compression,” *International Journal of Fracture*, vol. 10, no. 4, pp. 525–536, 1974.

- [31] L. N. Y. Wong and H. H. Einstein, "Systematic evaluation of cracking behavior in specimens containing single flaws under uniaxial compression," *International Journal of Rock Mechanics and Mining Sciences*, vol. 46, no. 2, pp. 239–249, 2009.
- [32] E. Z. Wang and N. G. Shrive, "Brittle fracture in compression: mechanisms, models and criteria," *Engineering Fracture Mechanics*, vol. 52, no. 6, pp. 1107–1126, 1995.
- [33] Z. Q. Cheng, *Fracture and energy mechanism of hard and brittle rocks under water-mechanical coupling*, Master's thesis of Chengdu University of Technology, 2015.
- [34] Z. Chen, C. He, D. Wu, G. Xu, and W. Yang, "Fracture evolution and energy mechanism of deep-buried carbonaceous slate," *Acta Geotechnica*, vol. 12, no. 6, pp. 1243–1260, 2017.
- [35] J. He, Y. Zhang, C. Yin, and X. Li, "Hydraulic fracturing behavior in shale with water and supercritical CO₂ under triaxial compression," *Geofluids*, vol. 2020, Article ID 4918087, 10 pages, 2020.

Research Article

Equivalent Permeability Distribution for Fractured Porous Rocks: Correlating Fracture Aperture and Length

Tao Chen 

Shandong Provincial Key Laboratory of Depositional Mineralization & Sedimentary Minerals, College of Earth Science and Engineering, Shandong University of Science and Technology, No. 579 Qianwangang Road, Qingdao 266590, China

Correspondence should be addressed to Tao Chen; chentao9330@gmail.com

Received 28 April 2020; Revised 22 August 2020; Accepted 18 September 2020; Published 10 October 2020

Academic Editor: Qian Yin

Copyright © 2020 Tao Chen. This is an open access article distributed under the Creative Commons Attribution License, which permits unrestricted use, distribution, and reproduction in any medium, provided the original work is properly cited.

Estimating equivalent permeability at grid block scale of numerical models is a critical issue for large-scale fractured porous rocks. However, it is difficult to constrain the permeability distributions for equivalent fracture models as these are strongly influenced by complex fracture properties. This study quantitatively investigated equivalent permeability distributions for fractured porous rocks, considering the impact of the correlated fracture aperture and length model. Two-dimensional discrete fracture models are generated with varied correlation exponent ranges from 0.5 to 1, which indicates different geomechanical properties of fractured porous rock. The equivalent fracture models are built by the multiple boundary upscaling method. Results indicate that the spatial distribution of equivalent permeability varied with the correlation exponent. When the minimum fracture length and the number of fractures increase, the process that the diagonal equivalent permeability tensor components change from a power law like to a lognormal like and to a normal-like distribution slows down as the correlation exponent increases. The average dimensionless equivalent permeability for the equivalent fracture models is well described by an exponential relationship with the correlation exponent. A power law model is built between the equivalent permeability of equivalent fracture models and fracture density of discrete fracture models for the correlated aperture-length models. The results demonstrate that both the fracture density and length-aperture model influence the equivalent permeability of equivalent fracture models interactively.

1. Introduction

Fractures are among the most common structures in the brittle rocks of the Earth's crust and span a wide range of length scales from millimeter to kilometers. The interconnected fracture networks in the rock matrix are the primary pathway for fluid to flow underground and have significant importance on practical applications, such as aquifer management, groundwater contamination, hydrocarbon and geothermal energy exploitation, geological disposal of nuclear waste, and coal mine water inrush [1–6]. As a quantitative measure of a rock mass's ability to conduct fluid, permeability is one of the most important properties affecting the flow in fractured porous rocks.

Due to the high heterogeneity and anisotropy of fractured rocks, the permeability of fractured porous rock gener-

ally has a symmetric full tensor form [7] and exhibits scale effects [8, 9]. Permeability of fractured rocks can be estimated by laboratory experiment [10], borehole flowmeter [11], field pumping test [12], discrete fracture characterization data from core samples [13], borehole well logs [14], and outcrops [15]. Such measurements can be roughly classified into continuum approaches and discrete fracture approaches [16]. The continuum approaches are often applied to explore the bulk rock flow regime for a scale of the measurement. In contrast, numerical or analytical calculating equivalent permeability from discrete fracture geometries provides an efficient way for estimating rock permeability and links the small scale fracture geometries and equivalent permeability for field-scale models, which is also known as upscaling [17, 18]. An understanding of the influence of discrete fractures on the equivalent permeability of grid blocks opens the

possibility of creating efficient and accurate equivalent fracture models based on the multiple-scale fracture characterization data.

For investigating the correlation between equivalent permeability and fracture geometries, analytical models and numerical models were developed since the 1960s [19] and since 1980s [20], respectively. With the development of fracture characterization, numerical models, and theoretic models, continuous efforts have been made for correlating the equivalent permeability and fracture geometries [21–23]. de Dreuzy et al. [24] studied the influence of a power law length distribution and a lognormal aperture distribution on the equivalent permeability for fractured rocks with an impervious matrix. Min et al. [25] developed a numerical procedure to calculate the permeability tensors of fractured rocks, using a stochastic REV concept based on discrete fracture network models. Based on a newly developed correlation equation, Baghbanan and Jing [26] investigated the permeability of fractured rocks, considering the correlation between distributed fracture aperture and length. Klimczak et al. [27] modeled flow through fracture networks for both correlated and uncorrelated fracture length-to-aperture relationships, calculated permeability of fractured rocks, and confirmed the importance of the correlated square root relationship of the aperture to length scaling. Leung and Zimmerman [28] established a methodology for estimating the macroscopic effective hydraulic conductivity based on the geometric parameters of the fracture network rather than solving the flow equations. However, compared to porous rocks (e.g., [29–31]), determining the bulk properties of fractured rocks is still challenging regarding the complexity of fracture geometries.

More recently, Miao et al. [32] derived an analytical model for estimating permeability for fractured rocks based on the fractal geometry theory and the cubic law for laminar flow in fractures. Liu et al. [33] proposed a fractal model to link the fractal characteristics of both the fluid flow tortuosity and fracture geometry with the equivalent permeability of the fracture networks. Hyman et al. [34] characterized how different fracture size and aperture relationships influence flow and transport simulations through sparse three-dimensional discrete fracture networks and observe that networks with a correlated relationship have consistently higher effective permeability values. The above study assumed that rock matrix permeability is impervious. Bisdorn et al. [35] compared the different aperture models and critical stress criteria and conclude that their impacts on equivalent permeability depend on matrix permeability for naturally fractured reservoirs. Xiong et al. [36] developed a numerical procedure about nonlinear flow in three-dimension discrete fracture networks by solving the Reynolds equation and Forchheimer equation. They found that the required hydraulic head gradient for the onset of nonlinear fluid flows reduces when the fracture surface becomes smooth and the fracture connectivity increases. Yin et al. [37] developed a high-precision apparatus to investigate the influence of shear processes on nonlinear flow within three-dimensional rough-walled fractures experimentally and found that the hydraulic aperture of fracture enlarges increases as the shear displacement increases. The

studies are conducted at the scale of the laboratory measurement. Nevertheless, the complexity of the interconnected fractures at the field scale has yet to be fully considered.

While many previous studies propose relationships between fracture length and aperture and illustrated their effects on fluid flow through fractured rocks (e.g., [33, 35, 38, 39]), yet they mainly address the equivalent permeability for a grid block at different scales. The influence of correlated length and aperture on equivalent permeability distributions of grid blocks for large-scale fractured porous media has yet to be clarified. The novelty of this study is that equivalent permeability distribution with correlated fracture aperture and length is analyzed for fractured porous media with state of the art upscaling method [40], which provides a potential link between fracture properties and stochastic equivalent fracture models and is possible for reducing uncertainty for equivalent fracture models.

The paper is organized as follows: first, the discrete fracture models with correlated fracture aperture and length are presented, and the multiple boundary upscaling method is introduced. Then, the equivalent permeability distribution for the discrete fracture models is analyzed stochastically based on histograms. Third, the relationship between the average equivalent permeability and correlated aperture and length model is interpreted. Forth, the effects of fracture geometry on the equivalent permeability are investigated based on the correlated aperture and length model. Finally, the results are discussed, and the conclusions are drawn.

2. Methodology

Two main procedures were conducted for analyzing the effects of fracture length-aperture correlation on equivalent permeability distribution for the two-dimensional fractured porous rocks: generating discrete fracture models correlating the fracture length and aperture and upscaling equivalent permeability for the discrete fracture model by using the multiple boundary method. The related techniques are described below.

2.1. Discrete Fracture Model Generation. Fracture apertures vary due to the mechanical misfit of fracture walls, chemical dissolution, and normal pressure due to the depth of overburden [41]. Fracture apertures cover a wide range of scales. They can be measured by a wide variety of methods, including direct measurements in core or outcrop and deduction from flow data. The aperture for fractured porous rocks can be described by constant (e.g., [24]), statistical models [42], correlation with fracture [27], and mechanical models [38]. The power law relationship between fracture aperture and length (including linear and sublinear) applied in this study is widely observed at the field scale [43] and is derived by linear elastic fracture mechanics [44], which can be expressed by [45]

$$w = \gamma l^D, \quad (1)$$

where w is fracture aperture, l is fracture length, γ is the coefficient related to mechanical properties of fractured rock,

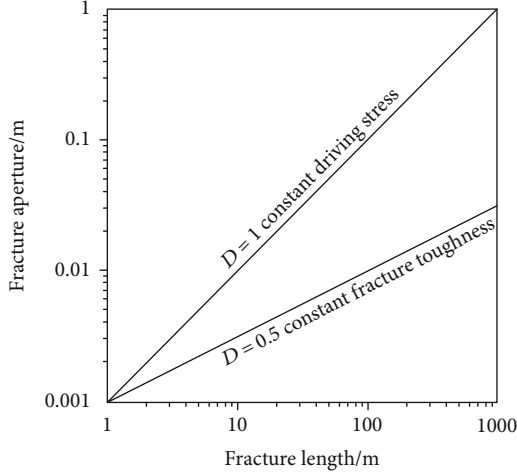


FIGURE 1: Theoretical scaling of fracture aperture with length for geologic structural discontinuities [45].

and the correlation exponent D indicates the mechanical interaction between closely spaced fractures (Figure 1). For isolated veins, faults, and shear deformation bands with constant driving stress, the correlation between fracture aperture and length tends to be linear, i.e., $D=1.0$ [45, 46]. For more complex open-mode fractures with a constant fracture toughness, the ability of a rock containing a fracture to resist further fracturing, D is around 0.5 [44, 47]. The correlation exponent D is greater than 0.5, and less than 1.0 could result from post-jointing relaxation [27]. In this study, the correlation exponent D ranges from 0.5 to 1.0, and γ is assumed to be 1.2×10^{-4} according to the field data [48].

Fracture length covers a wide scale and can be described by a power law model [41]:

$$n(l) = Al^{-a} dl, \quad (2)$$

where l is the fracture length, $n(l)$ is the number of fractures with sizes in the range $[l, l + dl]$, A is a density constant, and a is a power law exponent. As the length of fractures is measured upon a specific scale and is limited by the rock size in the Earth's crust, it has lower and upper bounds for the power law distribution. The power law exponent a represents the growth properties of the fractures and varies from 1.3 to 3.5 [41, 49], and in this study, a is assumed to be 2.5.

In this study, a series of two-dimensional synthetic fracture networks is generated in a squared domain of size $L = 20$ m (Figure 2). The location and orientation of fractures are assumed purely random, which is nominally homogeneous. The fracture length follows power law distribution as shown in equation (1) and the lower bound l_{\min} and the upper bound l_{\max} are 4 m and 40 m, respectively. The number of fractures N is 50. The fracture geometries vary by increasing l_{\min} from 4 m to 6 m, 8 m, and 10 m and by rising N from 50 to 75, 100, and 125. Thus, a total of 16 sets of discrete fracture networks with different geometric parameters are created with the Monte Carlo method based mainly on the ADFNE software [50]. In the following study, both the per-

meability of fractures and rock matrix are taken into account, which constitutes discrete fracture models.

2.2. Upscaling Permeability. The equivalent fracture models are built based on upscaling permeability for the discrete fracture models. The dimension of the Cartesian grid for the equivalent fracture model is $2 \text{ m} \times 2 \text{ m}$. After subdividing the fractures of the whole domain into the Cartesian grid, the multiple boundary upscaling method is applied for calculating equivalent permeability for each grid block. The multiple boundary upscaling method is applicable for both two-dimensional and three-dimensional discrete fracture models, which was tested for a rotated fracture by fitting with analytical solutions as well as for fracture networks [40].

The multiple boundary upscaling method involves mainly three steps. First, the linear boundary conditions, which mimic the flow across fractured porous rocks underground, are applied for the grid block with the pressure gradient of 1 Pa/m along the x -axis (Figure 3). Then, the steady flow problem is solved, and the fluxes q_x and q_y , from both the fracture and rock matrix are calculated with a multiple boundary expression [40]. Lastly, the equivalent permeability component k_{xx} and k_{yy} is calculated according to Darcy's law inversely. The equivalent permeability for two-dimensional discrete fracture models is a second-rank symmetric tensor with four components. k_{xy} and k_{yx} can be calculated by changing the direction of the linear boundary condition along the y -axis. It should be noted that the upscaled equivalent permeability is no inherently symmetric, and the symmetric permeability tensor is acquired by averaging the off-diagonal components.

The MRST code [51] is applied for solving flow problems in the fractures and rock matrix during the upscaling procedure. Flow equations in the fractures and rock matrix are based on mass conservation and Darcy's law, which are coupled based on the flow continuity on the fracture-rock matrix interface and are solved with a multipoint flux approximation [52]. The rock matrix and the fracture are represented by two-dimensional triangular grids of 0.2 m and one-dimensional line grids of 0.1 m, respectively. The matrix permeability is assumed as $k_m = 9.87 \times 10^{-16} \text{ m}^2$ (1 md) according to the actual data of fractured hydrocarbon reservoirs [53], and the fracture permeability is calculated according to the fracture aperture, that is, $k_f = w^2/12$. The numerical upscaling procedure is validated against analytical solutions. Considering a fully penetrated fracture with different correlation exponent D , the equivalent permeability can be calculated analytically and numerically with the multiple boundary method (Figure 4). It is shown that the numerical solutions match well with the analytical solution with varied correlation exponent D .

3. Equivalent Permeability Distribution

In this section, the influence of length-aperture correlation parameters on the histograms of equivalent permeability is demonstrated. The aperture-length correlation exponent D varied from 0.5 to 1.0 with a step of 0.1, which indicates

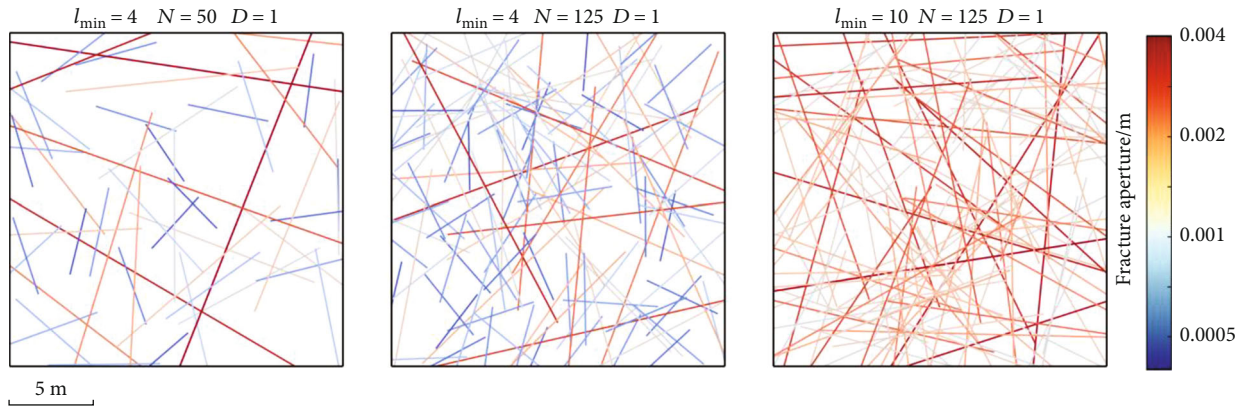


FIGURE 2: Discrete fracture models with correlated fracture aperture and length.

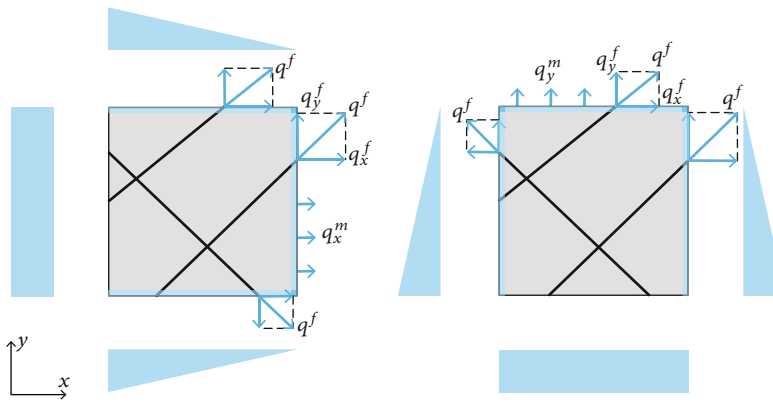


FIGURE 3: Calculating flow rates on multiple boundaries for a grid block under linear boundary conditions along the x -axis (left) and y -axis (right).

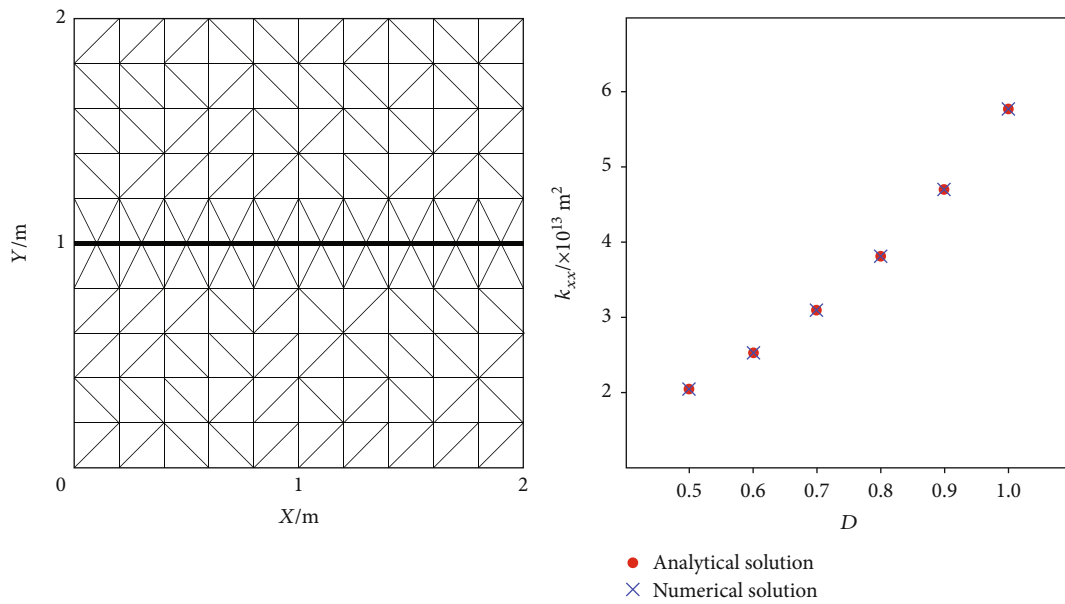


FIGURE 4: Meshes for the discrete fracture model, in which the bold lines denote fracture grids (left), and the corresponding equivalent permeability component k_{xx} for different correlation exponents D (right).

fracture mechanical state changes from constant fracture toughness to constant fracture driving force. For a specific correlation exponent D , 16 discrete fracture networks with varied fracture network geometries, i.e., the minimum fracture length l_{\min} and the number of fractures N , are generated. For generalizing the results, ten realizations are created for each group of fracture geometric parameters and thus a total of 960 discrete fracture models are generated for the following analysis.

Figure 5(a) shows the Cartesian grid of the equivalent fracture model for a realization of the discrete fracture models with $l_{\min} = 4, N = 125$, and $D = 1$. The spatial distributions of equivalent permeability components k_{xx} , k_{yy} , and k_{xy} are plotted in Figures 5(b)–5(d), respectively. The equivalent permeability ranges from $9.87 \times 10^{-16} \text{ m}^2$ (matrix permeability) to $3.5 \times 10^{-9} \text{ m}^2$. For the diagonal components k_{xx} and k_{yy} , the high permeable grid blocks are penetrated by long fractures which have large apertures as shown in the discrete fracture model. However, the spatial distribution for k_{xx} and k_{yy} is different from each other due to the random orientation of the fractures. For the off-diagonal component k_{xy} in Figure 5(d), they are either positive or negative, and the grid blocks with high absolute values correspond to those of large k_{xx} and k_{yy} in Figures 5(b) and 5(c).

For investigating the statistical distribution of equivalent permeability tensors, the histograms of k_{xx} , k_{yy} , and k_{xy} are plotted in Figures 5(e)–5(g), respectively. The fitting curves for histograms are also plotted. It is shown that both k_{xx} and k_{yy} exhibit a power law-like distribution whereas k_{xy} exhibits a normal distribution, which is similar to the results in three-dimensional fractured porous rock with poorly fracture connectivity [54].

For the discrete fracture model with different fracture geometric parameters, the fitting curves of the equivalent permeability tensor histograms for k_{xx} , k_{yy} , and k_{xy} are plotted in Figure 6. Rather than a single realization, the curves in Figure 6 represent fitting of all ten realizations for a given set of fracture geometric parameters. For $D = 0.5$, it shows that the shape and the magnitude of the diagonal components k_{xx} and k_{yy} are similar and tend to a power law distribution, whereas k_{xy} tends to a normal distribution. With the increase in l_{\min} and N , k_{xx} and k_{yy} change gradually from a power law to a lognormal to a normal distribution. The lognormal distribution of equivalent permeability is commonly assumed in the realistic reservoir models [55, 56]. Such transformation of the equivalent permeability distribution is partially due to the connectivity of fractures within grid blocks [49]. The shape of k_{xy} expands, which means an increase of the equivalent permeability. Furthermore, for evaluating the strength of the relationship for the fitting curves in Figure 6, the Spearman rank correlation coefficient between equivalent permeability and the frequency is calculated. The correlation coefficients for k_{xx} and k_{yy} are similar, with an average of about -0.75, which indicates a relatively strong negative correlation. For k_{xy} , the coefficient is less than -0.04, which almost denotes no correlation. It is reasonable as the off-diagonal component k_{xy} tends to be evenly distributed around zero due to the random fracture orientations.

With the increase in the correlation exponent D , the magnitude of the equivalent permeability tensor components also increases, which is due to that the equivalent permeability of the grid blocks is more controlled by long fractures with high aperture values [26]. However, with the increase in l_{\min} and N , the evolution of the histogram fitting curves differs for varied correlation exponent D . For a higher D (e.g., $D = 1$), the histograms do not show a clear normal distribution for large l_{\min} and N compared to those for a lower D , e.g., $D = 0.5$. They look like a transition shape for a lower D changing from a power law to a lognormal to a normal distribution. The difference is partially due to that the high correlation exponent D increases the heterogeneity of the discrete fracture model. And it is reasonable to speculate that with the increase in l_{\min} and N , the diagonal components tend to a lognormal distribution or normal distribution for a high D . Accordingly, for a specific fracture geometry, a high correlation exponent D means a higher heterogeneity which requires a sufficient number of fractures to reach a lognormal like distribution.

4. Correlating the Equivalent Permeability with the Aperture-Length Model

Before studying the effect of the length-aperture correlation exponent D on the equivalent permeability for the equivalent fracture models, the average dimensionless permeability \bar{k} for each discrete fracture model is defined as

$$\bar{k} = \frac{\sum_{n=1}^{N_m} (k_i/k_m)}{N_m}, \quad (3)$$

where N_m is the total number of grid blocks for the equivalent fracture model, and the rock matrix permeability k_m is equal to 1 md as assumed in the previous section. Under a specific aperture-length correlation exponent D , the average dimensionless permeability for all 160 realizations of discrete fracture models with varied fracture geometries is calculated. Figure 7 shows the relationship between the average dimensionless permeability \bar{k} and the aperture-length correlation exponent D of the discrete fracture models.

It shows in Figures 7(a) and 7(b) that for the diagonal components of equivalent permeability tensors, $\log(\bar{k}_{xx})$ and $\log(\bar{k}_{yy})$, increase linearly with the increase in the correlation exponent D , which can be expressed as the following exponential function:

$$\bar{k} = A \cdot 10^{B \cdot D}, \quad (4)$$

where the dimensionless coefficients A and B range from $10^{1.4}$ to $10^{2.4}$ and from 3.4 to 4.3, respectively. For the off-diagonal component k_{xy} , as the negative values exist, the absolute value $|k_{xy}|$ is used to analyze the correlation between the average dimensionless permeability and the aperture-length correlation exponent D (Figure 7(c)).

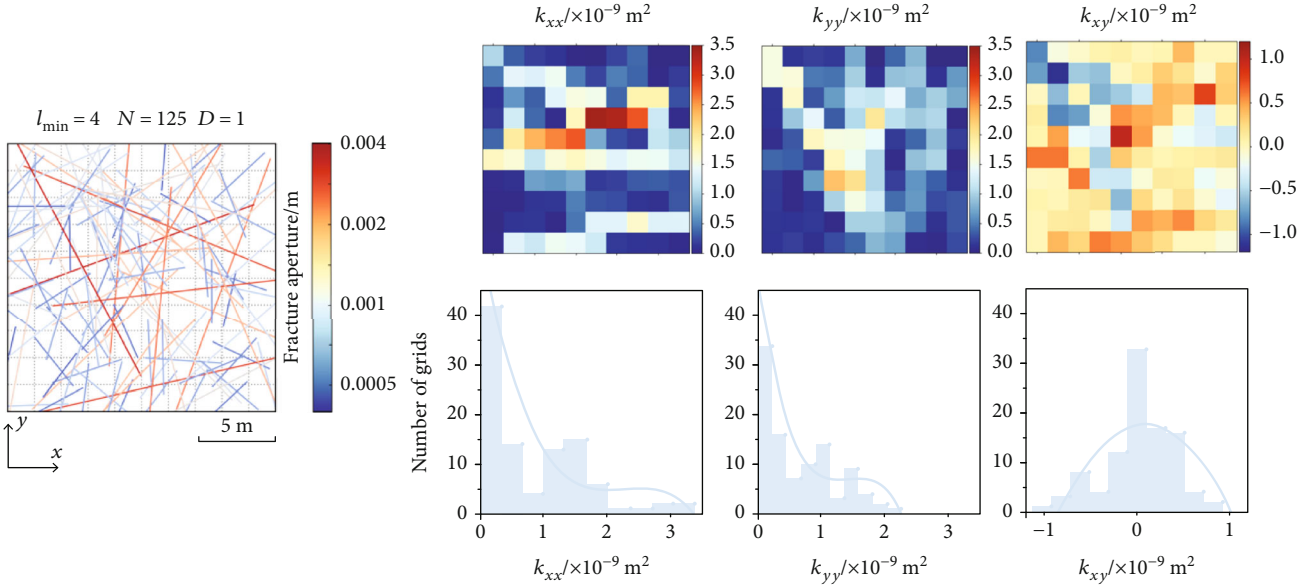


FIGURE 5: (a) Cartesian grid for the discrete fracture model, (b–d) spatial distributions, and (e–g) histograms for equivalent permeability components based on upscaling.

Likewise, the correlation can also be built in the framework of equation (4), which indicates that the exponential model can describe the relationship between the average dimensionless permeability \bar{k} and the aperture-length correlation exponent D . The observations also agree with the conclusions of Bisdom et al. [35] that the aperture-fracture model has an important effect on the magnitude of equivalent permeability.

We should note that although the correlation between \bar{k} of the equivalent fracture models and D of the discrete fracture models can be described by equation (4), the dimensionless coefficient B for k_{xx} and k_{yy} increases as the fracture geometric parameters l_{\min} and N raise (Figures 7(a) and 7(b)). In contrast, the dimensionless coefficient A does not show a clear change. It is reasonable as the large fracture length and number of fractures increase the permeability and connectivity of fractures and result in increased equivalent permeability. The coefficients A and B for $|k_{xy}|$ are of the same magnitude as those for k_{xx} and k_{yy} . However, for the coefficient A , the range is wider than those of k_{xx} and k_{yy} , which may be mainly due to the process of averaging the off-diagonal components. For the coefficient B , it is smaller than those of diagonal components. It is reasonable as the off-diagonal components are smaller than the diagonal components for a given discrete fracture model as shown in Figures 5(b)–5(d).

5. Effects of Fracture Geometry on the Equivalent Permeability

The influence of fracture geometries on the average dimensionless equivalent permeability for correlated length-aperture models is analyzed in this section. For each discrete

fracture model, the dimensionless fracture density is defined as [28]

$$\rho = \frac{1}{A} \sum_i^N \left(\frac{l_i}{2} \right)^2, \quad (5)$$

where A is the domain area, l_i is the length of the i -th fracture, and N is the total number of fractures of the discrete fracture model.

The correlations between the $\log(\bar{k})$ and $\log(\rho)$ are plotted for different length-aperture correlation exponents in Figure 8. It shows that for the diagonal components (Figures 8(a) and 8(b)), $\log(\bar{k})$ increases linearly with the increase in $\log(\rho)$ for a given length-aperture correlation exponent D , which can be fitted by the following power law relationship:

$$\bar{k} = \beta \cdot \rho^C, \quad (6)$$

where β and C are dimensionless coefficient in the ranges 10^3 – 10^5 and 1.1–1.3, respectively. Whereas for the off-diagonal components (Figure 8(c)), they are more scattered compared to the diagonal components. This characteristic is similar to that shown in Figure 7(c). It is shown in Figure 8 that the average dimensionless equivalent permeability scatters widely around the fitting line when the correlation exponent D increases. This is mainly because a higher correlation exponent D results in an enlarged difference in equivalent permeability. It indicates further that the higher D in the correlated length-aperture model, the higher heterogeneity for the equivalent fracture permeability field. It should be noted that C closing to 1 means a linear correlation between \bar{k} and ρ , which has been observed in the results for macroscopic hydraulic conductivity by Leung and Zimmerman [28]. Furthermore, when the

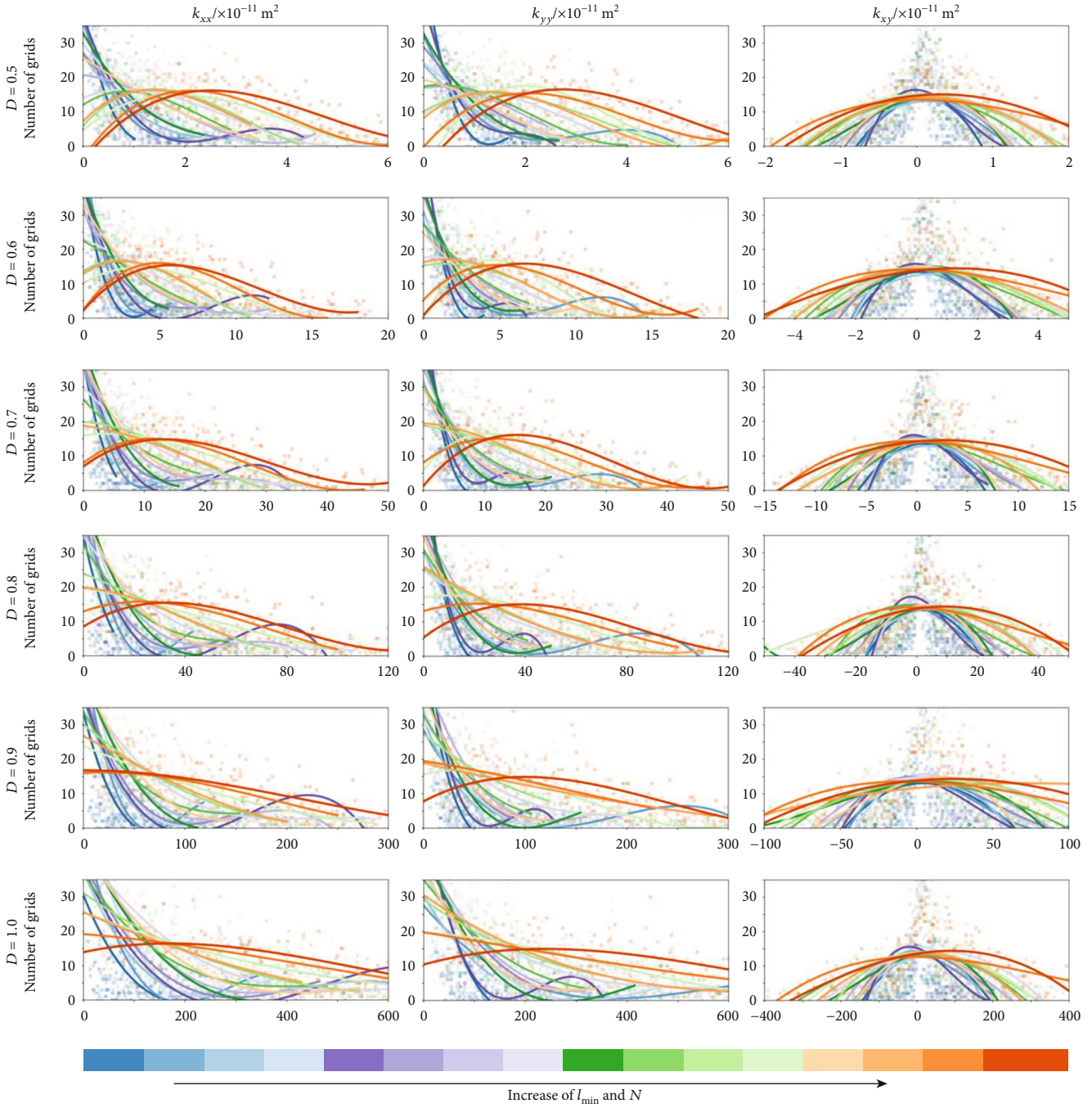


FIGURE 6: Fitting curves of histograms for equivalent permeability components with different aperture-length correlation exponent D and increasing l_{\min} and N .

correlation exponent D increases, β and C also increase (Figure 9). It shows that the aperture-length model influences the dimensionless coefficients β and C for the power model described by equation (6).

6. Discussion

In this study, the equivalent permeability distribution for discrete fracture models with correlated fracture aperture and length is investigated. Our results support the results

of Klimczak et al. [27], Leung and Zimmerman [28], and Bisdorn et al. [35], who highlight the importance of varied aperture models on equivalent permeability. Furthermore, the matrix permeability is considered for the fractured porous rocks as well in this study. In contrast to estimating the equivalent permeability at a given scale as in the above studies, this study investigates the statistical properties of equivalent permeability and the relationship between the averaged equivalent permeability rocks and the discrete fracture properties based on the multiple boundary

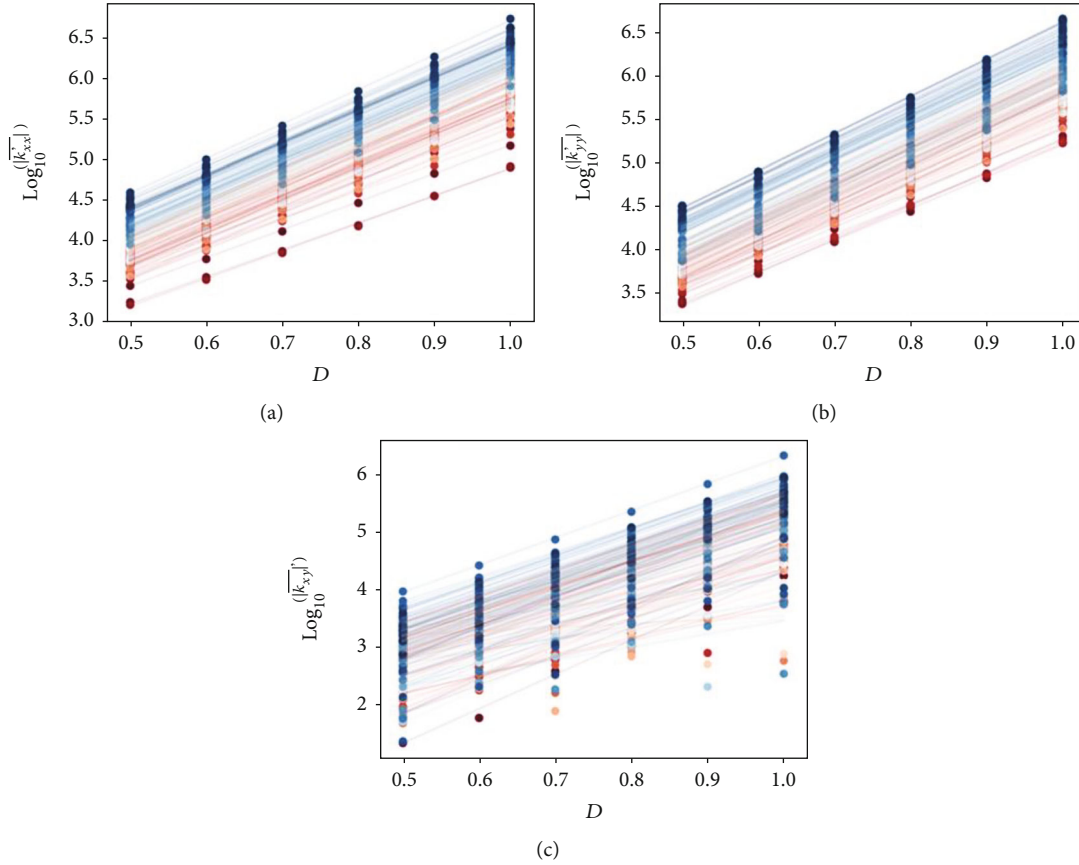


FIGURE 7: The average dimensionless permeability components of the equivalent fracture model versus aperture-length correlation exponent D of the discrete fracture model for increasing fracture geometric properties l_{\min} and N .

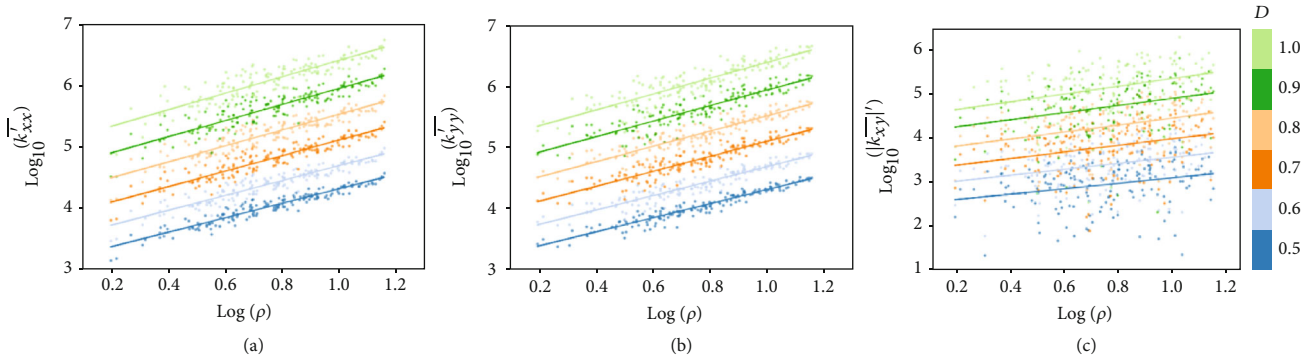


FIGURE 8: The average dimensionless permeability components of the equivalent fracture models versus dimensionless density of the discrete fracture models for varied aperture-length correlation exponent D .

upscaling method [54]. The methodology in the paper could be applied for efficient estimation of equivalent permeability distributions for fractured porous rocks correlating fracture length and aperture, which can be incorporated into stochastic equivalent fracture models. Thus, the results are meaningful for reducing uncertainty in numerical models for groundwater flow, solute, and heat transport processes (e.g., [56]) and for identifying key fracture geometric properties influencing rock hydraulic properties before fracture sampling at the field scale [2, 57].

The correlation exponent D varies from 0.5 to 1.0, which indicates fracture change from constant fracture toughness to constant driving stress [27, 44, 46]. The equivalent permeability for a fractured rock mass could be highly anisotropic, and the directional permeability can be estimated by the rotation of grid blocks [58]. In this study, the orientation and degree of anisotropy of equivalent permeability are analyzed based on coordinate rotations of the permeability tensor ellipse [39]. The directional permeability for grid blocks of equivalent fracture models is plotted in Figure 10. It should

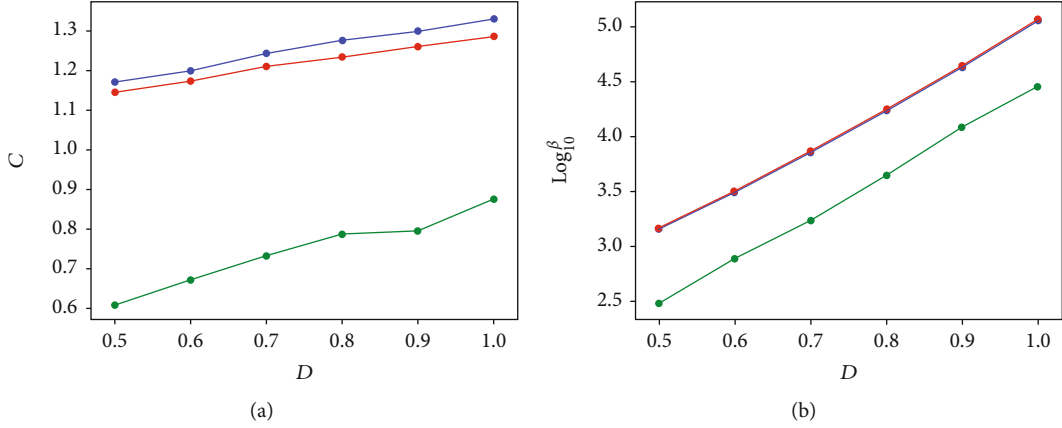


FIGURE 9: Variations of the dimensionless coefficient (a) C and (b) β regarding the correlation exponent D . The blue color, red color, and green color denote k_{xx} , k_{yy} , and k_{xy} , respectively.

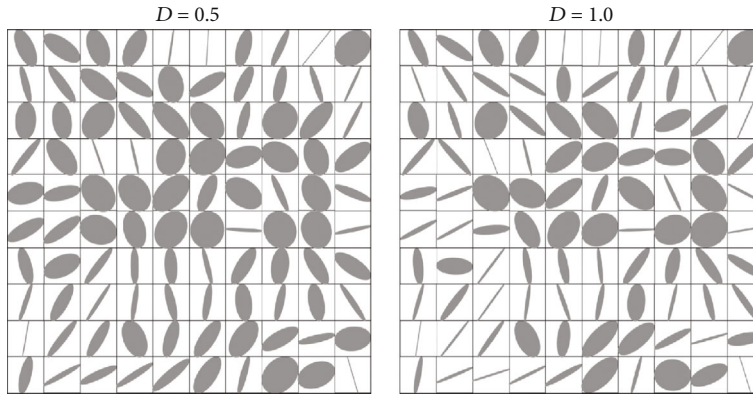


FIGURE 10: Equivalent permeability ellipse for correlated fracture aperture and length models for $D = 0.5$ and $D = 1.0$.

be noted that the permeability tensor ellipses are normalized, which only indicates the direction and anisotropy of equivalent permeability for a grid block rather than the magnitude of equivalent permeability for the grid blocks. It is shown that with the correlation exponent D changes from 0.5 to 1.0, the ratio of k_{max} (the major axis of the ellipse) to k_{min} (the minor axis of the ellipse) generally increased for the grid blocks, which suggest that the anisotropy of equivalent permeability increased.

Compared to the constant aperture model, the correlation of fracture length-aperture increases the heterogeneity of the discrete fracture model as well as that of the upscaled equivalent fracture model [26, 35]. The study emphasizes the importance of aperture-length model for building discrete fracture models and further for the equivalent permeability distributions. Previous studies mainly concentrate on the comparison between constant and varied aperture models on equivalent permeability of one grid block (e.g., [35]); this study investigates the influence of correlated fracture aperture and length model on equivalent permeability distributions, which helps link discrete fractures at the small scales to equivalent permeability of reservoir models at the field scales. However, we should note that the fractures are highly influenced by the mechanical properties and stress field of surrounding rocks [59, 60], and the variation of frac-

ture aperture is mechanical properties also be determined by constitutive models (e.g., [38]). Thus, how different aperture models affect on equivalent permeability distributions for grid blocks of equivalent fracture models should be further studied. Another limitation of the study is that the discrete fracture models are in two dimensions, which is a simplification for three-dimensional models. For investigating three-dimensional fractured porous media, realistic fracture geometric data and high computation platforms for meshing and simulation flow in discrete fracture models (e.g., [61]) are needed.

7. Conclusions

To conclude, a series of equivalent fracture models are built based on discrete fracture models with different aperture-length correlations and fracture geometries by the multiple boundary upscaling method, and the conclusions are as follows:

- (1) For the correlation exponent $D = 0.5$, with the increase in the minimum fracture length l_{min} and the number of fractures N , the diagonal components of equivalent permeability tensors change from a

power law like to a lognormal like to a normal like distribution

- (2) With the increase in correlation exponent D , k_{xx} and k_{yy} change “slower” from a power law distribution to a normal distribution, which is mainly due to the increase in heterogeneity. For k_{xy} , the spatial distribution keeps as normal distributions with a median of zero regarding the random orientation of fractures
- (3) The relationship between the average dimensionless equivalent permeability \bar{k} and the correlation exponent D follows an exponential function. The relationships for different aperture-length models are similar, which are partially related to the fracture geometries. The dimensionless coefficients for the exponential function are influenced by fracture geometry. That is, they increase as l_{\min} and N raise
- (4) The correlation between the average dimensionless equivalent permeability \bar{k} and dimensionless fracture density ρ model follows a power law for the correlated aperture-fracture models. Likewise, the dimensionless coefficients for the power law model are influenced by the correlation exponent D and increase as D raises. The analysis demonstrates that both the fracture geometric parameters and the length-aperture model influence the equivalent permeability of equivalent fracture models interactively

Data Availability

The data that support the findings of this study are available from the corresponding author upon request.

Conflicts of Interest

The author declared that he has no conflicts of interest to this work.

Acknowledgments

This work was funded by the Natural Science Foundation of Shandong Province, China (ZR2019BD028 and ZR2019MD013), the Scientific Research Foundation of Shandong University of Science and Technology for Recruited Talents (2019RCJJ004), and the National Natural Science Foundation of China (41702305). The author would also like to acknowledge the developers for the open-source codes MRST and ADFNE applied in the study.

References

- [1] P. M. Adler, J.-F. Thovert, and V. V. Mourzenko, *Fractured Porous Media*, Oxford University Press, Oxford, U. K., 2012.
- [2] B. Berkowitz, “Characterizing flow and transport in fractured geological media: a review,” *Advances in Water Resources*, vol. 25, no. 8–12, pp. 861–884, 2002.
- [3] S. Neuman, “Trends, prospects and challenges in quantifying flow and transport through fractured rocks,” *Hydrogeology Journal*, vol. 13, no. 1, pp. 124–147, 2005.
- [4] F. Xiong, W. Wei, C. Xu, and Q. Jiang, “Experimental and numerical investigation on nonlinear flow behaviour through three dimensional fracture intersections and fracture networks,” *Computers and Geotechnics*, vol. 121, article 103446, 2020.
- [5] H. Yin, J. Wei, L. Lefticariu et al., “Numerical simulation of water flow from the coal seam floor in a deep longwall mine in China,” *Mine Water and the Environment*, vol. 35, no. 2, pp. 243–252, 2016.
- [6] Y. Zhang, S. Cao, N. Zhang, and C. Zhao, “The application of short-wall block backfill mining to preserve surface water resources in northwest China,” *Journal of Cleaner Production*, vol. 121232, 2020.
- [7] S. Azizmohammadi and S. K. Matthäi, “Is the permeability of naturally fractured rocks scale dependent?,” *Water Resources Research*, vol. 53, no. 9, pp. 8041–8063, 2017.
- [8] C. Clauser, “Permeability of crystalline rocks,” *Eos, Transactions American Geophysical Union*, vol. 73, no. 21, pp. 233–238, 1992.
- [9] W. A. Illman, “Strong field evidence of directional permeability scale effect in fractured rock,” *Journal of Hydrology*, vol. 319, no. 1–4, pp. 227–236, 2006.
- [10] W. F. Brace, “Permeability of crystalline and argillaceous rocks,” *International Journal of Rock Mechanics and Mining Sciences & Geomechanics Abstracts*, vol. 17, no. 5, pp. 241–251, 1980.
- [11] A. E. Hess, “Identifying hydraulically conductive fractures with a slow-velocity borehole flowmeter,” *Canadian Geotechnical Journal*, vol. 23, no. 1, pp. 69–78, 1986.
- [12] T. Le Borgne, O. Bour, F. L. Paillet, and J. P. Caudal, “Assessment of preferential flow path connectivity and hydraulic properties at single-borehole and cross-borehole scales in a fractured aquifer,” *Journal of Hydrology*, vol. 328, no. 1–2, pp. 347–359, 2006.
- [13] H. Deng, J. P. Fitts, and C. A. Peters, “Quantifying fracture geometry with X-ray tomography: Technique of Iterative Local Thresholding (TILT) for 3D image segmentation,” *Computational Geosciences*, vol. 20, no. 1, pp. 231–244, 2016.
- [14] C. M. de Jesus, A. L. Martins Compan, and R. Surmas, “Permeability estimation using ultrasonic borehole image logs in dual-porosity carbonate reservoirs,” *Petrophysics*, vol. 57, no. 6, pp. 620–637, 2016.
- [15] A. Jafari and T. Babadagli, “Effective fracture network permeability of geothermal reservoirs,” *Geothermics*, vol. 40, no. 1, pp. 25–38, 2011.
- [16] S. P. Neuman, “Stochastic continuum representation of fractured rock permeability as an alternative to the REV and fracture network concepts,” in *Groundwater Flow and Quality Modelling*, pp. 331–362, Springer, Dordrecht, 1988.
- [17] B. Gong, M. Karimi-Fard, and L. J. Durlofsky, “Upscaling discrete fracture characterizations to dual-porosity, dual-permeability models for efficient simulation of flow with strong gravitational effects,” *SPE Journal*, vol. 13, no. 1, pp. 58–67, 2013.
- [18] X. Sanchez-Vila, A. Guadagnini, and J. Carrera, “Representative hydraulic conductivities in saturated groundwater flow,” *Reviews of Geophysics*, vol. 44, no. 3, article RG 3002, 2006.

- [19] D. T. Snow, "Anisotropic permeability of fractured media," *Water Resources Research*, vol. 5, no. 6, pp. 1273–1289, 1969.
- [20] J. C. Long and P. A. Witherspoon, "The relationship of the degree of interconnection to permeability in fracture networks," *Journal of Geophysical Research: Solid Earth*, vol. 90, no. B4, pp. 3087–3098, 1985.
- [21] A. Ebigbo, P. S. Lang, A. Paluszny, and R. W. Zimmerman, "Inclusion-based effective medium models for the permeability of a 3D fractured rock mass," *Transport in Porous Media*, vol. 113, no. 1, pp. 137–158, 2016.
- [22] R. Liu, B. Li, Y. Jiang, and N. Huang, "Mathematical expressions for estimating equivalent permeability of rock fracture networks," *Hydrogeology Journal*, vol. 24, no. 7, pp. 1623–1649, 2016.
- [23] M. Oda, "Permeability tensor for discontinuous rock masses," *Geotechnique*, vol. 35, no. 4, pp. 483–495, 1985.
- [24] J. R. de Dreuzy, P. Davy, and O. Bour, "Hydraulic properties of two-dimensional random fracture networks following a power law length distribution: 2. Permeability of networks based on lognormal distribution of apertures," *Water Resources Research*, vol. 37, no. 8, pp. 2079–2095, 2001.
- [25] K. B. Min, L. Jing, and O. Stephansson, "Determining the equivalent permeability tensor for fractured rock masses using a stochastic REV approach: method and application to the field data from Sellafield, UK," *Hydrogeology Journal*, vol. 12, no. 5, pp. 497–510, 2004.
- [26] A. Baghbanan and L. Jing, "Hydraulic properties of fractured rock masses with correlated fracture length and aperture," *International Journal of Rock Mechanics and Mining Sciences*, vol. 44, no. 5, pp. 704–719, 2007.
- [27] C. Klimczak, R. A. Schultz, R. Parashar, and D. M. Reeves, "Cubic law with aperture-length correlation: implications for network scale fluid flow," *Hydrogeology Journal*, vol. 18, no. 4, pp. 851–862, 2010.
- [28] C. T. Leung and R. W. Zimmerman, "Estimating the hydraulic conductivity of two-dimensional fracture networks using network geometric properties," *Transport in Porous Media*, vol. 93, no. 3, pp. 777–797, 2012.
- [29] D. Liu, Z. Gu, R. Liang et al., "Impacts of pore-throat system on fractal characterization of tight sandstones," *Geofluids*, vol. 2020, 17 pages, 2020.
- [30] D. Ren, D. Zhou, D. Liu, F. Dong, S. Ma, and H. Huang, "Formation mechanism of the upper Triassic Yanchang formation tight sandstone reservoir in Ordos Basin—Take Chang 6 reservoir in Jiyuan oil field as an example," *Journal of Petroleum Science and Engineering*, vol. 178, pp. 497–505, 2019.
- [31] N. Zhang, W. Liu, Y. Zhang, P. Shan, and X. Shi, "Microscopic pore structure of surrounding rock for underground Strategic Petroleum Reserve (SPR) caverns in bedded rock salt," *Energies*, vol. 13, no. 7, p. 1565, 2020.
- [32] T. Miao, B. Yu, Y. Duan, and Q. Fang, "A fractal analysis of permeability for fractured rocks," *International Journal of Heat and Mass Transfer*, vol. 81, pp. 75–80, 2015.
- [33] R. Liu, Y. Jiang, B. Li, and X. Wang, "A fractal model for characterizing fluid flow in fractured rock masses based on randomly distributed rock fracture networks," *Computers and Geotechnics*, vol. 65, pp. 45–55, 2015.
- [34] J. D. Hyman, G. Aldrich, H. Viswanathan, N. Makedonska, and S. Karra, "Fracture size and transmissivity correlations: implications for transport simulations in sparse three-dimensional discrete fracture networks following a truncated power law distribution of fracture size," *Water Resources Research*, vol. 52, no. 8, pp. 6472–6489, 2016.
- [35] K. Bisdom, G. Bertotti, and H. M. Nick, "The impact of different aperture distribution models and critical stress criteria on equivalent permeability in fractured rocks," *Journal of Geophysical Research: Solid Earth*, vol. 121, no. 5, pp. 4045–4063, 2016.
- [36] F. Xiong, Q. Jiang, C. Xu, X. Zhang, and Q. Zhang, "Influences of connectivity and conductivity on nonlinear flow behaviours through three-dimension discrete fracture networks," *Computers and Geotechnics*, vol. 107, pp. 128–141, 2019.
- [37] Q. Yin, G. Ma, H. Jing et al., "Hydraulic properties of 3D rough-walled fractures during shearing: an experimental study," *Journal of Hydrology*, vol. 555, pp. 169–184, 2017.
- [38] S. Azizmohammadi and M. Sedaghat, "The impact of stress orientation and fracture roughness on the scale dependency of permeability in naturally fractured rocks," *Advances in Water Resources*, vol. 141, article 103579, 2020.
- [39] P. S. Lang, A. Paluszny, and R. W. Zimmerman, "Permeability tensor of three-dimensional fractured porous rock and a comparison to trace map predictions," *Journal of Geophysical Research: Solid Earth*, vol. 119, no. 8, pp. 6288–6307, 2014.
- [40] T. Chen, C. Clauser, G. Marquart, K. Willbrand, and D. Mottaghy, "A new upscaling method for fractured porous media," *Advances in Water Resources*, vol. 80, pp. 60–68, 2015.
- [41] E. Bonnet, O. Bour, N. E. Odling et al., "Scaling of fracture systems in geological media," *Reviews of Geophysics*, vol. 39, no. 3, pp. 347–383, 2001.
- [42] G. Margolin, B. Berkowitz, and H. Scher, "Structure, flow, and generalized conductivity scaling in fracture networks," *Water Resources Research*, vol. 34, no. 9, pp. 2103–2121, 1998.
- [43] C. E. Renshaw and J. C. Park, "Effect of mechanical interactions on the scaling of fracture length and aperture," *Nature*, vol. 386, no. 6624, pp. 482–484, 1997.
- [44] J. E. Olson, "Sublinear scaling of fracture aperture versus length: an exception or the rule?," *Journal of Geophysical Research: Solid Earth*, vol. 108, no. B9, p. 2413, 2003.
- [45] R. A. Schultz, R. Soliva, H. Fossen, C. H. Okubo, and D. M. Reeves, "Dependence of displacement-length scaling relations for fractures and deformation bands on the volumetric changes across them," *Journal of Structural Geology*, vol. 30, no. 11, pp. 1405–1411, 2008.
- [46] J. M. Vermilye and C. H. Scholz, "Relation between vein length and aperture," *Journal of Structural Geology*, vol. 17, no. 3, pp. 423–434, 1995.
- [47] R. A. Schultz, C. Klimczak, H. Fossen et al., "Statistical tests of scaling relationships for geologic structures," *Journal of Structural Geology*, vol. 48, pp. 85–94, 2013.
- [48] R. A. Schultz and R. Soliva, "Propagation energies inferred from deformation bands in sandstone," *International Journal of Fracture*, vol. 176, no. 2, pp. 135–149, 2012.
- [49] O. Bour and P. Davy, "Connectivity of random fault networks following a power law fault length distribution," *Water Resources Research*, vol. 33, no. 7, pp. 1567–1583, 1997.
- [50] Y. F. Alghalandis, "ADFNE: open source software for discrete fracture network engineering, two and three dimensional applications," *Computers & Geosciences*, vol. 102, pp. 1–11, 2017.
- [51] K. A. Lie, *An Introduction to Reservoir Simulation Using MATLAB/GNU Octave: User Guide for the MATLAB Reservoir Simulation Toolbox (MRST)*, Cambridge University Press, Cambridge, UK, 2019.

- [52] T. H. Sandve, I. Berre, and J. M. Nordbotten, "An efficient multi-point flux approximation method for discrete fracture-matrix simulations," *Journal of Computational Physics*, vol. 231, no. 9, pp. 3784–3800, 2012.
- [53] F. A. Dullien, *Porous Media: Fluid Transport and Pore Structure*, Academic press, San Diego, CA, USA, 1992.
- [54] T. Chen, C. Clauser, G. Marquart, K. Willbrand, and T. Hiller, "Upscaling permeability for three-dimensional fractured porous rocks with the multiple boundary method," *Hydrogeology Journal*, vol. 26, no. 6, pp. 1903–1916, 2018.
- [55] R. S. Jayne, H. Wu, and R. M. Pollyea, "Geologic CO₂ sequestration and permeability uncertainty in a highly heterogeneous reservoir," *International Journal of Greenhouse Gas Control*, vol. 83, pp. 128–139, 2019.
- [56] C. Vogt, G. Marquart, C. Kosack, A. Wolf, and C. Clauser, "Estimating the permeability distribution and its uncertainty at the EGS demonstration reservoir Soultz-sous-Forêts using the ensemble Kalman filter," *Water Resources Research*, vol. 48, no. 8, article W08517, 2012.
- [57] D. J. Sanderson and C. W. Nixon, "The use of topology in fracture network characterization," *Journal of Structural Geology*, vol. 72, pp. 55–66, 2015.
- [58] M. Wang, P. H. S. W. Kulatilake, J. Um, and J. Narvaiz, "Estimation of REV size and three-dimensional hydraulic conductivity tensor for a fractured rock mass through a single well packer test and discrete fracture fluid flow modeling," *International Journal of Rock Mechanics and Mining Sciences*, vol. 39, no. 7, pp. 887–904, 2002.
- [59] G. Feng, Y. Kang, X. Wang, Y. Hu, and X. Li, "Investigation on the failure characteristics and fracture classification of shale under Brazilian test conditions," *Rock Mechanics and Rock Engineering*, pp. 1–16, 2020.
- [60] P. Shan and X. Lai, "An associated evaluation methodology of initial stress level of coal-rock masses in steeply inclined coal seams, Urumchi coal field, China," *Engineering Computations*, vol. 37, no. 6, pp. 2177–2192, 2020.
- [61] O. Kolditz, S. Bauer, L. Bilke et al., "OpenGeoSys: an open-source initiative for numerical simulation of thermo-hydro-mechanical/chemical (THM/C) processes in porous media," *Environment and Earth Science*, vol. 67, no. 2, pp. 589–599, 2012.

Review Article

Stability Monitoring and Analysis of High and Steep Slope of a Hydropower Station

Guangcheng Shi,^{1,2} Gongkai Gu,³ Hua Zhou,⁴ Zhigang Tao ,^{1,2} Hongyue Pan,³ and Ting Tang⁵

¹State Key Laboratory for Geomechanics and Deep Underground Engineering, China University of Mining and Technology-Beijing, Beijing 100083, China

²School of Mechanics and Civil Engineering, China University of Mining and Technology, Beijing 100083, China

³China Three Gorges Construction Management Co., Ltd., Beijing 100038, China

⁴Changjiang Survey, Planning, Design and Research Co. Ltd., Wuhan 430010, China

⁵Yangtze Ecology and Environment Co., Ltd., Wuhan 430062, China

Correspondence should be addressed to Zhigang Tao; taozhigang@263.net

Received 24 June 2020; Revised 25 July 2020; Accepted 29 August 2020; Published 6 October 2020

Academic Editor: Qian Yin

Copyright © 2020 Guangcheng Shi et al. This is an open access article distributed under the Creative Commons Attribution License, which permits unrestricted use, distribution, and reproduction in any medium, provided the original work is properly cited.

Slope deformation and failure are major challenges for hydropower station engineering. Taking the left bank slope at the exit of the flood discharge tunnel of the Wudongde Hydropower Station in China as an example, the deformation mechanism of the high-steep rock slope was studied. The height of the slope is about 200 m, which is affected by slope excavation, rainfall, and atomized rain. The results of multipoint displacement meters, surface deformation monitoring, and anchoring stress meters showed that the deformation and deformation rate of the slope have increased dramatically. Through the comprehensive analysis of the slope, it is found that the overall lithology of the slope is poor, the excavation disturbance causes the redistribution of the stress in the slope, and the excavation surface is relatively steep, which provides space for the deformation of the slope rock mass. Unloading relaxation leads to a large number of new fissures in the slope rock mass. These new fissures and fault fracture zones provide convenient conditions for rainfall and atomized rain infiltration. The rainwater infiltrated along the slope surface, formed the seepage field in the slope body, and weakened the rock-soil mass parameters. Meanwhile, saturated runoff is formed on the slope, causing large deformation of the slope rock mass. However, the migration of water in the slope has a time effect, and its influence on the stability of the slope also has a time effect. It is difficult for traditional monitoring methods to monitor the resulting changes in internal sliding force of the slope. Therefore, a remote monitoring and early warning system for landslide anchor cable force was introduced to monitor the slope stability changes caused by the impact of water flow and rainfall infiltration, which provided a reasonable and scientific reference for subsequent slope construction.

1. Introduction

The large deformation of high and steep slopes leads to widespread and catastrophic geological hazards. The high and steep slopes of a hydropower station are among the most common and dangerous morphologies. The construction and operation of the plant can trigger or reactivate such morphologies and significantly threaten human lives and properties [1, 2]. Consequently, significant efforts have been made to monitor such slopes and to design and implement effective countermeasures.

At present, although brilliant achievements have been made in the excavation disturbance [3–5] and rainwater seepage [6–8] of high and steep slope projects, they have also paid a heavy price. Deformation and destruction phenomena of different degrees and scales will affect the construction of high slope projects in water conservancy and hydropower projects. For example, the left and right abutment slopes of Miaowei Hydropower Station have undergone significant deformation during the excavation process. With the progress of the excavation, five significant deformations occurred

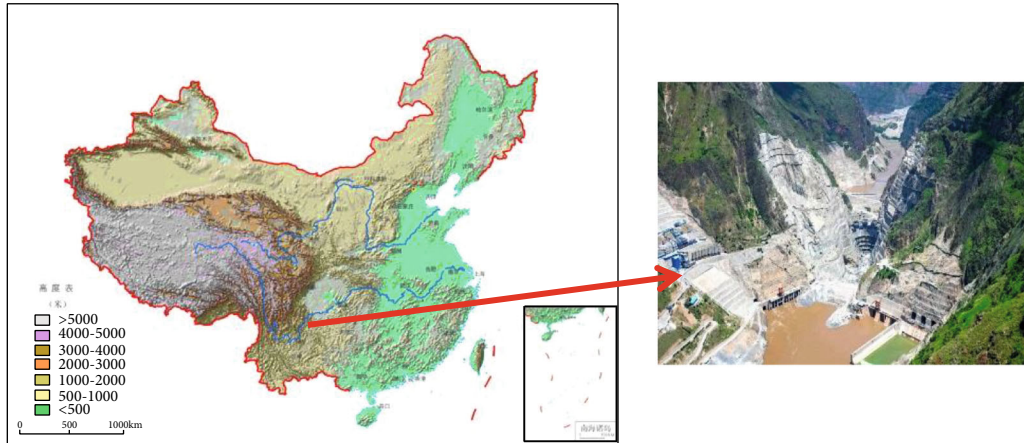


FIGURE 1: Geographical location of Wudongde Hydropower Station.

on the left abutment slope, and a landslide occurred on the right abutment slope from 1340 m to 1384 m, severely affecting the construction [9, 10]. Many scholars have analyzed the deformation mechanism of high steep slopes under excavation conditions. In order to analyze the loosening characteristics of columnar jointed basalts, the temporal-spatial evolution of the loosening depths and degrees of the left-bank slope were investigated through single-hole acoustic wave tests and visual inspections with borehole cameras. The tests were carried out in the columnar jointed basalt test section of the left bank dam foundation of Baihetan hydropower station [11–13]. For high dam projects with characteristics of high water head, large flood discharge, and narrow canyon, there is a class of rock slope instability problems that is induced by rainfall and flood discharge atomized rain. Here, atomized rain refers to the rain produced by the discharge of flood from high dams. Due to rainfall infiltration being the most frequent triggering factor for natural high steep rock slope failure, substantial research has been carried out to study the failure mechanisms of rainfall-induced landslides. This class of rock slope stability problems is mainly affected by the mechanical parameter reduction of structural planes and the internal pore water pressure [14–22].

The complex internal factors such as lithology and rock mass structure of the high-steep rock slope [23–25] and the external factors such as construction disturbances and heavy rain may change the slope during construction and operation. Many scholars have carried out microscopic experiments on rock crack growth to better understand the process and mechanism of rock slope failure, obtaining interesting research results [26–32]. In order to reflect the real mechanical effect of the rock mass and to ensure a stable state of the slope, slope monitoring projects are needed. Nowadays, many kinds of slope stability monitoring technologies and methods exist, from the traditional total station, the inclined pipe, the pressure gauge, the rain gauge, and the displacement meter [33] to the new type of the GPS [34], the laser range finder [35], the synthetic aperture radar [36], the ground-based interferometric radar [37], and the geological radar [38].

Research on slope stability monitoring and early warning technology is one of the leading research topics in the field of geotechnical engineering, and many scholars have investigated it. An early warning monitoring system is established to collect data such as seismic waves, pressures, and groundwater levels and activated the early warning signal when the instrument produced a signal outside the range [39], taking the excavation of the high slope on the left bank of Jinping I Hydropower Station as the research object. The monitoring results of the deformation of the graphite rod convergence meter of the flat hole, the horizontal observation of the valley width, the load of the anchor cable, and the deformation of the shear hole were comprehensively analyzed. Furthermore, the deformation law of the slope rock mass was obtained [40].

Based on the mechanics of the sliding body, sliding bed, and theory of monitoring anchor cable interaction as the theoretical basis, the principle of mechanical monitoring of the relative motion state of a sliding body and a sliding bed was put forward. Moreover, the multifactor monitoring was changed into single sliding force mechanical quantity monitoring, and the relationship between the sliding force and the monitoring pretightening force was given [41, 42]. Based on the above principles, a remote monitoring and forecasting system for landslide geological hazards was developed for the real-time remote monitoring of dynamic changes of disturbance forces. The proposed approach overcomes the bottleneck of conventional deformation monitoring and realizes monitoring and early warning of deep sliding forces [43–45].

This study takes the slope of Wudongde Hydropower Station as the research object and analyzes the slope deformation mechanism caused by excavation and rainwater infiltration through field investigation and slope deformation monitoring data. In addition, in order to better monitor the large deep deformation of the slope rock mass caused by the infiltration of atomized rain, a remote monitoring and early warning system for the force of the anchor cable is introduced. The monitoring system will provide a reasonable and scientific reference for subsequent slope construction.



FIGURE 2: Engineering slope.

2. Engineering Geology

2.1. Slope Engineering. Wudongde Hydropower Station is the first of the four cascade hydroelectric power stations in the lower reaches of the Jinsha River, which is of great significance to China's hydropower development. The plant is located on the Jinsha River at the junction of Luquan County, Kunming, Yunnan Province, and Huidong County, Liangshan Prefecture, Sichuan Province (Figure 1). The elevation of the left side slope of the outlet of the spillway tunnel of the hydropower station is more than 1070 m, which is a naturally exposed rock slope. The altitude from 1070 m to 1760 m is a steep slope with an average inclination of 55°. Before the excavation of the slope, the area below 1070 m elevation is a gentle slope formed by the Huashangou deposit, with an inclination of 10°~35°. The artificial slope structure is a transverse slope. The highest elevation line is about 970 m, the excavation of the plunge pond foundation corridor is of 786.5 m elevation, and that of the artificial slope is 183.5 m.

2.2. Stratigraphic Structure and Lithology. The engineering slope and natural slope above 925 m elevation are sedimentary caprock strata. The strata trending NNW-SSE dipping at an angle of 30° toward E, and the angle between the strike of the stratum and the strike of the slope is about 3°~37°, forming a gently inclined reverse slope. The engineering slope below 925 m elevation consists of folded strata that trend SW-NE and dip about 80° toward S. The strike of left side slope of the exit of the flood discharge tunnel is 193°, and the angle between the strike of the rock stratum and the slope forms a steep, transverse slope of about 57°~83° (Figure 2). The strata exposed before the excavation are the quaternary Huashangou accumulation body and the folded basement snowfall group, the sedimentary caprock Guanyinya Formation, and the Dengying Formation (Figure 3).

2.3. Hydrometeorological Conditions. Wudongde Hydropower Station is located in the dry and hot valley of Jinsha River. The average annual precipitation is 600 mm-800 mm, the rainfall is relatively concentrated, and the precipitation from June to October accounts for 81% of the annual precipitation. The average maximum temperature in the study area is 42.7°C, and the minimum temperature is -5.8°C; the difference between the two is as high as 48.5°C. The average max-

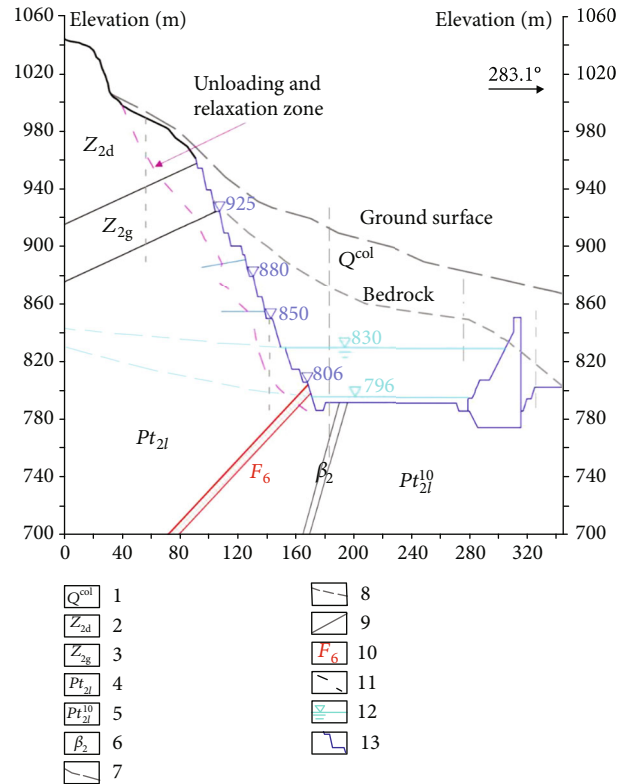


FIGURE 3: Engineering geology map of the slope. 1: collapse accumulation layer; 2: Dengying Formation grey to light grey thick dolomite; 3: Guanyinya group gray thin layer dolomite sandwich, ultrathin shale; 4: gray thin layer dolomite (specifically refers to the falling snow group stratum in the downstream of the Huashangou fault on the left bank); 5: gray interbedded with thin limestone; 6: diabase; 7: original terrain; 8: bedrock surface; 9: lithology boundary; 10: faults and numbers; 11: lower limit of relaxation zone of artificial slope; 12: groundwater level line; 13: designed excavation line.

imum ground temperature is 72.4°C, and the minimum ground temperature is -5.3°C; the difference between the two is as high as 77.7°C. The average maximum temperature in the study area is 42.7°C, and the minimum temperature is -5.8°C; the difference between the two is as high as 48.5°C. The average maximum ground temperature is 72.4°C, and the minimum ground temperature is -5.3°C; the difference between the two is as high as 77.7°C. This large temperature difference is beneficial to accelerate the physical weathering of the rock mass, especially after the rain and atomized rain infiltrate the slope rock mass, causing a large range of relaxation deformation on the rock mass surface in the study area.

There is a waterfall at the junction of the front side slope and the left side slope at the exit of the spillway tunnel, and the rainy season has a large amount of water. In addition, after the spillway is put into use, the two will produce strong atomized rain around the water cushion pond. Atomized rain often forms at the lower part of the slope. Perennial atomized rain will have a serious impact on the slope. The brown-yellow rusting phenomenon appears locally on the slope surface, which is caused by the Fe ions in the unevenly distributed pyrite in the rock layer near the unconformity

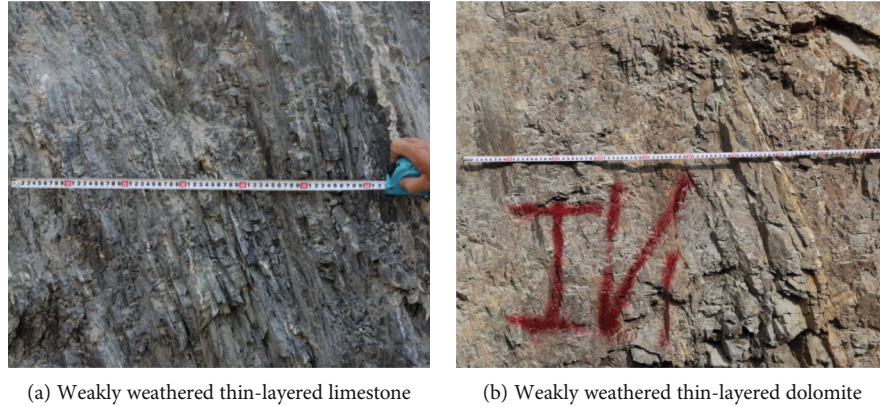


FIGURE 4: Typical rock mass of slope.



FIGURE 5: Distribution map of deformation monitoring points on the slope.

contact surface in the dam site, which oozes with water after oxidation and stains the concrete on the slope surface.

2.4. Engineering Geological Defects. The primary engineering geological defects revealed during the excavation of the slope include blocks, the fracture of the slope, the Huashangou fault (F_6), and the poor quality of the rock mass.

2.4.1. Block. A total of 213 blocks was found on the surface of the slope. There were 153 blocks with a volume of less than 100 m^3 , 54 blocks with a volume between 100 m^3 and 1000 m^3 , and six blocks with a volume between 1000 m^3 and 10000 m^3 , which accounted for 71.9%, 25.3%, and 2.8%, respectively. The maximum bulk volume was about 4691 m^3 . Among them, there were 12 stable blocks, 187 blocks with poor stability, and 14 blocks with the worst stability. The buried depth varied about from 2 m to 5 m, and the deepest was block found at about 29 m.

2.4.2. Fracture of Slope. The on-site geological investigation showed that the fracture of the slope surface was not developed. The excavation of the engineering slope revealed a strike of cracks at $240^\circ \sim 310^\circ$ with an angle of $40^\circ \sim 60^\circ$. The crack surface was generally straight and rough, mostly with mud and calcium, and only a few was filled with debris and mud. The extension of cracks was about 5~10 m. Only six fractures were longer than 20 m, and the longest was about 37 m. Most fracture surfaces were straight, rough, and mostly

closed or slightly stretched, with calcium membrane or mud calcium membrane attached to the surface.

2.4.3. Fault. Huashangou fault (F_6) is a large-scale geological structure of the entire slope. The strike of the fault was E-W, with an inclination angle of $70^\circ \sim 75^\circ$ and trending SE. It intersects with the river valley at an angle of about 60° . It is a normal fault and cuts through the sedimentary caprock, and the vertical offset is about 420 m. The fault through the slope, the plunge pool, and the tail drain guided the wall foundation. The F_6 was 3~8 m wide, mainly composed of clastic rock. Plasticized mudcracks or debris were found near the fault.

2.4.4. Poor Rock Mass Quality. The overall quality of the rock mass on the left side of the outlet of the spillway tunnel is poor, mainly grades IV1 to IV2, which are mainly distributed with weakly weathered thin-layered dolomite and limestone (Figure 4). The structural plane is dominated by layers, with microcracks developed, the layers are mostly straight and rough, filled with muddy calcareous, and the cracks are often attached with muddy calcium film, and the erosion and weathering along the structural plane are intensified.

3. Deformation Monitoring Results

The fault F_6 runs through the entire slope, and the rock mass of the fault fracture zone is very poor. At the same time, the slope has a series of isolated blocks and surface cracks. The existence of these geological defects seriously affects the stability of the slope. Moreover, frequent excavation disturbances cause severe unloading and relaxation of the slope, which leads to the extension and expansion of surface cracks into the rock mass. These geological defects and newly created fissures in the relaxation area will provide convenient conditions for the infiltration of rainwater and atomized rain, thereby increasing the effect of hydrostatic pressure in the fissure on the rock mass, accelerating the physical and chemical action of water on the rock mass structural plane, leading to the overall decline in rock mass quality, and ultimately leading to the deformation of the slope. Therefore, it was chosen as the main monitoring area for the slope project.

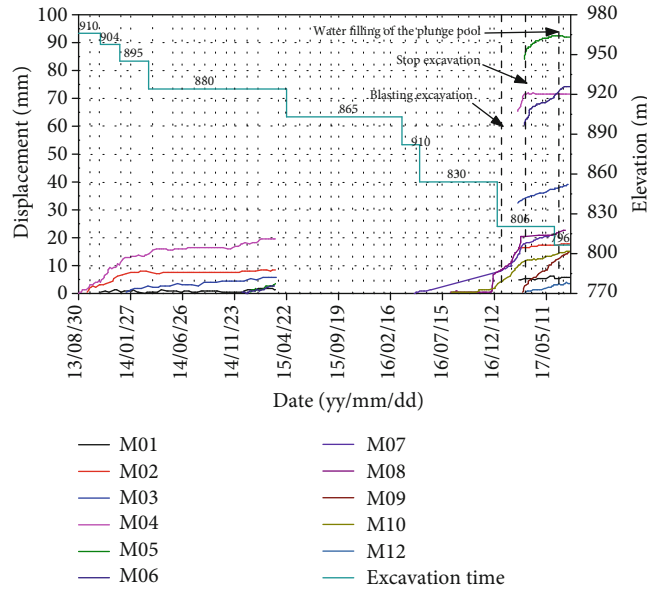


FIGURE 6: Relationship between the deformation of the multipoint displacement meter and the excavation process.

According to the different monitoring objects and monitoring depths, slope monitoring can be divided into appearance deformation monitoring, shallow deformation monitoring, and deep deformation monitoring. According to the characteristics of the project, six deformation monitoring sections (i.e., sections 1-1', 2-2', 3-3', 4-4', 5-5', and 6-6') were arranged on the slope. At the same time, 14 apparent monitoring piers, 17 sets of multipoint displacement meters, and 26 anchor stress meters were deployed (Figure 5).

3.1. Monitoring Results of Multipoint Displacement Meter. Seventeen sets of multipoint displacement meters, numbered M01~M17, were arranged on the slope. They were all placed at the downstream of F_6 and divided into two monitoring areas according to the structural characteristics of the slope. Among them, 11 sets were arranged between F_6 and the rear edge slope of the concrete system of 850 m elevation. Six sets were placed at the rear edge slope of the concrete system with an elevation of 850 m. The monitoring depth was about 30 m. Figure 5 shows the layout location. The monitoring time of each multipoint displacement meter is different, and the earliest time is May 5, 2013. Due to factors such as instrument failure and on-site environment, some data are missing. The whole process monitoring curve of the cumulative displacement of the multipoint displacement meter and the orifice is shown in Figure 6 and Table 1.

3.1.1. Cumulative Deformation. According to the analysis of the monitoring data in Table 1 and Figure 6, as of August 10, 2017, the cumulative deformation of the orifices of 13 multipoint displacement meters is less than 25 mm, accounting for 76.5% of all monitoring points. The deformation of one monitoring point is 38.86 mm, and that of three monitoring points is above 71 mm. Among them, the monitoring point with the most considerable deformation is M11, at 986.8m elevation, and the deformation is 92.15 mm. The parts with large local deformation monitored by multipoint

displacement meter are mainly located at section 4-4' of the slope, that is, 920~990 m high near the ridge-shaped terrain, and close to the fault F_6 . This data suggests that the slope unloading disturbance and fault structure affect the area significantly. The parts with small deformation monitored by the multipoint displacement meter are located near sections 2-2 and 3-3. That means they are at the trailing edge slope of 850 m elevation concrete system, suggesting a lighter effect of the excavation of the project on this part of the slope.

3.1.2. Deformation Depth. From Figure 6 and Table 1, among the 17 multipoint displacement meters, except for M11 and M03, the multipoint displacement meters at these two monitoring points show that there is still a large deformation at a depth of 30 m horizontally (note that the deformation at the monitoring depth of 30 m at both points is more significant than that at 20 m, which are abnormal data). The data from the remaining 15 sensors prove that the slope rock mass at the distance of 30 m from the slope surface does not deform or deforms very little. Therefore, the excavation disturbance at the left side slope at the outlet of the spillway tunnel deforms the rock mass for a depth of about 20~30 m.

3.1.3. Deformation Rate. The deformation rate of the slope rock mass can be divided into three stages, namely, deformation intensification stage, deformation slowdown stage, and deformation convergence stage (Figure 6).

The first stage is the deformation intensification stage. The deformation process of monitoring curves recorded by monitoring points M13, M14, and M16 reveals that the deformation aggravation occurs between December 24, 2016, and March 25, 2017. This period corresponds to the start and stops of blasting excavation of the slope below 830 m. The second stage is the deformation slowdown stage that happened after the site stopped blasting excavation on March 25, 2017. The third stage is the deformation convergence stage. Among the 17 multipoint displacement meters,

TABLE 1: Multipoint displacement meter cumulative deformation monitoring results.

Monitoring section	Number	Elevation (m)	Monitoring start time (yy/mm/dd)	40 m	Cumulative deformation by August 10, 2017 (mm)			Remarks	
					30 m	20 m	10 m		
1-1'	M01	925.5	13/10/20	0	1.42	4.33	6.16	15/3/27 damage 17/03/10 resume monitoring	
	M02	895.5	13/09/22	0	2.45	2.7	/	15/3/27 damage 17/03/10 resume monitoring	
	M03	865.5	14/01/03	0	36.83	27.13	33.69	15/3/27 damage 17/03/10 resume monitoring	
2-2'	M04	925.5	13/05/05	/	0	1.02	1.61	15/5/7 damage 17/04/5 resume monitoring	
	M05	895.5	13/05/05	/	0	0.77	3.5	13/7/6 damage 17/04/5 resume	
	M06	865.5	13/05/05	/	0	0.34	2.65	14/3/7 damage, 17/04/5 resume	
3-3'	M07	925.5	13/05/05	/	0	0.71	1.21	3.2	
	M08	895.5	13/05/05	/	0	1.8	2.43	4.55	15/10/23Damage 17/04/4 resume
	M09	865	13/05/05	/	0	1.39	2.07	3.33	15/10/23Damage 17/04/4 resume
4-4'	M10	925.5	13/08/31	0	-0.28	2.3	36.09	71.22	15/3/27 damage 17/3/10 resume
	M11	986.8	14/12/19	0	87.1	85.17	91.77	92.15	15/3/27 damage 17/3/29 resume
	M12	987.7	14/12/19	0	4.71	/	23.85	74.69	15/3/27 damage 17/3/29 resume
5-5'	M13	880.5	16/05/09	/	0	9.59	14.83	22.26	15/7/1 damage, 16/12/30 resume
	M14	850.3	16/08/20	/	0	-8.26	/	21.86	
	M15	830.3	17/03/25	/	0	3.32	8.17	14.51	
6-6'	M16	850.3	16/08/14	/	0	5.53	11.23	14.79	
	M17	830.3	17/03/25	/	0	1.68	2.62	3.66	17/03/25 start

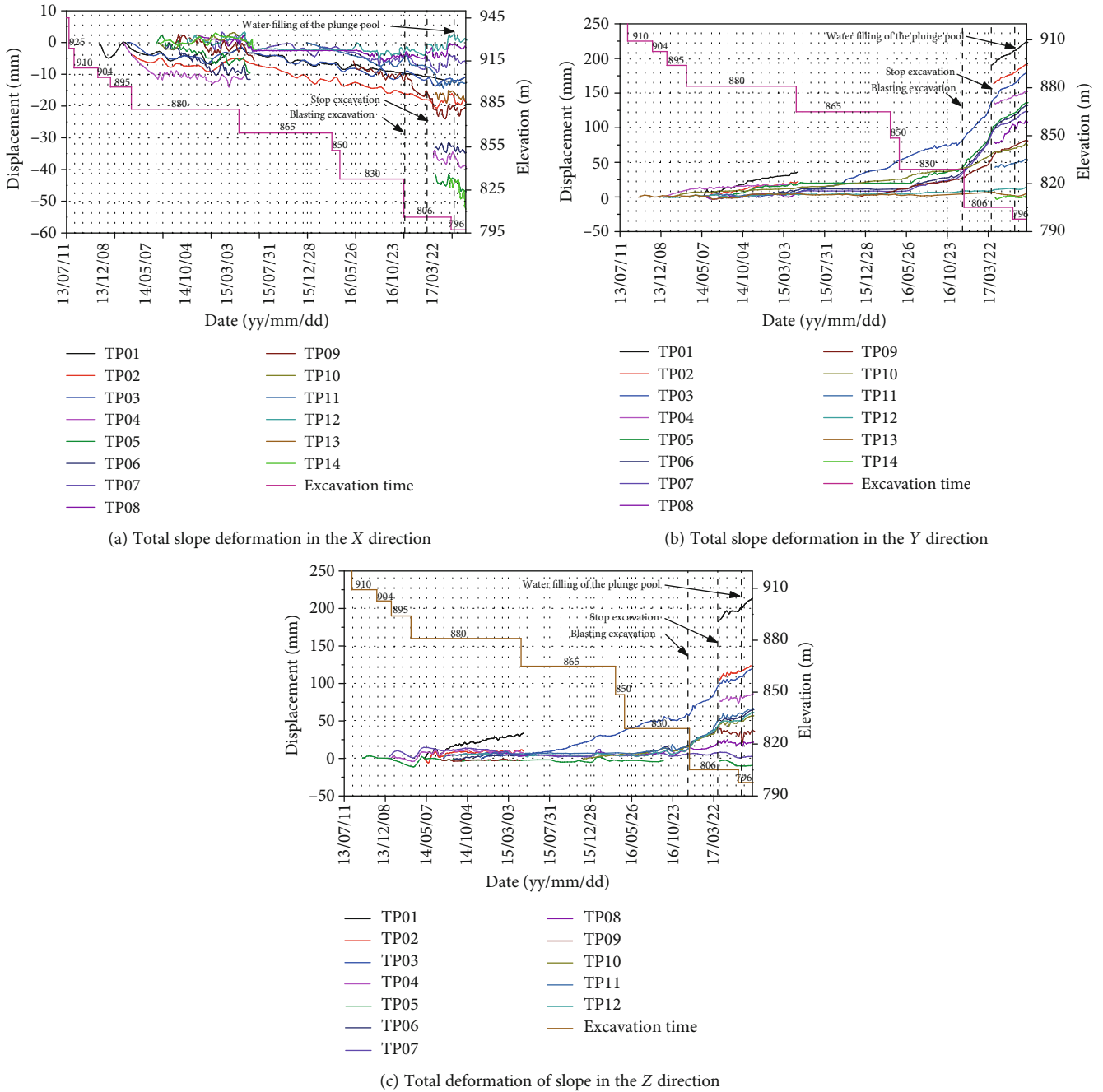


FIGURE 7: Comparison curve between the total deformation of apparent monitoring and the excavation process.

the time points of convergence of each point are quite different. Most of them gradually converge about half a month after stopping blasting excavation, that is, in the middle of April 2017. The convergence time of monitoring points M12 near the ridge terrain and M15 near the fault F_6 are the latest, while the convergence time of monitoring points M04~M09 at the rear edge of a concrete system is earlier. On June 24, 2017, after the plunge pool was filled with water, the deformation rate of the slope was temporarily unchanged. In summary, after stopping the blasting excavation, all the deformation monitoring data of multipoint displacement meters tend to converge.

3.2. *Apparent Deformation Monitoring Results.* The 14 apparent deformation monitoring piers TP01~TP14 were all arranged downstream the fault F_6 . Eleven piers were arranged between the fault F_6 and the rear edge slope of the concrete system at 850 m elevation; three were on the rear edge slope of the concrete system (Figure 5). Figure 7 compares the monitored total apparent deformation with the development of the excavation process. The horizontal deformation to the downstream of the river is the positive direction of X, and the upstream is the negative direction. The horizontal deformation to the outside of the slope is the positive direction of Y, and the deformation into the slope is the

TABLE 2: Apparent cumulative deformation monitoring results.

Section	Number	Elevation (m)	Monitoring start time (yy/mm/dd)	$\sum \Delta X$	$\sum \Delta Y$	$\sum \Delta Z$	Cumulative deformation by August 8, 2017 (mm)	Remarks
1-1'	TP01	942	13/12/16	-19.62	74.98	21.85	80.53	
	TP02	900	14/04/24	-18.1	51.87	16.52	57.37	15/3/12 damage 17/4/9 resume
	TP03	868	14/04/24	-54.63	108.83	36.63	127.16	15/4/13 damage 17/4/9 resume
2-2'	TP04	946	13/12/16	-12.2	14	2.88	18.79	
3-3'	TP05	897	17/04/09	-1.67	1.57	-0.5	2.35	
	TP06	925	13/12/16	-10.88	5.04	-9.23	15.13	16/9/12 damage 17/4/5 resume
4-4'	TP07	926	13/12/16	-34.39	152.19	86.47	178.39	15/5/27 damage 17/4/9 resume
	TP08	987	14/04/24	-39.36	223.75	214.5	312.45	15/4/23 damage 17/3/31 resume
	TP09	987	14/04/24	-47	190.86	124.03	232.42	15/4/23 damage 17/4/5 resume
	TP10	1013	14/07/09	-2.01	132.47	67.22	148.56	
	TP11	1012	14/07/09	-21.27	123.91	62.43	140	
	TP12	1018	14/08/19	0.72	136.47	64.14	150.79	
	TP13	1014	14/11/21	-6.72	179.35	120.22	216.02	
	TP14	1039	15/11/28	-12.74	81.29	57.33	100.29	15/3/12 damage 17/4/9 resume

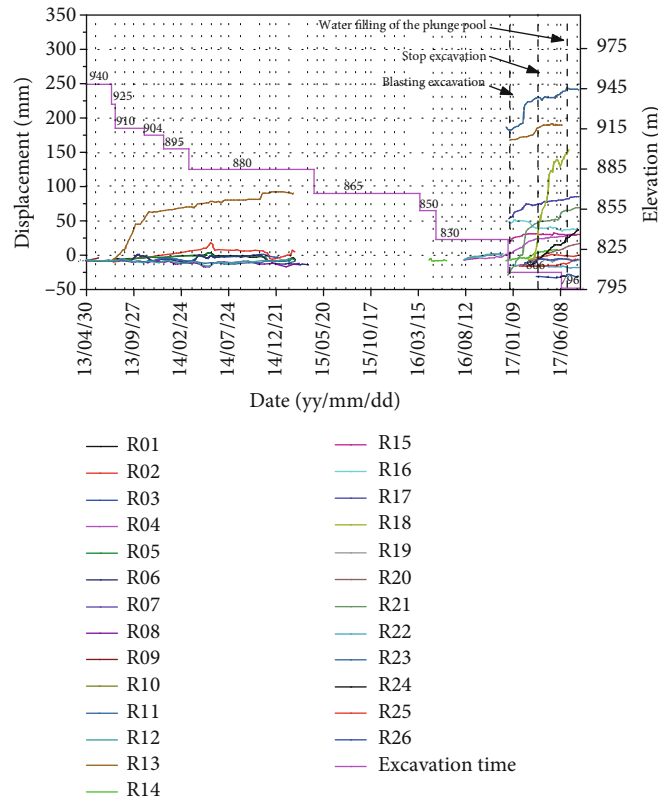


FIGURE 8: Comparison curve between the stress change of anchor stress meter and the excavation process.

negative direction. The vertical downward deformation is the positive direction of H , and the upward direction is the negative direction. The initial monitoring time of the apparent monitoring point was September 16, 2013. However, due to the influence of the on-site environment and equipment, only TP01, TP04, and TP10~TP14 recorded a relatively complete slope deformation process.

3.2.1. Cumulative Deformation. The deformation components of the apparent monitoring piers suggest that almost all the deformations in the river direction point to the upstream, and the cumulative deformation in this direction is the smallest, i.e., 8 to 23 mm. Moreover, the monitoring point with the most significant cumulative deformation of 54.63 mm is TP03, located at 868 m elevation. The cumulative deformation of all monitoring points to the outside of the slope is generally between 50 and 140 mm. The monitoring point with the most considerable cumulative deformation of 223.75 mm is TP08 at 987 m elevation. The monitoring points with large cumulative deformation after the excavation of the entire slope are higher than 980 m, i.e., they are located in the local ridge-like terrain of the slope. Excavation and unloading affect these monitoring points significantly. The cumulative vertical deformation of most monitoring points is between 14 and 80 mm; the monitoring point with the most substantial deformation (TP08) is at 987 m elevation; and the cumulative deformation is 214.5 mm. There are two monitoring points with a deformation greater than 100 mm, all of which are located above 980 m elevation. According to the apparent monitoring of the cumulative

deformation component characteristics, the deformation of the monitoring area mainly points to the outside of the slope and the upstream of the river.

3.2.2. Total Deformation. The total deformation represents the actual deformation distance of the apparent monitoring points. According to Table 2, as of August 8, 2017, the cumulative total deformation of three monitoring points (TP08, TP09, and TP13) is more significant than 200 mm. The TP08 monitoring point has the most considerable deformation (312.45 mm), and the cumulative total deformation of two monitoring points (TP07 and TP12) is 200~150 mm. These five monitoring points are mainly distributed in the ridge-like terrain at the top of the slope, which is greatly affected by excavation disturbance and rainfall infiltration.

In summary, since December 24, 2016, with the blasting excavation of the slope below 830 m, all monitored apparent deformation components and total deformations increase sharply, and the deformation rate is accelerated. The deformation generated at this stage accounts for 80% of the total deformation. After March 25, 2017, the deformation rate decreases significantly with the completion of the excavation, and as of August 8, 2017, eight out of the 14 apparent monitoring points converge, and the deformation rate of six points significantly reduces and tends to converge.

3.3. Anchor Stress Monitoring Results. Twenty-six sets of anchor stress meters, numbered R01~R26, were all arranged at the downstream of fault F_6 . Eighteen sets were placed between fault F_6 and the rear edge slope of the concrete

TABLE 3: Anchor stress meter monitoring results.

Section	Number	Elevation (m)	Monitoring start time (yy/mm/dd)	17/08/10 stress (MPa)	Remarks
1-1'	R01	939	13/09/27	-8.6	
	R02	924	13/09/22	& 4	
	R03	894	13/11/15	-27.3	
	R04	864	16/08/14	42.0	
2-2'	R05	939	13/05/05	-2.4	
	R06	924	13/05/05	29.5	15/05/07 damage
	R07	894	13/05/05	-0.4	13/07/06 damage
	R08	864	13/05/05	-14.2	
3-3'	R09	939	13/05/05	-16.8	13/07/06 damage
	R10	924	13/05/05	-13.1	
	R11	894	13/05/05	-12.4	
	R12	864	13/05/05	-10.7	
4-4'	R13	924	13/09/22	226.0	17/06/21 damage
	R14	879	16/05/09	19.7	
	R15	849	16/08/20	40.4	
	R16	849	16/08/20	53.0	
	R17	849	16/08/20	106.9	
	R18	829	17/03/25	181.8	
	R19	829	17/03/25	1.7	
	R20	829	17/03/25	9.9	
5-5'	R21	849	16/08/14	87.6	
	R22	849	16/08/14	0.5	
	R23	849	16/08/14	283.6	
	R24	829	17/03/25	50.8	
	R25	829	17/03/25	16.9	13/07/06 damage
	R26	829	17/03/25	27.9	

system at 850 m elevation, and eight sets were at the rear edge slope (Figure 5).

Figure 8 shows the monitoring results of all anchor stress meters, as summarized in Table 3. According to the data analysis, as of August 10, 2017, three monitoring points exceed 150 MPa, and the monitoring point R23 of 849 m elevation detects the most significant stress change, i.e., an increase of 283.6 MPa. The measured stress of five anchors is within 150~30 MPa, while the variation of the remaining sensors is less than 30 MPa.

According to the stress change curve analysis of all anchor stress meters, the stress change rate of each anchor stress meter increases sharply after blasting excavation of the slope below 830 m elevation on December 24, 2016. After March 25, 2017, with the blasting excavation stopped, except for the R16 anchor stress whose growth rate is still high, the stress growth rate is significantly reduced. As of August 10, 2017, 23 anchor stress monitoring curves have converged, and the stress growth rate of two anchors has reduced significantly and tends to converge. Only one set of R16 anchors at 829 m elevation remains at a higher stress growth rate.

To sum up, data from multipoint displacement meters, apparent deformation of the slope, and anchor stress meters showed that the deformation amount and deformation rate

of the slope keep relatively large from July 2016 to March 2017. It is the result of the combined effect of high-strength blasting excavation and long-term rainwater infiltration of the slope rock mass in the rainy season. The maximum deformation occurs at the 4-4' monitoring section, i.e., the protruding ridge topography, followed by the middle area of the slope, and the accumulated deformation amount of the slope behind the concrete system at 850 m elevation and other areas of the slope is small. At present, the slope deformation of the slope is at the stage of convergence. However, in the subsequent slope engineering, especially after the spillway is put into use, strong water impact and atomized rain infiltration will have a serious impact on the stability of the slope, so continuous monitoring is still required to ensure the stability of the slope.

4. Deformation Mechanism

4.1. The Poor Quality of Lithology. The upper cover of the engineering slope is a gently inclined thin layer of dolomite and thick layer dolomite with shale interlayer. The middle and lower part is a transverse thin layer of limestone and dolomite; the rock mass is poor. The fault F_6 , which is an antidip rock mass structure, runs through the entire slope

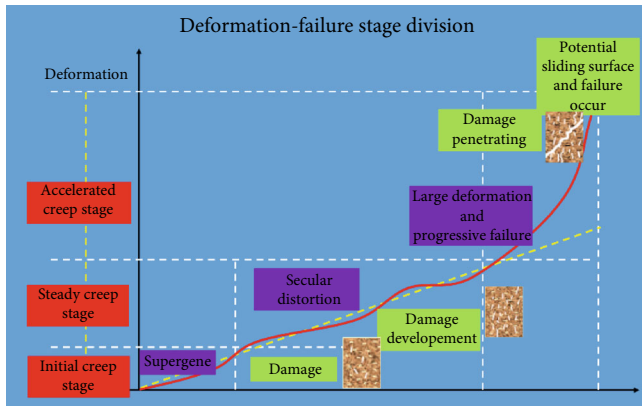


FIGURE 9: Deformation-failure evolution process of slope.

and steeply dip direction into the slope, intersecting the slope at a large angle. The fault F_6 divides the slope into two parts that form the weak boundary of the lower slope of the fault, which weakens the three-dimensional side restraining effect of the front slope of the flood discharge tunnel on the entire left slope. At the same time, due to the deformation of the downstream slope of fault F_6 , the fault and the lower rock mass squeeze under the action of the self-compression of the weak part of the fault and the deformation slip to the outer side of the slope. Due to the long construction period and the large annual temperature difference in the study area, the rock mass will inevitably be subjected to weathering, which will change the lithology of the slope surface rock mass, reduce the quality of the rock mass, and increase the permeability. The degree of weathering decreases with the depth of the slope, and the depth of weathering varies with the quality of the rock mass, which results in the heterogeneity of the seepage of the slope rock mass.

4.2. Disturbance of Engineering Activities. Although the engineering slope is a high-steep slope, before the excavation, the slope rock mass is in a relatively stable state. The excavation of the project redistributes the stress inside the rock mass. With the gradual expansion of the slope excavation, the rock mass on the slope is subjected to blasting dynamics to generate dynamic damage. On the other hand, the excavation changes the boundary conditions of the slope, and the rock mass undergoes unloading deformation. Part of the strain energy in the rock mass is released, and part of the strain energy is transferred to the deep part of the rock mass, resulting in stress redistribution. Moreover, the deformation of the slope body accompanies the redistribution causing the original structural plane in the rock mass to open and stagger, the expansion of the original joint fissure, or the generation of new cracks, especially in the vicinity of geological weak planes such as faults, soft rock areas, and strong unloading relaxation areas. The combination of new cracks and fault fracture zones generated in the unloading relaxation zone provides convenient conditions for rock mass seepage, and the slope rock mass seepage will vary with the degree of unloading (Figure 9).

4.3. Impact of Rainfall and Atomized Rain. The overall lithology of the slope, coupled with the slope rock mass stress relaxation and deep rock mass cracks caused by engineering disturbance and stress redistribution, provides convenient conditions for rainwater infiltration. Rain infiltrates along the cracks on the slope surface, weakening the mechanical properties of rock and soil. With the continuous heavy rainfall in the rainy season, seepage is formed in the rock mass above the depth of rainfall infiltration, and saturated runoff is formed on the surface of the slope. The infiltration of rainfall and atomized rain water forms a saturated zone that is detrimental to stability and unfavorable in the rock mass of the slope. Although the current saturation zone is not deep, it still causes the water level of the infiltration line on the surface of the slope to change. Especially the atomized rain produced by the waterfall is closer to the fault F_6 , the permeability of the fault fracture zone is stronger, and the overall quality of the slope rock mass is poor. The infiltration of rainwater increases the pore water pressure on the rock mass and reduces the effective stress, and the rock mass and rock mass structural surface are softened by the influence of groundwater. The mechanical properties of rock masses and structural planes change, which will have a very adverse effect on the slope stability.

In summary, due to the influence of stratum lithology, excavation disturbance, rainfall, and atomized rain infiltration, part of the apparent monitoring data of the slope surface suddenly increased from November 2016. As of the end of March 2017, the excavation above 806 m elevation was completed. The apparent monitoring data reveal that the deformation rate of the slope is still relatively fast, and the conventional monitoring bolt is subjected to a large force. In order to control the continuous large deformation of the slope, the excavation of the lower part of the slope was stopped on April 1, 2017. The excavated slope was systematically supported in time, and then the deformation rate of the slope slowed down. After filling the plunge pool with water on June 22, 2017, the excavation and support works of the slope were completely stopped. On October 26, 2017, the plunge pool was pumped after the flood season, and the excavation construction of the slope below 806 m fully started. Given the large deformation of the slope caused by the excavation between the 850 and 806 m elevation and considering the impact of strong atomized rain after the normal use of the spillway tunnel, flood discharge impact and atomized rain infiltration will be the most important factors affecting slope stability. In order to better understand the slope deformation law and avoid large deformation caused by the excavation of elevation below 806 m and to guarantee the safety and stability of the slope and integrate monitoring, early warning, reinforcement, and control, it is urgent to establish an early warning criterion and early warning mode suitable for the landslide monitoring of Wudongde Hydropower Station.

5. New Technology for Preventing and Monitoring the Slope Deformation

Although the left side high slope of the Wudongde flood discharge tunnel does not currently form a sliding surface, the

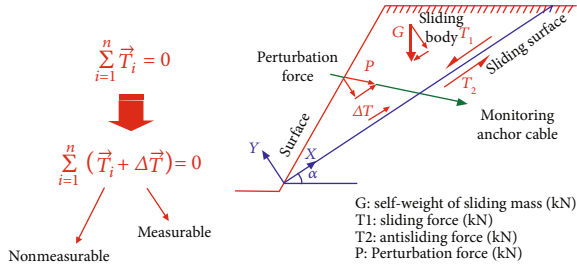


FIGURE 10: Schematic diagram of landslide measurable mechanical system.

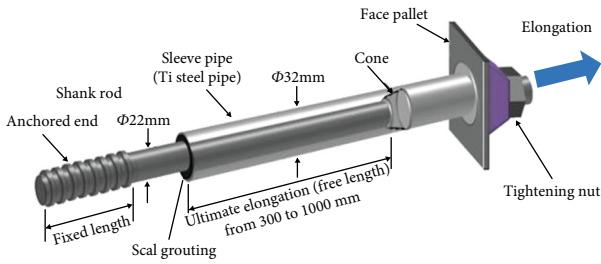


FIGURE 11: Structure diagram of CRLD cable.

excavation inevitably changes the stress distribution inside the slope body. At the same time, the deformation evolution of the slope is an irreversible process of the development of microfracture inside the rock mass, the weakening of the macromechanical characteristics of the rock mass, and the formation, development, and penetration of the sliding surface. Moreover, these new cracks caused by the construction of slope engineering will facilitate the infiltration of rainfall, especially the intense atomization rain caused by flood discharge. This will also be the most important factor affecting the stability of the hydropower station. At present, because the conventional anchor cable is easy to break during the process of slope deformation, the evolution law of the sliding force inside the slope is difficult to monitor. It is challenging to meet the requirements of landslide monitoring only by shallow displacement and deformation monitoring. Moreover, the conventional monitoring equipment on the slope surface is susceptible to failure due to the effects of strong atomizing rain. Therefore, it is necessary to consider the remote monitoring and early warning system of the slope anchor force developed by the State Key Laboratory of Geotechnical Mechanics and Underground Engineering of China University of Mining and Technology (Beijing) for real-time remote intelligent monitoring of the left side slope of Wudongde flood discharge tunnel.

5.1. Landslide Remote Monitoring and Early Warning System. Based on the monitoring principle of anchor cable force and the working principle of constant resistance large deformation anchor cable, Professor He Manchao developed a landslide monitoring and early warning system based on anchor cable force measurement [39]. The system is based on the principle that “sliding force greater than shear strength is a sufficient and necessary condition for landslide generation.”

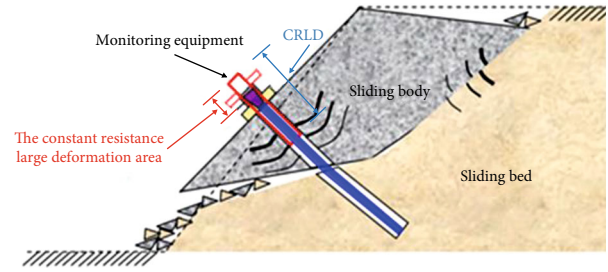


FIGURE 12: Reinforce and monitoring principle of CRLD cable.

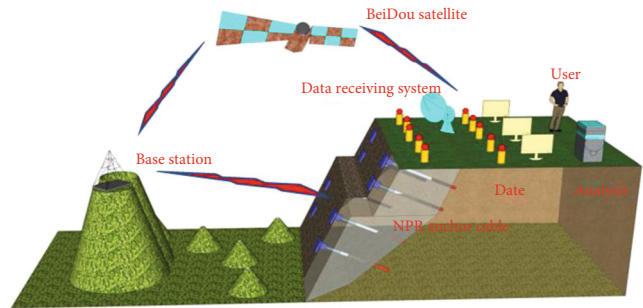


FIGURE 13: The principle of system operation.

The indirect measurement of the sliding force on the potential sliding surface is achieved by directly measuring and monitoring the axial force on the cable, thus breaking the bottleneck of traditional deformation monitoring. Also, the monitoring and early warning of the deep anchor cable force is realized for the first time.

5.1.1. Principle of Anchor Cable Force Remote Monitoring. The landslide will only occur if the sliding force is greater than the antisliding force. By considering the mechanical system of a natural landslide, three main forces are acting on it, i.e., sliding force (T_1), antisliding force (T_2), and self-weight of sliding mass (G). In the natural state, the sliding force and antisliding force on the sliding surface are in equilibrium, i.e., $T_1 \leq T_2$, and the slope is stable. However, when the external or internal factors affecting the slope stability change, the original equilibrium state breaks, and the stress in the landslide body redistributes. When $T_1 > T_2$, the slope is unstable. Therefore, it is only necessary to accurately measure T_1 and T_2 to judge the changing state of stress in the landslide body and predict the occurrence time and scale of landslide disaster in advance. In order to measure T_1 and T_2 , the magnitude of sliding force T_1 can be indirectly calculated through direct monitoring of disturbing force P after the artificial measurable force P is introduced. Figure 10 shows the complex mechanical system composed of the natural mechanical system and an artificial mechanical system.

5.1.2. Structure of Constant-Resistance Large-Deformation Anchor Cable and Working Principle. As a composite structure type stretchable anchor cable, the proposed Constant-Resistance Large-Deformation (CRLD) anchor cable mainly consists of rod body, constant resistance body, constant

TABLE 4: Warning level and warning criteria.

Warning level	Danger forecast	Level 1 criteria: cumulative increment T/t	Secondary criterion: daily slip of sliding force $\Delta T/t$		
Blue	Stability	0~50	10~20 up to yellow	20~35 up to orange	>35 up to red
Yellow	Substable	50~120			
Orange	Near slip	120~160			
Red	Impending slide	>160			

Anchor force $T = T_n - T_0$; sliding force increment $\Delta T = T_n - T_{n-1}$; initial prestress $T_0 = 30t$.

resistance sleeve, pallet, and nut (Figure 11). The constant resistance body and the constant resistance sleeve together form a constant resistance device to provide constant support resistance for the anchor cable.

When landslide occurs, with the slow release of deformation energy in the slope rock mass, the sliding body and sliding bed move relatively along the sliding surface. When the deformation energy of the rock mass exceeds the designed constant resistance, the constant resistance body frictionally slides along the inner wall of the constant resistance sleeve. The CRLD anchor cable stretches axially along with the large deformation of the slope rock mass and absorbs the energy generated by the slow landslide deformation (Figure 12). It avoids the failure of conventional monitoring anchor cable due to excessive deformation, meeting the targets of advanced monitoring and early warning for the landslide.

5.1.3. Structure of the Landslide Remote Monitoring and Early Warning System. The landslide remote monitoring and early warning system consists of indoor and on-site equipment. The indoor monitoring equipment includes a data receiving-processing-analysis system, 3S maps of monitoring point target areas, a 3D monitoring engineering image search system, and some auxiliary analysis software. The on-site monitoring equipment consists of BeiDou satellite receiving equipment, data processing system, and information display system. Figure 13 shows the schematics of the system’s working principle.

5.1.4. Landslide Monitoring and Warning Criteria. In order to improve the monitoring accuracy, this study establishes a landslide monitoring and early warning model. The model mainly relies on system equations and empirical equations. Through statistical analysis of the monitoring data of 354 existing monitoring systems in the past ten years and the results of indoor physical model experiments, a landslide four-level early warning mode is established. The model classifies the degree of hazard of the slope into four levels described by different colors, i.e., red (imminent slip early warning), orange (near slip early warning), yellow (metastable early warning), and blue (stable). Table 4 summarizes the specific grades and early warning criteria.

5.2. Monitoring Point Layout. Taking full account of the slope deformation trend, topography, rock lithology, geological structure, spatial distribution of the fracture, excavation

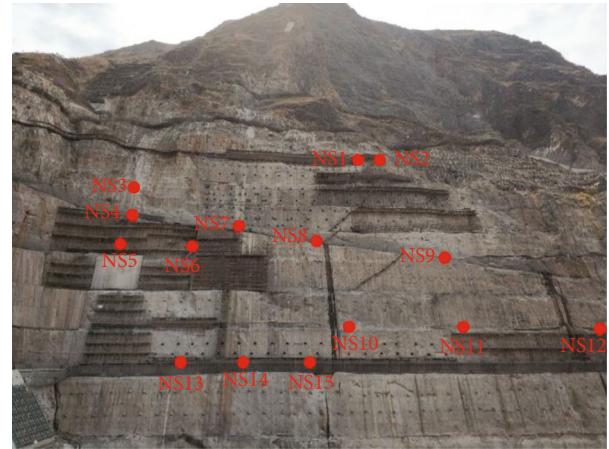


FIGURE 14: Layout of on-site monitoring points.

method, and schedule combined with the technical requirements of slope anchor cable force monitoring. A total of 15 monitoring points (NS1~NS15) were arranged within the scope of the engineering slope. The distribution of monitoring points is shown in Figure 14.

5.3. Monitoring Results and Analysis. From April 25, 2018, to October 18, 2018, eight sets of remote monitoring and early warning systems have been installed on the left side slope of the flood discharge tunnel, and the high slope has been continuously monitored for 24 hours. At present, about 14,000 series of data have been collected (Figure 15), which provides important data for monitoring the deformation and evolution characteristics of slopes and early warning.

Through the analysis of the monitoring curve and monitoring data that have been received so far, 75% of the monitoring curve is in a horizontal state or an approximate horizontal state, indicating that the slope is in a stable state. Also, the NS1 monitoring curve contains some unstable data, while the NS2 curve has a slow downward trend, indicating that the top slope is currently in a relatively stable state.

From a macroperspective, as the slope project is nearing completion, most of the slopes are in a stable state. However, as the spillway tunnel is put into use, the strong water impact and the infiltration of atomized rain generated by the flood discharge will have a long-term and continuous impact on the stability of the slope. Therefore, long-term real-time monitoring of slope stability is still needed.

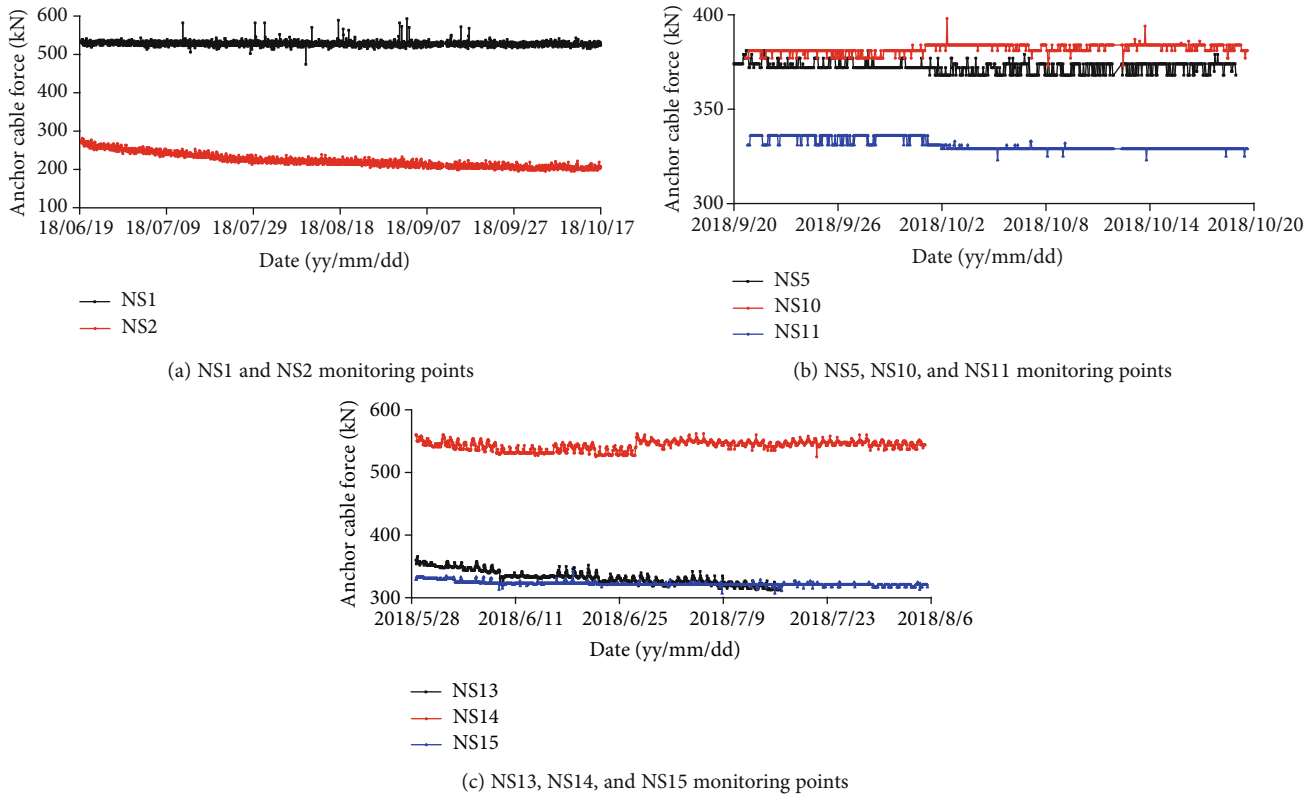


FIGURE 15: Curves of anchor cable force.

6. Conclusions

Based on the above analysis, a few conclusions can be drawn:

- (1) The data from multipoint displacement meters, the apparent deformation, and the anchor stress meters all show that the deformation amount and deformation rate of the slope are relatively large during the construction of the slope. It is the result of the combined effect of high-strength blasting excavation and long-term rainwater infiltration of the slope rock mass in the rainy season. The maximum deformation amount is located at the 4-4' deformation monitoring section, especially near the top of the opening line at this section, followed by the middle area of the slope
- (2) Through comprehensive analysis, the main reason for the large deformation of the slope is that after the excavation of the slope, the slope rock mass will inevitably be affected by weathering and unloading. In addition, the overall quality of the slope rock mass is poor. Weathering changes the lithology of the rock mass on the surface of the slope, reducing the quality of the rock mass and enhancing the permeability. The degree of weathering decreases with the depth of the slope, and the depth of weathering varies according to the quality of the rock mass. The unloading relaxation of rock mass changes the original stress field of the slope,

and different unloading degrees cause the cracks in the slope rock mass to open, slip, and expand to different degrees. Rock mass seepage is closely related to rock mass fissures. The degree of unloading decreases with the depth of the slope, and the degree of unloading varies with the quality of the rock mass, resulting in heterogeneity of the seepage of the slope rock mass

- (3) The newly created cracks and fault fracture zones in the weathering and unloading relaxation zone provide convenient conditions for rainfall and atomized rain infiltration. Rainfall and atomized rainwater infiltrate along the slope surface, forming a seepage field in the slope body, especially in areas with poor rock quality, such as near the fault fracture zone and the top ridged terrain area of the slope. The long-term infiltration of rainwater weakens the rock mass parameters, weakens the strength of the rock mass structural surface, increases the water pressure in the fissures, and causes large deformation of the slope
- (4) The impact of water flow and the infiltration of atomized rain caused by flood discharge will be the most important factors affecting the stability of this slope in the future. Therefore, the landslide anchor cable force remote monitoring system based on the constant resistance and large deformation anchor cable is used to monitor the stability of the slope. The

current monitoring results show that the slope is in a stable state. The research results will provide a scientific basis for the stability control of high and steep slopes of hydropower stations in the future

Conflicts of Interest

No conflict of interest exists in the submission of this manuscript.

Authors' Contributions

The manuscript was approved by all authors for publication.

Acknowledgments

This study was supported by the Zhejiang Province Key R&D Projects (No. 2019C03104) and the Fundamental Research Funds for the Central Universities, SCUT (No. 2015QB02).

References

- [1] C. R. J. Kilburn and D. N. Petley, "Forecasting giant, catastrophic slope collapse: lessons from Vajont, Northern Italy," *Geomorphology*, vol. 54, no. 1-2, pp. 21–32, 2003.
- [2] C. Zhu, M. He, M. Karakus, X. Cui, and Z. Tao, "Investigating toppling failure mechanism of anti-dip layered slope due to excavation by physical modelling," *Rock Mechanics and Rock Engineering*, 2020.
- [3] J. Xu, A. Haque, W. Gong et al., "Experimental study on the bearing mechanisms of rock-socketed piles in soft rock based on micro X-ray CT analysis," *Rock Mechanics and Rock Engineering*, vol. 53, no. 8, pp. 3395–3416, 2020.
- [4] N. Jiang, C. X. Wang, H. Y. Pan, D. Yin, and J. Ma, "Modeling study on the influence of the strip filling mining sequence on mining-induced failure," *Energy Science & Engineering*, vol. 8, no. 6, pp. 2239–2255, 2020.
- [5] C. X. Wang, B. T. Shen, J. T. Chen et al., "Compression characteristics of filling gangue and simulation of mining with gangue backfilling: an experimental investigation," *Geomechanics and Engineering*, vol. 20, no. 6, pp. 485–495, 2020.
- [6] Q. Yin, G. W. Ma, H. W. Jing et al., "Hydraulic properties of 3D rough-walled fractures during shearing: an experimental study," *Journal of Hydrology*, vol. 555, pp. 169–184, 2017.
- [7] H. Huang, T. Babadagli, X. Chen, H. Li, and Y. Zhang, "Performance comparison of novel chemical agents for mitigating water-blocking problem in tight gas sandstones," *SPE Reservoir Evaluation & Engineering*, 2020.
- [8] Y. Zhang, S. Cao, N. Zhang, and C. Zhao, "The application of short-wall block backfill mining to preserve surface water resources in northwest China," *Journal of Cleaner Production*, vol. 261, article 121232, 2020.
- [9] J. Cai, N. Ju, R. Huang et al., "Mechanism of toppling and deformation in hard rock slope: a case of bank slope of Hydropower Station, Qinghai Province, China," *Journal of Mountain Science*, vol. 16, no. 4, pp. 924–934, 2019.
- [10] X. Wang, C. Liu, S. Chen, L. Chen, K. Li, and N. Liu, "Impact of coal sector's de-capacity policy on coal price," *Applied Energy*, vol. 265, article 114802, 2020.
- [11] Y. X. Xiao, X. T. Feng, G. L. Feng, H. J. Liu, Q. Jiang, and S. L. Qiu, "Mechanism of evolution of stress–structure controlled collapse of surrounding rock in caverns: a case study from the Baihetan hydropower station in China," *Tunnelling and Underground Space Technology*, vol. 51, pp. 56–67, 2016.
- [12] F. Dai, B. Li, N. Xu, G. Meng, J. Wu, and Y. Fan, "Microseismic monitoring of the left bank slope at the Baihetan hydropower station, China," *Rock Mechanics and Rock Engineering*, vol. 50, no. 1, pp. 225–232, 2017.
- [13] N. Xu, J. Wu, F. Dai, Y. Fan, T. Li, and B. Li, "Comprehensive evaluation of the stability of the left-bank slope at the Baihetan hydropower station in southwest China," *Bulletin of Engineering Geology and the Environment*, vol. 77, no. 4, pp. 1567–1588, 2018.
- [14] Z. Zhang, X. Huang, W. Liu, and L. Wang, "Study on the hydraulic parameters of Woshaxi landslide soils during water level drawdown of three gorges reservoir," *Geofluids*, vol. 2020, Article ID 6283791, 14 pages, 2020.
- [15] C. Meisina, M. Bittelli, R. Valentino, M. Bordoni, and R. Tomás-Jover, "Advances in shallow landslide hydrology and triggering mechanisms: a multidisciplinary approach," *Geofluids*, vol. 2019, Article ID 1607684, 2 pages, 2019.
- [16] A. Wayllace, B. Thunder, N. Lu, A. Khan, and J. W. Godt, "Hydrological behavior of an infiltration-induced landslide in Colorado, USA," *Geofluids*, vol. 2019, Article ID 1659303, 14 pages, 2019.
- [17] B. Han, B. Tong, J. Yan, C. Yin, L. Chen, and D. Li, "The monitoring-based analysis on deformation-controlling factors and slope stability of reservoir landslide: Hongyanzi landslide in the southwest of China," *Geofluids*, vol. 2018, 7391514 pages, 2018.
- [18] N. Zhang, W. Liu, Y. Zhang, P. Shan, and X. Shi, "Microscopic pore structure of surrounding rock for underground strategic petroleum reserve (SPR) caverns in bedded rock salt," *Energies*, vol. 13, no. 7, article 1565, 2020.
- [19] P. Shan and X. Lai, "An associated evaluation methodology of initial stress level of coal-rock masses in steeply inclined coal seams, Urumchi coal field, China," *Engineering Computations*, vol. 37, no. 6, pp. 2177–2192, 2020.
- [20] H. Y. Pan, D. W. Yin, N. Jiang, and Z. G. Xia, "Crack initiation behaviors of granite specimens containing crossing-double-flaws with different lengths under uniaxial loading," *Advances in Civil Engineering*, vol. 2020, pp. 1–13, 2020.
- [21] Q. Yin, R. Liu, H. Jing, H. Su, L. Yu, and L. He, "Experimental study of nonlinear flow behaviors through fractured rock samples after High-Temperature exposure," *Rock Mechanics and Rock Engineering*, vol. 52, no. 9, pp. 2963–2983, 2019.
- [22] Q. Yin, H. Jing, H. Su, and H. Zhao, "Experimental study on mechanical properties and anchorage performances of rock mass in the fault fracture zone," *International Journal of Geomechanics*, vol. 18, no. 7, article 04018067, 2018.
- [23] X. Wang, W. Yuan, Y. T. Yan, and X. Zhang, "Scale effect of mechanical properties of jointed rock mass: a numerical study based on particle flow code," *Geomechanics and Engineering*, vol. 21, no. 3, pp. 259–268, 2020.
- [24] D. Liu, Z. Gu, R. Liang et al., "Impacts of pore-throat system on fractal characterization of tight sandstones," *Geofluids*, vol. 2020, Article ID 4941501, 17 pages, 2020.
- [25] S. C. Hu, Y. L. Tan, H. Zhou et al., "Anisotropic modeling of layered rocks incorporating planes of weakness and volumetric stress," *Energy Science & Engineering*, vol. 8, no. 3, pp. 789–803, 2020.

- [26] D. Z. Ren, D. S. Zhou, D. K. Liu, F. Dong, S. Ma, and H. Huang, "Formation mechanism of the Upper Triassic Yanchang Formation tight sandstone reservoir in Ordos Basin-Take Chang 6 reservoir in Jiyuan oil field as an example," *Journal of Petroleum Science and Engineering*, vol. 178, pp. 497–505, 2019.
- [27] J. Chen, J. Zhao, S. Zhang, Y. Zhang, F. Yang, and M. Li, "An experimental and analytical research on the evolution of mining cracks in deep floor rock mass," *Pure and Applied Geophysics*, 2020.
- [28] J. Wang, Y. Zhang, Z. Qin, S. G. Song, and P. Lin, "Analysis method of water inrush for tunnels with damaged water-resisting rock mass based on finite element method-smooth particle hydrodynamics coupling," *Computers and Geotechnics*, vol. 126, article 103725, 2020.
- [29] F. Q. Ren, C. Zhu, and M. C. He, "Moment tensor analysis of acoustic emissions for cracking mechanisms during schist strain burst," *Rock Mechanics and Rock Engineering*, vol. 53, no. 1, pp. 153–170, 2020.
- [30] J. Xu, G. Dai, W. Gong, Q. Zhang, A. Haque, and R. P. Gamage, "A review of research on the shaft resistance of rock-socketed piles," *Acta Geotechnica*, 2020.
- [31] G. Feng, X. C. Wang, M. Wang, and Y. Kang, "Experimental investigation of thermal cycling effect on fracture characteristics of granite in a geothermal-energy reservoir," *Engineering Fracture Mechanics*, vol. 235, article 107180, 2020.
- [32] G. Feng, Y. Kang, X. C. Wang, Y. Hu, and X. Li, "Investigation on the failure characteristics and fracture classification of shale under Brazilian test conditions," *Rock Mechanics and Rock Engineering*, vol. 53, no. 7, pp. 3325–3340, 2020.
- [33] Y. Zhang, H. Li, Q. Sheng, K. Wu, and G. Chen, "Real time remote monitoring and pre-warning system for highway landslide in mountain area," *Journal of Environmental Sciences*, vol. 23, pp. S100–S105, 2011.
- [34] Y. Yin, H. Wang, Y. Gao, and X. Li, "Real-time monitoring and early warning of landslides at relocated Wushan Town, the Three Gorges Reservoir, China," *Landslides*, vol. 7, no. 3, pp. 339–349, 2010.
- [35] O. A. Conte and R. A. Coffman, "Slope stability monitoring using remote sensing techniques," in *GeoCongress 2012: State of the Art and Practice in Geotechnical Engineering*, pp. 3060–3068, Oakland, California, USA, March 2012.
- [36] C. Atzeni, M. Barla, M. Pieraccini, and F. Antolini, "Early warning monitoring of natural and engineered slopes with ground-based synthetic-aperture radar," *Rock Mechanics and Rock Engineering*, vol. 48, no. 1, pp. 235–246, 2015.
- [37] P. K. Miller, M. Vessely, L. D. Olson, and Y. Tinkey, "Slope stability and rock-fall monitoring with a remote interferometric radar system," in *Geo-Congress 2013: Stability and Performance of Slopes and Embankments III*, pp. 304–318, San Diego, California, USA, February 2013.
- [38] G. J. Dick, E. Eberhardt, A. G. Cabrejo-Liévano, D. Stead, and N. D. Rose, "Development of an early-warning time-of-failure analysis methodology for open-pit mine slopes utilizing ground-based slope stability radar monitoring data," *Canadian Geotechnical Journal*, vol. 52, no. 4, pp. 515–529, 2015.
- [39] L. Zan, G. Latini, E. Piscina, G. Polloni, and P. Baldelli, "Landslides early warning monitoring system," in *IEEE International Geoscience and Remote Sensing Symposium*, pp. 188–190, Toronto, Ontario, Canada, June 2002.
- [40] N. W. Xu, C. A. Tang, L. C. Li et al., "Microseismic monitoring and stability analysis of the left bank slope in Jinping first stage hydropower station in southwestern China," *International Journal of Rock Mechanics and Mining Sciences*, vol. 48, no. 6, pp. 950–963, 2011.
- [41] M. He, W. Gong, J. Wang et al., "Development of a novel energy-absorbing bolt with extraordinarily large elongation and constant resistance," *International Journal of Rock Mechanics and Mining Sciences*, vol. 67, pp. 29–42, 2014.
- [42] Z. Tao, H. Zhang, Y. Chen, and C. Jiang, "Support principles of NPR bolt/cable and control techniques of large-deformation disasters," *International Journal of Mining Science and Technology*, vol. 26, no. 6, pp. 967–973, 2016.
- [43] M. C. HE, Z. G. TAO, and B. ZHANG, "Application of remote monitoring technology in landslides in the Luoshan mining area," *Mining Science and Technology (China)*, vol. 19, no. 5, pp. 609–614, 2009.
- [44] X. Yang, D. Hou, Z. Tao, Y. Peng, and H. Shi, "Stability and remote real-time monitoring of the slope slide body in the Luoshan mining area," *International Journal of Mining Science and Technology*, vol. 25, no. 5, pp. 761–765, 2015.
- [45] Z. Tao, Y. Wang, C. Zhu, H. Xu, G. Li, and M. He, "Mechanical evolution of constant resistance and large deformation anchor cables and their application in landslide monitoring," *Bulletin of Engineering Geology and the Environment*, vol. 78, no. 7, pp. 4787–4803, 2019.

Research Article

Failure Behavior of Hot-Dry-Rock (HDR) in Enhanced Geothermal Systems: Macro to Micro Scale Effects

Hongwei Zhang ^{1,2}, Zhijun Wan ³, and Derek Elsworth ²

¹School of Energy and Mining Engineering, China University of Mining & Technology, Beijing 100089, China

²Department of Energy and Mineral Engineering, EMS Energy Institute, and G3 Center, The Pennsylvania State University, University Park, PA 16802, USA

³Key Laboratory of Deep Coal Resource Mining (CUMT), Ministry of Education of China, School of Mines, China University of Mining & Technology, Xuzhou 221116, China

Correspondence should be addressed to Zhijun Wan; zhjwan@163.com and Derek Elsworth; elsworth@psu.edu

Received 19 June 2020; Revised 9 July 2020; Accepted 26 July 2020; Published 21 September 2020

Academic Editor: Qian Yin

Copyright © 2020 Hongwei Zhang et al. This is an open access article distributed under the Creative Commons Attribution License, which permits unrestricted use, distribution, and reproduction in any medium, provided the original work is properly cited.

Evaluations of the mechanical properties and failure modes of granite at high temperatures are important issues for underground projects such as enhanced geothermal systems and nuclear waste disposal. This paper presents the results of laboratory experiments that investigated the physico-mechanical failure behavior of granites at high temperatures. The results allowed several important conclusions to be drawn. Both the uniaxial compressive strength (UCS) and tangent modulus decrease with increasing temperature. Specifically, the UCS-temperature curve can be divided into three sections: a section (20–200°C) where UCS shows a slight decrease, a section (200–300°C) where the UCS decreases significantly, and a third section (300–500°C) where the rate of UCS decrease stabilizes. However, in the entire temperature range from 20 to 500°C, the tangent modulus decreases exponentially. The number of acoustic emission (AE) counts decrease and the counts occur less frequently at higher temperatures. Individual grains are surrounded by a large number of microcracks at 200°C and the crack length increased significantly when heating to 300°C. Specifically, the length of micro-cracks in the granite at 300°C could be 10 times longer than that at 200°C. Quenching or injecting cold water into HDRs would further weaken the rock and induce thermal damage to the rock structure. The strength of rock would be further quench-weakened by 10%, 20% and 30% at 200°C, 300°C and 500°C, respectively. Therefore, in Enhanced/Engineered Geothermal Systems (EGS), quenching is much more destructive than normal thermal stress.

1. Introduction

Rocks hosting Enhanced/Engineered Geothermal Systems (EGS) are subjected to elevated temperatures (e.g., heating during heat restoring) or reduced temperatures (e.g., quenching during hydraulic fracturing), as shown in Figure 1. These thermal treatments typically result in modifications to the mechanical properties of the rock and the response of the couple THMC processes [1–6]. The modifications include rock softening, strength weakening, and degradation of the elastic modulus. Since the 1970s, numerous studies have been conducted to determine the effects of elevated temperatures on the physico-mechanical properties and deformation of granitic rocks [7–17]. However, most studies have concen-

trated on the changes to the samples after the sample had been heated [13, 18–27] rather than to follow the changes that take place during heating. Since heat restoring is of great significance to the next turn of heat extraction, the thermal crack damage process during heating should be considered. To monitor the thermal microcracking effect of temperature on crystalline rocks, some scholars employed various methods, such as direct wave velocity measurement, coda wave interferometry (CWI), permeability test and acoustic emissions (AE) to track the thermal cracking process during heating and thus reveal the thermal cracking mechanism [7, 16, 28, 29]. Hence, it is necessary to understand the failure response of granite under high temperature, particularly under high temperature that above 200°C. At

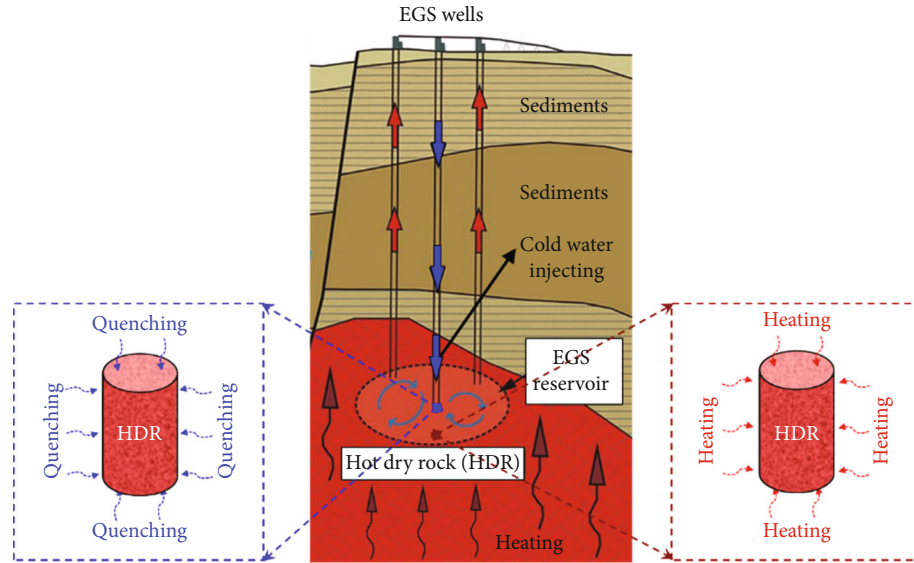


FIGURE 1: Heating and quenching of HDR in a typical EGS.

these temperatures, the properties of the rock are dramatically different than when they are at Earth-surface temperatures. In addition, understanding the HDR's performances during straightforward heating and quenching would be helpful to improve thermal treatment efficiency during EGS reservoir building.

Generally, higher temperatures result in a lower UCS and a reduced elastic modulus of brittle rock. However, the downward trends varies owing to the different compositions of the specimens tested and differences in experimental techniques. For the straightforward heating tests, cooling methods, such as quenching, cooling in air, or cooling in a furnace, can significantly affect the mechanical and physical properties of the specimen [19, 30]. In addition, both thermal cracking and the quartz α - β phase transition [31] can contribute to the dramatic changes. The uncertainties introduced by different cooling methods could be eliminated by conducting high-temperature tests.

The main mechanisms that weaken the granite are physical damages caused by thermal expansion and the thermal changes in rock minerals [32]. Specifically, spatial and temporal changes in temperature can induce microcracking as a result of differential thermal expansion between grains with different thermoelastic moduli and thermal conductivities. However, there are also other mechanisms involved like resistance to crack initiation and propagation under high temperatures (toughening mechanisms) [27]. By using computed tomography (micro-CT scans), Zhao and coworkers [16, 33] revealed that thermal cracks develop as the temperature increases. A few microfissures were observed at temperatures under 200°C. With increasing temperature, more microfissures were initiated and coalesced, leading to the development of new microcracks and the propagation of pre-existing cracks. To provide a link between the microstructural parameters and the mechanical behaviour of rock, Griffiths et al. [34] provided robust measurements of microcrack characteristics to constrain micromechanical models

for rock strength and stiffness, which bridged the gap between the measurements of microcrack density at the microscale and the measurements of mechanical properties at the sample scale. During heating, a number of physical and mineralogical changes take place and these phenomena eventually result in thermal damage. The α - β quartz phase transformation occurs at 573°C and consequently, causing the volume of the quartz crystal to increase. This causes cracks in the rock resulting in weakened mechanical properties [20, 35–37]. These complex mineral thermal transitions are also important factors causing weakening and the brittle-ductile transition during deformation [38–40].

It is necessary to understand the real-time response of granite to deformation at high temperatures at both macro and micro scales. For this study, uniaxial compression tests on Luhui granite were conducted at temperatures ranging from 20°C to 500°C. This research focused on investigating: (1) the influence of high temperatures on the UCS, elastic modulus, and acoustic emissions (AE) from the Luhui granite; (2) the quenching effect and heating effect of hot dry rock. The following sections describe the experimental methods and then present and discuss the results. Finally, several important findings are set forth in the conclusion part.

2. Materials and Methods

2.1. Luhui Granite Sample Preparation. Samples of Luhui granite were collected from an open-pit quarry in Zoucheng city, Shandong province, China. The Luhui granite blocks were carefully selected to avoid fractures, discontinuities, and microcracks that would influence the test results. The granite block (Figure 2(a)) was cut into smaller blocks (200 mm × 200 mm × 120 mm) for further processing in the laboratory. These smaller blocks were cored to produce 50 mm diameter cylinders 100 mm long (Figure 2(b)). Both ends of the cylindrical samples were ground to ensure the ends of the cylinders were flat and parallel to each other

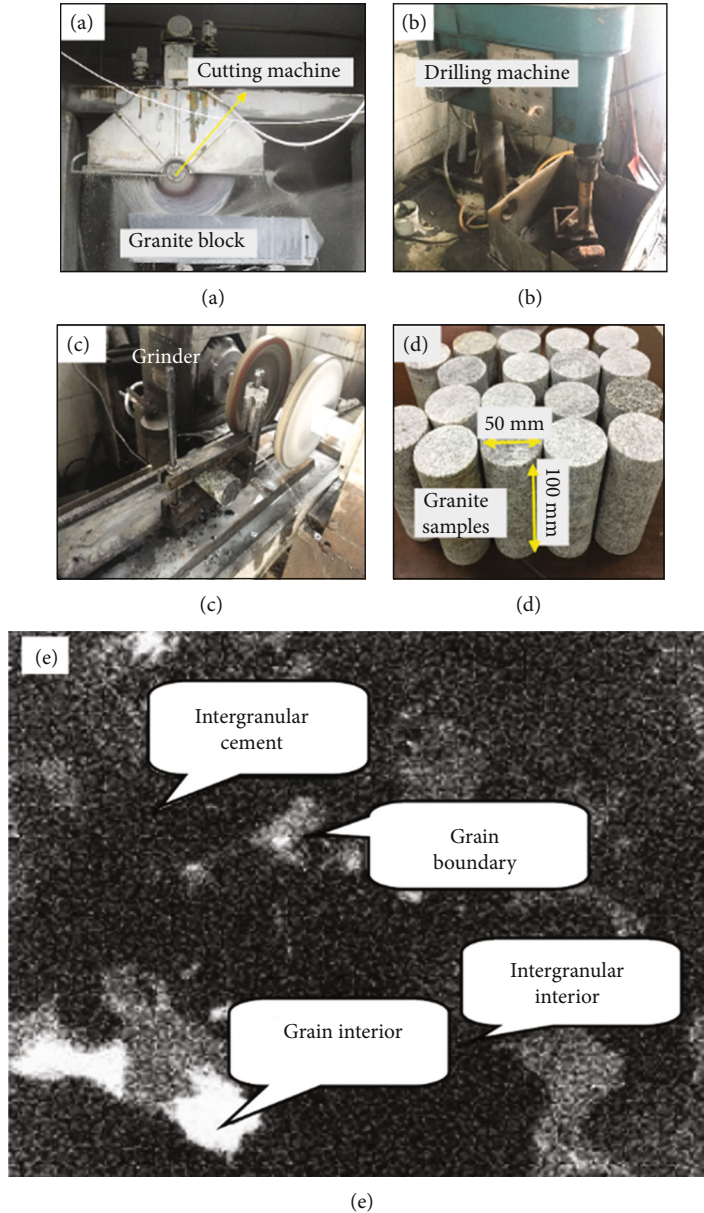


FIGURE 2: Photographs showing sample preparation and the meso-images of Luhui granite structure. (a) Rock saw cutting the granite block; (b) Core drill coring a smaller granite block; (c) Grinding the ends of a granite core; (d) Finished granite specimens 50 mm in diameter and 100 mm long; (e) Meso-image of Luhui granite structure at room temperature [7, 41].

(Figure 2(c)). Finished granite specimens are shown in Figure 2(d).

The Luhui granite is a strongly heterogeneous brittle and hard rock, mainly consist of feldspar, quartz, etc. Figure 2(e) shows the meso-structure of granite in the room temperature using high-accuracy micro-CT. Crystal grain, the boundary of grain, binding material among grain and grain pore can be clearly differentiated [41]. The main mineral compositions (feldspar, quartz) have almost the same proportion. However, the mechanical properties of these minerals differ greatly, making granites intensively heterogeneous.

2.2. *Uniaxial Compression and Acoustic Emissions Test Procedures.* The uniaxial compression experiments were

carried out on a servo-controlled testing system with a maximum loading capacity of 300 kN and a displacement resolution of 0.001 mm. This servo-controlled system can test samples in either load (stress) or displacement (strain) control modes. In this test, the displacement (strain) control mode was employed. Specifically, the displacement rate for these tests on the Luhui granite specimens was set at 0.5 mm/min which equals to a strain rate of $8.33 \times 10^{-5}/s$.

To heat the samples, a temperature-controlled electric furnace was used to heat the samples to the target temperature at a heating rate of 4°C/min. The samples were held at the target temperature for two hours to achieve thermal equilibration and allow thermal reactions to proceed. For this study, the target temperatures were 20, 200, 300, 400, and

TABLE 1: The UCS and tangent modulus of granite under high temperatures.

Sample number	Temperature (°C)	UCS (MPa)	Average UCS (MPa)	Tangent modulus (GPa)	Average tangent modulus (GPa)
G-20C-1	20	86.7	116.0	18.0	13.6
G-20C-2		148.4		18.1	
G-20C-3		128.2		15.1	
G-20C-4		124.9		15.3	
G-20C-5		173.0		14.2	
G-20C-6		100.1		11.3	
G-20C-7		90.0		9.9	
G-20C-8		99.4		10.7	
G-20C-9		111.7		12.9	
G-20C-10		97.7		10.4	
G-200C-1	200	120.6	102.3	10.9	11.0
G-200C-2		111.5		11.7	
G-200C-3		84.3		10.1	
G-200C-4		92.7		11.2	
G-300C-1	300	72.1	84.5	9.4	10.0
G-300C-2		63.6		9.4	
G-300C-3		82.0		10.1	
G-300C-4		90.2		9.8	
G-300C-5		114.4		11.4	
G-400C-1	400	62.4	80.1	9.7	9.8
G-400C-2		99.9		10.8	
G-400C-3		78.4		8.9	
G-400C-4		79.7		9.8	
G-500C-1	500	80.8	79.7	9.0	9.8
G-500C-2		79.1		10.7	
G-500C-3		80.2		9.8	
G-500C-4		78.9		9.6	

500°C. Four uniaxial compression tests were run for each target temperature. Sample numbers and experimental conditions are listed in Table 1. To run a test, a cylindrical sample was placed in the center of the furnace and the piston applied compression to the ends of the sample after AE sensors were attached. Piston displacement and load were recorded simultaneously during the test as were the AE signals. It should be noted that AE sensors cannot be attached directly to the hot sample. Alternatively, these AE sensors were attached to the piston (Figure 3).

3. Results

3.1. Uniaxial Compression Results

3.1.1. Stress–Strain Curves for Granite Samples at High Temperatures. The uniaxial stress–strain curves for granite samples at different temperatures ranging from 20°C to 500°C are presented in Figure 4. The stress–strain curves

for this brittle granite can be roughly divided into three stages, namely an original microcrack closure stage, an elastic deformation stage, and a final stage signaled by a sudden stress drop.

The first two stages, the microcrack closure and elastic deformation stages, occur before the maximum stress. During the microcrack closure (sealing) stage, the stress–strain curve is concave downward and this shape may result from the closure of primary pores and voids in the sample, although as pointed out by [42], some of the test conditions and imperfections in sample preparation can also contribute to the shape of the downward concave stress–strain curve. During the elastic deformation stage, axial stress increases and elastic deformation dominates the stress–strain curve. The stress–strain relationship remains linear despite the fact that there are some irreversible changes at this stage, such as crack initiation. The elastic deformation stage ends when peak strength is attained and the stage is followed by a sudden stress drop in stress. At the sudden stress drop stage, the stress decreases abruptly from the peak to essentially zero resulting in the stress–strain curve becoming a vertical line.

From Figure 4, it can be seen that the stress–strain curves are temperature dependent. Specifically, the peak strength and rigidity vary with the temperature. This is discussed in the following section.

3.1.2. Uniaxial Compressive Strength and Tangent Modulus

(1) Effect of temperature on UCS. Figure 5 presents a graph showing UCS for the granite samples versus temperature; the corresponding UCS and tangent modulus values are listed in Table 1. It can be seen that the average UCS value decreases with increasing temperature. The UCS–temperature curve can be divided into three sections by the UCS degradation rate. From 20°C to 200°C, the average UCS decreases from 112.7 MPa to 102.3 MPa. Thus, in this range the UCS decreases slightly with a UCS degradation rate of 0.058 MPa/°C. From 200°C to 300°C, the average UCS drop is more significant. In this range, the UCS value drops from 102.3 MPa to 84.5 MPa, in other words, the UCS degradation rate equals 0.178 MPa/°C. Above 300°C, the average UCS continues to decrease but the degradation rate is very low (only 0.024 MPa/°C). It appears that the thermal damage to the granite may be initiated between 20°C and 200°C, is enhanced between 200°C and 300°C, but little additional damage takes place above 300°C.

As shown in Figure 5, the UCS of the granite at 200–300°C is lower than that at room temperature. During the loading process, the thermal stresses enhance fissure expansion and stress softening. Therefore, the UCS decreases with increasing temperature. In addition, the changes in mineral composition and microcracking lead to degradation of the mechanical properties. In the aspect of data scattering, the large scattering in the UCS data at room temperature disappeared almost completely at 500°C. The large scattering at room temperature may be due to sample imperfections and the heterogeneity of rock. Granite is one of the crystalline rocks, which is mainly composed of quartz, feldspar and

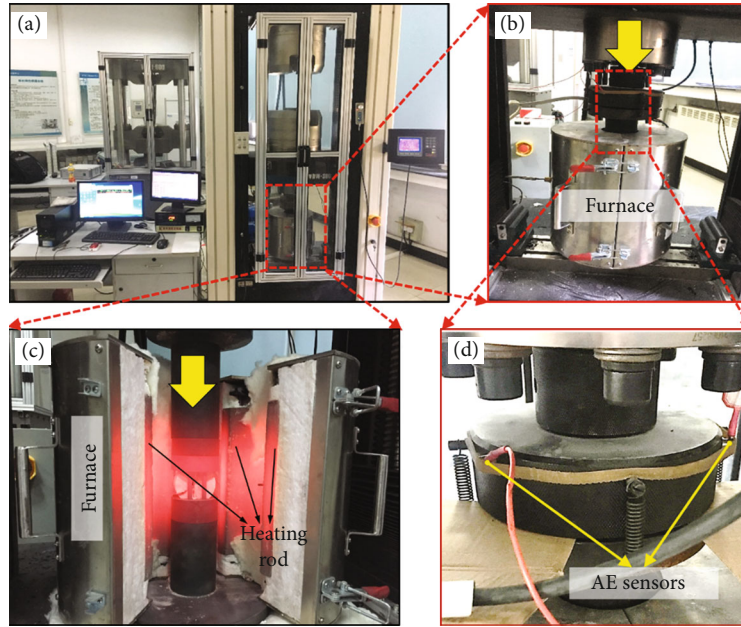


FIGURE 3: Photographs of the test systems showing the uniaxial compression test machine with the test control and data acquisition equipment (a), the furnace surrounding a sample (b and c) and a more detailed view of the acoustic emission sensors attached to the piston (d).

other minerals. During compression at room temperature, cracking is rather random, thus the strength was mostly controlled by the sample imperfections. However, the variations in UCS tend to be uniform at high temperatures, because more and more thermally induced microcracks controlled the strength of rock. That is to say, thermal cracking in rock, to some extent, could release the imperfection and the heterogeneity of rock.

(2) *Effect of temperature on tangent modulus.* The parameter of tangent modulus (E) represents the resistance of a sample during the stage of elastic compressing. On a stress-strain curve, the tangent modulus is defined as the slope of the elastic deformation portion of the curve. During the elastic deformation stage, the compressive stress increases linearly with the axial strain and elastic deformation dominates a stress-strain curve in the pre-peak region. The elastic moduli for the granite at different temperatures can be derived from the stress-strain curves; they are listed in Table 1 and plotted in Figure 6. The average tangent modulus of the granite decreases with increasing temperature. The curve in Figure 6 can be divided into two sections. In the temperature range 20–300°C, the tangent modulus decreases significantly from 13.6 GPa to 10.0 GPa, whereas at temperatures above 300°C, only a slight decrease, from 10.0 GPa to 9.8 GPa, occurs - the granite softens at high temperatures.

3.2. *Acoustic Emission Results.* Microcracking was monitored by counting dynamic rupture events in the granite samples using AE. Figure 7 shows typical stress-strain curves for each test temperature plotted on AE count vs. time axes for granite samples under the five different high-temperature test environments.

The microcracking activity shown in each of the panels on Figure 8 can clearly be divided into two periods, namely a quiescent period and an active period. During the quiescent period, there are few or no AE counts recorded. During the active AE period, the stress-strain curve reflects two different types of deformation, a stage of elastic deformation and a stage of crack growth and propagation. In the elastic deformation stage, there are one or more stress drops that may represent microfracture propagation. This fracturing is not in all cases evident in the stress-strain curves but is detected by the AE sensors and is manifested by a sudden increase in AE counts.

The intensity of the microcracking in the granite samples changes with temperature. As shown in Figure 8, the number of AE counts decreases and counts are recorded less frequently at higher temperatures indicating that the granite becomes much more ductile at high temperatures. This result is consistent with the lower tangent modulus at these temperatures. Interestingly, the cumulative AE count versus time curves show distinct steps at the higher temperatures indicating several failures in the samples. These failures will be discussed in the following sections on failure modes and grain size distributions.

4. Discussion

4.1. *Thermal Micro-Cracking Effect of Granite.* Zhai et al. [43] investigated thermal effects on the strength of granite from the aspect of energy storage and release. A higher temperature implies greater thermal energy in the granite, and this can result in a larger energy releases when fissures coalesce and propagate before failure. After completing a study on thermal cracking, Zhao and coworkers [16] reported that

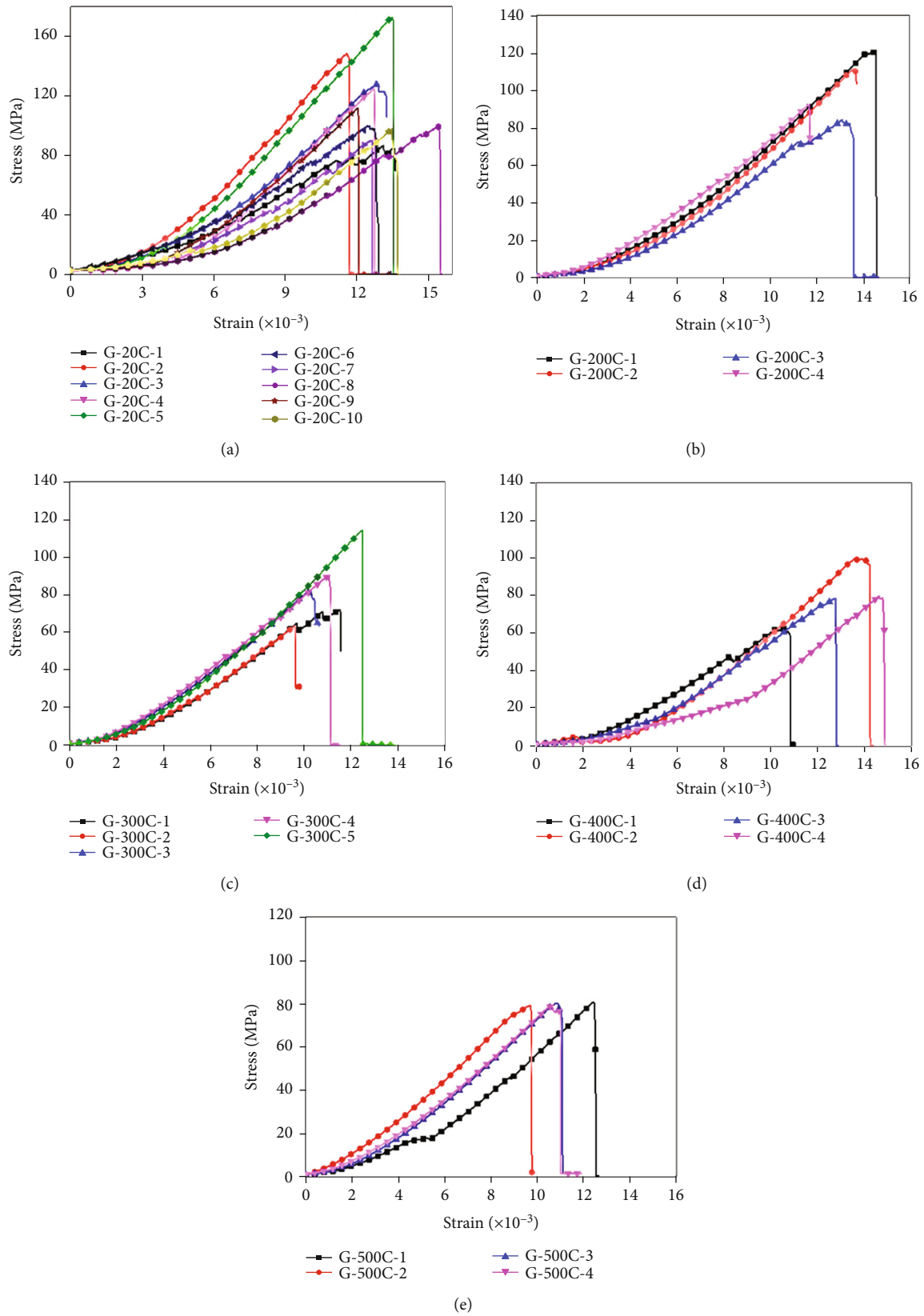


FIGURE 4: Uniaxial stress versus strain curves for granite at different temperatures. (a) room temperature ($\sim 20^{\circ}\text{C}$); (b) 200°C ; (c) 300°C ; (d) 400°C ; (e) 500°C .

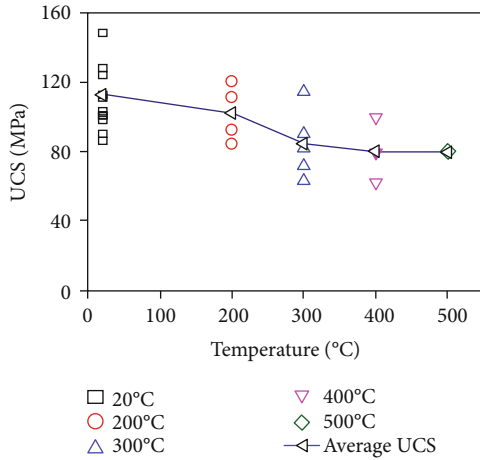


FIGURE 5: Uniaxial compressive strength of the granite samples vs. temperature.

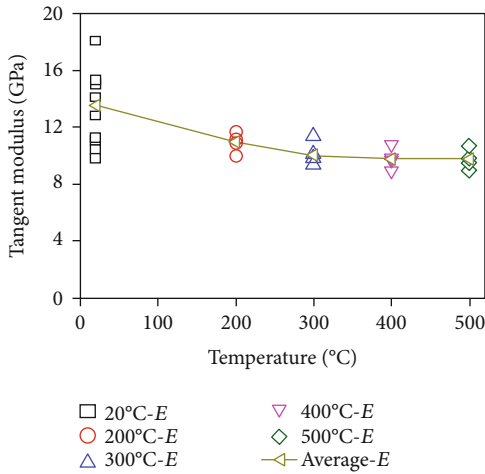


FIGURE 6: Effect of temperature on the tangent modulus of granite samples.

thermal fracturing in the Luhui granite increased at higher temperatures. Figure 7(a) shows the CT images of the meso-structure of Luhui granite specimens under different temperatures (20°C, 200°C, 300°C and 500°C). There are no obvious micro-cracks at room temperature. A few micro-fractures were observed at temperatures below 200°C. The crystal particles are surrounded by a large majority of micro-cracks in weakening lines when heated to 200°C. But a large-closed polygon crack around granitic particles has not yet been formed. Large cracks can be observed, and the crack length increased significantly when heating to 300°C. Specifically, the length of a fissure in the granite could be 10 times longer at 300°C than a fissure at 200°C, which would significantly destroy the tight and intact structure of rock and thus weaken its strength. Importantly, when the temperature increased to 500°C, the crystal grains in the granite were almost surrounded by micro-fractures. More than 90% of the micro-fractures (either boundary or cleavage cracks [17, 26, 44]) occurred on the boundaries of rock grains, although minor transgranular cracks [45, 46] cut across mineral grains. In addition, Yang et al. [26] indicated that mineral

grains in granites are closely arranged and linked. At 400–600°C, the boundary cracks and transgranular cracks in the feldspar and quartz grains would diminish the strength and stiffness of the rock. The knowledge that thermal cracking generates these cracks and fissures suggests that, after failure, the grain sizes of the failure fragments would be smaller.

By conducting MPV micro-photometer test, Feng et al. [7] revealed the micro-crack quantity change with temperature in thermally cracked Luhui granite. As shown in Figure 7(b), for the quantity of micro-crack curve (Length>5 μm), there are two peaks and the corresponding temperature are 100–150°C and 250–300°C, respectively. The second peak of micro-crack quantity occurs at around 300°C which is larger than the first peak. The explanation of thermally induced micro-crack occurrence is inharmonious thermal expansion, which can result in thermal stress in granite. When the temperature in granite increased to 100–150°C, thermal stress among the majority of mineral grains may exceed bonding stress and intergranular micro-cracks largely occur. The quantity peak of Length>5 μm micro-cracks thus occurs. When the temperature increased further to 250–300°C, thermal stress may exceed inner bonding stress in mineral crystal and transgranular microcracks largely happen, which causes a second large increment of microcracks. The quantity of micro-crack whose length is greater than 10 μm (Length>10 μm) has the same evolution. The temperature of quantity increasing of Length>10 μm micro-crack corresponds to that of Length>5 μm micro-crack quantity reduction. It can illustrate that small micro-cracks propagate and interconnect each other to form large micro-crack after small micro-crack initiating with the temperature rising. These results are consistent with the CT image results shown in Figure 7(a). These findings can explain why the UCS changes with temperature, especially the sharp UCS drop at 200–300°C.

4.2. Comparison of Rock’s Mechanical Property between Straightforward Heating and Quenching Treatments. In EGS system, injecting cold water into HDR occurs a lot for thermal stimulation [47–50]. As above mentioned, the increase of temperature may reduce the compressive strength, tangent modulus and other mechanical parameters of HDR to a certain degree. During quenching, both strength and elastic properties of granite could significantly decrease due to the intense thermal shock which creates considerable thermal damage to the rock structure. Therefore, it is necessary to understand how does the mechanical property changes in straightforward heating and quenching conditions.

Xi and Zhao conducted the quenching tests of Luhui granite from room temperature to 500°C. After heating the Luhui granite samples [23], cold water was utilized to quench these samples and the UCS values were obtained afterwards. Figure 9(a) presents the variation of UCS values versus the temperature and Figure 9(b) shows the normalized USC-temperature curve. Black lines show our high-temperature test results, while the dotted lines are quenched test results. Noted that the normalized UCS is the ratio between the UCS value at various temperatures and the UCS value that gained at room temperature. Similarly, Figures 9(c) and 9(d) present the relationship between the actual tangent

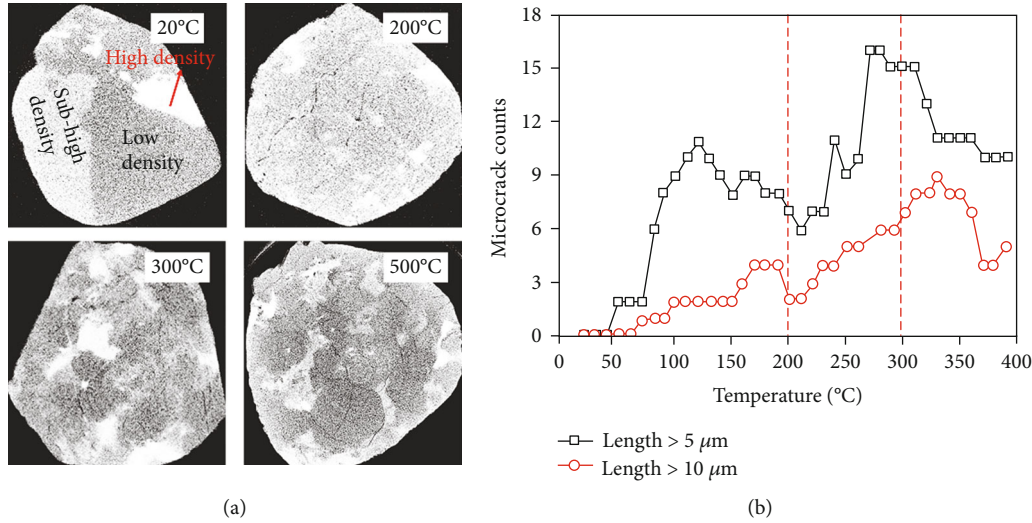


FIGURE 7: CT images of meso-structure during thermal cracking of Luhui granite specimen (modified from Zhao et al. [16]) (a); Variation in the quantity of micro-crack of Luhui granite (modified from Feng et al. [7]) (b).

modulus values as well as the normalized tangent modulus and the temperature, respectively.

The UCS values of Luhui granite at room temperature varies because of the difference of sampling locations and weathering conditions of rock specimen, for instance, the UCS value of Luhui granite that we obtained is 116 MPa, which differs from Xi and Zhao's result [23]. However, the tendency of UCS variation with temperatures is consistent. Three sections are observed from the UCS vs temperature curves. Section I: UCS values decrease slightly at the temperature range of 20-200°C. Section II: UCS values decreases sharply from 200 to 300°C. Section III: The decreasing rate of UCS stabilizes from 300 to 500°C. Specifically, the strength of rock would be further quenching weakened by 10%, 20% and 30% at 200°C, 300°C and 500°C, respectively. Apart from the UCS values, the relationship between the tangent modulus of the Luhui granite specimens and the temperature is also obtained. It was found that the tangent modulus decreases with the temperature for both straightforward heated and quenched granite specimens (Figures 9(c) and 9(d)).

In addition, the normalized UCS and tangent modulus values obtained from the quenching test are smaller than those values that gained from the high-temperature conditions. Furthermore, the quenched normalized curves decrease faster than that of high-temperature curves, meaning that quenching or injecting cold water into HDR would further weaken the rock and creates thermal damage to the rock structure.

Granite is one of the crystalline rocks. In the heterogeneous rock, thermal cracking is rather random. The main reason for thermally induced micro-crack occurrence is inharmonious thermal expansion of mineral grains, which can result in thermal stress in granite. Temperature change (i.e. thermal gradient) is the main factor that induces thermal stress. Specifically, a larger temperature change always implies a higher thermal stress. Once local thermal stress exceeds the binding stress among the same/different constituted particles, thermal cracking would occur and thus result in micro-crack initiation, propagation and interconnection. Therefore, quench-

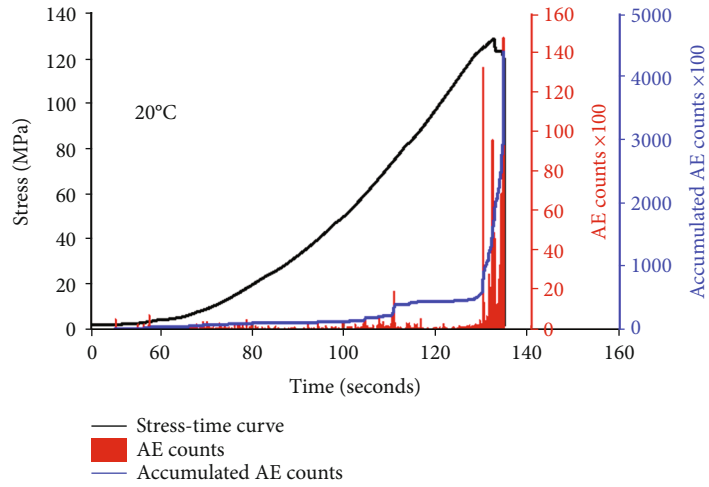
ing (with a sharp temperature change) induced rock damage is much more destructive than normal temperature rising.

5. Implications of Geothermal Mining in HDR by EGS

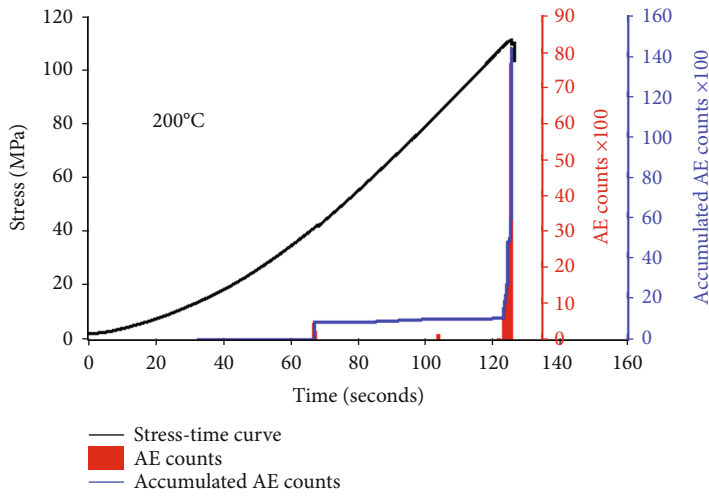
The temperature variation may induce the change of mechanical parameters and may result in the thermal shock to the granite specimens [23, 51, 52]. The temperature has a great influence on the mechanical parameters of granite, which is mainly reflected in the tangent modulus, compressive strength, etc..

As shown in Figure 1, the concept of EGS is to exploit geothermal resources from the earth by drilling wells into HDR. A well is drilled first to inject cold water at high pressure to stimulate or hydraulically fracturing the natural rock joints, thereby creating a geothermal reservoir. Injected cold water picks up heat and returns to the surface via the production well. In the process injecting cold water to HDR, the rock would rapidly be cooled at a high rate, inevitably leading to the thermal shock within the reservoir rock. Because of the rapid cooling, a relatively higher thermal gradient will be generated compared to that from the steady heat flow. This higher thermal gradient will certainly generate a greater thermal stress component.

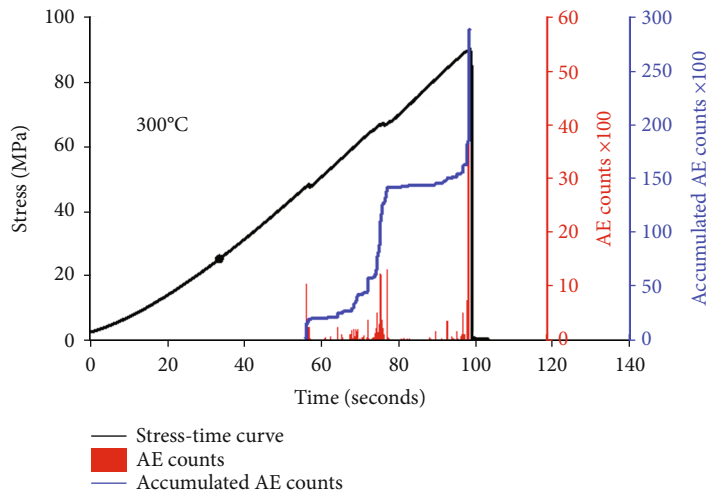
This study investigated the failure response of granite specimen, and discussed the difference of rock mechanical properties between straightforward heating and quenching treatments. Macroscopic failure rock is always caused by micro-crack initiation, propagation, interconnection etc. Fracture in rocks under compressive boundary loads is a result of the coalescence of many microcracks, not the growth of a single crack [17]. As compression stress increases and rock failure is approached, the microcrack population changes spatially from random to locally intense zones of cracking. High thermal treatment on an impermeable rock, such as quenching, is likely to create new thermal cracks. The implication of HDR is that when wells are drilled into



(a)

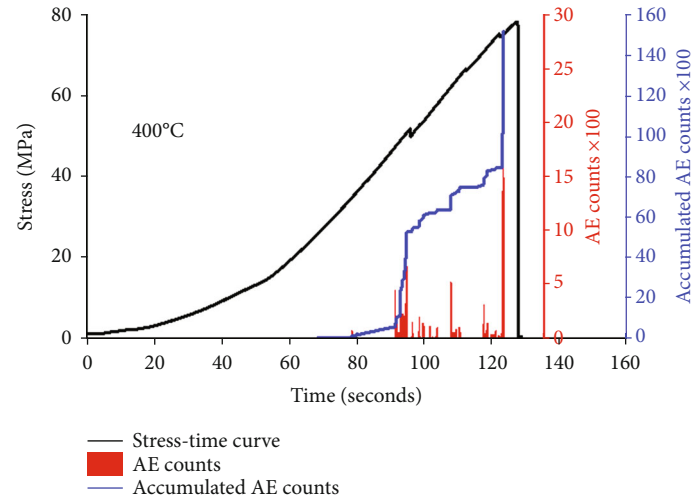


(b)

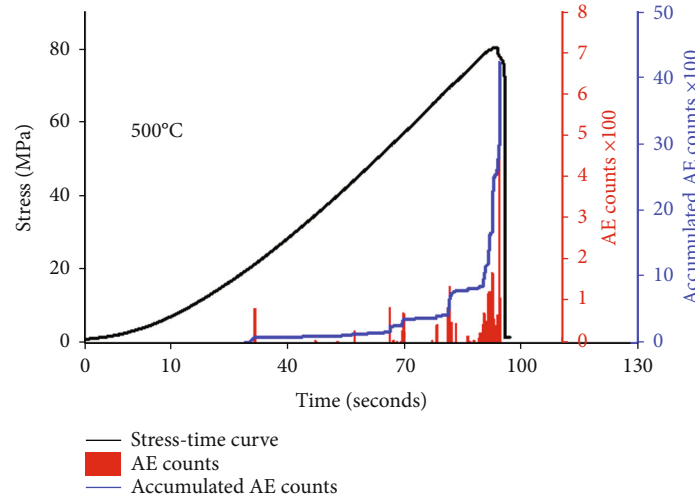


(c)

FIGURE 8: Continued.



(d)



(e)

FIGURE 8: Typical stress–strain curves and acoustic emission counts for granite samples at high temperatures. (a) 20°C; (b) 200°C; (c) 300°C; (d) 400°C; (e) 500°C.

high-temperature rocks, but with poor flow circulation because of lacking flow path, thermal cracking processes could be a worthwhile pursuit to enhance the permeability. Therefore, in the process of geothermal reservoir stimulation and enhancement, rock failure response under heating and quenching treatments cannot be ignored. During drilling, injecting, hydraulic fracturing and hydroshearing [53, 54], rock failure response and the mechanisms due to the temperature variation should be fully utilized to improve well drilling and reservoir building efficiency.

6. Conclusions

Understanding the influence of temperature on granite failure is of great interest to engineers involved with enhanced geothermal energy systems and nuclear waste disposal projects. In this study, the mechanical behavior and deformation of granite at high temperatures ranging from 20°C to 500°C were

systematically studied at both macro to micro scales. Several conclusions can be drawn.

- (1) Both the uniaxial compressive strength (UCS) and tangent modulus decrease with increasing temperature. The UCS–temperature curve can be divided into three sections: the UCS decreases slightly between 20°C and 200°C, significantly between 200°C and 300°C, and then the rate of decrease slows drastically in the interval 300°C to 500°C. However, as the temperature increases from 20°C to 500°C, the tangent modulus decreases exponentially.
- (2) The number of acoustic emission (AE) counts recorded also changes with temperature. At higher temperatures, the number of AE counts decreases and counts are recorded less frequently. This indicates that the granite becomes much more ductile at high temperatures.

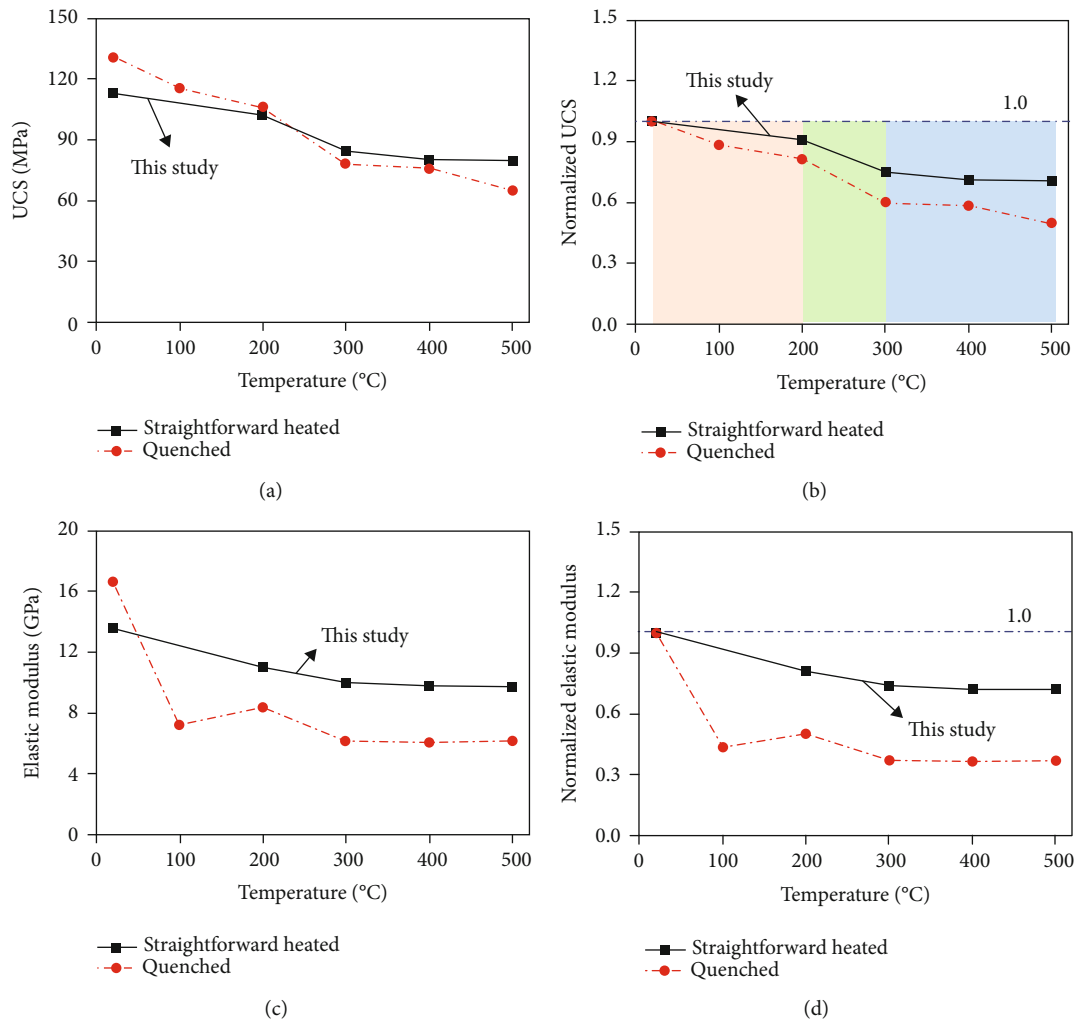


FIGURE 9: UCS and elastic modulus of granite under different thermal treatments. (a) UCS versus temperature curves; (b) Normalized UCS versus temperature curves; (c) Tangent modulus versus temperature curves; (d) Normalized tangent modulus versus temperature curves.

(3) Quenching or injecting cold water into HDR would further weaken the rock and create thermal damage to the rock structure. The strength of rock would be further quench-weakened by 10%, 20% and 30% at 200°C, 300°C and 500°C, respectively. Therefore, in EGS systems, quenching is much more destructive than the application of normal thermal stresses, which could be fully utilized to improve well drilling and reservoir stimulation.

Data Availability

The data used to support the findings of this study are available from the corresponding author upon request.

Additional Points

Highlights. (1) Both the uniaxial compression strength (UCS) and tangent modulus of granite decrease with increasing temperature. (2) The UCS-temperature curve follows a three-stage strain-dependent evolution. (3) Quenching is much more destructive than normal thermal stress.

Conflicts of Interest

The authors declare that there is no conflict of interest regarding the publication of this paper.

Acknowledgments

This work was supported by the Fundamental Research Funds for the Central Universities (2020XJNY03 and 2017XKZD06) and the YueQi Distinguished Scholar Project of China University of Mining & Technology, Beijing.

References

- [1] R. G. S. Araújo, J. L. A. O. Sousa, and M. Bloch, "Experimental investigation on the influence of temperature on the mechanical properties of reservoir rocks," *International Journal of Rock Mechanics & Mining Sciences*, vol. 34, no. 3-4, pp. 298.e1-298.16, 1997.
- [2] S. J. Bauer and J. Handin, "Thermal expansion and cracking of three confined water-saturated igneous rocks to 800°C," *Rock Mechanics & Rock Engineering*, vol. 16, no. 3, pp. 181-198, 1983.

- [3] R. D. Dwivedi, R. K. Goel, V. V. R. Prasad, and A. Sinha, "Thermo-mechanical properties of Indian and other granites," *International Journal of Rock Mechanics & Mining Sciences*, vol. 45, no. 3, pp. 303–315, 2008.
- [4] Y. Mahmutoglu, "Mechanical behaviour of cyclically heated fine grained rock," *Rock Mechanics & Rock Engineering*, vol. 31, no. 3, pp. 169–179, 1998.
- [5] J. Fan, P. Liu, J. Li, and D. Jiang, "A coupled methane/air flow model for coal gas drainage: model development and finite-difference solution," *Process Safety and Environmental Protection*, vol. 141, pp. 288–304, 2020.
- [6] A. Liu, S. Liu, X. Hou, and P. Liu, "Transient gas diffusivity evaluation and modeling for methane and helium in coal," *International Journal of Heat and Mass Transfer*, vol. 159, article 120091, 2020.
- [7] Z. Feng, Y. Zhao, Y. Zhang, and Z. Wan, "Real-time permeability evolution of thermally cracked granite at triaxial stresses," *Applied Thermal Engineering*, vol. 133, pp. 194–200, 2018.
- [8] C. Goetze, "High temperature rheology of westerly granite," *Journal of Geophysical Research*, vol. 76, no. 5, pp. 1223–1230, 1971.
- [9] F. E. Heuze, "High-temperature mechanical, physical and Thermal properties of granitic rocks– A review," *International Journal of Rock Mechanics & Mining Sciences & Geomechanics Abstracts*, vol. 20, no. 1, pp. 3–10, 1983.
- [10] S. Kou, "Effect of thermal cracking damage on the deformation and failure of granite," *Acta Mechanica Sinica*, vol. 242, pp. 235–240, 1987.
- [11] S. Liu and J. Xu, "An experimental study on the physico-mechanical properties of two post-high- temperature rocks," *Engineering Geology*, vol. 185, no. 4, pp. 63–70, 2015.
- [12] I. van der Molen, "The shift of the α - β transition temperature of quartz associated with the thermal expansion of granite at high pressure," *Tectonophysics*, vol. 73, no. 4, pp. 323–342, 1981.
- [13] Q. Sun, W. Zhang, L. Xue, Z. Zhang, and T. Su, "Thermal damage pattern and thresholds of granite," *Environmental Earth Sciences*, vol. 74, no. 3, pp. 2341–2349, 2015.
- [14] Z. Wan, Y. Zhao, F. Dong, Z. Feng, N. Zhang, and J. Wu, "Experimental study on mechanical characteristics of granite under high temperatures and triaxial stresses," *Chinese Journal of Rock Mechanics & Engineering*, vol. 27, no. 1, pp. 72–77, 2008.
- [15] T. F. Wong, "Effects of temperature and pressure on failure and post-failure behavior of westerly granite," *Mechanics of Materials*, vol. 1, no. 1, pp. 3–17, 1982.
- [16] Y. S. Zhao, Z. J. Wan, Z. J. Feng, Z. H. Xu, and W. G. Liang, "Evolution of mechanical properties of granite at high temperature and high pressure," *Geomechanics and Geophysics for Geo-Energy and Geo-Resources*, vol. 3, no. 2, pp. 199–210, 2017.
- [17] R. L. Kranz, "Microcracks in rocks: a review," *Tectonophysics*, vol. 100, no. 1-3, pp. 449–480, 1983.
- [18] X. Xu, Z. Kang, M. Ji, W. Ge, and J. Chen, "Research of micro-cosmic mechanism of brittle-plastic transition for granite under high temperature," *Procedia Earth & Planetary Science*, vol. 1, no. 1, pp. 432–437, 2009.
- [19] H. Zhu, Z. Yan, T. Deng, J. Yao, L. Zeng, and J. Qiang, "Testing study on mechanical properties of tuff, granite and breccia after high temperatures," *Chinese Journal of Rock Mechanics & Engineering*, vol. 25, no. 10, pp. 1945–1950, 2006.
- [20] S. Yin, R. Shu, X. Li, P. Wang, and X. Liu, "Comparison of mechanical properties in high temperature and thermal treatment granite," *Transactions of Nonferrous Metals Society of China*, vol. 26, no. 7, pp. 1926–1937, 2016.
- [21] L. P. Zhi, J. Y. Xu, J. Z. Jin, S. Liu, and T. F. Chen, "Research on ultrasonic characteristics and mechanical properties of granite under post-high temperature," *Chinese Journal of Underground Space and Engineering*, vol. 8, no. 4, pp. 54–59, 2012.
- [22] Y. Chen, W. Shao, and Y. Zhou, "Experimental study on mechanical properties of granite after high temperature," *Chinese Quarterly of Mechanics*, vol. 32, no. 3, pp. 397–402, 2011.
- [23] B. Xi and Y. Zhao, "Experimental research on mechanical properties of water-cooled granite under high temperatures within 600°C," *Chinese Journal of Rock Mechanics & Engineering*, vol. 29, no. 5, pp. 892–898, 2010.
- [24] S. J. Du, H. Liu, H. T. Zhi, and H. H. Chen, "Testing study on mechanical properties of post-high-temperature granite," *Chinese Journal of Rock Mechanics & Engineering*, vol. 23, no. 14, pp. 2359–2364, 2004.
- [25] Y. L. Chen, S. R. Wang, J. Ni, R. Azzam, and T. M. Fernándezsteeger, "An experimental study of the mechanical properties of granite after high temperature exposure based on mineral characteristics," *Engineering Geology*, vol. 220, pp. 234–242, 2017.
- [26] S. Q. Yang, P. G. Ranjith, H. W. Jing, W. L. Tian, and Y. Ju, "An experimental investigation on thermal damage and failure mechanical behavior of granite after exposure to different high temperature treatments," *Geothermics*, vol. 65, pp. 180–197, 2017.
- [27] G. M. N. Rao and C. R. Murthy, "Dual role of microcracks: toughening and degradation," *Canadian Geotechnical Journal*, vol. 38, no. 2, pp. 427–440, 2001.
- [28] L. Griffiths, O. Lengliné, M. J. Heap, P. Baud, and J. Schmittbuhl, "Thermal cracking in westerly granite monitored using direct wave velocity, coda wave interferometry and acoustic emissions," *Journal of Geophysical Research Solid Earth*, vol. 123, no. 3, pp. 2246–2261, 2018.
- [29] J. Browning, P. Meredith, and A. Gudmundsson, "Cooling-dominated cracking in thermally stressed volcanic rocks," *Geophysical Research Letters*, vol. 43, no. 16, pp. 8417–8425, 2016.
- [30] K. Kim, J. Kemeny, and M. Nickerson, "Effect of rapid thermal cooling on mechanical rock properties," *Rock Mechanics & Rock Engineering*, vol. 47, no. 6, pp. 2005–2019, 2014.
- [31] C. V. Raman and T. M. K. Nedungadi, "The α - β transformation of quartz," *Nature*, vol. 145, no. 3665, pp. 147–1912, 1940.
- [32] Y. Chen, D. Li, Q. Jiang, and C. Zhou, "Micromechanical analysis of anisotropic damage and its influence on effective thermal conductivity in brittle rocks," *International Journal of Rock Mechanics & Mining Sciences*, vol. 50, no. 2, pp. 102–116, 2012.
- [33] Y. Zhao, Q. Meng, T. Kang, N. Zhang, and B. Xi, "Micro-ct experimental technology and meso-investigation on thermal fracturing characteristics of granite," *Chinese Journal of Rock Mechanics & Engineering*, vol. 27, no. 1, pp. 28–34, 2008.
- [34] L. Griffiths, M. J. Heap, P. Baud, and J. Schmittbuhl, "Quantification of microcrack characteristics and implications for stiffness and strength of granite," *International Journal of Rock Mechanics Mining Sciences*, vol. 100, pp. 138–150, 2017.
- [35] G. Dolino and J. P. Bachheimer, "Fundamental and second-harmonic light scattering by the α - β coexistence state of quartz," *Physica Status Solidi*, vol. 41, no. 2, pp. 673–677, 2010.

- [36] S. Kume and N. Kato, "A furnace for high-temperature X-ray diffraction topography," *Journal of Applied Crystallography*, vol. 7, no. 4, pp. 427–429, 2010.
- [37] C. M. E. Zeyen, G. Dolino, and J. P. Bachheimer, "Neutron and calorimetric observation of a modulated structure in quartz just above the α - β phase transition," *Physica B+C*, vol. 120, no. 1-3, pp. 280–282, 1983.
- [38] J. T. Fredrich and T. Wong, "Micromechanics of thermally induced cracking in three crustal rocks," *Journal of Geophysical Research Solid Earth*, vol. 91, no. B12, pp. 12743–12764, 1986.
- [39] Z. Zhang, F. Gao, and X. Xu, "Experimental study of temperature effect of mechanical properties of granite," *Rock and Soil Mechanics*, vol. 32, no. 8, pp. 2346–2352, 2011.
- [40] S. Shao, P. G. Ranjith, P. L. P. Wasantha, and B. K. Chen, "Experimental and numerical studies on the mechanical behaviour of Australian Strathbogie granite at high temperatures: an application to geothermal energy," *Geothermics*, vol. 54, no. 54, pp. 96–108, 2015.
- [41] Y. Zhao, Z. Feng, Y. Zhao, and Z. Wan, "Experimental investigation on thermal cracking, permeability under HTHP and application for geothermal mining of HDR," *Energy*, vol. 132, pp. 305–314, 2017.
- [42] A. Korinets and H. Alehossein, "Technical note on the initial non-linearity of compressive stress-strain curves for intact rock," *Rock Mechanics & Rock Engineering*, vol. 35, no. 4, pp. 319–328, 2002.
- [43] S. Zhai, G. Wu, Y. Zhang, C. Luo, and Y. Li, "Research on acoustic emission characteristics of granite under high temperature," *Chinese Journal of Rock Mechanics & Engineering*, vol. 32, no. 1, pp. 126–134, 2013.
- [44] M. Sarfarazi and S. K. Ghosh, "On the micromechanical theories of stress-induced cleavage microcracking in crystalline solids," *Engineering Fracture Mechanics*, vol. 27, no. 2, pp. 215–230, 1987.
- [45] V. M. Goritskii, "A criterion of failure of steels susceptible to propagation of brittle microcracks along crystal boundaries," *Strength of Materials*, vol. 19, no. 4, pp. 479–486, 1987.
- [46] B. Obara, "Identification of transcrystalline microcracks observed in microscope images of a dolomite structure using image analysis methods based on linear structuring element processing," *Computers & Geosciences*, vol. 33, no. 2, pp. 151–158, 2007.
- [47] P. A. Siratovich, M. C. Villeneuve, J. W. Cole, B. M. Kennedy, and F. Bégué, "Saturated heating and quenching of three crustal rocks and implications for thermal stimulation of permeability in geothermal reservoirs," *International Journal of Rock Mechanics Mining Sciences*, vol. 80, pp. 265–280, 2015.
- [48] A. Ghassemi, "A review of some rock mechanics issues in geothermal reservoir development," *Geotechnical Geological Engineering*, vol. 30, no. 3, pp. 647–664, 2012.
- [49] G. Izadi and D. Elsworth, "Reservoir stimulation and induced seismicity: roles of fluid pressure and thermal transients on reactivated fractured networks," *Geothermics*, vol. 51, pp. 368–379, 2014.
- [50] J. Taron and D. Elsworth, "Thermal-hydrologic-mechanical-chemical processes in the evolution of engineered geothermal reservoirs," *International Journal of Rock Mechanics Mining Sciences*, vol. 46, no. 5, pp. 855–864, 2009.
- [51] C. Zhou, Z. Wan, Y. Zhang, and B. Gu, "Experimental study on hydraulic fracturing of granite under thermal shock," *Geothermics*, vol. 71, pp. 146–155, 2018.
- [52] W. G. P. Kumari, P. G. Ranjith, M. S. A. Perera, and B. K. Chen, "Experimental investigation of quenching effect on mechanical, microstructural and flow characteristics of reservoir rocks: thermal stimulation method for geothermal energy extraction," *Journal of Petroleum Science Engineering*, vol. 162, pp. 419–433, 2018.
- [53] A. P. Rinaldi and J. Rutqvist, "Joint opening or hydroshearing? Analyzing a fracture zone stimulation at Fenton Hill," *Geothermics*, vol. 77, pp. 83–98, 2019.
- [54] Q. Yin, H. Jing, G. Ma, H. Su, and R. Liu, "Investigating the roles of included angle and loading condition on the critical hydraulic gradient of real rock fracture networks," *Rock Mechanics Rock Engineering*, vol. 51, no. 10, pp. 3167–3177, 2018.

Research Article

Experimental Investigation on the Stress-Dependent Permeability of Intact and Fractured Shale

Yongxiang Zheng ^{1,2} Jianjun Liu ^{2,3} Yichen Liu,^{2,4} Di Shi,^{2,3} and Bohu Zhang²

¹School of Civil Engineering, Shijiazhuang Tiedao University, Shijiazhuang, China

²School of Geoscience and Technology, Southwest Petroleum University, Chengdu, China

³Institute of Rock and Soil Mechanics, Chinese Academy of Science, Wuhan, China

⁴Team 141 of Sichuan Coalfield Geological Bureau, Deyang, China

Correspondence should be addressed to Jianjun Liu; jjliu@whrsm.ac.cn

Received 3 March 2020; Revised 29 July 2020; Accepted 21 August 2020; Published 10 September 2020

Academic Editor: Qian Yin

Copyright © 2020 Yongxiang Zheng et al. This is an open access article distributed under the Creative Commons Attribution License, which permits unrestricted use, distribution, and reproduction in any medium, provided the original work is properly cited.

The permeability of shale is extremely low. Therefore, the shale reservoir needs fracturing. The fracture network by fracturing can increase the permeability in a stimulated shale reservoir. To understand the permeability evolution in the stimulated shale reservoir, this study measured the permeability of intact and fractured shale samples with different pore pressure and confining pressure by the transient pulse test. And the differences between the two kinds of samples in permeability were analyzed. The results show that permeability magnitude of fractured shale is increased by 5 orders compared to the intact shale. It means that fracture networks after fracturing can effectively improve the permeability. Besides, the change in matrix permeability is the result of the combined effect of slippage effect and matrix deformation. At low pore pressure, the influence of slippage effect is more significant. Based on the results, an improved exponential function was established to describe the relationship between permeability and effective stress of shale matrix. Moreover, the permeability of fractured shale is still bigger than that of the shale matrix when the confining pressure is larger than pore pressure. This paper provides theoretical guidance for studying the evolution of reservoir permeability before and after fracturing.

1. Introduction

Low permeability and porosity of shale cause difficulties in shale gas exploitation [1]. Fortunately, combined with the complex structure of deep underground formation [2], the reservoir can be stimulated by hydraulic fracturing. Hydraulic fracturing is an effective method for shale gas exploitation. Fracturing is designed to create fracture networks by producing more fractures. The flow paths of gas in the stimulated shale reservoir include shale matrix and fracture network [3, 4]. It is difficult to flow in matrix with low permeability. Therefore, fractures are the main flow paths for shale gas.

Firstly, the permeability of matrix is affected by stress and flow regimes [5, 6]. Previous studies indicated that permeability is affected by the stress condition of shale reservoir. The stress of formation is affected by underground resource development [7, 8]. With the exploitation of shale gas, the

reservoir pressure decreases and the effective stress increases, which will lead to the deformation of the shale matrix and the change of reservoir permeability [9]. Stress sensitivity is defined to describe the effect of pore-throat shrinkage on permeability [10]. Therefore, understanding the relationship between permeability and stress in shale reservoir can provide guidance for effective exploitation of shale gas. In addition, permeability of matrix is also affected by the porosity of the matrix. Due to the small porosity of the matrix, the slippage effect of gas in the matrix is significant at low pressure [5].

The stress sensitivity is the effect of pore-throat shrinkage on permeability. The pore-throat shrinkage is the result of effective stress change. Therefore, the effective stress is a vital factor on shale permeability. There are many studies on permeability and effective stress. The relationship between them can be described by exponential, logarithmic, and power

relationships [11]. Based on the laboratory experiment, Dong et al. [12] adopted the power law to describe the relationship between permeability and effective stress. And some other scholars [13, 14] suggested that power functions are appropriate to describe this relationship. There are also some studies that applied the logarithmic relationship to describe the stress sensitivity of permeability. Jones [15] described fractured carbonate permeability with respect to effective stress by a logarithmic empirical relationship. Walsh [16] represented the theoretical derivation procedure of this logarithmic relationship by using Poiseuille's equation of fracture system. Among them, the most popular empirical relationship is the exponential relationship. Zhang et al. [17] measured the permeability of shale in Lower Silurian Longmaxi Formation and suggested that the exponential law can well describe the relationship between shale permeability and various effective stress. Other studies [18–20] about shale permeability also showed that the exponential law was an appropriate method to present the relationship. In conclusion, the exponential relationship is the most widely accepted. Therefore, exponential function was chosen as the basic relationship to describe permeability and effective stress.

The fractures are the main flow path. Therefore, permeability considering fractures is of great importance to shale reservoir. There are some laboratory or theoretical studies about permeability of fractured shale. Wu et al. [21] and Tan et al. [22] studied the permeability evolution of proppant-supported fractures under dynamic stress conditions by a series of laboratory experiments. Generally, the cracks in fractured shale were created by artificial splitting. Besides, some splitting fractures were generated after high-temperature exposure in Yin et al.'s experiment [23]. Based on the fractured cores, Su et al. [24] studied the effect of mechanical opening (normal displacement) of fractures on the permeability. Zhou et al. [25] indicated that the fracture permeability was mainly determined by several factors including the shear displacement, integral roughness of the fracture planes, and the local roughness. Ma et al. [26] investigated the anisotropic permeability of cubic samples from Lower Silurian Longmaxi Formation. The results suggested that microfractures were critical to permeability in the parallel to bedding direction. And Zhou et al. [27] investigated the permeability change in a stimulated shale gas reservoir under high effective stress. Then, they derived a stress-dependent fracture permeability model based on the fracture compressibility models. Yin et al. [28] conducted stress-dependent flow tests on real rock specimens containing fracture networks with various included angles. Chen et al. [29] derived a theoretical correlation between shale permeability and effective stress. The results indicated that fracture permeability might decrease significantly with the reservoir pressure drawdown.

There are some meaningful results about the permeability of shale in previous studies. However, the researches on the stress sensitivity of shale matrix were mainly based on the research with high pore pressure, and less consideration was given to the permeability variation rule with low pore pressure. In this study, the permeability of intact shale (shale matrix) and fractured shale as a function of pressure was

measured. For the permeability of shale matrix, we measured the stress sensitivity of permeability under both low and high pore pressures. In addition, we improved the exponential model to characterize the permeability and effective stress of shale matrix. By comparing the new model with the experimental results and the experimental data in the existing literature, it is found that the improved exponential relation has a higher fitting accuracy. For fractured shale, we analyze the permeability evolution law of fractured shale and discuss the reason why stimulated new fractures can still increase reservoir permeability after closure. In addition, equivalent fracture width is applied to characterize the permeability of fractures, and the relationship between equivalent fracture width and effective stress is established. The results include the permeability evolution of shale matrix and fracture system, which provides a theoretical basis for the permeability evolution of stimulated reservoir in the process of shale gas development.

The innovation of this article is mainly reflected in the following three aspects. The first innovation of this article is to supplement and improve the experimental plan. The experiment tests the permeability changes under low pore pressure and high pore pressure conditions and discusses the effect of slippage effect and effective stress on permeability. Most of the previous people only considered the effect of effective stress under high pore pressure conditions. In addition, this experiment also measured the permeability of fractured shale and intact shale and analyzed the influence of fracture on the overall permeability of shale sample by comparison. The second innovation is the improvement of the traditional exponential relationship. The fitting results of the experimental results in this experiment and other literatures indicate that the improved relationship has higher fitting accuracy. The third innovation is to analyze the reason why the permeability of the fracture after the fracturing is still higher than that of the matrix when the confining pressure is greater than the pore pressure.

2. Materials and Methods

2.1. Introduction of Samples. The samples were taken from the Longmaxi Formation in the Changning section of Shuanghe Town, Sichuan Basin. The sampling site is located in Yanzi Village, Shuanghe Town, Yibin City, Sichuan Province, China. The Silurian Longmaxi Formation is composed of black, gray-black, and dark gray calcareous and siliceous shale and sandy shale. And it is in integrated contact with the underlying Upper Ordovician.

The uniaxial compression test and SEM test were chosen to determine the mechanical properties and microstructure of the samples. The uniaxial compression test showed that the elastic modulus was in the range of 14.04–25.69 GPa and the Poisson's ratio was in the range of 0.14–0.389. The results indicated that the samples were hard to deform with a higher elastic modulus. Elastic modulus is a measure of the ability of an object to resist elastic deformation. Then, the greater the elastic modulus, the greater the object's ability to resist elastic deformation. Under a certain load, the greater the elastic modulus, the smaller the deformation.

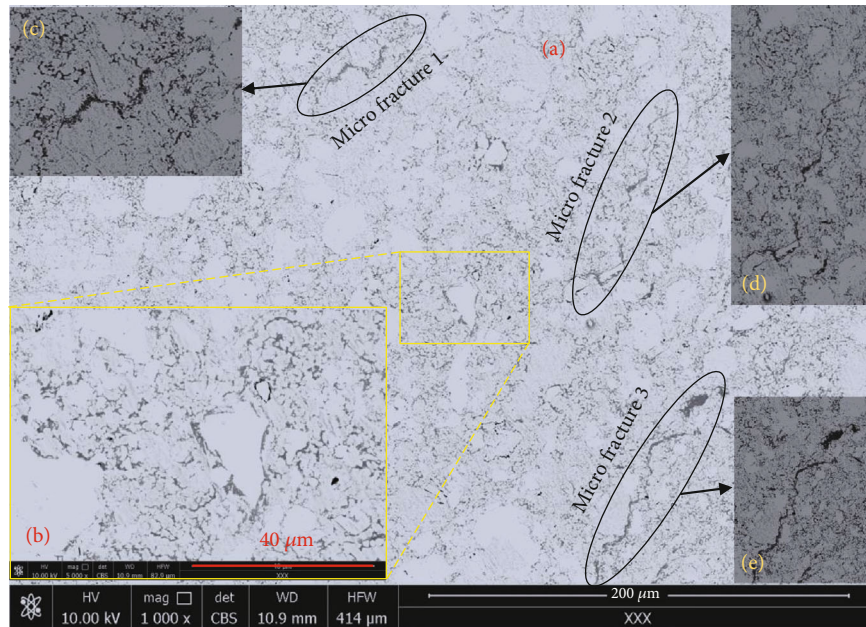


FIGURE 1: The microscopic pore of shale samples.

The SEM test has an ultrahigh resolution and can produce secondary electron images of the surface appearance of various solid specimens and comprehensively analyzes the surface characteristics of rocks [30, 31]. The SEM test was employed to understand the microscopic pore structure of shale samples. The results are shown in Figure 1. Figure 1(a) is a SEM photo of the shale surface magnified 1000 times. The figure shows that the voids mainly include microfractures and pores. The main of void volume on the surface is micropores. To show the micropores more clearly, the local micropores (yellow rectangle in Figure 1) were enlarged. Figure 1(b) shows the SEM photo magnified 5000 times. In the figure, the reference scale is $40\ \mu\text{m}$. As can be seen from the figure, the pore size is significantly smaller than the scale length. Therefore, the scale of micropores in the matrix is in nanoscale. In addition to micropores, there are some scattered fractures on the surface. The fracture area is amplified locally to observe the morphology of those fractures. Figures 1(c)–1(e) show the morphology of the three microfractures, respectively. As shown in the figures, the fracture length is much larger than the radius of micropores. The micropores are connected by those long fractures. As the microstructure of matrix shows, the scale of pore in matrix is very small. The small pores result in the low permeability. Besides, there are some fractures. However, the fractures are not long enough to connect with other fractures. Therefore, the permeability of matrix is still low. To some extent, it can be considered that few microfractures do not increase permeability.

2.2. Sample Preparation. The main purpose is to study the permeability variation of the intact and fractured shale. As shown in Figure 2, there are 4 cylindrical samples with a diameter of 25 mm and a height of 50 mm drilled from the outcrop. Among them, KJ1 and KJ2 are intact cores without

fractures. KJ3 and KJ4 are fractured cores with artificial fractures. A schematic view of the fractured core is shown in Figure 2(b). As shown in the figure, a fracture located approximately in the middle of core penetrates this core. An end surface is shown in Figure 2(c). To obtain accurate experimental results, the geometry, weight, and porosity of each core were measured. The details are listed in Table 1.

From Table 1, the porosity range of the shale matrix falls in the range from 4.08% to 4.71%, while the porosity range of the fractured cores is from 6.77% to 7.01%. The porosity of each sample is at a low scale overall. Besides, the porosity of the fractured core is slightly bigger than that of the intact core. This indicated that fractures increased the porosity of the samples.

2.3. Laboratory Measurement System. The Black-Stone II stress-sensitive pulse tester, which was jointly developed by the Institute of Rock and Soil Mechanics of the Chinese Academy of Sciences and Southwest Petroleum University, was chosen to measure the permeability. The photo of this device is shown in Figure 3(a). And this device measures permeability by the transient pulse method. This test system mainly includes a confining system, upstream system, downstream system, and core holder. The details are plotted in Figure 3(b). The confining pressure (CP) of the system can be up to 60 MPa, and the pore pressure (PP) can be up to 40 MPa.

This device measures permeability by the transient pulse method. First, the pressure within the system should be balanced. Once the pressure is balanced, a transient pulse is applied to the upstream chamber (V1, Figure 3). Then, the pressure in V1 will gradually transfer to downstream chamber V2. Consequently, the pressure in V1 decreases, and the pressure in V2 increases until reaching a new pressure balance. A pressure decay curve at V1 can be plotted during

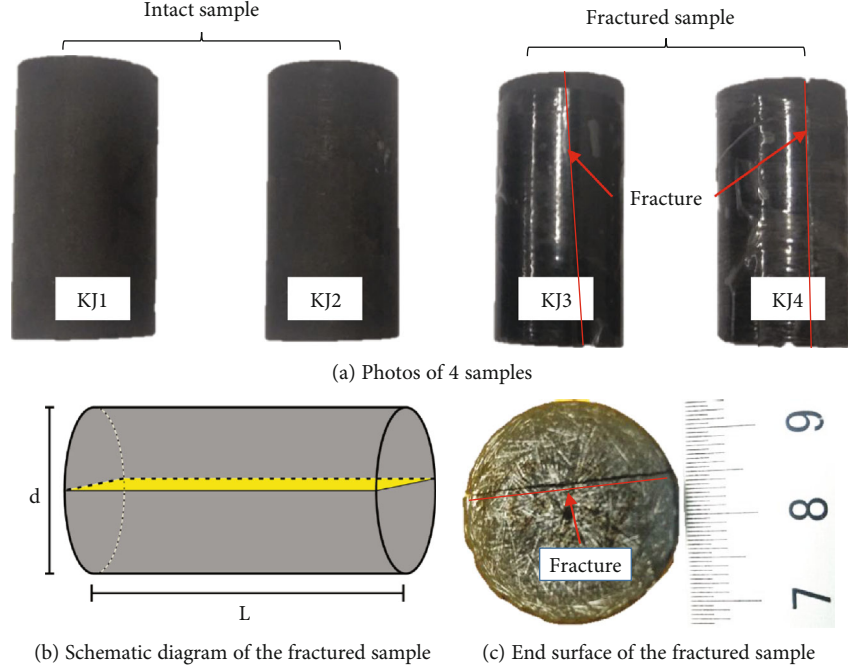


FIGURE 2: The intact and fractured samples.

TABLE 1: The parameter values of samples.

No.	Length (cm)	Diameter (cm)	Weight (g)	Porosity
KJ1	4.998	2.535	63.87	4.08%
KJ2	4.987	2.536	63.56	4.71%
KJ3	5.025	2.418	56.65	7.01%
KJ4	5.011	2.422	57.27	6.77%

the pressure change. Based on this curve, the permeability of the test sample can be obtained. The mathematical model of permeability by the transient pulse method is [32, 33]

$$\frac{\partial^2 p}{\partial l^2} = \left[\frac{\mu}{k} \phi \left(C_f + \frac{C_{\text{eff}}}{\phi} - \frac{1 + \phi}{\phi} C_s \right) \right] \frac{\partial p}{\partial t}, \quad t > 0, 0 < l < L, \quad (1)$$

where p is the pressure (MPa), l is the distance along the length of the measured rock sample (cm), k is the permeability of the measured rock sample (μm^2), μ is the dynamic viscosity of the fluid (10^{-3} Pa·s), ϕ is the porosity, C_f is the compression coefficient of the fluid (MPa^{-1}), C_s is the compression coefficient of samples (MPa^{-1}), and C_{eff} is the pore compression coefficient samples (MPa^{-1}). The boundary condition is

$$\begin{aligned} \frac{\partial p}{\partial l} &= \frac{\mu V_u C_f}{kA} \frac{\partial p}{\partial t}, \quad t > 0, l = 0, \\ \frac{\partial p}{\partial l} &= -\frac{\mu V_d C_f}{kA} \frac{\partial p}{\partial t}, \quad t > 0, l = L, \end{aligned} \quad (2)$$

where A is the cross-section area (cm^2), V_u is the volume of upstream chamber (cm^3), and V_d is the volume of downstream chamber (cm^3). The initial condition is

$$\begin{aligned} p_u(0, 0) &= p_i, \quad t = 0, l = 0, \\ p_R(l, 0) &= p_0, \quad t = 0, 0 < l < L, \\ p_d(L, 0) &= p_0, \quad t = 0, l = L, \end{aligned} \quad (3)$$

where p_i is the pressure of upstream chamber when the pulse pressure is applied (MPa).

The mathematical models of the transient pulse method mainly include an approximation method, plate method, and Jones' method. Due to the fact that the medium in this experiment was nitrogen, Jones' method was chosen for this test [34]. Jones' method is a simplification of a mathematical model for the transient pulse method. The analytical solution of the gas permeability can be expressed as

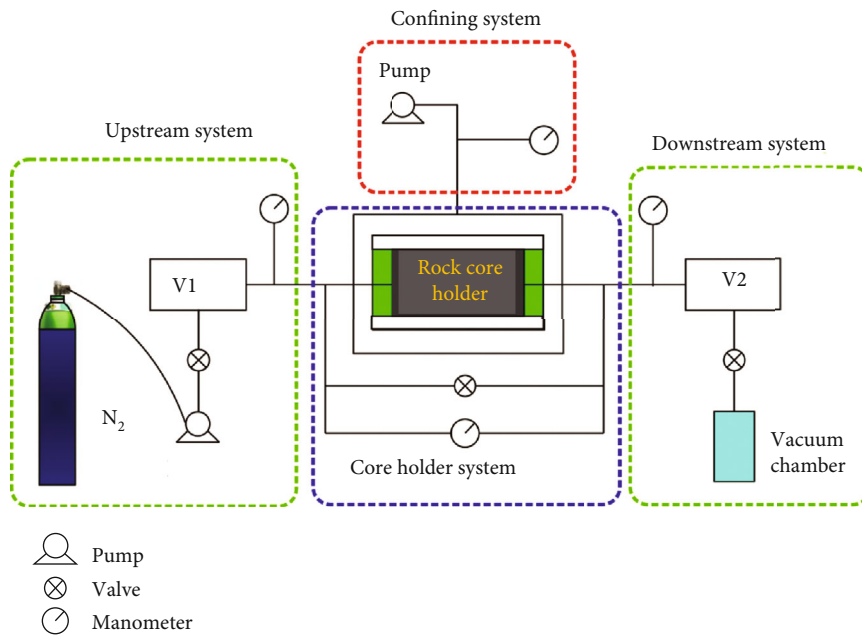
$$k_g = \frac{-14696 m_1 \mu_g L f_z}{f_1 A p_m \left(\frac{1}{V_u} + \frac{1}{V_d} \right)}, \quad (4)$$

where m_1 is the slope of the pressure decay curve, μ_g is the viscosity (10^{-3} Pa·s), f_z is the correction factor of gas compression, f_1 is the correction factor of mass flow, and p_m is the average pore pressure (MPa).

2.4. Experimental Testing Process and Design. Transient pulse testing of shale permeability can be divided into two parts: aging test and measurement. The aging test plays a crucial role in the measurement of stress sensitivity of permeability. The aging test eliminates irreversible deformation in the test by the loading and unloading process of the confining



(a) Photo of Black-Stone II pulse tester



(b) Equipment composition diagram

FIGURE 3: The measurement system.

pressure. Therefore, the rock samples were first subjected to the aging test. Through the aging test, the stability and reliability of the test results can be improved. The steps of the aging test are as follows. First, the pore pressure and the chamber pressure should be stabilized. And the pore pressure is maintained at 0.8 MPa. Then, the confining pressure was sequentially increased from 5 MPa to 40 MPa with a step of 5 MPa. Next, the confining pressure is reduced from 40 MPa to 5 MPa with every step of 5 MPa. When the confining pressure is stabilized for every step, a pulse pressure is applied to determine the corresponding permeability. Repeat the loading-unloading pressure process.

After the aging test was completed, the permeability of sample can be measured. At first, the permeability changed by the pore pressure with a fixed confining pressure of 30 MPa was measured. The measured results are plotted in Figure 4. The permeability declines first and then rises with the increase of pore pressure. As the figure shows, the pore pressure at turning point is 6 MPa. According to the literature [5], the slippage effect in the matrix is obvious with low pore pressure. The slippage effect can increase gas permeability. The slippage effect becomes weaker as the pore pressure rises. Therefore, the permeability drops as the pore pressure rises. The slippage effect only occurs in the shale

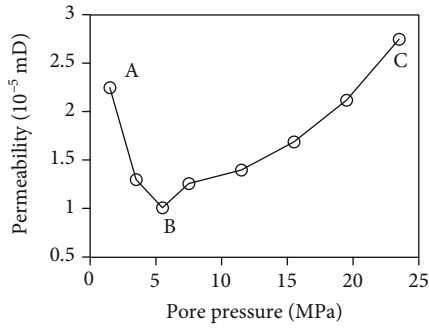


FIGURE 4: Relationship of permeability and pore pressure.

matrix, while the gas is in laminar flow in the fracture system. Therefore, this experiment discusses both low pore pressure (2-6 MPa) and high pore pressure (8-24 MPa) for intact shale. In addition, to analyze the permeability evolution of fractured shale, a permeability test scheme for fractured shale was designed. The details about experiments design are summarized in Table 2.

3. Results

3.1. Permeability of Intact Shale. Figure 4 shows the permeability curve of KJ1 changing with pore pressure at a fixed confining pressure of 30 MPa. As pore pressure rises, permeability drops first and then rises. When the pore pressure is less than 6 MPa, permeability reduces as the pore pressure rises. Qian et al. [35] and Yang et al. [5] also had the similar results by experiments. They believed that the effective stress decreased with the increase of pore pressure and then the matrix pores were larger. Consequently, the permeability of matrix is affected by both matrix deformation and slippage effects. In a low pore pressure (0-6 MPa), the slippage effect of gas is obvious, and its influence on the permeability is large. When the pore pressure is bigger than 6 MPa, the matrix deformation becomes the main factor. In this condition, the permeability increases with the increase of pore pressure.

In most cases, a pore with a large radius means large permeability. But a pore with a small radius may have a larger flow capacity than that with a large radius with a little difference in pore structure due to the slippage effect. The pore radius of the shale is too small to ignore the slippage effect due to low pore pressure. And the slippage effect is the main factor affecting permeability. Therefore, pores with a small radius have larger flow capacity. Conversely, when pores are larger, the slippage effect can be ignored. Matrix deformation becomes the main factor affecting permeability. Then, the large pore radius means large permeability.

In short, the slippage effect of gas on permeability is dominant when pore pressure is small. And permeability decreases as pore pressure rises. When pore pressure is larger than the critical pressure (6 MPa in this study), the key factor affecting permeability is matrix deformation. And permeability increases as pore pressure rises. It is worth noting that regardless of the low or high pore pressure, the permeability of matrix is affected by both slippage effect and matrix

deformation. One factor will be the dominant factor under a certain condition. As mentioned above, the change of permeability with pore pressure is different under different pressure conditions. Therefore, the test about matrix permeability is divided into two cases: low pore pressure and high pore pressure.

3.1.1. Permeability Variation under Low Pore Pressure. Permeability variation under low pore pressure is discussed in this section. The matrix permeability is measured by changing confining pressure (abbreviated as CP in the next figures) with a fixed pore pressure (abbreviated as PP in the next figures). Figure 5(a) shows the results of permeability change with confining pressure when the pore pressure is 2, 4, and 6 MPa, respectively. First of all, it can be clarified that permeability decreases as confining pressure rises under a constant pore pressure. Besides, the decaying rate of permeability is faster at a low confining pressure. With the increase of confining pressure, it is more difficult for the shale matrix to be compressed. Consequently, the decaying rate of permeability reduces significantly. In addition, for one fixed confining pressure, permeability decreases as pore pressure increases. Moreover, the decrease magnitude of permeability between 2 and 4 MPa is greater than that of the interval of 4-6 MPa. It indicates that the decay rate of the permeability reduces as the pore pressure rises. This is consistent with the results of the A-B interval in Figure 4.

Permeability variation with effective stress is shown in Figure 5(b). For a fixed pore pressure, permeability is negatively related to effective stress. Moreover, the permeability is different even though the effective stress is the same. It can be deduced that the pore pressure is the reason for the difference. Overall, the permeability at lower pore pressure is bigger. It indicates that the effective stress is not the key factor for permeability change at low pore pressure. The key factor should be the slippage effect. Consequently, the pore pressure condition cannot be ignored for the relationship between permeability and effective stress at low pore pressure.

Generally, the reservoir pressure is maintained at a higher condition during gas development. The low pore pressure condition always appears in the late development period. At this time, the permeability of matrix would rise gradually as the reservoir pressure gradually decreases. Therefore, this conclusion is mainly used to guide the development of gas reservoir in the late period.

3.1.2. Permeability Variation at High Pore Pressure. Generally, the reservoir pressure is maintained at a higher value. With the gas production, the pore pressure gradually decreases, while the in situ stress of formation does not change significantly. Therefore, the experimental scheme of changing pore pressure with fixed confining pressure was selected. The results are shown in Figure 6. The order of matrix permeability is $1e^{-5}$ mD. The matrix permeability varies from $1e^{-5}$ to $5e^{-5}$ mD. Matrix permeability increases as the pore pressure increases. The slope of the curves is larger for higher pore pressure, indicating that the permeability is greatly affected by the pore pressure. Conversely, the curve

TABLE 2: Design of experiments.

	Samples	Test type	Confining pressure (MPa)	Pore pressure (MPa)
	KJ1	Basic case	30	2, 4, 6, 8, 10, 12, 14, 16, 18, 20
Intact shale	KJ1	Low pore pressure	10, 15, 20, 25, 30	2, 4, 6
	KJ1, KJ2	High pore pressure	30, 35, 40	8, 12, 16, 20, 24
Fractured shale	KJ3, KJ4	High pore pressure	30, 35, 40	8, 12, 16, 20, 24

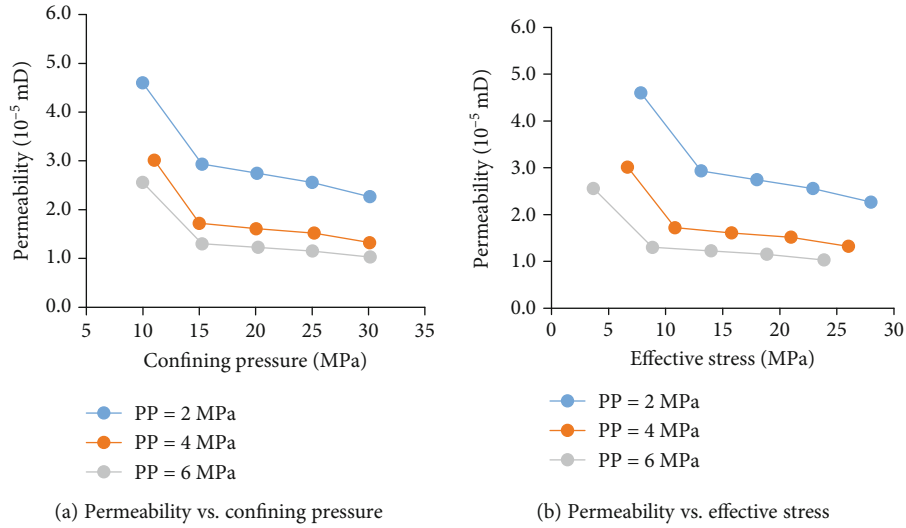


FIGURE 5: Matrix permeability at low pore pressure.

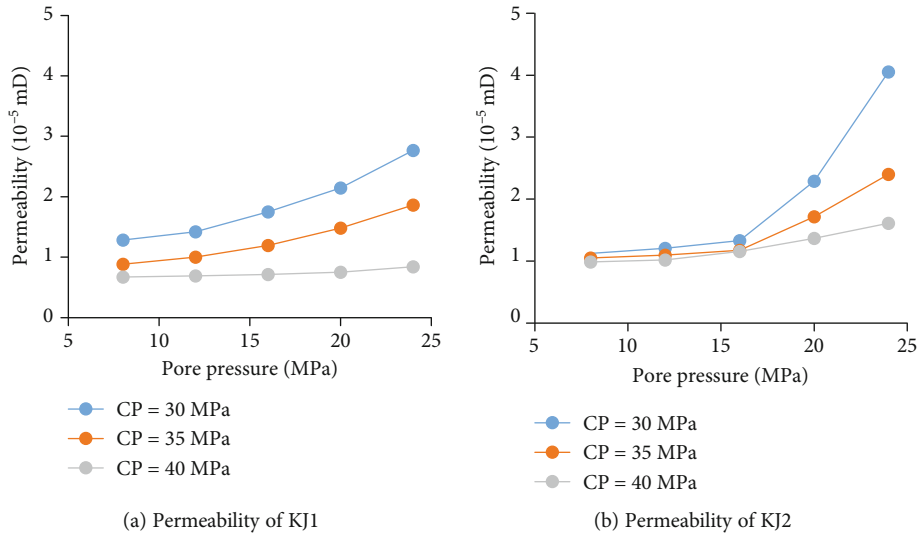


FIGURE 6: Relationship between permeability and pore pressure.

slope is smaller for lower pore pressure, indicating that the influence of pore pressure on the permeability reduces gradually. In the early period of development, the pore pressure is high. Consequently, the pore pressure has a great influence on the permeability during the early period. Then, the permeability gradually becomes stable in the late period of development when pore pressure reduces.

In addition, the permeability of matrix is also affected by confining pressure. As shown in the figures, the permeability varies greatly as pore pressure is 30 MPa. But the permeabil-

ity varies little as pore pressure is 40 MPa. The confining pressure means a change in the depth of the reservoir. Therefore, the greater the depth of reservoir is, the less permeability of shale matrix is affected by pore pressure.

In short, the permeability of matrix is affected by both slippage effect and effective stress under different pore pressure and confining pressure. At the condition of low pore pressure, the permeability decreases with pore pressure increase, while at the condition of high pore pressure, the permeability rises with pore pressure increase. Besides, the

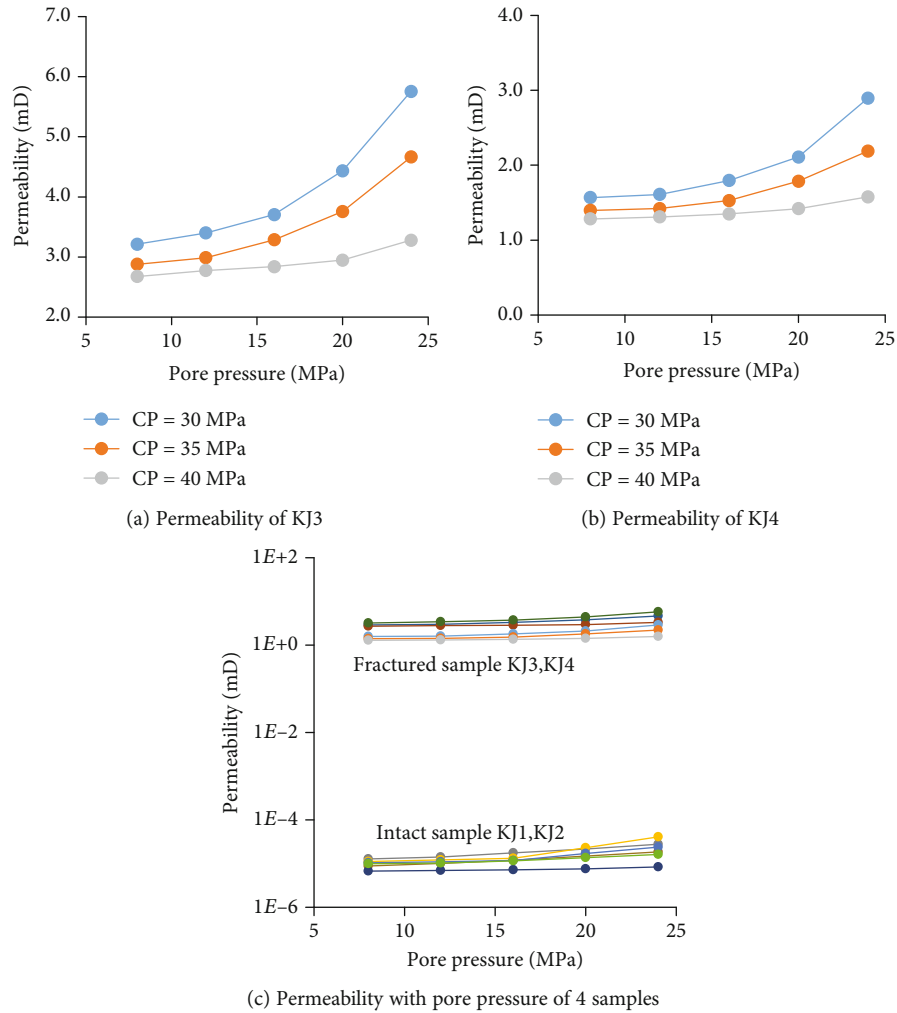


FIGURE 7: Relationship between permeability and pore pressure.

permeability of matrix reduces as confining pressure rises. The effect of gas slippage on permeability is significant at low pore pressure and weakened at high pore pressure.

3.2. Permeability of Fractured Shale. The permeability of fractured shale is discussed in this section. Figure 7 illustrates the influence of confining pressure and pore pressure on permeability of fractured shale. The permeability of fractured shale sample ranges from 1 mD to 6 mD. Permeability variation of fractured shale is similar to that of intact shale. The permeability rises as the pore pressure increases and reduces as the confining pressure increases.

The results of permeability for both intact and fractured shale are summarized in Figure 7(c). As the figure shows, permeability magnitude of fractured shale is raised by five orders compared to the intact shale. The fractures in this experiment do not contain proppants and can be considered self-supporting fractures. From the results above, we can safely draw a conclusion that the self-supporting fractures greatly enlarge the permeability of sample. And the fractures are the main flow paths for shale gas. For an ideal situation, if

a fracture was completely closed by the confining pressure, there would no conductivity theoretically. Actually, the measured permeability is much bigger than the matrix permeability. This result is consistent with Gutierrez's conclusion: the fracture permeability remained much higher than the intact shale (or matrix) permeability [36]. Gutierrez just described the results but did not explain why. We would discuss the reason why the samples can still increase the permeability after the fractures closed in Section 4.2 as a discussion.

4. Discussion

4.1. Relationship between the Permeability of Matrix and Effective Stress

4.1.1. Improved Exponential Function. For the cases of high pore pressure, the permeability of matrix is mainly affected by matrix deformation. The main factor affecting matrix deformation is effective stress. Previous studies established some relationships to describe the influence of effective stress on matrix permeability. The exponential relationship is the

TABLE 3: The fitting results.

	Samples	$a(a_0)$	$b(b_0)$	$c(c_0)$	R^2
Traditional exponential function	KJ1	$3.918e-5$	0.04872	0.7157	0.9233
	KJ2	$4.031e-5$	0.04745	0.04336	0.8811
	(KJ1 + KJ2)/2	$4.744e-5$	0.05781	0.4081	0.9030
Improved exponential function	KJ1	$6.505e-5$	0.1356	$9.197e-6$	0.9540
	KJ2	$4.238e-5$	0.1006	$9.586e-6$	0.9007
	(KJ1 + KJ2)/2	$6.459e-5$	0.1415	$1.078e-5$	0.9769

most common approach. The traditional exponential function is shown in Equation (5). Based on the exponential relationship, this study improved traditional exponential function. The improved exponential relationship is shown in Equation (6).

$$k = a_0 e^{-b_0(\sigma_e - c_0)}, \quad (5)$$

$$k = a e^{-b\sigma_e} + c. \quad (6)$$

The results about the relationship between permeability and effective stress of samples KJ1 and KJ2 are listed in Table 3. Besides, the third set of experimental data was taken by the average of the two sets of data. Then, there are 3 sets of data. The traditional and improved relationship can be fitted, respectively, using these 3 sets of data by Matlab. The fitting is based on the Levenberg-Marquardt algorithm built into the software. The coefficients for the two relationships and the goodness of fit are shown in Table 3. The fitting results of the two relationships are shown in Figure 8.

As shown in Figure 8, permeability decreases as the effective stress rises. Different with the results of low pore pressure in Figure 5(b), the difference in permeability values for one effective stress value is small, indicating that the matrix deformation is the key factor affecting permeability at high pore pressure. We also focus on the slope of curves. The decaying rate of permeability is large when the effective stress is low. And as the effective stress rises, the decaying rate of permeability is gradually slowing down. It can be explained by the reason that the deformation of compacted rock is more difficult for higher effective stress.

It is generally believed that in situ stress in the reservoir remains stable. The reservoir pressure in the early period of development is high, and the effective stress is small consequently. In such a condition, the pressure change induced by gas extraction would have great impact on permeability. In the late period of development, the pore pressure reduces and the effective stress rises. In such a condition, the change of pore pressure has little effect on the overall permeability.

The fit goodness (R^2) is a mathematical index reflecting the effect of data fitting. As Table 3 shows, the fit goodness for the improved exponential function is 0.9540, 0.9007, and 0.9769. The R^2 of improved exponential function is higher than that of the traditional exponential function. The new function can better fit the relationship between permeability and effective stress.

In order to verify whether the model is suitable for other data, the improved function is applied to fit the results from other results. The fitted data is derived from the results of Duan et al.'s study [37]. The fitting results are shown in Figure 9. The red dots in the figure are the measured data points. The dashed lines are the fitting results by the traditional exponential function in Equation (5). The solid lines are the fitting result by the improved exponential function in Equation (6). As the figure shows, the fitting goodness of samples 209, 215, and 239 by the improved exponential function was 0.9988, 0.9966, and 0.9741, respectively. It means that the improved exponential function proposed in this paper is better than the traditional exponential function in fitting accuracy.

4.1.2. Parameter Analysis of the Three Coefficients in the Improved Exponential Function. Each coefficient of the improved exponential function has its own attributes. Compared with the traditional exponential function, there is a constant c in the new function. When the effective stress is zero, the permeability is $a + c$. And when the effective stress tends to infinity, the permeability is c . According to the traditional exponential relationship, a is the corresponding permeability when effective stress is zero. In addition, when the effective stress tends to infinity, the permeability should be zero. Actually, the permeability is not zero. Therefore, the fitting effect of the new model is better after adding a new constant c . The constant c can be understood as the deviation due to the experimental system or other factors. It can also be seen from the data in Table 3 that the value of the constant c is generally small compared to the value of a . However, the fitting effect of the experimental results after introducing the constant c is better.

The effect of each coefficient on the permeability curve is shown in Figure 10. The values of the three coefficient are selected according to the value in Table 3. In Table 3, the value of coefficient a is from $4.23e-5$ to $6.50e-5$. Therefore, $5e-5$ was set as the basic value. Then, the range was selected from $0.5e-4$ to $2.5e-4$. Figure 10(a) shows the effect of the constant a on the curve. According to the traditional exponential relationship, the constant a represents the corresponding permeability when the effective stress is zero. The initial permeability is defined as the corresponding permeability when the effective stress is 0. As the figure shows, the initial permeability rises as the value of a rises. The permeability curves with different constants a would converge when effective stress reaches 30 MPa.

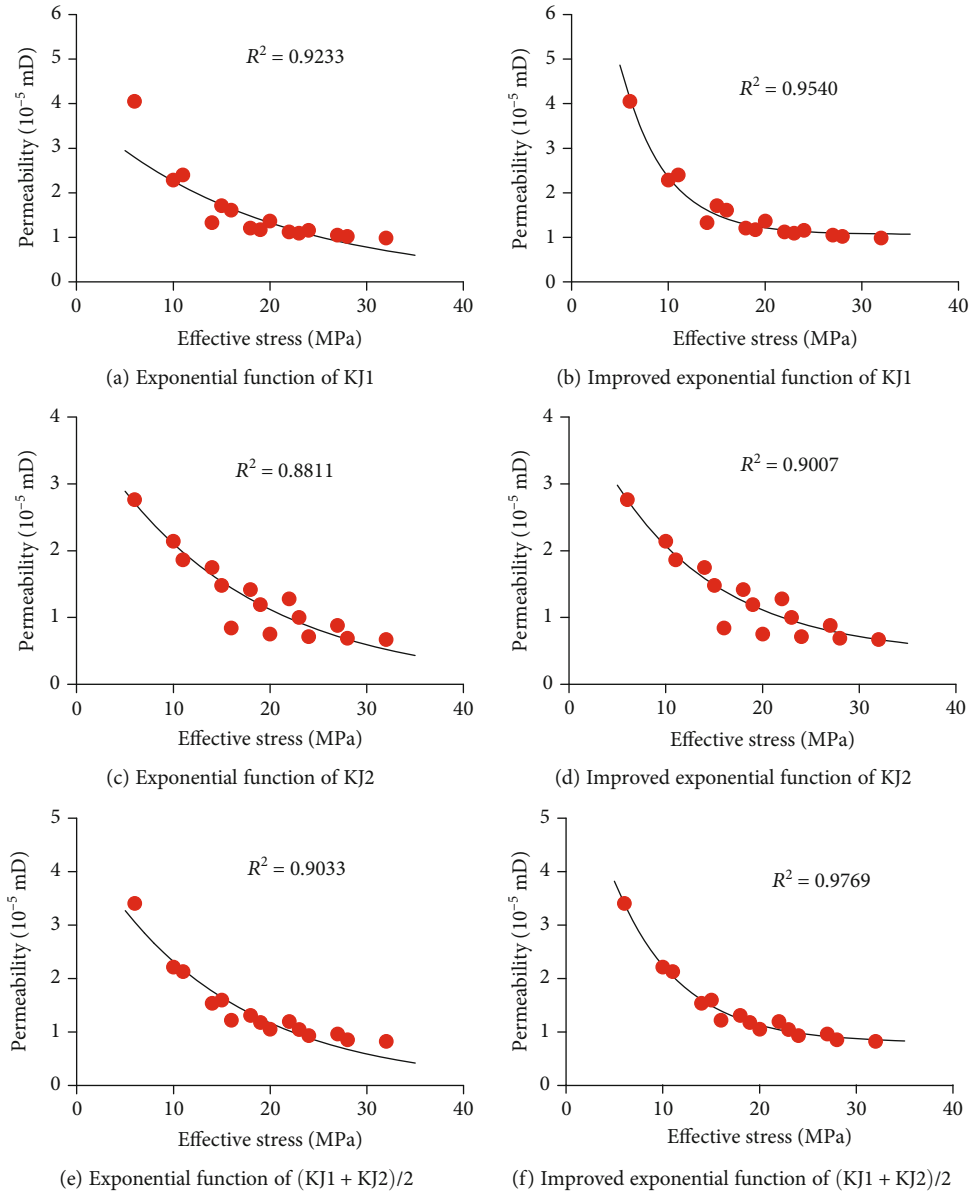


FIGURE 8: Fitting results of permeability with effective stress.

Figure 10(b) shows the effect of the coefficient b on the permeability curves. The coefficient b is considered the stress sensitivity coefficient. As shown in the figure, the influence of coefficient b on permeability is divided into two aspects. The first aspect is the effect on the decaying rate of permeability. The larger the coefficient b value is, the larger the decaying rate of the curve is. When b is equal to 0.1, the decay rate of the curve is small and the curve is gradual. As b rises, the curves become more curved. The second aspect is the sensitive range of effective stress. According to the curves, permeability is greatly affected by the effective stress with small effective stress, and the permeability gradually becomes stable with large effective stress. Therefore, the permeability sensitivity is very obvious within a certain range. It can be seen from the figure that the larger the b value is, the smaller

the range where the permeability is significantly affected by the effective stress is. Then, the influence of the constant b on the permeability can be obtained. Naming the range where permeability is more significantly affected by the effective stress as sensitivity range. The sensitivity range decreases as the constant b increases.

Figure 10(c) shows the effect of the coefficient c on permeability curves. The curves only shift vertically as c changes, and the shape of the curves does not change. As mentioned above, the value of c is very small compared to the initial permeability a . This coefficient c can be considered the fluctuation of the permeability test caused by the experimental system or other reasons. The introduction of the coefficient c is more conducive to the fit of the relationship between permeability and effective stress, although c is small.

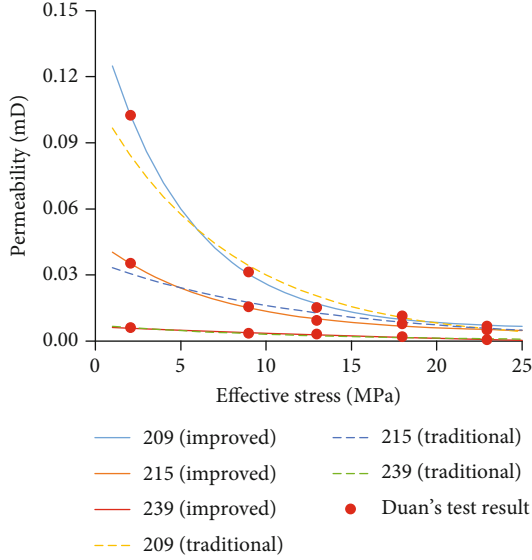


FIGURE 9: Model verification of the improved exponential relationship.

4.1.3. *Comparison of Traditional and Improved Models.* There are three advantages of the new model compared with the traditional model. Firstly, the new model can get better fitting accuracy. The new model is verified by the results of this experiment and a previous experiment. Both of these indicate that the fitting accuracy of the new model is better.

Secondly, although the expressions of the two models seem similar, there are differences in the mathematical form. Let $A = a_0 e^{b_0 c_0}$; then, the traditional model becomes

$$k = A e^{-b_0 \sigma_e} \quad (\text{traditional model}). \quad (7)$$

The new model is

$$k = a e^{-b \sigma_e} + c \quad (\text{improved model}). \quad (8)$$

Comparing the two models, the effect of the parameter c_0 in the traditional model is essentially on A . The parameter A is a multiplication factor, which will enlarge or reduce the entire curve. The parameter c is just a constant term. Therefore, the constant c can be more flexible in the fitting process and leads to the up and down translations of the curve. Consequently, the new model can have better fitting accuracy.

Third, as mentioned in the second point, the new model can express the up and down translations of the curve. Therefore, the new model can reflect the overall error caused by the equipment and measurement process. This can make the fitting result more accurate.

4.2. The Permeability of Self-Supporting Fractures

4.2.1. *Conductivity of Self-Supporting Fractures.* Fractures are the main flow channels of shale gas. Therefore, it is of great significance to understand the permeability variation induced by fractures. Generally, fractures can be divided into self-supporting fractures and supporting fractures depending

on whether or not the proppants are contained. The self-supporting fractures without proppants were measured in this experiment. In this section, the permeability variation of self-supporting fractures would be discussed.

Although the self-supporting fracture closes apparently, it still plays a major role in permeability of the shale system. In an ideal state, fractures would be closed when confining pressure is greater than pore pressure. If a fracture is closed completely, the measured permeability should be the same with the permeability of the matrix. However, the actual measured permeability was much greater than the permeability of matrix. As shown in the results of this experiment, the fractures without proppants are still permeable when the confining pressure is larger than pore pressure. It indicates that the fractures are not closed completely. Therefore, the permeable fractures without proppants are called self-supporting fractures.

Ren et al. [31] shared the same idea that the fracture did not close completely. Then, why does the fracture cannot close completely? Self-supporting fractures without proppants are permeable. The profiles of the samples in Figure 11(a) show that fracture surfaces are of certain roughness. The fracture surfaces may be slightly distorted under stress conditions. A slight displacement between the fracture faces results in the incomplete contact between two fracture faces. Therefore, the small displacement between the rough fracture faces is one of the main reasons for the unclosed fractures. In the real stratum, the in situ stress conditions are complex, and the fracture surfaces are relatively dislocated under the action of shear stress after fracturing. As Yin et al.'s experiment about the influence of shear processes on nonlinear flow behavior through 3D rough-walled rock fractures shows, the relative displacement of the rough surfaces under shearing would form a flow passage between the fractures [38]. The permeability of fractured shale is related to the roughness and relative shear displacement of the fracture surfaces.

In addition, another reason is the flaking of particles during the prefabrication of fractures. When the fracture was prefabricated, some of the blocks on the fracture surfaces peeled off. The blocks in our other related experiments about fracking are shown in Figure 11(b). The size and scale of the peeling block are different. Its size ranges from strip to powder. These blocks contribute to the permeability of self-supporting fractures in two ways. First, there will be gaps between the surfaces which are the flow channels for gas after block peeling off. It increases the permeability of the rock sample, which may also be a reason for the experiment in this paper. Another reason is that these particles would remain in the fractures. At this point, the particles act as proppants and the fractures cannot be closed completely. In the real stratum, some powdery particles may be carried away by the fracturing fluid, but the larger particles still stay in the fractures. In a word, those residues act as proppants. Hence, the fracture cannot be completely closed even if there is no added proppants in the fractures.

4.2.2. *Equivalent Width of Fractures.* The above discussed the reason why self-supporting fractures were still permeable.

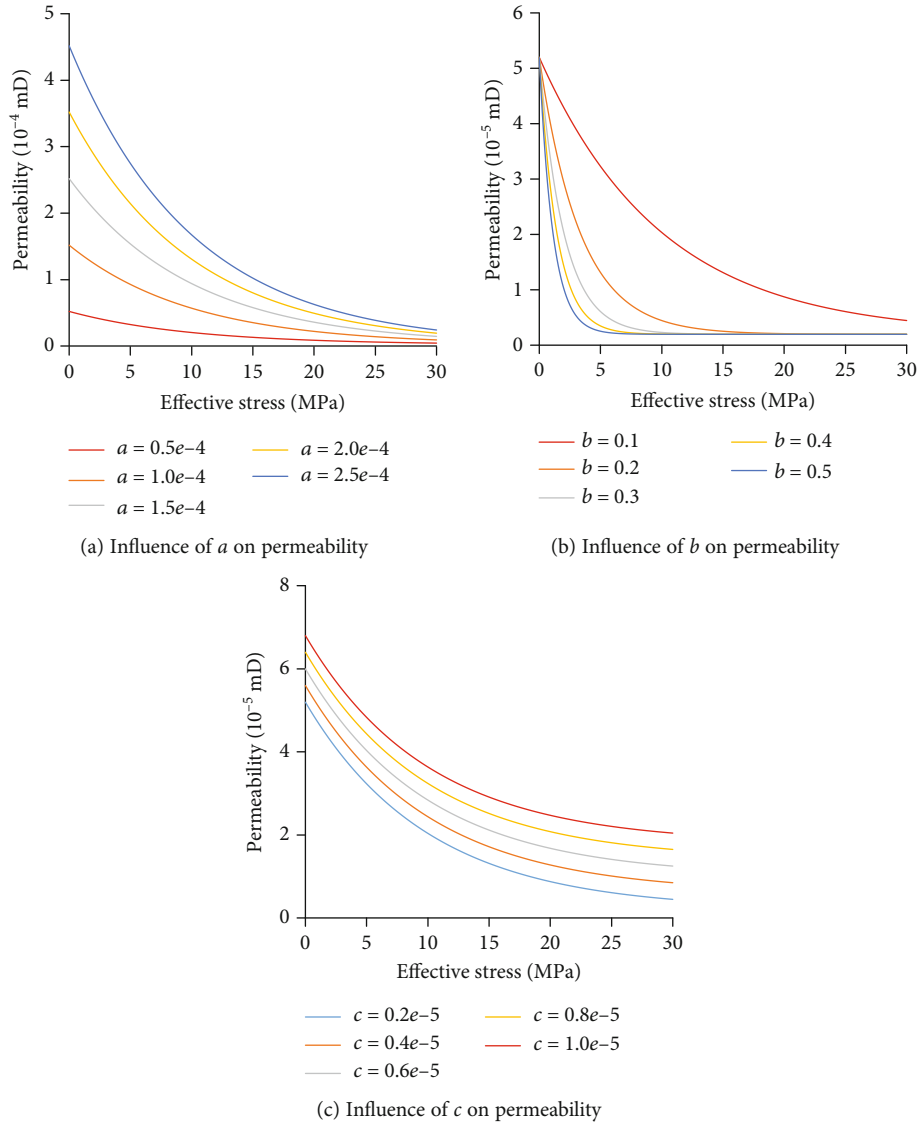


FIGURE 10: The parameter analysis for the improved exponential model.

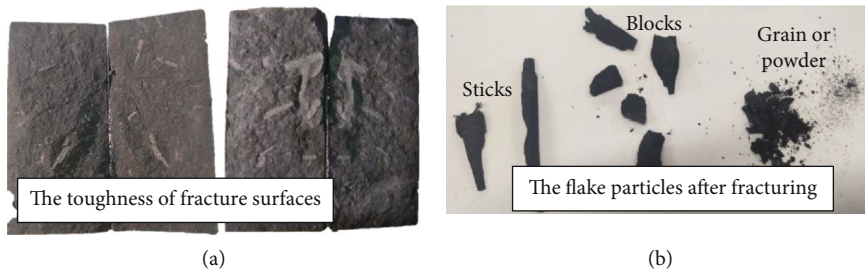


FIGURE 11: Fracture surfaces and flaking particles.

The essential reason is a nonclosed fracture. The fracture is difficult to describe because of its roughness. In order to describe the self-supporting fractures, the equivalent fracture width is proposed to evaluate the fracture width in this study. Referring to Figure 2(b), the fracture surfaces are assumed as smooth surfaces in the middle of the core. Then,

the permeability of fractured shale depends on the equivalent width of fracture. The equivalent width of fracture describes the permeability change with effective stress. According to Darcy's law and Reynold's equation for laminar flow between parallel surfaces, the equivalent width of fracture can be calculated.

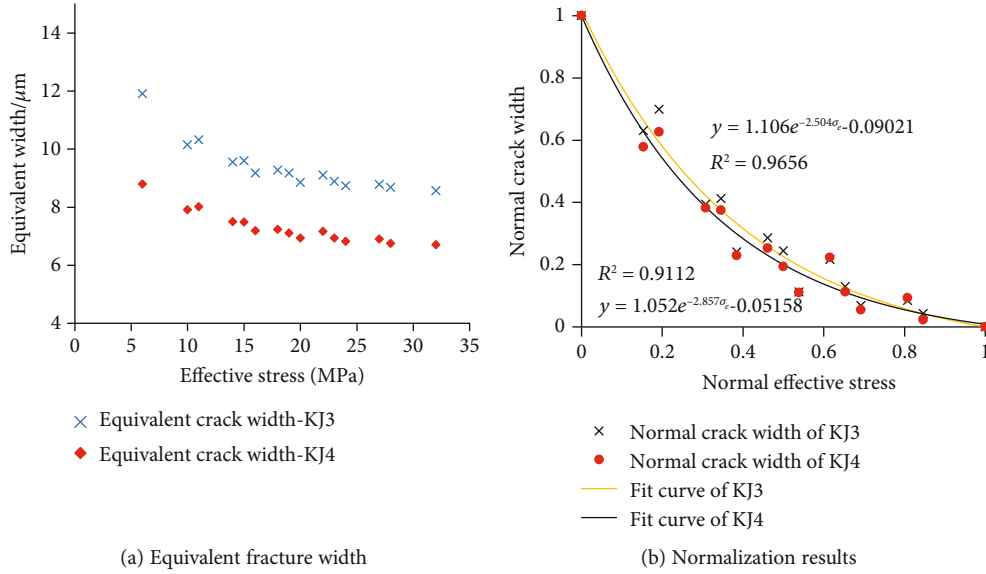


FIGURE 12: Relationship between equivalent width of fracture and effective stress.

By Darcy's law, the flow through the matrix can be expressed as

$$q_m = \frac{k_m A \Delta p}{\mu L}. \quad (9)$$

The flow through the fracture can be expressed as

$$q_f = \frac{k_f A \Delta p}{\mu L}. \quad (10)$$

The total flow is the sum of the flow in matrix and fracture

$$q_t = q_m + q_f. \quad (11)$$

By Darcy's law, the flow rate of the entire sample is

$$q_t = \frac{k_t A \Delta p}{\mu L} \quad (12)$$

Available from Equation (11),

$$q_f = q_t - q_m = q_m = \frac{(k_t - k_m) A \Delta p}{\mu L}. \quad (13)$$

In sum,

$$k_f = k_t - k_m. \quad (14)$$

Assuming that the fracture surfaces are a set of smooth planes and the fluid is laminar in the fracture, Reynold's equation for the parallel plate flow can be expressed as

$$q_f = \frac{e^3 \Delta p}{12 \mu L} * 2r. \quad (15)$$

Available from Equation (12) to Equation (15)

$$k_t - k_m = - \frac{(q_f + q_m - q_m) \mu L}{A \Delta p} = \frac{((e^3 \Delta p / 12 \mu L) \cdot 2r) \mu L}{A \Delta p} = \frac{r e^3}{6A}. \quad (16)$$

The equivalent width of fracture is

$$e = \sqrt[3]{\frac{6A(k_t - k_m)}{r}}. \quad (17)$$

$$A = \pi r^2. \quad (18)$$

Substituting Equation (18) into Equation (17), the equivalent width can be simplified to

$$e = \sqrt[3]{6\pi r(k_t - k_m)}. \quad (19)$$

In the condition where the fracture is not closed, the pore pressure and confining pressure affect the width of the fracture. Figure 12(a) shows the variation of the equivalent fracture width with effective stress. As the figure shows, the equivalent width of fracture reduces as the effective stress rises. The equivalent width of fracture ranges from 6 to 12 μm. This value is small, but it has a great influence on the permeability of the fractured shale core. The experimental results shows that the artificial fractures effectively raise the permeability of the fractured sample. The core permeability is very sensitive to change in the fracture width. Because of the difference in rock samples, there is a certain difference in the equivalent fracture width in Figure 12(a). Then, what is the relationship between the fracture width and the effective stress?

The equivalent fracture width and the effective stress are normalized separately to investigate the relationship between them. The results after normalization are plotted

in Figure 12(b). The relationship between the equivalent width and the effective stress is attempted by the improved exponential relationship established above. The calculated fit goodness is greater than 0.9, so that the fitting effect is well. Therefore, the stress sensitivity of the fracture width can also be described by the improved exponential relationship. As a result, we can characterize the stress influence on the permeability of fractured shale according to stress sensitivity of the fracture width curve.

5. Conclusions

In this paper, the permeability of intact shale and fracture shale is measured by the transient pulse method. The relationship between shale permeability and stress was analyzed. The main conclusions are as follows:

- (1) Comparing the results of fractured shale and intact shale, the fracture can greatly increase the permeability of the test rock sample. In this experiment, the permeability of the sample was increased by five orders of magnitude by the fractures
- (2) The permeability of intact shale under low pore pressure and high pore pressure is measured. The results show that the variation of permeability with pore pressure shows different results under two different conditions. Under the condition of low pore pressure, the slippage effect in the matrix is significant, so the slippage effect is a key factor affecting the permeability change, and the permeability decreases with the increase of pore pressure. Under the condition of high pore pressure, the deformation of the matrix is the main factor affecting the change of permeability. At this time, the permeability increases with the increase of pore pressure. This result also indicates that the change in permeability is the result of the combined effect of slippage effect and matrix deformation
- (3) The exponential function was improved in this paper. The improved exponential function can better fit the relationship between shale matrix permeability and effective stress for high pore pressure. It has a higher fitting accuracy compared with the traditional relationship. There are three advantages of the new model compared with the traditional model: better fitting accuracy, better mathematical form, and reflection of the overall error
- (4) The fractures in fractured shale samples cannot be closed completely even when the confining pressure is bigger than the pore pressure. The fracture is still the main flow channel of the gas, and the permeability of fractured shale is still much larger than the matrix. It means that the permeability of reservoir would increase after fracturing. There are two explanations for this. One reason is that the fracture surfaces are rough. The displacement of the surfaces under shear stress causes the unclosed fractures.

Another reason is the peeling of surface particles. The void forms after particle peeling. In addition, the exfoliated particles can act as a proppant to hinder the fracture closure

- (5) Aiming at the problem that the fracture width is difficult to describe due to the roughness of the fracture surfaces, this paper proposes the concept of equivalent fracture width. The change in permeability can be characterized by the equivalent fracture width. The fitting results show that the relationship between the equivalent fracture width and the effective stress also satisfies the improved exponential relationship proposed in this paper
- (6) The improved exponential relationship proposed in this paper is established under the condition of high pore pressure, only considering the relationship between permeability and effective stress and ignoring the slippage effect. Therefore, the improved exponential relationship in this paper is only applicable to high pore pressure conditions. In future research, different pore pressures should be combined to establish a permeability characterization equation that comprehensively considers the combined effect of slippage effect and matrix deformation

Data Availability

The data used to support the findings of this study are included within the article.

Conflicts of Interest

The authors declare that there is no conflict of interest regarding the publication of this article.

References

- [1] S. C. Maxwell, T. I. Urbancic, N. Steinsberger, and R. Zinno, *Microseismic imaging of hydraulic fracture complexity in the Barnett Shale*, Society of Petroleum Engineers, San Antonio, Texas, 2002.
- [2] G. Feng, X. Wang, M. Wang, and y. Kang, "Experimental investigation of thermal cycling effect on fracture characteristics of granite in a geothermal-energy reservoir," *Engineering Fracture Mechanics*, vol. 235, article 107180, pp. 1–16, 2020.
- [3] W. Shen, X. Li, X. Lu, W. Guo, S. Zhou, and Y. Wan, "Experimental study and isotherm models of water vapor adsorption in shale rocks," *Journal of Natural Gas Science and Engineering*, vol. 52, pp. 484–491, 2018.
- [4] W. Shen, F. Song, X. Hu, G. Zhu, and W. Zhu, "Experimental study on flow characteristics of gas transport in micro- and nanoscale pores," *Scientific Reports*, vol. 9, no. 1, p. 10196, 2019.
- [5] D. Yang, W. Wang, W. Chen, S. Wang, and X. Wang, "Experimental investigation on the coupled effect of effective stress and gas slippage on the permeability of shale," *Scientific Reports*, vol. 7, 2017.
- [6] D. Ren, D. Zhou, D. Liu, F. Dong, S. Ma, and H. Huang, "Formation mechanism of the Upper Triassic Yanchang

- Formation tight sandstone reservoir in Ordos Basin—Take Chang 6 reservoir in Jiyuan oil field as an example,” *Journal of Petroleum Science and Engineering*, vol. 178, pp. 497–505, 2019.
- [7] J. T. Chen, J. H. Zhao, S. C. Zhang, Y. Zhang, F. Yang, and M. Li, “An experimental and analytical research on the evolution of mining cracks in deep floor rock mass,” *Pure and Applied Geophysics*, 2020.
- [8] J. Wang, Y. Zhang, Z. Qin, S. G. Song, and P. Lin, “Analysis method of water inrush for tunnels with damaged water-resisting rock mass based on finite element method-smooth particle hydrodynamics coupling,” *Computers and Geotechnics*, vol. 126, article 103725, 2020.
- [9] K. Wu, Z. Chen, X. Li, C. Guo, and M. Wei, “A model for multiple transport mechanisms through nanopores of shale gas reservoirs with real gas effect-adsorption-mechanic coupling,” *International Journal of Heat and Mass Transfer*, vol. 93, pp. 408–426, 2016.
- [10] G. Sheng, F. Javadpour, and Y. Su, “Effect of microscale compressibility on apparent porosity and permeability in shale gas reservoirs,” *International Journal of Heat and Mass Transfer*, vol. 120, pp. 56–65, 2018.
- [11] D. Yang, W. Wang, and K. Li, “Experimental investigation on the stress sensitivity of permeability in naturally fractured shale,” *Environmental Earth Sciences*, vol. 78, no. 2, 2019.
- [12] J. J. Dong, J. Y. Hsu, W. J. Wu et al., “Stress-dependence of the permeability and porosity of sandstone and shale from TCDP hole-A,” *International Journal of Rock Mechanics and Mining Sciences*, vol. 7, pp. 1141–1157, 2010.
- [13] Y. Shi and C. Wang, “Pore pressure generation in sedimentary basins: overloading versus aquathermal,” *Journal of Geophysical Research: Solid Earth*, vol. 91, no. B2, pp. 2153–2162, 1986.
- [14] C. A. Morrow, L. Q. Shi, and J. D. Byerlee, “Permeability of fault gouge under confining pressure and shear stress,” *Journal of Geophysical Research: Solid Earth*, vol. 89, no. B5, pp. 3193–3200, 1984.
- [15] F. O. Jones Jr., “A laboratory study of the effects of confining pressure on fracture flow and storage capacity in carbonate rocks,” *Journal of Petroleum Technology*, vol. 27, no. 1, pp. 21–27, 2013.
- [16] J. B. Walsh, “Effect of pore pressure and confining pressure on fracture permeability,” *International Journal of Rock Mechanics and Mining Sciences & Geomechanics Abstracts*, vol. 18, no. 5, pp. 429–435, 1981.
- [17] R. Zhang, Z. Ning, F. Yang, X. Wang, H. Zhao, and Q. Wang, “Impacts of nanopore structure and elastic properties on stress-dependent permeability of gas shales,” *Journal of Natural Gas Science and Engineering*, vol. 26, pp. 1663–1672, 2015.
- [18] A. Ghanizadeh, M. Gasparik, A. Amann-Hildenbrand, Y. Gensterblum, and B. M. Krooss, “Experimental study of fluid transport processes in the matrix system of the European organic-rich shales: I. Scandinavian Alum Shale,” *Marine and Petroleum Geology*, vol. 51, pp. 79–99, 2014.
- [19] G. Cui, J. Liu, M. Wei, R. Shi, and D. Elsworth, “Why shale permeability changes under variable effective stresses: new insights,” *Fuel*, vol. 213, pp. 55–71, 2018.
- [20] M. Gutierrez, D. Katsuki, and A. Tutuncu, “Determination of the continuous stress-dependent permeability, compressibility and poroelasticity of shale,” *Marine and Petroleum Geology*, vol. 68, pp. 614–628, 2015.
- [21] Y. Wu, Z. Pan, D. Zhang, D. I. Down, Z. Lu, and L. D. Connell, “Experimental study of permeability behaviour for proppant supported coal fracture,” *Journal of Natural Gas Science and Engineering*, vol. 51, pp. 18–26, 2018.
- [22] Y. Tan, Z. Pan, J. Liu, Y. Wu, A. Haque, and L. D. Connell, “Experimental study of permeability and its anisotropy for shale fracture supported with proppant,” *Journal of Natural Gas Science and Engineering*, vol. 44, pp. 250–264, 2017.
- [23] Q. Yin, R. Liu, H. Jing, H. Su, L. Yu, and L. He, “Experimental study of nonlinear flow behaviors through fractured rock samples after high-temperature exposure,” *Rock Mechanics and Rock Engineering*, vol. 52, no. 9, pp. 2963–2983, 2019.
- [24] K. Su, Y. Sanz Perl, A. Onaisi, H. Pourpark, and S. Vidal-Gilbert, *Experimental study of hydromechanical behavior of fracture of Vaca Muerta Gas Shale*, American Rock Mechanics Association, San Francisco, California, USA, 2017.
- [25] T. Zhou, S. Zhang, Y. Feng, Y. Shuai, Y. Zou, and N. Li, “Experimental study of permeability characteristics for the cemented natural fractures of the shale gas formation,” *Journal of Natural Gas Science and Engineering*, vol. 29, pp. 345–354, 2016.
- [26] Y. Ma, Z. Pan, N. Zhong et al., “Experimental study of anisotropic gas permeability and its relationship with fracture structure of Longmaxi Shales, Sichuan Basin, China,” *Fuel*, vol. 180, pp. 106–115, 2016.
- [27] J. Zhou, L. Zhang, X. Li, and Z. Pan, “Experimental and modeling study of the stress-dependent permeability of a single fracture in shale under high effective stress,” *Fuel*, vol. 257, 2019.
- [28] Q. Yin, H. Jing, G. Ma, H. Su, and R. Liu, “Investigating the roles of included angle and loading condition on the critical hydraulic gradient of real rock fracture networks,” *Rock Mechanics and Rock Engineering*, vol. 51, no. 10, pp. 3167–3177, 2018.
- [29] C. Dong, Z. Pan, and Y. Zhihui, “Dependence of gas shale fracture permeability on effective stress and reservoir pressure: model match and insights,” *Fuel*, vol. 139, pp. 383–392, 2015.
- [30] Z. Gu, R. Liang, J. Su et al., “Impacts of pore-throat system on fractal characterization of tight sandstones,” *Geofluids*, vol. 2020, Article ID 4941501, 2020.
- [31] F. Ren, C. Zhu, and M. He, “Moment tensor analysis of acoustic emissions for cracking mechanisms during schist strain burst,” *Rock Mechanics and Rock Engineering*, vol. 53, no. 1, pp. 153–170, 2020.
- [32] C. E. Neuzil, C. Cooley, S. E. Silliman, J. D. Bredehoeft, and P. A. Hsieh, “A transient laboratory method for determining the hydraulic properties of ‘tight’ rocks—II. Application,” *International Journal of Rock Mechanics and Mining Sciences & Geomechanics Abstracts*, vol. 18, no. 3, pp. 253–258, 1981.
- [33] P. A. Hsieh, J. V. Tracy, C. E. Neuzil, J. D. Bredehoeft, and S. E. Silliman, “A transient laboratory method for determining the hydraulic properties of ‘tight’ rocks—I. Theory,” *International Journal of Rock Mechanics and Mining Sciences & Geomechanics Abstracts*, vol. 18, no. 3, pp. 245–252, 1981.
- [34] S. C. Jones, “A technique for faster pulse-decay permeability measurements in tight rocks,” *SPE Formation Evaluation*, vol. 12, no. 1, pp. 19–26, 2013.
- [35] C. Qian, G. Yanjie, and F. Tailiang, “The effect of pressure variation on gas permeability in fractured tight sandstone reservoir,” *Science Technology and Engineering*, vol. 18, no. 26, pp. 60–67, 2018.
- [36] Ø. Gutierrez, “Stress-dependent permeability of a de-mineralised fracture in shale,” *Marine and Petroleum Geology*, vol. 17, no. 8, pp. 895–907, 2000.

- [37] X. G. Duan, W. G. An, Z. M. Hu, S. S. Gao, L. Y. Ye, and J. Chang, "Experimental study on fracture stress sensitivity of Silurian Longmaxi shale formation, Sichuan Basin," *Natural Gas Geoscience*, vol. 28, no. 9, pp. 1416–1424, 2017.
- [38] Q. Yin, G. Ma, H. Jing et al., "Hydraulic properties of 3d rough-walled fractures during shearing: an experimental study," *Journal of Hydrology*, vol. 555, pp. 169–184, 2017.

Research Article

Scale Dependence of Waviness and Unevenness of Natural Rock Joints through Fractal Analysis

Yingchun Li ¹, Shengyue Sun,¹ and Hongwei Yang²

¹State Key Laboratory of Coastal and Offshore Engineering, Dalian University of Technology, Dalian, China 116024

²Institute for Geology, Mineralogy and Geophysics, Ruhr University Bochum, Bochum, Germany D-44780

Correspondence should be addressed to Yingchun Li; yingchun_li@dlut.edu.cn

Received 19 May 2020; Revised 7 July 2020; Accepted 29 July 2020; Published 25 August 2020

Academic Editor: Qian Yin

Copyright © 2020 Yingchun Li et al. This is an open access article distributed under the Creative Commons Attribution License, which permits unrestricted use, distribution, and reproduction in any medium, provided the original work is properly cited.

The scale dependence of surface roughness is critical in characterising the hydromechanical properties of field-scale rock joints but is still not well understood, particularly when different orders of roughness are considered. We experimentally reveal the scale dependence of two-order roughness, i.e., waviness and unevenness through fractal parameters using the triangular prism surface area method (TPM). The surfaces of three natural joints of granite with the same dimension of 1000 mm × 1000 mm are digitised using a 3D laser scanner at three different measurement resolutions. Waviness and unevenness are quantitatively separated by considering the area variation of joint surface as grid size changes. The corresponding fractal dimensions of waviness and unevenness in sampling window sizes ranging from 100 mm × 100 mm to 1000 mm × 1000 mm at an interval of 100 mm × 100 mm are determined. We find that both the fractal dimensions of waviness and unevenness vary as the window size increases. No obvious stationarity threshold has been found for the three rock joint samples, indicating the surface roughness of natural rock joints should be quantified at the scale of the rock mass in the field.

1. Introduction

Rock masses contain a large body of joints. The mechanical and hydraulic behaviours of rock joints highly affect the hydromechanical properties of rock masses. Due to geological processes, rock joints with natural surfaces occur over a broad scale from millimeters to kilometers. Accurate description of joint roughness at the relevant scale is crucial for predicting the hydromechanical coupling of the rock mass.

The surfaces of natural rock joints exhibit varying degrees of roughness. Roughness refers to the inherent unevenness and waviness of a rock joint surface relative to its mean plane [1]. Initially, waviness and unevenness represent large-scale undulations observed in the field and small-scale roughness sampled in the laboratory, respectively [2, 3]. Large-scale undulations dominate joint dilatancy since they are too large to be sheared off, and small-scale roughness affects joint shear strength as it is usually damaged under shear. The surface of a laboratory-sized rock joint also exhibits two-order asperities, i.e., first-order waviness and second-order uneven-

ness [4–8]. Waviness with comparatively larger wavelength and amplitude primarily contributes to dilation, whereas unevenness of a smaller asperity size is sheared and damaged, providing shear resistance to the shear movement. That is to say, a rock joint surface is characterised by two-order roughness at various scales [9]. Although numerous empirical and statistical approaches have been proposed to quantify the roughness of rock joints [10–15], they have rarely taken into account the two-order roughness of a joint surface that plays distinct roles in the mechanical and hydraulic behaviours of rock joints [7, 16, 17].

The roughness of a natural rock joint surface depends on the scale of examination, which is referred to as scale effect. Bandis et al. [18] reported that the value of *JRC* (joint roughness coefficient) decreased as the rock joint size increased, i.e., negative scale effect. On the other hand, conflicting results including positive and no scale effects have been observed [19–22]. By examining the morphological characteristics of the surface roughness of a large-scale rock joint replica (1000 mm × 1000 mm), Fardin et al. [23] also stated that there was a stationarity threshold beyond which

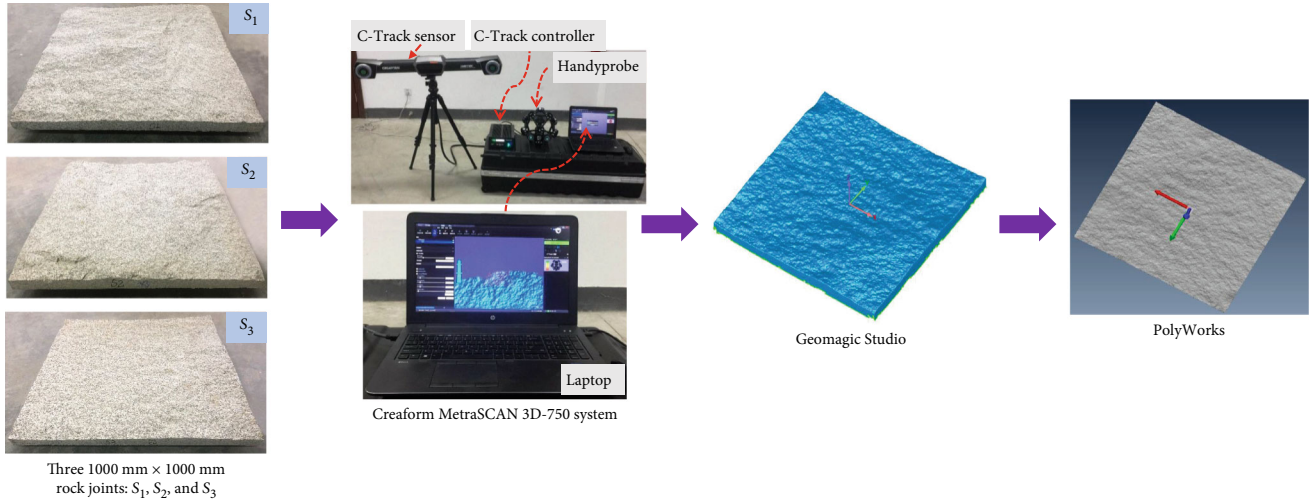


FIGURE 1: Digitisation of a 1000 mm × 1000 mm rock joint surface.

the scale dependency of surface roughness vanished, i.e., the roughness remained unvaried once the scale exceeded the size of the stationarity threshold. Due to these controversial findings, the nature of how scale affects the surface roughness remains enigmatic.

Fractal theory [24, 25] has been successfully applied to characterise the roughness of rock joints at varying scales. Many approaches to estimate the fractal dimension of a rock joint profile have been proposed, including ruler length [26], box counting [27], variogram [28, 29], spectral [30, 31], roughness length [9, 23, 32, 33], and line scaling [34]. The triangular prism surface area method (TPM) [35–37], project covering method (PCM) [38–40], and cubic covering method (CCM) [41] are shown to be applicable for determining the fractal geometry of a three-dimensional joint surface. However, few of them have considered the individual fractal dimensions of waviness and unevenness since a universal single value was commonly assumed.

In this paper, we examine the fractal characteristics of waviness and unevenness of three natural granite rock joints dimensioned up to 1000 mm × 1000 mm. We find that each-order roughness possesses individual fractal dimension at varying sizes from 100 mm × 100 mm to 1000 mm × 1000 mm. The waviness and unevenness of a rock joint surface are separated by considering the surface area variation as grid size changes. The fractal dimension of each-order roughness is calculated using TPM (triangular prism surface area method). Evident scale dependency of fractal dimension of each-order roughness has been observed. However, the stationarity threshold of the joint surface roughness is possibly absent.

2. Data Acquisition

We scanned and reconstructed the three-dimensional surfaces of three natural granite joints 70 (labeled S_1 , S_2 , and S_3 , respectively) sourced from a quarry in Fujian Province, China (Figure 1).

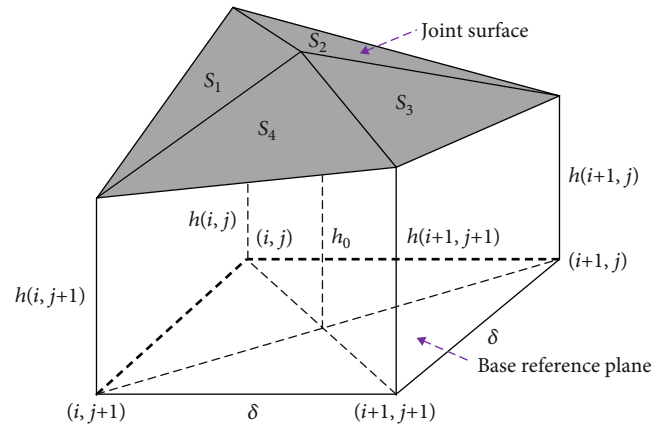


FIGURE 2: Illustration of the triangular prism surface area method (after Clarke [35]). δ is the grid size, S_1 , S_2 , S_3 , and S_4 represent the areas of four triangles; (i, j) , $(i, j+1)$, and $(i+1, j+1)$ are, respectively, the coordinates of the four points of the triangular prism, h_0 denotes the elevation at the center of the grid cell, and $h(i, j)$, $h(i+1, j)$, $h(i, j+1)$, and $h(i+1, j+1)$ are the elevations of the four points, respectively.

The dimension of each rock joint surface was 1000 mm × 1000 mm. The rock joint surfaces were initially covered by a very thin layer of dust. We carefully cleaned the dust with wipes to avoid damaging the surface roughness. Visual observation suggested that the granite joints are light gray and unweathered.

When the rock joint surfaces were naturally dried in the laboratory, a Creaform MetraSCAN 3D 750 system was employed to digitise the joint surface at three measurement resolutions with point spacings being 0.5 mm, 1.0 mm, and 2.0 mm, respectively. The optical scanning system consists of a HandyPROBE for scanning, a C-Track sensor to locate the position of the HandyPROBE, a C-Track controller for data acquisition, and a laptop for image processing and display (Figure 1). It ideally can acquire the topographic information of an object up to several meters at a minimum point spacing of 0.05 mm. During data acquisition, we

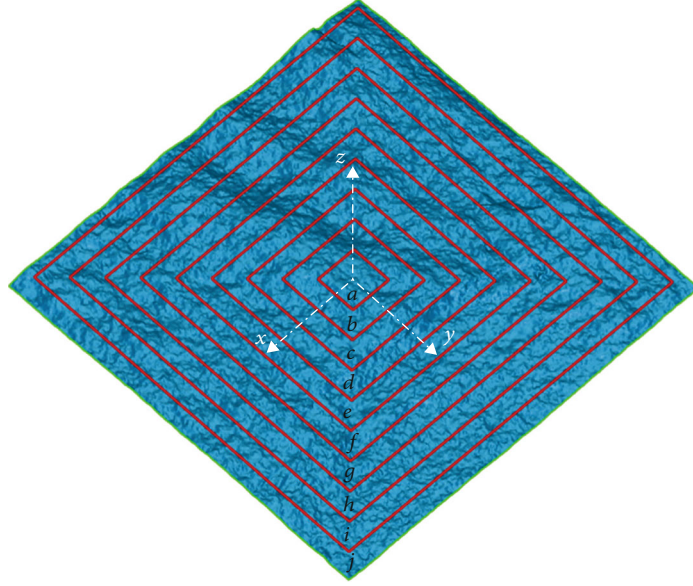


FIGURE 3: Illustration of the square windows of different sizes from $a = 100 \text{ mm} \times 100 \text{ mm}$ to $j = 1000 \text{ mm} \times 1000 \text{ mm}$ chosen from the central part of a rock joint surface.

scanned the rock joint surface region by region very slowly and carefully to fully capture the morphological properties of the rock joint surfaces. The digitised surface of the rock joint was visualised simultaneously over scanning through the laptop monitor, which ensured that each surface was thoroughly reconstructed without small empty areas remained. We attempted to obtain a more detailed joint surface at the point spacing of 0.2 mm but failed due to memory limitation of the laptop. The graphic processing software, Geomagic Studio, was employed to coordinate the data acquired through the scanner. The graphic processing software, PolyWorks, converted the format of the data imported from Geomagic Studio to the format that is readable by the data processing software, MATLAB.

3. Fractal Dimensions of Waviness and Unevenness

We used the well-established triangular prism surface area method (TPM) [35, 37] to estimate the fractal dimensions of waviness and unevenness. The principle of TPM is that the true surface area of a joint surface is measurable once the heights of all points on the joint surface above a base reference plane are established. For a square grid with a side length of δ (Figure 2), the elevation at the center of the grid cell (h_0) is determined by the elevations of its four points:

$$h_0 = \frac{1}{4} [h(i, j) + h(i, j + 1) + h(i + 1, j) + h(i + 1, j + 1)], \quad (1)$$

where $h(i, j)$, $h(i, j + 1)$, $h(i + 1, j)$, and $h(i + 1, j + 1)$ are the elevations of the four points, respectively (Figure 2).

The area of one of the triangles, S_1 , is as follows:

$$S_1 = \sqrt{l_1(l_1 - a_1)(l_1 - b_1)(l_1 - c_1)}, \quad (2)$$

where $l_1 = 1/2(a_1 + b_1 + c_1)$,

$$\begin{aligned} a_1 &= \sqrt{[h(i, j) - h(i, j + 1)]^2 + \delta^2}, \\ b_1 &= \sqrt{[h(i, j) - h_0]^2 + \frac{1}{2}\delta^2}, \\ c_1 &= \sqrt{[h(i, j + 1) - h_0]^2 + \frac{1}{2}\delta^2}. \end{aligned} \quad (3)$$

Similarly, the areas of the other three triangles, i.e., S_2 , S_3 , and S_4 , are calculated, respectively. The true area of a joint surface in a given grid cell sized of $\delta \times \delta$ is as follows:

$$S_{i,j} = S_1 + S_2 + S_3 + S_4. \quad (4)$$

The joint surface area is as follows:

$$S(\delta) = \sum_{i,j=1}^{N(\delta)} S_{i,j}, \quad (5)$$

where $N(\delta)$ denotes the number of total grid cells. The joint surface area is a function of grid size (δ) by [37]:

$$S(\delta) = A\delta^{2-D}, \quad (6)$$

where D is the fractal dimension of a joint surface, and A is a coefficient. Note that the original approach of Clarke [35] estimated the fractal dimension (D) through the relationship

TABLE 1: Grid sizes used in TMP calculation for estimating the fractal dimensions of the rock joint samples of varying window sizes.

Window size (mm × mm)	Point spacing (ω) (mm)	Grid size (δ) (mm)
100 × 100	0.5	[100, 50, 40, 25, 20, 10, 8, 5, 4, 2, 1] × 0.5
	1.0	[50, 25, 20, 10, 5, 4, 2, 1] × 1.0
	2.0	[50, 25, 20, 10, 5, 4, 2, 1] × 2.0
200 × 200	0.5	[200, 100, 80, 50, 40, 25, 20, 16, 10, 8, 5, 4, 2, 1] × 0.5
	1.0	[100, 50, 40, 25, 20, 10, 8, 5, 4, 2, 1] × 1.0
	2.0	[50, 25, 20, 10, 5, 4, 2, 1] × 2.0
300 × 300	0.5	[300, 200, 150, 120, 100, 75, 60, 50, 40, 30, 25, 24, 20, 15, 12, 10, 8, 6, 5, 4, 3, 2, 1] × 0.5
	1.0	[150, 100, 75, 60, 50, 30, 25, 20, 15, 12, 10, 6, 5, 4, 3, 2, 1] × 1.0
	2.0	[75, 50, 30, 25, 15, 10, 6, 5, 3, 2, 1] × 2.0
400 × 400	0.5	[400, 200, 160, 100, 80, 50, 40, 32, 25, 20, 16, 10, 8, 5, 4, 2, 1] × 0.5
	1.0	[200, 100, 80, 50, 40, 25, 20, 16, 10, 8, 5, 4, 2, 1] × 1.0
	2.0	[100, 50, 40, 25, 20, 10, 8, 5, 4, 2, 1] × 2.0
500 × 500	0.5	[500, 250, 200, 125, 100, 50, 40, 25, 20, 10, 8, 5, 4, 2, 1] × 0.5
	1.0	[250, 125, 100, 50, 25, 20, 10, 5, 4, 2, 1] × 1.0
	2.0	[125, 50, 25, 10, 5, 2, 1] × 2.0
600 × 600	0.5	[600, 400, 300, 240, 200, 150, 120, 100, 80, 75, 60, 50, 48, 40, 30, 25, 24, 20, 16, 15, 12, 10, 8, 6, 5, 4, 3, 2, 1] × 0.5
	1.0	[300, 200, 150, 120, 100, 75, 60, 50, 40, 30, 25, 24, 20, 15, 12, 10, 8, 6, 5, 4, 3, 2, 1] × 1.0
	2.0	[150, 100, 75, 60, 50, 30, 25, 20, 15, 12, 10, 6, 5, 4, 3, 2, 1] × 2.0
700 × 700	0.5	[700, 350, 280, 200, 175, 140, 100, 70, 56, 50, 40, 35, 28, 25, 20, 14, 10, 8, 7, 5, 4, 2, 1] × 0.5
	1.0	[350, 175, 140, 100, 70, 50, 35, 28, 25, 20, 14, 10, 7, 5, 4, 2, 1] × 1.0
	2.0	[175, 70, 50, 35, 25, 14, 10, 7, 5, 2, 1] × 2.0
800 × 800	0.5	[800, 400, 320, 200, 160, 100, 80, 64, 50, 32, 40, 25, 20, 16, 10, 8, 5, 4, 2, 1] × 0.5
	1.0	[400, 200, 160, 100, 80, 50, 40, 32, 25, 20, 16, 10, 8, 5, 4, 2, 1] × 1.0
	2.0	[200, 100, 80, 50, 40, 25, 20, 16, 10, 8, 5, 4, 2, 1] × 2.0
900 × 900	0.5	[900, 600, 450, 360, 300, 225, 200, 180, 150, 120, 100, 90, 75, 72, 60, 50, 45, 40, 36, 30, 25, 24, 20, 18, 15, 12, 10, 9, 8, 6, 5, 4, 3, 2, 1] × 0.5
	1.0	[450, 300, 225, 180, 150, 100, 90, 75, 60, 50, 45, 36, 30, 25, 20, 18, 15, 12, 10, 9, 6, 5, 4, 3, 2, 1] × 1.0
	2.0	[225, 150, 90, 75, 50, 45, 30, 25, 18, 15, 10, 9, 6, 5, 3, 2, 1] × 2.0
1000 × 1000	0.5	[1000, 500, 400, 250, 200, 125, 100, 80, 50, 40, 25, 20, 16, 10, 8, 5, 4, 2, 1] × 0.5
	1.0	[500, 250, 200, 125, 100, 50, 40, 25, 20, 10, 8, 5, 4, 2, 1] × 1.0
	2.0	[250, 125, 100, 50, 25, 20, 10, 5, 4, 2, 1] × 2.0

between joint surface area $S(\delta)$ and grid size square (δ^2), i.e., $S(\delta) = A(\delta^2)^{2-D}$. However, Equation (6) using grid size is proven to be mathematically correct and experimentally reliable [36, 37, 42] as the use of the grid size underestimated fractal dimension [43].

To double-logarithmise Equation (6), we have:

$$\ln(S(\delta)) = \ln A + (2 - D) \ln(\delta), \quad (7)$$

where D and A are estimated from the slope and intercept of the $\ln(S(\delta)) - \ln(\delta)$ plot, respectively.

To investigate the scale dependency of surface roughness, the fractal dimensions of waviness and unevenness of the three rock joint samples at varying window sizes from 100 mm \times 100 mm to 1000 mm \times 1000 mm are estimated (Figure 3). The square window of different sizes is selected from the central part of a rock joint surface. We first plot the relationship between $\ln(S(\delta))$ and $\ln(\delta)$ based on Equations (1), (2), (4), (5), (6), and (7). The joint surface area is computed at varying grid sizes through Equation (5). Table 1 shows the grid size used in calculating the joint surface area at varying window sizes of different measurement resolutions from 100 mm \times 100 mm to 1000 mm \times 1000 mm at the interval of 100 mm \times 100 mm. As illustrated in Figure 4, the principle of grid size determination is to ensure that the side length of the sampling window is divisible by the grid size (δ) that is a multiple of the point spacing. Figure 5 demonstrates the double-logarithmic relationship between surface area ($\ln(S(\delta))$) and grid size ($\ln(\delta)$) of the three rock joint samples at the dimension of 800 mm \times 800 mm under the resolution of point spacing at 1.0 mm. The surface areas of the three joint samples are calculated through TPM with each grid size ranging from 1 mm to 400 mm, i.e., $\delta = [400, 200, 160, 100, 80, 50, 40, 32, 25, 20, 16, 10, 8, 5, 4, 2, 1] \times 1$ mm. Waviness and unevenness are separated by considering the area variation of a joint surface at varying grid sizes. Specifically, as the grid size decreases, the joint surface area increases to approximately the real surface area. When the grid size exceeds 30 mm, the slope of the $\ln(S(\delta)) - \ln(\delta)$ plot decreases remarkably. Under this circumstance, the joint surface area is primarily contributed by waviness, whereas the surface area of unevenness is excluded. For all the three rock joint samples, the slopes of the $\ln(S(\delta)) - \ln(\delta)$ curves vary noticeably at the grid size of 30 mm at which waviness and unevenness are separated. Figure 6 illustrates the decomposition of a rock joint surface into profiles of waviness and unevenness.

The unevenness is acquired by subtracting the waviness from the whole joint surface. The fractal dimensions of waviness (D_w) and unevenness (D_u) of a rock joint surface are determined from the two slopes of each bilinear curve, respectively (Figure 4). Actually, similar bilinearity of the $\ln(S(\delta)) - \ln(\delta)$ plot of tension-induced rock joint surfaces has been reported by several researchers [40, 41]. They found that the rock joint surface has nonuniversal fractal dimensions, depending on the measurement scale. However, the nature of the two-order fractal dimensions that are explained above was not unveiled by the authors.

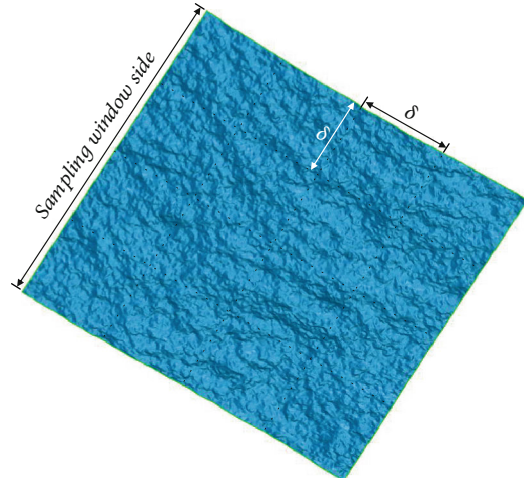


FIGURE 4: Illustration of grid size (δ) determination in TPM calculation. The rationale is that the side length of sampling window is divisible by the grid size (δ) that is a multiple of the point spacing.

4. Results

4.1. Scale Effect. Figure 7 shows that the fractal dimensions of two-order roughness are scale-dependent for the three rock joint samples digitised at three measurement resolutions. Tables 2–4 list the fractal dimensions of waviness and unevenness of rock joint samples S_1 to S_3 at varying sizes, respectively. For joint sample S_1 at a fixed point spacing, the fractal dimension of waviness is the highest at the sampling window of 100 mm \times 100 mm, followed by a decrease once the sampling window grows to 200 mm \times 200 mm. As the side length of the sampling window increases to 400 mm, the fractal dimension of waviness peaks with a value smaller than that at the sampling window of 100 mm \times 100 mm. When the side length of the sampling window increases from 400 mm to 1000 mm, the fractal dimension of waviness generally decreases with slight fluctuations at the side lengths of 700 mm and 900 mm. The fractal dimension of unevenness of joint sample S_1 at a certain point spacing, however, is the smallest at the window size of 100 mm \times 100 mm. The fractal dimension of unevenness rises continuously to a peak value as the sampling window size increases to 400 mm \times 400 mm, followed by an overall decrease as the sampling window size is increased to the maximum value of 1000 mm \times 1000 mm.

For rock joint sample S_2 under a certain measurement resolution, the fractal dimension of waviness fluctuates slightly as the window side length increases from 100 mm to 400 mm, preceding a gradual decrease when the window size grows to 700 mm \times 700 mm. As the sampling window size increases from 700 mm \times 700 mm to 1000 mm \times 1000 mm, the fractal dimension of waviness increases marginally. The fractal dimension of unevenness seemingly exhibits no general tendency. The magnitude of the fractal dimension of unevenness roughly levels off with several unremarkable fluctuations at different sampling window sizes.

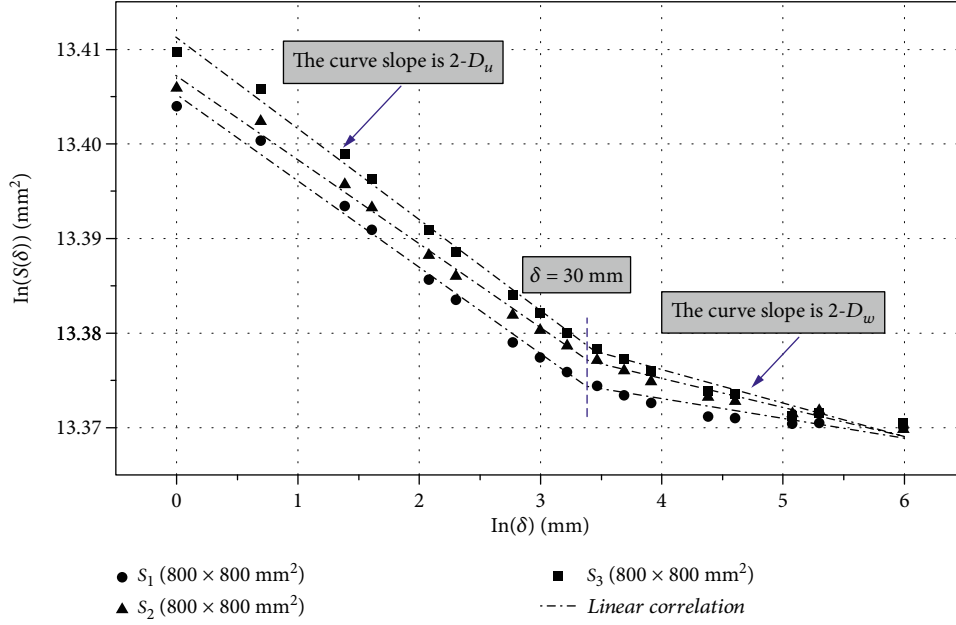


FIGURE 5: Double-logarithmic relationship between joint surface area ($S(\delta)$) and grid size (δ). D_w and D_u denote the fractal dimensions of waviness and unevenness, respectively.

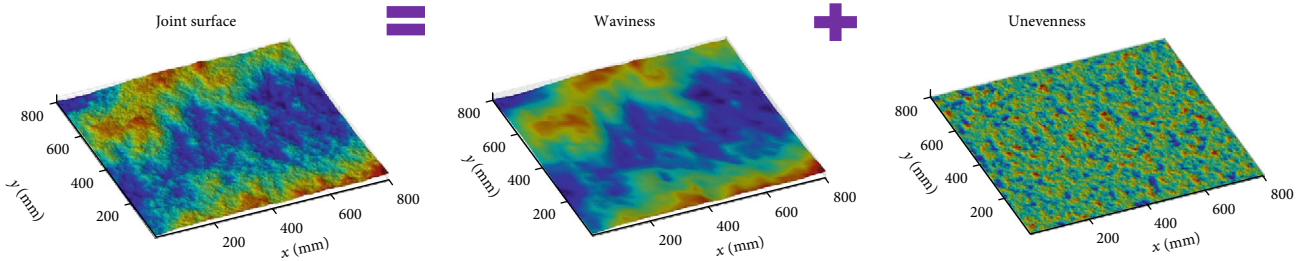


FIGURE 6: Decomposition of a rock joint surface into waviness and unevenness.

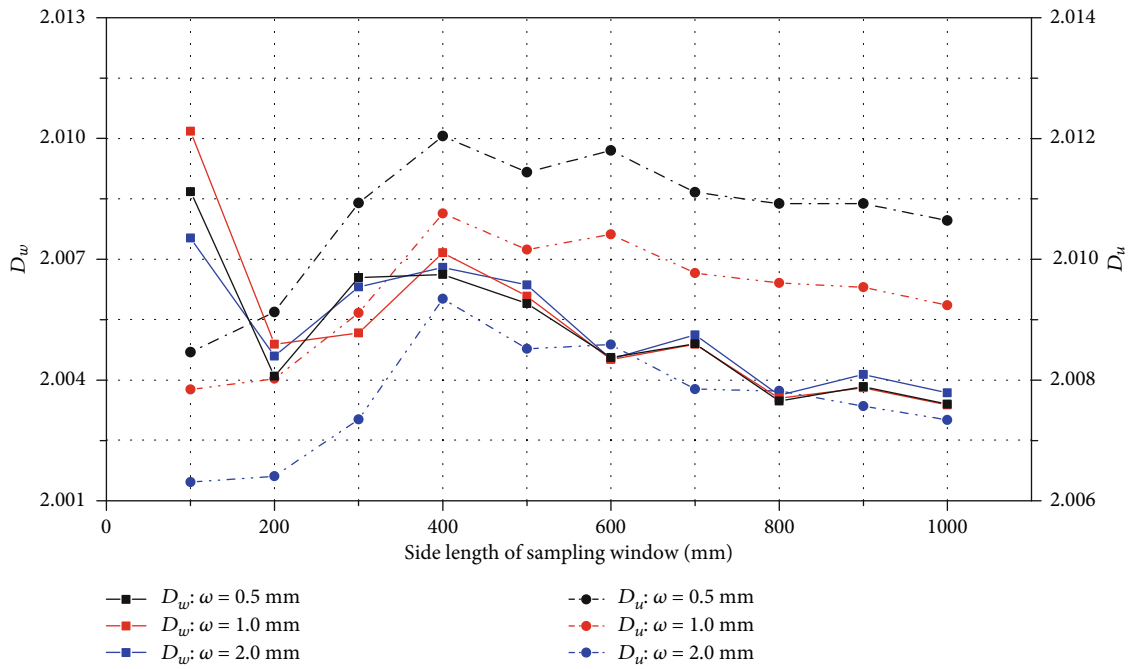
For rock joint sample S_3 at a fixed point spacing, the fractal dimension of waviness is maximum at the window size of $100 \text{ mm} \times 100 \text{ mm}$ and then predominantly declines as the window side length increases to 1000 mm with slight fluctuations. The variation of fractal dimension of unevenness resembles that of rock joint sample S_2 without noticeable trend.

To quantify the variation of fractal dimensions of waviness and unevenness as the window size is enlarged, the percent error relative to the value of window size of $100 \text{ mm} \times 100 \text{ mm}$ is calculated as follows:

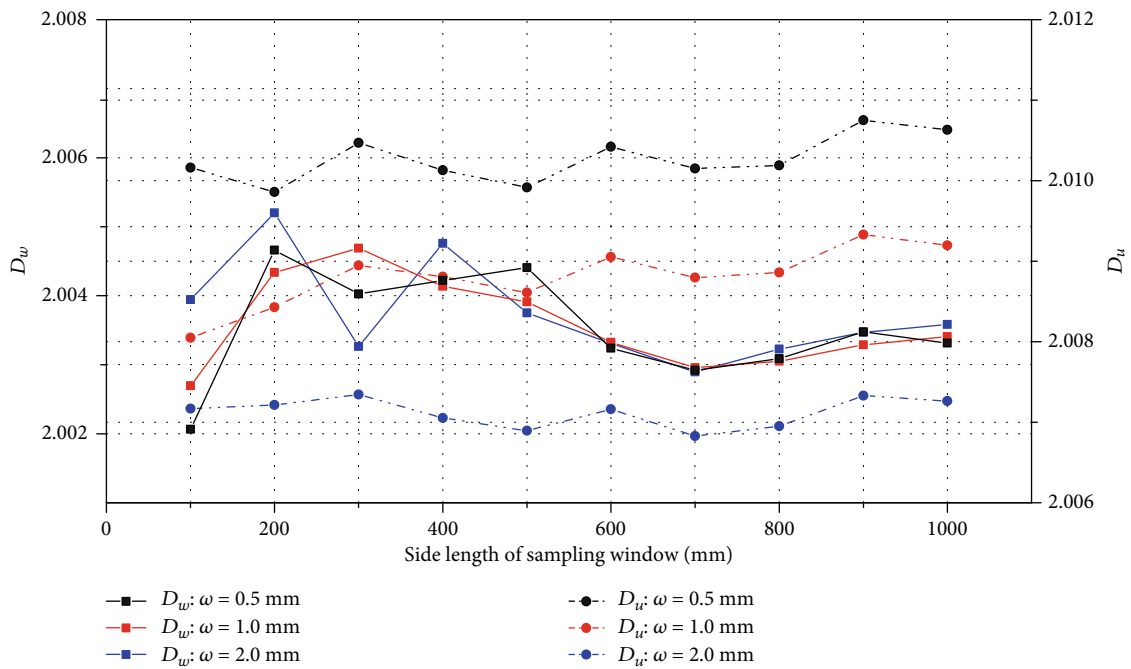
$$\delta_i = \frac{|D_i - D_{100}|}{D_{100}} \times 100\%, \quad (8)$$

where δ_i and D_i represent the percent error and fractal dimension of waviness or unevenness at a window size between $200 \text{ mm} \times 200 \text{ mm}$ to $1000 \text{ mm} \times 1000 \text{ mm}$, respectively. D_{100} is the fractal dimension of waviness or unevenness at the window size of $100 \text{ mm} \times 100 \text{ mm}$.

Figure 8 presents the percent errors of waviness and unevenness of the three rock joint samples at window sizes from $200 \text{ mm} \times 200 \text{ mm}$ to $1000 \text{ mm} \times 1000 \text{ mm}$ at three measurement resolutions. Generally, the effect of window size on the fractal dimension of waviness is more pronounced than that of unevenness. Particularly for rock joint samples S_2 and S_3 , the percent errors of fractal dimension of unevenness are lower than 0.1%. The variations of fractal dimensions of both waviness and unevenness of rock joint sample S_1 are overall larger than those of rock joint samples S_2 and S_3 at the same window size and resolution. For rock joint sample S_1 , the percent errors of the fractal dimension of waviness at varying window sizes under the resolution of 1.0 mm are unanimously the highest, and 2.0 mm the lowest. The percent error of the fractal dimension of unevenness under the resolution of 0.5 mm is the highest, and 2.0 mm the lowest except at the window size of $400 \text{ mm} \times 400 \text{ mm}$ where the percent error of the fractal dimension of unevenness under the point spacing of 1.0 mm is marginally smaller than that under 2.0 mm . For rock joint sample S_2 , the percent errors of the fractal dimension of waviness at varying window sizes under the resolution of

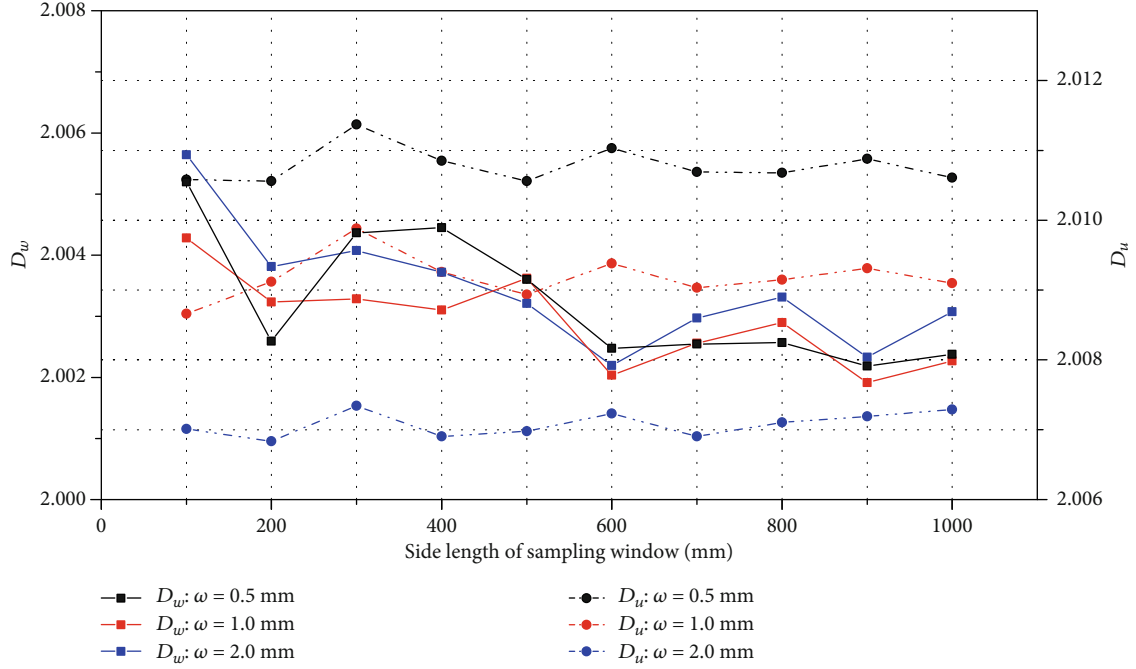


(a) Two-order fractal dimensions of surface roughness of joint sample S_1



(b) Two-order fractal dimensions of surface roughness of joint sample S_2

FIGURE 7: Continued.

(c) Two-order fractal dimensions of surface roughness of joint sample S_3 FIGURE 7: Fractal dimensions of waviness and unevenness of three rock joints of three resolutions at varying window sizes. D_w and D_u are fractal dimensions of waviness and unevenness, respectively. ω denotes the point spacing.TABLE 2: Fractal dimensions of waviness and unevenness of rock joint sample S_1 at varying window sizes.

Point spacing (mm)	Fractal estimation	Window size (mm \times mm)									
		100 \times 100	200 \times 200	300 \times 300	400 \times 400	500 \times 500	600 \times 600	700 \times 700	800 \times 800	900 \times 900	1000 \times 1000
0.5	D_w	2.008677	2.004098	2.006542	2.006624	2.005897	2.004557	2.004899	2.00348	2.003838	2.0034
	A_w	10360	40920	93180	166200	258300	369600	503400	653400	827600	964300
	R^2_w	0.999	0.9116	0.9621	0.9671	0.9561	0.9599	0.9694	0.9179	0.9543	0.9056
	D_u	2.008463	2.009124	2.01093	2.01204	2.01144	2.0118	2.01111	2.01092	2.01092	2.01064
	A_u	10350	41610	94500	169400	263500	378800	513900	669900	846800	988400
	R^2_u	0.9906	0.9873	0.9893	0.9907	0.9904	0.9909	0.9908	0.9906	0.9783	0.9886
1.0	D_w	2.01018	2.004889	2.00517	2.007159	2.006078	2.004509	2.004889	2.003546	2.003809	2.003378
	A_w	10420	41060	92560	166600	258600	369500	503400	653600	827500	964500
	R^2_w	0.999	0.9365	0.9264	0.9818	0.9686	0.9641	0.982	0.9367	0.9589	0.9172
	D_u	2.007841	2.008021	2.009109	2.01076	2.01016	2.01041	2.009771	2.009609	2.009538	2.009236
	A_u	10330	41500	93710	168800	262500	377300	51190	667400	843900	984600
	R^2_u	0.9944	0.9943	0.9916	0.9931	0.9931	0.993	0.9941	0.994	0.9934	0.9921
2.0	D_w	2.007528	2.004591	2.006311	2.006796	2.00636	2.004521	2.005116	2.003627	2.004135	2.003681
	A_w	10320	41000	93040	166300	259000	369600	503800	653800	828500	966100
	R^2_w	0.999	0.945	0.9412	0.9766	0.9518	0.9546	0.9688	0.9164	0.9636	0.9025
	D_u	2.006311	2.006409	2.007347	2.009343	2.008571	2.008585	2.007849	2.007821	2.007567	2.00734
	A_u	10280	41280	93470	168000	261000	375200	508800	663700	838800	978600
	R^2_u	0.9879	0.9894	0.9891	0.9843	0.993	0.9857	0.9948	0.9878	0.9903	0.9905

Note: D_w and D_u are fractal dimensions of waviness and unevenness, respectively. A_w and A_u are the coefficients during linear correlations for estimating D_w and D_u , respectively. R^2_w and R^2_u represent the coefficients of determination during linear correlations for estimating D_w and D_u , respectively.

TABLE 3: Fractal dimensions of waviness and unevenness of rock joint sample S_2 at varying window sizes.

Point spacing (mm)	Fractal estimation	Window size (mm \times mm)									
		100 \times 100	200 \times 200	300 \times 300	400 \times 400	500 \times 500	600 \times 600	700 \times 700	800 \times 800	900 \times 9000	1000 \times 1000
0.5	D_w	2.002065	2.004658	2.004025	2.004222	2.004405	2.003238	2.002918	2.003086	2.003475	2.003312
	A_w	10140	40920	91850	163500	25590	366900	49870	651800	82650	963700
	R^2_w	0.999	0.971	0.9343	0.9728	0.9756	0.981	0.9442	0.9449	0.9664	0.9589
	D_u	2.01016	2.009858	2.01047	2.01013	2.009915	2.01042	2.01015	2.01075	2.01075	2.01063
	A_u	10410	41620	93790	166600	26070	375600	2.01015	667200	84620	987600
	R^2_u	0.9876	0.9893	0.9893	0.9886	0.9858	0.989	51090	0.9893	0.9719	0.9882
1.0	D_w	2.002696	2.004337	2.004687	2.004136	2.003912	2.003324	2.002957	2.003051	2.003287	2.003409
	A_w	10150	40860	92090	163400	25550	367100	49890	651700	82590	964300
	R^2_w	0.999	0.9652	0.9654	0.954	0.9623	0.9777	0.9399	0.9465	0.9604	0.9578
	D_u	2.008048	2.008427	2.008947	2.008806	2.008611	2.009051	2.008796	2.008859	2.009329	2.009198
	A_u	10350	41430	93410	166000	25980	374200	50900	664700	84320	983800
	R^2_u	0.9849	0.9919	0.9902	0.9924	0.9907	0.9928	0.9934	0.9932	0.9921	0.9908
2.0	D_w	2.003945	2.005202	2.003265	2.004757	2.003571	2.003308	2.002896	2.003225	2.00347	2.003585
	A_w	10190	41000	91580	163900	25520	367000	49870	652300	82640	956300
	R^2_w	0.999	0.9499	0.9362	0.9418	0.9384	0.9771	0.9547	0.9387	0.9538	0.9417
	D_u	2.00717	2.007215	2.007344	2.007052	2.006896	2.00716	2.006828	2.006952	2.00733	2.007264
	A_u	10310	41290	92930	165100	25810	372100	50590	660800	83810	977700
	R^2_u	0.9799	0.9895	0.9885	0.9919	0.9927	0.9886	0.9927	0.9909	0.9894	0.9899

Note: D_w and D_u are fractal dimensions of waviness and unevenness, respectively. A_w and A_u are the coefficients during linear correlation for estimating D_w and D_u , respectively. R^2_w and R^2_u represent the coefficients of determination during linear correlations for estimating D_w and D_u , respectively.

0.5 mm generally are the highest, and 2.0 mm the lowest except at the window side lengths of 300 mm and 800 mm. The percent errors of the fractal dimension of unevenness of rock joint samples S_2 and S_3 at the resolution of 1.0 mm are the highest.

Figures 7 and 8 show that the fractal dimension of each-order roughness varies from 2.001 to 2.014, and the percent errors of fractal dimensions of waviness and unevenness of the three rock joint samples are numerically small, which are less than 1%. One may draw the conclusion that the scale effect of the fractal dimensions of waviness and unevenness could be neglected. Actually, the low values of percent errors result from the low values of the fractal dimensions (Figure 7) which are common for the rough surfaces of naturally formed rock joints [39, 41, 44]. Many studies reported that the fractal geometry of the surface roughness of three-dimensional rock joints is slightly larger than 2.0 [38–41]. Zhou and Xie [41] showed that the fractal dimensions of the surface roughness of tension-induced rock joints of varying degrees of roughness are all smaller than 2.07. Similarly, several rock joints collected from in situ also exhibited surface roughness of fractal dimensions around 2.05, whereas the JRC (joint roughness coefficient) values [10] of these joint surfaces reached as high as 14.0 [38]. That is to say, a naturally surfaced rock joint possesses a fractal dimension varying in a very narrow band. A small variation in fractal

dimension likely leads to noticeable change of surface roughness [26, 45].

The low values of the percent errors of fractal dimensions do not necessarily mean that the variation of surface roughness is negligible as window size change, because the widely used indicators of surface roughness such as JRC and asperity slope can be mathematically related with fractal dimension through certain relationships [45, 46]. These relationships commonly involve scaling coefficients of quite high values [45].

To illustrate the effect of fractal dimension variation on the joint roughness change, the well-established relationship linking fractal dimension (D) and JRC is employed [26]:

$$JRC = -0.87804 + 37.7844 \left(\frac{D-1}{0.015} \right) - 16.9304 \left(\frac{D-1}{0.015} \right)^2 \quad (9)$$

Equation (9) was originally proposed to estimate JRC through the fractal dimension (D) of a two-dimensional joint profile. Since the relationship between JRC and the fractal dimension (D) of a three-dimensional joint surface is unavailable, the above formulation is directly adopted by extending the two-dimension to three-dimension by replacing ($D-1$) with ($D-2$). Additionally, our purpose is not to

TABLE 4: Fractal dimensions of waviness and unevenness of rock joint sample S_3 at varying window sizes.

Point spacing (mm)	Fractal estimation	Window size (mm × mm)									
		100 × 100	200 × 200	300 × 300	400 × 400	500 × 500	600 × 600	700 × 700	800 × 800	900 × 900	1000 × 1000
0.5	D_w	2.005199	2.00259	2.004366	2.00445	2.003602	2.002477	2.002543	2.00257	2.002184	2.002377
	A_w	10120	40950	91870	163500	254600	364700	496700	649000	820100	957800
	R^2_w	0.999	0.9685	0.9246	0.9634	0.9582	0.9101	0.9252	0.9042	0.9158	0.9196
	D_u	2.01058	2.01056	2.01137	2.01085	2.01056	2.01103	2.01069	2.01068	2.01088	2.01061
	A_u	10390	41580	93880	166900	260600	375100	510300	666400	843300	984100
	R^2_u	0.9739	0.9859	0.9883	0.9864	0.9846	0.9883	0.9897	0.9894	0.9704	0.9858
1.0	D_w	2.004282	2.003235	2.003286	2.003104	2.003623	2.002034	2.002557	2.002896	2.001913	2.002271
	A_w	10180	40600	91430	162600	25460	364100	496800	647700	819100	955500
	R^2_w	0.999	0.9092	0.9133	0.9028	0.9321	0.9013	0.9124	0.929	0.9102	0.9049
	D_u	2.00866	2.009118	2.009879	2.009258	2.008936	2.009383	2.009035	2.009148	2.009312	2.0091
	A_u	10340	41410	93450	166100	259300	373400	507900	663500	839900	979800
	R^2_w	0.9831	0.9887	0.9899	0.9893	0.99	0.9927	0.9929	0.9927	0.9915	0.9901
2.0	D_w	2.00564	2.003815	2.004073	2.00372	2.00321	2.002192	2.002969	2.003313	2.002331	2.003075
	A_w	10230	40690	91750	163100	254300	364400	497600	648500	820600	963300
	R^2_w	0.999	0.9013	0.9109	0.9069	0.9065	0.9091	0.929	0.9184	0.9347	0.9201
	D_u	2.007011	2.006835	2.007341	2.006906	2.006979	2.007231	2.006903	2.007105	2.007191	2.007291
	A_u	10280	41120	92820	164900	257700	371000	504600	659400	834700	977300
	R^2_u	0.99	0.989	0.9918	0.9922	0.9922	0.991	0.9906	0.9924	0.9907	0.9921

Note: D_w and D_u are fractal dimensions of waviness and unevenness, respectively. A_w and A_u are the coefficients during linear correlation for estimating D_w and D_u , respectively. R^2_w and R^2_u represent the coefficients of determination during linear correlations for estimating D_w and D_u , respectively.

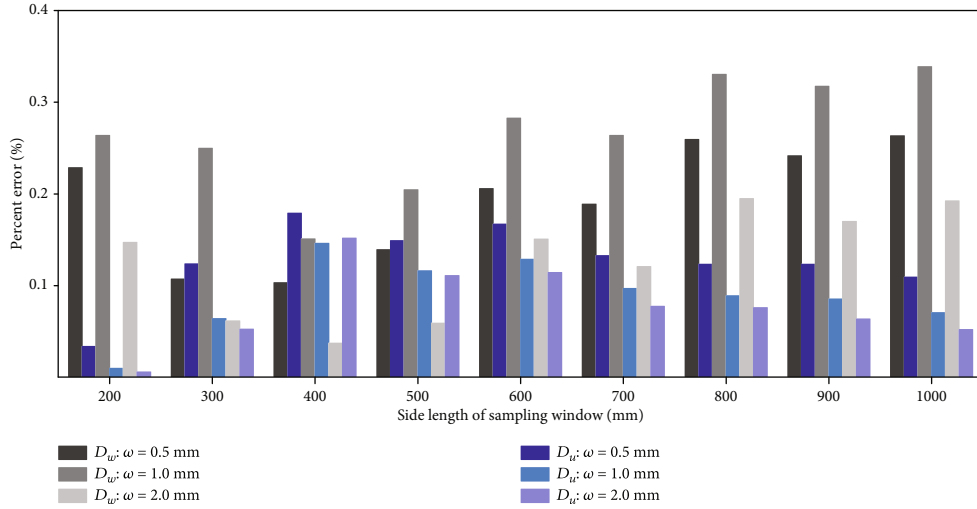
quantify JRC through fractal dimension (D), but to demonstrate the significant joint roughness variation due to the small change of fractal dimension. Considering the two-order roughness separation, JRC values of waviness and unevenness (JRC_w and JRC_u) are, respectively,

$$\begin{aligned}
 JRC_w &= -0.87804 + 37.7844 \left(\frac{D_w - 2}{0.015} \right) - 16.9304 \left(\frac{D_w - 2}{0.015} \right)^2, \\
 JRC_u &= -0.87804 + 37.7844 \left(\frac{D_u - 2}{0.015} \right) - 16.9304 \left(\frac{D_u - 2}{0.015} \right)^2.
 \end{aligned} \tag{10}$$

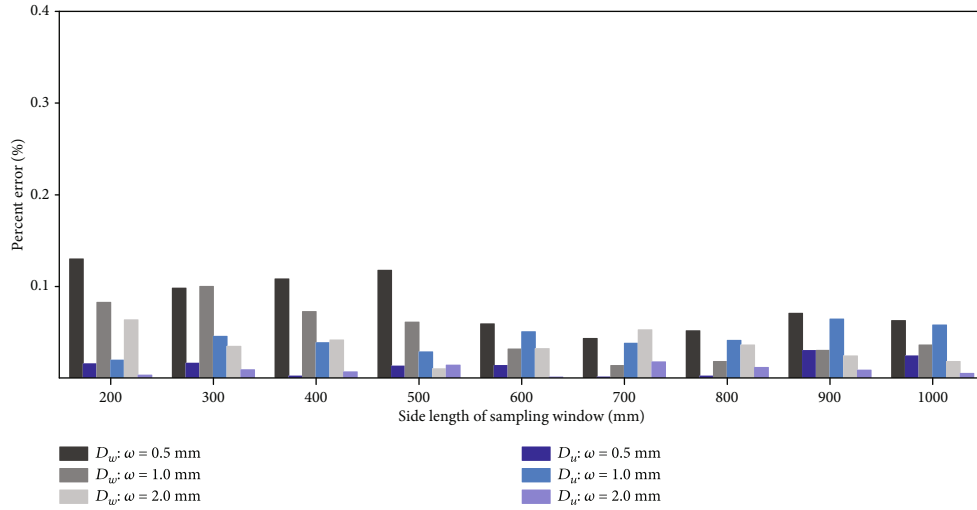
Figure 9 shows the effect of window size on the percent errors of JRC values of waviness and unevenness (JRC_w and JRC_u) of the three rock joint samples of different measurement resolutions. For joint samples S_1 to S_3 , JRC values of waviness (JRC_w) exhibit strong scale dependency without general trend. The maximum percent errors of JRC_w of joint samples S_1 , S_2 , and S_3 occur on window sizes of 1000 mm × 1000 mm, 200 mm × 200 mm, and 600 mm × 600 mm, respectively, suggesting the randomness of the scale effect. Additionally, similar to the fractal dimension, the effect of window size on JRC_w is much more pronounced than on JRC_u . For joint sample S_1 , the percent errors of JRC_w are generally appreciably larger than those of JRC_u with a maximum

value smaller than 40%. For joint samples S_2 and S_3 , the percent errors of JRC_w can be as high as 130%, whereas the percent errors of JRC_u are all lower than 15% with a majority less than 10%, which indicates that the scale effect of JRC_u may be insignificant.

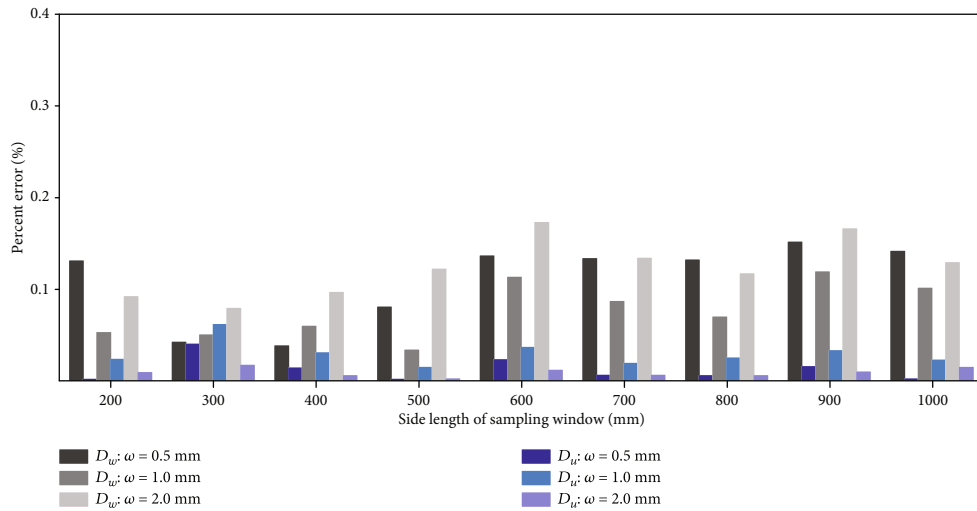
4.2. Effect of Measurement Resolution. We digitised the surface of each rock joint sample using three different resolutions. Figure 10 shows the percent errors of the fractal dimensions of waviness and unevenness of the three rock joint samples at resolutions of 1.0 mm and 2.0 mm, respectively, relative to the point spacing of 0.5 mm. Both the fractal dimensions of waviness and unevenness are dependent of measurement resolution. The fractal dimension of unevenness is much more sensitive to the measurement resolution compared with that of waviness. For all the three samples, the fractal dimension of unevenness is the largest at the highest resolution and vice versa. The percent error of fractal dimension of unevenness under the point spacing of 2.0 mm is roughly two times that under point spacing of 0.5 mm. Nevertheless, the fractal dimension of waviness of all the three samples is seemingly unaffected by the resolution. In this study, waviness are asperities in wavelength longer than 30 mm that is substantially greater than the prescribed point spacings. The fractal dimension of waviness is theoretically independent on the resolution of point spacing less than 30 mm. In many cases, the difference of fractal



(a) Percent errors of fractal dimensions of waviness and unevenness of joint sample S_1

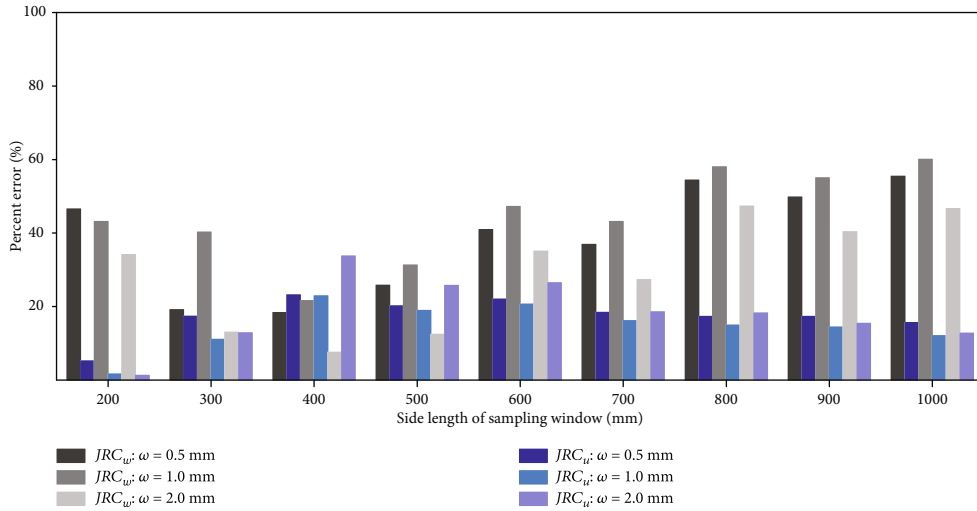


(b) Percent errors of fractal dimensions of waviness and unevenness of joint sample S_2

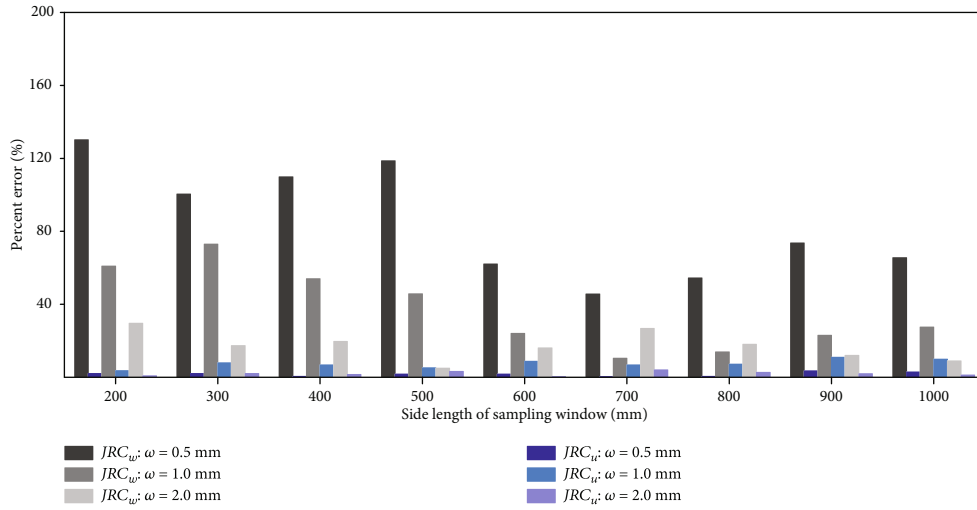


(c) Percent errors of fractal dimensions of waviness and unevenness of joint sample S_3

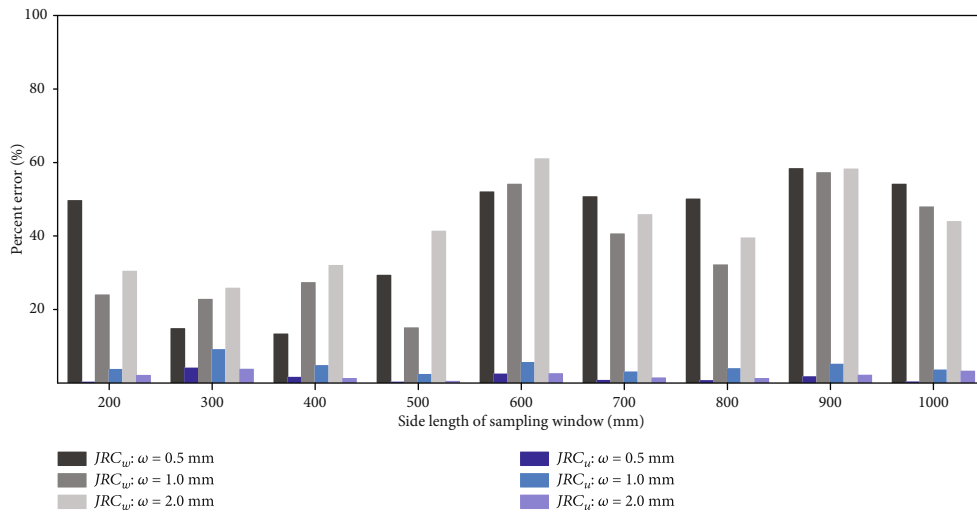
FIGURE 8: Effect of window size on the fractal dimensions of waviness and unevenness of three rock joints of three resolutions. Percent errors are relative to the values of window size of 100 mm \times 100 mm. D_w and D_u are fractal dimensions of waviness and unevenness. ω denotes the point spacing.



(a) Percent errors of the JRC values of waviness and unevenness of joint sample S_1

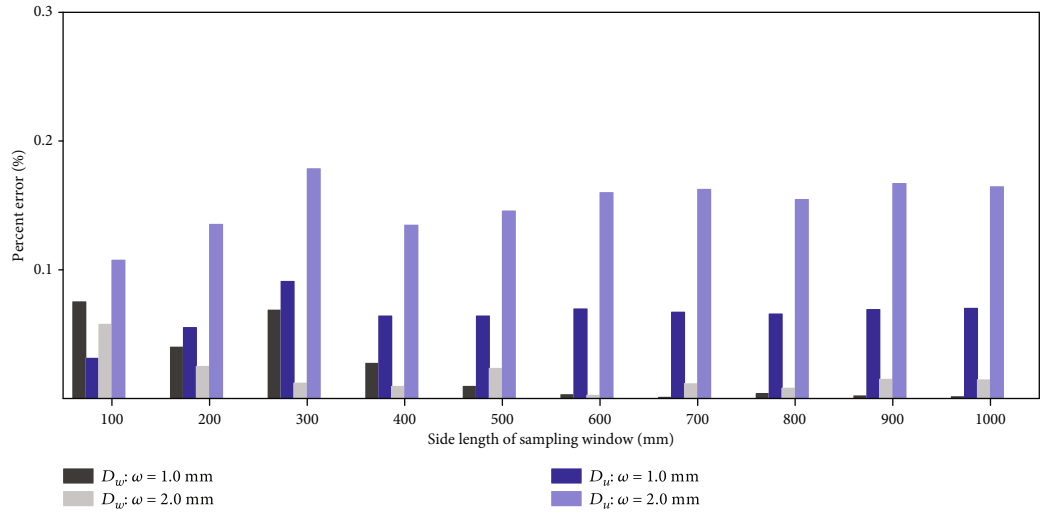


(b) Percent errors of the JRC values of waviness and unevenness of joint sample S_2

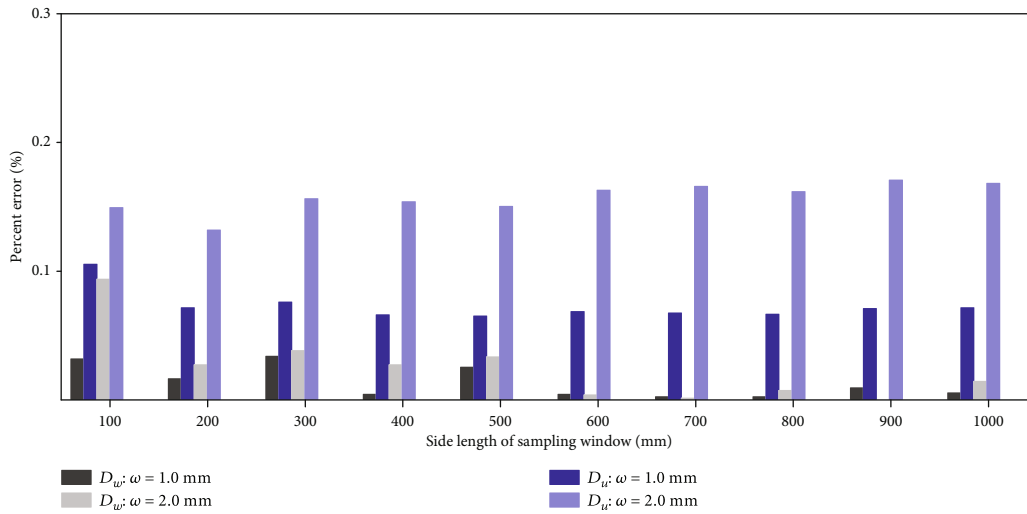


(c) Percent errors of the JRC values of waviness and unevenness of joint sample S_3

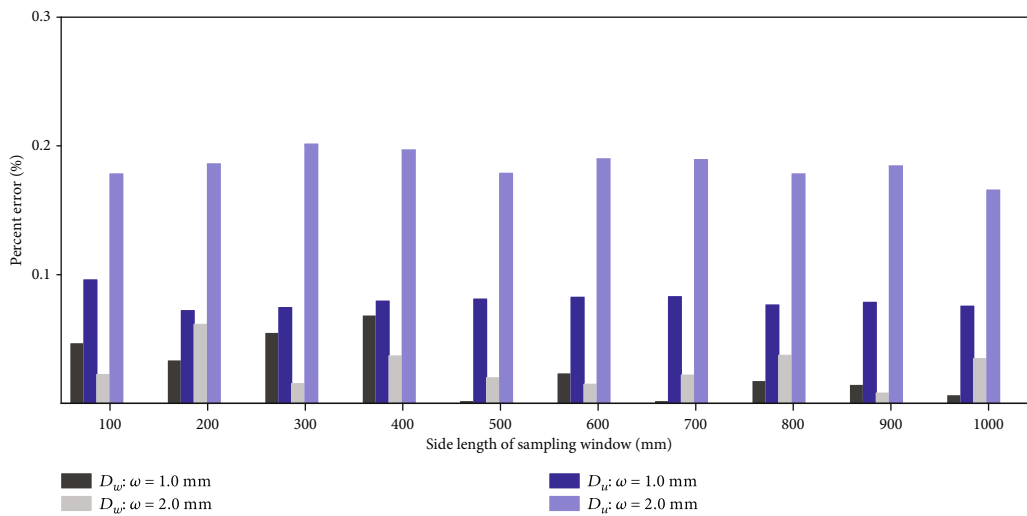
FIGURE 9: Effect of window size on the JRC values of waviness and unevenness of three rock joints of three resolutions. Percent errors are relative to the values of window size of 100 mm \times 100 mm. JRC_w and JRC_u are the JRC values of waviness and unevenness, respectively. ω denotes the point spacing.



(a) Percent errors of fractal dimensions of waviness and unevenness of joint sample S_1

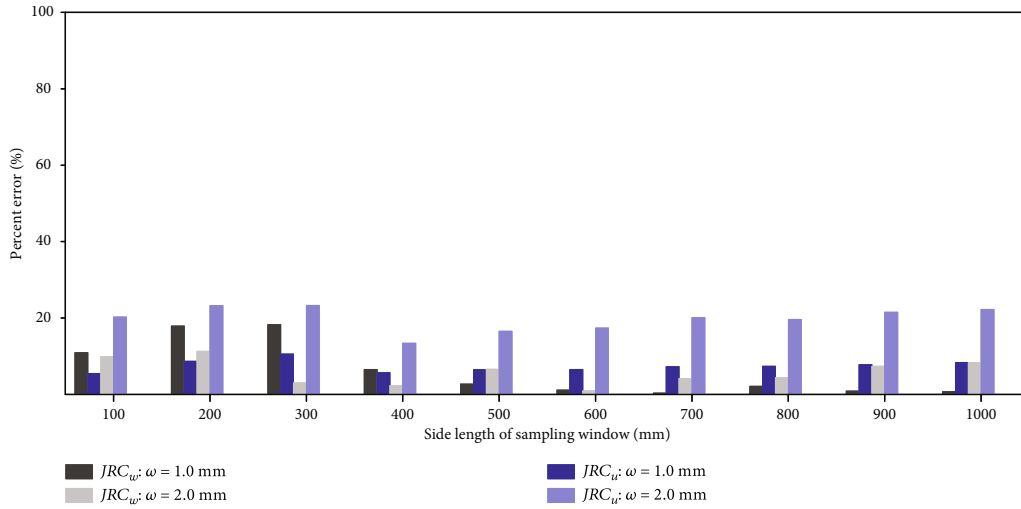


(b) Percent errors of fractal dimensions of waviness and unevenness of joint sample S_2

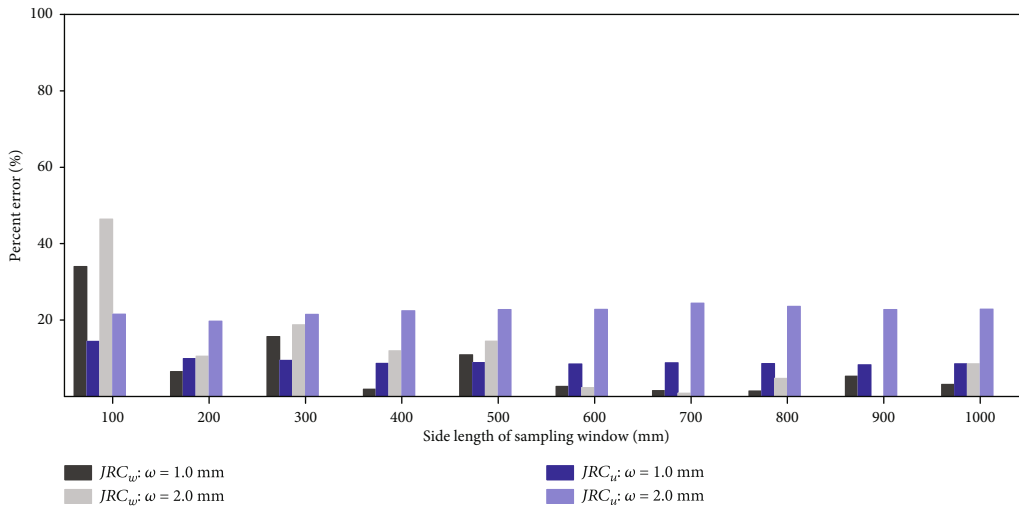


(c) Percent errors of fractal dimensions of waviness and unevenness of joint sample S_3

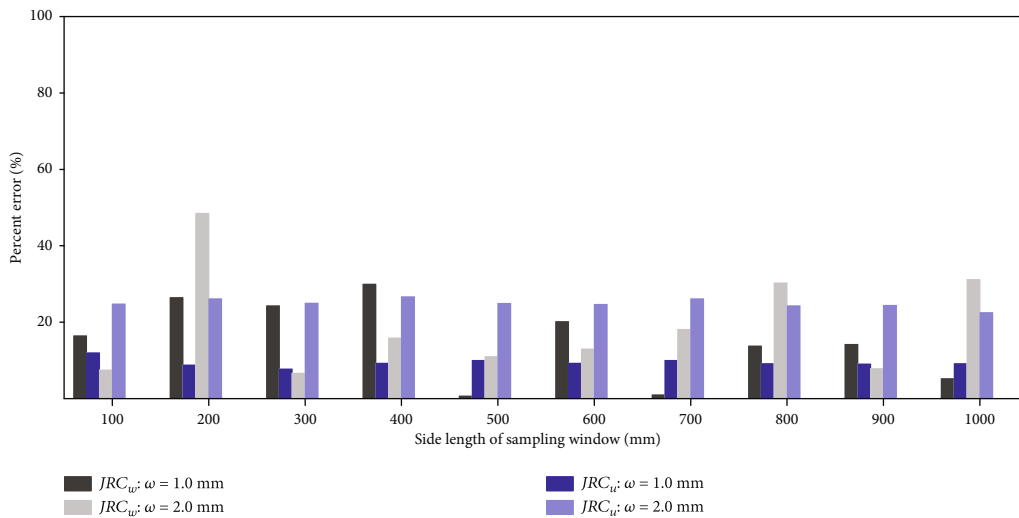
FIGURE 10: Effect of resolution on the fractal dimensions of waviness and unevenness of three rock joints of varying sampling window sizes. Percent errors are calculated relative to the values of resolution of 0.5 mm. D_w and D_u are fractal dimensions of waviness and unevenness, respectively. ω denotes the point spacing.



(a) Percent errors of the JRC values of waviness and unevenness of joint sample S_1



(b) Percent errors of the JRC values of waviness and unevenness of joint sample S_2



(c) Percent errors of the JRC values of waviness and unevenness of joint sample S_3

FIGURE 11: Effect of resolution on the JRC values of waviness and unevenness of three rock joint samples of varying sampling window sizes. Percent errors are calculated relative to the values of resolution of 0.5 mm. JRC_w and JRC_u are the JRC values of waviness and unevenness, respectively. ω denotes the point spacing.

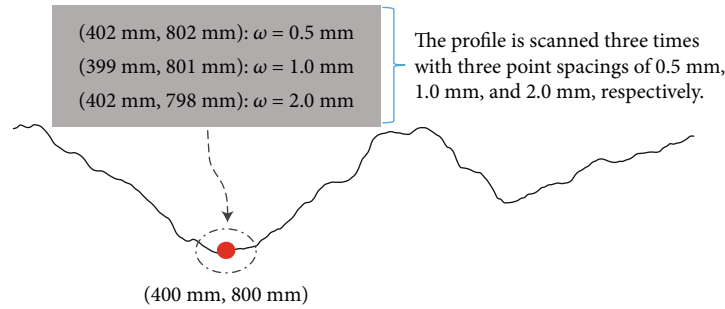


FIGURE 12: Illustration of the coordinate deviation due to manual operation.

dimension of waviness of the three samples is negligible (Figures 8 and 11). The minor discrepancies mainly originated from the fact that it is impossible to acquire exactly the same coordinates of a certain point due to the error caused by the manual operation of the HandyPROBE. For the example, in Figure 12, the coordinates (400 mm, 800 mm) of a point of a profile are perhaps digitised as (402 mm, 802 mm), (399 mm, 801 mm), and (402 mm, 798 mm) during the scanning with point spacings of 0.5 mm, 1.0 mm, and 2.0 mm, respectively.

Figures 8 and 10 show that both window size and measurement resolution affect the fractal dimensions of waviness and unevenness. The measurement resolution has no less influence than window size on the variation of fractal dimension. Previous studies [18–23] have reported positive, negative, and no scale effects when large-scale rock joint surfaces are measured. The controversial results may be stemmed from the combinative effects of sample size and measurement resolution. Most of the studies on large-scale rock joints in the literature [21, 23, 47] used inconsistent measurement resolutions to digitise rock joint surfaces of varying scales. In these studies, the point spacing was increased as larger areas (or lengths) of the rock joint surface were examined. Therefore, the change in roughness with increased rock joint size reported in this work was also possibly a result of the varying measurement resolution besides the variation in roughness [22].

5. Discussion and Implications

We explored the fractal characteristics of two-order asperities of natural rock joints in window sizes from 100 mm × 100 mm to 1000 mm × 1000 mm with three different resolutions.

Both the fractal dimensions of waviness and unevenness vary as the window size increases.

Nevertheless, no apparent stationarity threshold has been found for the three natural granite joints. The findings contrast with the results reported in Fardin et al. [23]. Using the roughness length method [33], Fardin et al. [23] studied the fractal dimension of the surface roughness of a rock joint up to the window size of 1000 mm × 1000 mm.

They claimed that for sampling windows having a size larger than a stationarity threshold of roughly 500 mm × 500 mm, the fractal dimension remained almost unvaried and can be considered as reliable estimation. The discrepancy

between Fardin et al. [23] and our study possibly resulted from the following reasons. First, a single fractal dimension, i.e., the fractal dimension of unevenness, was estimated by Fardin et al. [23]. In the calculation of the roughness length method, the local trend, the asperities with long wavelength (which is termed waviness in this study) are excluded to avoid overestimating roughness in small windows [32, 33]. Second, the fractal dimension of unevenness with relatively small and similar wavelength and amplitude probably keeps almost constant as the sampling data reaches a certain large volume since fractal dimension is essentially determined based on statistical consideration. For example, the fractal dimensions of unevenness of rock joint samples S_2 and S_3 in this study (Figures 7(b) and 7(c)) appear unchanged when the window size exceeds 400 mm × 400 mm. Moreover, the surface of merely one rock joint was studied by Fardin et al. [23], based on which affirmative conclusions cannot be drawn without examining the fractal features of several more large-scale rock joints with varying surface roughness.

Quantification of the surface roughness of a natural rock joint is critical for predicting the mechanical and hydraulic properties of a rock mass. Particularly, the shear behaviour of rock joints is strongly affected by surface roughness. Under a low normal stress (relative to rock strength), a rock joint fails in shear due to asperity dilation. In this case, both waviness and unevenness contribute to the degree of dilatancy. When the normal stress is high, joint shear behaviour is mainly controlled by the damage or degradation of waviness since unevenness is much more easily sheared off. The permeability of rock joints under shearing is closely associated with the dilation and degradation of asperities [48–53]. That is to say, waviness and unevenness of the surface roughness of a natural rock joint should be separately considered for accurately predicting the hydromechanical behaviour of a rock mass. Currently, surface roughness of rock joints at field scales is commonly evaluated from laboratory experimentation on small joint samples through scaling laws [18, 54]. These laws are unable to, respectively, take into account the variations of waviness and unevenness at different scales.

Additionally, our findings based on three natural rock joints sized 1000 mm × 1000 mm show that the fractal dimensions of waviness and unevenness seemingly vary without a universal trend as the joint sample size changes. In other words, waviness and unevenness of rock joints should be quantified at the scales of rock masses in the field

mainly due to the random nature of asperity distribution along a joint surface [55].

6. Conclusions

We investigated the scale effect of surface roughness of natural rock joints using fractal approach. Three natural granite joints dimensioned of 1000×1000 mm were digitised and reconstructed at three different measurement resolutions. The fractal characteristics of two-order roughness, i.e., waviness and unevenness, were separately quantified through the classic triangular prism surface area method (TPM). We found that each-order roughness of a natural rock joint in window sizes varying from $100 \text{ mm} \times 100 \text{ mm}$ to $1000 \text{ mm} \times 1000 \text{ mm}$ owns individual fractal dimension. Although both the fractal dimensions of waviness and unevenness are scale-dependent, no noticeable stationarity threshold of scale effect has been found primarily due to the randomness of roughness distribution. Additionally, the measurement resolution has remarkable influence on the fractal dimension of unevenness, whereas its effect on that of waviness is negligible. Surface roughness quantification plays a key role in predicting the hydromechanical behaviour of rock masses. Our findings suggest that waviness and unevenness should be separately characterised at the field scale of the rock mass with an appropriate consistent measurement resolution. The conclusions are drawn by examining three natural rock joints with the dimension up to $1000 \text{ mm} \times 1000 \text{ mm}$. The existence of a stationarity threshold of a larger value remains questionable due to the absence of experimental data. One may argue that the surface roughness of a natural rock joint likely exhibits more than two-order roughness.

However, roughness characterisation with two-order roughness is sufficient for the purpose of accurately estimating the mechanical and hydraulic properties of rock joints. Further studies are to investigate the anisotropy of the fractal features of surface roughness since the hydromechanical behaviours of rock joints are strongly direction-dependent.

Data Availability

The experimental data used to support the findings of this study are included within the article.

Conflicts of Interest

The authors declare they have no conflicts of interest to this work.

Acknowledgments

Yingchun Li thanks the financial support from the National Natural Science Foundation (51809033), the China Postdoctoral Science Foundation (2019T120208), the National Key Research and Development Plan (2018YFC1505301), and the Fundamental Research Funds for the Central Universities (DUT20LK15).

References

- [1] B. Brady and E. Brown, *Rock Mechanics for Underground Mining*, Kluwer Academic Publishers, 2006.
- [2] International Journal of Rock Mechanics and Mining Sciences, "Commission on standardization of laboratory and field tests of the international society for rock mechanics: 'suggested methods for the quantitative description of discontinuities,'" *Int J Rock Mech Min*, vol. 15, no. 6, pp. 320–368, 1978.
- [3] F. Patton, *Multiple failure modes of rock and related materials*, [Ph.D. thesis], University of Illinois, 1966.
- [4] Q. He, Y. Li, J. Xu, and C. Zhang, "Prediction of mechanical properties of igneous rocks under combined compression and shear loading through statistical analysis," *Rock Mechanics and Rock Engineering*, vol. 53, no. 2, pp. 841–859, 2020.
- [5] L. Jing, E. Nordlund, and O. Stephansson, "An experimental study on the anisotropy and stress-dependency of the strength and deformability of rock joints," *International Journal of Rock Mechanics and Mining Sciences & Geomechanics Abstracts*, vol. 29, no. 6, pp. 535–542, 1992.
- [6] H. Lee, Y. Park, T. Cho, and K. You, "Influence of asperity degradation on the mechanical behavior of rough rock joints under cyclic shear loading," *International Journal of Rock Mechanics and Mining Sciences*, vol. 38, no. 7, pp. 967–980, 2001.
- [7] Y. Li, J. Oh, R. Mitra, and B. Hebblewhite, "A constitutive model for a laboratory rock joint with multi-scale asperity degradation," *Computers and Geotechnics*, vol. 72, pp. 143–151, 2016.
- [8] Z. Yang, C. Di, and K. Yen, "The effect of asperity order on the roughness of rock joints," *International Journal of Rock Mechanics and Mining Sciences*, vol. 38, no. 5, pp. 745–752, 2001.
- [9] Y. Li, J. Oh, R. Mitra, and I. Canbulat, "A fractal model for the shear behaviour of large-scale opened rock joints," *Rock Mechanics and Rock Engineering*, vol. 50, no. 1, pp. 67–79, 2017.
- [10] N. Barton and V. Choubey, "The shear strength of rock joints in theory and practice," *Rock Mechanics*, vol. 10, no. 1-2, pp. 1–54, 1977.
- [11] H. Dong, G. Poropat, I. Gratchev, and A. Balasubramaniam, "Improvement of photogrammetric JRC data distributions based on parabolic error models," *International Journal of Rock Mechanics and Mining Sciences*, vol. 80, pp. 19–30, 2015.
- [12] Y. Li, C. Tang, D. Li, and C. Wu, "A new shear strength criterion of three-dimensional rock joints," *Rock Mechanics and Rock Engineering*, vol. 53, no. 3, pp. 1477–1483, 2020.
- [13] G. Morelli, "On joint roughness: measurements and use in rock mass characterization," *Geotechnical and Geological Engineering*, vol. 32, no. 2, pp. 345–362, 2014.
- [14] R. Tse and D. Cruden, "Estimating joint roughness coefficients," *International Journal of Rock Mechanics and Mining Sciences & Geomechanics Abstracts*, vol. 16, no. 5, pp. 303–307, 1979.
- [15] X. Yu and B. Vayssade, "Joint profiles and their roughness parameters," *International Journal of Rock Mechanics and Mining Sciences & Geomechanics Abstracts*, vol. 28, no. 4, pp. 333–336, 1991.
- [16] Y. Li, S. Sun, and C. Tang, "Analytical prediction of the shear behaviour of rock joints with quantified waviness and unevenness through wavelet analysis," *Rock Mechanics and Rock Engineering*, vol. 410, pp. 1–13, 2019.

- [17] L. Zou, L. Jing, and V. Cvetkovic, "Roughness decomposition and nonlinear fluid flow in a single rock fracture," *International Journal of Rock Mechanics and Mining Sciences*, vol. 75, pp. 102–118, 2015.
- [18] S. Bandis, A. Lumsden, and N. Barton, "Experimental studies of scale effects on the shear behaviour of rock joints," *International Journal of Rock Mechanics and Mining Sciences & Geomechanics Abstracts*, vol. 18, no. 1, pp. 1–21, 1981.
- [19] M. Cravero, G. Iabichino, and V. Piovano, "Analysis of large joint profiles related to rock slope instabilities," in *Proceedings of the 8th ISRM Congress*, pp. 423–428, Tokyo, Japan, 1995.
- [20] N. Fardin, "Influence of structural non-stationarity of surface roughness on morphological characterization and mechanical deformation of rock joints," *Rock Mechanics and Rock Engineering*, vol. 41, no. 2, pp. 267–297, 2008.
- [21] N. Maerz and J. Franklin, "Roughness scale effects and fractal dimension," in *Proceedings of the First International Workshop on Scale Effects in Rock Masses*, pp. 121–125, Loen, Norway, 1990.
- [22] B. Tatone and G. Grasselli, "An investigation of discontinuity roughness scale dependency using high-resolution surface measurements," *Rock Mechanics and Rock Engineering*, vol. 46, no. 4, pp. 657–681, 2013.
- [23] N. Fardin, O. Stephansson, and L. Jing, "The scale dependence of rock joint surface roughness," *International Journal of Rock Mechanics and Mining Sciences*, vol. 38, no. 5, pp. 659–669, 2001.
- [24] B. Mandelbrot, "How long is the coast of Britain? Statistical self-similarity and fractional dimension," *Science*, vol. 156, no. 3775, pp. 636–638, 1967.
- [25] B. Mandelbrot, "Self-affine fractals and fractal dimension," *Physica Scripta*, vol. 32, no. 4, pp. 257–260, 1985.
- [26] Y. Lee, J. Carr, D. Barr, and C. Haas, "The fractal dimension as a measure of the roughness of rock discontinuity profiles," *International Journal of Rock Mechanics and Mining Sciences & Geomechanics Abstracts*, vol. 27, no. 6, pp. 453–464, 1990.
- [27] L. Liebovitch and T. Toth, "A fast algorithm to determine fractal dimensions by box counting," *Physics Letters A*, vol. 141, no. 8–9, pp. 386–390, 1989.
- [28] P. Kulatilake, P. Balasingam, J. Park, and R. Morgan, "Natural rock joint roughness quantification through fractal techniques," *Geotechnical and Geological Engineering*, vol. 24, no. 5, pp. 1181–1202, 2006.
- [29] M. Kwasniewski and J. Wang, "Application of laser profilometry and fractal analysis to measurement and characterization of morphological features of rock fracture surfaces," in *Geotechnique et Environnement, Colloque Franco-Polonais*, pp. 163–176, CRC Press, Balkema, Rotterdam, 1993.
- [30] S. Brown, "A Note on the description of surface roughness using fractal dimension," *Geophysical Research Letters*, vol. 14, no. 11, pp. 1095–1098, 1987.
- [31] H. Yang, B. Baudet, and T. Yao, "Characterization of the surface roughness of sand particles using an advanced fractal approach," *Proceedings of the Royal Society A: Mathematical, Physical and Engineering Sciences*, vol. 472, no. 2194, article 20160524, 2016.
- [32] P. H. S. W. Kulatilake, J. Um, and G. Pan, "Requirements for accurate quantification of self-affine roughness using the variogram method," *International Journal of Solids and Structures*, vol. 35, no. 31–32, pp. 4167–4189, 1998.
- [33] A. Malinverno, "A simple method to estimate the fractal dimension of a self-affine series," *Geophysical Research Letters*, vol. 17, no. 11, pp. 1953–1956, 1990.
- [34] M. Matsushita and S. Ouchi, "On the self-affinity of various curves," *Physica D*, vol. 38, no. 1–3, pp. 246–251, 1989.
- [35] K. C. Clarke, "Computation of the fractal dimension of topographic surfaces using the triangular prism surface area method," *Computers & Geosciences*, vol. 12, no. 5, pp. 713–722, 1986.
- [36] W. Ju and S. Lam, "An improved algorithm for computing local fractal dimension using the triangular prism method," *Computers & Geosciences*, vol. 35, no. 6, pp. 1224–1233, 2009.
- [37] D. Santis, M. Fedi, and T. Quarta, "A revisitation of the triangular prism surface area method for estimating the fractal dimension of fractal surfaces," *Annals of Geophysics*, vol. 40, no. 4, 1997.
- [38] Y. Jiang, B. Li, and Y. Tanabashi, "Estimating the relation between surface roughness and mechanical properties of rock joints," *International Journal of Rock Mechanics and Mining Sciences*, vol. 43, no. 6, pp. 837–846, 2006.
- [39] H. Xie, J. Wang, and M. Kwasniewski, "Multifractal characterization of rock fracture surfaces," *International Journal of Rock Mechanics and Mining Sciences*, vol. 36, no. 1, pp. 19–27, 1999.
- [40] H. Xie and J. Wang, "Direct fractal measurement of fracture surfaces," *International Journal of Solids and Structures*, vol. 36, no. 20, pp. 3073–3084, 1999.
- [41] H. Zhou and H. Xie, "Direct estimation of the fractal dimensions of a fracture surface of rock," *Surface Review and Letters*, vol. 10, no. 5, pp. 751–762, 2003.
- [42] N. Lam, H. Qiu, D. Quattrochi, and C. Emerson, "An evaluation of fractal methods for characterizing image complexity," *Cartography and Geographic Information Science*, vol. 29, no. 1, pp. 25–35, 2002.
- [43] S. Jaggi, D. A. Quattrochi, and N. S.-N. Lam, "Implementation and operation of three fractal measurement algorithms for analysis of remote-sensing data," *Computers & Geosciences*, vol. 19, no. 6, pp. 745–767, 1993.
- [44] M. Sakellariou, B. Nakos, and C. Mitsakaki, "On the fractal character of rock surfaces," *International Journal of Rock Mechanics and Mining Sciences & Geomechanics Abstracts*, vol. 28, no. 6, pp. 527–533, 1991.
- [45] Y. Li and R. Huang, "Relationship between joint roughness coefficient and fractal dimension of rock fracture surfaces," *International Journal of Rock Mechanics and Mining Sciences*, vol. 75, pp. 15–22, 2015.
- [46] Y. Li, *A constitutive model of opened rock joints in the field*, [Ph.D. thesis], University of New South Wales, Sydney, 2016.
- [47] M. Cravero, G. Iabichino, and A. Ferrero, "Evaluation of joint roughness and dilatancy of schistosity joints," in *Proceedings of Eurock 2001: Rock Mechanics—a Challenge for Society*, pp. 217–222, Espoo, Finland, 2001.
- [48] N. Huang, R. Liu, and Y. Jiang, "Numerical study of the geometrical and hydraulic characteristics of 3D self-affine rough fractures during shear," *Journal of Natural Gas Science and Engineering*, vol. 45, pp. 127–142, 2017.
- [49] B. Li, Y. Jiang, T. Koyama, L. Jing, and Y. Tanabashi, "Experimental study of the hydro-mechanical behavior of rock joints using a parallel-plate model containing contact areas and artificial fractures," *International Journal of Rock Mechanics and Mining Sciences*, vol. 45, no. 3, pp. 362–375, 2008.

- [50] R. Liu, Y. Jiang, B. Li, and X. Wang, "A fractal model for characterizing fluid flow in fractured rock masses based on randomly distributed rock fracture networks," *Computers and Geotechnics*, vol. 65, pp. 45–55, 2015.
- [51] R. Liu, B. Li, and Y. Jiang, "A fractal model based on a new governing equation of fluid flow in fractures for characterizing hydraulic properties of rock fracture networks," *Computers and Geotechnics*, vol. 75, pp. 57–68, 2016.
- [52] X. Xiong, B. Li, Y. Jiang, T. Koyama, and C. Zhang, "Experimental and numerical study of the geometrical and hydraulic characteristics of a single rock fracture during shear," *International Journal of Rock Mechanics and Mining Sciences*, vol. 48, no. 8, pp. 1292–1302, 2011.
- [53] Y. Li, C. Wu, and B. Jang, "Effect of bedding plane on the permeability evolution of typical sedimentary rocks under triaxial compression," *Rock Mechanics and Rock Engineering*, 2020.
- [54] J. Oh, E. Cording, and T. Moon, "A joint shear model incorporating small-scale and large-scale irregularities," *International Journal of Rock Mechanics and Mining Sciences*, vol. 76, pp. 78–87, 2015.
- [55] S. Hencher and L. Richards, "Assessing the shear strength of rock discontinuities at laboratory and field scales," *Rock Mechanics and Rock Engineering*, vol. 48, no. 3, pp. 883–905, 2015.

Research Article

A New Decision Method of Filling Ratio Based on Energy Matching of Surrounding Rock and Backfill

Yanlong Zhou , Keping Zhou , and Yun Lin 

School of Resources and Safety Engineering, Central South University, Changsha 410083, China

Correspondence should be addressed to Yun Lin; yunlin617@csu.edu.cn

Received 23 June 2020; Revised 13 July 2020; Accepted 23 July 2020; Published 5 August 2020

Academic Editor: Qian Yin

Copyright © 2020 Yanlong Zhou et al. This is an open access article distributed under the Creative Commons Attribution License, which permits unrestricted use, distribution, and reproduction in any medium, provided the original work is properly cited.

In order to simplify the ratio decision process of cemented backfill in underground mines and achieve fine decision of filling ratio, the research on the energy matching between surrounding rock and cemented backfill in underground mines was conducted in this study. Based on the cubic function strength model of cemented backfill, the peak specific energy equation of backfill was improved by inversion analysis of the data of filling ratio experiment, and the functional relationship between the peak specific energy and the filling ratio was obtained by regression analysis. Then, based on the energy balance principle between the deformation energy released by the excavation of the underground rock mass and the peak specific energy of the cemented backfill, considering the physical and mechanical parameters of the surrounding rock of the goaf, including bulk density, elastic modulus, and burial depth, a ratio decision model of cemented backfill is established. The application results suggested that the calculation result of the model is reliable, and it can realize the rapid and accurate decision of the ratio of cement backfill in underground mines.

1. Introduction

Underground mineral resources provide indispensable materials for human use, but the excavation of underground mineral resources may cause a number of safety accidents, such as goaf instability caused by the excavation of underground ore bodies [1–6]. To ensure the stability of goafs in underground mines, underground rock mechanics [7–13] has been used to propose many measures, such as retaining isolated mine pillars and filling the goafs. Among them, filling the goafs is a more effective method [14–17] and has been gradually promoted in underground mines [18–21]. It is worth noting that the rock mass excavation and filling involved in underground mining is a typical fluid-solid coupling problem, and there are many influencing factors that make it difficult to obtain filling ratio of backfill quickly and accurately. In practical applications, the filling ratio of backfill is generally determined according to engineering experience, and the adopted values of the filling ratios are generally too large [22, 23]. Although the goaf stability is guaranteed with high

filling ratios, some other problems can arise, such as a waste of filling materials. Therefore, it is necessary to carry out research to determine a rapid and accurate decision-making method of the filling ratios of underground mines.

At present, most of the related research focuses on the mechanical properties of surrounding rock and backfill. For example, Fang and Fall [24] studied the shear mechanical properties of the interface between backfill and a rock mass. The characteristics of the mechanical interaction between backfill and a rock mass under the condition of creep behaviour were investigated by Qi and Fourie [25]. Hou et al. [26] analyzed the change law of mechanical properties during the process of the joint support of backfill and ore pillars. Liu et al. [27] explored the damage patterns of backfill and surrounding rock. Yan et al. [28] conducted a numerical analysis of the stress distribution characteristics of backfill.

The determination of the size of the filling body is one of the most critical issues in the mining process, but few related studies have been presented, and these earlier studies mainly concentrated on traditional methods, including ratio

experiments and numerical simulation analyses [29–33]. For example, Wu et al. [34] chose the uniaxial compressive strength (UCS), slurry slump, and unit C binder consumption as response variables and then optimized the filling ratio of cemented backfill. Through the orthogonal experimental method, the best prescription of hemihydrate phosphogypsum was determined by Lan et al. [35]. Wen et al. [23] and Sun et al. [36] explored the optimal ratios of composite cementitious material based on fill tests and simulation analyses.

The traditional methods have the disadvantages of a long decision-making period, single results, and inflexibility. Aiming to establish a fast and accurate decision method for the filling ratio of cemented backfill, research on the energy balance between rock mass and backfill will be studied in this work.

2. Establishment of the Energy Model of Backfill

A goaf is formed in the excavation of an underground rock mass, and after the rock mass is excavated, its energy is released, which in turn causes the backfill to be gradually compressed and produce deformation energy. Considering the unconfined uniaxial compression characteristics, combined with the research results of relevant scholars [37], the peak specific energy of the unit volume backfill when it reaches the peak state can be expressed as

$$V_M = \int_0^{\varepsilon_M} \sigma d\varepsilon, \quad (1)$$

where V_M is the peak specific energy, MJ/m^3 , σ is the stress, MPa , ε is the strain, and ε_M is the peak strain of the backfill.

By establishing the stress-strain relationship of the backfill, the peak specific energy of the backfill can be calculated. Many scholars have carried out research and analyses on model functions and established many damage functions that characterize the damage characteristics of backfill, but these functions have the following problems: (1) the form is generally very complicated, (2) the fitting effect is poor, and (3) the calculation is difficult. Considering that the strength curve of the backfill (shown in Figure 1) can be better described by a cubic function, some scholars have proposed cubic (shown in Equation (2)) stress-strain relationships of backfill. Thus, a cubic function will be utilized to analyze the energy of the backfill in this study.

$$\sigma = a\varepsilon + b\varepsilon^2 + c\varepsilon^3 + d, \quad (2)$$

where a , b , c , and d are constants, and ε represents the strain of the backfill.

According to the characteristics of the stress-strain curve of the backfill, the following boundary conditions are considered [38].

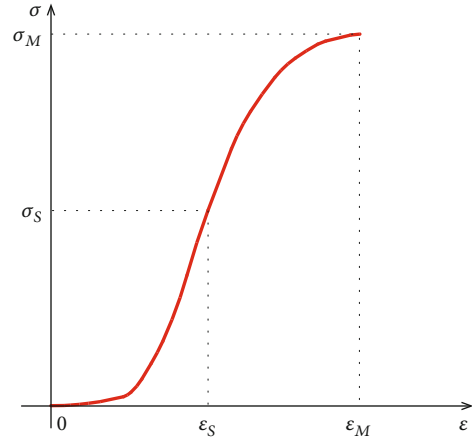


FIGURE 1: Schematic diagram of the stress-strain curve and inflection point of the backfill.

$$\begin{cases} \sigma|_{\varepsilon=0} = 0, \\ \sigma|_{\varepsilon=\varepsilon_M} = \sigma_M, \\ \left. \frac{d\sigma}{d\varepsilon} \right|_{\varepsilon=\varepsilon_M} = 0, \\ \left. \frac{d^2\sigma}{d\varepsilon^2} \right|_{\varepsilon=\varepsilon_S} = 0, \end{cases} \quad (3)$$

where ε_S represents the strain at the inflection point of the curve.

Substituting Equation (2) into Equation (3), the following relationships can be obtained.

$$\begin{cases} a = \frac{\sigma_M(6\varepsilon_S - 3\varepsilon_M)}{\varepsilon_M(3\varepsilon_S - 2\varepsilon_M)}, \\ b = \frac{-3\varepsilon_S\sigma_M}{\varepsilon_M^2(3\varepsilon_S - 2\varepsilon_M)}, \\ c = \frac{\sigma_M}{\varepsilon_M^2(3\varepsilon_S - 2\varepsilon_M)}, \\ d = 0. \end{cases} \quad (4)$$

Substituting Equation (4) into Equation (1), we have

$$V_M = \int_0^{\varepsilon_M} \sigma d\varepsilon = \frac{\sigma_M \varepsilon_M (8\varepsilon_S - 5\varepsilon_M)}{12\varepsilon_S - 8\varepsilon_M}. \quad (5)$$

3. The Peak Specific Energy of Backfill

3.1. Experimental Materials. The tailings used in this paper came from Baoshan Mine. The size distribution of the tailings is shown in Figure 2. The nonuniformity coefficient C_u is 10.3 ($C_u > 5$), and the curvature coefficient C_c is 1.27 ($1 < C_c < 3$). Therefore, the tailings are coarse sand, and the gradation is good. The elemental components of the tailing are shown in Table 1. It is known that Si, Al, and Fe contain less, which is helpful for strength performance. To reflect

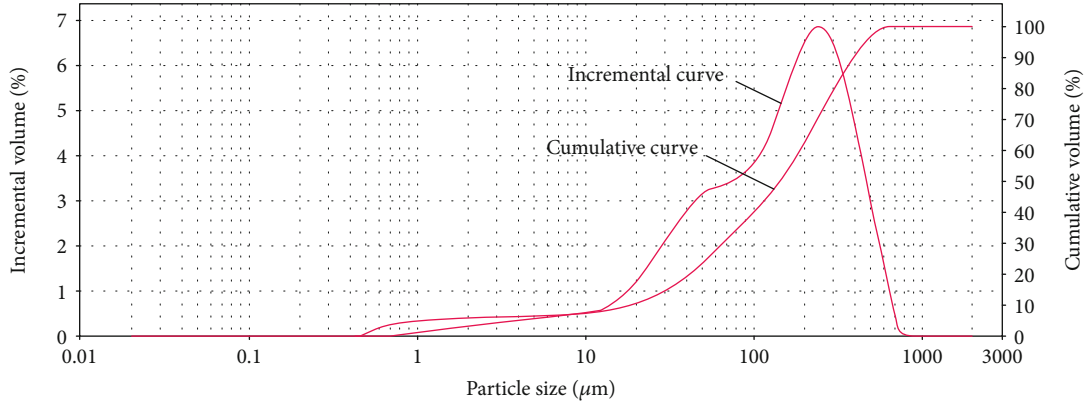


FIGURE 2: Size distribution curve of the tailings.

TABLE 1: Elemental components of the tailings.

Element	O	Na	Mg	Al	Si	S	Cl	K	Ca	Ti
Content (%)	42.5	0.019	5.695	0.781	2.29	0.676	0.018	0.239	33.02	0.037
Element	Cr	Mn	Fe	Cu	Zn	As	Rb	Sr	Zr	Pb
Content (%)	0.006	0.468	1.316	0.0141	0.104	0.13	0.002	0.0252	0.0013	0.179

with the actual situation on site and the elemental components of the tailing, ordinary 425 Portland cement was used as the cementing material and was mixed with tap water.

3.2. Experiment of Backfilling Ratio. The tailings were dried at 105°C for 12 hours and then sieved. As required by the standards of ISRM suggested, a high-quality standard $\varnothing 50 \text{ mm} \times \text{H}100 \text{ mm}$ cylindrical mould was used to prepare the samples [39]. The cement-tailings ratio (designated R) of the backfill were set to 1:4, 1:6, 1:8, 1:10, 1:12, 1:15, and 1:20 according to the actual mine conditions and engineering experience, and the mass concentration was 80% (shown in Figure 3). Then, the samples were placed in the standard curing box. After being cured for 28 days under standard curing conditions (temperature of 20°C and humidity of 95%), unconfined uniaxial compressive strength test was carried out (results shown in Figure 4).

3.3. Parameter Determination. It can be seen from Equation (5) that the determination of the inflection point is the key in the calculation of the peak specific energy of the cemented backfill. Considering the characteristics of the stress-strain curves of the cemented backfill, the coefficient k was introduced. If $0 < k < 1$ and substituting k into Equation (5), we have

$$V_M = \int_0^{\varepsilon_M} \sigma d\varepsilon = \frac{\sigma_M \varepsilon_M (8\varepsilon_S - 5\varepsilon_M)}{12\varepsilon_S - 8\varepsilon_M} = \frac{\sigma_M \varepsilon_M (8k - 5)}{12k - 8}. \quad (6)$$

According to Equation (6), the coefficient k can be expressed as

$$k = \frac{8V_M - 5\sigma_M \varepsilon_M}{12V_M - 8\sigma_M \varepsilon_M}. \quad (7)$$

According to Equation (1), the peak specific energy of the cemented backfill could be calculated based on the stress and strain data of the cemented backfill obtained through the experiments. Then, according to Equation (7), the coefficient k of the cemented backfill under different filling ratios can be obtained [40, 41]. The experimental and statistical results are shown in Table 2, and the representative stress-strain curve (filling ratio is 1:4) is shown in Figure 5.

The test results show that the materials have a better bonding effect and higher strength due to a more suitable gelling material and a better tailings gradation. Furthermore, the curve characteristics before the peak closely match the characteristics of the cubic function curve. There was an operation error during the data acquisition from the test of a filling ratio of 1:12; thus, these data are omitted in subsequent calculations.

As shown in Table 1, the k values under different ratios is relatively close and fluctuate at approximately 0.55. Considering the simplicity of the calculation equation, the k value is 0.55 in this study. Taking the value of k into Equation (6), we have

$$V_M = \int_0^{\varepsilon_M} \sigma d\varepsilon = \frac{\sigma_M \varepsilon_M (8\varepsilon_S - 5\varepsilon_M)}{12\varepsilon_S - 8\varepsilon_M} = \frac{\sigma_M \varepsilon_M (8k - 5)}{12k - 8} \approx \frac{\sigma_M \varepsilon_M}{2.4}. \quad (8)$$

Compared with the calculation results of the peak specific energy of cemented backfill based on the test data (shown in Figure 6), it can be found that the calculation results based on Equation (8) are accurate and reliable. Thus, it can be concluded that it is feasible to fix the coefficient k to 0.55 in this study.

According to the peak specific energy of cemented backfill under different cement-tailings ratios R in Table 1, the



FIGURE 3: Filling ratio experiment.



FIGURE 4: Uniaxial compressive strength test.

relationship between these factors was analyzed [42, 43]. Figure 7 shows that the peak specific energy of the cemented backfill has an exponential relationship with the filling ratio, and the correlation coefficient R^2 can reach 0.995 [44, 45]. The relationship can be written as

$$V_M = \frac{\sigma_M \varepsilon_M}{2.4} = 0.00166 + 0.11656e^{-1/3.06302R}. \quad (9)$$

4. Analysis of Energy Balance between Surrounding Rock and Cemented Backfill

4.1. Specific Energy of Surrounding Rock. Under the original stress environment, the original rock is compressed and stores deformation energy [37]. After excavation, the energy released per unit of rock mass in the goaf is

$$V_R = \int_{\varepsilon_0}^0 \sigma d\varepsilon = -\frac{\sigma_0^2}{2E_0}, \quad (10)$$

where V_R represents the specific energy of the surrounding rock, MJ/m^3 , σ_0 is the rock stress, MPa , and E_0 is the elastic modulus of the surrounding rock, GPa .

Regardless of the tectonic stress, the specific energy of the surrounding rock in the goaf can be expressed as

$$V_R = \int_{\varepsilon_0}^0 \sigma d\varepsilon = -\frac{\sigma_0^2}{2E_0} = -\frac{\gamma^2 H^2}{2E_0}, \quad (11)$$

where γ is the bulk density of the overlying strata, kN/m^3 , and H represents the thickness of the overlying strata, m .

4.2. Analysis of Energy Balance. Excavation of the stope causes the energy of the surrounding rock to be released. After filling into the goaf, the cemented backfill is compressed to produce deformation energy. Considering the stability of the goaf, the peak deformation energy (peak specific energy) of the cemented backfill should be able to withstand the release of energy from the surrounding rocks. Introducing the balance coefficient ($K > 1$) [46–48], the energy relationship between the cemented backfill and the surrounding rock is

$$V_M = -KV_R. \quad (12)$$

Substituting Equation (9) into Equation (12), we have

$$0.00166 + 0.11656e^{-1/3.06302R} = K \frac{\gamma^2 H^2}{2E_0}. \quad (13)$$

Then, the filling ratio R can be written as

$$\frac{1}{R} = -3.06302 \ln \frac{K\gamma^2 H^2 - 0.00332E_0}{0.23312E_0}. \quad (14)$$

5. Application Analysis

The surrounding rock of the Baoshan Mine is sandstone. Laboratory experiments have indicated that the physical and mechanical properties of the surrounding rock at different burial depths remain approximately unchanged. The bulk density of the surrounding rock is $22 \text{ kN}/\text{m}^3$, and the elastic modulus is 3.7 GPa . At present, the burial depths of the main production level are 582 m , 622 m , and 702 m . The filling ratio of the backfill is not determined according to the amount of energy released by the surrounding rock at different burial depths, and the current filling ratio is assumed to be $1:6-1:8$, which causes excessive consumption of materials. Therefore, it is necessary to adopt a more rapid and effective method to determine reasonable filling ratio of cemented backfill at different burial depths. According to the characteristics of the physical and mechanical parameters of the surrounding rocks, combined with the actual conditions of the mine, the balance coefficient K is set to 1.5 , and then, the filling ratios of the backfill at different burial depths are calculated based on Equation (14). The results are shown in Table 3, where R' represents the recommended filling ratio based on the actual application.

According to the calculation results, the filling ratios of the cemented backfill with the levels of 582 m , 622 m , and 702 m were selected as $1:13$, $1:12$, and $1:11$, respectively.

TABLE 2: The experimental results and the value of k under different ratios of cemented backfill.

Number	Ratio parameter	Elastic modulus (MPa)	Stress (MPa)	Strain (%)	Peak specific energy (MJ/m ³)	k
1	1:4	1140.24	8.21	0.9624	0.03449	0.546
2	1:6	769.2	5.18	0.8986	0.01851	0.563
3	1:8	532.33	2.66	0.8039	0.00846	0.564
4	1:10	371.13	2.02	0.7212	0.00606	0.556
5	1:12	328.06	1.35	0.7066	—	0.597
6	1:15	282.74	0.99	0.7028	0.00350	0.497
7	1:20	169.21	0.67	0.6609	0.00207	0.527

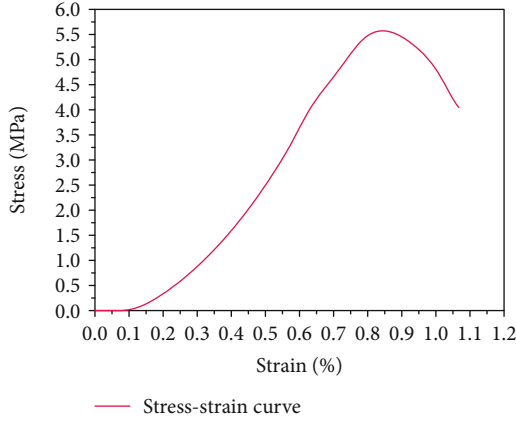


FIGURE 5: Representative stress-strain curve.

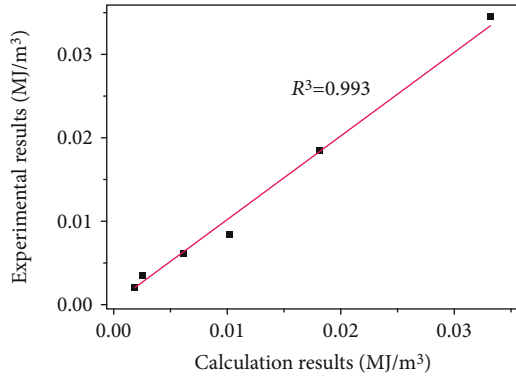


FIGURE 6: Correlation between calculation results and experimental results.

Then, the filling ratios were applied to the actual engineering of this time. In the field application, it was found that the goafs have remained stable since filling, which indicates that the filling ratios of the cemented backfill determined by this method are reasonable and can be applied to engineering practice. It also further suggests that it is feasible to determine the filling ratios of backfill based on the method proposed in this study. At the same time, the filling ratio determined by the conventional engineering experience is relatively high. However, when the determination of the filling ratio based on the method in this study was applied, excessive consumption of materials is thus avoided to a certain extent.

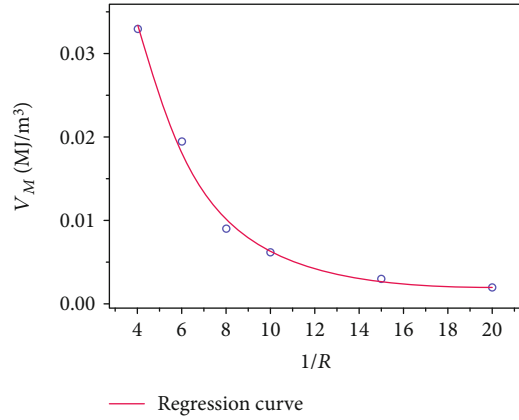


FIGURE 7: The relationship between the peak specific energy of the backfill and the filling ratio.

TABLE 3: Results of filling ratios of the backfill with different burial depths.

Depth (m)	$-KV_R$	R	R'
582	0.00332	1:13.01688	1:13
622	0.00380	1:12.25097	1:12
702	0.00483	1:11.03655	1:11

6. Discussion

Although the proposed method was only tested on one mine, it is expected that this method can also be applied to other mines because the principle of energy balance between surrounding rock and backfill is universal. Moreover, it should be noted that because different mines have different geological characteristics, the value of the coefficient k should be determined according to experimental results of surrounding rock and backfill when this method is applied to other mines.

In addition, to simplify the calculation, the value of k was fixed at 0.55. Although the application results suggest this simplification is feasible, the research of different k values is still necessary and will be carried out in the future.

7. Conclusions

The purpose of this research was to determine a new methodology for assessing the filling ratios of backfill in mines, and

the following conclusions were drawn based on the results obtained in this study:

- (1) The coefficient k was introduced to characterize the position of the inflection point in the stress-strain curve, and the value of k was fixed at 0.55 through experimental data. The verification results showed that this simplification is reasonable and feasible
- (2) The peak energy equation of cemented backfill was improved, and it was found that the peak specific energy of the cemented backfill has a linear relationship with the peak stress and strain of the backfill
- (3) Based on the energy balance principle of the surrounding rock and backfill, considering the bulk density, elastic modulus, and burial depth of the surrounding rock, a relational function model of the filling ratio was established. The application results indicated that the model established in this study is simple and accurate and can be used to determine the backfill ratios of underground mines. Moreover, it is expected that this method can also be applied to other mines as described in the section of discussion

Data Availability

Most of the data generated or analysed during this study are included in this manuscript, and all of the data are available from the corresponding author on reasonable request.

Conflicts of Interest

The authors declare that they have no conflicts of interest.

Acknowledgments

The research presented in this paper was jointly supported by the National Natural Science Foundation of China (Grant no. 51774323).

References

- [1] E. Yilmaz, "Stope depth effect on field behaviour and performance of cemented paste backfills," *International Journal of Mining Reclamation and Environment*, vol. 32, no. 4, pp. 273–296, 2018.
- [2] C. Zhu, M. C. He, M. Karakus, X. B. Cui, and Z. G. Tao, "Investigating toppling failure mechanism of anti-dip layered slope due to excavation by physical modelling," *Rock Mechanics and Rock Engineering*, vol. 2020, pp. 1–20, 2020.
- [3] D. Ren, D. Zhou, D. Liu, F. Dong, S. Ma, and H. Huang, "Formation mechanism of the Upper Triassic Yanchang Formation tight sandstone reservoir in Ordos Basin—Take Chang 6 reservoir in Jiyuan oil field as an example," *Journal of Petroleum Science and Engineering*, vol. 178, pp. 497–505, 2019.
- [4] P. Shan and X. Lai, "An associated evaluation methodology of initial stress level of coal-rock masses in steeply inclined coal seams, Urumchi coal field, China," *Engineering Computations*, vol. 37, no. 6, pp. 2177–2192, 2020.
- [5] N. Zhang, W. Liu, Y. Zhang, P. Shan, and X. Shi, "Microscopic pore structure of surrounding rock for underground strategic petroleum reserve (SPR) caverns in bedded rock salt," *Energies*, vol. 13, no. 7, article 1565, 2020.
- [6] S. Bacha, Z. Mu, A. Javed, and S. Al Faisal, "A review of rock burst's experimental progress, warning, prediction, control and damage potential measures," *Journal of Mining and Environment*, vol. 11, no. 1, pp. 31–48, 2020.
- [7] Q. Yin, R. C. Liu, H. W. Jing, H. J. Su, L. Y. Yu, and L. X. He, "Experimental study of nonlinear flow behaviors through fractured rock samples after High-Temperature exposure," *Rock Mechanics and Rock Engineering*, vol. 52, no. 9, pp. 2963–2983, 2019.
- [8] Q. Yin, G. W. Ma, H. W. Jing et al., "Hydraulic properties of 3D rough-walled fractures during shearing: an experimental study," *Journal of Hydrology*, vol. 555, pp. 169–184, 2017.
- [9] Q. Yin, H. W. Jing, G. W. Ma, H. J. Su, and R. C. Liu, "Investigating the roles of included angle and loading condition on the critical hydraulic gradient of real rock fracture networks," *Rock Mechanics and Rock Engineering*, vol. 51, no. 10, pp. 3167–3177, 2018.
- [10] G. Feng, Y. Kang, X. Wang, Y. Hu, and X. Li, "Investigation on the failure characteristics and fracture classification of shale under brazilian test conditions," *Rock Mechanics and Rock Engineering*, vol. 53, no. 7, pp. 3325–3340, 2020.
- [11] G. Feng, X. C. Wang, M. Wang, and Y. Kang, "Experimental investigation of thermal cycling effect on fracture characteristics of granite in a geothermal-energy reservoir," *Engineering Fracture Mechanics*, vol. 235, article 107180, 2020.
- [12] D. Liu, Z. Gu, R. Liang et al., "Impacts of pore-throat system on fractal characterization of tight sandstones," *Geofluids*, vol. 2020, Article ID 4941501, 17 pages, 2020.
- [13] H. Huang, T. Babadagli, X. Chen, H. Z. Li, and Y. M. Zhang, "Performance comparison of novel chemical agents for mitigating water-blocking problem in tight gas sandstones," *SPE Reservoir Evaluation & Engineering*, 2020.
- [14] J. Wang, D. P. Qiao, R. S. Han, G. T. Li, and J. C. Xie, "Strength model of cemented backfill in subsequent filling at the stage of open stope and its application," *Rock and Soil Mechanics*, vol. 40, no. 3, pp. 1105–1112, 2019.
- [15] B. A. Lingga, D. B. Apel, M. Sepehri, and Y. Y. Pu, "Assessment of digital image correlation method in determining large scale cemented rockfill strains," *International Journal of Mining Science and Technology*, vol. 29, no. 5, pp. 771–776, 2019.
- [16] Z. Z. Zhang, W. J. Wang, S. Q. Li, and X. Y. Yu, "Analysis on rockbolt support interaction with roof dilatancy above roadside backfill area in gob-side entry retaining," *Geotechnical and Geological Engineering*, vol. 36, no. 4, pp. 2577–2591, 2018.
- [17] Y. Zhang, S. G. Cao, N. Zhang, and C. Z. Zhao, "The application of short-wall block backfill mining to preserve surface water resources in northwest China," *Journal of Cleaner Production*, vol. 261, article 121232, 2020.
- [18] S. J. Chen, D. W. Yin, N. Jiang, F. Wang, and Z. H. Zhao, "Mechanical properties of oil shale-coal composite samples," *International Journal of Rock Mechanics and Mining Sciences*, vol. 123, article 104120, 2019.
- [19] S. Zhu, Q. S. Chen, Q. L. Zhang, and D. M. Zhang, "Recycling lead-zinc tailings for cemented paste backfill and stabilisation of excessive metal," *Minerals*, vol. 9, no. 11, article 710, 2019.

- [20] N. Jiang, C. Wang, H. Pan, D. Yin, and J. Ma, "Modeling study on the influence of the strip filling mining sequence on mining-induced failure," *Energy Science & Engineering*, vol. 8, no. 6, pp. 2239–2255, 2020.
- [21] C. Wang, B. Shen, J. Chen et al., "Compression characteristics of filling gangue and simulation of mining with gangue backfilling: an experimental investigation," *Geomechanics and Engineering*, vol. 20, no. 6, pp. 485–495, 2020.
- [22] C. C. Qi, A. Fourie, Q. S. Chen, and Q. L. Zhang, "A strength prediction model using artificial intelligence for recycling waste tailings as cemented paste backfill," *Journal of Cleaner Production*, vol. 183, pp. 566–578, 2018.
- [23] Z. J. Wen, Q. Gao, Y. D. Wang, and X. B. Yang, "Development of composite cementitious material and optimization of slurry proportion based on fuzzy comprehensive evaluation," *The Chinese Journal of Nonferrous Metals*, vol. 30, no. 3, pp. 698–707, 2020.
- [24] K. Fang and M. Fall, "Shear behavior of the interface between rock and cemented backfill: effect of curing stress, drainage condition and backfilling rate," *Rock Mechanics and Rock Engineering*, vol. 53, no. 1, pp. 325–336, 2020.
- [25] C. C. Qi and A. Fourie, "Numerical investigation of the stress distribution in backfilled stopes considering creep behaviour of rock mass," *Rock Mechanics and Rock Engineering*, vol. 52, no. 9, pp. 3353–3371, 2019.
- [26] C. Hou, W. C. Zhu, B. X. Yan, K. Guan, and L. L. Niu, "Analytical and experimental study of cemented backfill and pillar interactions," *International Journal of Geomechanics*, vol. 19, no. 8, article 04019080, 2019.
- [27] Z. X. Liu, M. Lan, S. Y. Xiao, and H. Q. Guo, "Damage failure of cemented backfill and its reasonable match with rock mass," *Transactions of Nonferrous Metals Society of China*, vol. 25, no. 3, pp. 954–959, 2015.
- [28] B. X. Yan, W. C. Zhu, C. Hou, and H. W. Jia, "A comparative study on the stress distribution in mine backfill through theoretical and numerical analysis," *Journal of Northeastern University (Natural Science)*, vol. 40, no. 12, pp. 1773–1778, 2019.
- [29] J. Wang, J. X. Fu, W. D. Song, Y. F. Zhang, and Y. Wang, "Particle flow simulation of mechanical properties and microcrack evolution characteristics of rock-backfill combined model," *Journal of China University of Mining & Technology*, vol. 49, no. 3, pp. 453–462, 2020.
- [30] H. Suhara, Y. Sawa, M. Nishimura et al., "Efficacy of a new coating material, PMEA, for cardiopulmonary bypass circuits in a porcine model," *Annals of Thoracic Surgery*, vol. 71, no. 5, pp. 1603–1608, 2001.
- [31] C. Hou, W. Zhu, B. Yan, K. Guan, and J. du, "Influence of binder content on temperature and internal strain evolution of early age cemented tailings backfill," *Construction and Building Materials*, vol. 189, pp. 585–593, 2018.
- [32] Y. Wang, C. H. Li, Z. Q. Hou, X. F. Yi, and X. M. Wei, "In vivo X-ray computed tomography investigations of crack damage evolution of Cemented Waste Rock Backfills (CWRB) under uniaxial deformation," *Minerals*, vol. 8, no. 11, article 539, 2018.
- [33] M. Li, J. X. Zhang, P. Huang, and R. Gao, "Mass ratio design based on compaction properties of backfill materials," *Journal of Central South University*, vol. 23, no. 10, pp. 2669–2675, 2016.
- [34] H. Wu, G. Z. Zhao, Y. Chen, and H. Y. Zhang, "Optimization of mix proportioning of mine filling materials using RSM-DF experiments design method," *Journal of Basic Science and Engineering*, vol. 27, no. 2, pp. 453–461, 2019.
- [35] W. T. Lan, A. X. Wu, Y. M. Wang, and J. Q. Li, "Optimization of filling ratio of hemihydrate phosphogypsum based on orthogonal test," *The Chinese Journal of Nonferrous Metals*, vol. 29, no. 5, pp. 1083–1091, 2019.
- [36] G. J. Sun, P. Wang, T. Feng, W. J. Yu, and J. H. Liu, "Strata movement characteristics of the deep well gangue filling on the fully mechanized mining face," *Journal of Mining & Safety Engineering*, vol. 37, no. 3, pp. 562–570, 2020.
- [37] K. Du, L. I. Xi-bing, D.-y. Li, and L. Weng, "Failure properties of rocks in true triaxial unloading compressive test," *Transactions of Nonferrous Metals Society of China*, vol. 25, no. 2, pp. 571–581, 2015.
- [38] Y. X. Ke, X. M. Wang, Q. L. Zhang, and E. Y. Liu, "Strength determination of crude tailings backfill in deep mine based on non-linear constitutive model," *Journal of Northeastern University (Natural Science)*, vol. 38, no. 2, pp. 280–283, 2017.
- [39] W. Xu, M. Han, and P. Li, "Influence of freeze-thaw cycles on mechanical responses of cemented paste tailings in surface storage," *International Journal of Mining Reclamation and Environment*, vol. 34, no. 5, pp. 326–342, 2020.
- [40] T. Alkhamaiseh, L. Mejus, I. Yusoff, and R. Yaccup, "Relationships between geophysical and geotechnical parameters focusing on a site specific results of a landslide risk area," *Amazonia Investiga*, vol. 7, no. 15, pp. 386–398, 2018.
- [41] K. Fang and M. Fall, "Effects of curing temperature on shear behaviour of cemented paste backfill- rock interface," *International Journal of Rock Mechanics and Mining Sciences*, vol. 112, pp. 184–192, 2018.
- [42] S. Zamiran and A. Osouli, "Seismic motion response and fragility analyses of cantilever retaining walls with cohesive backfill," *Soils and Foundations*, vol. 58, no. 2, pp. 412–426, 2018.
- [43] H. Basarir, H. Bin, and A. Fourie, "An adaptive neuro fuzzy inference system to model the uniaxial compressive strength of cemented hydraulic backfill," *Mining of Mineral Deposits*, vol. 12, no. 2, pp. 1–12, 2018.
- [44] E. Tavasoli, G. Asadollahfardi, A. Khodadadi Darban, and M. Asadi, "Simulation of cyanide oxidation using calcium and sodium hypochlorite in the Moteh Gold Mine Tailing Dam, Iran," *Desalination and Water Treatment*, vol. 145, pp. 273–279, 2019.
- [45] L. Peng, J. J. Mei, N. Wang et al., "Quantitative inversion of water quality parameters in industrial and mining cities from hyperspectral remote sensing," *Spectroscopy and Spectral Analysis*, vol. 39, no. 9, pp. 2922–2928, 2019.
- [46] N. H. Alaei, A. Mozafari, M. Mirzaee, A. Faghihi, and K. Tolouei, "Fuzzy evaluation method for the identification of subsidence susceptibility in an underground mine (case study in Tabas coal mine of Iran)," *Natural Hazards*, vol. 99, no. 2, pp. 797–806, 2019.
- [47] B. X. Yan, W. C. Zhu, and C. Hou, "Theoretical analysis of maximum exposure height of the backfill when mining underground adjacent stope," *Hazard Control in Tunnelling and Underground Engineering*, vol. 1, no. 2, pp. 100–106, 2019.
- [48] G. Feng, Z. Li, Y. Guo et al., "175 Mix ratio optimization of cemented Coal Gangue Backfill (CGB) based on response surface method," *Journal of Residuals Science & Technology*, vol. 13, no. 3, pp. 175–184, 2016.

Research Article

Numerical Simulation on Heat Transfer Characteristics of Water Flowing through the Fracture of High-Temperature Rock

Xiaohu Zhang,^{1,2} Zhaolun Wang,³ Yanhua Sun,¹ Chun Zhu,^{2,4} Feng Xiong,⁵
and Qiongqiong Tang⁴ 

¹School of Civil Engineering, Guizhou University of Engineering Science, Bijie 551700, China

²State Key Laboratory for Geomechanics and Deep Underground Engineering, Beijing 100083, China

³Henan College of Transportation, Zhengzhou, 450006, China

⁴College of Construction Engineering, Jilin University, Changchun 130026, China

⁵School of Civil Engineering, Wuhan University, Hubei 430072, China

Correspondence should be addressed to Qiongqiong Tang; 1012846844@qq.com

Received 6 April 2020; Revised 25 May 2020; Accepted 11 June 2020; Published 11 July 2020

Academic Editor: Qian Yin

Copyright © 2020 Xiaohu Zhang et al. This is an open access article distributed under the Creative Commons Attribution License, which permits unrestricted use, distribution, and reproduction in any medium, provided the original work is properly cited.

Deep geothermal resources are becoming an increasingly important energy source worldwide. To achieve the optimal efficiency of this resource, the heat transfer characteristics between flowing water and rock need to be further studied. Using the stereotopometric scanning system 3D CaMega, the fracture geometry data of five cuboid granite rocks were obtained to determine the effects of fracture roughness on the heat transferability of rock. A 3-D model was built based upon the scanned geometry data to assess the effects of rock temperature, water velocity, and roughness, and aperture size of fracture surface on the heat transfer coefficient. The simulation tests show that water velocity has the most noticeable effect, followed by aperture size and rock roughness. On the other hand, the initial rock temperature has the least influence. A new heat transfer coefficient was proposed considering aperture size, water flow velocity, and rock fracture roughness. The calculated values of Reynolds, Prandtl, and Nusselt numbers obtained using this coefficient are in good agreement with the numerical simulation results. This study provides a reference for enhancing the heat transfer coefficient to benefit the exploitation of heat energy of hot dry rock.

1. Introduction

Clean energy can help solve the problems of air pollution and energy shortages as fossil fuels become exhausted in the coming generations. The deep geothermal energy of hot dry rock (HDR) has been utilized worldwide, including in China [1–3]. China is rich in coal resources and has a well-developed mining system [4–7]. At the same, China is also a vast country with abundant geothermal resources, mostly of the low-medium temperature type. China's geothermal resources potential is about 8% of the total global geothermal potential (Zhao et al. 2014). Thus, it is necessary to further develop this sustainable energy technology to meet the growing energy demand.

Fluid circulation and heat transmission are essential in conventional or enhanced geothermal systems (Figure 1). Hot water and steam can be extracted from fluids flowing through the fractures found in natural hydrothermal systems. However, dry reservoirs with low permeability require an enhanced geothermal system in which man-made fractures provide a heat exchange surface and pathways for fluids to flow. The existence of fractures is important for affecting the rock mass properties [8–10]. For both natural and man-made fractures, the characteristics of fluid flowing through fractures in the subsurface vary based upon water velocity, surface roughness, temperature, and porosity/permeability characteristics. Further research is needed to accurately model the geothermal

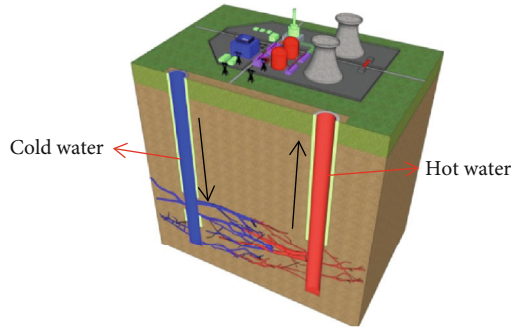


FIGURE 1: Diagram of a geothermal system.

system in these reservoirs to properly develop geothermal energy.

To explicitly represent the heat transfer of fluid through a fractured surface, a heat transfer coefficient (HTC) was proposed to predict hot water production from an enhanced geothermal reservoir. There has been much in-depth research on this parameter (Zhao et al. 2014; Ganguly et al. 2014; [11–14]; Teke et al. 2018; [15]). For example, Mohais et al. [16] proposed a simplified interpretation and mathematical analysis of flow and heat transfer through a single horizontal fracture in an enhanced geothermal system. Bai et al. [17] proposed an analytical method to develop a more effective equation for the HTC based on the temperature distribution in the fracture wall along the direction of the sample radius. Finally, Abbasi et al. [18] proposed an analytical method to describe the transient temperature distribution in a single fracture model to help investigate water injection into a fractured geothermal reservoir.

Understanding the heat transfer process between fluids and rocks is critical for efficiently exploiting geothermal systems. Many laboratory experiments have been conducted to determine the heat transfer properties of various rock types [19–21]. Huang et al. [22] performed convective heat transfer experiments to study the behavior of water flowing in a simulated rock specimen. Based on two rock specimens with different roughness coefficients, the influence of rock roughness on the seepage characteristics was determined. The secondary damage characteristics of HDR reservoirs were studied through experiments. Guo et al. [23] obtained the damage formulas of granite rock properties based on experimental results.

Although various parameters for specific rock types have been determined, the effects of the flow path and changes in rock temperature on the evolution of fluid temperature have not yet been studied in-depth. Luo et al. [24] used two groups of granite samples with a single fracture obtained from the Gonghe Basin, China, to determine the influence of the flow path. The results showed that the larger the fracture area ratio, the higher the hydraulic conductivity of the rock. Ma et al. [25] created rock samples with different rough surfaces by 3D printing to study heat transfer of water flowing through rough fractures. They found that the tortuosity of a fracture surface influences local fluctuations in temperature. In another study, distilled water was passed through artificial

smooth and rough fractures of rock samples to study the impact of fracture surface roughness on the heat transfer intensity [26]. The results showed that the roughness of the rock fracture surface improves the overall heat transfer intensity to a certain extent. While surface roughness has been studied, the effect of variations in aperture size on heat transfer in geothermal systems has not been extensively studied.

The evaluation of the potential of geothermal energy and accurate prediction of hot water production remains a challenge because of its complexity. As the increasing confining pressure caused by geothermal energy production affects the fracture geometry to some extent, the influence of the aperture size of the fracture on the heat transfer characteristics needs to be studied. While it is known that aperture size affects temperature and production, the increase in aperture size is on the micron level under typical conditions. Therefore, it is difficult to measure the fluid temperature and inner surface temperature at various points along the flow direction in the laboratory or in-situ experiments.

Numerical simulation can easily determine the heat transfer process between water and hot dry rock under the typical complex environment of geothermal reservoirs [27–29]. Kolditz et al. (1998) used a fully 3-D finite-element model to study the heat transfer during forced water circulation through fractured crystalline rock. The applicability of this model was proven by a 900-day test at an HDR site in the United Kingdom. Bai et al. [30] built a numerical model to simulate the local heat transfer coefficient (LHTC) of fluid flowing through a single fracture under confining pressure, and the numerical results were verified by test data. To study the coupled thermal-mechanical-hydraulic process in fractured porous media, Lee et al. [31] proposed the TOUGH-UDEC numerical software to simulate heat transfer and multiphase fluid flow in fractured porous media. To study the effects of heat transfer between fluid and rock on economic hot water production from geothermal systems, Shaik et al. [32] proposed a numerical approach to simulate the heat transfer process by coupling fluid flow with heat transfer. Most of the previous studies on the heat transfer process are mainly based on 2-D analysis, and influencing factors such as rock temperature, roughness, and aperture size of the fracture surface, and water velocity are not comprehensively considered.

Herein, a 3-D numerical model was adopted to quantitatively investigate the characteristics of the heat transfer process between flowing water and rough granite fracture wall. Rock properties, including rock temperature, roughness, and aperture size of the fracture surface, and water velocity, were included in the model to create a comprehensive heat convection process of water in rock fractures.

2. Heat Transfer Coefficient

The heat transfer coefficient is an important parameter that describes the heat transfer characteristics of working fluid flowing through a fractured rock. The average heat transfer coefficient h can be obtained based on energy conservation because the heat absorbed by water in the entire fracture pathway equals the heat transfer by convection between the

water and the inner surface of the fracture [30]. It can be expressed as follows:

$$h = \frac{c_{p,w}\rho_w v s (T_2 - T_1)}{2L(T_i - T_1 + T_2/2)}, \quad (1)$$

where $c_{p,w}$ is the specific heat capacity of water at constant pressure, ρ_w is the density of water, v is the steady flow velocity of water, s is the aperture width, T_2 and T_1 are the water temperatures at outlet and inlet ends, respectively, T_i is the inner wall temperature of the rock fracture, and L is the length of the rock sample.

Equation (1) requires information on the temperature distribution on the inner wall of the fracture. Here, the formula of the inner wall temperature T_i presented by Carslaw and Jaeger (1973) is adopted:

$$T_i = T_c - \frac{\pi c_{p,w}\rho_w v ds (T_2 - T_1)}{42.32K_r L}, \quad (2)$$

where K_r is the rock thermal conductivity, and d is the equivalent radius of fracture.

Substituting Eq. (2) into Eq. (1), the following equation is obtained:

$$h = \frac{c_{p,w}\rho_w v s (T_2 - T_1)}{2L(T_c - \pi c_{p,w}\rho_w v ds (T_2 - T_1)/42.32K_r L - T_1 + T_2/2)}. \quad (3)$$

Compared with previous calculation formulas ([33]; Zhao et al. 1992), this proposed equation does not consider a simplification of specimen section shape. Nevertheless, it can obtain the temperature on the fracture wall by solving the two-dimensional heat conduction equation on a semi-disk region.

The Reynolds number Re is calculated as follows:

$$Re = \frac{2q}{dv}, \quad (4)$$

where v is the fluid viscosity, and q is the flow rate.

The Prandtl number Pr is calculated as follows:

$$Pr = \frac{v}{a}, \quad (5)$$

where a is the thermal diffusivity. $a = \lambda/\rho c$. λ is the fluid thermal conductivity coefficient; ρ is water density, and c is fluid specific heat.

The Nusselt number Nu is calculated as follows:

$$Nu = \frac{hl}{\lambda}, \quad (6)$$

where l is the characteristic length.

However, the characteristics of rough-walled fracture are not included in most of the established relationships of Nu , Re , and Pr .

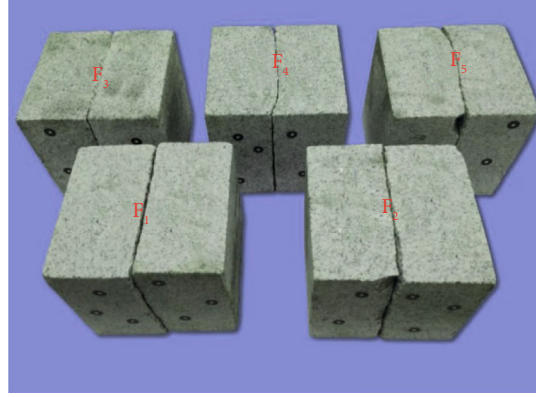


FIGURE 2: Scanned rock samples, each with different roughness values.

3. Numerical Modeling and Simulation

It is difficult to directly obtain the temperature inside the fracture surface using microscale sensors. Moreover, the installment of such sensors would affect the natural flow of water through the fracture. Numerical simulation is an effective method to explore the heat transfer process at the microscale. According to the previous research of Bai et al. [30], numerical modeling is an alternative method to obtain the necessary heat transfer characteristics values. Many scholars have studied heat transfer processes primarily based on 2-D analysis, whereas the influencing factors such as rock temperature, roughness, and aperture size of fracture surface along with water velocity have not been comprehensively considered. Based on the previous detailed research [30], COMSOL software was used in this work to study the heat transfer process between the water and fracture surface.

In COMSOL, the single-phase water flow in the fracture follows the Navier-Stokes equations ([34–38]), which can be written:

$$\begin{aligned} \nabla \mathbf{u} &= 0, \\ \rho_w \frac{\partial \mathbf{u}}{\partial t} + \rho_w \mathbf{u} \nabla \mathbf{u} &= -\nabla p + \nabla \left(\mu \left(\nabla \mathbf{u} + (\nabla \mathbf{u})^T \right) \right) \\ &\quad - \frac{2}{3} \mu ((\nabla \mathbf{u}) I), \\ \rho_w c_{p,w} \left(\frac{\partial T_w}{\partial t} + (\mathbf{u} \nabla) T_w \right) &= -\nabla \mathbf{q}_w, \end{aligned} \quad (7)$$

where ρ_w is the density, \mathbf{u} is the velocity vector, p is the pressure, $c_{p,w}$ is the specific heat capacity, T_w is the absolute temperature, and \mathbf{q}_w is the heat flux vector in water. The heat conduction equation in the rock can be given by:

$$\rho_s c_{p,s} \frac{\partial T_s}{\partial t} = -\nabla \mathbf{q}_s, \quad (8)$$

where \mathbf{q}_s is the heat flux in rock specimen. The boundary condition of the outlet is the standard atmospheric pressure corresponding to the experiment.

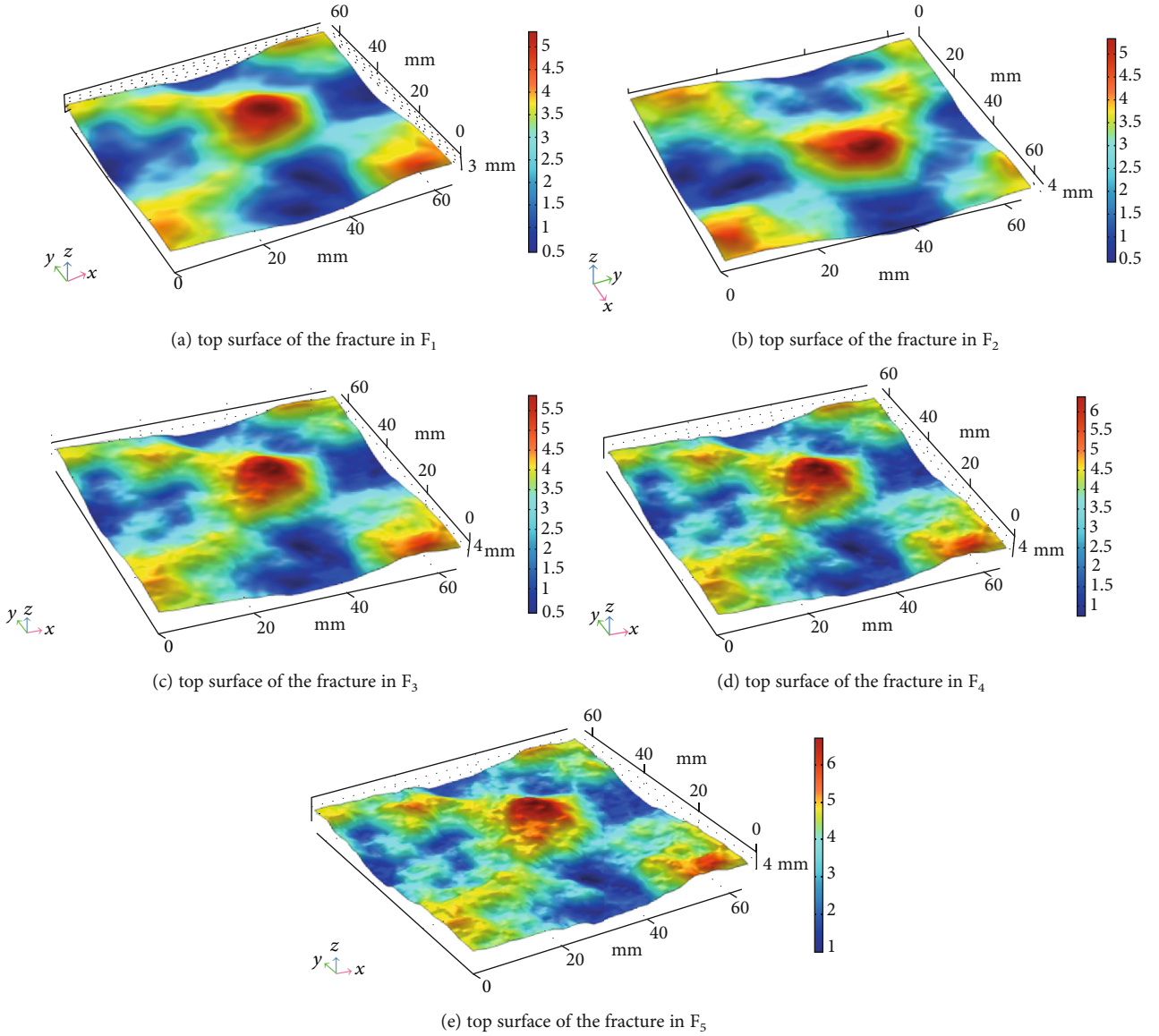


FIGURE 3: 3D discretization of the fracture surfaces in the five samples.

The fracture geometries of five cuboid granite rocks (Figure 2) were obtained through the stereotopometric scanning system 3D CaMega with high measurement speed and precision [34]. The resolution of a sampling point obtained by the scanning system was $\pm 25 \mu\text{m}$, which is defined as the error of 3D space along the x , y , and z directions. Roughness measurements were performed on the 64 mm \times 64 mm lower and upper halves of the five fracture replicas. 3D discretization of the fracture surface is shown in Figure 3.

The fracture geometries were then imported into Comsol software. The initial inlet temperature of water was set at 293.15 K. The fractal dimension of the fracture surface (D) for each sample, rock temperature, water velocity, and aperture size of the fracture surface (s) for each simulation are listed in Table 1. The fractal dimension was calculated according to the variogram function of 2D profiles. More detailed information can be seen in Xiong et al. [34].

The heat transfer process between water and fracture surface was calculated based on the finite element method through precision meshing on these models after setting each simulation parameter of the model in COMSOL. The calculation results of water pressure and rock temperature are plotted in Figure 4, and the calculation results of different heat transfer processes are shown in Table 2.

4. Simulation Results Analysis

4.1. Effects of Fracture Aperture Size on the Heat Transfer Characteristics. The distribution of the temperature field is an important indicator of the efficiency of the heat transfer process. The temperature field of water flowing within granite with different aperture sizes (0.5 mm, 0.7 mm, and 0.9 mm) was taken as an example, and the effects of fracture aperture size on heat transfer were studied. The flow velocity

TABLE 1: Fracture parameters influencing the heat transfer coefficient.

Fractal dimension D	Rock temperature t (K)	Velocity of water v (m/s)	Aperture width of fracture surface s (mm)
1.2 (I rock)	323.15	0.0025	0.3
1.4 (II rock)	343.15	0.0050	0.5
1.6 (III rock)	363.15	0.0075	0.7
1.8 (IV rock)	/	/	/
2.0 (V rock)	/	/	/

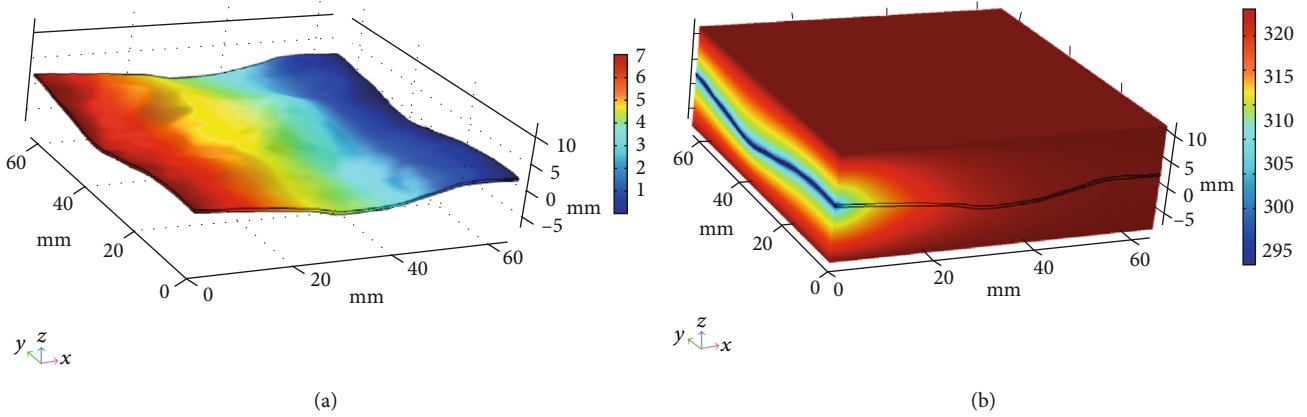


FIGURE 4: Calculation results of water pressure and rock temperature (Temperature: K).

of water and rock temperature were set as 0.005 m/s and 343.15 K, and the 1.4 roughness fracture surface (F_2 sample) was chosen as the flow surface. The calculation results are shown in Figure 5. Similar temperature trends are observed for the results of the other samples with water flowing through the fracture.

Overall, the aperture size has a significant influence on the heat transfer process (Table 2). As the fracture aperture size increases, the heat transfer coefficient [39–47] increases. When water flows along the fracture surface of a rock, it absorbs the surrounding heat energy of the rock. The temperature of the water gradually increases during the flow process, and the temperature of the surrounding rock decreases slowly along the flow direction. The most significant decrease in temperature occurs at the water inlet. As seen from Figure 5, with the increase in aperture size, the water heating rate decreases and the lower temperature area at the inlet further expands. This is mainly because the increase in aperture size leads to a rise in water flow to maintain a constant flow rate. The total volume of water flowing inside the fracture surface to absorb heat energy increases. Thus, the heat energy stored in the surrounding rock decreases. Overall, the heat transfer coefficient increases.

4.2. *Effects of Flow Velocity on the Heat Transfer Characteristics.* Using the same rock and aperture size conditions as above, the temperature field of water flowing

through granite at different velocities (0.005 m/s, 0.01 m/s, and 0.015 m/s) was taken as an example, and the effects of flow velocity on the heat transfer characteristics were studied. The fracture aperture size and rock temperature were set to 0.5 mm and 343.15 K, and the 1.4 roughness fracture surface (F_2) was chosen as the flow surface. The calculation results are shown in Figure 6. The results of the other surfaces with varying water velocities exhibit similar trends.

The water velocity has a more significant influence on the heat transfer process than the fracture aperture size (Table 2). With the increase in flow velocity, the heat transfer coefficient markedly increases, although the inner wall temperature and outlet temperature of rock fracture also decrease to some extent. Increase in flow velocity results in an increase in the total volume of water flowing inside the rock to absorb the heat energy. Thus, the heat energy stored in the rock transfers to the water (Figure 6). Finally, the water reaches equilibrium with the rock closer to the outlet with increasing velocity.

4.3. *Effects of Rock Temperature on the Heat Transfer Characteristics.* At constant water velocity and aperture size of the fracture surface, the effects of rock temperature on the heat transfer characteristics were studied, taking the example of the temperature field of water flowing through granite at different temperatures (323.15 K, 343.15 K, and 363.15 K). The fracture aperture size and flow velocity of

TABLE 2: Calculation results of different heat transfer processes.

Roughness	Aperture (m)	Water velocity (m/s)	Rock temperature (K)	Ti (K)	Outlet temperature (K)	Heat transfer coefficient		
1.2	5e-4	0.0025	323.15	319.5125	323.043	107.4001		
			343.15	337.0955	342.985	107.4214		
			363.15	354.6715	362.915	107.416		
		0.005	323.15	316.0465	322.241	285.7587		
			343.15	331.3185	341.65	285.8437		
			363.15	346.5825	361.041	285.7897		
		0.0075	323.15	313.0875	320.591	543.1123		
			343.15	326.3865	338.903	543.4135		
			363.15	339.6895	357.223	543.6105		
		7e-4	0.0025	323.15	318.027	322.831	169.814	
				343.15	334.6085	342.612	169.7923	
				363.15	351.202	362.415	169.8297	
	0.005		323.15	313.5595	320.84	484.4274		
			343.15	327.1735	339.318	484.6754		
			363.15	340.7835	357.798	484.955		
	0.0075		323.15	310.255	318.017	916.9923		
			343.15	321.666	334.614	917.6287		
			363.15	333.0795	351.218	918.0965		
	9e-4		0.0025	323.15	316.542	322.367	245.5782	
				343.15	332.144	341.86	245.6567	
				363.15	347.7375	361.334	245.6099	
		0.005	323.15	311.4425	318.989	710.0856		
			343.15	323.64	336.229	710.6735		
			363.15	335.8445	353.481	711.0104		
		0.0075	323.15	308.11	315.376	1279.624		
			343.15	318.09	330.212	1280.801		
			363.15	328.063	345.021	1279.712		
		1.4	5e-4	0.0025	323.15	319.5595	323.043	106.9598
					343.15	337.1745	342.984	106.9772
					363.15	354.782	362.913	106.9723
	0.005			323.15	316.1265	322.261	283.5782	
				343.15	331.4415	341.662	283.531	
				363.15	346.7535	361.057	283.4858	
	0.0075			323.15	313.181	320.618	536.74	
				343.15	326.543	338.949	537.0395	
				363.15	339.9085	357.288	537.2532	
7e-4	0.0025			323.15	317.987	322.827	170.4365	
				343.15	334.5415	342.605	170.4152	
				363.15	351.1095	362.406	170.4481	
	0.005		323.15	313.5105	320.834	487.7402		
			343.15	327.0915	339.29	487.4112		
			363.15	340.676	357.764	487.5822		
	0.0075		323.15	310.212	318.001	923.32		
			343.15	321.594	334.586	923.8931		
			363.15	332.979	351.18	924.4104		
	9e-4		0.0025	323.15	316.5125	322.363	246.3158	
				343.15	332.094	341.853	246.4041	
				363.15	347.6675	361.325	246.3648	

TABLE 2: Continued.

Roughness	Aperture (m)	Water velocity (m/s)	Rock temperature (K)	Ti (K)	Outlet temperature (K)	Heat transfer coefficient	
1.6	5e-4	0.005	323.15	311.4085	318.979	713.6627	
			343.15	323.5885	336.216	714.0491	
			363.15	335.773	353.463	714.3618	
		0.0075	323.15	308.0825	315.371	1287.704	
			343.15	318.0445	330.202	1288.598	
			363.15	327.999	345.008	1287.639	
		7e-4	0.0025	323.15	319.734	323.049	105.4043
				343.15	337.454	342.977	105.3962
				363.15	355.0385	362.755	105.401
	0.005		323.15	316.1165	322.141	280.7423	
			343.15	331.4165	341.452	280.7037	
			363.15	346.5535	360.559	280.7069	
	0.0075		323.15	312.981	320.29	533.38	
			343.15	326.343	338.579	533.4634	
			363.15	339.7085	356.888	533.9026	
	9e-4	0.0025	323.15	317.787	322.457	168.5644	
			343.15	334.3415	342.195	168.9517	
			363.15	350.9095	361.93	169.0013	
		0.005	323.15	313.3105	320.524	485.6311	
			343.15	326.8915	338.97	485.8183	
			363.15	340.476	357.425	485.9981	
		0.0075	323.15	310.062	317.771	921.7325	
			343.15	321.394	334.266	921.5292	
			363.15	332.779	350.838	921.4334	
	7e-4	0.0025	323.15	316.3125	322.04	244.6681	
			343.15	331.894	341.483	244.7837	
			363.15	347.4675	360.93	244.9673	
0.005		323.15	311.2085	318.669	711.0851		
		343.15	323.3885	335.886	711.3734		
		363.15	335.573	353.11	711.522		
0.0075		323.15	307.8825	315.062	1285.096		
		343.15	317.8445	329.88	1285.271		
		363.15	327.999	344.99	1285.894		
1.8	5e-4	0.0025	323.15	319.334	322.009	100.6993	
			343.15	337.054	341.55	100.7489	
			363.15	354.6385	360.855	100.4835	
		0.005	323.15	315.7165	321.49	276.8732	
			343.15	331.5165	341.32	276.6828	
	7e-4	0.0075	363.15	346.1535	359.659	276.2579	
			323.15	312.981	320.29	533.38	
			343.15	326.343	338.579	533.4634	
		0.0025	363.15	339.7085	356.888	533.9026	
			323.15	317.387	321.7	164.5648	
	9e-4	0.005	343.15	333.9415	341.24	164.8952	
			363.15	350.5095	360.79	164.9999	
			323.15	312.9105	319.9	481.101	
		0.0075	343.15	326.4915	338.3	481.6045	
			363.15	340.076	356.7	481.7055	

TABLE 2: Continued.

Roughness	Aperture (m)	Water velocity (m/s)	Rock temperature (K)	Ti (K)	Outlet temperature (K)	Heat transfer coefficient
2.0	9e-4	0.0075	323.15	309.162	316.442	919.013
			343.15	320.994	333.66	919.552
			363.15	332.379	350.23	919.9104
		0.0025	323.15	317.9125	323.82	240.1812
			343.15	331.494	340.65	240.293
			363.15	347.0675	360.01	240.9346
		0.005	323.15	310.8085	318.078	708.5908
			343.15	322.9885	335.275	708.7534
			363.15	335.173	352.48	708.8886
	5e-4	0.0075	323.15	307.4795	314.167	1218.251
			343.15	317.4195	328.75	1218.772
			363.15	327.5555	343.62	1218.943
		0.0025	323.15	318.734	320.53	94.41801
			343.15	336.654	339.75	94.60147
			363.15	354.2385	358.655	94.81679
		0.005	323.15	315.3165	320.82	272.4365
			343.15	331.1165	340.57	272.8525
			363.15	345.7535	358.859	272.9349
7e-4	0.0075	323.15	312.581	319.68	529.4248	
		343.15	325.843	337.79	529.5298	
		363.15	339.3085	356.18	529.6305	
	0.0025	323.15	316.787	320.7	160.4109	
		343.15	333.3415	340.01	160.5339	
		363.15	349.9095	359.4	160.9596	
	0.005	323.15	312.3105	318.99	475.5328	
		343.15	325.8915	337.31	475.6835	
		363.15	334.576	349.03	475.8615	
9e-4	0.0075	323.15	308.562	315.53	913.1465	
		343.15	320.394	332.715	913.4476	
		363.15	331.279	348.53	913.8874	
	0.0025	323.15	317.3125	322.8	234.4315	
		343.15	330.894	339.48	234.6153	
		363.15	346.4675	358.61	234.7439	
	0.005	323.15	309.6085	316.322	702.2043	
		343.15	322.3885	334.32	702.4912	
		363.15	334.573	351.48	702.626	
0.0075	323.15	306.8795	313.26	1212.152		
	343.15	316.8195	327.82	1212.229		
	363.15	326.9555	342.67	1212.526		

water were set as 0.5 mm and 0.005 m/s, and the 1.4 roughness fracture surface (F_2) was chosen as the flow surface. The calculation results are shown in Figure 7. The other samples have similar trends for temperature.

Initial rock temperature has a limited influence on the heat transfer process (Table 2). With the increase in surrounding rock temperature, the water temperature at outlet increases, but the heat transfer coefficient remains

essentially constant with only a small increase. The increase in the initial temperature of the rock results in a relatively constant rock temperature (Figure 7). The position where water has a similar temperature as the rock has no obvious deviation and is still near the inlet. Thus, the heat transfer characteristics between flowing water and the rock fracture are not significantly affected by the initial rock temperature.

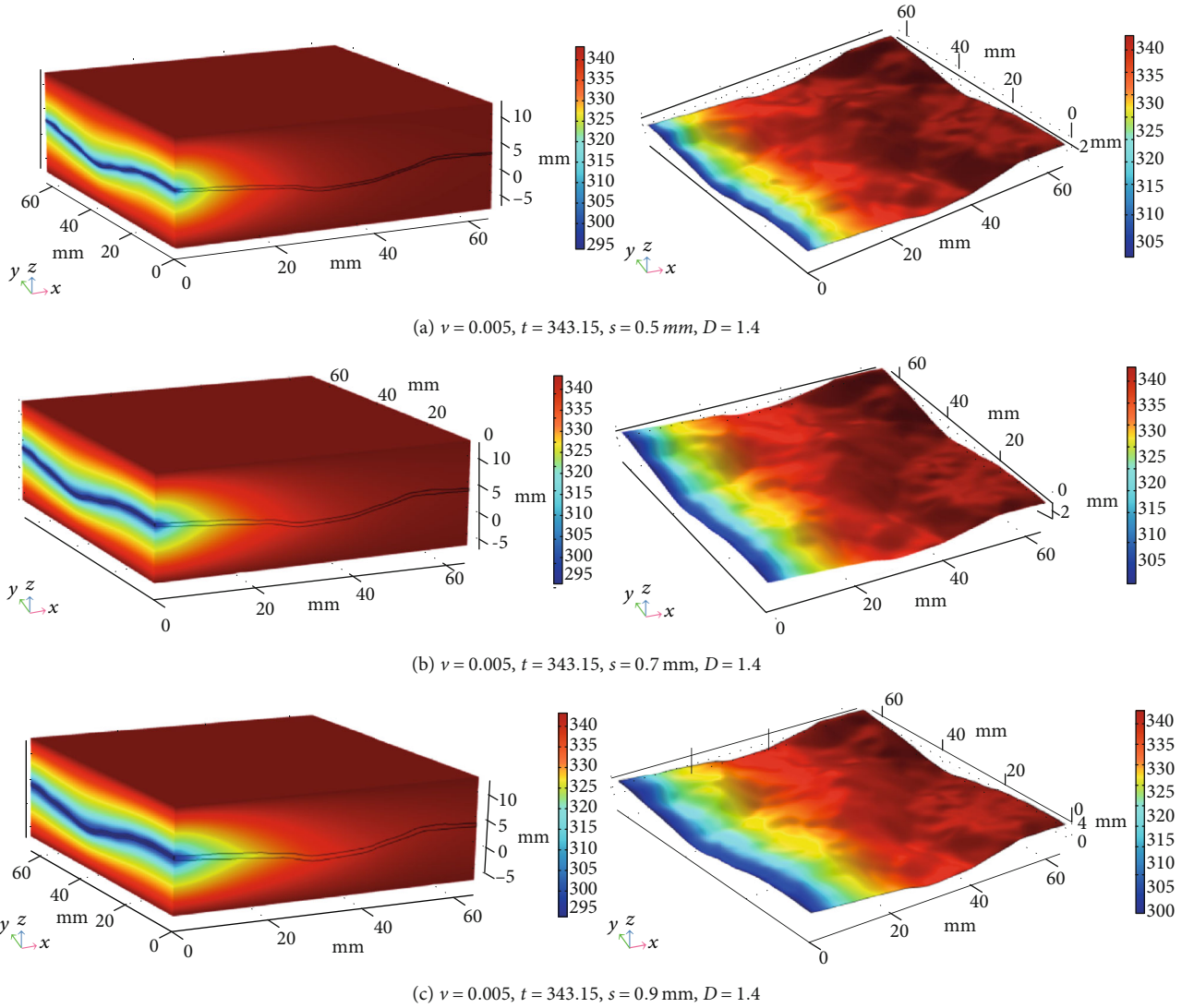


FIGURE 5: Temperature field of water flowing through F_2 granite sample with various aperture sizes (Temperature: K).

4.4. Effects of Fracture Roughness on the Heat Transfer Characteristics. Using constant water velocity, the aperture size of the fracture surface, and initial rock temperature, the effects of fracture roughness on the heat transfer characteristics were studied, taking the temperature field of water flowing through granite rock with different roughness values of fracture surface (1.2, 1.4, 1.6, 1.8, and 2.0 roughness fracture surface) as an example. The rock temperature, fracture aperture size, and flow velocity of water were set to 343.15 K, 0.5 mm, and 0.005 m/s, respectively. The calculation results are shown in Figure 8. The other water velocities, aperture sizes, and initial rock temperatures have similar trends.

Fracture roughness has a slight influence on the heat transfer process (Table 2). The increase in fracture roughness results in increased contact area. However, some bumps and recesses in the fracture surface hinder effective heat transfer between flowing water and rock fracture. Overall, the heat

transfer coefficient decreases with the increase in the roughness coefficient. An increase in fracture roughness under the same flow velocity, rock temperature, and fracture aperture size results in gradually decreasing heat transfer abilities between flowing water and rock (Figure 8). A greater flow distance is needed to increase and maintain the water temperature at the rock temperature. Thus, the position where water has a similar temperature as the surrounding rock slowly moves towards the outlet. Overall, the decreasing temperature area of the rock becomes relatively large.

5. Discussion

To better represent the geothermal system based upon the above results, a new heat transfer coefficient is proposed. Water velocity has the most significant influence on the heat transfer coefficient, followed by fracture aperture size, and

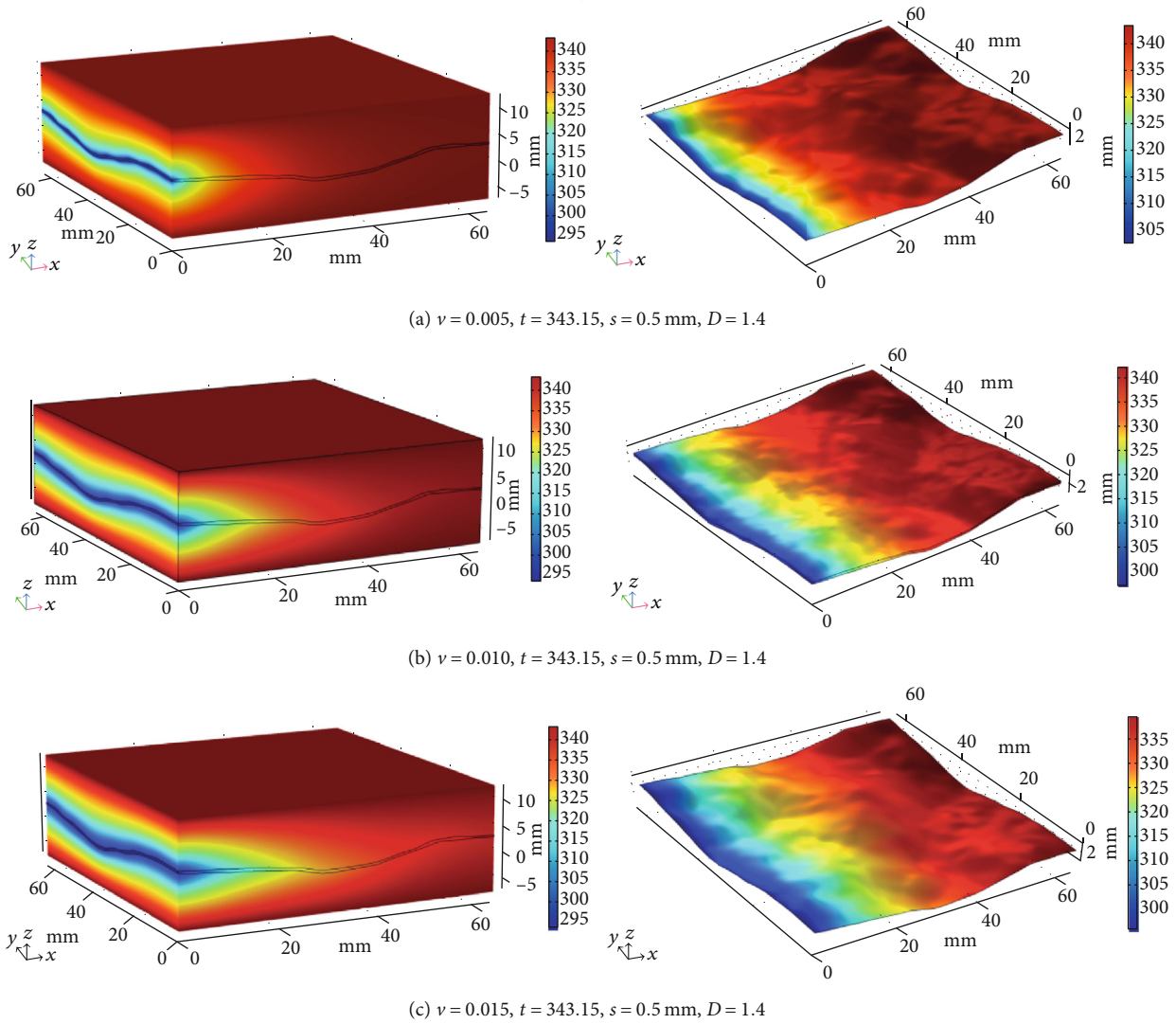


FIGURE 6: Temperature field of water flowing through granite sample F_2 with various velocities (Temperature: K).

rock fracture roughness; whereas initial rock temperature has the least influence. Therefore, the initial rock temperature can be ignored in the newly proposed heat transfer coefficient. The new heat transfer coefficient model considers aperture size, flow velocity of water, and rock fracture roughness and can be expressed as:

$$h = 6e9v^{1.4} \exp(-0.16D)s^{1.2}. \quad (9)$$

From Eq. (9), the heat transfer coefficient can be estimated approximately by water velocity, rock fracture roughness, and aperture size. With the increase in the rock aperture size and water velocity, and decrease in the rock fracture roughness, the heat transfer coefficient increases. Therefore, to enhance the heat transfer coefficient of fluid through the rock fracture surface, the water velocity and rock aperture size should be increased

appropriately, and the rock fracture surface should be as smooth as possible.

Additionally, the Reynolds, Prandtl, and Nusselt numbers were calculated by Eqs. (4)–(6), respectively. Figure 9 illustrates the positively correlated relationship between the Nusselt number and the Reynolds/Prandtl number ratio. The Reynolds number is within the range of 7.4–20.5 in the above experiments. Based on the characteristics of the curves plotted in Figure 9, a semiempirical relationship between the Nusselt number and Reynolds number/Prandtl number ratio is proposed below in the form of Eq. (10):

$$Nu = 0.94Pr^{1/3} Re^{1.23} \quad (10)$$

Figure 9 also presents the best-fitted curves of the numerical data for all the above cases. The results show that Eq. (10) fits well with the experimental data with a high correlation coefficient ($R^2 = 0.95$).

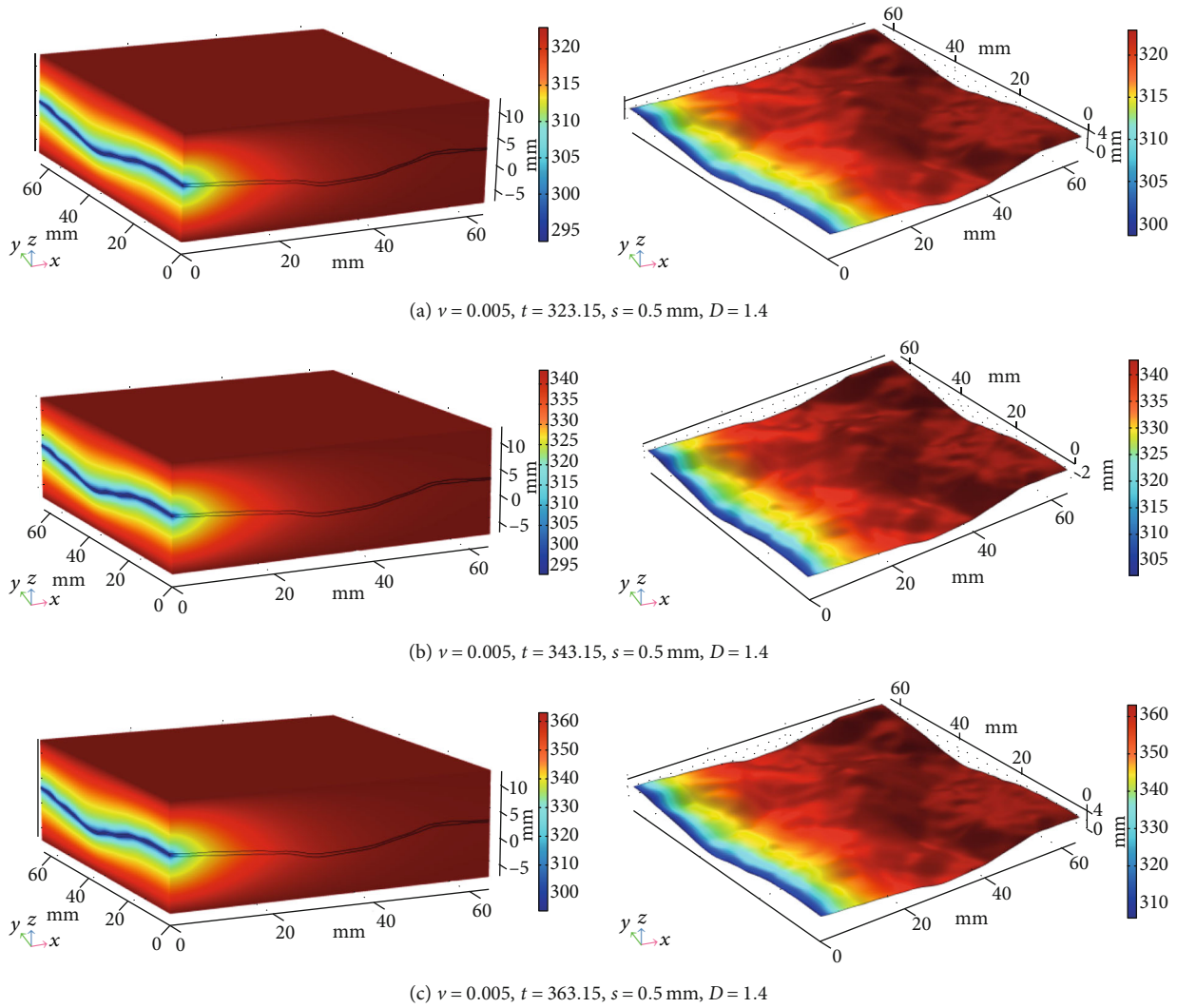


FIGURE 7: Temperature field of water flowing through a fracture in granite with various starting temperatures (Temperature: K).

Equations (9) and (10) were proposed based on a number of numerical simulations. However, the reliability of numerical simulation results is not acceptable. Hence, a series of heat transfer experiments should be conducted to verify the proposed Eqs. (9) and (10). In addition, the heat transfer coefficient model should be considered for future application in large scale engineering simulation.

6. Conclusion

Using a 3-D numerical model, the effects of rock temperature, roughness, and aperture size of fracture surface, and water velocity on the heat transfer characteristics of rock were studied in detail. The following are the main conclusions of this work:

- (1) The fracture geometry of five cuboid granite rocks was obtained using 3D CaMeta stereotopometric scanning system, and 3-D models were built using

Comsol software by importing the geometry data. Based on previous research, a reasonable 3-D model was built to investigate the effects of rock temperature, roughness, and aperture size of fracture surface, and water velocity on the heat transfer characteristics between flowing water and a rock fracture. The simulation results were highly consistent with previous experimental results, which verifies the precision and practicality of the model

- (2) The test results showed that water velocity has the most significant influence on the heat transfer coefficient, followed by fracture aperture size and rock fracture roughness. The initial rock temperature has the least influence. The simulation results provide a foundation for the exploitation of heat energy of hot dry rock for renewable energy resources
- (3) A new heat transfer coefficient model was proposed considering aperture size, flow velocity of water,

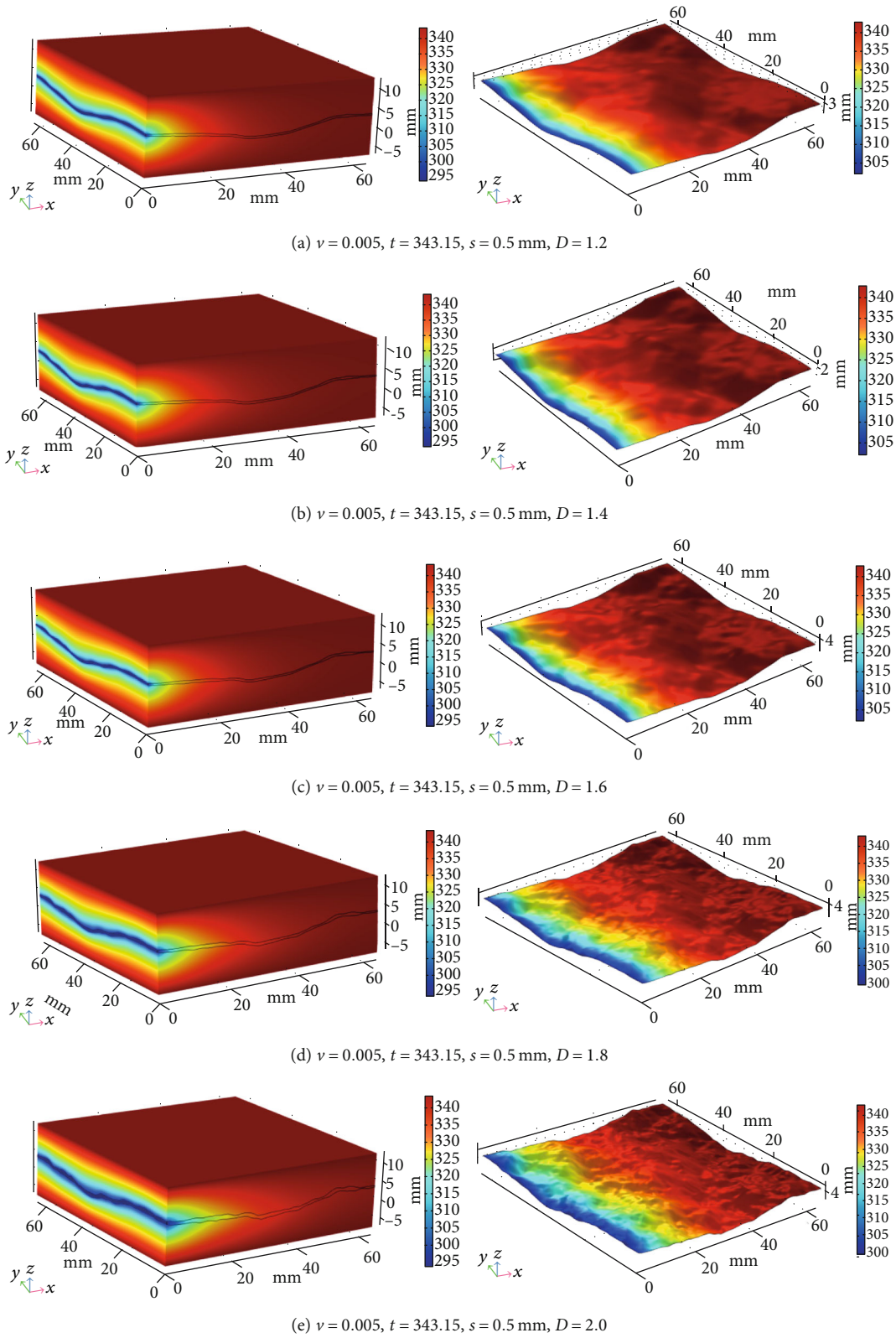


FIGURE 8: Temperature field of water flowing through granite with various roughness values of fracture surface (Temperature: K).

and rock fracture roughness. The initial rock temperature was not taken into account because it has a negligible effect on the temperature of the water as

it passes through the fracture. The heat transfer coefficient can be estimated approximately by the water velocity, rock fracture roughness, and aperture

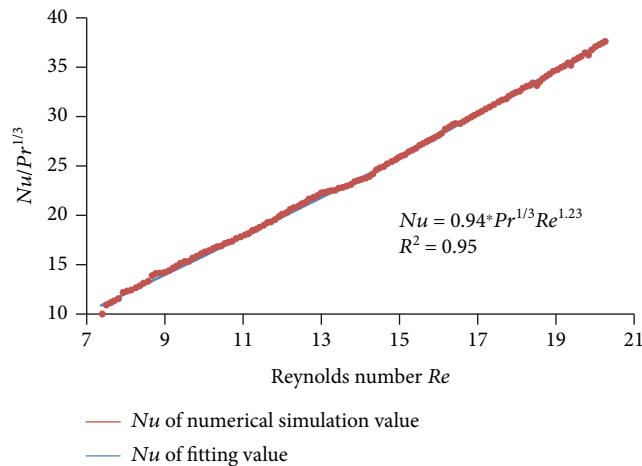


FIGURE 9: The relationship between Re and $Nu/Pr^{1/3}$.

size in this new coefficient model. The heat transfer coefficient of water flowing through a fracture in the hot dry rock can be enhanced by increasing the water velocity and aperture size and by decreasing the roughness of the fracture surface. Additionally, a relationship between Nusselt number and Reynolds number/Prandtl number ratio was also proposed based upon the relationships determined through the simulation results

Data Availability

The data are available and explained in this article, readers can access the data supporting the conclusions of this study.

Conflicts of Interest

The authors have no conflicts of interest to declare.

Acknowledgments

This work was supported by the Research and Development Project of Guizhou University of Engineering Science (Grant No: G2018016), the Technology Top Talent Support Project of Guizhou Provincial Education Department ([2017]098), and the Technology Platform and Talent Team Plan Project ([2018]5622).

References

- [1] P. Olasolo, M. C. Juárez, M. P. Morales, S. D'Amico, and I. A. Liarte, "Enhanced geothermal systems (EGS): a review," *Renewable and Sustainable Energy Reviews*, vol. 56, pp. 133–144, 2016.
- [2] F. Xiong, Q. Jiang, C. Xu, X. Zhang, and Q. Zhang, "Influences of connectivity and conductivity on nonlinear flow behaviours through three-dimension discrete fracture networks," *Computers and Geotechnics*, vol. 107, pp. 128–141, 2019.
- [3] F. Xiong, W. Wei, C. Xu, and Q. Jiang, "Experimental and numerical investigation on nonlinear flow behaviour through three dimensional fracture intersections and fracture networks," *Computers and Geotechnics*, vol. 121, p. 103446, 2020.
- [4] N. Jiang, C. Wang, H. Pan, D. Yin, and J. Ma, "Modeling study on the influence of the strip filling mining sequence on mining-induced failure," *Energy Science & Engineering*, vol. 8, no. 6, pp. 2239–2255, 2020.
- [5] J. Wang, J. G. Ning, P. Q. Qiu, S. Yang, and H. F. Shang, "Microseismic monitoring and its precursory parameter of hard roof collapse in longwall faces: a case study," *Geomechanics and Engineering*, vol. 17, no. 4, pp. 375–383, 2019.
- [6] J. Wang, P. Q. Qiu, J. G. Ning, L. Zhuang, and S. Yang, "A numerical study of the mining-induced energy redistribution in a coal seam adjacent to an extracted coal panel during long-wall face mining: a case study," *Energy Science & Engineering*, vol. 8, no. 3, pp. 817–835, 2020.
- [7] N. Wu, Z. Z. Liang, J. R. Zhou, and Y. Z. Zhang, "Energy evolution characteristics of coal specimens with preformed holes under uniaxial compression," *Geomechanics and Engineering*, vol. 20, no. 1, pp. 55–66, 2020.
- [8] G. Feng, Y. Kang, X. C. Wang, Y. Hu, and X. Li, "Investigation on the failure characteristics and fracture classification of shale under brazilian test conditions," *Rock Mechanics and Rock Engineering*, vol. 53, pp. 3325–3340, 2020.
- [9] A. Li, Y. Liu, F. Dai, K. Liu, and M. D. Wei, "Continuum analysis of the structurally controlled displacements for large-scale underground caverns in bedded rock masses," *Tunnelling and Underground Space Technology*, vol. 97, p. 103288, 2020.
- [10] X. Wang, W. Yuan, Y. T. Yan, and X. Zhang, "Scale effect of mechanical properties of jointed rock mass: a numerical study based on particle flow code," *Geomechanics and Engineering*, vol. 21, no. 3, pp. 259–268, 2020.
- [11] J. Dirker, J. P. Meyer, and B. W. Kohlmeyer, "Local heat transfer coefficients at the inlet of an annular flow passage," *International Journal of Heat and Mass Transfer*, vol. 113, pp. 268–280, 2017.
- [12] T. Heinze, S. Hamidi, and B. Galvan, "A dynamic heat transfer coefficient between fractured rock and flowing fluid," *Geothermics*, vol. 65, pp. 10–16, 2017.
- [13] Q. Yin, G. W. Ma, H. W. Jing et al., "Hydraulic properties of 3D rough-walled fractures during shearing: an experimental study," *Journal of Hydrology*, vol. 555, pp. 169–184, 2017.
- [14] Q. Yin, H. W. Jing, H. J. Su, and H. Zhao, "Experimental study on mechanical properties and anchorage performances of rock mass in the fault fracture zone," *International Journal of Geomechanics*, vol. 18, no. 7, 2018.
- [15] A. Alkhasov, N. Bulgakova, and M. Ramazanov, "Studies of the heat and mass transfer phenomena when flowing a vapor-water mixture through the system of geothermal reservoir-well," *Geomechanics and Geophysics for Geo-energy and Geo-resources*, vol. 6, no. 1, 2020.
- [16] R. Mohais, C. Xu, and P. Dowd, "Fluid flow and heat transfer within a single horizontal fracture in an enhanced geothermal system," *Journal of Heat Transfer*, vol. 133, no. 11, 2011.
- [17] B. Bai, Y. Y. He, S. B. Hu, and X. C. Li, "An analytical method for determining the convection heat transfer coefficient between flowing fluid and rock fracture walls," *Rock Mechanics and Rock Engineering*, vol. 50, no. 7, pp. 1787–1799, 2017.
- [18] M. Abbasi, M. Mansouri, A. Daryasafar, and M. Sharifi, "Analytical model for heat transfer between vertical fractures in fractured geothermal reservoirs during water injection," *Renewable Energy*, vol. 130, pp. 73–86, 2019.

- [19] B. Bai, Y. Y. He, X. C. Li, J. Li, X. X. Huang, and J. L. Zhu, "Experimental and analytical study of the overall heat transfer coefficient of water flowing through a single fracture in a granite core," *Applied Thermal Engineering*, vol. 116, pp. 79–90, 2017.
- [20] L. L. Guo, Y. Zhang, Z. Yu, Z. Hu, C. Lan, and T. Xu, "Hot dry rock geothermal potential of the Xujiaweizi area in Songliao Basin, northeastern China," *Environmental Earth Sciences*, vol. 75, no. 6, 2016.
- [21] Y. Y. He, B. Bai, S. B. Hu, and X. C. Li, "Effects of surface roughness on the heat transfer characteristics of water flow through a single granite fracture," *Computers and Geotechnics*, vol. 80, pp. 312–321, 2016.
- [22] Y. B. Huang, Y. J. Zhang, Z. W. Yu, Y. Q. Ma, and C. Zhang, "Experimental investigation of seepage and heat transfer in rough fractures for enhanced geothermal systems," *Renewable Energy*, vol. 135, pp. 846–855, 2019.
- [23] L. L. Guo, Y. B. Zhang, Y. J. Zhang, Z. W. Yu, and J. N. Zhang, "Experimental investigation of granite properties under different temperatures and pressures and numerical analysis of damage effect in enhanced geothermal system," *Renewable Energy*, vol. 126, pp. 107–125, 2018.
- [24] J. Luo, Y. M. Qi, Q. Zhao, L. Tan, W. Xiang, and J. Rohn, "Investigation of flow and heat transfer characteristics in fractured granite," *Energies*, vol. 11, no. 5, p. 1228, 2018.
- [25] Y. Q. Ma, Y. J. Zhang, Z. W. Yu, Y. B. Huang, and C. Zhang, "Heat transfer by water flowing through rough fractures and distribution of local heat transfer coefficient along the flow direction," *International Journal of Heat and Mass Transfer*, vol. 119, pp. 139–147, 2018.
- [26] Z. W. Li, X. T. Feng, Y. J. Zhang, C. Zhang, T. F. Xu, and Y. S. Wang, "Experimental research on the convection heat transfer characteristics of distilled water in manmade smooth and rough rock fractures," *Energy*, vol. 133, pp. 206–218, 2017.
- [27] M. Abbasi, N. Khazali, and M. Sharifi, "Analytical model for convection-conduction heat transfer during water injection in fractured geothermal reservoirs with variable rock matrix block size," *Geothermics*, vol. 69, pp. 1–14, 2017.
- [28] T. Lee, K. Kim, K. Lee, H. Lee, and W. Lee, "Development of fluid flow and heat transfer model in naturally fractured geothermal reservoir with discrete fracture network method," *Geosciences Journal*, vol. 22, no. 3, pp. 477–485, 2018.
- [29] P. Popov, G. Qin, L. Bi, Y. Efendiev, R. E. Ewing, and J. Li, "Multiphysics and multiscale methods for modeling fluid flow through naturally fractured carbonate karst reservoirs," *SPE Reservoir Evaluation and Engineering*, vol. 12, no. 2, pp. 218–231, 2013.
- [30] B. Bai, Y. He, X. Li et al., "Local heat transfer characteristics of water flowing through a single fracture within a cylindrical granite specimen," *Environmental Earth Science*, vol. 75, no. 22, 2016.
- [31] J. Lee, K. I. Kim, K. B. Min, and J. Rutqvist, "TOUGH-UDEC: a simulator for coupled multiphase fluid flows, heat transfers and discontinuous deformations in fractured porous media," *Computers and Geosciences*, vol. 126, pp. 120–130, 2019.
- [32] A. R. Shaik, S. S. Rahman, N. H. Tran, and T. Tran, "Numerical simulation of fluid-rock coupling heat transfer in naturally fractured geothermal system," *Applied Thermal Engineering*, vol. 31, no. 10, pp. 1600–1606, 2011.
- [33] A. J. Chapman, *Heat Transfer*, Macmillan publishing company, New York, NY, 4th edition, 1989.
- [34] F. Xiong, Q. Jiang, Z. Ye, and X. Zhang, "Nonlinear flow behavior through rough-walled rock fractures: the effect of contact area," *Computers and Geotechnics*, vol. 102, pp. 179–195, 2018.
- [35] W. Zheng, S. C. Silva, and D. D. Tannant, "Crushing characteristics of four different proppants and implications for fracture conductivity," *Journal of Natural Gas Science and Engineering*, vol. 53, pp. 125–138, 2018.
- [36] Z. Qin, H. Fu, and X. Chen, "A study on altered granite meso-damage mechanisms due to water invasion-water loss cycles," *Environmental Earth Sciences*, vol. 78, no. 14, 2019.
- [37] Q. Yin, H. W. Jing, G. W. Ma, H. Su, and R. Liu, "Investigating the roles of included angle and loading condition on the critical hydraulic gradient of real rock fracture networks," *Rock Mechanics and Rock Engineering*, vol. 51, no. 10, pp. 3167–3177, 2018.
- [38] Q. Yin, R. Liu, H. Jing, H. Su, L. Yu, and L. He, "Experimental study of nonlinear flow behaviors through fractured rock samples after High-Temperature exposure," *Rock Mechanics and Rock Engineering*, vol. 52, no. 9, pp. 2963–2983, 2019.
- [39] D. Z. Ren, D. S. Zhou, D. K. Liu, F. J. Dong, S. W. Ma, and H. Huang, "Formation mechanism of the Upper Triassic Yanchang Formation tight sandstone reservoir in Ordos Basin-Take Chang 6 reservoir in Jiyuan oil field as an example," *Journal of Petroleum Science and Engineering*, vol. 178, pp. 497–505, 2019.
- [40] H. Huang, T. Babadagli, X. Chen, H. Z. Li, and Y. M. Zhang, "Performance comparison of novel chemical agents for mitigating water-blocking problem in tight gas sandstones," *SPE Reservoir Evaluation & Engineering*, vol. 2020, pp. 1–9, 2020.
- [41] S. J. Chen, D. W. Yin, N. Jiang, F. Wang, and Z. H. Zhao, "Mechanical properties of oil shale-coal composite samples," *International Journal of Rock Mechanics and Mining Sciences*, vol. 123, article 104120, 2019.
- [42] N. Zhang, W. Liu, Y. Zhang, P. F. Shan, and X. L. Shi, "Microscopic pore structure of surrounding rock for underground strategic petroleum reserve (SPR) caverns in bedded rock salt," *Energies*, vol. 13, no. 4, article 1565, 2020.
- [43] Y. Zhang, S. G. Cao, N. Zhang, and C. Z. Zhao, "The application of short-wall block backfill mining to preserve surface water resources in northwest China," *Journal of Cleaner Production*, vol. 261, article 121232, 2020.
- [44] P. F. Shan and X. P. Lai, "An associated evaluation methodology of initial stress level of coal-rock masses in steeply inclined coal seams, Urumchi coal field, China," *Engineering Computations*, vol. 37, no. 6, pp. 2177–2192, 2020.
- [45] H. Y. Wang, A. Dyskin, P. Dight, E. Pasternak, and A. Hsieh, "Review of unloading tests of dynamic rock failure in compression," *Engineering Fracture Mechanics*, vol. 225, article 106289, 2020.
- [46] C. X. Wang, B. T. Shen, J. T. Chen et al., "Compression characteristics of filling gangue and simulation of mining with gangue backfilling: an experimental investigation," *Geomechanics and Engineering*, vol. 20, no. 6, pp. 485–495, 2020.
- [47] W. Zheng and D. D. Tannant, "Influence of proppant fragmentation on fracture conductivity - insights from three-dimensional discrete element modeling," *Journal of Petroleum Science and Engineering*, vol. 177, pp. 1010–1023, 2019.

Research Article

Model Experimental Study on the Seepage and Failure Features of Tunnel under Wetting-Drying Alternation with Increasing Water Pressure

Haijian Su ¹, Yujie Feng,¹ Qingzhen Guo,¹ Hongwen Jing ¹ and Wenxin Zhu²

¹State Key Laboratory for Geomechanics and Deep Underground Engineering, China University of Mining and Technology, Xuzhou, Jiangsu 221116, China

²School of Traffic and Civil Engineering, Shandong Jiaotong University, Jinan, Shandong 250357, China

Correspondence should be addressed to Haijian Su; hjsu@cumt.edu.cn

Received 29 April 2020; Revised 8 June 2020; Accepted 18 June 2020; Published 4 July 2020

Academic Editor: Qian Yin

Copyright © 2020 Haijian Su et al. This is an open access article distributed under the Creative Commons Attribution License, which permits unrestricted use, distribution, and reproduction in any medium, provided the original work is properly cited.

Wetting-drying alternation caused by seasonal rainfall and water fluctuation has a negative effect on the rock mass. Model experiments were conducted in this paper to investigate the role of wetting-drying alternation on the seepage and failure features of a tunnel. Water-bearing structure was located in the lateral position of tunnel. The stratum thickness between the tunnel and water-bearing structure was ranged from 20 to 100 mm. The results showed that, with an increase in the wetting-drying alternation number, the pore water pressure increases gradually. The critical water pressure also increases gradually with the increasing thickness of water-resisting stratum. With the increase of the stratum thickness, the permeable area is gradually widened and the water storage capacity becomes stronger. The failure mode of water-resisting stratum under geostress and water pressure can be summarized as two types: fracture failure (thickness of 20 mm) and slippage failure (thickness between 40 and 100 mm), respectively.

1. Introduction

With the vigorous development of economics, the focus of major engineering construction has shifted from plains to the mountainous and karst areas with extremely complex topographic and geological conditions. Deep and long tunnel engineering with high risk has been conducted in karst areas. However, a series of special geological hazards like fractured weak zone, rock burst, and water inrush are encountered in the process of construction [1–4]. Karst tunnel water inrush is one of most common and harmful of these geological hazards [5–9]. According to the statistics, water inrush and other geological hazards induced by water inrush account for 77.3% of the total number of major accidents in tunnel project during the first decade of 21st century in China [10, 11].

The stratum thickness between the tunnel and water-bearing structure is especially crucial to the safety of the karst tunnel. Xu et al. [12] investigated the minimum safety thick-

ness of the rock resisting water inrush from filling-type karst caves located in the top, bottom, and lateral positions to the tunnel. Based on the Yuelongmen tunnel of Chengdu to the Lanzhou railway line in China, Jiang et al. [13] carried out a series of large-scale geomechanical model tests to study the effect of waterproof-resistant slab thickness of surrounding rock on water inrush disaster and established a simplified model to simulate the whole disaster process. Yang and Zhang [14] obtained the expression of the minimum thickness for rock plug in a karst tunnel by means of the upper bound theorem in combination with variational principle. In the area with obvious seasonal rainfall characteristics, the water-bearing cave is often connected with outside by an open channel. The water level in the water-bearing cave rises during the rainy season and falls in the dry season. Under the influence of wetting-drying alternation, fine mineral particles and cementing material in the surrounding rock are dissolved in water and flowed out due to water

pressure, leading to the deterioration of rock mass. With the accumulation of the deterioration effect, the risk of water inrush gradually increases [15–18].

Water environment is one of the important factors affecting rock properties because it can soften and disintegrate the rock and soil mass [19–21]. The grain structure, cementation degree, mineral composition, and crack propagation of rock mass will all change after it is exposed to water, which will eventually lead to the deterioration of physical and mechanical properties of rock mass [22–24]. In recent years, lots of scholars have drawn many valuable conclusions about the effect of wetting-drying alternation on the rock mass. For instance, Doostmohammadi et al. [25] studied the influence of cyclic wetting and drying on mudstone, and they found that the increasing wetting and drying cycles can reduce the time required to reach ultimate swelling. Vergara and Triantafyllidis [26] investigated the swelling behavior of volcanic rocks from the Central Andes of Chile under cyclic wetting and drying. Their results indicated that swelling potential is affected by wetting and drying cycles and this phenomenon only occurs during the wetting phase. Ozbek [27] investigated the variations in physical and mechanical properties of ignimbrites under the influence of wetting-drying and freezing–thawing cycles and discovered the effects of chemical composition, color, and cyclic period on the physical and mechanical properties of rock. Wang et al. [28] examined the irreversible phenomena of argillaceous rocks during wetting and drying processes by combining environmental scanning electron microscope (ESEM) imaging and digital image correlation (DIC) techniques. A modified split Hopkinson pressure bar (SHPB) technique was applied by Zhou et al. [29] to study the influence of wetting and drying cycles on dynamic compressive properties of sandstone. The results showed that the generation of microcracks caused by wetting and drying cycles primarily leads to the reduction in dynamic compressive strength. Qin et al. [30] investigated the effects of drying-wetting cycles on the mechanical properties of altered rock and found that uniaxial compressive strength and elastic modulus gradually decrease with the increase of the drying-wetting cycle number. Zhao et al. [31] studied the evolution of micropores of mudstones under periodic wetting-drying conditions by low-field nuclear magnetic resonance (NMR) and established a significant linear relationship between the increment of porosity and wetting-drying cycle number.

The Liupanshan tunnel is located in Ningxia Hui Autonomous Region of China. The main aquifer types of the rock mass around tunnel are pore and fissure waters in Quaternary loose rock and the bedrock fissure water. In addition, the rainfall is unevenly distributed, depending on the seasons. For example, the rainfall is relatively large in summer and autumn, whereas the rainfall is relatively small in spring and winter. Therefore, in order to investigate the characteristics of water inrush and instability modes of the tunnel under the influence of wetting-drying alternation, large-scale geomechanical models were set up based on the engineering geological background of the Liupanshan tunnel. The effects of stratum thickness on the seepage and failure modes of surrounding rock were also analyzed.

2. Model Experimental Method

2.1. Test Materials and Similarity Ratio. The test materials were selected according to the similarity theory. To improve the accuracy of the test, river sand and talcum powder were selected as the aggregate materials, paraffin as cementing material, and hydraulic oil as the auxiliary material. Preparation and molding of similar material depend on the hot melting and the hardening by cooling of paraffin. In the wetting-drying alternation process, talcum powder and hydraulic oil will be precipitated and separated gradually, which can be used to simulate the loss of clay mineral of surrounding rock mass. The similar material specimens were prepared using these materials with a rational mix ratio.

According to the principle of orthogonal test, the test specimens were designed and fabricated, which include $\varnothing 50 \times 100$ mm, $\varnothing 50 \times 25$ mm, and $\varnothing 50 \times 50$ mm. Based on the test results of uniaxial compressive, Brazilian splitting and shear tests, the density ρ , porosity Φ , uniaxial compressive strength σ_c , elastic modulus E_c , tensile strength σ_t , cohesion C , and internal friction φ_0 were measured. The test method was based on the specification of “the specification of engineering rock test method standard (GB/T 50266-2013)” [32]. The mix ratio of similar materials was determined from the specific value of river sand, talcum, paraffin, and hydraulic oil, i.e., 23.0:3.5:1.5:1.0. According to the experimental data on rocks and similar materials, the physical and mechanical properties are listed in Table 1. Besides, according to the engineering geological condition, the geometric similarity ratio and volume-weight similarity ratio in this model experiment were determined as 100 and 1.24, respectively [33, 34].

2.2. Experimental System. In order to investigate the formation process of water inrush with different thickness of water-resisting stratum under wetting-drying alternation, a set of visualization test system for karst tunnel water-inrush disaster was independently developed, as shown in Figure 1. The system mainly consists of geostress loading device, water pressure loading device, data acquisition system, and overall framework. The experimental overall framework is made of a seamless welded steel plate with a thickness of 12 mm, and the net size of the framework is $1000 \times 1000 \times 300$ mm. The 5 cm-apart bolt holes around the frame are reserved to connect the reinforcing plate. A transparent high-strength glass panel is equipped between the frame and reinforcing plate to observe the deformation and failure process of surrounding rock. In addition, in order to provide stable water pressure for the water-bearing structure, the water pressure loading device uses a group of nitrogen cylinder with servo control to provide pressure for the water, which has the advantage of gas-liquid combination. The water-bearing structure is fabricated using the PVC pipe with an inner diameter of 50 mm and thickness of 1.5 mm combined with a stripper rubber.

2.3. Experiment Condition and Production Procedure. Figure 2 shows the sensor arrangement around the tunnel. The height and width of the tunnel are 72 mm and 110 mm, respectively. The stratum thickness d between the water-bearing structure and tunnel was ranged from 20 to 100 mm.

TABLE 1: Physical–mechanical properties of prototype and similar material.

	ρ	Φ	σ_c	σ_t	E_c	C	φ_0
Sandstone	2.51 g/cm ³	8.27%	81.83 MPa	11.74 MPa	8.89 GPa	18.61 MPa	43.08°
Similar material	2.02 g/cm ³	8.73%	323.73 kPa	43.50 kPa	25.78 MPa	79.40 kPa	37.34°

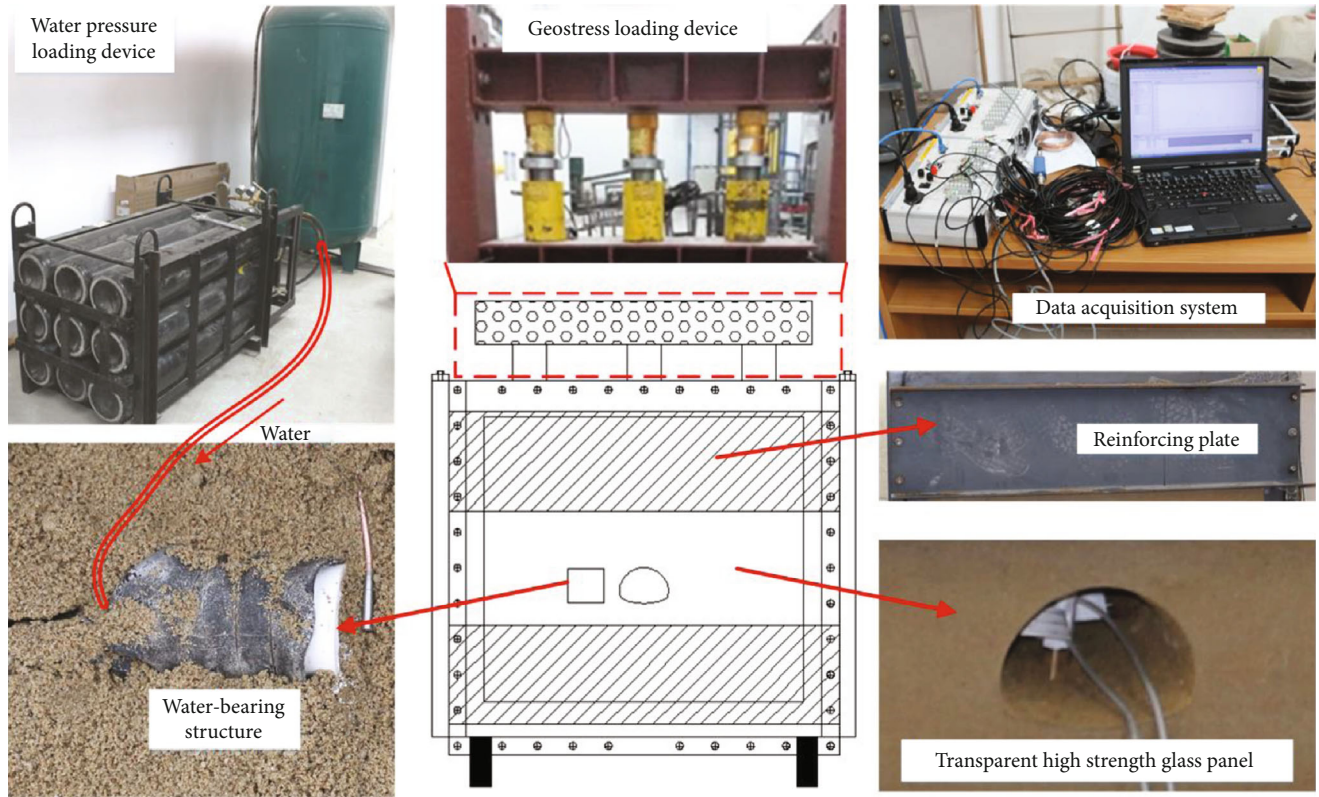


FIGURE 1: Experimental system.

An osmotic pressure gauge, with the measuring range of 1 MPa, was arranged at $d/2$ away from the right boundary of the water-bearing structure and was connected to data acquisition system via a fixed signal amplifier. The direction of the osmotic pressure gauge is the same with the seepage direction. Three pressure cells were distributed around the tunnel as shown in Figure 2. These pressure cells could measure 1 MPa maximally, with the diameter and thickness of 17 and 8 mm, respectively. The pressure cells were arranged horizontally to collect the vertical stress of surrounding rock mass.

The components of similar material were weighted separately in proportion before stirring. In order to achieve the uniform stirring, the talcum powder and river sand were firstly mixed evenly in the blender and the bottom of blender was heated continuously meanwhile. Then, hydraulic oil and melted paraffin were added in the blender, which were stirred well with previous mixed materials.

The lubricating oil was brushed on the frame and interior of the reinforcing plate to reduce the friction. Then, the well-stirred similar materials were poured into test-bed in batches. The similar materials need to be vibrated and tamped one time every 10 cm thick. In addition, water-

bearing structure, pressure box, osmotic pressure gauge, and other sensors were buried, respectively, on a preset schedule, once similar materials were laid to the specified position. After pouring similar materials, the model was kept for 48 hours to cool solidified. The geostress loading device was installed on the upper part of the model with a specified in situ stress load applied. The tunnel excavation was carried out after 6 hours' constant in situ stress. Then, the displacement sensor was installed to measure the top-bottom and two walls approaches of tunnel.

The water pressure applied to the model was calculated through a similarity calculation based on the field test data. As shown in Figure 3, when the wetting-drying alternation number $N = 1$, the water pressure was increased from 0 to 0.03 MPa firstly. The water pressure loading and drying times are about 30 and 120 minutes, respectively. In this drying process, the water in the storage structure will continue to flow out from the surrounding rock of the tunnel, which is actually a process of unloading water pressure. Therefore, the water pressure at the next alternation returns to zero, so as to simulate the wetting-drying alternation process of tunnel surrounding rock. When $N = 2$, the water pressure

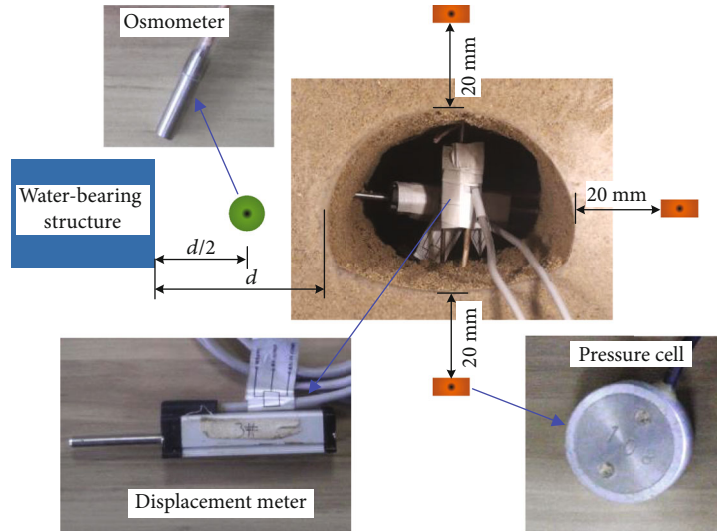


FIGURE 2: Sensor arrangement.

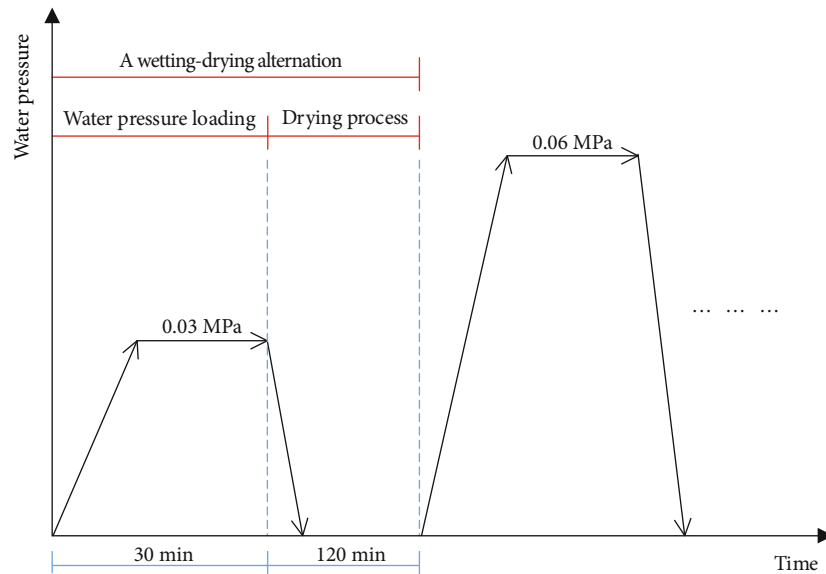


FIGURE 3: Schematic diagram of wetting-drying alternation.

was increased from 0 to 0.06 MPa, and the rest of the process was the same. The increments in each loading cycle are also 0.03 MPa until the formation of water inrush.

3. Results Analysis

3.1. Stable Pore Water Pressure. Figure 4 demonstrates the variation of the pore water pressure in the surrounding rock in a complete water pressure loading and unloading process when the stratum thickness is 80 mm and the wetting-drying alternation number is 11. The whole process of the variation of pore water pressure can be divided into four stages: rising stage, unstable stage, stable stage, and declining stage. In the rising stage, the pore water pressure increases dramatically, which indicates that the surrounding rock of the tunnel is sensitive to the increment of the groundwater level. When the pore water pressure increases to about

40 kPa, the surrounding rock of the tunnel begins to seep water, but the pore water pressure is still unstable and fluctuates around 40 kPa. After a period of adjustment, the pore water pressure gets to the stable stage. The stable and continuous seepage occurs on the surface of tunnel surrounding rock. Finally, the water pressure in the cave decreases to zero at the end of this wetting-drying alternation; the pore water pressure gradually decreases from the previous stable value. The same evolution curve of the pore water pressure also exhibits in other wetting-drying alternation.

In the rising and unstable seepage stages, the tested pore water pressure of the surrounding rock mass is affected by the water flowing to a certain extent. Therefore, in this study, the average value of pore water pressure in the stable stage was calculated to investigate the influence of wetting-drying alternation on the seepage feature of surrounding rock. Figure 5 displays the variation characteristics of the stable pore water

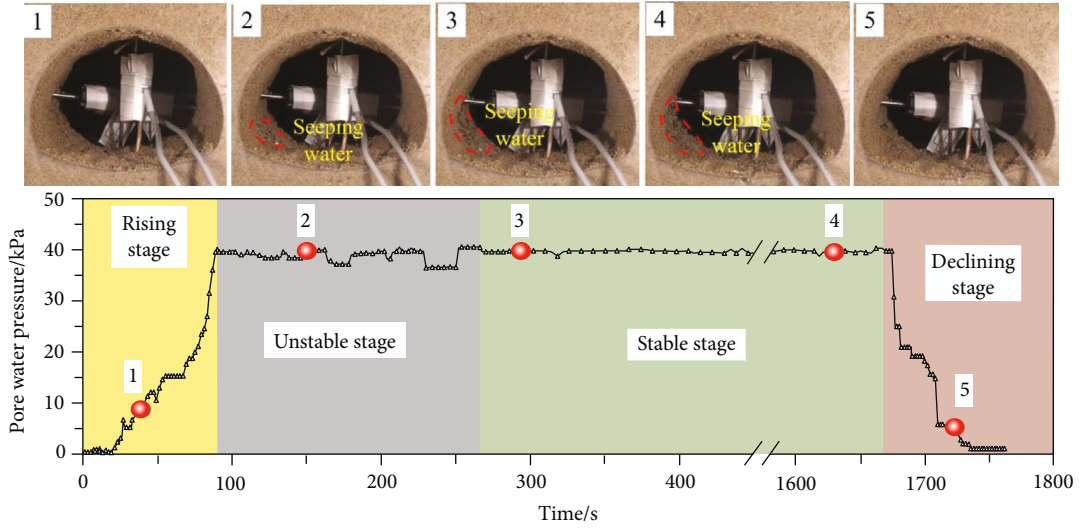


FIGURE 4: Actual curve of pore water pressure in a water pressure loading process ($d = 80$ mm, $N = 11$).

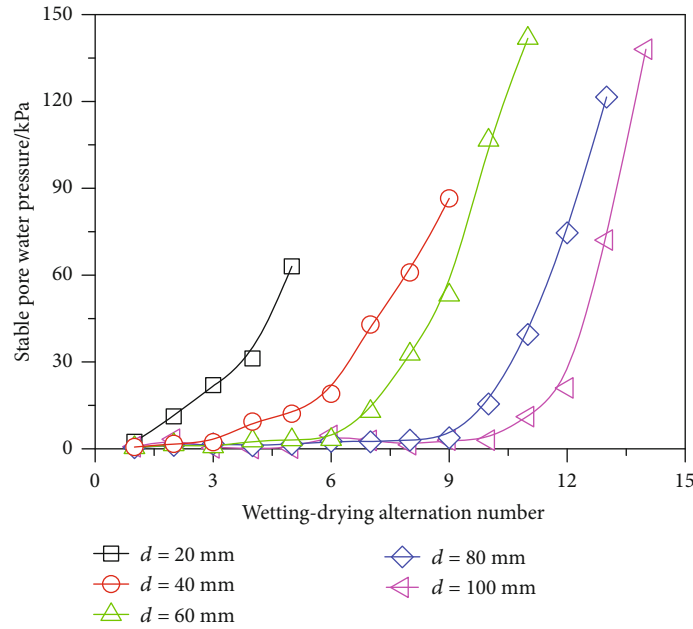


FIGURE 5: Variation in stable water pressure with the increase of wetting-drying alternation number.

pressure in the surrounding rock of the tunnel with different stratum thicknesses and different wetting-drying alternation numbers. When the stratum thickness is fixed, the stable pore water pressure presents a gradual increasing trend with the increment of the wetting-drying number, and the increasing process can be divided into two stages: slow increase and rapid increase. For instance, when the stratum thickness is 80 mm, the stable pore water pressure increases from 0.4 to 3.8 kPa within the first 9 wetting-drying alternations but quickly increases to 121.5 kPa in the following 4 wetting-drying alternations. The variation trend of the pore water pressure in the rock mass is different with different stratum thicknesses. The pore water pressure responds quickly and obviously to the change of the wetting-drying alternation number when the stratum thickness is thin ($d = 20$,

40 mm). A sharp increase of the pore water pressure only occurs after the wetting-drying alternation number reaches a certain value when the stratum thickness is over 40 mm. In addition, the pore water pressure decreases with the increment of the stratum thickness under the same wetting-drying alternation, which may due to the hysteresis of sensor caused by the large stratum thickness. This phenomenon further indicates that, for porous media, the pore water pressure tends to decline with the increase of seepage path.

Figure 6 shows the seepage and failure process of the tunnel when the stratum thickness is 40 mm. For $N \leq 4$, the fluid has not penetrated through the entire thickness of strata and there is no fluid overflow on the tunnel surface. For $N = 5$, the left side wall of the tunnel starts to seep the water. Then, the area where seepage occurs gradually expands with the

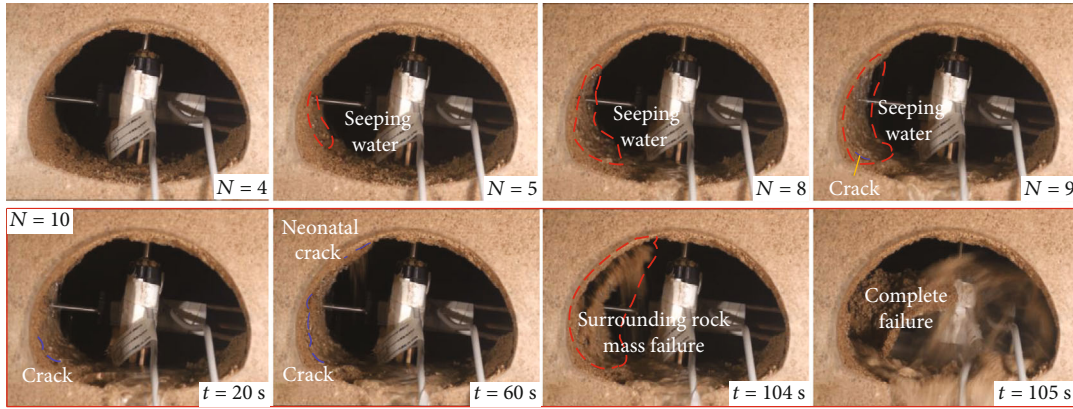


FIGURE 6: Seepage and failure process of tunnel ($d = 40$ mm).

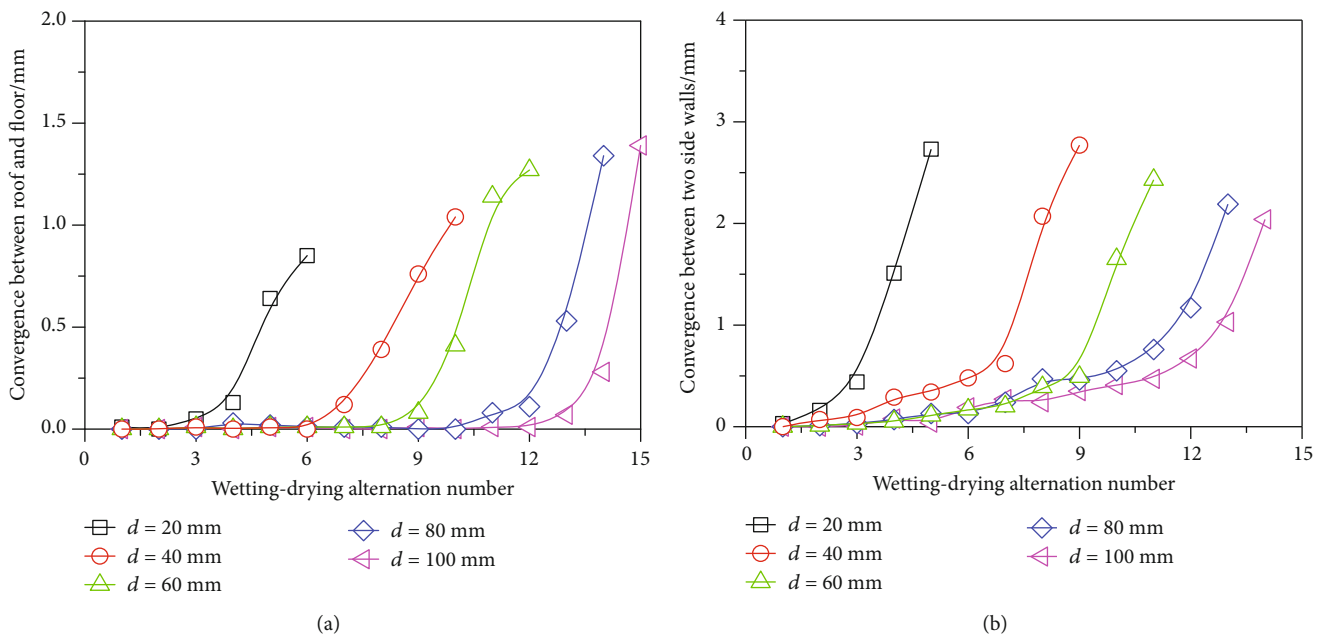


FIGURE 7: Variations in tunnel deformations with the increase of wetting-drying alternation number: (a) convergence between roof and floor and (b) convergence between two side walls.

increase of the wetting-drying alternation number and the current becomes more and more apparent. For $N = 9$, the seepage extends to the entire left wall and a macroscopic crack is observed. For $N = 10$, preserved crack grows and neonatal crack generates at the beginning of the loading process, and the surrounding rock mass continues to separate until the peeling surface is pushed out and caved into the tunnel under the influence of the water pressure. At last, the confined water gushes out quickly from the rock barrier, and the phenomenon of water inrush is formed.

3.2. Displacement and Stress of Surrounding Rock. In order to investigate the evolution characteristics of the surface displacement of the tunnel surrounding rock during the whole process, the displacement meters were embedded in the test model body. The tunnel deformations can be characterized by the relative displacement of the left and right side

walls and the top and bottom surfaces of the tunnel. Figure 7 shows the variations of tunnel deformations in the stable stage with the increase of wetting-drying alternation number. For the surrounding rocks with different stratum thicknesses, the roof and floor are close to each other with the increase of the wetting-drying alternation number so are the left and right side walls. On the whole, under the influence of wetting-drying alternation, the surrounding rock of the tunnel is deformed and the whole tunnel section is in a state of convergence. The horizontal and vertical convergences of the tunnel change slightly and fluctuate in a small range before the complete water inrush but increase sharply in the late stage of water inrush. The peak values of the horizontal and vertical convergences of the tunnel occur at the critical moment of water inrush. The greater the stratum thickness is, the better the integrity of surrounding rock and the smaller the horizontal convergence of two side walls is. It

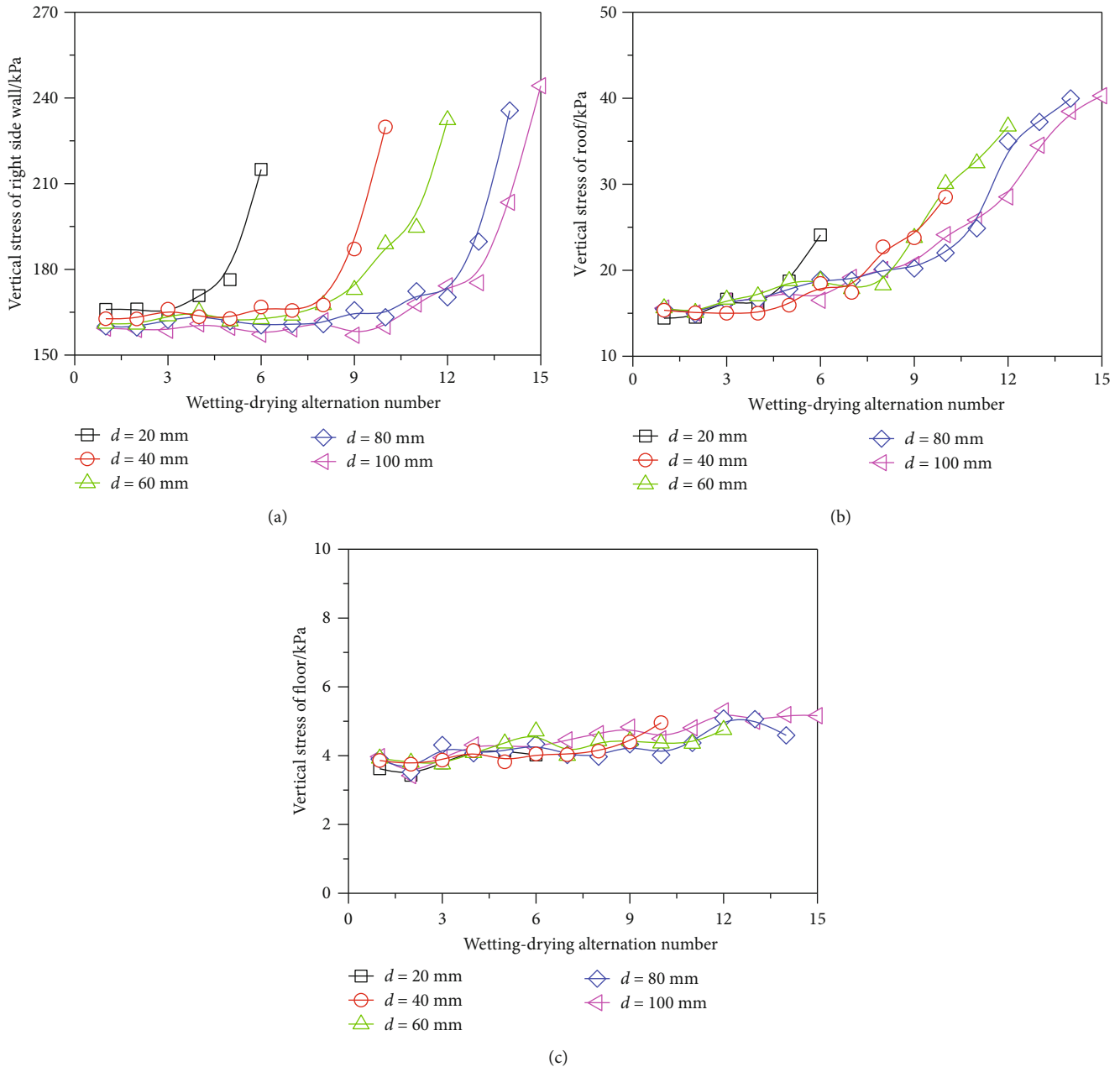


FIGURE 8: Variations in vertical stresses of surrounding rock with the increase of wetting-drying alternation number: (a) right side wall, (b) roof, and (c) floor, respectively.

is found that the change of horizontal convergence is more significant than vertical convergence in terms of the response speed and response scale. In the model test, the cave was arranged at different positions on the left side of the tunnel, the water pressure in the cave acts directly on the left surrounding rock, which leads to the first deformation of the left surrounding rock. The vertical convergence between the roof and floor before water inrush primarily comes from the vertical displacement of the roof and the heave deformation of the floor. In addition, the roof loses the support of the lower rock mass on account of tunnel excavation; the vertical displacement of the roof would occur due to the dead weight and the pressure of the upper rock mass.

Figure 8 shows the changes of vertical stresses of the surrounding rock with the increase of the wetting-drying alternation number. It is found that vertical stresses of the right side wall; the roof and floor get different levels of increment with the increase of the wetting-drying alternation number. The increasing trend of vertical stresses of the right side wall and roof is obvious. They both rise slowly at first and then increase rapidly after reaching a critical value. However, the increase of vertical stress of the floor is hysteretic and the increasing extent is smaller in general than that of the roof. For $d = 20 - 100$ mm, the increasing extents of the vertical stress of the right side wall are 29.51%, 41.24%, 44.27%, 47.21%, and 53.24%, respectively. The vertical stress of the

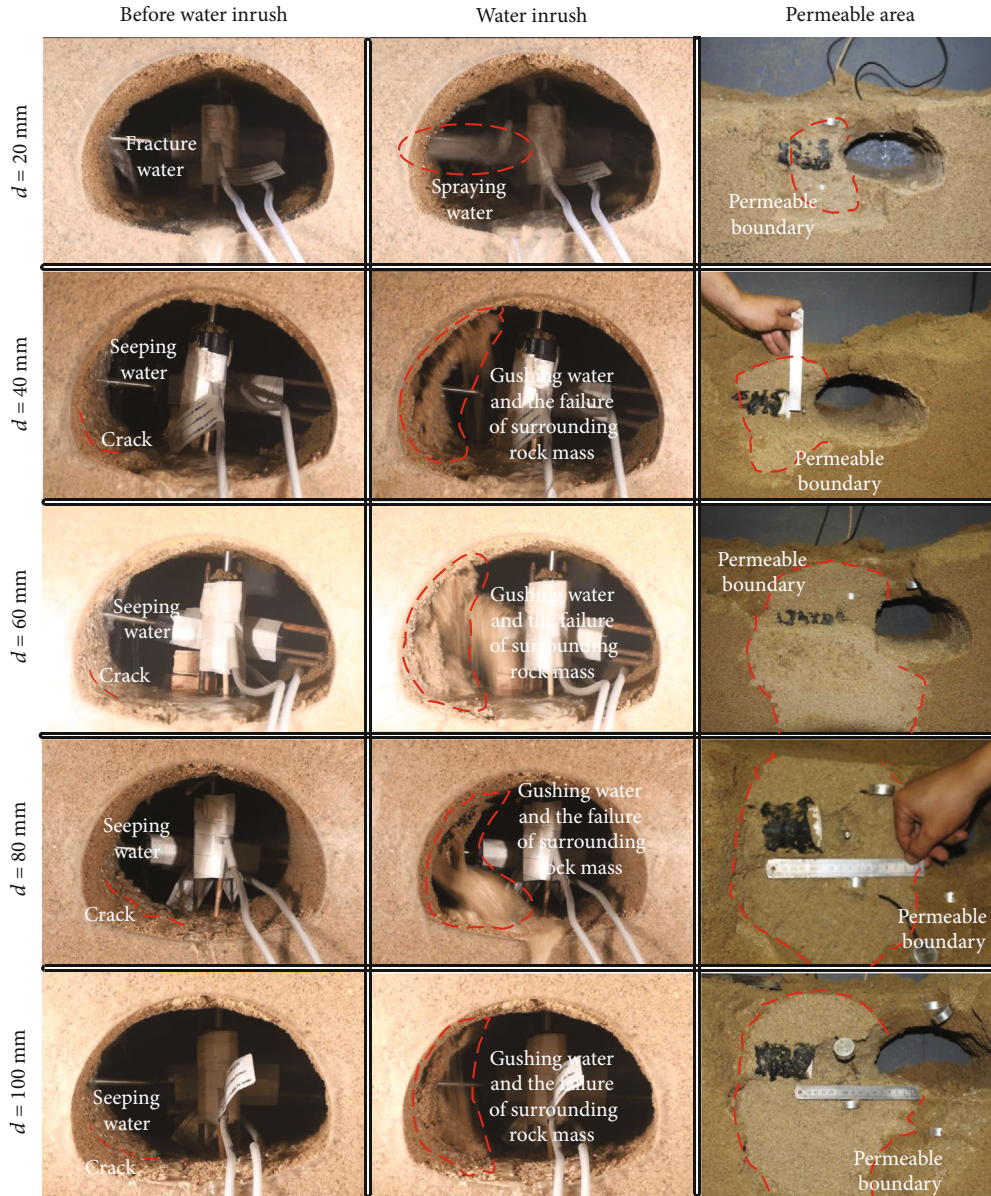


FIGURE 9: Water inrush and failure mode of tunnels.

roof increases by 67.13%, 85.67%, 135.60%, 158.04%, and 158.43%, respectively. The greater stratum thickness and more wetting-drying alternations result in the corresponding increment of the permeable area, seepage velocity, and seepage discharge, which further leads to the strength deterioration of the surrounding rock and the increase of porosity. In addition, the roof and side wall of the tunnel are in an unstable state because of the tunnel excavation. This can help explain why the vertical stresses of the roof and right side wall rise with the wetting-drying alternation number. Tunnel excavation makes the roof of the tunnel lose the supporting function of the lower rock mass, and under the influence of the dead weight, it is the most unstable compared with other rock mass. There are differences in the sensitivity and response of the right side wall and roof to the seepage and the strength degradation of the surrounding caused by wetting-drying alternation. The vertical stress of the floor is relatively the least

sensitive to the wetting-drying alternation number and stratum thickness, and it always fluctuates around a small value. So, tunnel excavation and wetting-drying alternation have no significant effect on the vertical stress of the floor.

3.3. Failure Feature of Tunnel. Figure 9 exhibits the water inrush and failure mode of tunnels with different stratum thicknesses. It is found that the larger the stratum thickness is, the less obvious the water gushing process is before occurrence of water inrush. When $d = 20$ mm, the water gushing from the surrounding rock appears to have a “spraying” shape. In general, under the same wetting-drying alternation number, the thicker the water-resisting stratum is, the safer the surrounding rock is. While with the increase of the stratum thickness, the water gushing from the surrounding rock appears in a “linear” shape accompanied by the failure of the surrounding rock mass. The mineral composition and fine

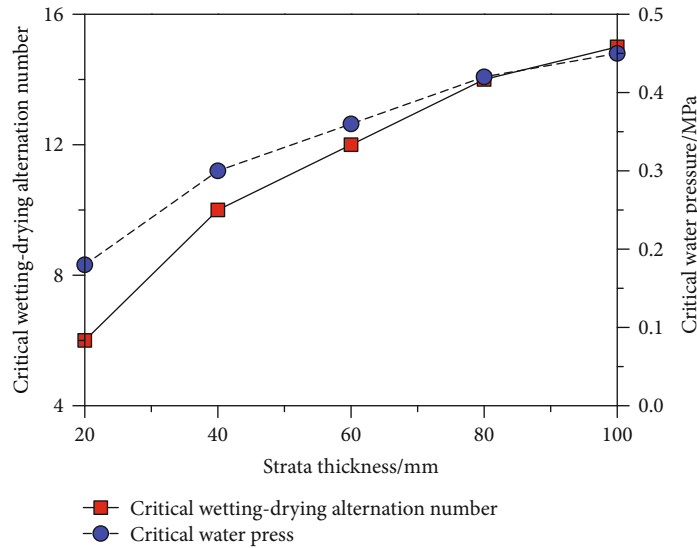


FIGURE 10: Variations in critical wetting-drying alternation number and critical water pressure with different stratum thicknesses.

clay particles of the water-resisting stratum will be separated out with the influence of wetting-drying alternation, leading to the continuous increase in porosity and reduction in water storage capacity. The majority of water before water inrush is stored in the water-resisting stratum, and the water pressure gradually declines with the flow of water. Therefore, the water gushing process of the tunnel with thick water-resisting stratum is not obvious and the water discharge is small.

The ultimate failure patterns of the tunnel with different stratum thicknesses are significantly different during the instability of the tunnel under the influence of wetting-drying alternation. For $d = 20$ mm, the surrounding rock is broken by water from the middle part of the left side wall. For $d = 40 - 100$ mm, the left side wall overall slides to the right and the failure of rock mass occurs at the roof and floor of the left side wall. With the increase of stratum thickness, more wetting-drying alternations are conducted, and the strength of surrounding rock gets continuous degradation. Therefore, the whole surrounding rock is at an unstable state and finally broken by the water pressure accompanied with serious mud inrush.

For the water-resisting stratum with different thicknesses, the final permeable areas show different characteristics after the water inrush of surrounding rock. After comparing the permeable areas showed in Figure 9, it is found that the permeable area is gradually widened with the increase of the stratum thickness. For $d = 100$ mm, the permeable area extends about 140 mm upwards and 300 mm downwards from the center of the water-bearing structure. The permeable area can intuitively reflect the water storage capacity of the stratum. The thicker water-resisting stratum suffers more wetting-drying alternations, and the pore water pressure gets a continuous increase, which can help explain why the water gushing process before water inrush of thick stratum is not apparent. In addition, according to the principle of minimum energy, water always chooses to flow along the path with the largest slope. So, the water flow path of the cave must be in the direction of the tunnel excavation face.

The completed wetting-drying alternation number and the real-time water pressure in the water-bearing structure when tunnel water inrush happens are, respectively, defined as the critical wetting-drying alternation number and critical water pressure. Figure 10 displays the changes of the critical wetting-drying alternation number and the critical water pressure with different stratum thicknesses. It is found that both the critical wetting-drying alternation number and critical water pressure are positively correlated with stratum thickness as a whole. For $d = 20$ mm, the water inrush occurs after 6 wetting-drying alternations and the critical water pressure is 0.18 MPa. For $d = 100$ mm, the water inrush occurs after 15 wetting-drying alternations and the critical water pressure is 0.45 MPa.

Generally, the failure modes of stratum with different thicknesses ranged from 20 to 100 mm under wetting-drying alternation with the increasing water pressure can be divided into two types (fracture failure and slippage failure) in this study, as shown in Figure 11. As stratum thickness is 20 mm, the instability feature presents the fracture failure. The stratum is broken off under geostress and water pressure. When stratum thickness is between 40 and 100 mm, the stratum ends are damaged and fractured, and the stratum structure shows overall slippage.

4. Conclusions

In this study, based on the engineering background of the Liupanshan tunnel (China), physical model tests were set up to explore the seepage and failure features of the karst tunnel with different thicknesses of the water-resisting stratum under the wetting-drying alternation. Some of the conclusions drawn are as follows:

- (1) Both the critical wetting-drying alternation number and critical water pressure increase gradually with the increasing thickness of water-resisting stratum. Besides, with the increase of the alternation number,

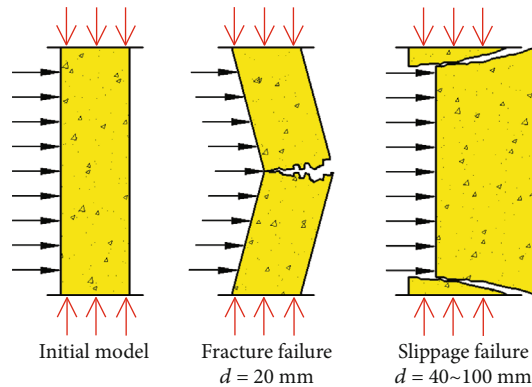


FIGURE 11: Failure modes of stratum.

the pore water pressure of the surrounding rock mass increases gradually, which shows a trend of small fluctuation at first and then rapid increase

- (2) The smaller the thickness of water-resisting stratum is, the more obvious the change of pore water pressure will be. In addition, with the increase in the thickness of water-resisting stratum, the permeable area is gradually widened. The water storage capacity also becomes stronger
- (3) The vertical stresses of the right side wall, roof, and floor get different levels of increment with the increase of the wetting-drying alternation number. The stress variation of the roof surrounding rock is the most significant, followed by the right wall, and the floor-surrounding rock is the smallest. And the horizontal and vertical convergences of tunnel change slightly and fluctuate in a small range before the complete water inrush but increase sharply in the late stage of water inrush

In the actual tunnel projects, the location and scale of karst cave are also crucial to the stability of the tunnel. In addition, more model tests will be conducted to study the whole deformation field evolution process of the surrounding rock mass around the tunnel by the digital image correlation method.

Data Availability

The original data used to support the findings of this study are available from the corresponding author (hjsu@cumt.edu.cn) upon request.

Conflicts of Interest

The authors declare that there are no conflicts of interest regarding the publication of this paper.

Acknowledgments

This study is financed by the National Natural Science Foundation of China (Nos. 51704279 and 51734009) and the Natural Science Foundation of Jiangsu Province of China (No. BK20170270).

References

- [1] L. Li, W. Tu, S. Shi, J. Chen, and Y. Zhang, "Mechanism of water inrush in tunnel construction in karst area," *Geomatics, Natural Hazards and Risk*, vol. 7, no. sup1, pp. 35–46, 2016.
- [2] D. Liang, Z. Jiang, S. Zhu, Q. Sun, and Z. Qian, "Experimental research on water inrush in tunnel construction," *Natural Hazards*, vol. 81, no. 1, pp. 467–480, 2016.
- [3] T. T. Zhu and D. Huang, "Experimental investigation of the shear mechanical behavior of sandstone under unloading normal stress," *International Journal of Rock Mechanics and Mining Sciences*, vol. 114, pp. 186–194, 2019.
- [4] Y. Bai, R. Shan, Y. Ju, Y. Wu, P. Sun, and Z. Wang, "Study on the mechanical properties and damage constitutive model of frozen weakly cemented red sandstone," *Cold Regions Science and Technology*, vol. 171, article 102980, 2020.
- [5] S. Li, Z. Zhou, L. Li, Z. Xu, Q. Zhang, and S. Shi, "Risk assessment of water inrush in karst tunnels based on attribute synthetic evaluation system," *Tunnelling and Underground Space Technology*, vol. 38, pp. 50–58, 2013.
- [6] Q. Zhu, Q. Miao, and S. Jiang, "On karst water inrush (gushing) geological environment in Pingyang tunnel," *Applied Mechanics and Materials*, vol. 580–583, pp. 1008–1012, 2014.
- [7] S. Wang, L. P. Li, S. Cheng, H. J. Hu, M. G. Zhang, and T. Wen, "Risk assessment of water inrush in tunnels based on attribute interval recognition theory," *Journal of Central South University*, vol. 27, no. 2, pp. 517–530, 2020.
- [8] X. Li and Y. Li, "Research on risk assessment system for water inrush in the karst tunnel construction based on GIS: case study on the diversion tunnel groups of the Jinping II Hydro-power Station," *Tunnelling and Underground Space Technology*, vol. 40, pp. 182–191, 2014.
- [9] D. D. Pan, S. C. Li, Z. H. Xu, P. Lin, and X. Huang, "Experimental and numerical study of the water inrush mechanisms of underground tunnels due to the proximity of a water-filled karst cavern," *Bulletin of Engineering Geology and the Environment*, vol. 78, no. 8, pp. 6207–6219, 2019.
- [10] J. Q. Guo, Y. Qian, J. X. Chen, and F. Chen, "The minimum safe thickness and catastrophe process for water inrush of a karst tunnel face with multi fractures," *Processes*, vol. 7, no. 10, p. 686, 2019.
- [11] B. Zhang and Z. Lin, "A computing method for sand inrush quantity through a borehole in Longde coal mine," *Advances in Civil Engineering*, vol. 2018, Article ID 4842939, 11 pages, 2018.
- [12] Z. H. Xu, J. Wu, S. C. Li, B. Zhang, and X. Huang, "Semianalytical solution to determine minimum safety thickness of rock resisting water inrush from filling-type karst caves," *International Journal of Geomechanics*, vol. 18, no. 2, article 04017152, 2018.
- [13] H. M. Jiang, L. Li, X. L. Rong, M. Y. Wang, Y. P. Xia, and Z. C. Zhang, "Model test to investigate waterproof-resistant slab minimum safety thickness for water inrush geohazards," *Tunnelling and Underground Space Technology*, vol. 62, pp. 35–42, 2017.
- [14] Z. H. Yang and J. H. Zhang, "Minimum safe thickness of rock plug in karst tunnel according to upper bound theorem," *Journal of Central South University*, vol. 23, no. 9, pp. 2346–2353, 2016.
- [15] F. Zhao, Q. Sun, and W. Zhang, "Combined effects of salts and wetting-drying cycles on granite weathering," in *Bulletin of Engineering Geology and the Environment*, 2020.

- [16] W. Liu and Z. H. Zhang, "Experimental characterization and quantitative evaluation of slaking for strongly weathered mudstone under cyclic wetting-drying condition," *Arabian Journal of Geosciences*, vol. 13, no. 2, 2020.
- [17] Y. J. Qi, T. Li, R. H. Zhang, and Y. Chen, "Interannual relationship between intensity of rainfall intraseasonal oscillation and summer-mean rainfall over Yangtze River basin in eastern China," *Climate Dynamics*, vol. 53, no. 5-6, pp. 3089–3108, 2019.
- [18] S. Phakula, W. A. Landman, and A. F. Beraki, "Forecasting seasonal rainfall characteristics and onset months over South Africa," *International Journal of Climatology*, vol. 38, pp. E889–E900, 2018.
- [19] E. Kim and H. Changani, "Effect of water saturation and loading rate on the mechanical properties of red and buff sandstones," *International Journal of Rock Mechanics and Mining Sciences*, vol. 88, pp. 23–28, 2016.
- [20] Q. Yin, G. Ma, H. Jing et al., "Hydraulic properties of 3d rough-walled fractures during shearing: an experimental study," *Journal of Hydrology*, vol. 555, pp. 169–184, 2017.
- [21] Y. Ju, Q. G. Zhang, Y. M. Yang, H. P. Xie, F. Gao, and H. J. Wang, "An experimental investigation on the mechanism of fluid flow through single rough fracture of rock," *Science China–Technological Sciences*, vol. 56, no. 8, pp. 2070–2080, 2013.
- [22] P. Sumner and M. J. Loubser, "Experimental sandstone weathering using different wetting and drying moisture amplitudes," *Earth Surface Processes and Landforms*, vol. 33, no. 6, pp. 985–990, 2008.
- [23] Z. Zhou, X. Cai, D. Ma, L. Chen, S. Wang, and L. Tan, "Dynamic tensile properties of sandstone subjected to wetting and drying cycles," *Construction and Building Materials*, vol. 182, pp. 215–232, 2018.
- [24] Q. Sun and Y. L. Zhang, "Combined effects of salt, cyclic wetting and drying cycles on the physical and mechanical properties of sandstone," *Engineering Geology*, vol. 248, pp. 70–79, 2019.
- [25] R. Doostmohammadi, M. Moosavi, T. Mutschler, and C. Osan, "Influence of cyclic wetting and drying on swelling behavior of mudstone in south west of Iran," *Environmental Geology*, vol. 58, no. 5, pp. 999–1009, 2008.
- [26] M. Vergara and T. Triantafyllidis, "Swelling behavior of volcanic rocks under cyclic wetting and drying," *International Journal of Rock Mechanics and Mining Sciences*, vol. 80, pp. 231–240, 2015.
- [27] A. Ozbek, "Investigation of the effects of wetting–drying and freezing–thawing cycles on some physical and mechanical properties of selected ignimbrites," *Bulletin of Engineering Geology and the Environment*, vol. 73, no. 2, pp. 595–609, 2014.
- [28] L. Wang, M. Bornert, E. Heripre, D. Yang, and S. Chanchole, "Irreversible deformation and damage in argillaceous rocks induced by wetting/drying," *Journal of Applied Geophysics*, vol. 107, pp. 108–118, 2014.
- [29] Z. Zhou, X. Cai, L. Chen, W. Cao, Y. Zhao, and C. Xiong, "Influence of cyclic wetting and drying on physical and dynamic compressive properties of sandstone," *Engineering Geology*, vol. 220, pp. 1–12, 2017.
- [30] Z. Qin, X. Chen, and H. Fu, "Damage features of altered rock subjected to drying-wetting cycles," *Advances in Civil Engineering*, vol. 2018, Article ID 5170832, 10 pages, 2018.
- [31] Y. Zhao, S. Ren, D. Jiang, R. Liu, J. Wu, and X. Jiang, "Influence of wetting-drying cycles on the pore structure and mechanical properties of mudstone from Simian Mountain," *Construction and Building Materials*, vol. 191, pp. 923–931, 2018.
- [32] People's Republic of China National Standard, *Engineering rock test method standard (GB/T 50266–2013)*, China Planning Publishing House, Beijing, 2013.
- [33] L. Liu, Z. Li, X. Liu, and Y. Liu, "Frost front research of a cold-region tunnel considering ventilation based on a physical model test," *Tunneling and Underground Space Technology*, vol. 77, pp. 261–279, 2018.
- [34] Q. Tian, J. Zhang, and Y. Zhang, "Similar simulation experiment of expressway tunnel in karst area," *Construction and Building Materials*, vol. 176, pp. 1–13, 2018.

Research Article

Visualization of Gas Diffusion-Sorption in Coal: A Study Based on Synchrotron Radiation Nano-CT

Yingfeng Sun ^{1,2,3,4}, Yixin Zhao ^{1,2,3}, Hongwei Zhang ^{1,2,3} and Cun Zhang ^{1,2,3}

¹Beijing Key Laboratory for Precise Mining of Intergrown Energy and Resources, China University of Mining and Technology (Beijing), Beijing 100083, China

²State Key Laboratory of Coal and CBM Co-mining, Jincheng Anthracite Mining Group, Jincheng 048204, China

³School of Energy and Mining Engineering, China University of Mining and Technology (Beijing), Beijing 100083, China

⁴School of Emergency Management and Safety Engineering, China University of Mining and Technology (Beijing), Beijing 100083, China

Correspondence should be addressed to Yixin Zhao; zhaoyx@cumtb.edu.cn

Received 30 May 2020; Revised 10 June 2020; Accepted 12 June 2020; Published 2 July 2020

Academic Editor: Qian Yin

Copyright © 2020 Yingfeng Sun et al. This is an open access article distributed under the Creative Commons Attribution License, which permits unrestricted use, distribution, and reproduction in any medium, provided the original work is properly cited.

Gas diffusion-sorption is a critical step in coalbed methane (CBM) exploitation and carbon dioxide sequestration. Because of the particularity of gas physical properties, it is difficult to visualize the gas diffusion-sorption process in coal by experimental methods. Due to the limitation of experimental approaches to image the three-dimensional coal pore structure, it is impossible to obtain the three-dimensional pore structure images of coal. As a result, the visualization of gas diffusion-sorption in coal pore structure by numerical ways is impossible. In this study, gas diffusion coefficients were firstly estimated by experiments. Then, a gas diffusion-sorption coupled model was developed which can be applied to the nanoscale geometry imaged by synchrotron radiation nano-CT. The dynamic process of gas diffusion and ad-/desorption in the nanoscale microstructure of coal was visualized by the developed gas diffusion-adsorption coupled model and the numerical simulation based on MATLAB. The simulation results show a good agreement with the experimental results. The gas diffusion-sorption coupled model and numerical method can help to investigate the effect of microstructure on gas diffusion and ad-/desorption and provides a possibility to investigate the multiscale gas transportation and adsorption in coal pore-fracture system.

1. Introduction

Coal, as a porous medium, exhibits high gas adsorption affinity [1]. As a result, coal is not only a methane reservoir but also can be considered as a potential place for carbon dioxide storage [2, 3]. The recoverable coalbed methane (CBM) is between 500 and 3000×10^{12} scf (14.2 to 84.9×10^{12} m³) in the world [4]. Carbon dioxide storage capabilities in deep coal seam are nearly 150 Gt in the world [5]. During coalbed methane (CBM) production, the gas needs to diffuse through the coal matrix and finally flows to the producing well [6–8]. When carbon dioxide sequestration is considered, carbon dioxide is physically adsorbed on the pore surface of coal through a reverse process [9]. Therefore, gas diffusion is an indispensable step in both CBM production and carbon dioxide sequestration. A significant amount of researches

has been conducted to study gas diffusion behavior in coal by experimental and numerical methods. Experimental research is focused on the factors that affect gas diffusion behavior, such as particle size [10], temperature [11], and gas pressure [12, 13]. Numerical methods are mainly used to calculate the gas diffusion coefficient by the bidisperse diffusion model [14]. Currently, widely implemented methods for diffusion coefficient calculation are the unipore model assuming a uniform pore size distribution [15, 16] and bidisperse model assuming bimodal pore size distribution [17]. Compared to bidisperse model, the unipore model is much easier in mathematical calculations. Some researchers found that the unipore model is sufficient to model the experimental data [11, 18–20], while other researchers found that bidisperse model is needed to achieve satisfactory accuracy [21–24].

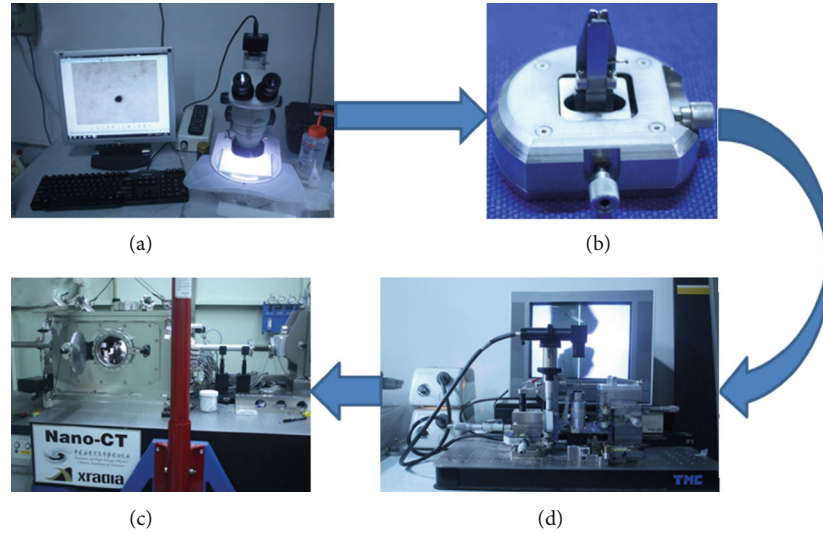


FIGURE 1: Photographs of the instruments for synchrotron radiation nano-CT imaging. (a) Instruments for placing the sample particle on the tip of a pin. (b) Sample turntable for clipping the pin. (c) Transmission X-ray microscopy (TXM) instrument. (d) Instruments for mounting gold particle on the sample.

Among the factors of reparticle size, temperature, and pressure that affect gas diffusion behavior, pressure attracts relatively more attention. Because the gas pressure in coal matrix is continuously changing during gas production and carbon dioxide sequestration [13]. As for the relationship between gas diffusivity and gas pressure, there are two opposite results in prior studies. One conclusion is that diffusivity increased with the increase of pressure [25], while other results show that diffusivity drops with increasing pressure [13].

Previous researches on gas diffusion behavior can only provide macro (statistical) diffusion characteristics, such as diffusion coefficient, and are incapable of providing the real-time gas distribution in coal three-dimensional microstructure which is caused by the limitations of pore structure imaging approaches, especially in nanoscale [26–28]. In this paper, the synchrotron-based nano-CT at the Beijing Synchrotron Radiation Facility (BSRF) is applied to obtain the image of coal microstructure. Benefiting from a monochromatic beam and high X-ray coherency, synchrotron-based nano-CT can achieve nanometer-scale resolution with very good data quality [29].

In this study, methane and carbon dioxide diffusion coefficients during the adsorption and desorption process were measured and comprehensively analyzed. Based on an experimental study, a gas diffusion-sorption coupled model was developed. Finally, real-time gas diffusion-sorption process in coal was visualized by the combination of nanoscale microstructure and the coupled model of gas diffusion-sorption.

2. Experimental

2.1. Sample. Coal samples were collected from Xinzhouyao coal mine and Tangshan coal mine and were named as sam-

ple XZY and sample TS in the following sections of this paper. Because the true density of coal samples will be used in the following numerical study, the true density was measured. The true density of two samples is 1.3502 g/cm^3 (sample XZY) and 1.5355 g/cm^3 (sample TS), respectively.

For synchrotron radiation nano-CT imaging, the first step is to pulverize the coal samples, and then the particle with size close to $10 \mu\text{m}$ was selected and placed on the tip of a pin by the instruments shown in Figure 1(a). Figure 1(b) shows the turntable with the pin. Using the instruments shown in Figure 1(c), the gold particle was placed on the sample to facilitate the images alignment.

For gas diffusivity test, in order to eliminate the cracks and macropores, which have impacts on the test results, the coal sample size is 60–80 mesh ($180\text{--}250 \mu\text{m}$). Prior to tests, samples were degassed for 24 h at 303 K.

2.2. 3D Nanoscale Microstructure of Coal. The 3D nanoscale microstructure of coal was imaged by the synchrotron radiation nano-CT at BSRF. For more details about the nano-CT and imaging method, refer to the paper [29]. Before numerical investigation, the nano-CT images were processed in the following three steps: region of interest (ROI) selection, noise filtration [30], and images segmentation [31]. For more details about the nano-CT images processing, refer to the paper [32]. Figure 2 shows the flowchart of the images processing, and the processed synchrotron radiation nano-CT images were used for subsequent numerical investigation.

2.3. Gas Diffusivity Setup. Diffusion coefficient tests are similar to sorption isotherm measurements both in setup and experimental procedures. In diffusion measurements, the time of adsorption and desorption is recorded [13]. The gas diffusivity tests were completed by H-Sorb 2600 adsorption analyzer (Gold APP Instruments Corporation, China). For

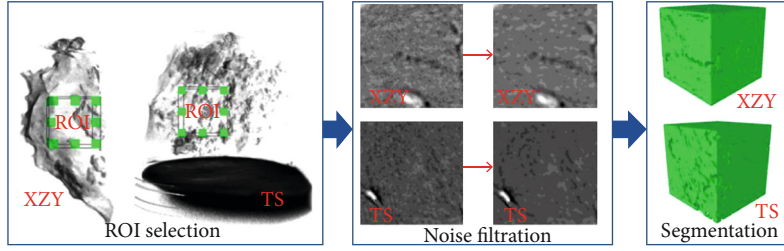


FIGURE 2: Flowchart of synchrotron radiation nano-CT images processing. ROI size is $200 \times 200 \times 200$ voxels. Voxel size is $0.01459 \times 0.01459 \times 0.01459 \mu\text{m}$. XZY represents sample from Xinzhouyao coal mine, and TS represents sample from Tangshan coal mine.

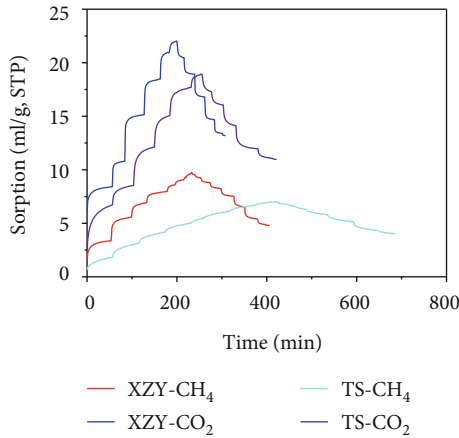


FIGURE 3: Gas sorption amount variation with time during the adsorption and desorption period.

more details about H-Sorb 2600 adsorption analyzer, refer to Sun et al. [33]. The gas pressure is up to 8 MPa for methane and is up to 5 MPa for carbon dioxide in diffusivity tests at the temperature 303 K. Figure 3 shows the test procedure. It can be found from Figure 3 that there are more significant leaps of the amount of adsorbed CO_2 at the initial stage of each pressure level than that of CH_4 . There are also more significant leaps in sample XZY than that in sample TS. It is because of the difference in gas diffusivity characteristics discussed in the following section. The experimental and Langmuir isotherms are shown in Figure 4, and the Langmuir parameters are listed in Table 1.

2.4. Estimation of Diffusion Coefficients and Discussion.

According to the prior studies, there are two widely-used models to estimate the diffusion coefficient of coal, unipore model, and bidisperse model [5]. Compared to the bidisperse model, the unipore model is relatively simple in the mathematical calculation [12]. The unipore model was used to estimate the gas diffusion coefficient in this study.

According to Fick's second law,

$$\frac{M_t}{M_\infty} = 1 - \frac{6}{\pi^2} \sum_{n=1}^{\infty} \frac{1}{n^2} \exp \left[-\frac{Dn^2\pi^2 t}{r_p^2} \right] \quad (1)$$

For the convenience of calculation, equation (1) can also be written as,

$$\frac{V_t}{V_\infty} = 1 - \frac{6}{\pi^2} \sum_{n=1}^{\infty} \frac{1}{n^2} \exp \left[-\frac{Dn^2\pi^2 t}{r_p^2} \right] \quad (2)$$

According to equation (2) [34], the diffusion coefficients of CH_4 and CO_2 were calculated, as shown in Figures 5(a)–5(d).

It can be found in Figure 5 that the diffusion coefficients are in the range of 10^{-13} to $10^{-11} \text{m}^2/\text{s}$, which is at the same magnitude as the results obtained by other researchers [11].

According to the results by other researchers, there is a positive relationship between gas diffusion coefficient and adsorbed gas volume [12]. The gas diffusion coefficient in sample XZY is higher than that in sample TS (Figure 5), which can be explained by the difference in the gas adsorption capacity. In this work, the gas adsorption capacity was quantified by the adsorbed gas amount on unit pore surface area, which can be obtained from the ad-/desorption isotherms in Figure 4, when the pore surface area of unit mass was obtained. The pore surface area in unit mass was calculated by the following equation (3).

$$F = \frac{f}{N_{\text{solid}} V_{\text{voxel}} \rho_{\text{true}}} \quad (3)$$

The ratio of pore surface area of two samples was estimated,

$$\frac{F_{\text{XZY}}}{F_{\text{TS}}} = \frac{f_{\text{XZY}}}{f_{\text{TS}}} \cdot \frac{N_{\text{solid,TS}}}{N_{\text{solid,XZY}}} \cdot \frac{\rho_{\text{true,TS}}}{\rho_{\text{true,XZY}}} = 0.7809 < 1 \quad (4)$$

As shown in equation (4), the pore surface area in unit mass of sample XZY is less than that of sample TS, while the adsorbed gas amount on unit mass in sample XZY is higher, as shown in Figure 4, which indicates that the gas adsorption capacity of sample XZY is higher. It verifies that there is a positive relationship between the gas diffusion coefficient and adsorbed gas volume.

During the adsorption period, CH_4 diffusion coefficient peaks at the inflection-point pressure of adsorption isotherm (7.15 MPa for sample XZY and 5.12 MPa for sample TS) where capillary condensation begins (Figures 4(a), 4(b), and 5(a)). When capillary condensation begins, the gas

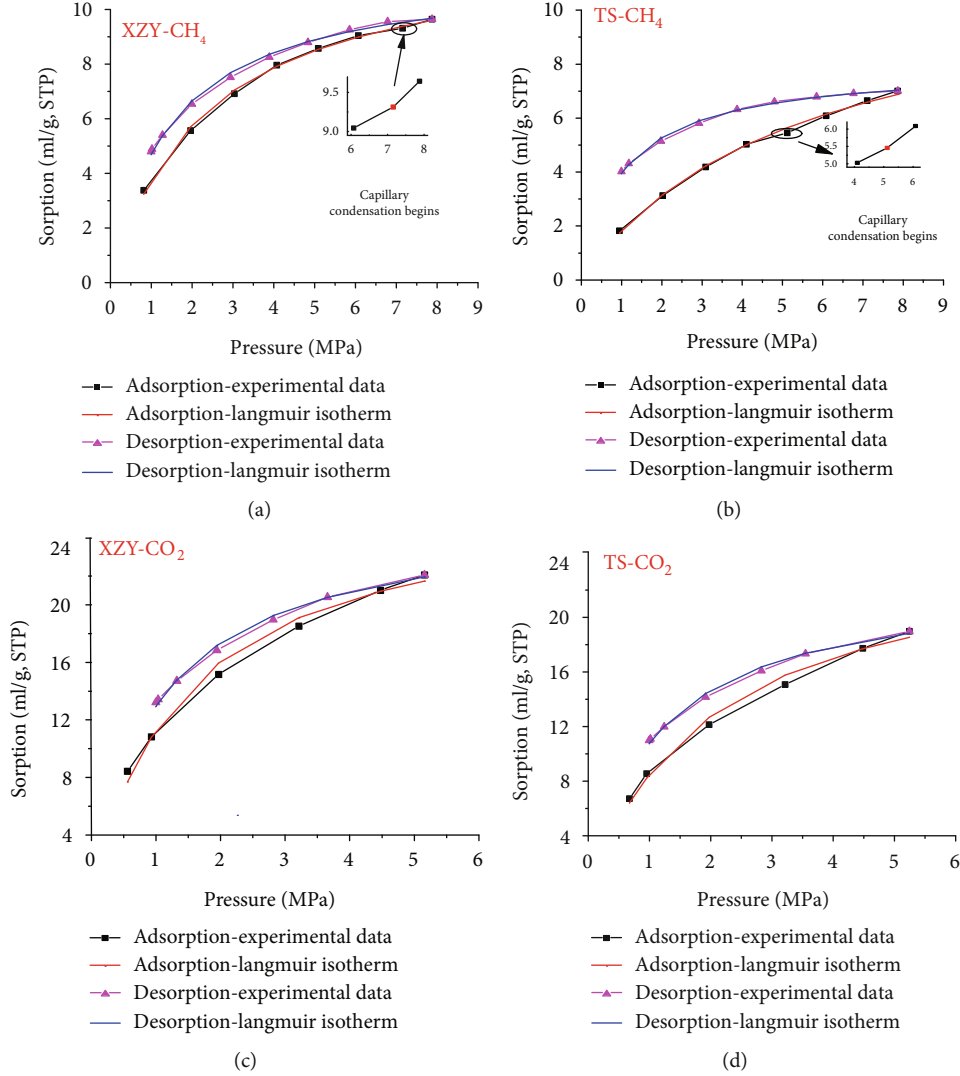


FIGURE 4: Experimental and Langmuir isotherms for adsorption and desorption of two coal samples.

TABLE 1: Langmuir constants.

Gas	Adsorption				Desorption			
	XZY		TS		XZY		TS	
	V_L (ml/g)	P_L (MPa)	V_L (ml/g)	P_L (MPa)	V_L (ml/g)	P_L (MPa)	V_L (ml/g)	P_L (MPa)
CH ₄	12.41	2.31	11.55	5.35	11.45	1.44	7.94	1.01
CO ₂	27.80	1.46	25.71	2.03	26.36	1.04	22.87	1.12

adsorption rate significantly increases. According to the positive correlation between gas diffusion coefficients and adsorbed gas volume [12], the increase of gas adsorption rate facilitates gas diffusion. Because there is no capillary condensation in CO₂ diffusion tests, which may be caused by the smaller test gas pressure range in CO₂ diffusion tests, CO₂ diffusion coefficients calculated from the adsorption stage are relatively constant although there is a fluctuation with gas pressure (Figure 5(c)). The reasons why the diffusion coefficient is relatively constant during the adsorption period

except at the gas pressure where capillary condensation begins needs further research.

During the desorption period, as shown in Figures 5(b) and 5(d), there is a U-shape relationship between gas pressure and diffusion coefficients. At the low-pressure regime, the amount of adsorbed gas is small and the effect of adsorbed gas is small. According to the Lennard–Jones fluid model (Figure 6(a)) [35], there is a negative relationship between gas diffusion coefficient and gas pressure (Figures 5(b) and 5(d)). Subsequently, with the increase of

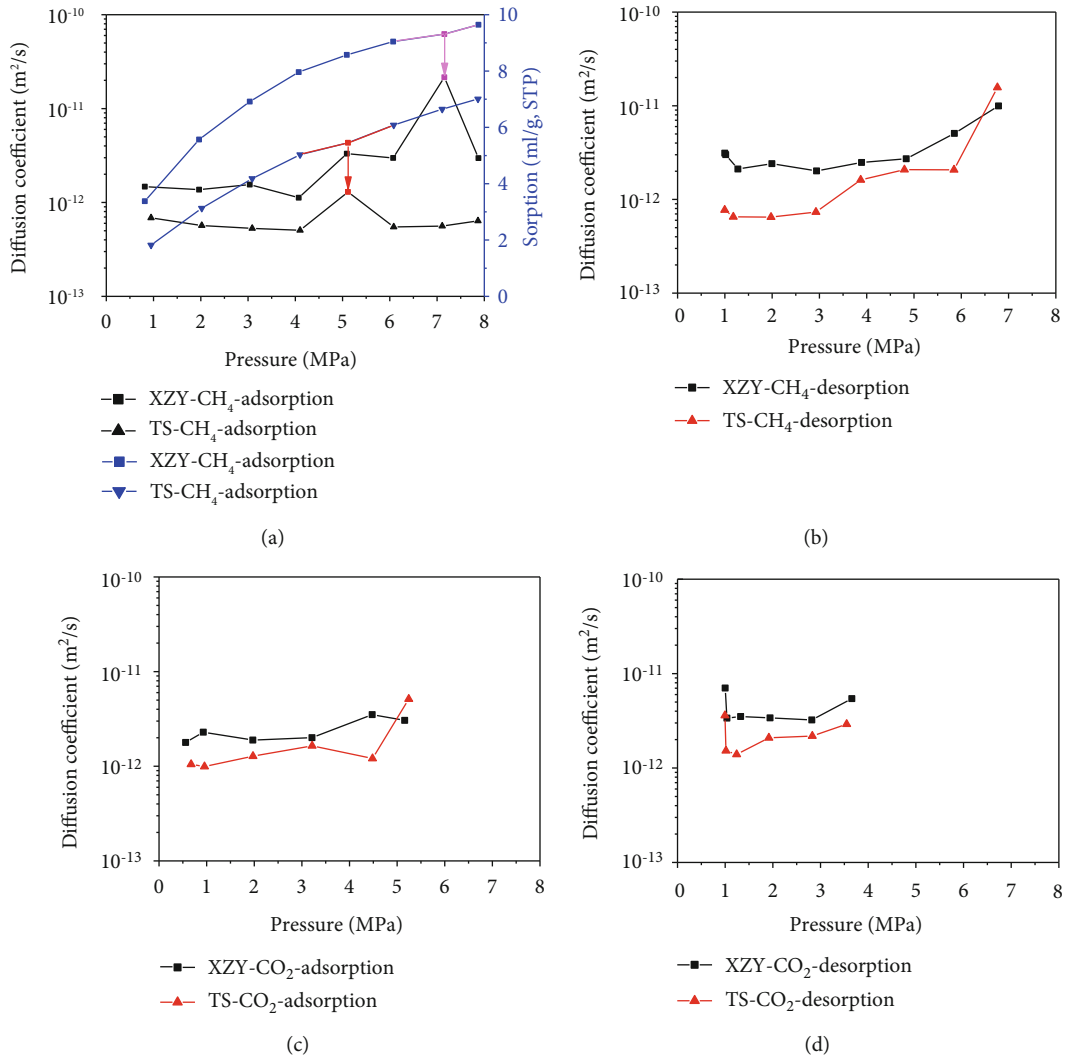


FIGURE 5: Gas diffusion coefficient variation with gas pressure.

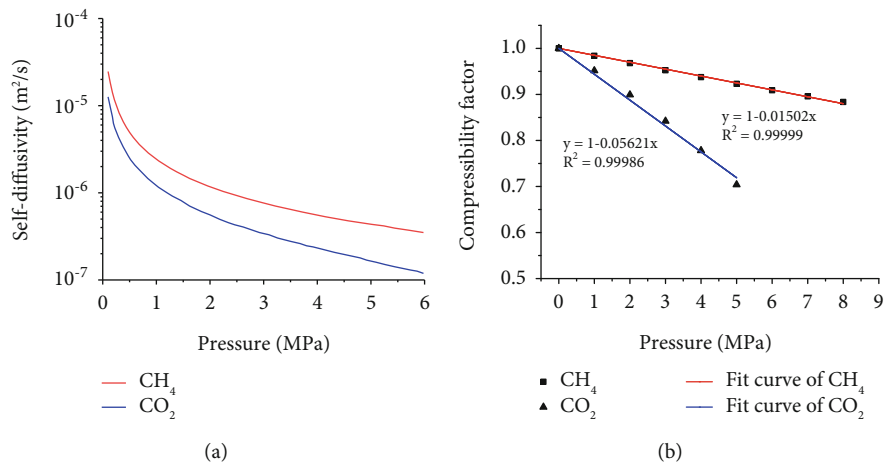


FIGURE 6: Pressure-related parameters of gas. (a) The relationship between self-diffusivities and pressure [35]. (b) The relationship between compressibility factor and pressure.

gas pressure, the impact of adsorbed gas becomes stronger, which causes the positive relationship between diffusion coefficient and gas pressure (Figures 5(b) and 5(d)) [13]. The different laws presented in adsorption and desorption needs further investigation.

Moreover, it can be found that CO₂ diffusivity is consistently higher than that of CH₄, which has also been found by some other researchers [12], because the kinetic diameter of carbon dioxide is smaller (CO₂: 0.33 nm; CH₄: 0.38 nm) [10].

3. Visualization of Gas Diffusion-Sorption

3.1. Coupled Model of Gas Diffusion-Sorption. In current researches on gas transport behavior in coal, insufficient attentions have been paid to the visualization of dynamic gas diffusion-sorption process in the real geometrical morphology of coal microstructure. In this work, gas diffusion-sorption visualization in the real coal microstructure was achieved by the combination of high-resolution images of coal microstructure and the coupled model of gas diffusion and adsorption.

According to the continuum equation,

$$\frac{\partial C}{\partial t} + \nabla J = S \quad (5)$$

Gas flow in the coal matrix can be described by the Fick's first law [36],

$$J = -D\nabla C \quad (6)$$

Substituting the equation (6) to the equation (5), Fick's second law containing the source term S is derived,

$$\frac{\partial C}{\partial t} - D\Delta C = S \quad (7)$$

$$S = -\frac{\partial C_{ad}}{\partial t}$$

C_{ad} can be formulated as equation (8),

$$C_{ad} = \frac{n_{ad}}{V_e} = \frac{sv/V_m}{V_e} = \frac{sv}{V_e V_m} \quad (8)$$

Because the internal pore surface is the place where gas adsorbs, the identification equation of the internal pore surface was built,

$$\left\{ \begin{array}{l} g(x, y, z) - g(x + 1, y, z) = -1, \text{ or} \\ g(x, y, z) - g(x, y + 1, z) = -1, \text{ or} \\ g(x, y, z) - g(x, y, z + 1) = -1, \text{ or} \\ g(x - 1, y, z) - g(x, y, z) = 1, \text{ or} \\ g(x, y - 1, z) - g(x, y, z) = 1, \text{ or} \\ g(x, y, z - 1) - g(x, y, z) = 1 \end{array} \right. \quad (9)$$

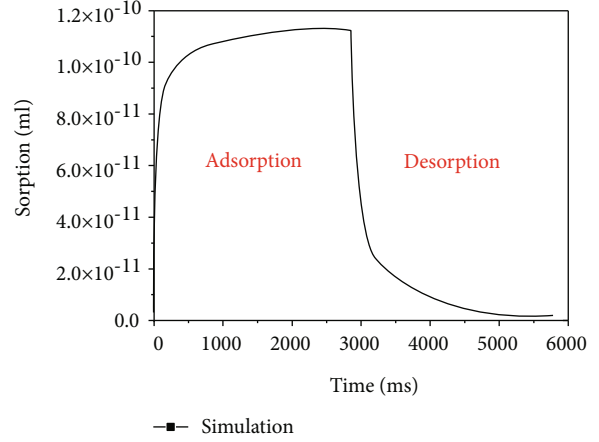


FIGURE 7: Variation of the gas sorption amount with time in numerical simulation.

In this study, the grey value of solid and pore is 0 and 1, respectively.

The amount of adsorbed gas on unit pore surface area can be estimated by equation (10).

$$v = \frac{V}{F} \quad (10)$$

Gas adsorption here follows Langmuir isotherm model by equation (11) [37],

$$V = \frac{PV_L}{P + P_L} \quad (11)$$

Figure 4 shows the Langmuir isotherms, and the Langmuir parameters are listed in Table 1.

The coupled model of gas diffusion and sorption is developed as,

$$\frac{\partial C}{\partial t} - D\Delta C = -\frac{\partial}{\partial t} \left[\frac{sPV_L}{1000V_m FV_e(P + P_L)} \right] \quad (12)$$

The gas state equation is,

$$C = \frac{n}{V} = \frac{P}{ZRT} \quad (13)$$

$$Z = f(T, P)$$

Figure 6(b) shows the gas compressibility factor [38]. Now, equation (14) can be written as,

$$\frac{\partial P}{\partial t} - D\Delta P = -ZRT \frac{\partial}{\partial t} \left[\frac{sPV_L}{1000V_m FV_e(P + P_L)} \right] \quad (14)$$

The visualization of gas diffusion-sorption in coal can be achieved by solving equation (14).

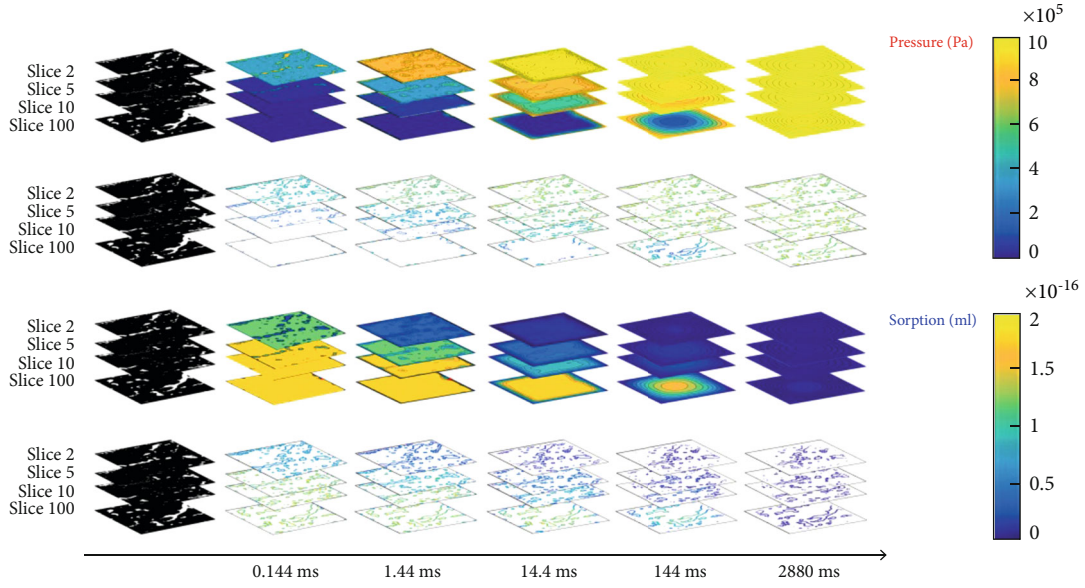


FIGURE 8: The gas pressure and adsorbed gas distribution during the process of adsorption and desorption.

3.2. Parameters Determination. In the simulation, the equilibrium pressure is 1 MPa. A cube from sample XZY was used as the simulation geometry. The size of the cube is $200 \times 200 \times 200$ voxels, and the voxel size is $0.01459 \times 0.01459 \times 0.01459 \mu\text{m}$ (Figure 2). Adsorption and desorption stage were both investigated in numerical study. At the stage of adsorption and desorption, the pressure on the simulation geometry surface is 1 MPa and 0 MPa, respectively.

Gas diffusion in coal is mainly impacted by pore structure, matrix, gas molecular, and the characteristics of sorption [12]. Gas transport mechanism in pores can be determined by Knudsen number described by equation (15) [39].

$$K_n = \frac{\lambda}{D_p} \quad (15)$$

$$\lambda = \frac{k_B T}{\sqrt{2\pi} \delta^2 P} \quad (16)$$

Gas transport can be divided into different flow patterns by Knudsen number, and for each flow regime, gas transport follows different control equations [40].

As the methane pressure is equal to 1 MPa, the Knudsen number in sample XZY is calculated to be 0.07. Moreover, as shown in Figure 5(a), at the low-pressure regime, the trend of CH_4 diffusion coefficients complies with Lennard–Jones fluid model (Figure 6(a)) [35], which indicates the gas diffusion can be approximately treated as bulk diffusion. Therefore, in the simulations, the value from Lennard–Jones model (Figure 6(a)) was set as the diffusion coefficient in pores.

The pore radius from the synchrotron-based nano-CT in this study is in the range of 9–279 nm. According to the prior test results by NMR cryoporometry, the pore volume of pores with radius in the range of 0.84–9 nm account for 43% of the

total pore volume in the range of 0.84–250 nm [41]. Coal matrix and pores out of nano-CT detection coverage account for the majority of the coal. Therefore, the gas diffusion coefficient in matrix was from the value measured in experimental study (Figure 5). Through pores range (9–288 nm) detected in this paper do not cover the entire pore size range, gas adsorbed on these pores surfaces can proportionally reflect the dynamic process of adsorbed gas distribution and the gas pressure distribution in this simulation can relatively accurately reflect the free gas distribution in real situation.

3.3. Numerical Simulation Results and Discussion. Figure 7 shows the total amount of adsorbed gas varies with time during the adsorption and desorption period. It can be found that adsorption and desorption rate is significantly faster at the initial stage of adsorption and desorption, and the amount of adsorbed gas becomes steady eventually after a certain time, which is the same as the experimental data in Figure 3. There is a contradiction between resolution and sample size in CT imaging, and the sample size needs to be small enough to meet the resolution requirements. In the synchrotron radiation nano-CT imaging, the sample size is less than $10 \mu\text{m}$, while the sample mass needs to achieve a certain amount to ensure the accuracy of experimental measurement in gas ad-/desorption. Therefore, the geometric scale of experiments and simulations is not at the same scale. Moreover, there is the diffusion in the space between the coal particles in experiments. As a result, it is not comparable between the experimental and numerical results in the sorption-time coordinate system. In the future, the numerical method for investigating the gas diffusion-sorption considering the effect of scale and the diffusion in the space between the coal particles should be studied.

In Figure 8, the dynamic process of gas diffusion-sorption during the adsorption process is visualized in the rows 1 and

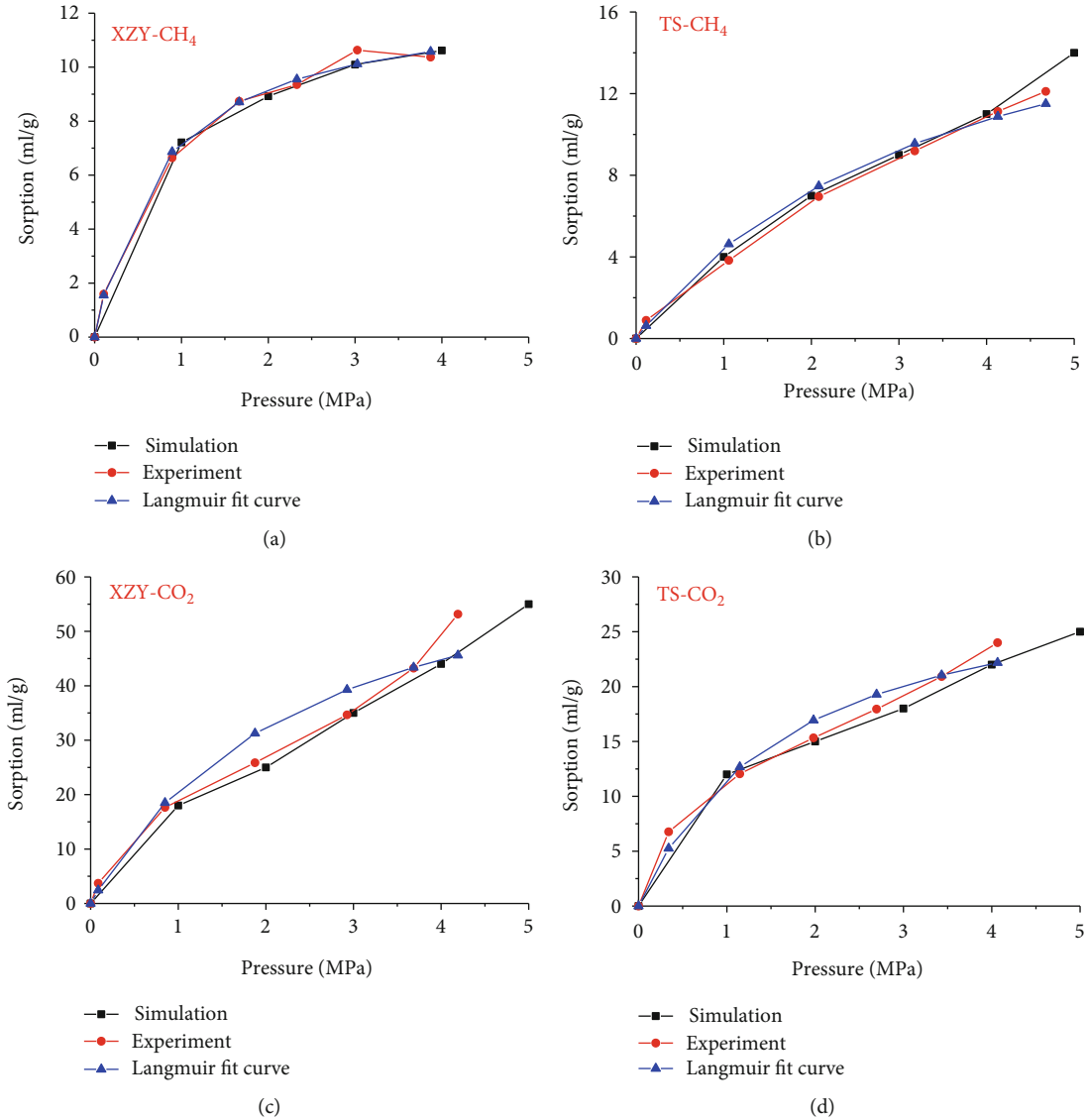


FIGURE 9: The comparison between simulation and experiment results.

2, and the dynamic process of gas diffusion-sorption during the process of desorption is visualized in the rows 3 and 4. The nano-CT image slices were numbered 1-200 from top to bottom. The first column is the slices numbered 2, 5, 10, and 100. The dynamic gas pressure evolution over time is presented in rows 1 and 3. The dynamic adsorbed gas evolution over time is presented in rows 2 and 4. It can be found that gas diffusion dominates the gas adsorption. When gas diffuses to a pore, there can be gas adsorption on the surface of the pore. Moreover, gas pressure determines the amount of gas adsorbed and the amount of adsorbed gas is higher when the gas pressure is higher.

Because of the particularity of gas physical properties, it is difficult to visualize the gas diffusion-sorption process in coal by experimental methods. Due to the limitation of previous means to characterize coal pore structure, it is impossible to obtain the three-dimensional pore structure images of coal. As a result, it is not possible to realize the visualization of

gas diffusion-sorption process based on the real three-dimensional microstructure by numerical means. In the previous study of gas transportation in coal by numerical method, only one parameter (porosity) was given to characterize the effect of pore structure on gas transportation in coal [42, 43], which cannot precisely investigate the influence of pore structure on gas transportation, because the size and spatial distribution of pore structure was not considered. In this study, based on the nanoscale microstructure, the simulation visualizes the dynamic process of gas diffusion-sorption in coal microstructure and obtains the variation of total adsorbed gas amount with time. Besides, various numerical methods have been developed to generate porous media [44–46]. The coupled model of gas diffusion and sorption and the numerical method for simulating gas diffusion and sorption in 3D porous media, which are developed in this paper, provides an option for further researches on the impact of microstructure on the gas diffusion and sorption.

Although there is adsorption-swelling effect [47], this study intends to develop the method to visualize gas diffusion and sorption in coal, so the adsorption-swelling effect was not investigated, but the improved model will be developed in the future.

Although it is not comparable between the experimental and numerical results in the adsorption-time coordinate system as mentioned above, it is comparable between the experimental and numerical results in the adsorption isotherm, because the effect of scale and the diffusion in the space between the coal particles is ignorable when the adsorption reaches equilibrium. In order to validate the numerical method to visualize the dynamic process of gas diffusion and ad-/desorption in coal microstructure, the adsorption isotherms from numerical simulations are compared with the experimental results. As shown in Figure 9, adsorption isotherms from numerical simulations are consistent with the experimental results, which validate the numerical method. The application of nano-CT and the coupled model of gas diffusion and adsorption developed in this paper make it possible to investigate the dynamic process of pressure distribution and adsorbed gas distribution during the adsorption and desorption period. Moreover, the pore-scale model in this study can be combined with the fracture-scale models, such as discrete fracture model (DFM) [48], to investigate the multiscale gas transportation and adsorption in coal reservoir.

4. Conclusions

Visualization of gas diffusion-sorption in coal is very important for investigating the impact of pore structure on gas diffusion-sorption and multiscale gas transportation and adsorption in coal pore-fracture system. In this study, based on the nanoscale images of coal pore structure, the dynamic process of gas diffusion-sorption in coal was visualized. Before the visualization of gas diffusion-sorption in coal, methane and carbon dioxide diffusion coefficients during the adsorption and desorption processes in two coal samples were tested and comprehensively analyzed. Coal with higher gas adsorption capacity presents higher diffusivity. The smaller kinetic diameter of CO_2 causes the diffusivity of CO_2 is higher than that of CH_4 . During the adsorption process, gas diffusion coefficient peaks at the gas pressure where capillary condensation begins. There is a U-shape relationship between gas diffusion coefficient and gas pressure during the desorption process. In order to investigate the dynamic process of gas diffusion and ad-/desorption in coal, a gas diffusion-sorption coupled model was developed. Based on the nanoscale microstructure, the dynamic process of gas diffusion and ad-/desorption in coal nanoscale microstructure was visualized. The numerical simulation results show a good agreement with the experimental results. The gas diffusion-adsorption coupled model and numerical method can help to investigate the influence of microstructure on gas diffusion and ad-/desorption and provides a possibility to investigate the multiscale gas transportation and adsorption in coal pore-fracture system.

Nomenclature

M_t :	Total desorbed gas mass in time t (g)
M_∞ :	Total desorbed gas mass in infinite time (g)
D :	Diffusion coefficient (m^2/s)
r_p :	Diffusion path length (m)
V_t :	Total volume of gas ad/de-sorbed in time t (ml)
V_∞ :	volume of gas ad/de-sorbed in infinite time (ml)
f :	Total pore surface area in ROI (m^2)
N_{solid} :	Total number of solid voxel in ROI
V_{voxel} :	Volume of per voxel (m^3)
ρ_{true} :	True density (g/cm^3)
X :	Coal sample collected from Xinzhouyao coal mine
TS :	Coal sample collected from Tangshan coal mine
C :	Gas concentration (mol/m^3)
J :	Diffusion flux ($\text{mol}/(\text{m}^2 \cdot \text{s})$)
S :	Source term ($\text{mol}/(\text{m}^3 \cdot \text{s})$)
C_{ad} :	Gas concentration impacted by gas adsorption (mol/m^3)
n_{ad} :	Amount of adsorbed gas (mol)
V_e :	Volume of mesh element in numerical calculation (m^3)
s :	Pore surface area in the element (m^2)
v :	Adsorbed gas amount on unit pore surface area (ml/m^2)
V_m :	Molar volume of gas ($22.4\text{L}/\text{mol}$, STP)
$g(x, y, z)$:	The grey value in the location (x, y, z)
V :	Volume of gas adsorbed on unit mass of coal (ml/g)
F :	Pore surface area in unit mass of coal (m^2/g)
P :	Gas pressure (Pa)
V_L :	Langmuir volume (ml/g)
P_L :	Langmuir pressure (MPa)
Z :	Gas compressibility factor
D_p :	Mean diameter of the pore (m)
λ :	Mean free path of gas molecules (m)
k_B :	Boltzmann constant ($1.3805 \times 10^{-23}\text{J}/\text{K}$)
T :	Temperature (K)
δ :	Collision diameter (m).

Data Availability

The data used to support the findings of this study are available from the corresponding author upon request.

Conflicts of Interest

The authors declare that there is no conflict of interest regarding the publication of this paper.

Acknowledgments

The research is financially supported by the National Natural Science Foundation (Nos. U1910206, 51861145403, 51874312) and China Postdoctoral Science Foundation (No. 2018M641526).

References

- [1] X. Tang, Z. Wang, N. Ripepi, B. Kang, and G. Yue, "Adsorption affinity of different types of coal: mean isosteric heat of adsorption," *Energy & Fuels*, vol. 29, no. 6, pp. 3609–3615, 2015.
- [2] C. M. White, D. H. Smith, K. L. Jones et al., "Sequestration of carbon dioxide in coal with enhanced coalbed methane RecoveryA Review†," *Energy & Fuels*, vol. 19, no. 3, pp. 659–724, 2005.
- [3] N. C. Dixit, M. Ahmadi, C. L. Hanks, and O. Awoleke, "Preliminary study of the carbon sequestration and enhanced coal bed methane production potential of subbituminous to high-volatile bituminous coals of the healy creek formation, Nenana Basin, Interior Alaska," in *2018 IEEE International Conference on Smart Cloud*, vol. 26, pp. 339–363, 2017.
- [4] Z. Dong, S. A. Holditch, W. B. Ayers, and W. J. Lee, "Probabilistic estimate of global Coalbed-methane recoverable resources," *Spe Economics & Management*, vol. 7, no. 4, pp. 148–156, 2015.
- [5] D. J. Beecy and V. A. Kuuskraa, "Status of U.S. geologic carbon sequestration research and technology," *Environmental Geosciences*, vol. 8, no. 3, pp. 152–159, 2001.
- [6] Q. Yin, R. Liu, H. Jing, H. Su, L. Yu, and L. He, "Experimental study of nonlinear flow behaviors through fractured rock samples after High-Temperature exposure," *Rock Mechanics and Rock Engineering*, vol. 52, no. 9, pp. 2963–2983, 2019.
- [7] Q. Yin, H. Jing, G. Ma, H. Su, and R. Liu, "Investigating the roles of included angle and loading condition on the critical hydraulic gradient of real rock fracture networks," *Rock Mechanics and Rock Engineering*, vol. 51, no. 10, pp. 3167–3177, 2018.
- [8] Q. Yin, G. Ma, H. Jing et al., "Hydraulic properties of 3D rough-walled fractures during shearing: an experimental study," *Journal of Hydrology*, vol. 555, pp. 169–184, 2017.
- [9] C. Stewart and M. A. Hessami, "A study of methods of carbon dioxide capture and sequestration—the sustainability of a photosynthetic bioreactor approach," *Energy Conversion & Management*, vol. 46, no. 3, pp. 403–420, 2005.
- [10] A. Busch, Y. Gensterblum, B. M. Krooss, and R. Littke, "Methane and carbon dioxide adsorption-diffusion experiments on coal: upscaling and modeling," *International Journal of Coal Geology*, vol. 60, no. 2–4, pp. 151–168, 2004.
- [11] D. Charriere, Z. Pokryszka, and P. Behra, "Effect of pressure and temperature on diffusion of CO₂ and CH₄ into coal from the Lorraine basin (France)," *International Journal of Coal Geology*, vol. 81, no. 4, pp. 373–380, 2010.
- [12] X. Cui, R. M. Bustin, and G. Dipple, "Selective transport of CO₂, CH₄, and N₂ in coals: insights from modeling of experimental gas adsorption data," *Fuel*, vol. 83, no. 3, pp. 293–303, 2004.
- [13] M. Pillalamarry, S. Harpalani, and S. Liu, "Gas diffusion behavior of coal and its impact on production from coalbed methane reservoirs," *International Journal of Coal Geology*, vol. 86, no. 4, pp. 342–348, 2011.
- [14] J. Q. Shi and S. Durucan, "A bidisperse pore diffusion model for methane displacement desorption in coal by CO₂ injection*, " *Fuel Guildford*, vol. 82, no. 10, pp. 1219–1229, 2003.
- [15] C. R. Clarkson and R. M. Bustin, "The effect of pore structure and gas pressure upon the transport properties of coal: a laboratory and modeling study. 2. Adsorption rate modeling," *Fuel*, vol. 78, no. 11, pp. 1345–1362, 1999.
- [16] J. Crank, *Mathematics of Diffusion*, Oxford University Press, London, 1975.
- [17] E. Ruckenstein, A. S. Vaidyanathan, and G. R. Youngquist, "Sorption by solids with bidisperse pore structures," *Chemical Engineering Science*, vol. 26, no. 9, pp. 1305–1318, 1971.
- [18] A. Ciembroniewicz and A. Marecka, "Kinetics of CO₂ sorption for two Polish hard coals," *Fuel*, vol. 72, no. 3, pp. 405–408, 1993.
- [19] X. Jian, P. Guan, and W. Zhang, "Carbon dioxide sorption and diffusion in coals: experimental investigation and modeling," *Science China Earth Sciences*, vol. 55, no. 4, pp. 633–643, 2012.
- [20] M. Svabova, Z. Weishauptova, and O. Pribyl, "The effect of moisture on the sorption process of CO₂ on coal," *Fuel*, vol. 92, no. 1, pp. 187–196, 2012.
- [21] L. D. Connell, R. Sander, Z. Pan, M. Camilleri, and D. Heryanto, "History matching of enhanced coal bed methane laboratory core flood tests," *International Journal of Coal Geology*, vol. 87, no. 2, pp. 128–138, 2011.
- [22] Z. Pan, L. D. Connell, M. Camilleri, and L. Connelly, "Effects of matrix moisture on gas diffusion and flow in coal," *Fuel*, vol. 89, no. 11, pp. 3207–3217, 2010.
- [23] R. Sander, L. D. Connell, Z. Pan, M. Camilleri, D. Heryanto, and N. Lupton, "Core flooding experiments of CO₂ enhanced coalbed methane recovery," *International Journal of Coal Geology*, vol. 131, pp. 113–125, 2014.
- [24] G. Staib, R. Sakurovs, and E. M. A. Gray, "A pressure and concentration dependence of CO₂ diffusion in two Australian bituminous coals," *International Journal of Coal Geology*, vol. 116, pp. 106–116, 2013.
- [25] S. P. Nandi and P. L. Walker Jr., "Activated diffusion of methane from coals at elevated pressures," *Fuel*, vol. 54, no. 2, pp. 81–86, 1975.
- [26] P. Liu, Y. Jiang, and B. Fu, "A novel approach to characterize gas flow behaviors and air leakage mechanisms in fracture-matrix coal around in-seam drainage borehole," *Journal of Natural Gas Science and Engineering*, vol. 77, p. 103243, 2020.
- [27] P. Liu, Y. Qin, S. Liu, and Y. Hao, "Non-linear gas desorption and transport behavior in coal matrix: experiments and numerical modeling," *Fuel*, vol. 214, pp. 1–13, 2018.
- [28] P. Liu, Y. Qin, S. Liu, and Y. Hao, "Numerical modeling of gas flow in coal using a modified dual-porosity model: A multi-mechanistic approach and finite difference method," *Rock Mechanics & Rock Engineering*, vol. 51, no. 9, pp. 2863–2880, 2018.
- [29] Q. Yuan, K. Zhang, Y. Hong et al., "A 30 nm-resolution hard X-ray microscope with X-ray fluorescence mapping capability at BSRF," *Journal of Synchrotron Radiation*, vol. 19, no. 6, pp. 1021–1028, 2012.
- [30] N. Gallagher and G. Wise, "A theoretical analysis of the properties of median filters," *IEEE Transactions on Acoustics, Speech, and Signal Processing*, vol. 29, no. 6, pp. 1136–1141, 1981.
- [31] M. O. Baradez, C. P. MCGuckin, N. Forraz, R. Pettengell, and A. Hoppe, "Robust and automated unimodal histogram thresholding and potential applications," *Pattern Recognition*, vol. 37, no. 6, pp. 1131–1148, 2004.
- [32] Y. Zhao, Y. Sun, S. Liu, Z. Chen, and L. Yuan, "Pore structure characterization of coal by synchrotron radiation nano-CT," *Fuel*, vol. 215, pp. 102–110, 2018.
- [33] Y. Sun, Y. Zhao, and L. Yuan, "Impact of coal composition and pore structure on gas adsorption: a study based on a

- synchrotron radiation facility,” *Greenhouse Gases: Science and Technology*, vol. 10, no. 1, pp. 116–129, 2019.
- [34] H. Liu, J. Mou, and Y. Cheng, “Impact of pore structure on gas adsorption and diffusion dynamics for long-flame coal,” *Journal of Natural Gas Science and Engineering*, vol. 22, pp. 203–213, 2015.
- [35] Y. Zhu, X. Lu, J. Zhou, Y. Wang, and J. Shi, “Prediction of diffusion coefficients for gas, liquid and supercritical fluid: application to pure real fluids and infinite dilute binary solutions based on the simulation of Lennard-Jones fluid,” *Fluid Phase Equilibria*, vol. 194–197, pp. 1141–1159, 2002.
- [36] A. Fick, “On liquid diffusion,” *Journal of Membrane Science*, vol. 100, no. 1, pp. 33–38, 1995.
- [37] I. Langmuir, “The adsorption of gases on plane surfaces of glass, mica and platinum,” *Journal of the American Chemical Society*, vol. 40, no. 9, pp. 1361–1403, 1918.
- [38] <https://www.webbook.nist.gov/chemistry/fluid/n.d>.
- [39] Y. Yang and S. Liu, “Estimation and modeling of pressure-dependent gas diffusion coefficient for coal: a fractal theory-based approach,” *Fuel*, vol. 253, pp. 588–606, 2019.
- [40] S. Roy, R. Raju, H. F. Chuang, B. A. Cruden, and M. Meyyappan, “Modeling gas flow through microchannels and nanopores,” *Journal of Applied Physics*, vol. 93, no. 8, pp. 4870–4879, 2003.
- [41] Y. Zhao, Y. Sun, S. Liu, K. Wang, and Y. Jiang, “Pore structure characterization of coal by NMR cryoporometry,” *Fuel*, vol. 190, pp. 359–369, 2017.
- [42] X. R. Wei, G. X. Wang, P. Massarotto, S. D. Golding, and V. Rudolph, “Numerical simulation of multicomponent gas diffusion and flow in coals for CO₂ enhanced coalbed methane recovery,” *Chemical Engineering Science*, vol. 62, no. 16, pp. 4193–4203, 2007.
- [43] P. Thararoop, Z. T. Karpyn, and T. Ertekin, “Development of a multi-mechanistic, dual-porosity, dual-permeability, numerical flow model for coalbed methane reservoirs,” *Journal of Natural Gas Science & Engineering*, vol. 8, no. 8, pp. 121–131, 2012.
- [44] I. Hidajat, A. Rastogi, M. Singh, and K. K. Mohanty, “Transport properties of porous media reconstructed from thin-sections,” *SPE Journal*, vol. 7, no. 1, pp. 40–48, 2013.
- [45] P. Oren and S. Bakke, “Process based reconstruction of sandstones and prediction of transport properties,” *Transport in Porous Media*, vol. 46, no. 2/3, pp. 311–343, 2002.
- [46] C. L. Y. Yeong and S. Torquato, “Reconstructing random media,” *Physical Review E*, vol. 57, no. 1, pp. 495–506, 1998.
- [47] Z. Pan and L. D. Connell, “A theoretical model for gas adsorption-induced coal swelling,” *International Journal of Coal Geology*, vol. 69, no. 4, pp. 243–252, 2007.
- [48] Y. Zhang, B. Gong, J. Li, and H. Li, “Discrete fracture modeling of 3D heterogeneous enhanced coalbed methane recovery with prismatic meshing,” *Energies*, vol. 8, no. 6, pp. 6153–6176, 2015.

Research Article

Numerical Simulation on Non-Darcy Flow in a Single Rock Fracture Domain Inverted by Digital Images

Jianli Shao ^{1,2} Qi Zhang ³ Wenbin Sun ^{1,2} Zaiyong Wang,¹ and Xianxiang Zhu ¹

¹State Key Laboratory of Mining Disaster Prevention and Control Co-Founded by Shandong Province and the Ministry of Science and Technology, Shandong University of Science and Technology, Qingdao 266590, China

²Mining Engineering National Experimental Teaching Demonstration Center, Shandong University of Science and Technology, Qingdao 266590, China

³Department of Civil and Environmental Engineering, Stanford University, Stanford, CA 94305, USA

Correspondence should be addressed to Qi Zhang; qzhang94@stanford.edu and Wenbin Sun; swb@sdust.edu.cn

Received 14 March 2020; Revised 29 May 2020; Accepted 6 June 2020; Published 27 June 2020

Academic Editor: Qian Yin

Copyright © 2020 Jianli Shao et al. This is an open access article distributed under the Creative Commons Attribution License, which permits unrestricted use, distribution, and reproduction in any medium, provided the original work is properly cited.

The influence of rock seepage must be considered in geotechnical engineering, and understanding the fluid flow in rock fractures is of great concern in the seepage effect investigation. This study is aimed at developing a model for inversion of rock fracture domains based on digital images and further study of non-Darcy flow. The visualization model of single rock fracture domain is realized by digital images, which is further used in flow numerical simulation. We further discuss the influence of fracture domain geometry on non-Darcy flow. The results show that it is feasible to study non-Darcy flow in rock fracture domains by inversion based on digital images. In addition, as the joint roughness coefficient (JRC) increases or the fracture aperture decreases, distortion of the fluid flow path increases, and the pressure gradient loss caused by the inertial force increases. Both coefficients of the Forchheimer equation decrease with increasing fracture aperture and increase with increasing JRC. Meanwhile, the critical Reynolds number tends to decrease when JRC increases or the fracture aperture decreases, indicating that the fluid tends to non-Darcy flow. This work provides a reference for the study of non-Darcy flow through rock fractures.

1. Introduction

Many important underground resources, such as groundwater, oil, gas, coalbed methane, and geothermal energy, are exploited in low-permeability reservoirs with highly developed fractures [1, 2]. Hydraulic fracturing of oil- and gas-rich strata and coal seams requires accurate control of the amount of fluid injected into the rock fractures. The deep burial of nuclear waste and CO₂ geological storage should reduce the fluid infiltration into the rock mass as much as possible [3]. In situ leaching (ISL), an alternative mining technology, requires the injection of leaching solution into the artificial fracture to dissolve target minerals in impervious host rocks [4]. Compared with intact low-permeability rocks, the fractures formed by rock failure greatly improve its permeability. The fractures formed by rock cracked change the stability and permeability of surrounding rocks, which are easy to induce geological disasters [5–10]. Obtain-

ing the fracture flow characteristics is the premise of rock seepage control. Therefore, the fluid flow through fractures of the rock mass has always been the focus of engineering research [11].

The classical cubic law of linear laminar flow was developed in the early study of rock fracture flow using a smooth parallel plate model. It was used to evaluate the flow capacity of fractures [12, 13]. However, due to the complexity of the fracture geometry and flow regime, the cubic law does not adequately describe fluid flow behavior in natural fractures, and non-Darcy flow may occur as a result of nonnegligible inertial losses. Previous experimental investigations reported that Darcy's law fails to predict pressure drops in fractures when inertial effects are relevant before the fully developed turbulence [14, 15]. The rough structure of the fracture surface causes non-Darcy flow [16], and the exact solution must be obtained by solving the Navier–Stokes equation, which is difficult to obtain in engineering applications [17]. Therefore,

scholars have tried to develop a characterization method for determining the fracture roughness and the reduction of the coarse structure of natural fractures to conduct non-Darcy flow behavior research. Su et al. [18] used artificial rough surface fractures to simulate natural rock mass fractures, but the actual rough fracture surface is much more complicated than the artificial rough surface. Barton and Choubey [19] used the joint roughness coefficient (JRC) to define the roughness and created 10 standard curves, which quantitatively reflect the fracture roughness. Ju et al. [20] used polymethyl methacrylate (PMMA) to make planar models of fractures with different roughness and used a high-speed camera to record the entire rough fracture water seepage process. Xie et al. [21] used a laser scanner system with a spacing grid of 0.1 mm to conduct a two-dimensional numerical simulation of single fractures during shear displacement with the Navier–Stokes equations. However, a fracture is a three-dimensional space with irregular scale and characteristics, so only the accurate inversion of a three-dimensional fracture domain with actual rough surfaces can objectively reflect the geometric characteristics of a natural fracture.

As an accurate spatial structure measurement and digital representation on the microscopic scale of materials, digital image processing technology has been widely used in the analysis of geotechnical microstructures. Angelin et al. [22] used image processing techniques of K-means algorithms and Watershed algorithms to analyze microscopic images for void identification in cement matrices. Based on digital image analysis, Thomas et al. [23] analyzed the distribution and size of macroporosity under different mixing conditions by computerized axial tomography, scanning electron microscopy, and a new developed methodology. Zhu et al. [24, 25] utilized the digital image technique to numerically characterize the heterogeneity of the structural characteristics of coal and rock masses, and they studied the influence of heterogeneity on coal rock fractures and seepage using numerical analysis. In view of the fact that the roughness of the fracture surface results in different pixel values, in this paper, we attempt to restore the rough structure of the fracture surface by converting the pixels into a 0 to 1 data distribution (normalization).

There are many types of non-Darcy flow such as low-velocity non-Darcy flow caused by boundary layer [26] and high-velocity non-Darcy flow caused by inertia force, of which the latter type is adopted in this manuscript. The Forchheimer equation [27–30] is commonly used to describe non-Darcy flow. Because the coefficients in the Forchheimer equation are closely related to the geometric characteristics of fractures [26, 31], the variation in the coefficients is a necessary condition for describing non-Darcy flow. Many studies have found that surface roughness determines the nonlinear characteristics of fluid flow in natural rock fractures [32, 33]. Xia et al. [34] observed that non-Darcy seepage in rough fractures depends on the void space and composite morphology of the fracture surface. Yin et al. [35–37] reported a large number of experimental studies on nonlinear flow characteristics of fractured rock samples. Zhang et al. [38] presented a hydromechanical framework for porous materials exhibiting two dominant porosity scales

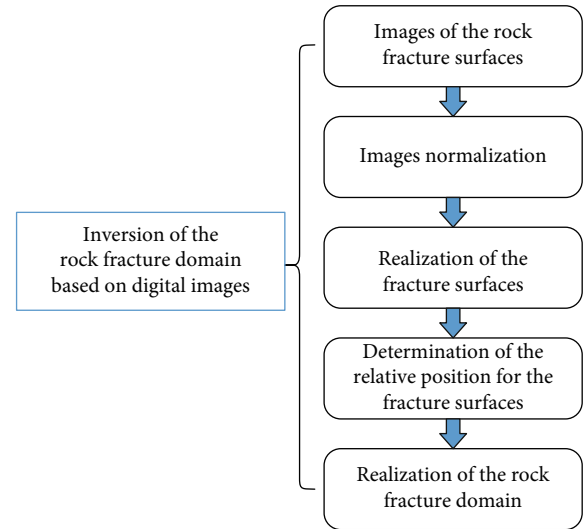


FIGURE 1: Process chart of inverting the fracture domain.

that accommodates transverse isotropy induced by distributed microfractures and non-Darcy flow through the nanometer-scale pore spaces. Therefore, it is necessary to quantitatively study the influence of the fracture’s geometric characteristics on non-Darcy flow behavior.

In this work, the reverse model for rock fracture domain will be carried out according to the digital images of rock fracture surfaces, and the model will be implemented to numerical simulation to realize the visualization of non-Darcy flow in rock fracture. The simulation results are fitted according to the Forchheimer equation describing the non-linear flow, and the effects of the geometric characteristics of the fracture domain on the non-Darcy flow are further analyzed. This paper provides a reference for the current methods of non-Darcy flow in rough rock fractures.

2. Inversion of the Fracture Domain Based on Digital Images

The digital image is the reflection of the objective object, which is composed of many pixels with a matrix arrangement, so the digital image can reflect the fluctuation height of the rock fracture surface. In gray level images or binarization images [39, 40], the gray values are 0–1 and 0–255, respectively. The discrete function of the gray value or chromaticity of the corresponding digital image can accurately reflect the distribution characteristics of the material surface, which is the basis of inversion of the fracture domain based on digital image technology. The process of inverting the fracture domain based on the digital image is shown in Figure 1.

Fractured rocks form fracture domains of different scales, which are actually surrounded by rough rock surfaces. As shown in Figure 2, a single fracture domain is formed between the upper and lower surfaces. Therefore, we used CCD camera to get the images of rock fracture surfaces, which are 24-bit true color pictures with pixel size 1000×600 . In addition, the images are denoised to reduce the interference of external factors.

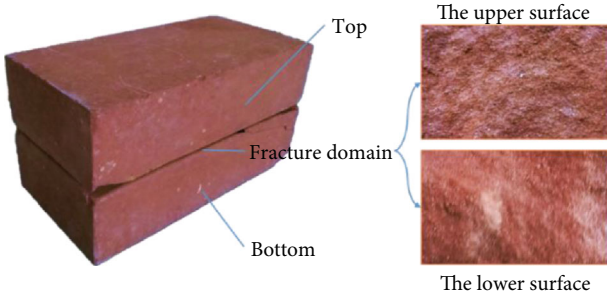


FIGURE 2: Images of rock fracture surfaces.

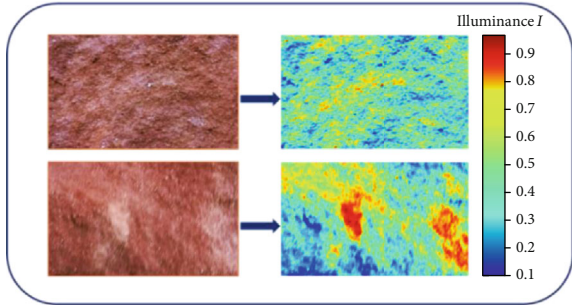


FIGURE 3: Image normalization.

The images of the fracture surface have a wealth of information, which can well reflect the mesostructure of the surface through different grayscales and colors. Digital image is composed of rectangular image elements, also known as pixel points. The digital image of the surface of the rock sample can be stored as an image of different accuracy by image processing software. The so-called accuracy here is controlled by pixels. There are many kinds of color space such as RGB composed of three primary colors and HSI composed of three variables, i.e., hue, saturation, and illuminance [41, 42]. To facilitate the transition of both kinds of color space, illuminance (I) is generally defined as the arithmetic mean of the three RGB components, i.e., $I = (R + G + B)/3$ [43, 44], which is also used in this paper. In the digital image of the rock fracture surface, the values of R , G , and B range from 0 to 255. After the image is normalized, the values of R , G , and B are converted to the I value, which has a 0-1 distribution. It shows the normalized result of the rock fracture surface images in Figure 3. The lowest pit on the rock fracture surface is considered to be in the horizontal plane, so the I value is always distributed between 0 and 1.

In this section, the fracture reconstruction method of Zhao et al. [45] is referenced and improved for inversion of the fracture domain. For the lower surface of the fracture, the digital image matrix function of the fracture surface is obtained and recorded as $[B]$, and then, $[B]$ is normalized to obtain the normalization matrix $[\bar{B}]$. The minimum and maximum values in $[B]$ are determined using MATLAB and are recorded as b_{\min} and b_{\max} , respectively. Thus, the height distribution of the lower surface of the fracture is as follows:

$$B = (b_{\max} - b_{\min}) \cdot [\bar{B}]. \quad (1)$$

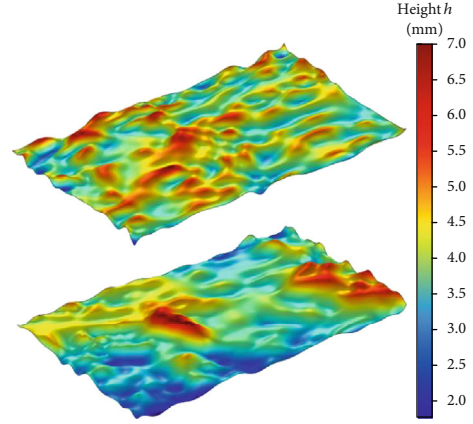


FIGURE 4: The restored surfaces.

For the upper surface of the fracture, the digital image matrix function of the fracture surface is obtained and recorded as $[T]$, and then, normalization processing is carried out to obtain the normalization matrix $[\bar{T}]$. Using the same method, the minimum t_{\min} and maximum t_{\max} in $[T]$ are determined. Thus, the surface height distribution on the fracture is as follows:

$$T = (t_{\max} - t_{\min}) \cdot [\bar{T}]. \quad (2)$$

As shown in Figure 4, the height distribution of the upper and lower surfaces of the fracture is restored. By comparison, the results of the restored surfaces are consistent with the actual height distribution on the fracture surfaces. When further inversion of the fracture domain is needed, the relative positions of the upper surface and the lower surface need to be determined. As shown in Figure 5, we select the horizontal plane, where b_{\min} is located, as the reference plane I with height h_1 , so the height function of any point on the lower surface of the fracture will be

$$B_{h(x)} = (b_{\max} - b_{\min}) \cdot [\bar{B}] + h_1. \quad (3)$$

Then, we select the horizontal plane, where t_{\max} is located, as the reference plane II with height h_2 , so the height function of any point on the surface of the same fracture will be

$$T_{h(x)} = h_2 - (t_{\max} - t_{\min}) \cdot (1 - [\bar{T}]). \quad (4)$$

By combining the top and bottom of the fracture specimen (see Figure 6), the rock fracture domain is obtained, and the spatial distribution function of the fracture aperture $e(x)$ will be:

$$e(x) = T_{h(x)} - B_{h(x)} = h_2 - (t_{\max} - t_{\min}) \cdot (1 - [\bar{T}]) - (b_{\max} - b_{\min}) \cdot [\bar{B}] - h_1. \quad (5)$$

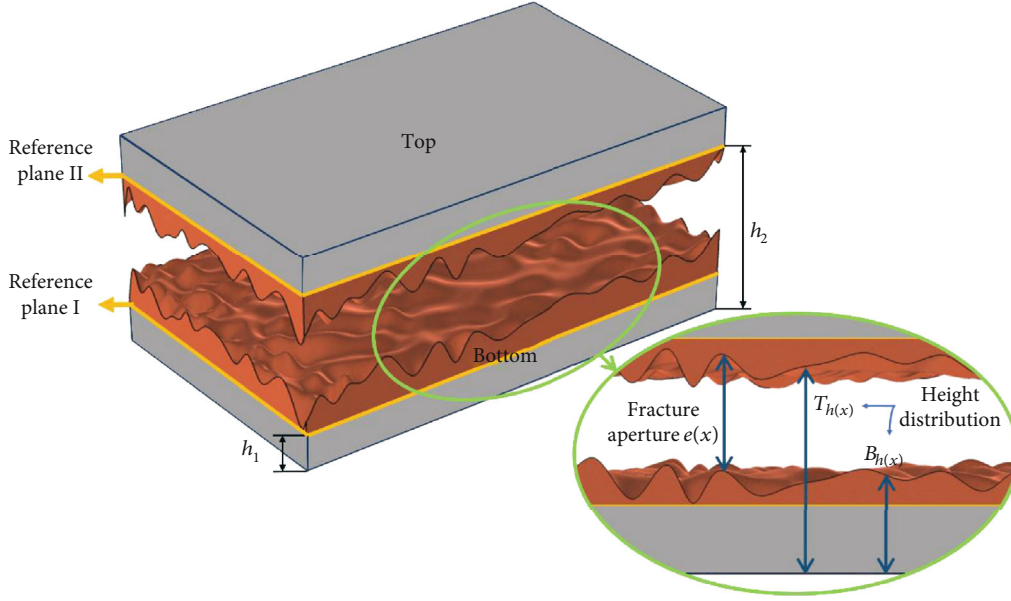


FIGURE 5: The relative position of the surfaces.

3. Model Implementation

3.1. Mathematical Model. The single-phase flow of incompressible fluid in rock fractures can be expressed by mass conservation and Navier–Stokes equations, which can be expressed as [12]

$$\rho \left(\frac{\partial \mathbf{u}}{\partial t} + (\mathbf{u} \cdot \nabla) \mathbf{u} \right) = -\nabla P + \mu \nabla^2 \mathbf{u} + \mathbf{F}, \quad (6)$$

where \mathbf{u} , ρ , ∇P , μ , and \mathbf{F} represent the flow velocity vector (m/s), the fluid density (kg/m^3), the fluid pressure gradient along the flow direction (MPa/m), the viscosity coefficient ($\text{N}\cdot\text{s}/\text{m}^2$), and the body force vector (N), respectively.

Due to the increasingly obvious inertia effect as the flow rate and fracture roughness increase [28, 46], the fluid usually exhibits non-Darcy flow behavior in rough rock fractures. In general, Forchheimer equation in porous media seepage theory is introduced to describe the non-Darcy flow [26], which is defined as

$$-\nabla P = A Q + B Q^2, \quad (7)$$

where Q (m^3/s) is the flow rate; A ($\text{kg}\cdot\text{s}^{-1}\cdot\text{m}^{-5}$) is the coefficient of the linear term; B ($\text{kg}\cdot\text{m}^{-8}$) is the coefficient of the nonlinear term. Both coefficients A and B rely on knowledge of the fluid properties and the geometric characteristics of rough fractures [29], which can be expressed as

$$A = \frac{\mu}{k A_h} = \frac{12\mu}{w e^3}, \quad (8)$$

$$B = \frac{\beta \mu}{A_h^2} = \frac{\beta \rho}{w^2 e^2}, \quad (9)$$

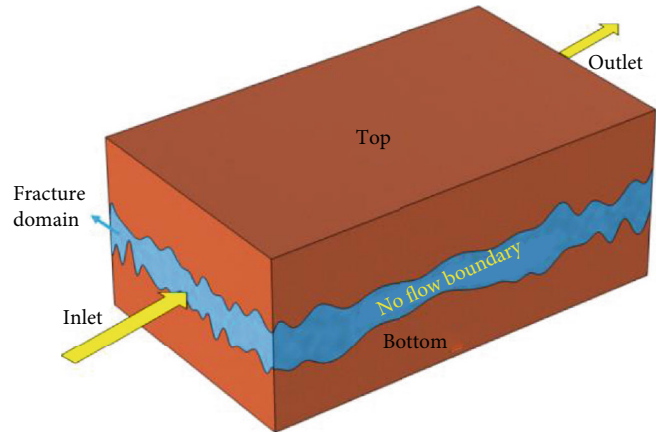


FIGURE 6: Inversion of the fracture domain.

where β (m^{-1}) is the non-Darcy coefficient, which varies with the geometric characteristics of the fractures.

Reynolds number Re is a hydraulic parameter, which is a dimensionless number used to judge the flow state of viscous fluid. Its physical meaning is the ratio between the inertial force and the viscous force of the fluid, which can be expressed as

$$Re = \frac{\rho v e}{\mu} = \frac{\rho Q}{\mu w}. \quad (10)$$

In order to further explain the mechanism of non-Darcy flow, Zeng and Grigg [47] proposed a non-Darcy flow effect factor E , which is defined as

$$E = \frac{BQ}{A + BQ}. \quad (11)$$

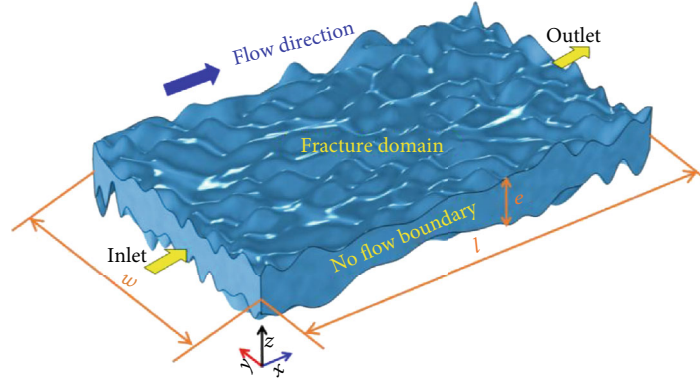


FIGURE 7: Geometry and boundary conditions for numerical simulation.

The non-Darcy flow effect factor E indicates the degree of non-Darcy flow, which is between 0 and 1. Combining equations (8), (9), (10), and (11), the Reynolds number Re can be rewritten as

$$Re = \frac{A\rho E}{B\mu w(1-E)} = \frac{12E}{\beta e_h(1-E)}. \quad (12)$$

The critical Reynolds number Re_c characterizes the onset of the flow transition from linear flow to nonlinear flow. In recent studies, the critical condition for the onset of nonlinear flow has been defined as the point at which the nonlinear pressure drop contributes 10% to the overall pressure drop [28], which is equal to $E = 0.1$. Considering this condition, the critical Reynolds number for nonlinear fluid flow in rough fractures was suggested by Javadi et al. [29]:

$$Re_c = \frac{A\rho}{9B\mu w}. \quad (13)$$

3.2. Numerical Model. We consider a 3D single fracture domain 50 mm wide and 90 mm long, and the roughness varies with different fracture domains. The geometric profile and boundary conditions are shown in Figure 7. The fracture aperture distribution of each single fracture domain can be obtained by equation (5). In order to analyze the influence of fracture aperture on non-Darcy flow, the average value of fracture aperture distribution is selected as the relative description of fracture aperture size, in which of the model is 10 mm. We assume a single fluid flow in the fracture domain, the pressure at the inlet boundary on the left was 1.0 MPa, and the pressure at the outlet boundary on the right was 0.1 MPa. The other boundaries are set as no flow boundaries. The following water parameters are assumed in the simulations: temperature $T = 20^\circ\text{C}$; density $\rho = 998.2 \text{ kg/m}^3$; dynamic viscosity $\mu = 0.001 \text{ Pa}\cdot\text{s}$.

In this work, the COMSOL Multiphysics code is used for the numerical model implementation based on the Finite Element Method (FEM). The model was divided into 133082 grids using free tetrahedral node. The numerical simulations are obtained by computational convergence of the stationary studies.

Using the rock fracture domain inversion method, we obtained 4 fracture domains with different roughness as shown in Figure 8. Table 1 lists the JRC range of some fracture contours of these 4 samples, which can be used to evaluate the overall roughness of the fracture domains.

4. Results and Discussion

4.1. Effects of the Different JRCs. Figure 9 shows the velocity distribution in the fracture domains with different JRCs. Overall, the undulating structure of the fracture surface makes the velocity distribution very uneven. On the upper surface of the fracture, each protruding position is relatively low, while the concave position has a relatively high velocity. There is a low-speed boundary layer at the entrance of each sample, which surrounds the high-speed mainstream area. As the JRC increases, the effect of the boundary layer becomes more significant, resulting in an uneven velocity distribution at the entrance. In Figure 9, because the fracture surface of Sample 1 is relatively smooth, the velocity fluctuation is not significant, and the maximum velocity is up to 0.6 m/s. As the surface roughness increases, the fluctuation in the fracture surface increases gradually, and the maximum velocity decreases gradually. The maximum velocity of Sample 4 is only 0.4 m/s.

The essence of non-Darcy flow is that the growth of the flow and the pressure gradient no longer satisfies a linear relationship. In order to investigate this nonlinear flow behavior, different water pressures were set at the inlet boundary in the simulations. The relationship between the hydraulic gradient and the flow rate is shown in Figure 10. $-\nabla P$ represents the macroscopic pressure gradient along the flow direction, which is equal to the pressure drop between the inlet and outlet divided by the fracture length l . Based on the relationship between the hydraulic gradient and the flow rate, the relationship between each pressure gradient and flow rate deviates from the linear relationship. Because the influence of the inertial force becomes more significant as the flow rate increases, the degree of deviation increases. When the flow rate is the same, as the JRC increases, the hydraulic gradient increases, the slope between the pressure gradient and the flow rate becomes steeper, and the deviation from the linear relationship increases. When the

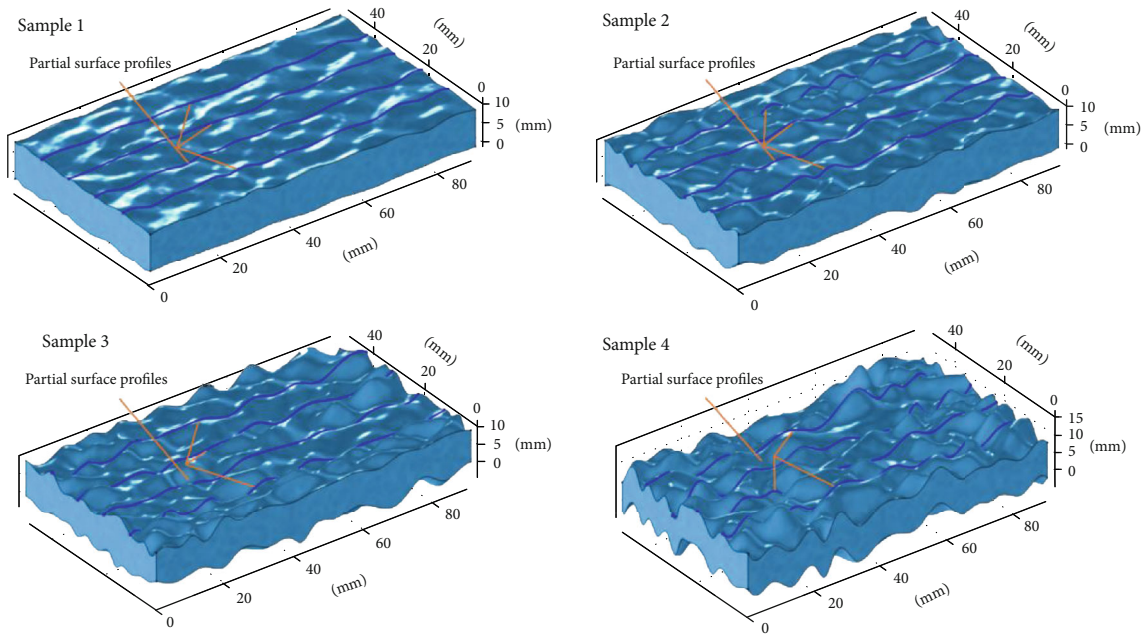


FIGURE 8: Morphology characterization of the fracture domains.

TABLE 1: JRC value of the partial surface profiles.

Sample no.	Position	Surface profiles	JRC value
Sample 1	Y = 10		2-4
	Y = 20		2-4
	Y = 30		0-2
	Y = 40		4-6
Sample 2	Y = 10		8-10
	Y = 20		8-10
	Y = 30		6-8
	Y = 40		8-10
Sample 3	Y = 10		14-16
	Y = 20		14-16
	Y = 30		12-14
	Y = 40		16-18
Sample 4	Y = 10		18-20
	Y = 20		18-20
	Y = 30		16-18
	Y = 40		18-20

pressure gradient is the same, the flow rates of the four samples are significantly different. The sample with the lowest roughness has the highest flow rate, and the roughness of the other samples increases gradually and the flow rate decreases.

As the fracture roughness increases, the circuitous degree of the fracture flow path increases, and the inertial force of the fluid flow increases. The nonlinear pressure gradient loss caused by the inertial force accounts for most of the total

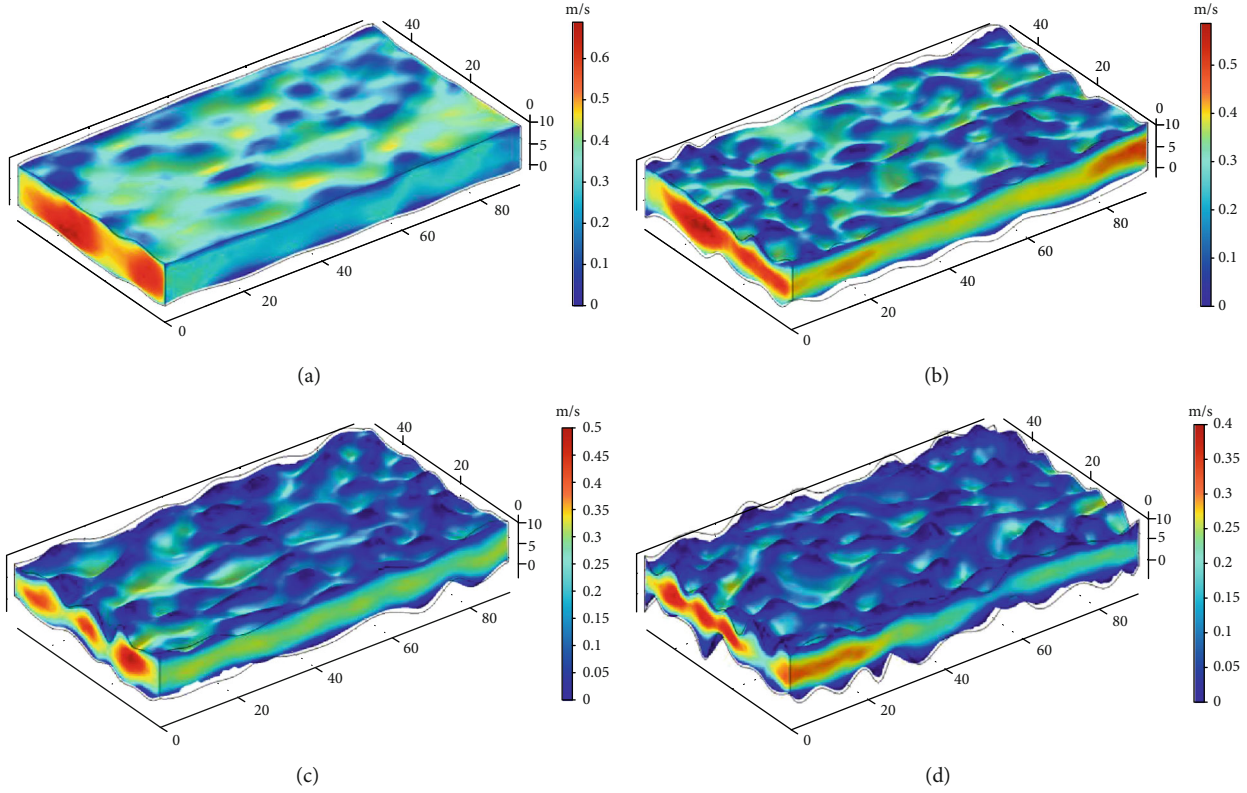


FIGURE 9: Velocity distribution of the samples with different JRCs. (a) Sample 1. (b) Sample 2. (c) Sample 3. (d) Sample 4.

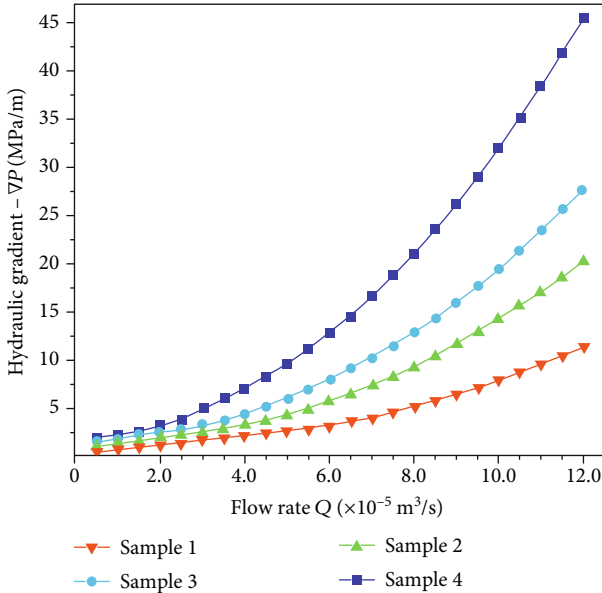


FIGURE 10: Pressure gradient versus flow rate for the samples.

pressure gradient loss, and the proportion transformed into fluid kinetic energy decreases, so the nonlinear characteristic of fluid flow is more significant.

4.2. Effect of Fracture Aperture. In this section, we explore the influence of the change of fracture aperture on fluid flow. Numerical simulations are carried out for Sample 3 with

the fracture apertures of 6 mm, 8 mm, 10 mm, and 12 mm, respectively. And the surface and internal velocity distributions of the different fracture apertures were obtained as shown in Figure 11. Overall, there are always relatively low velocity boundary layers within the fracture domains, which surround the high-speed mainstream area. Observing the internal section, there are significant differences in the velocity at different positions in the fracture aperture. For the position where the fracture aperture is small, the velocity increases rapidly, while for the position where the fracture aperture is large, the velocity decreases accordingly. For the same pressure gradient, the maximum velocity is 0.3 m/s when the fracture aperture is 6 mm. The maximum velocity increases as the fracture aperture increases, and the velocity reaches 0.5 m/s when the fracture aperture is 12 mm. The streamline color represents the velocity distribution, and the change in the streamline color reflects the increase of the overall velocity in the fracture domain with increasing fracture aperture. Based on the flow direction, as the fracture aperture increases, the streamline tends to become smoother.

As shown in Figure 12, based on the Forchheimer fitting curves of the pressure gradient and the flow rate, the relationship between the pressure gradient and the flow rate is still nonlinear regardless of the change in the fracture aperture. The determination coefficients R^2 of fitting curves are 0.9993, 0.9997, 0.9998, and 0.9996, respectively, indicating that the fitting effect is satisfactory. As can be seen from the diagram, when the flow rate is the same, i.e., the x value of each regression equation is the same, the y value, i.e., the required pressure gradient, decreases with increasing fracture

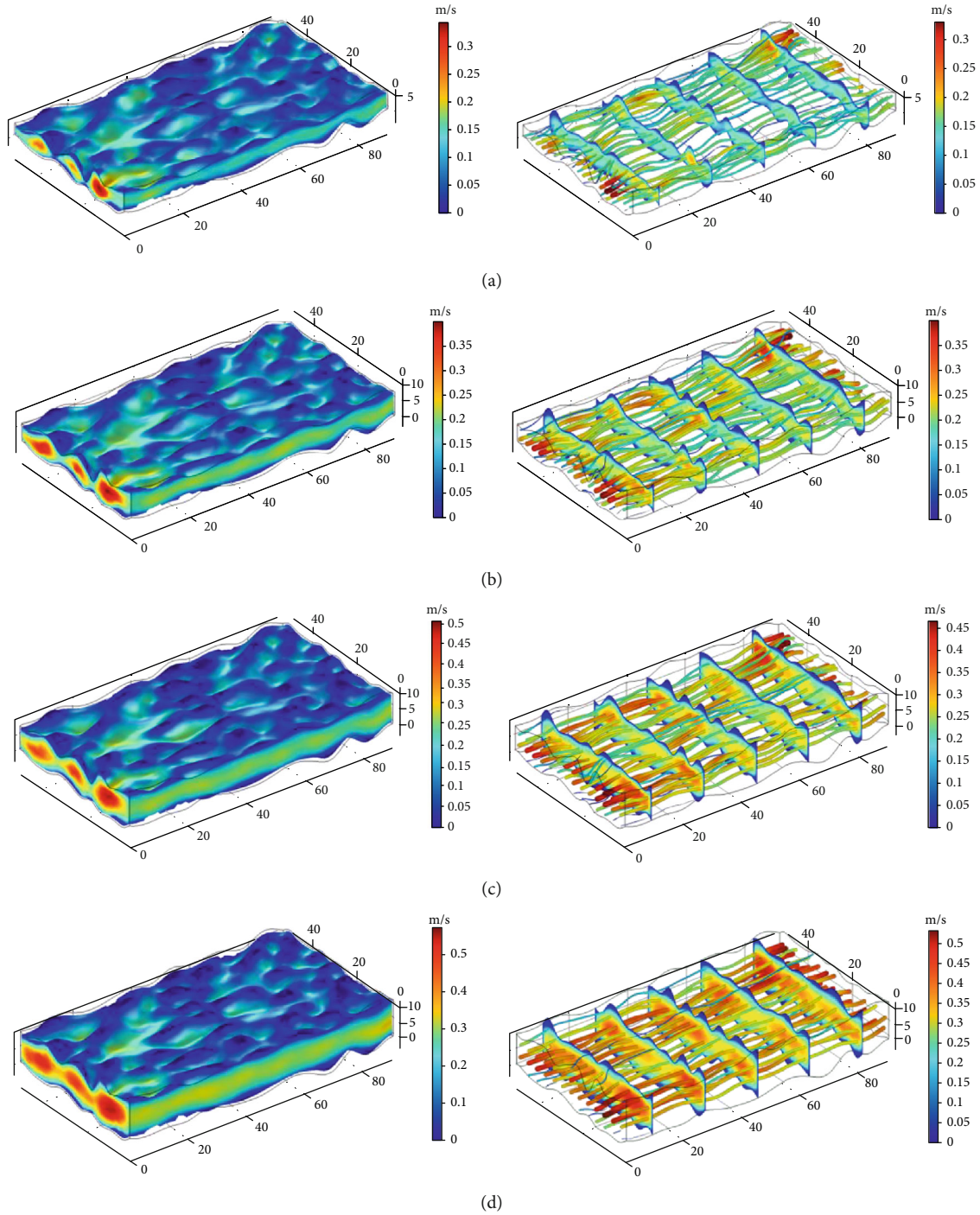


FIGURE 11: Velocity and streamline distribution of various fracture apertures. (a) $e = 6$ mm. (b) $e = 8$ mm. (c) $e = 10$ mm. (d) $e = 12$ mm.

aperture e . When the pressure gradient is the same, the flow rate increases with increasing fracture aperture e .

The flow path of a single fracture with the same JRC becomes relatively relaxed and smooth with increasing fracture aperture, which means that the corresponding tortuous degree decreases and the inertial force becomes weaker in the fluid flow. The nonlinear pressure gradient loss caused by the inertial force accounts for part of the total pressure gradient loss and increases the proportion of the fluid kinetic energy. In addition, due to the difference in the fracture aper-

ture e , the primary term coefficient A and the quadratic term coefficient B of each regression equation are also different. The variation in these coefficients will be further analyzed in the next section.

4.3. Variation of the Coefficients of the Forchheimer Equation.

According to the physical meaning of the Forchheimer equation (equation (7)), A ($\text{kg} \cdot \text{s}^{-1} \cdot \text{m}^{-5}$) is the coefficient of the linear term, which represents the energy losses due to viscous dissipation mechanisms; and B ($\text{kg} \cdot \text{m}^{-8}$) is the coefficient of

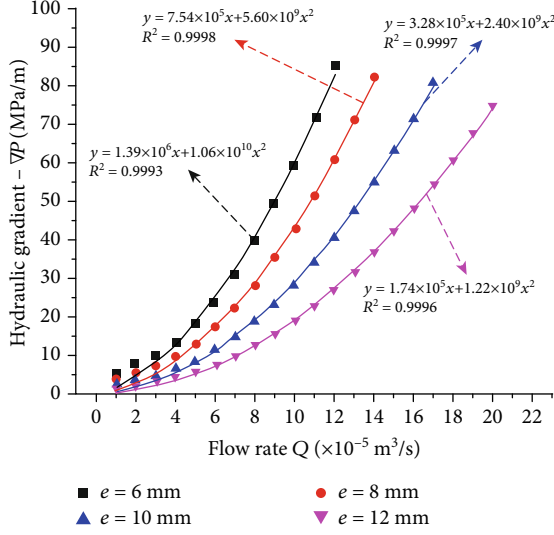


FIGURE 12: Fitted pressure gradient versus flow rate curves under various fracture apertures.

TABLE 2: Summary of the fitted coefficients A , B of the Forchheimer equation.

Sample no.	Fracture aperture e (mm)	Coefficient A ($\text{kg} \cdot \text{s}^{-1} \cdot \text{m}^{-5}$)	Coefficient B ($\text{kg} \cdot \text{m}^{-8}$)	Coefficient of determination R^2
Sample 1	6	$9.32E+5$	$6.78E+9$	0.9997
	8	$5.10E+5$	$3.51E+9$	0.9999
	10	$2.25E+5$	$1.52E+9$	0.9998
	12	$1.14E+5$	$7.68E+8$	0.9997
	14	$5.93E+4$	$3.84E+8$	0.9996
Sample 2	6	$1.21E+6$	$9.08E+9$	0.9999
	8	$6.64E+5$	$4.91E+9$	0.9988
	10	$2.94E+5$	$2.11E+9$	0.9998
	12	$1.48E+5$	$1.04E+9$	0.9991
	14	$7.22E+4$	$4.98E+8$	0.9986
Sample 3	6	$1.39E+6$	$1.06E+10$	0.9993
	8	$7.54E+5$	$5.60E+9$	0.9998
	10	$3.28E+5$	$2.40E+9$	0.9997
	12	$1.74E+5$	$1.22E+9$	0.9996
	14	$8.98E+4$	$6.32E+8$	0.9978
Sample 4	6	$1.67E+6$	$1.29E+10$	0.9998
	8	$9.09E+5$	$6.87E+9$	0.9969
	10	$3.95E+5$	$2.94E+9$	0.9993
	12	$2.06E+5$	$1.51E+9$	0.9997
	14	$9.91E+4$	$7.11E+8$	0.9989

the nonlinear term, which describes the energy losses arising from the inertial effects [26]. Both coefficients A and B rely on knowledge of the fluid properties and the geometric characteristics of rough fractures [14, 15]. In order to

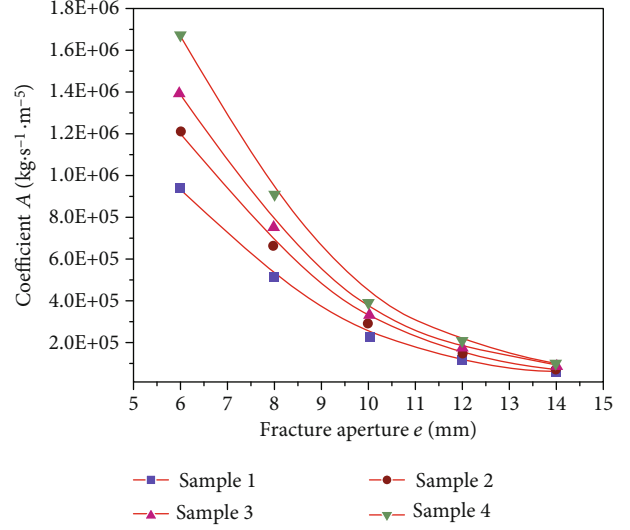


FIGURE 13: Variation of coefficient A with fracture apertures.

further analyze the change in the coefficients of the Forchheimer equation, we carried out numerical simulation for all four samples when the fracture apertures were adjusted to 6 mm, 8 mm, 10 mm, and 12 mm, respectively. The relationship between the pressure gradient and the flow rate was extracted, and the results of coefficients A and B were obtained by polynomial fitting (Table 2).

Figure 13 shows the relationship between coefficient A of the Forchheimer equation (equation (8)) and the fracture aperture e . For fractures with the same JRC, coefficient A decreases with increasing the fracture aperture e , indicating that the viscous effect has been gradually weakened. For the same fracture aperture, coefficient A also increases with increasing JRC, which also means that the viscous force is increasing. This is consistent with the observation of Xiong et al. [48].

Figure 14 shows the relationship between coefficient B of the Forchheimer equation (equation (7)) and the fracture aperture e . From the point of view of the changing trend, the JRC and the fracture aperture e are closely related to coefficient B . For the same JRC, coefficient B decreases with increasing fracture aperture e , indicating that the fluid inertial force weakens. For the same fracture aperture e , as the JRC increases, coefficient B also increases, which indicates that the inertial force of the fluid is increasing. This observation is consistent with the observation of Chen et al. [49].

Variation of the coefficients A and B shows a much similar pattern. For the same JRC, both coefficients A and B decrease with increasing fracture aperture e . For the same fracture aperture e , both coefficients A and B increase with increasing JRC. Both coefficients A and B of rough samples experience a decrease in 2 orders of magnitude while those coefficients of smooth samples decrease in 1 order of magnitude as the fracture aperture increases from 6 to 14 mm.

4.4. Variation of the Critical Reynolds Number. Based on the data in Table 2 produced from the calculations using equation (13), the distribution of the critical Reynolds number

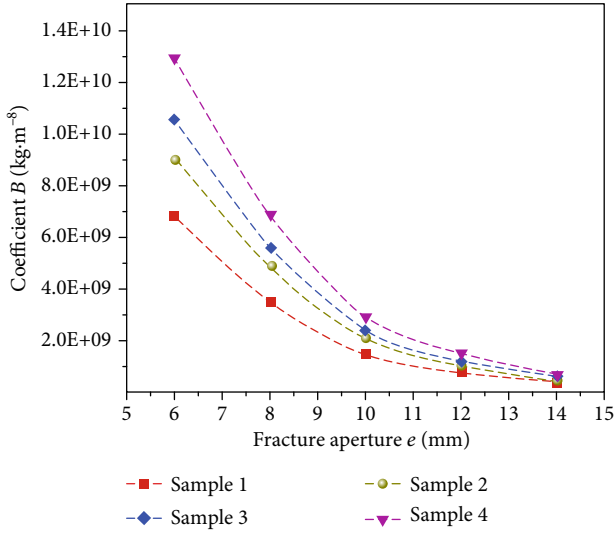


FIGURE 14: Variation of coefficient B with fracture apertures.

Re_c is obtained. As shown in Figure 15, the critical Reynolds number Re_c increases with increasing fracture aperture e , and rougher samples have smaller critical Reynolds numbers Re_c . Combined with the previous analysis, rougher fractures and smaller fracture apertures will make the flow paths more tortuous. Then, the proportion of the nonlinear pressure gradient loss increases. This easily leads to nonlinear flow, resulting in a smaller critical Reynolds number Re_c .

The critical Reynolds number (CRN) model in equation (14) provides a simple method of clear physical significance to quantify Re_c for fluid flow through rock fractures. This model is useful for numerical simulation of fluid flow in fractured networks, in which a decision can be flexibly made to include the nonlinear effect [50].

$$Re_c = \frac{12\rho}{w^2} \frac{E}{1-E} \cdot \frac{1}{10^{6m}\lambda} \cdot e^{m-3}, \quad (14)$$

where λ and m are regression coefficients. As illustrated in Figure 15, simulation data are fitted well the results of the CRN model, which manifest that the numerical simulation can suit for fluid flow in the fracture domain.

In further analysis, the effects of fracture aperture and roughness on the coefficients A and B should be related to the physical meaning of the fluid flow process. In fact, the small fracture aperture and the great rough extent are generally accompanied with more tortuous flow paths, which results in significant inertial effects. This statement is similar to many previous studies. For example, Javadi et al. [29] investigated the role of shear processes on nonlinear flow through rough-walled rock fractures, showing that the coefficients A and B experience 4 and 7 orders of magnitude reduction with increasing shear displacement, respectively, mainly as a result of shear dilation (or equivalently, the increase in fracture aperture) of the fractures. Xiong et al. [51] developed a numerical procedure about nonlinear flow in three-dimension discrete fracture networks (DFN), showing that both the linear coefficient A and the nonlinear coefficient B

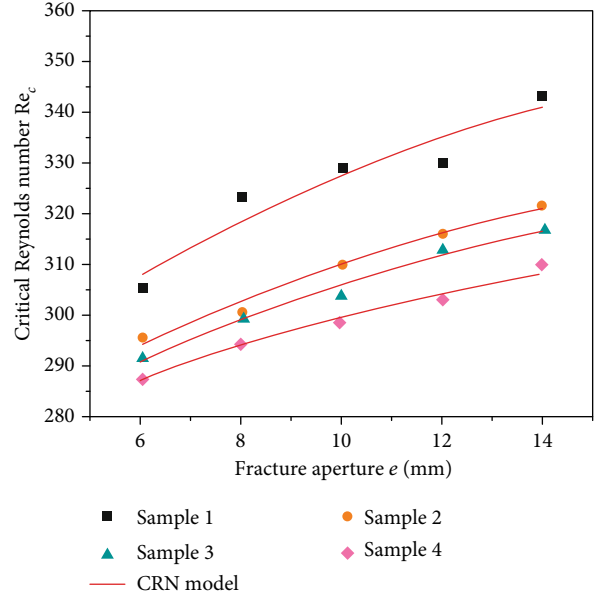


FIGURE 15: Variation of critical Reynolds number with the fracture apertures.

of the Forchheimer law decrease with increasing percolation density, but increase with increasing JRC. The experimental results conducted by Ni et al. [15] on a seepage apparatus have shown that the monomial coefficient and the quadratic coefficient decrease with the increase of the fracture aperture, and with the increase of joint roughness coefficient, the non-Darcy influence coefficient of rough fracture increases.

5. Conclusions

This paper presents a model to investigate non-Darcy flow in single rock fracture domain inverted by digital images, which is further used in flow numerical simulation. In addition, we further discuss the influence of the geometric characteristics of rock fracture domain on the non-Darcy flow. The main conclusions are as follows.

- (1) The rough structure of the fracture surface produces different pixel values in the image. The rough undulating structure of the rock fracture surface can be accurately reduced using digital image processing technology, and then, it can be combined with the actual measurement data to determine the relative position of the upper and lower surfaces of the fracture. This method can be used for inversion of rock fracture domains
- (2) The JRC and fracture aperture significantly influence the fracture fluid flow. For the same conditions, as the JRC increases, the tortuous degree of the fracture flow path increases, the pressure gradient loss caused by the inertial force increases, and the proportion of the kinetic energy of the transformed fluid decreases. For the same conditions, as the fracture aperture increases, the fluid flow path becomes relaxed, the

pressure gradient loss caused by the inertial force decreases, and the fluid velocity increases

- (3) The geometric characteristics of fracture domain have obvious influence on the coefficients of Forchheimer equation. Both coefficients A and B decrease with increasing fracture aperture and increase with increasing JRC. Meanwhile, as the JRC increases or the fracture aperture decreases, the tortuous degree of the fracture seepage path increases, leading to an increase in the proportion of nonlinear pressure gradient loss caused by the inertial force. The critical Reynolds number Re_c decreases accordingly, indicating that the nonlinear flow is more likely to occur at this time
- (4) The conclusion of non-Darcy flow in rock fracture in this paper is consistent with the previous studies, which verifies the feasibility of understanding non-Darcy flow in rock fracture domains by inversion based on digital images

Although the inversion model for the fracture domain presented in this paper provides some insights into the investigation of non-Darcy flow behaviors, compared with CT image method, the inversion method of the fracture domain has limitations in accuracy. Thereby, the inversion method of the fracture domain by digital image needs further improvement.

Data Availability

The data used to support the findings of this study are available from the corresponding author upon request.

Conflicts of Interest

The authors declare that they have no conflicts of interest.

Acknowledgments

The research was funded by the National Natural Science Foundation of China (51774199 and 51974172) and the Natural Science Foundation of Shandong Province (2019MEE004). The authors are thankful for all the support for this basic research.

References

- [1] S. P. Neuman, "Trends, prospects and challenges in quantifying flow and transport through fractured rocks," *Hydrogeology Journal*, vol. 13, no. 1, pp. 124–147, 2005.
- [2] K. Nandlal and R. Weijermars, "Impact on drained rock volume (DRV) of storativity and enhanced permeability in naturally fractured reservoirs: upscaled field case from hydraulic fracturing test site (HFTS), Wolfcamp Formation, Midland Basin, West Texas," *Energies*, vol. 12, no. 20, p. 3852, 2019.
- [3] J. Jing, Y. Yang, and Z. Tang, "Effects of formation dip angle and salinity on the safety of CO₂ geological storage - a case study of Shiqianfeng strata with low porosity and low permeability in the Ordos Basin, China," *Journal of Cleaner Production*, vol. 226, pp. 874–891, 2019.
- [4] V. R. S. De Silva, P. G. Ranjith, M. S. A. Perera, B. Wu, and W. A. M. Wanniarachchi, "A low energy rock fragmentation technique for in-situ leaching," *Journal of Cleaner Production*, vol. 204, pp. 586–606, 2018.
- [5] Y. Xue, W. Sun, and Q. Wu, "The influence of magmatic rock thickness on fracture and instability law of mining surrounding rock," *Geomechanics and Engineering*, vol. 20, no. 6, pp. 547–556, 2020.
- [6] F. Zhou, W. Sun, J. Shao, L. Kong, and X. Geng, "Experimental study on nano silica modified cement base grouting reinforcement materials," *Geomechanics and Engineering*, vol. 20, no. 1, pp. 67–73, 2020.
- [7] W. Sun, F. Zhou, J. Liu, and J. Shao, "Experimental study on Portland cement/calcium sulfoaluminate binder of paste filling," *European Journal of Environmental and Civil Engineering*, pp. 1–16, 2020.
- [8] Z. Zhao, Q. Ma, Y. Tan, and X. Gao, "Load transfer mechanism and reinforcement effect of segmentally yieldable anchorage in weakly consolidated soft rock," *Simulation*, vol. 95, no. 1, pp. 83–96, 2018.
- [9] J. Wang, P. Qiu, J. Ning, L. Zhuang, and S. Yang, "A numerical study of the mining-induced energy redistribution in a coal seam adjacent to an extracted coal panel during longwall face mining: a case study," *Energy Science & Engineering*, vol. 8, no. 3, pp. 817–835, 2020.
- [10] T. F. Fu, T. Xu, M. J. Heap, P. G. Meredith, and T. M. Mitchell, "Mesoscopic time-dependent behavior of rocks based on three-dimensional discrete element grain-based model," *Computers and Geotechnics*, vol. 121, 2020.
- [11] Y. L. He, Y. J. Tao, and L. Z. Yang, "Experimental research on hydraulic behaviors in a single joint with various values of JRC," *Chinese Journal of Rock Mechanics and Engineering*, vol. 29, no. S1, pp. 3237–3240, 2010.
- [12] R. W. Zimmerman and G. S. Bodvarsson, "Hydraulic conductivity of rock fractures," *Transport in Porous Media*, vol. 23, no. 1, pp. 1–30, 1996.
- [13] P. A. Witherspoon, J. S. Y. Wang, K. Iwai, and J. E. Gale, "Validity of cubic law for fluid flow in a deformable rock fracture," *Water Resources Research*, vol. 16, no. 6, pp. 1016–1024, 1980.
- [14] A. Nowamooz, G. Radilla, and M. Fourar, "Non-Darcian two-phase flow in a transparent replica of a rough-walled rock fracture," *Water Resources Research*, vol. 45, no. 7, pp. 4542–4548, 2009.
- [15] X. Ni, Y. Niu, Y. Wang, and K. Yu, "Non-Darcy flow experiments of water seepage through rough-walled rock fractures," *Geofluids*, vol. 2018, Article ID 8541421, 12 pages, 2018.
- [16] H. G. Zhu, H. P. Xie, C. Yi et al., "Analysis of properties of fluid flow in rock fractures," *Chinese Journal of Rock Mechanics and Engineering*, vol. 32, no. 4, pp. 657–663, 2013.
- [17] X. Xiong, B. Li, Y. Jiang, T. Koyama, and C. Zhang, "Experimental and numerical study of the geometrical and hydraulic characteristics of a single rock fracture during shear," *International Journal of Rock Mechanics and Mining Sciences*, vol. 48, no. 8, pp. 1292–1302, 2011.
- [18] B. Y. Su, M. L. Zhan, and J. Zhao, "Study on fracture seepage in the imitative nature rock," *Chinese Journal of Geotechnical Engineering*, vol. 17, no. 5, pp. 19–24, 1995.

- [19] N. Barton and V. Choubey, "The shear strength of rock joints in theory and practice," *Rock Mechanics*, vol. 10, no. 1-2, pp. 1-54, 1977.
- [20] Y. Ju, Q. G. Zhang, Y. M. Yang, H. P. Xie, F. Gao, and H. J. Wang, "An experimental investigation on the mechanism of fluid flow through single rough fracture of rock," *Science China Technological Sciences*, vol. 56, no. 8, pp. 2070-2080, 2013.
- [21] L. Z. Xie, C. Gao, L. Ren, and C. B. Li, "Numerical investigation of geometrical and hydraulic properties in a single rock fracture during shear displacement with the Navier-Stokes equations," *Environmental Earth Sciences*, vol. 73, no. 11, pp. 7061-7074, 2015.
- [22] A. F. Angelin, F. M. da Silva, L. A. G. Barbosa, R. C. C. Lintz, M. A. G. de Carvalho, and R. A. S. Franco, "Voids identification in rubberized mortar digital images using K-Means and Watershed algorithms," *Journal of Cleaner Production*, vol. 164, pp. 455-464, 2017.
- [23] C. Thomas, J. Setién, J. A. Polanco, J. de Brito, and F. Fiol, "Micro- and macro-porosity of dry- and saturated-state recycled aggregate concrete," *Journal of Cleaner Production*, vol. 211, pp. 932-940, 2019.
- [24] W. C. Zhu, T. H. Yang, Z. G. Huo, W. Z. Wei, and C. H. Wei, "Numerical simulation on gas flow through coal seam based on digital image-based technique," *Journal of China Coal Society*, vol. 34, no. 1, pp. 18-23, 2009.
- [25] W. C. Zhu, Y. M. Kang, T. H. Yang, Z. H. Li, and J. S. Liu, "Application of digital image-based heterogeneity characterization in coupled hydromechanics of rock," *Chinese Journal of Geotechnical Engineering-Chinese Edition*, vol. 28, no. 12, pp. 2087-2091, 2006.
- [26] Y.-F. Chen, J.-Q. Zhou, S.-H. Hu, R. Hu, and C.-B. Zhou, "Evaluation of Forchheimer equation coefficients for non-Darcy flow in deformable rough-walled fractures," *Journal of Hydrology*, vol. 529, pp. 993-1006, 2015.
- [27] L. C. Zou, L. Jing, and V. Cvetkovic, "Shear-enhanced nonlinear flow in rough-walled rock fractures," *International Journal of Rock Mechanics and Mining Sciences*, vol. 97, pp. 33-45, 2017.
- [28] R. W. Zimmerman, A. Al-Yaarubi, C. C. Pain, and C. A. Grattoni, "Non-linear regimes of fluid flow in rock fractures," *International Journal of Rock Mechanics and Mining Sciences*, vol. 41, pp. 163-169, 2004.
- [29] M. Javadi, M. Sharifzade, K. Shahriar, and Y. Mitani, "Critical Reynolds number for nonlinear flow through rough-walled fractures: the role of shear processes," *Water Resources Research*, vol. 50, no. 2, pp. 1789-1804, 2014.
- [30] Z. Zhang and J. Nemeik, "Fluid flow regimes and nonlinear flow characteristics in deformable rock fractures," *Journal of Hydrology*, vol. 477, pp. 139-151, 2013.
- [31] M. Wang, Y. F. Chen, G. W. Ma, J. Q. Zhou, and C. B. Zhou, "Influence of surface roughness on nonlinear flow behaviors in 3D self-affine rough fractures: Lattice Boltzmann simulations," *Advances in Water Resources*, vol. 96, pp. 373-388, 2016.
- [32] Z. Zhang, J. Nemeik, and S. Ma, "Micro- and macro-behaviour of fluid flow through rock fractures: an experimental study," *Hydrogeology Journal*, vol. 21, no. 8, pp. 1717-1729, 2013.
- [33] S. H. Lee, I. W. Yeo, K. K. Lee, and R. L. Detwiler, "Tail shortening with developing eddies in a rough-walled rock fracture," *Geophysical Research Letters*, vol. 42, no. 15, pp. 6340-6347, 2015.
- [34] C. C. Xia, X. Qian, P. Lin, W. M. Xiao, and Y. Gui, "Experimental investigation of nonlinear flow characteristics of real rock joints under different contact conditions," *Journal of Hydraulic Engineering*, vol. 143, no. 3, p. 04016090, 2017.
- [35] Q. Yin, G. Ma, H. Jing et al., "Hydraulic properties of 3D rough-walled fractures during shearing: an experimental study," *Journal of Hydrology*, vol. 555, pp. 169-184, 2017.
- [36] Q. Yin, H. Jing, G. Ma, H. Su, Y. Wang, and R. Liu, "Investigating the roles of included angle and loading condition on the critical hydraulic gradient of real rock fracture networks," *Rock Mechanics and Rock Engineering*, vol. 51, no. 10, pp. 3167-3177, 2018.
- [37] Q. Yin, R. Liu, H. Jing, H. Su, L. Yu, and L. He, "Experimental study of nonlinear flow behaviors through fractured rock samples after High-Temperature exposure," *Rock Mechanics and Rock Engineering*, vol. 52, no. 9, pp. 2963-2983, 2019.
- [38] Q. Zhang, J. Choo, and R. I. Borja, "On the preferential flow patterns induced by transverse isotropy and non-Darcy flow in double porosity media," *Computer Methods in Applied Mechanics and Engineering*, vol. 353, pp. 570-592, 2019.
- [39] H. Kim, E. Ahn, S. Cho, M. Shin, and S. H. Sim, "Comparative analysis of image binarization methods for crack identification in concrete structures," *Cement and Concrete Research*, vol. 99, pp. 53-61, 2017.
- [40] X. Wei, S. Sonoda, C. Mishra et al., "Comparison of choroidal vascularity markers on optical coherence tomography using two-image binarization techniques," *Investigative Ophthalmology & Visual Science*, vol. 59, no. 3, pp. 1206-1211, 2018.
- [41] S. Gontani, T. Ohashi, K. Miyanaga, T. Kurata, Y. Akatani, and S. Matsumoto, "Structural comparison of two bisphenol S derivatives used as colour developers in high-performance thermal paper," *Dyes and Pigments*, vol. 139, pp. 549-555, 2017.
- [42] M. Prashasthi, K. S. Shrivaya, A. Deepak, M. Mulimani, and K. G. Shashidhar, "Image processing approach to diagnose eye diseases," in *Asian Conference on Intelligent Information and Database Systems*, pp. 245-254, Springer, Cham, 2017.
- [43] R. Lukac and K. N. Plataniotis, "A taxonomy of color image filtering and enhancement solutions," *Advances in imaging and electron physics*, vol. 140, no. 5, pp. 187-264, 2006.
- [44] M. W. Schwarz, W. B. Cowan, and J. C. Beatty, "An experimental comparison of RGB, YIQ, LAB, HSV, and opponent color models," *ACM Transactions on Graphics (TOG)*, vol. 6, no. 2, pp. 123-158, 1987.
- [45] J. Zhao, L. Yin, and W. Guo, "Stress-seepage coupling of cataclastic rock masses based on digital image technologies," *Rock Mechanics and Rock Engineering*, vol. 51, no. 8, pp. 2355-2372, 2018.
- [46] P. G. Ranjith and D. R. Viete, "Applicability of the 'cubic law' for non-Darcian fracture flow," *Journal of Petroleum Science and Engineering*, vol. 78, no. 2, pp. 321-327, 2011.
- [47] Z. W. Zeng and R. Grigg, "A criterion for non-Darcy flow in porous media," *Transport in Porous Media*, vol. 63, no. 1, pp. 57-69, 2006.
- [48] F. Xiong, Q. Jiang, Z. Ye, and X. Zhang, "Nonlinear flow behavior through rough-walled rock fractures: the effect of contact area," *Computers and Geotechnics*, vol. 102, pp. 179-195, 2018.
- [49] Y. Chen, H. Lian, W. Liang, J. Yang, V. P. Nguyen, and S. P. A. Bordas, "The influence of fracture geometry variation on non-Darcy flow in fractures under confining stresses," *International*

Journal of Rock Mechanics and Mining Sciences, vol. 113, pp. 59–71, 2019.

- [50] J. Q. Zhou, S. H. Hu, S. Fang, Y. F. Chen, and C. B. Zhou, “Nonlinear flow behavior at low Reynolds numbers through rough-walled fractures subjected to normal compressive loading,” *International Journal of Rock Mechanics and Mining Sciences*, vol. 80, pp. 202–218, 2018.
- [51] F. Xiong, Q. Jiang, C. Xu, X. Zhang, and Q. Zhang, “Influences of connectivity and conductivity on nonlinear flow behaviours through three-dimension discrete fracture networks,” *Computers and Geotechnics*, vol. 107, pp. 128–141, 2019.

Research Article

Permeability Experiment of Fractured Rock with Rough Surfaces under Different Stress Conditions

Zilong Zhou,¹ Jing Zhang,¹ Xin Cai ,¹ Shanyong Wang,² Xueming Du,³ and Haizhi Zang^{1,2}

¹School of Resources and Safety Engineering, Central South University, Changsha 410083, China

²Faculty of Engineering and Built Environment, ARC Centre of Excellence for Geotechnical Science and Engineering, The University of Newcastle, Callaghan 2308, Australia

³College of Water Conservancy and Environmental Engineering, Zhengzhou University, Zhengzhou 450001, China

Correspondence should be addressed to Xin Cai; xincai@csu.edu.cn

Received 24 February 2020; Accepted 20 May 2020; Published 1 June 2020

Academic Editor: Qian Yin

Copyright © 2020 Zilong Zhou et al. This is an open access article distributed under the Creative Commons Attribution License, which permits unrestricted use, distribution, and reproduction in any medium, provided the original work is properly cited.

To investigate the permeability changes and the mechanisms of fractured rock under dynamic and static stresses produced by earthquakes, permeability experiments on fractured rock with rough surfaces under axial dynamic and static stresses were conducted on the MTS815 Rock Mechanics Testing System. Surface asperity was investigated by scanning the specimen surfaces before and after testing. The results show that the roughness of fracture surface has a great influence on the permeability when the axial displacement is not enough to cause the fracture rock to slip. Moreover, the rougher fracture surface leads to severer surface damage as indicated by the more gouge productions. The accumulation of gouge materials on larger roughness fracture surfaces causes a slow drop in permeability. The fracture surfaces experience larger degradations, but it has small weights of gouge materials on fracture surface after testing under axial dynamic stress. The reason is that the gouge material transport and mobilization tend to occur in process of dynamic loading. Therefore, the permeability drops of axial dynamic stress are larger than those of axial static stress.

1. Introduction

Permeability of rock fracture is governing fluid filtration rates and particle mobilization [1] and the main parameter of the safety properties of fractured rock mass [2]. Permeability varies with the changes of roughness [3] and the production of gouge materials [4], when the deformation of fracture occurs under stress [5–7]. It is known that fractured rock is often subjected to significant dynamic and static stresses produced by earthquakes [8–19]. Therefore, the permeability changes and the mechanisms of fractured rock under dynamic stress and static stress are very important to predict seismic activity.

Permeability changes caused by various mechanisms, including the unclogging and clogging of fractures, variations in the fracture aperture, and the particle mobilization, under static stress have been observed in both the field and the laboratory. Some researchers found the permeability of fracture decreases with the increase effective static stress [20–26]. Vogler et al. found that gouge material production may have

caused clogging of the main fluid flow channels, resulting in reductions of permeability by up to one order of magnitude [4]. Zhao et al. investigated that the permeability decreases with the fracture apertures decrease in effective stress, and the effect of fracture roughness on the permeability is related to the magnitude of effective stress [27]. Wu et al. measured the roughness and the permeability drop with effective stress. The permeability of natural fracture only partially recovers after effective stress returns to initial value and decreases due to produced gouge blocking fluid flow pathways [3].

Some studies suggested that dynamic stress can lead to the severe fatigue damage or failure of rock even when the stress level is significantly lower than the static strength [28–31] and can change permeability. Brodsky [32] and Elkhoury et al. [33] found that distant earthquakes may even increase the permeability in faults by unclogging of fractures in the field. Xue et al. [34] and Shi and Wang [35] studied that after a large earthquake, the fault zone permeability transiently increases because of earthquakes generating fractures

in a damage fault in Wenchuan earthquake. Faoro et al. [36] showed transient increase in the effective permeability of the rock mass caused by dilates in the fracture aperture with fluid pressure at laboratory scale. Candela et al. [37] conducted that transient fluid pressure in fractured rock commonly involves permeability increases and has been attributed to mobilization of fine particles in laboratory experiments. In addition, a few studies have detected that earthquakes could decrease permeability [38–40]. For example, Shi et al. found the earthquake-induced permeability decrease in the fault zone reduced the recharge from deep hot water [39]. Given the azimuthal distribution of distant earthquakes, the observed permeability decrease could be attributed to the seismic wave-induced clogging of fractures that compose the flow paths in the shallow crust [40]. Shmonov et al. [8] applied oscillatory stresses to unfractured cores at high confining pressures and temperatures and found that permeability is more likely to increase. Liu and Manga [41] conducted similar experiments on already fractured sandstone cores saturated with deionized water and showed that the permeability in fractured sandstone can potentially decrease under the effect of dynamic stresses. Various mechanisms have been tried to explain the increases in permeability caused by dynamic stresses induced by the passage of seismic waves [40]. However, these mechanisms are poorly understood, and thus, it is difficult to predict permeability increase or decrease under dynamic stress and static stress.

In this study, the experiments of effect of axial dynamic stress and static stress on permeability were conducted on the MTS815 Rock Mechanics Testing System. The fracture roughness change was investigated by scanning the sample surfaces before and after testing. The permeability characteristics under axial dynamic stress and axial static stress were analyzed considering the asperity degradations and gouge materials of fracture surfaces. This provides the information on the impact of production, transport, and flow mobilization of gouge material on permeability changes under dynamic stress.

2. Test Preparation

2.1. Sample Preparation. The rock material used in this study is a fine-grained sandstone collected from the northwest of Kunming, Yunnan province of China. A series of preliminary tests have been conducted on standard rock samples to determine the crucial mechanical parameters of the sandstone, such as Young's modulus (34 GPa), Poisson's ratio (0.3), and uniaxial compressive strength (86 MPa).

All samples were extracted from one single sandstone slab to minimize the variations in properties [42]. Then, samples were manufactured into cylindrical geometry with 50 mm in diameter and 100 mm in length. Each sample was split at a 30-degree angle with respect to the axis to form a fracture surface, as shown in Figure 1(a). Subsequently, one borehole with 3 mm diameter was drilled parallel to the axial direction, at the corner of each half to facilitate fluid flow from core holders into the fracture (Figure 1(b)). After that, samples were saturated by soaking in water for more than 12 hours.

2.2. Surface Roughness Measurements. Fracture surface characteristics were scanned with an optical three-dimensional scanner manufactured by GOM (ATOS III TRIPLE SCAN). The ATOS Core sensor projects fringe patterns on the object surface, which are recorded by two cameras. The patterns form a phase shift that is based on a sinusoidal intensity distribution which enables one to calculate the three-dimensional (3D) surfaces. The photogrammetry scanner is calibrated with two tests. The diameter and shape of a sphere and the distance between two spheres that are mounted on a plate are measured with the photogrammetry scanner to derive calibration errors and accuracy. All equipment used for calibration are specifically developed by the company GOM, which manufactures the scanner. The overall scanning accuracy is less than 0.01 mm within the scanning range of $100 \times 75 \text{ mm}^2$, and length deviation errors are between 0.009 and 0.027 mm. The measurement resolution is 3692×2472 pixel with optimized calibration deviations of 0.014 ± 0.001 pixels. In addition, the tensile fractures were prepared carefully with a high degree of fracture matching; therefore, the joint matching coefficient of the fractures is close to 1.0. So we only use one fracture surface of each sample in the scanning contour before and after testing. After the 3D scanning, the digitized data were exported in xyz file format to estimate the fracture roughness. The surface roughness parameter, Z_2 , the root mean square of the slope of a 2D profile, is widely used to correlate with the JRC value [43–46]. For a 2D profile, Z_2 is given by

$$Z_2 = \left[\frac{1}{(n-1)(\Delta x)^2} \sum_{i=1}^{i=n-1} (Z_{i+1} - Z_i)^2 \right]^{0.5}, \quad (1)$$

$$\text{JRC} = 61.79Z_2 - 3.47, \quad (2)$$

where Z_2 is the root mean square of the slope of a given 2D profile, n is the number of data points along the 2D profile, Δx is the interval between the data points, Z_i is the value of the asperity height at point i , and JRC is the joint roughness coefficient.

As in many previous studies, an interval of 0.5 mm for sampling points was selected to estimate the roughness [43–46]. JRC of each profile on the fracture surface was calculated using equation (2), and the mean value of JRC was calculated to characterize the roughness of the fracture surface as listed in Table 1. They are a set of 10 typical roughness profiles as shown in Figure 2. The mean JRC values of samples Ss-1 and Sd-1 belong to the roughness profile type 4, that of samples Ss-2 and Sd-2 is the roughness profile type 5, and that of samples Ss-3 and Sd-3 is of the roughness profile type 10. The same process was repeated for the damaged surfaces after testing to analyze the surface changes that occurred during the experiments and compare these to the changes in permeability during the experiment.

2.3. Experimental Setup and Procedure. All experiments were conducted on a servo-controlled Rock Mechanics Testing System (MTS815) housed at the Advanced Research Center

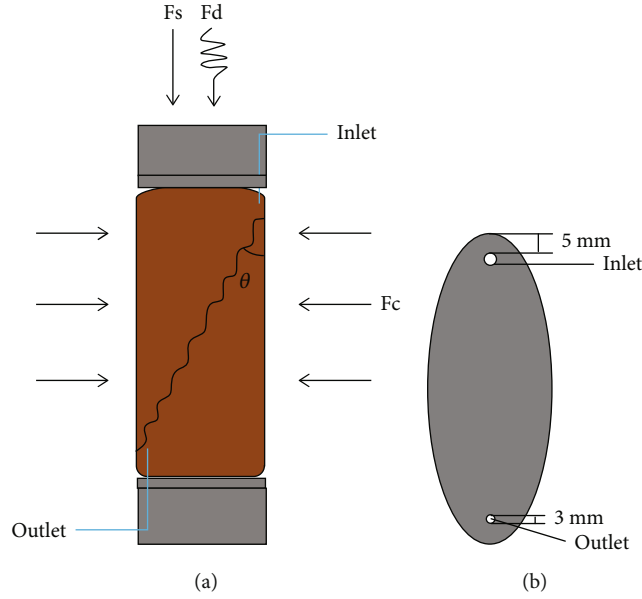


FIGURE 1: (a) Sketch of fractured rock sample and (b) a rough fracture with boreholes for fluid flow.

in Central South University. The system consists of five main units: a triaxial cell, a loading unit, a water supply unit, a deformation and pressure monitoring unit, and a data-acquisition unit. The maximum loading capacity of the system is up to 4600 kN. The maximum confining pressure and pore water pressure are 140 MPa. The axial deformation of the sample is measured by a pair of linear variable displacement transducers (LVDTs). The system is configured with a transient pulse apparatus for the permeability test of cylinder rock specimen. The permeability was measured with a pressure pulse-decay technique testing method as shown in Figure 3.

Two suites of permeability experiments on fractured rock were conducted. In the “axial dynamic test” suite of experiments, three groups (Sd-1, Sd-2, and Sd-3) of tests were designed. The experimental procedure includes the following steps:

- (1) Each sample was wrapped in a Teflon tape to avoid the slippage in the opening fracture when exerting the confining stress and preaxial static stress. Then, the sample was circumferentially sealed in a thermo-shrinking plastic membrane to separate the sample from the confining fluid. After that, the rock sample was placed at the triaxial cell filled with hydraulic oil
- (2) The confining stress (σ_3) and static axial stress (σ_s) were successively increased to the designed levels at a constant loading rate of 0.1 MPa/s. They were, respectively, set at 5 MPa and 10 MPa in all tests and kept constant during the whole test
- (3) Five minutes later, the sample and the loading system became stable. The successive axial sine wave was applied to the top of the sample by a

rigid loading bar. The actual axial stress is the superposition of the static prestress and the cyclic stress as

$$\sigma_{sd} = \sigma_s + \sigma_d \sin(2\pi ft), \quad (3)$$

where σ_{sd} is the superimposed axial stress, σ_s is static axial stress, σ_d is the amplitude of dynamic axial stress, f is the frequency, and t is the time. Preliminary compression tests on the fracture rock sample suggested that the critical axial stress for the slippage of the sample under the confining pressure of 5 MPa is 15 MPa. Hence, the superimposed axial stress should be limited below the critical stress. In this study, the axial stress was independent variables as listed in Table 1. Three groups of tests were designed according to the amplitude of dynamic stress, i.e., 0.25, 1.25, 2.5, 3.75, and 5 MPa. The loading paths with the frequency of 1 Hz were plotted in Figure 4

- (4) After the sample was subjected to 100 cycles of dynamic disturbance, the cyclic loading stopped, and then, the confining pressure and static axial stress were still maintained at 5 MPa and 10 MPa. Then, an initial water pressure was applied to both the upstream and downstream reservoirs, at a loading rate of 0.2 MPa/min. Next, the water pressure in the upstream reservoir suddenly increased to form a differential pressure (i.e., an initial pulse pressure) which makes the water flow from the top to the bottom through the fracture, as shown in Figure 3. The time pulse pressure (ΔP) decreased over time until equilibrium was attained. It was automatically monitored and recorded by two pressure gages in the water

TABLE 1: Test parameter for stress conditions.

Sample	Mean JCR value	Roughness profile type	Subset	σ_3 (MPa)	Fs (MPa)	Fd (MPa)	Cycles	f (Hz)
Sd-1	6.26	4	1	5	10	0.25	100	1
			2			1.25		
			3			2.5		
			4			3.75		
			5			5		
Sd-2	9.256	5	1	5	10	0.25	100	1
			2			1.25		
			3			2.5		
			4			3.75		
			5			5		
Sd-3	19.35	10	1	5	10	0.25	100	1
			2			1.25		
			3			2.5		
			4			3.75		
			5			5		
Ss-1	7.025	4	1	5	5	0	100	0
			2		7.5			
			3		10			
			4		12.5			
			5		15			
Ss-2	9.135	5	1	5	5	0	100	
			2		7.5			
			3		10			
			4		12.5			
			5		15			
Ss-3	20	10	1	5	5	0	100	0
			2		7.5			
			3		10			
			4		12.5			
			5		15			

tank. Accordingly, the permeability of the fractured sample can be obtained (see Section 2.4)

In the ‘‘axial static test’’ suite of experiments, three groups (Ss-1, Ss-2, and Ss-3) of tests were also designed. In each experiment, the axial stress was raised from 5 to 15 MPa in step of 2.5 MPa, and the confining pressure was kept at 5 MPa as listed in Table 1. The permeability of fractured rock was measured at each axial loading.

2.4. Permeability Measurements. Rock permeability can be measured using a steady state method, in which the flow rate of a fluid through a sample is measured for a known hydraulic pressure gradient. When permeability is low, however, a long time may be required to establish a steady state. This method is based on the analysis of the decay of a small-step change of the pressure imposed at one end of a specimen.

In this study, the differential pressure along the fault plane after achieving a pressure step is measured; then, the permeability is calculated as [3]

$$k = \frac{cL\mu}{A_2 P_m (1/V_1 + 1/V_2)}, \quad (4)$$

where P_m is the average value of P_{V_1} and P_{V_2} , P_{V_1} and P_{V_2} are the upstream and downstream pressure, μ is the water viscosity (1.01×10^{-3} Pa · s), L is the distance between the two drilled boreholes along the fault plane, A_2 is the cross-sectional area of the fracture, V_1 and V_2 are the upstream and downstream reservoir volumes ($V_1 = V_2 = 3.32 \times 10^{-7}$ m³ for the MTS experimental setup as shown in Figure 3), and c is the rate of the variation rate of the time pulse pressure with time, which can be determined according to the evolution of the time pulse pressure (ΔP). Brace et al. [47] and Jang et al.

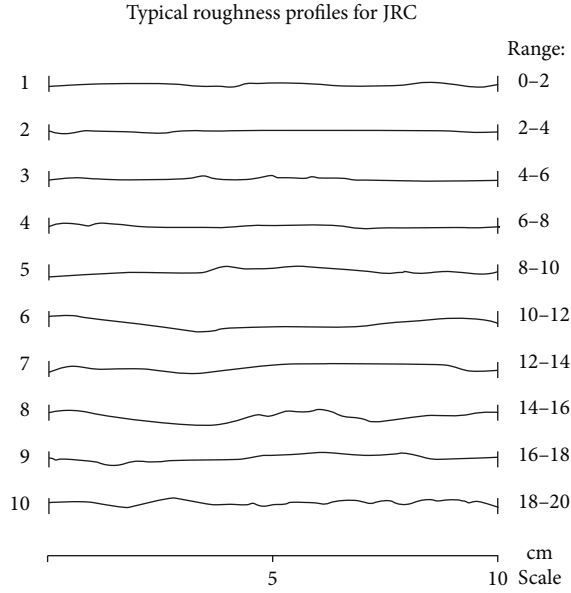


FIGURE 2: 10 typical roughness profiles showing the range of JRC values [44].

[48] suggested that the time pulse pressure exponentially attenuates with time as

$$\Delta P(t) = P_0(e^{-ct}) + c_0, \quad (5)$$

where P_0 is the initial pulse pressure at time $t = 0$ and c_0 is a fitting constant. Figure 5 presents the variation of the time pulse pressure versus time. It can be seen that the decay model of the time pulse pressure (equation (5)) matches the trend of test data well. Clearly, the coefficient c is 0.0021.

3. Results and Discussions

Our data shows that (1) the permeability changes are negatively correlated with the axial stress, (2) the permeability changes are affected by the roughness of fracture surfaces, and (3) the fractures of dynamic stress have slightly higher permeability drops compared to the fracture of static stress. We consider three influencing factors for transient permeability changes: (i) initial mean value of JRC, (ii) asperity degradation and gouge materials, and (iii) particle mobilization.

3.1. Permeability Changes. Figure 6 depicts the permeability evolution and axial displacements under axial dynamic stress. Figure 6 shows the permeability variation of Sd-1 and Sd-2 decreases at similar rates, while the axial displacements of Sd-1 and Sd-2 increase at similar rates. The permeability of Sd-3 drops slower and the axial displacement rises faster. Overall, three groups show an apparent reduction in the permeability with the rising amplitude under axial dynamic stress, an enhancement in axial displacement with that. This phenomenon does not match those observed in earlier studies that the decrease of permeability is sharp with increasing slip displacement [3, 4, 49, 50]. Figure 7 indicates the changes of permeability before and after testing under

axial dynamic stress and axial static stress. It is found that the permeability of Sd-1 and Sd-2 drops with 35% and 37% decline rate, and that of Sd-3 goes down 44% as presented in Figure 7. However, the mean JRC values of samples Sd-1 and Sd-2 belonging to the roughness profile types 4 and 5 are lower than those of sample Sd-3 in Table 1.

The similar phenomenon occurs under static stress. The changes of permeability and axial displacements of Ss-1 and Ss-2 are similar, while the permeability of Ss-3 decreases slowly and the axial displacements increase largely as presented in Figure 8. The roughness of fracture surfaces of Ss-1 and Ss-2 is smaller than that of Ss-3 under axial static stress (Table 1). The permeability values of Ss-1, Ss-2, and Ss-3, respectively, decrease with the decline rates 13%, 14%, and 20% in Figure 9. Figures 7 and 8 show that all the axial displacements are less than 1 mm and the fracture rocks are not damaged in two suites of permeability experiments. This indicates that when the axial displacement is not enough to cause the fracture rock to slip under the same stress conditions, the roughness of fracture surface has a great influence on the permeability.

3.2. Topographic Changes of Fracture Surfaces. Due to the large axial forces, significant surface deformation is expected in the fracture plane of the sample. For detailed analysis, the photogrammetric surface scans of the fracture sample and the mean values of JRC are generated before and after two suites of permeability experiments as shown in Figures 10–13. Photogrammetric scans produced profiles of the surfaces, which are oriented according to a best-fit plane in the $x - y$ coordinates. For visualization and comparison, an asperity height of 0 mm is assigned to the lowest point of the surface for Figures 10 and 12. Note that the same color scales are used. The changes of the mean values of JRC before and after testing under dynamic stress and that under static stress are, respectively, presented in Figure 13.

Figures 10 and 11 show the surface scans and the changes of the mean values of JRC of samples Sd-1, Sd-2, and Sd-3 before and after testing under axial dynamic stress. Comparing the fracture surfaces before and after testing, the maximum surface reliefs of Sd-1, Sd-2, and Sd-3 are, respectively, from 3.635 mm to 3.406 mm, 8.897 mm to 6.625 mm, and 5.448 mm to 4.835 mm in asperity height (Figure 10). Figure 11 indicates that the mean values of JRC of Sd-1 and Sd-2 are, respectively, from 6.26 to 3.45 and from 9.26 to 4.01 with the reductions of 2.81 and 5.25, while the mean values of JRC of Sd-3 drop from 19.35 to 6.42 with a higher reduction of 12.93. Therefore, the larger fracture roughness of Sd-3 is more decreased. This means that fracture surfaces with a high degree of relief and a large mean value of JRC variability experience more degradation during testing.

Under axial static stress, the initial maximum surface reliefs of Ss-1, Ss-2, and Ss-3 are 4.413 mm, 9.688 mm, and 5.443 mm and the initial mean values of JRC of Ss-1, Ss-2, and Ss-3 are 7.03, 9.14, and 20 as shown in Figures 12 and 13. After testing, the mean values of JRC are 4.75, 5.67, and 13.15. This means that the JRC degradations of 2.28, 3.47, and 6.85 are induced on the fracture surfaces under static stress.

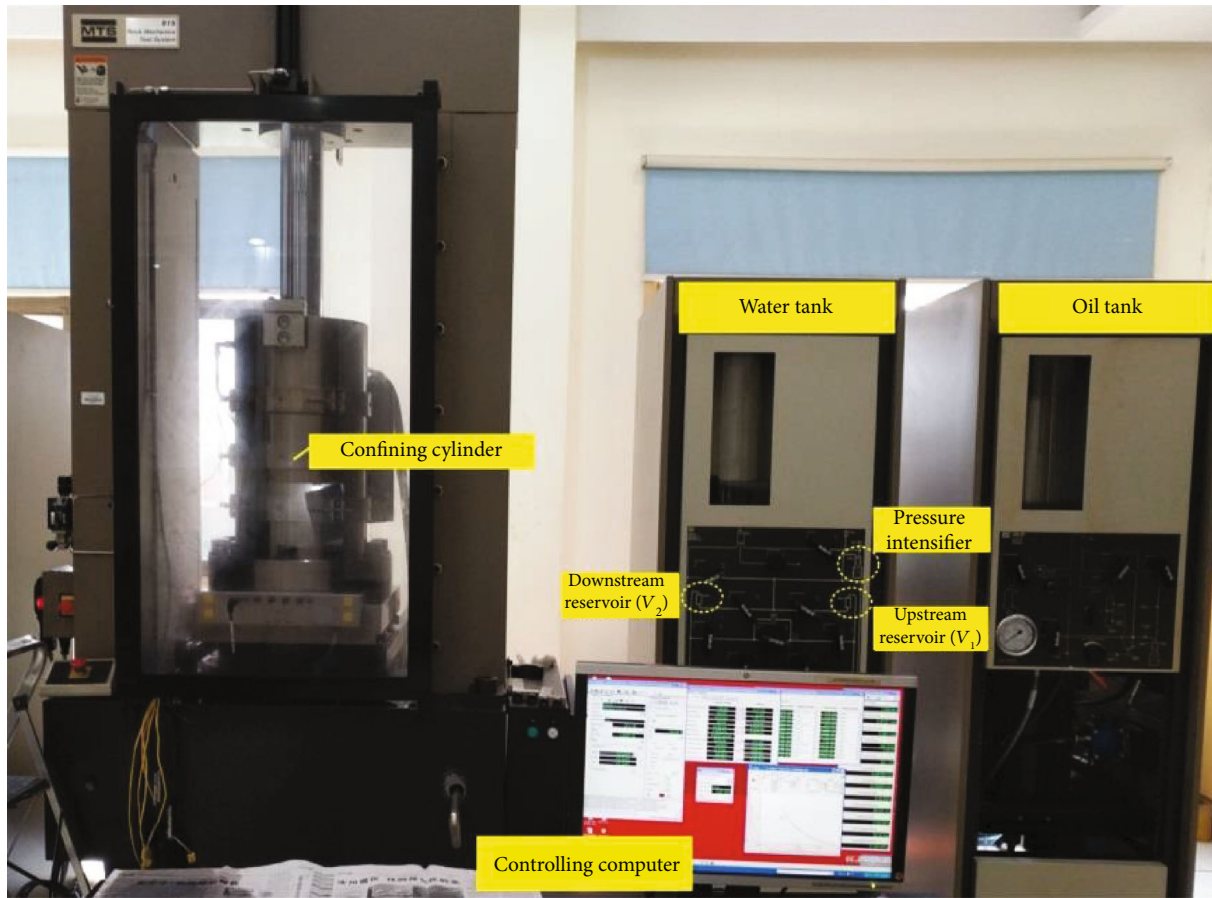


FIGURE 3: Schematic of transient permeability system.

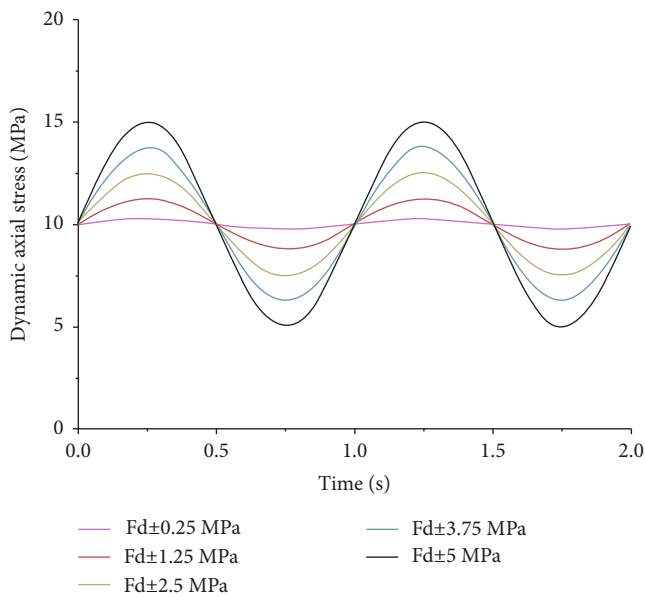


FIGURE 4: Schematic of loading paths.

3.3. Analysis of Gouge Material. Due to the experimental setup, the gouge material was not collected at the outflow end of the experiment, but that left on the fracture surface

after testing was collected. The gouge material was then brushed off the surface and weighed. The weight of gouge material collected after testing is shown in Figures 14 and 15. The weights of gouge material on fracture surface of samples Sd-1, Sd-2, and Sd-3 under dynamic stress are 1.20 g, 1.23 g, and 1.44 g, while those on fracture surface of samples Ss-1, Ss-2, and Ss-3 under static stress are 2.07 g, 2.11 g, and 2.24 g.

The mean value drop of JRC and the weight of the generated gouge materials under dynamic stress were compared as shown in Figure 14. The initial mean value of JRC of Sd-1 is smaller than that of Sd-2, and the initial mean value of JRC of Sd-1 and Sd-2 is lower than that of Sd-3 (Table 1), while the drop of mean value of JRC and the weights of fracture gouge produced by Sd-1 and Sd-2 are lower than those of Sd-3 during dynamic loading.

The same phenomenon occurs under static stress in Figure 15. The initial mean value of JRC of Ss-1 and Ss-2 is smaller than that of Ss-3 under axial static stress (Table 1). The drop of mean value of JRC and the weights of fracture gouge produced by Ss-1 and Ss-3 are lower than those of Ss-2 during static loading. This means that the larger mean value of JRC of fracture surface leads to larger surface damage as indicated by the more gouge productions. This observed gouge material production could potentially cause the hysteretic behavior by subsequently clogging flow paths, thus

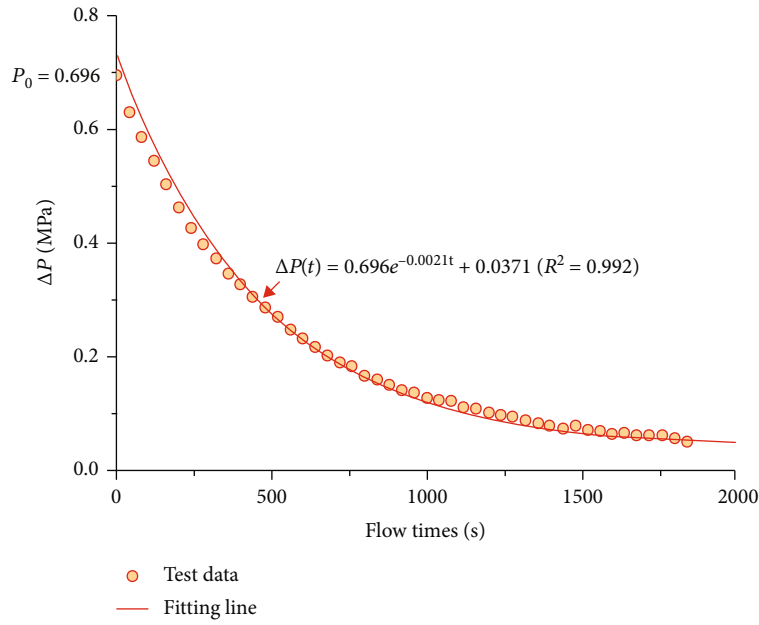


FIGURE 5: A representative differential pressure versus flow time curve.

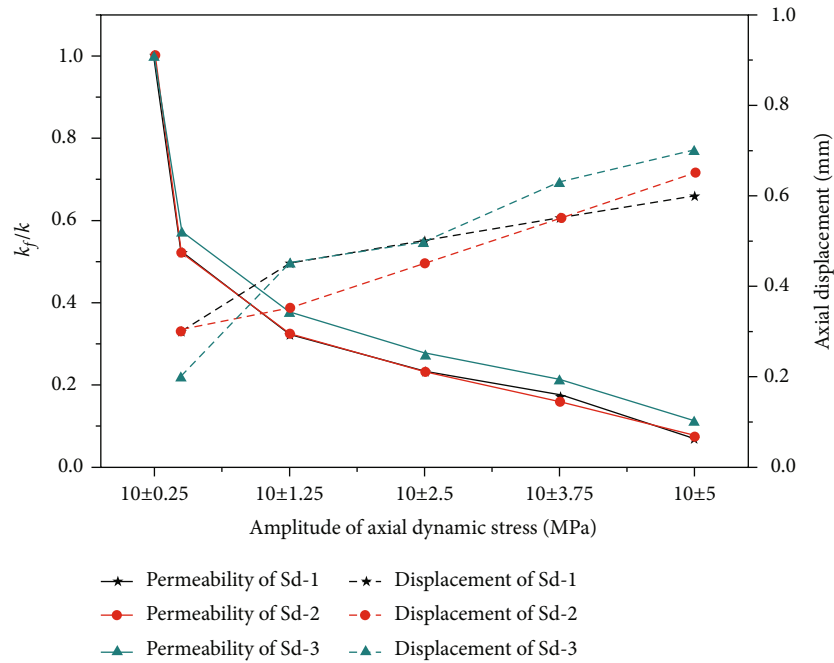


FIGURE 6: Permeability evolution and axial displacement of Sd-1, Sd-2, and Sd-3 under different amplitudes of axial stress of 10 MPa.

lowering the fracture permeability and bringing about the irregular permeability values [4]. This helps to explain that the permeability of Sd-2 drops slower than that of Sd-1 and Sd-2 under dynamic stress (Figure 6). The changes of permeability of Ss-1 and Ss-2 are similar, while the permeability of Ss-3 decreases slowly under static stress (Figure 8). Generally, under the same stress conditions, the accumulation of gouge materials on larger roughness fracture surfaces causes slower drops of permeability.

3.4. Comparing Dynamic Stress and Static Stress. Comparing the permeability changes before and after testing under dynamic and static stresses, the permeability drop, the mean value drop of JRC, and the weight of gouge material are indicated in Figure 16. Under similar roughness profile type for JRC, the permeability drops of fracture surfaces of Sd-1, Sd-2, and Sd-3 more than 35% under axial dynamic stress are larger than the drops of permeability less than 20% under axial static stress. The mean value drop of JRC of Sd-1, Sd-

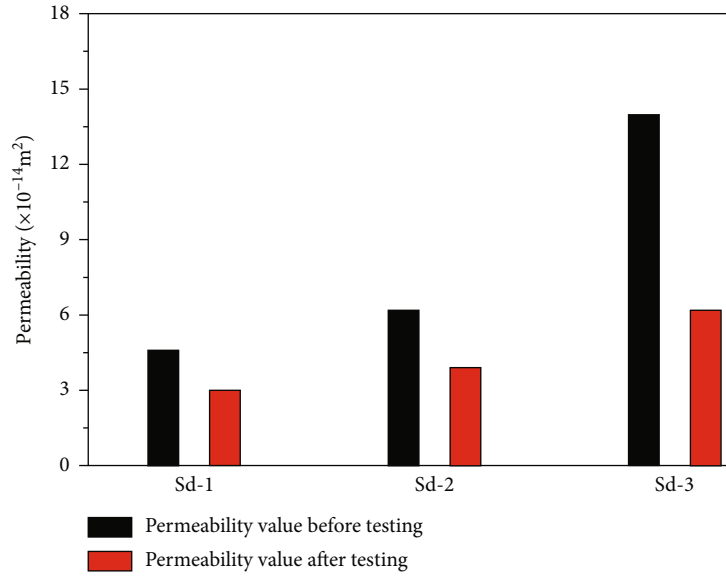


FIGURE 7: Permeability changes before and after testing under axial dynamic stress.

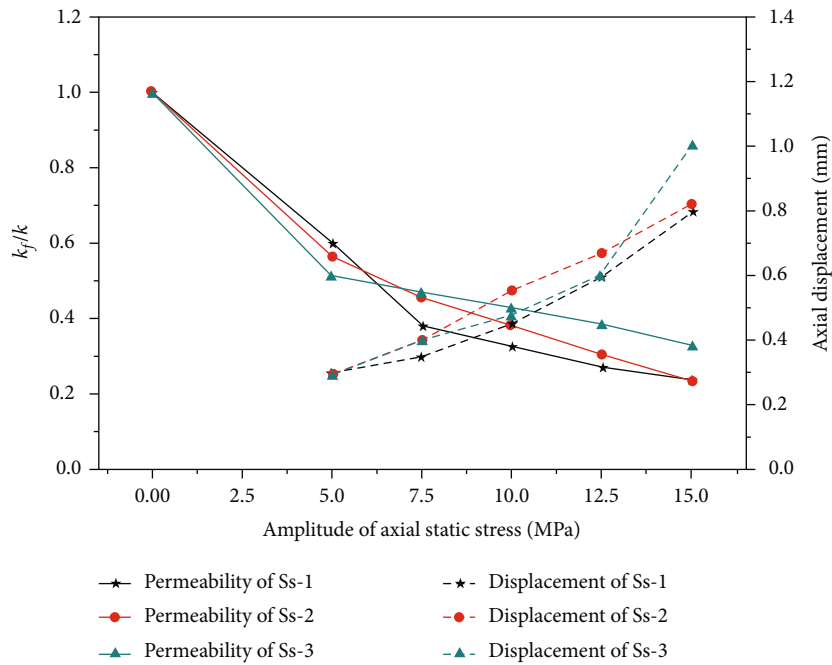


FIGURE 8: Permeability evolution and axial displacement of Ss-1, Ss-2, and Ss-3 under axial static stress.

2, and Sd-3 is larger than that of fracture surfaces of Ss-1, Ss-2, and Ss-3. This suggests that the permeability drops of fracture surfaces under dynamic stress are greater than those under static stress, and the asperity degradations under dynamic stress are larger than those under static stress. However, the weights of gouge materials on fracture surface after testing under axial dynamic stress are smaller than those under axial static stress, which is different from more gouge materials with larger asperity degradations. Overall, under the similar rough surface, the permeability decreases of fracture surfaces are easily caused by dynamic stress through

larger asperity degradations. But fewer gouge materials remain in fracture surfaces under dynamic stress conditions.

These observed responses can be summarized with a proposed conceptual model that considers permeability evolution modes of gouge material transport and flow mobilization, as shown in Figure 17. Figure 17(a) indicates that the gouge materials are more likely to stick to the fracture surface under static stress. When the forces increase, the compacted gouge materials will close the aperture, thus slowing down the rate of permeability reduction of the rock fracture (Figure 17(c)). However, the gouge materials migrate

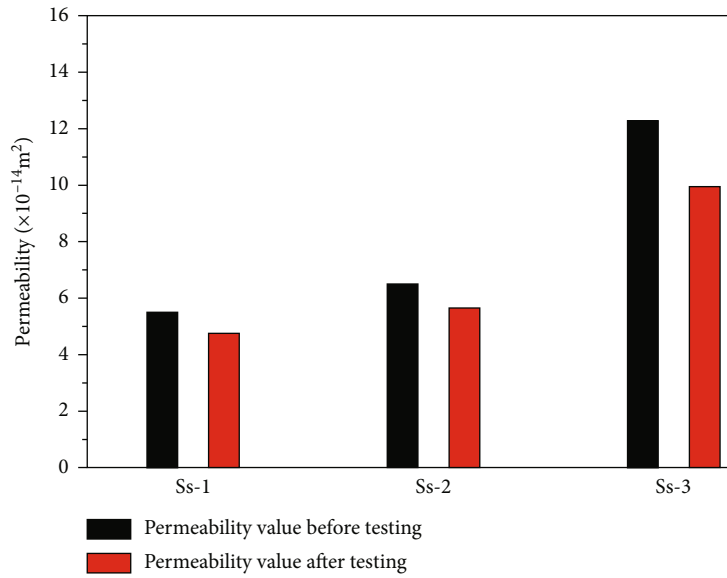


FIGURE 9: Permeability changes before and after testing under axial state stress.

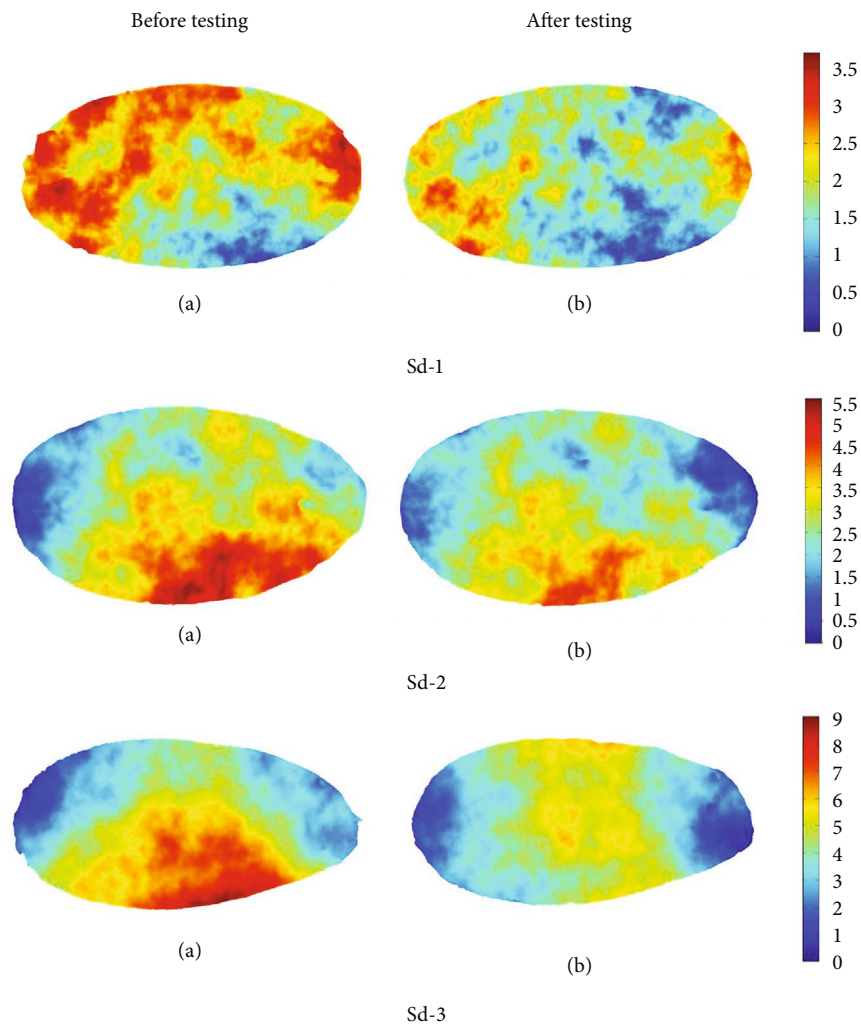


FIGURE 10: (a, b) Surface scans of samples Sd-1, Sd-2, and Sd-3 before and after testing under dynamic stress.

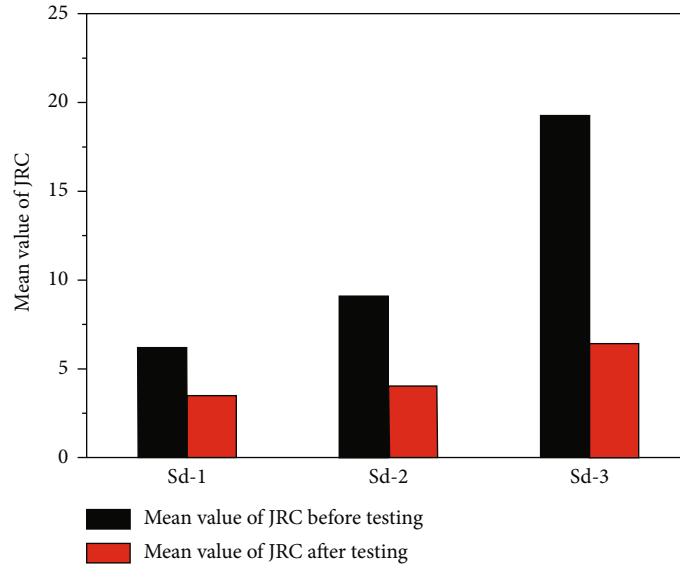


FIGURE 11: Mean value changes of JRC of samples Sd-1, Sd-2, and Sd-3 before and after testing under dynamic stress.

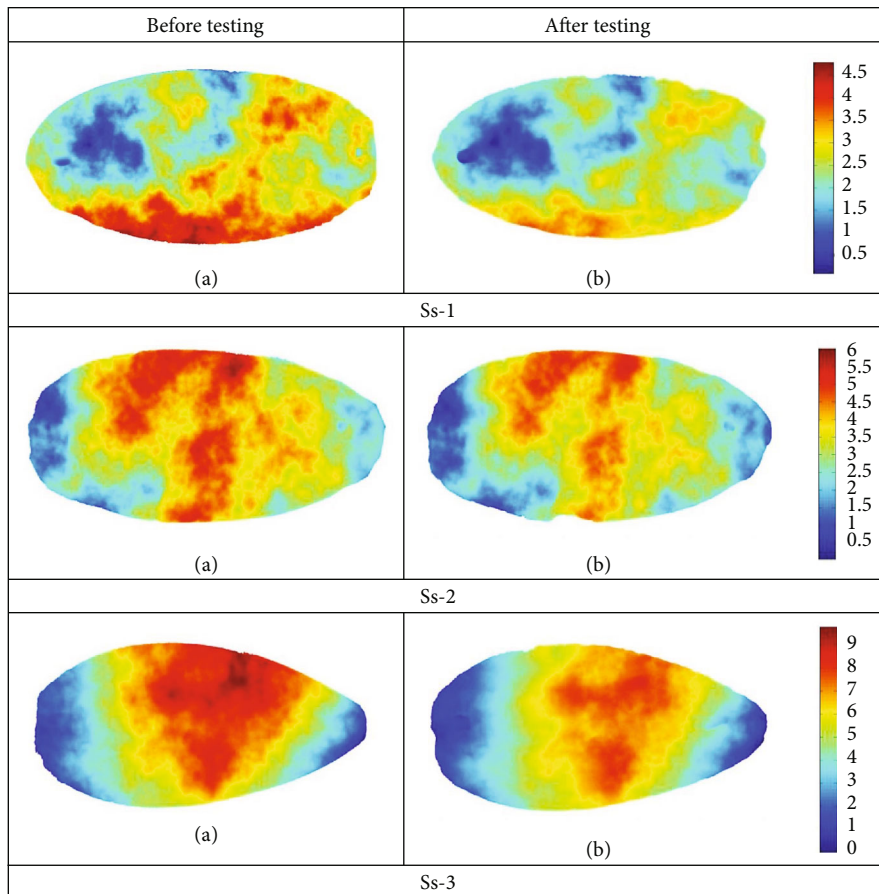


FIGURE 12: (a, b) Surface scans of samples Ss-1, Ss-2, and Ss-3 before and after testing under static stress.

gradually between fracture asperities (or the pore throats) under dynamic stress as described in Figure 17(b). During the amplitude of dynamic stress increasing, the gouge materials initially plugged between fracture asperities (or in the

pore throats) are flushed, producing the permeability drop enhancement under dynamic stress than static stress observed in our experiments (Figure 17(d)). Generally, when the rough fracture surfaces are crushed under more intensive

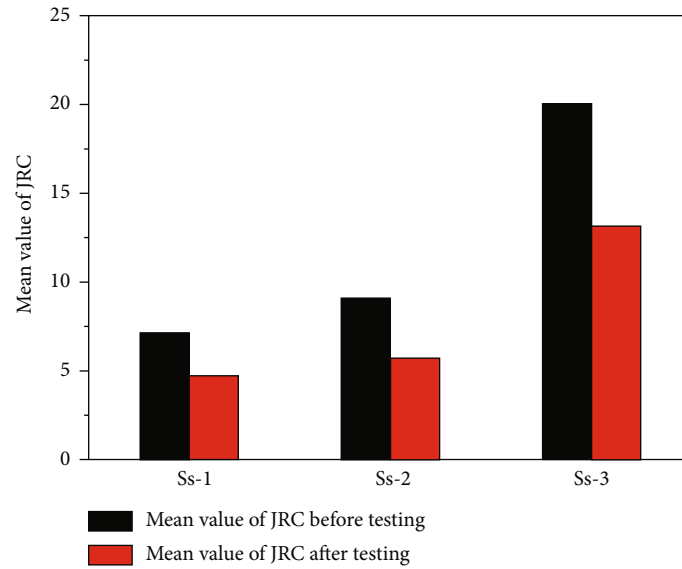


FIGURE 13: Mean value changes of JRC of samples Ss-1, Ss-2, and Ss-3 before and after testing under static stress.

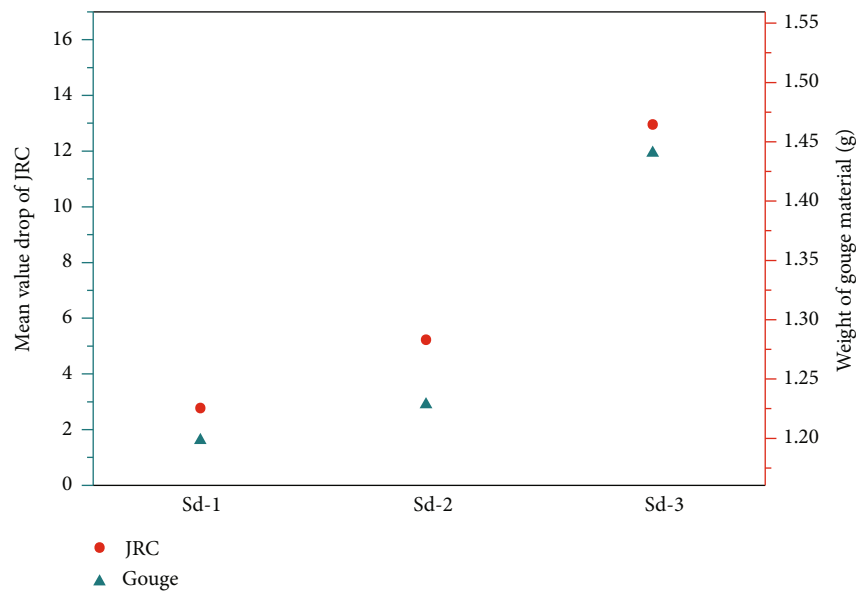


FIGURE 14: Mean value drop of JRC and weights of gouge material after testing under dynamic stress.

multiple dynamic impacts, the transport of gouge materials and the flow mobilization tend to occur during dynamic stress, causing the permeability drops of axial dynamic stress to be larger than those of axial static stress.

4. Conclusions

The permeability changes of nature rock fracture were investigated before and after testing under axial dynamic stress and static stress, so as to simulate the mechanisms of permeability changes of preexisting fractures via dynamic stress in fracture rock engineering. Six series of experiments under different amplitudes of cyclic axial forces and different axial static forces were conducted; the influence of surface rough-

ness was investigated by scanning the specimen surfaces before and after testing; and by which, gouge material transport and flow mobilization of rock fracture were analyzed. The main findings of this paper can be summarized as follows:

- (1) The axial displacements of Sd-1 and Sd-2 are lower than those of Sd-3 with dynamic stress, but the permeability of Sd-1 and Sd-2 is larger than that of Sd-3. In fact, the initial maximum and the mean value of JRC of fracture surfaces of Sd-1 and Sd-2 are smaller than those of Sd-3. This indicates that the roughness of fracture surface has a great influence on the permeability when the axial displacement is not enough to cause the fracture rock to slip

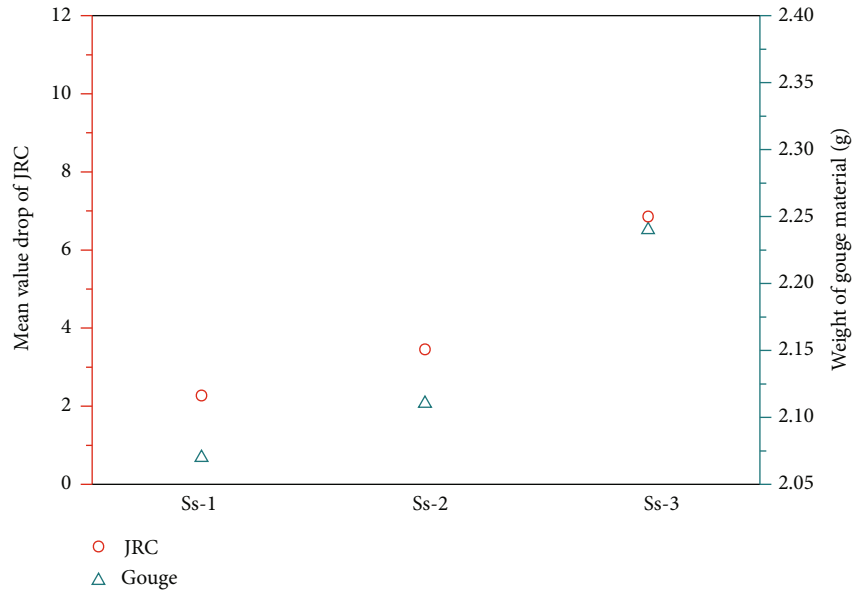


FIGURE 15: Mean value drop of JRC and weights of gouge material after testing under static stress.

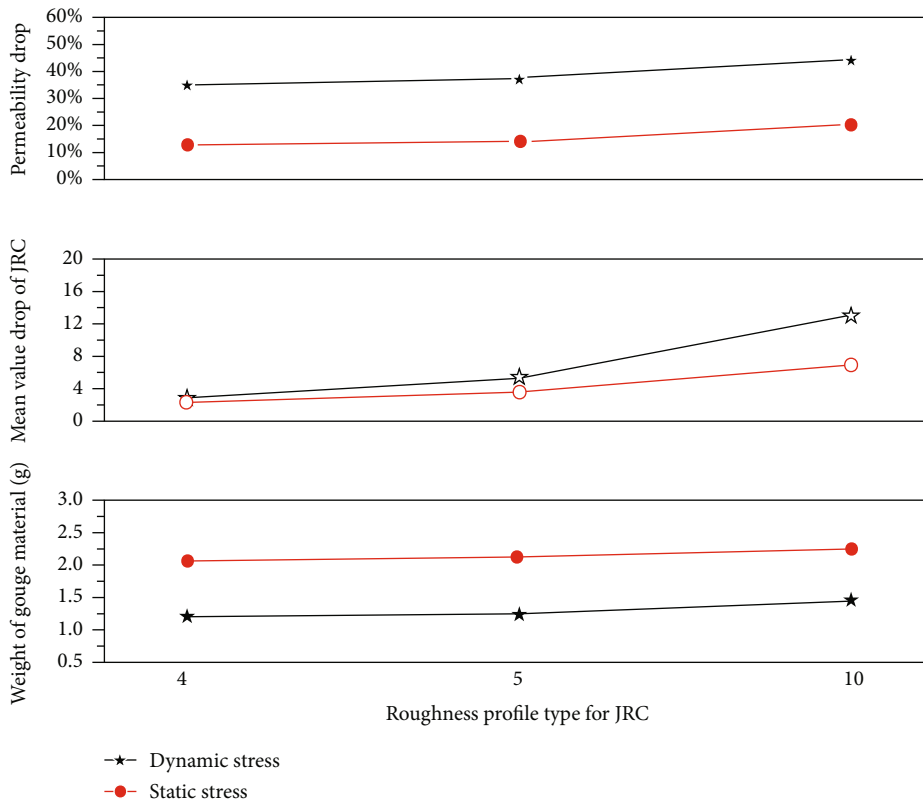


FIGURE 16: Comparing permeability drop, mean value drop of JRC, and weight of gouge material after testing under dynamic stress and static stress.

(2) The initial mean value drop of JRC of Sd-1 and Sd-2 is smaller than that of Sd-3 under dynamic stress, and the weights of fracture gouge produced of Sd-1 and Sd-2 are lower than those of Sd-3 during dynamic loading. This means that the larger

roughness fracture surface leads to larger surface damage as indicated by more gouge production. The accumulation of gouge materials on larger roughness fracture surfaces causes slow drops of permeability

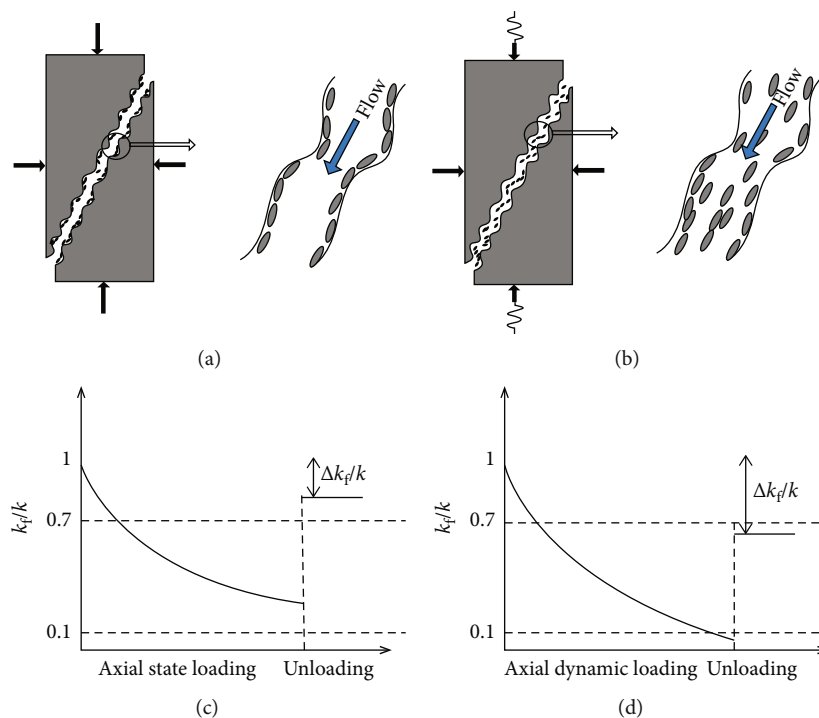


FIGURE 17: Permeability evolution modes of gouge material transport and flow mobilization. (a, b) Gouge material transport and flow mobilization under static stress and dynamic stress. (c, d) Permeability changes under static stress and dynamic stress.

(3) The permeability evolution modes considering gouge material transport and flow mobilization indicate that the gouge material transport and the flow mobilization tend to occur during dynamic stress. When the rough fracture surfaces are crushed under more intensive multiple dynamic impacts, the permeability drops of axial dynamic stress are larger than those of axial static stress. This interprets that the asperity degradations on fracture surface after testing under axial dynamic stress are larger than those under axial static stress. However, the weights of gouge materials on fracture surface after testing under axial dynamic stress are smaller than those under axial static stress

Data Availability

Data is included in the manuscript.

Conflicts of Interest

The authors declare that there is no conflict of interest regarding the publication of this paper.

Acknowledgments

This work was supported by the National Natural Science Foundation of China (41772313), Hunan Science and Technology Planning Project (No. 2019RS3001), and the Graduated Students' Research and Innovation Fund Project of Hunan Province (CX20190135 and 2019zzts079).

References

- [1] M. Manga, I. Beresnev, E. E. Brodsky et al., "Changes in permeability caused by transient stresses: field observations, experiments, and mechanisms," *Reviews of Geophysics*, vol. 50, no. 2, 2012.
- [2] Y. Liu, F. Dai, L. Dong, N. W. Xu, and P. Feng, "Experimental investigation on the fatigue mechanical properties of intermittently jointed rock models under cyclic uniaxial compression with different loading parameters," *Rock Mechanics and Rock Engineering*, vol. 51, no. 1, pp. 47–68, 2018.
- [3] W. Wu, J. S. Reece, Y. Gensterblum, and M. D. Zoback, "Permeability evolution of slowly slipping faults in shale reservoirs," *Geophysical Research Letters*, vol. 44, no. 22, pp. 11,368–11,375, 2017.
- [4] D. Vogler, F. Amann, P. Bayer, and D. Elsworth, "Permeability evolution in natural fractures subject to cyclic loading and gouge formation," *Rock Mechanics and Rock Engineering*, vol. 49, no. 9, pp. 3463–3479, 2016.
- [5] K. Peng, Y. Q. Wang, Q. Le Zou, Z. P. Liu, and J. H. Mou, "Effect of crack angles on energy characteristics of sandstones under a complex stress path," *Engineering Fracture Mechanics*, vol. 218, article 106577, 11 pages, 2019.
- [6] K. Peng, J. Zhou, Q. Zou, and F. Yan, "Deformation characteristics of sandstones during cyclic loading and unloading with varying lower limits of stress under different confining pressures," *International Journal of Fatigue*, vol. 127, pp. 82–100, 2019.
- [7] K. Peng, J. Q. Zhou, Q. Le Zou, and X. Song, "Effect of loading frequency on the deformation behaviours of sandstones subjected to cyclic loads and its underlying mechanism," *International Journal of Fatigue*, vol. 131, article 105349, 2020.

- [8] V. M. Shmonov, V. M. Vitovtova, and A. V. Zharikov, "Experimental study of seismic oscillation effect on rock permeability under high temperature and pressure," *International Journal of Rock Mechanics and Mining Sciences*, vol. 36, no. 3, pp. 405–412, 1999.
- [9] D. Ma, M. Rezaia, H. S. Yu, and H. B. Bai, "Variations of hydraulic properties of granular sandstones during water inrush: effect of small particle migration," *Engineering Geology*, vol. 217, pp. 61–70, 2017.
- [10] Z. L. Zhou, X. Cai, X. B. Li, W. Z. Cao, and X. M. Du, "Dynamic response and energy evolution of sandstone under coupled static–dynamic compression: insights from experimental study into deep rock engineering applications," *Rock Mechanics and Rock Engineering*, vol. 53, no. 3, pp. 1305–1331, 2020.
- [11] X. Cai, Z. Zhou, and X. Du, "Water-induced variations in dynamic behavior and failure characteristics of sandstone subjected to simulated geo-stress," *International Journal of Rock Mechanics and Mining Sciences*, vol. 130, article 104339, 2020.
- [12] W. G. Dang, H. Konietzky, L. F. Chang, and T. Frühwirth, "Velocity-frequency-amplitude-dependent frictional resistance of planar joints under dynamic normal load (DNL) conditions," *Tunnelling and Underground Space Technology*, vol. 79, pp. 27–34, 2018.
- [13] W. G. Dang, H. Konietzky, T. Frühwirth, and M. Herbst, "Cyclic frictional responses of planar joints under cyclic normal load conditions: laboratory tests and numerical simulations," *Rock Mechanics and Rock Engineering*, vol. 53, no. 1, pp. 337–364, 2020.
- [14] Z. Y. Song, H. Konietzky, and M. Herbst, "Bonded-particle model-based simulation of artificial rock subjected to cyclic loading," *Acta Geotechnica*, vol. 14, no. 4, pp. 955–971, 2019.
- [15] D. Ma, H. Y. Duan, X. B. Li, Z. H. Li, Z. L. Zhou, and T. Bin Li, "Effects of seepage-induced erosion on nonlinear hydraulic properties of broken red sandstones," *Tunnelling and Underground Space Technology*, vol. 91, article 102993, 2019.
- [16] D. Ma, J. Wang, X. Cai et al., "Effects of height/diameter ratio on failure and damage properties of granite under coupled bending and splitting deformation," *Engineering Fracture Mechanics*, vol. 220, article 106640, p. 106640, 2019.
- [17] D. Ma, J. J. Wang, and Z. H. Li, "Effect of particle erosion on mining-induced water inrush hazard of karst collapse pillar," *Environmental Science and Pollution Research*, vol. 26, no. 19, pp. 19719–19728, 2019.
- [18] W. G. Dang, W. Wu, H. Konietzky, and J. Y. Qian, "Effect of shear-induced aperture evolution on fluid flow in rock fractures," *Computers and Geotechnics*, vol. 114, article 103152, 2019.
- [19] Z. Y. Song, T. Frühwirth, and H. Konietzky, "Inhomogeneous mechanical behaviour of concrete subjected to monotonic and cyclic loading," *International Journal of Fatigue*, vol. 132, article 105383, 2020.
- [20] M. D. Zoback and J. D. Byerlee, "Permeability and effective stress: geologic notes," *AAPG Bulletin*, vol. 59, pp. 154–158, 1976.
- [21] K. Iwai, "Fundamental studies of fluid flow through a single fracture," *International Journal of Rock Mechanics and Mining Sciences, PhD Thesis*, University of California, Berkeley, 1976.
- [22] Y. W. Tsang and P. A. Witherspoon, "Hydromechanical behavior of a deformable rock fracture subject to normal stress," *Journal of Geophysical Research*, vol. 86, no. B10, pp. 9287–9298, 1981.
- [23] H. S. Lee and T. F. Cho, "Hydraulic characteristics of rough fractures in linear flow under normal and shear load," *Rock Mechanics and Rock Engineering*, vol. 35, no. 4, pp. 299–318, 2002.
- [24] B. Li, Y. J. Jiang, T. Koyama, L. R. Jing, and Y. Tanabashi, "Experimental study of the hydro-mechanical behavior of rock joints using a parallel-plate model containing contact areas and artificial fractures," *International Journal of Rock Mechanics and Mining Sciences*, vol. 45, no. 3, pp. 362–375, 2008.
- [25] Q. Yin, H. Jing, G. Ma, H. Su, and R. Liu, "Hydraulic properties of 3D rough-walled fractures during shearing: an experimental study," *Journal of Hydrology*, vol. 555, pp. 169–184, 2017.
- [26] Q. Yin, H. Jing, G. Ma, H. Su, and R. Liu, "Investigating the roles of included angle and loading condition on the critical hydraulic gradient of real rock fracture networks," *Rock Mechanics and Rock Engineering*, vol. 51, no. 10, pp. 3167–3177, 2018.
- [27] Y. L. Zhao, L. Y. Zhang, W. J. Wang, J. Z. Tang, H. Lin, and W. Wan, "Transient pulse test and morphological analysis of single rock fractures," *International Journal of Rock Mechanics and Mining Sciences*, vol. 91, pp. 139–154, 2017.
- [28] Y. T. Wang, X. P. Zhou, and M. M. Kou, "An improved coupled thermo-mechanic bond-based peridynamic model for cracking behaviors in brittle solids subjected to thermal shocks," *European Journal of Mechanics, A/Solids*, vol. 73, pp. 282–305, 2019.
- [29] S. Wang, X. Li, J. Yao et al., "Experimental investigation of rock breakage by a conical pick and its application to non-explosive mechanized mining in deep hard rock," *International Journal of Rock Mechanics and Mining Sciences*, vol. 122, article 104063, 2019.
- [30] M. M. Kou, X. R. Liu, S. D. Tang, and Y. T. Wang, "3-D X-ray computed tomography on failure characteristics of rock-like materials under coupled hydro-mechanical loading," *Theoretical and Applied Fracture Mechanics*, vol. 104, article 102396, 2019.
- [31] Z. Zhou, J. Zhang, X. Cai et al., "Permeability evolution of fractured rock subjected to cyclic axial load conditions," *Geofluids*, vol. 2020, Article ID 4342514, 12 pages, 2020.
- [32] E. E. Brodsky, "A mechanism for sustained groundwater pressure changes induced by distant earthquakes," *Journal of Geophysical Research*, vol. 108, no. B8, pp. 1–10, 2003.
- [33] J. E. Elkhoury, E. E. Brodsky, and D. C. Agnew, "Seismic waves increase permeability," *Nature*, vol. 441, no. 7097, pp. 1135–1138, 2006.
- [34] L. Xue, H.-B. Li, E. E. Brodsky et al., "Continuous permeability measurements record healing inside the Wenchuan Earthquake Fault Zone," *Science*, vol. 340, no. 6140, pp. 1555–1559, 2013.
- [35] Z. M. Shi and G. C. Wang, "Sustained groundwater level changes and permeability variation in a fault zone following the 12 May 2008, Mw7.9 Wenchuan earthquake," *Hydrological Processes*, vol. 29, no. 12, pp. 2659–2667, 2015.
- [36] I. Faoro, D. Elsworth, and C. Marone, "Permeability evolution during dynamic stressing of dual permeability media," *Journal of Geophysical Research: Solid Earth*, vol. 117, no. 1, pp. 1–10, 2012.
- [37] T. Candela, E. E. Brodsky, C. Marone, and D. Elsworth, "Laboratory evidence for particle mobilization as a mechanism for permeability enhancement via dynamic stressing," *Earth and Planetary Science Letters*, vol. 392, pp. 279–291, 2014.

- [38] R. Yan, G. C. Wang, and Z. M. Shi, "Sensitivity of hydraulic properties to dynamic strain within a fault damage zone," *Journal of Hydrology*, vol. 543, pp. 721–728, 2016.
- [39] Z. Shi, S. Zhang, R. Yan, and G. Wang, "Fault zone permeability decrease following large earthquakes in a hydrothermal system," *Geophysical Research Letters*, vol. 45, no. 3, pp. 1387–1394, 2018.
- [40] Y. Shi, X. Liao, D. Zhang, and C. P. Liu, "Seismic waves could decrease the permeability of the shallow crust," *Geophysical Research Letters*, vol. 46, no. 12, pp. 6371–6377, 2019.
- [41] W. Q. Liu and M. Manga, "Changes in permeability caused by dynamic stresses in fractured sandstone," *Geophysical Research Letters*, vol. 36, no. 20, pp. 2–5, 2009.
- [42] X. Cai, Z. Zhou, K. Liu, X. Du, and H. Zang, "water-weakening effects on the mechanical behavior of different rock types: phenomena and mechanisms," *Applied Sciences*, vol. 9, no. 20, p. 4450, 2019.
- [43] N. Barton, "Review of a new shear-strength criterion for rock joints," *Engineering Geology*, vol. 7, no. 4, pp. 287–332, 1973.
- [44] R. Tse and D. M. Cruden, "Estimating joint roughness coefficients," *International Journal of Rock Mechanics and Mining Sciences*, vol. 16, no. 5, pp. 303–307, 1979.
- [45] N. Huang, R. C. Liu, and Y. J. Jiang, "Numerical study of the geometrical and hydraulic characteristics of 3D self-affine rough fractures during shear," *Journal of Natural Gas Science and Engineering*, vol. 45, pp. 127–142, 2017.
- [46] Z. Ye and A. Ghassemi, "Injection-induced shear slip and permeability enhancement in granite fractures," *Journal of Geophysical Research: Solid Earth*, vol. 123, no. 10, pp. 9009–9032, 2018.
- [47] W. F. Brace, J. B. Walsh, and W. T. Frangos, "Permeability of granite under high pressure," *Journal of Geophysical Research*, vol. 73, no. 6, pp. 2225–2236, 1968.
- [48] H. C. Jang, J. Lee, and W. Lee, "Experimental apparatus and method to investigate permeability and porosity of shale matrix from Haenam Basin in Korea," *Environmental Earth Sciences*, vol. 74, no. 4, pp. 3333–3343, 2015.
- [49] Y. Fang, D. Elsworth, C. Wang, T. Ishibashi, and J. P. Fitts, "Frictional stability-permeability relationships for fractures in shales," *Journal of Geophysical Research*, vol. 122, no. 3, pp. 1760–1776, 2017.
- [50] H. Zhang, Z. Wan, Z. Feng, and J. Wu, "Shear-induced permeability evolution of sandstone fractures," *Geofluids*, vol. 2018, Article ID 2416481, 11 pages, 2018.